The Hong Kong Polytechnic University

Modelling and Simulation of Nano-surface Generation in Ultra-precision Machining

by

Cheung Chi Fai, BEng(Hons), MPhil.

A thesis submitted to The Hong Kong Polytechnic University in accordance with the regulations for the Degree of Doctor of Philosophy

Department of Manufacturing Engineering
The Hong Kong Polytechnic University
April 2000

MODELLING AND SIMULATION OF NANO-SURFACE GENERATION IN ULTRA-PRECISION MACHINING

by

Cheung Chi Fai, BEng(Hons), MPhil.

A thesis submitted to The Hong Kong Polytechnic University in accordance with the regulations for the Degree of Doctor of Philosophy

Members of the Board of Examiners (BOE):

_____

Professor T. P. Leung, Chairman of the BOE

_____

Professor W. B. Lee, Thesis Supervisor

_____

Professor P. A. McKeown, External Examiner

_____

Professor M. Masuda, External Examiner

Department of Manufacturing Engineering
The Hong Kong Polytechnic University

April 2000

Abstract of thesis entitled 'Modelling and Simulation of Nano-surface Generation in Ultra-precision Machining' submitted by Cheung Chi Fai
for the degree of Doctor of Philosophy
at The Hong Kong Polytechnic University in April, 2000.

In ultra-precision diamond turning, the quality of a machined surface that can be generated is important in assessing the performance of the machining system. This process of surface generation has attracted a lot of research interest. However, most of the work to date is based on empirical studies. Relatively little quantitative work has been reported. Although some attempts have been made in the development of machining models to simulate surface topography of a workpiece, most of them focused on the synthesis of surface topography from the data derived from interferometry or Scanning Electron Microscopy (SEM). Few deterministic models have been found to simulate the generation of surface topography based on machine kinematics, material science and cutting theories. The influences of crystallographic orientation and other properties of the work materials, and their interaction with the surface generation have been overlooked in most of the current models.

In this research, an investigation has been conducted into the factors affecting the surface generation in ultra-precision diamond turning. Experimental results indicate that the quality of a diamond turned surface is affected by both the process factors and material factors. The former involves cutting conditions like spindle speed, feed rate, tool geometry as well as the relative tool-work vibration due to machine vibration and spindle error motions. These process factors are related to the cutting geometry and the dynamic characteristics of the cutting system. The material factors considered are material anisotropy, swelling, and crystallographic orientation of the work materials. This study shows that the influence due to external factors like tool wear or machine chatter can be suppressed or even eliminated through a proper selection of operational settings and control of the dynamic characteristics of the machine. However, the influence of material factors would still persist even if cutting is performed under an optimal cutting condition.

In order to measure quantitatively the effect of material swelling and anisotropy on the surface generation, a Multi-spectrum Analysis Method has been adopted in the study. In this method, various features of a diamond turned surface are extracted and analyzed by the spectrum analysis of its surface roughness profiles measured at a finite number of radial sections of the diamond turned surface. It is found that the tool feed rate, the spindle rotational speed, the tool geometry, the material properties as well as the relative tool-work vibration are not the only dominant components contributing to the generation of surface roughness. The vibration induced by the variation of crystallographic orientation of the workpiece material is another major factor. Such a vibration can cause a significant variation in the frequency of surface modulation formed on the machined surface.

However, the multi-spectrum analysis method is incapable of determining the exact contribution of each factor upon the overall surface roughness. To overcome this shortcoming, a Multiple Data Dependent Systems (MDDS) analysis method is proposed. The metal cutting dynamics are characterized by the natural frequency, the damping ratio, and the relative contribution of the central wavelength components which make up the roughness profiles at a finite number of radial sections of a workpiece. Experimental results indicate that the cutting dynamics are dominated by the relative vibration between the tool and the workpiece, the spindle axial error motion and the swelling of the work materials. The contribution and the natural frequency of the tool-work vibration components are found to vary with the crystallographic orientation of the workpiece.

Based on the results of the experimental findings and the quantitative analysis, a 3-D surface topography simulation model for ultra-precision diamond turning is proposed. The model takes into account the effect of tool geometry, machining conditions and tool-workpiece vibration. It makes use of the surface roughness profiles predicted at a finite number of radial sections of the workpiece to construct the surface topography of a diamond turned surface. The model has been evaluated through a series of cutting experiments. Satisfactory results have been achieved in the prediction of surface roughness

parameters and the 3-D surface topography in diamond turning of polycrystalline aggregates.

A captioned model has been further developed to account for the influence of materials induced vibration in diamond turning of highly anisotropic single crystal materials. This leads to the establishment of a model-based simulation system. It is composed of several model-elements which include a microplasticity model, a dynamic model and an enhanced surface topography model. The microplasticity model is used for predicting the variation of micro-cutting forces with the changing crystallographic orientations of the workpiece during cutting. A dynamic model is built for determining the vibration induced by the variation of the cutting forces. The influence of this vibration on the surface roughness is estimated by an enhanced surface topography model. The system has been successfully implemented and evaluated through a series of cutting experiments. The simulation results are found to agree well with the experimental ones.

Ultra-precision diamond turning is an expensive process. Nowadays, the achievement of a super mirror finish in many current industrial applications still depends much on the experience and skills of the machine operator through an expensive trial and error approach when new materials or new machine tools are used. The successful development of the surface topography model and the model-based simulation system can help to identify the optimal cutting conditions for different work materials without the need for costly trial and error cutting tests. It also helps to find the best surface quality that can be achieved under particular dynamic conditions for a specific machine. Moreover, this is the first of its kind in which a deterministic model-based system has been successfully built which accounts for the effect of materials induced vibration in diamond turning anisotopic materials. This contributes significantly to the knowledge of ultra-precision machining and the further improvement of the performance of ultra-precision machines.

Acknowledgements

The author would like to express his sincere thanks to his academic supervisor, Professor W.B.Lee, Chair Professor of Manufacturing Engineering and Head of the Ultra-precision Machining Centre of The Hong Kong Polytechnic University, for his guidance, encouragement and support during the PhD. research project. The author also wishes to thank the Research Committee of The Hong Kong Polytechnic University for the award of a studentship and for financial support of the research work.

Many thanks are also due to Mr. T.W.Chung of the Ultra-precision Machining Centre who shared his invaluable experience and provided the technical support for the project.

Finally, the author would like to express his gratitude to his colleagues and friends within and outside The Hong Kong Polytechnic University for their kind encouragement and support during the course of the work.

TABLE OF CONTENTS

List of Figures

List of Tables

Chapter 1

Introduction

Ultra-precision diamond turning is one of the most important techniques for the manufacture of high precision components with a surface roughness of a few nanometres and with a tolerance which is in the submicrometer range (McKeown, 1987 and Ikawa et al., 1991a). Spherical and aspherical surfaces produced by this method can be of high quality without the need for any post-machining polishing. The machining accuracy is affected by a number of factors which include the performance of the machine tools (Bispink, 1992), the quality of the diamond tools (Masuda et al., 1989) and the properties of the workpiece materials (Sugano and Takeuchi, 1987). The superior surface finish is produced primarily by the transfer of the tool profile onto the workpiece. The quality of the surface roughness is governed by both the machine tool motion and the fidelity of the tool profile cutting the workpiece. The former is related to the machine accuracy and dynamic stiffness, the process parameters (e.g. cutting speed, feed rate, depth of cut, etc) and the machining environment, whereas the latter depends greatly on the properties of the work material being cut.

The surface roughness of a finished surface has attracted much research interest. This is due to the increasing demand in various industrial fields for better surface finish, as exemplified by surface characteristic improvement of magnetic disks for higher packing density or the reflection mirror for lasers in terms of longer life. A large amount of research and development has been done to design ultra-precision machine tools and the design methodology has been firmly established. As to the performance evaluation tests of ultra-precision machine tools, the effect of machine dynamics, in particular the fine vibration between the tool and the workpiece upon surface roughness has been analyzed by Takasu et al. (1985). The chipping and the wear of the diamond tool edge have been examined in the view of cutting capability by Nishiguchi et al. (1988). However, our understanding of the removal process at the micro to nano-scale and its relation to the surface generation mechanisms in ultra-precision machining is still far from complete.

Ultra-precision machining presents problems which are not encountered in conventional machining. The increase in specific cutting force as well as its periodic fluctuation has been reported by a number of researchers. It was found that the fluctuation in cutting forces depends very much on the crystallographic orientation of the slip systems of the grain, which is highly anisotropic with respect to both elastic and plastic properties. Zhou and Lee (1993) have successfully made use of the microplasticity theory to predict the variation of shear angle with the crystallographic orientation of work material and good results have been attained. However, the effect of such a variation on surface topography has not been explored deterministically by any researchers so far.

Although most of the ultra-precision machines available in the world markets are constructed to achieve extremely high loop stiffness, say several hundred N/μm, and can eliminate most of the vibration and the thermal expansion caused by the motion of machine parts, the vibration induced by the variation of the intrinsic properties of the workpiece material is an intrinsic part of the process and cannot be eliminated. As the depth of cut becomes finer, the influences of work material properties on the micro cutting mechanism can be decisive (Furukawa, 1988). In ultra-precision machining, the depth of cut is usually less than the average grain size of a polycrystalline aggregate. The variation of the work material properties due to the crystallographic nature of individual grain exerts great influence on the surface generation mechanism. Therefore, it cannot be treated as a continuous and homogeneous body as in the conventional analysis (Yuan et al., 1994) and should be treated as a series of single crystals which may have quite random orientations and are highly anisotropic in nature. It is difficult to predict the influences of material crystallography on the surface generation based on the current understanding of the theories of ultra-precision cutting.

Nowadays, ultra-precision metal cutting has satisfied many of the present industrial needs in the manufacture of optical, electronic and mechanical parts for use in advanced technology products. However, the mechanics of micromachining phenomena is still under development and the previous research work has only contributed a little to the establishment of predictable performance parameters. Most aspects of ultra-precision

machining still rely on empirical procedures and the technical skills of individual operators. Currently, the selection of optimum tool setting still relies on the trial cutting tests which are both time-consuming and costly. The choice of cutting parameters depends largely on the experience of the operator and empirical experimental results found in the literature. In practice, the optimal cutting conditions could easily drift due to the change in the machining environment and the materials being cut. Frequently re-calibrations are therefore needed to ensure a certain level of surface finish quality. There is a need to develop a deterministic model for the prediction and the optimization of surface quality under a wide range of cutting conditions.

With these circumstances in mind, the objectives of this research work are:

(i) To investigate into the factors affecting surface roughness in ultra-precision machining;

(ii) To develop analytical tools and methodologies for identifying, quantifying and hence measuring the effect of these factors on the roughness of a machined surface;

(iii) To explore the relationship between material properties (eg. material anisotropy, swelling and materials induced vibration) and the surface roughness parameters;

(iv) To develop a deterministic model for predicting the nano-surface generation and hence to establish a strategy for the selection of the optimal cutting conditions;

(v) To formulate a model-based simulation system for predicting the magnitude of materials induced vibration and its effect on the surface generation.

The research project is divided into two parts, i.e. Part I and Part II. Part I focuses on the experimental investigation of the various factors affecting the surface generation in ultra-precision diamond turning. Analytical tools and methodologies are developed for identifying and quantifying the effect of these factors on the surface quality. The

implications of the findings in the improvement of surface quality are also discussed. These form the basis for the establishment of a deterministic surface topography model and hence a model-based simulation system to account for the process and the material factors on the surface generation in Part II. The developed model together with the simulation system is further used in the evaluation and the optimization of diamond turning process.

The thesis is divided into nine chapters. The first Chapter is an introduction. Chapter 2 gives a literature review discussing the development of ultra-precision machining technology, the theory of cutting mechanics, the dynamic systems analysis, and the surface generation which forms the background of the study. Chapters 3, 4 and 5 constitute the first part of the research work. In Chapter 3, the experimental work and the results of an investigation into the factors affecting the surface generation are described. Chapter 4 presents the development of a Multi-spectrum Analysis Method to analyze the effect of swelling, plastic anisotropy and crystallographic orientation of the work material on surface generation in the diamond turning process. Based on this method, some proxy parameters are proposed to characterize the effect of material swelling and plastic anisotropy. Furthermore, the patterns of materials induced vibration and their significance are also discussed. The theoretical background, the experimental procedures and the results of a Multiple Data Dependent System (MDDS) analysis of the cutting dynamics are presented in Chapter 5. Chapters 6 and 7 cover the details of the modelling and the simulation of surface generation based on the findings in Part I and these constitute the second part of the research work. In Chapter 6, the emphasis is placed on the development of a surface topography simulation model to account for the process effects in diamond turning of polycrystalline materials. The details of the experimental verification and the use of the model for process optimization and machine capability evaluation are also discussed. The model forms the basis for the formulation of a model-based simulation system which takes into account both the process and the material effects on the surface generation. The theoretical basis, the system design and the experimental verification are discussed thoroughly in Chapter 7. Chapter 8 gives an overall conclusion of the research project. The recommendations for further work and the potential applications of the research results in the industry are highlighted in Chapter 9.

Chapter 2

Background to the Study

2.1 OVERVIEW OF THE DEVELOPMENT OF ULTRA-PRECISION MACHINING TECHNOLOGY

2.1.1 Ultra-precision diamond turning

Historically, ultra-precision machining had began to be investigated in the 1950's with the advent of demands in advanced science and technology for energy, computer, electronics and defense application. In the 1950's, Taylor & Hobson developed a numerically controlled, polar coordinate aspheric generating machine for the production of high quality camera lenses (Horne, 1981). At about the same time, Bell and Howell developed a cartesian coordinate machine using "a high speed diamond burr for generating the aspheric curve on a glass surface" (Evans, 1989). It must be noted that the pioneering work led by J.B. Bryan was carried out at Lawrence Livermore National Laboratory. In the 1970's, experimental work was carried out in its application to optical components of complex forms. With the accelerated development by the US Government weapons laboratories in the early 1970's, ultra-precision diamond turning became an indispensable tool for the economic production of high precision products (Ikawa et al., 1991a). Ultra-precision diamond turning is a machining process making use of a monocrystal diamond cutting tool which can possess nanometric edge radius, form reproducibility and wear resistance. Figure 2.1 depicts the process of diamond turning of aluminium alloy. The depth of cut being used is in the order of a micrometer or less. The process is capable of producing components with micrometer to sub-micrometer form accuracy and surface roughness in the nanometre range. Non-ferrous work materials like aluminium, copper alloy, silver, gold, electroless nickel and acrylic plastic workpiece can be directly machined to optical quality without the need for subsequent post-polishing. Some "infrared materials" such as silicon and germanium can also be finished to a surface roughness (R_t) of a few tens of nanometers (Nakasuji et al., 1990). Hundreds of ultra-precision components are continuing to grow in the fields of optics, ophthalmics, consumer

electronics, computers, communications, medicine, and aerospace. Traditional manufacturing industries such as automotive and diesel engine fabrication are also actively pursuing the development of lower cost ultra-precision components which in the future will necessitate fully automated ultra-precision machining systems.

The superior surface finish and form accuracy of ultra-precision diamond turning allows the technology to be widely adopted for the manufacturing of a variety of precision mechanical and optical parts. Applications are now seen in the manufacturing of inserts for injection-moulded plastic camera lenses, scanner mirrors, photoconductor drums in photo-copiers and substrates for memory disks, etc. More recent applications are for the manufacture of optical parts with complex forms like aspheric surfaces (Cheung et al., 1997, and Cheung and To, 1998). The use of the techniques for the manufacture of glancing incidence mirrors for X-ray telescopes is a particularly demanding example of non-conventional optics with the following accuracies: 0.2 μm p-v, axial form accuracy; 2 μm roundness accuracy on diameters up to 1.5 m; 5 nm rms roughness. (Wills-Moren et al., 1982, and McKeown et al., 1987). Figure 2.2 shows some examples of curved mirror being produced by diamond turning.

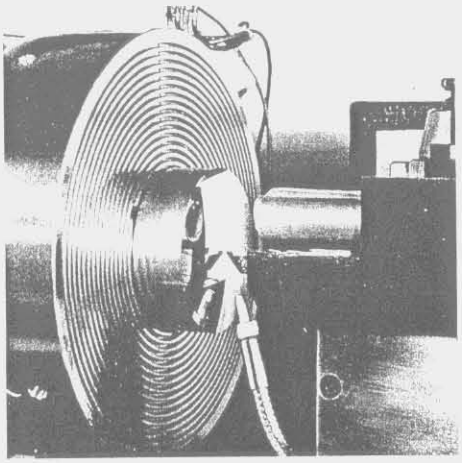

Figure 2.1 Ultra-precision diamond turning of aluminium alloy on a Nanoform 300 machine from Taylor Hobson Pneumo Co.

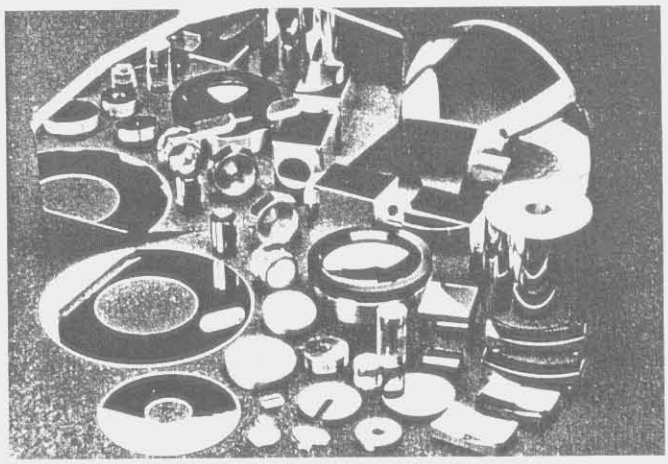

Figure 2.2 Examples of diamond turned workpiece (From Taylor Hobson Pneumo Co.)

2.1.2 Machine tools and controls

The success of ultra-precision machining technology relies on high precision machine tools, an advanced control system, laser metrology and single crystal diamond tools (Chiu et al., 1997). Improving spindle rotational accuracy, both axial and radial, the adoption of externally pressurised air bearing spindles (see Figure 2.3) played a dominant role through their ability to operate at submicron rotational accuracy. This kind of spindle has been proved to be effective in the reduction of vibrations and spindle error motions as well as in heat generation accompanying high speed rotation of spindles (Kobayashi et al., 1978).

In the field of ultra-precision machining, high accuracy of feed drive systems is necessary. Smallest depths of cut, smooth surfaces and minimal shape errors of complex parts are demanded. In order to satisfy these requirements, hydrostatic oil bearing guideways (see Figure 2.4) are used in many ultra-precision machines for reducing the static friction of the slide surface of the slides (Bryan, 1979a, and Donaldson and Patterson, 1983). For achieving nanometric resolution for linear motion and positioning of the feed drive systems, laser metrology is incorporated into the machine tool for feed and position controls at a resolution down to 1.25 nm (Kanai, 1983, Simokohbe, 1991, and Mckeown, 1998). In the case of machining complex component geometry, the performance of the feed drive system influences the quality of the workpiece to a considerable extent. Methods have been developed for the assessment of the performance of feed-drive systems in diamond turning, such as the ball-bar test and the circular test (Bryan et al., 1982, Knapp, W., 1983). Weck and Bispink (1991) have presented four different test methods which can be used to analyse the properties of high-precision feed drive systems. However, a pre-requisite for these procedures is expensive measurement and analysis equipment. Their applicability is therefore limited. Refining and simplifying these techniques for practical application in the industry is one of the on-going areas for improving the performance of feed drive systems in modern machines (Bispink, 1992).

For work alignment and tool setting, capacitance gages and LVDT (Linear Variable Differential Transformer) and photoelectronic sensors are usually employed for their high resolution down to subnanometer levels. High-speed, multi-axis CNC processor systems are also essential for efficient control, not only of servo drives in high precision position loop synchronism for contouring control, but also for thermal and geometrical error compensation (Figure 2.5), optimised tool setting (Figure 2.6) and direct entry of the equation of shape so as to avoid lengthy post-processing (McKeown et al., 1990).

In order to minimise thermal distortions and 'thermal drift' of the tool to the workpiece datum (Debra et al. 1986), it is essential to eliminate or minimise thermal inputs either externally or internally. This is achievable by a temperature controlled machining environment. The use of structural materials of low thermal expansion coefficient and high dimensional stability such as granite, super-Invar, synthetic granite/polymer concrete, ceramics and Zerodur is also a turn key solution (Willis-Moren, 1989). It is also essential to take special care in work-holding devices i.e., for stiff clamping with minimal distortion of the workpiece down to sub-micron values. The common techniques used include vacuum clamping or chucking (Figure 2.7), the use of intermediate fixtures, together with very precise dynamic balancing of the work spindle/chuck/workpiece system (Ikawa et al., 1991a).

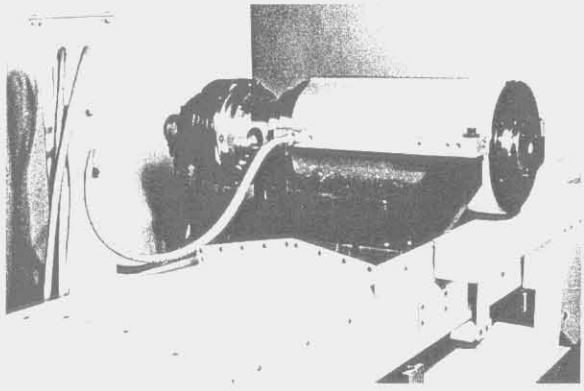

Figure 2.3 Air bearing spindle minimising the vibration and spindle error motions (From Ultra-precision Machining Centre of The Hong Kong Polytechnic University)

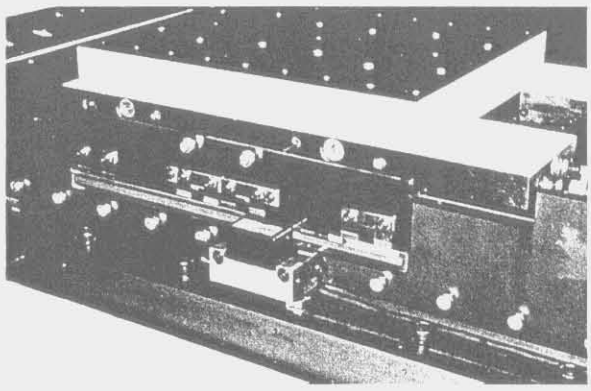

Figure 2.4 Hydrostatic oil-bearing guideway for reducing static friction of the bearing surface in the slide (Photo from Taylor Hobson Pneumo Co.)

2.1.3 Machining environment

The profile of a diamond turned surface is formed as a result of the motion of the tool edge in relation to the workpiece on a machine tool. The vibration control of the cutting system is of vital importance. In most designs of ultra-precision machines, the use of "air-mounts" (Figure 2.8) to support the machine base is often needed for preventing the vibration from the foundation. Some analyses of the undesired relative motion between the tool and workpiece reported that a few nanometer P-V amplitude seems to be the feasible limit of vibration control. There is a limit set by the current systems used for seismic vibration isolation. Vibration with small amplitude and low frequency (less than 10 Hz) is still inevitable even if the machine is housed on a specially constructed foundation. There are also problems set by imperfect coupling of machine components, e.g. spindle and their drive motors, eccentricity and manufacturing errors in machine components etc.

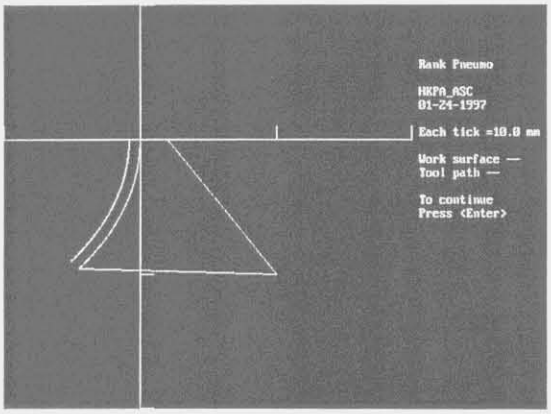

Figure 2.5 Tool path generation and error compensation (From aspheric generator of Taylor Hobson Pneumo Co.)

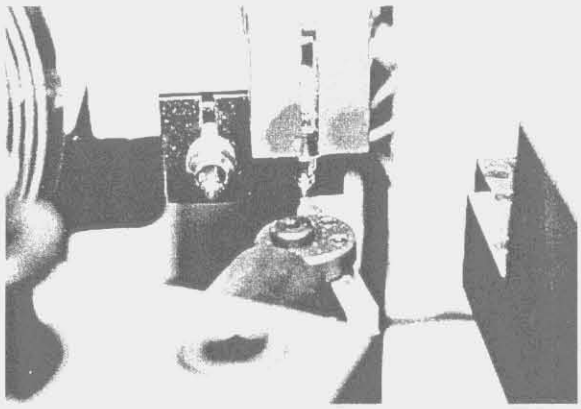

Figure 2.6 Linear Variable Differential Transformer (LVDT) Tool Probe for tool geometry determination (From Ultra-precision Machining Centre of The Hong Kong Polytechnic University)

Although vibration-free machining is ideal, this is difficult to realize economically or technically in industrial applications. Research (Takasu et al., 1985) has been attempted to optimize cutting conditions so as to improve the surface roughness under relative vibration between the tool and the workpiece. This direction seems to be more scientific and proactive for improving performance of the machining process than the preventive ones.

Other environmental controls like housing the machine in clean and temperature controlled rooms as well as the use of vacuum chip extractors for preventing the fine chips from scratching the surfaces. These are also found to be essential for improving the surface quality in diamond turning.

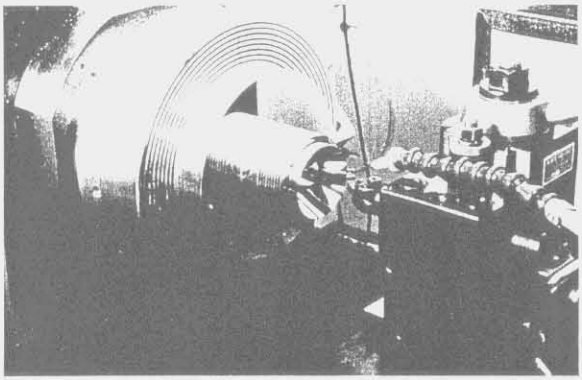

Figure 2.7 Vacuum chuck for workpiece holding (Photo from Taylor Hobson Pneumo Co.)

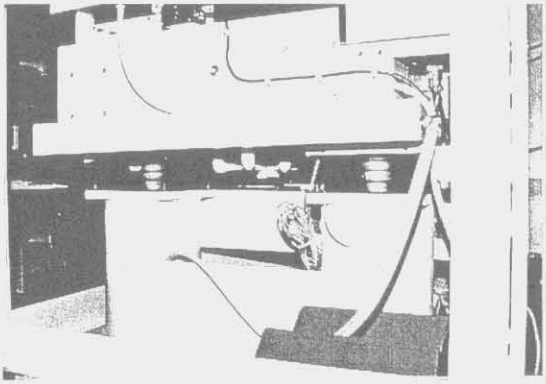

Figure 2.8 Vibration isolation foundation for absorbing environmental vibration (From Ultra-precision Machining Centre of The Hong Kong Polytechnic University)

2.1.4 Associated metrology

The success of ultra-precision machining technology not only relies on sophisticated machine design and control but also depends on its associated metrology. Knowledge of surface topography at nanometer and increasingly at the atomic scale is important in understanding the functional performance of that surface (McKeown, 1998). For nanometer level surface roughness and sub-micrometer level form accuracy, extremely high precision measuring instruments are needed to inspect the quality of the machined surfaces. A wide range of instruments has been developed for the metrology of surface topography. These instruments can be classified by their working principles into two main types which are the stylus type and the optical interferometric type.

2.1.4.1 Stylus type instrument

Stylus type instruments make use of the touch probing (i.e. the stylus) technique to capture the surface data from a work surface. Based on a very high resolution a Linear Variable Differential Transformer (LVDT) or Laser Interferometric sensor such as those used in Talysurf and Talystep, with a diamond probe with a tip radius of typically 1 μm can achieve a profile height resolution of 1 nm and approaching 0.2 nm. However, this type of instrument suffers from the potential risk of making scratch marks on the measured surface and limitations are imposed by the physical dimension of the stylus head. To overcome these shortcomings and for higher resolution, scanning probe microscopes such as the Scanning Tunnelling Microscope (STM) and the Atomic Force Microscope (AFM) have been developed which are capable of achieving atomic resolution (McKeown, 1998).

2.1.4.2 Optical interferometric instrument

The first optical interferometer system was developed by Albert A. Michelson during the period from 1852 to 1931. He exploited his knowledge of optics, and how interference fringes are formed by light waves interfering with each other. Modern electronics enables us to use optical interferometry for nano surface profile and roughness measurements. Figure 2.9 and Figure 2.10 show the interferometric plots of an ultra-precision diamond turned surface with submicrometer form accuracy and nanometer surface finish, respectively.

Interferometric techniques are limited by the amount of light which is reflected, or scattered off the test surface and returned through the microscope objective. Therefore, the performance is affected by the reflectivity of material of the test piece. For highly reflective material like aluminium, special filters are needed but are unnecessary for low reflective material like glass.

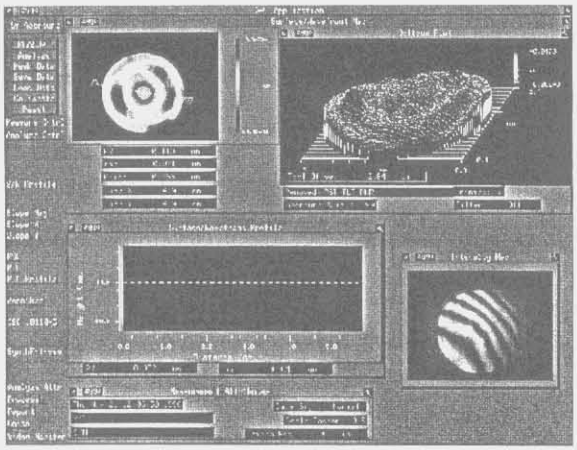

Figure 2.9 Form accuracy measurement using non-contact type laser interferometric profiler

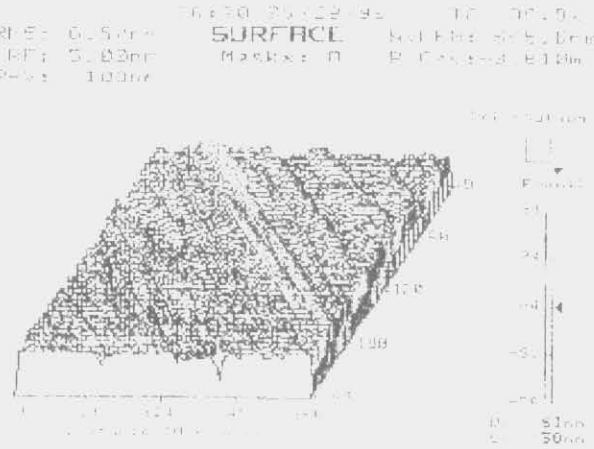

Figure 2.10 Surface roughness measurement using non-contact interferometric type microsurface measurement system

2.1.5 Single crystal diamond cutting tools

The cutting tool in ultra-precision diamond turning must possess nanometer edge radius and the capability of stable cutting in the submicron region for many kilometres length of cutting. Single crystal diamond tools are extensively used for their nanometric edge radius, form reproducibility and excellent wear resistance. Figure 2.11 shows a picture of some commercially available single crystal diamond cutting tools.

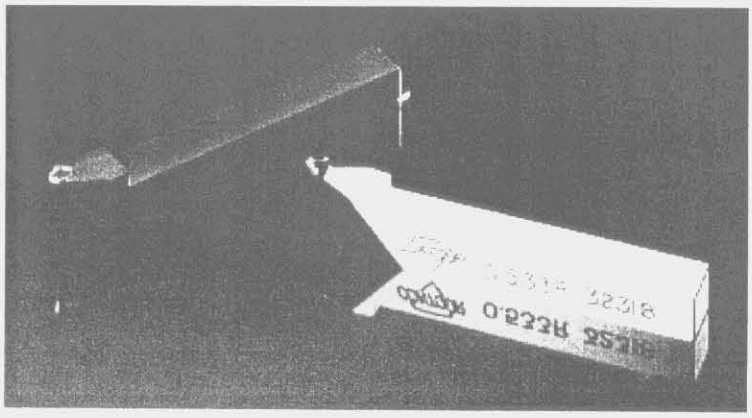

Figure 2.11 Single crystal diamond cutting tools (From Contour Fine Tooling)

The fabrication of diamond tools has, in the past, relied very much on empirical procedures. More scientific effort is now being put in the qualification of diamonds at the

raw material stages (Yuan et al., 1992) for selection of orientation, diamond polishing and analysis of wear mechanisms, etc. Several investigations have been reported on the qualification of diamonds, intended for prolonging the tool life by means of optical scattering, infrared absorption, electron spin resonance, etc. Each of these techniques reflects the existence of several types of defect in the diamonds (Wilks et al., 1978, 1980, and Shimada et al., 1989). These scientific analyses and evaluation of diamond is of primary importance for producing more predictable and reliable tools to meet future needs.

There are two types of damage in diamond tools, namely cutting edge chipping and chemical-abrasive wear. Cutting edge chipping takes place when the stress level in a tool edge exceeds the strength of the diamond at a specific location. Progressive wear occurs on both flank and rake faces on a submicron scale over a cutting distance of normally up to several hundreds of kilometres. Some experimental work (Komanduri et al., 1975, and Evans, C., 1991) highlighted the fact that thermal effects play an essential role in tool wear. The diffusion wear problem in diamond turning of ferrous materials limits the application of the technology to the manufacturing of precision steel moulds. The diffusion wear of a diamond tool is caused by the chemical affinity of the diamond with carbon in the steel being machined. Some research has done on the cutting of steel in a carbon-saturated atmosphere (Casstevens, 1983). However, this is not cost effective in industrial uses. A more interesting and practical ways forward can be seen in the ultra-precision machining of stainless steel by ultrasonic vibration cutting (Moriwaki et al., 1991).

2.1.6 Work materials

The material removal process is not only governed by the cutting tool but also by the work materials. Work materials must be chosen to give an acceptable machinability on which nanometric surface finish can be achieved. At present, typical work materials used in diamond turning can be classified into four main types which include ductile materials like copper and aluminium; brittle materials like silicon and germanium; single crystal materials like KDP and amorphous materials like electroless nickel and PMMA. Although

there has been some research work in the machinability of special materials like SiCw/Al composites (Yuan et al., 1993) and Al/SiC_p composites (Chan et al., 2000 and Cheung et al., 2000), these materials are not commonly used in industry.

2.1.6.1 Ductile materials

Ductile materials like aluminium and copper are the most common type of work materials used in diamond turning. Applications are found in the manufacture of VCR cylinders, optical quality reflectors and mould inserts for injection moulding of plastic lenses (see Figure 2.12 and Figure 2.13). The theoretical basis for the diamond turning of ductile materials is better established than that for the other types of materials, especially for polycrystalline materials. The machinability of these materials has been investigated by a number researchers (Sugano et al., 1987, Moriwaki and Okuda, 1989, Masuda et al., 1989, and Furukawa and Moronuki, 1988). Sugano et al. (1987) carried out an investigation of the residual stress on diamond turned aluminium alloy. They reported that the effect of the slip in crystals on surface roughness must be considered in diamond turning. Besides, the magnitude of the residual stress on the work surface was found to depend on the nose radius of the cutting tools and the feed rate, but the effect of depth of cut is small. Moriwaki and Okuda (1989) have made a comprehensive investigation into the machinability of copper and they found that there exists an optimum feed rate at which surface roughness becomes the minimal and continuous chips can be formed at nominal depths of cut from 3 μm to 0.0025 μm. Shear front-lamellar structures at the top of the chip have been reported to correlate with grain orientations (Black, 1972, and von Turkovich and Black, 1971). The variation of shear angles with crystallographic orientations of the work materials has been studied based on the experimental observations of chip formation (Ueda and Iwata, 1980). However, relatively little research work has been done on the effect of the crystallographic orientation on the diamond cutting process from the viewpoint of microplasticity. Nevertheless, most of this research focused on empirical experimental work and comparatively few quantitative analyses have been reported in the literature.

2.1.6.2 Brittle materials

During the past two decades, mirror finishing of brittle materials has been an important research topic in diamond turning. Brittle materials like glass and silicon have been widely used for a variety of devices which are incorporated into electronic, optical and some laser optical products. It is well known that in the general terms, the cutting of brittle materials is performed by brittle fracture. Plastic chip formation is only feasible at an extremely small depth of cut, so-called the "critical depth of cut". In other words, the material removal mechanism may change from brittle fracture to plastic deformation when an extremely small amount of material is removed. Some research work has studied in studying the diamond turning of brittle materials (Syn et al., 1988, and Nakasuji et al., 1990). Their findings show that the brittle-ductile transition depends on the material properties, magnitude of the applied force and volume of material to be removed. On the other hand, brittle-ductile transition was also found to depend on the crystallographic orientation in single crystals since the resolved stresses on the cleavage plane and on the slip plane vary with their orientations. Variation of localised surface finish always appears when the cutting direction relative to the crystal orientation varies successively in face turning. Nakasuji et al. (1990) has established a criterion for determining the critical thickness of cut at which the brittle-ductile transition occurs.

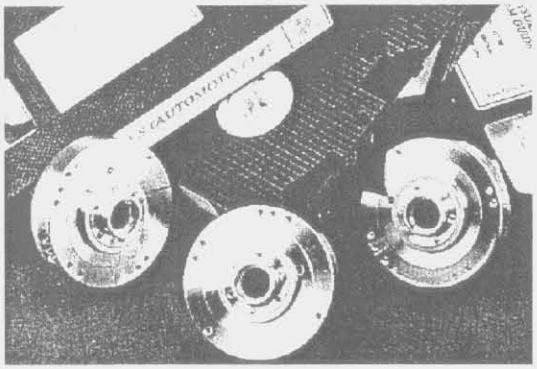

Figure 2.12 VCR cylinders (Photo from Taylor Hobson Pneumo Co.)

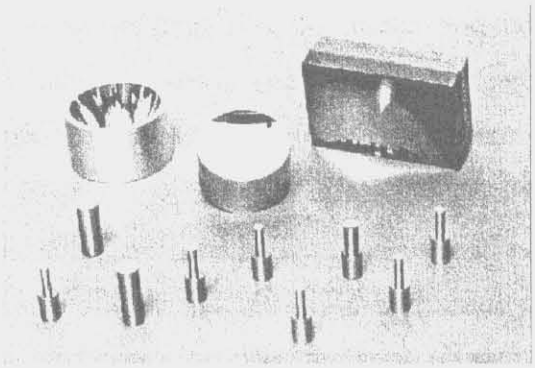

Figure 2.13 Reflectors and mould inserts

Ductile machining of brittle materials is now recognised as an emerging technology with important applications. By keeping the depth of cut and the feed rate below certain critical values, the transition from brittle fracture to plastic flow occurs (Nakasuji et al., 1991 and Puttick et al., 1989). However, it is difficult to keep the depth of cut and the feed rate stable at an extremely low level over a wide range of cutting regions even with ultra-precision machine tools. Some attempts (Hara, 1990, and Kim and Kim, 1998) have been made to develope micro-feed devices for precise control of the depth of cut so as to achieve ductile mode chip removal in diamond turning brittle material. It should be noted that the pioneering work in the development of micro-feed devices was first done at Cranfield Unit for Precision Engineering (CUPE) of Cranfield University in 1987/89. The use of ultrasonic vibration (Moriwaki, 1992) is another ongoing research area for achieving ductile machining of brittle materials.

2.1.6.3 Single crystal materials

Although diamond turning of polycrystalline aggregates which are considerably more usual than the single crystals, there will inevitably be the use of single crystal materials for some special applications. Examples include the use of single crystal KDP material in laser system and single crystal silicon for high precision infrared optical system. Single crystal materials are known to be highly anisotropic in their physical and mechanical properties. The local variation of machinability due to variation of the crystallographic orientation induces a local variation in the surface qualities (Nakasuji, 1990). The fluctuation of micro-cutting forces with crystallographic orientation has also been reported by a number researchers (Lee, 1990 and Yuan et al., 1994). However, our technological know-how on the machinability of single crystal material is still far from perfect. Although some research work (Zhang, 1991) has been found on studying the machinability of single crystal materials and their effect on surface quality in ultra-precision diamond turning, most of these works were focused on qualitative analysis (Nakasuji et al., 1990). Only limited quantitative works have been reported (Lee and Zhou, 1993).

2.1.6.4 Amorphous materials

Amorphous metals like electroless nickel and Fe-based amorphous alloy (METGLAS 2605S-2) have been found to possess a structure which consists of random aggregation of atoms, and they exhibit interesting and distinctive characteristics when compared to crystalline materials. Because of the superior magnetic, electrical and mechanical properties of amorphous metals, they have been attracting much attention as an advanced material for micromachining (Kanji and Keiji, 1992, and Ueda and Manade, 1992). Although there has been much discussion in the literature on the mechanical properties of amorphous metals in tension, bending and indentation, etc (Gilman, 1975, Leamy et al., 1972, and Masumoto and Maddin, 1971), little investigation on the cutting of these materials has been found.

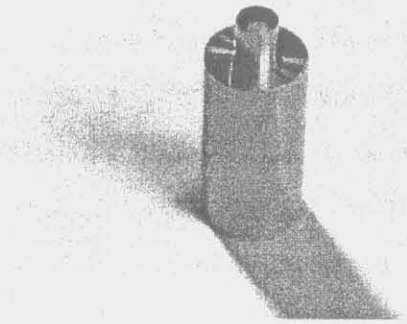

Figure 2.14 Electroless nickel plated mould insert for contact lenses manufacturing

Figure 2.15 Prototype plastic lenses directly made by diamond turning

The amorphous metals have neither slip systems nor lattice defects, such as dislocations, grain boundaries, stacking faults, etc. Accordingly, they exhibit isotropic homogeneous behaviour with no obvious strain hardening, and are thus adequate to simulate plastic deformation in the cutting processes. These properties minimise or even eliminate the localised variation of machinability encountered in diamond turning. Some research work has been found on the diamond turning of nickel plated steel substrate for precision mould making (Figure 2.14). On the other hand, it was on amorphous

(electroplated) copper that Ikawa et al. (1991a) demonstrated undeformed chip thickness of one nanometer.

Currently, ultra-precision diamond turning is widely used in the manufacturing of prototype plastic lenses of variety shapes (Figure 2.15) made of acrylic (PMMA). Experimental results showed that PMMA gives random and little variation of dynamic cutting forces as well as continuous chip formation during cutting (Furukawa and Moronuki, 1988). This is highly preferable in ultra-precision diamond turning. The amorphous and ductile properties of PMMA allow it to be directly diamond turned to optical quality without the need for additional polishing (Cheung, 1998).

2.2 THEORY OF CUTTING MECHANICS IN ULTRA-PRECISION DIAMOND TURNING

The shaping of components by machining represents a mature technology that dates back to the eighteenth century. There have been many improvements in machines, cutting tools and materials that have led to significant benefits (Moon, 1998). In the conventional cutting process, most of the deformation occurs in the metal layer which is cut into chips, while the deformation below the machined surface is of a lesser degree. However, the cutting mechanisms in single point diamond turning (SPDT) are quite different from ordinary turning. (Zhang, 1991). In diamond turning, the deformation below the machined surface is very important. This is because, in diamond turning, the undeformed chip thickness is very small, while the deformation caused by the compression and friction between the tool and the machined surface plays a significant role in the cutting process (Zhang, 1991). With small depth of cut and feed, cutting naturally becomes of a single-crystal nature. Therefore the cutting behaviour and mechanism of chip formation depend on crystallographic factors such as the orientation, the slip system and the dislocation that occurs. However, the material factors have received relatively little attention in the research on the mechanism of single point diamond turning.

2.2.1 Mechanism of plastic deformation

Plastic deformation of metals in metal cutting can be explored from different length scales, i.e. angstrom or atomic particle scale (10^{-9} to 10^{-8} m), microstructure scale and macroscopic continuum scale. A comprehensive discussion on the plasticity mechanisms and representations in different length scales was given by Drucker (1984 and 1985). The macroscopic theory of plastic deformation in a polycrystalline metal is based on the observations of the behaviour of the metal in bulk. The theory so constructed is found to be adequate as a first approximation when applied to many problems in engineering and metal-cutting technology.

However, the depth of cut in ultra-precision machining is usually less than the average grain size of a polycrystalline aggregate. As cutting is performed within a grain, the mechanics of the cutting problem in such a micro-region of the crystal should be investigated using a micro-structural scale (Yang and Lee, 1993). The studies of the effect of large deformations on a micro-structural scale form the bulk of so-called microplasticity, which contains four different length scales, namely the scale of dislocation, continuous slip, sub-grain structure and grain. A metal can be deformed by dislocation slip, mechanical twinning, grain boundary sliding as well as phase transformation. As the dislocation slip and mechanical twinning are more related to metal cutting, they will be discussed in greater detail.

Dislocation slip occurs when metals are deformed by a crystallographic slip process in which blocks of crystals slide over one another along definite crystallographic planes. A dislocation is a linear lattice defect which provides the mechanism for the crystallographic slip. The concept of the dislocation was proposed independently by Orowan, Polanyi and Taylor (Honeycombe, 1984) to explain the micro-mechanics of slip. They proposed essentially the same crystal defect known as an 'edge' dislocation for which the displacement vector is perpendicular to the dislocation line. Taylor's (1934) dislocation model shows that slip is accomplished by the glide of the dislocation across the slip plane one lattice spacing at a time. The result is to displace the material on either side of the

plane by the unit lattice spacing. Taylor argued that the shear stress required to cause incremental dislocation motion would be very low and thus propagation of such defects would result in shear strengths consistent with those observed. Studies on the motion and the velocity of dislocation were later quantitatively performed by Nabarro (1947), Frank (1949) and Eshelby (1949). The application of dislocation theory to the study of chip formation mechanism began in 1950's (Shaw, 1950). Since then, much research work has been done on investigating the shear slip process in metal cutting based on dislocation theory (Ramalingam, 1970, von Turkovich, 1970, and Black, 1971). However, it must be emphasised that the shear band observed in metal cutting is of macroscopic nature and the shear band may not be parallel to a particular crystallographic slip plane of the crystal. However, the shear in the band has to be accomplished by homogeneously distributed slip i.e. operative slip systems co-operate in the shear band development. Figure 2.16 shows a SEM micrograph of the shear zone formation in a copper single crystal when cutting is performed along a [001] direction on a (230) plane.

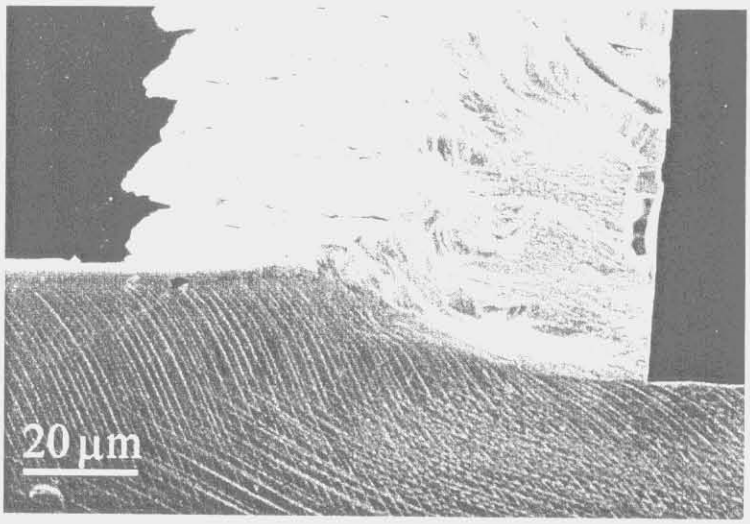

Figure 2.16 A SEM micrograph of the shear zone formation in a copper single crystal when cutting is performed along a [001] direction on a (230) plane. (From Lee and Zhou, 1993)

Twinning is another mechanism of plastic deformation, particularly when straining is carried out at low temperatures or at high speeds (Hall, 1954 and Hertzberg, 1983). This has been observed in faced-centred-cubic (FCC) metals especially in low-stacking fault energy metals (Duggan et al., 1978). In FCC metals, there are twelve deformation twinning

systems of (111)[112] type. Similar to slip, twinning enables a crystal to undergo a permanent change of shape with a negligible change in volume. Unlike slip, twinning involves the shearing of part of a crystal by a fixed magnitude, characteristic of the crystal structure. This may accomplish an extensive change in shape or may bring potential slip system planes into a more favourable position for slip. Twinning is a movement of planes of atoms in the lattice parallel to a specific plane so that the lattice is divided into two symmetrical parts which are differently orientated. The amount of movement of each plane of atoms in the twinned region is proportional to its distance from the twinning plane, so that a mirror image is formed across the twin plane. The formation of twinning is affected not only by the crystal structure but also by the deformation conditions. The critical stress of twinning is much greater than that of slip. Therefore, the twinning can be produced only in the case that slip is exhausted.

2.2.2 Chip formation

The limits to further improvement in ultra-precision machining are governed by a host of interrelated processing details and by the ability to measure accurately their effects. In particular, a basic understanding of the material removal process at the tip of the cutting tool is needed. In conventional machining, chip formation has been studied by a number of researchers (Childs and Mahdi, 1989, Nakayama and Arai, 1992, and Shaw, 1993) and various chip formation models have been proposed. Early works (Albrecht, 1961) can be found on the development of analytical models for the chip formation processes based on the combined effect of shear and bending stresses in the shear zone. Albrecht, (1962) conducted an investigation of the periodic patterns in segmented chips. Ostafiev et al. (1994) has developed a chip formation model which has proposed trapezium shaped lamellar structure formation process. This model has described chip curve, its contact length and contact load distribution taking into account both the plastic and elastic chip deformations. More recently, Xie et al. (1998) have made use of finite element analysis (FEA) to model and simulate the chip formation and the shear localisation phenomenon in the metal cutting process.

In ultra-precision machining, there are some differences in the chip formation mechanisms. The cutting process leads to a multiplication of defects and is affected by the imperfections which exist in a material. During cutting, the work material under the shear zone is subject to a large compression deformation exerted by the cutting tool. This will cause the atomic arrangement and distribution of defects in the metal to be distorted and hence lead to a multiplication of dislocations. The zone of the workpiece material in contact with the tool tip acts as a strong source of dislocations (Iwata et al., 1984). Fine cracks are produced near the vicinity of the tool tip and trigger the primary shearing process. Large numbers of dislocations are moved due to the compression loading ahead of the tool toward the free surface. As the tool advances, the material ahead of it is compressed in the cutting direction and a shear band joining the tool to the surface of the work material develops and hence the chip forms (Yuan, 1994).

Zhang (1991) has reported continuous chip formation and lamellar slip structure at the shear zone in machining pure metals at sufficiently small depth of cut compatible to the grain size. This shows that the shear slip leads to the formation of the lamellar structure of the chip. Similar results have been obtained by To et al. (1997) on diamond turning of aluminium single crystals with various crystallographic orientations. It was also found that continuous chip formation occurred under all cutting conditions. Lamella structure was observed on the free surface of all the chips examined, which was indicative of the highly inhomogeneous strain distribution in the chip. The surface underneath that was in contact with the tool was found to be much smoother and possessed long scratch marks on it similar to those found on a freshly machined surface (Figure 2.17). Considerable variations in the chip thickness were also noted. These provided significant evidence that the shear angle varies with the variations of crystallographic orientations.

It has been experimentally confirmed that very fine chips of order of 1 nm can be removed in diamond turning of free machining materials (Ikawa et al., 1988 and Ikawa et al., 1991a). This fact proves that nanometric metal cutting is feasible. There is a need to analyse the chip removal mechanism and surface generation processes on the atomistic or molecular scale. Molecular dynamics analysis is a branch of mechanics that attempts to

analyse the behaviour of an atomistic solid model from an atomistic point of view (Shimada. et al., 1992). The progressive motion including lattice vibration of individual atoms, which compose the model, can be traced by solving sequentially the differential equations of motion of the atoms. Based on molecular dynamics analysis, several kinds of computer simulations of nano-cutting have been developed (Inamura et al., 1990 and Stowers et al., 1991). These computer simulation techniques can be useful for understanding the nano-cutting process under nanometric uncut chip thickness. However, molecular dynamics analysis suffered from the inevitable difficulties in the analysis under large uncut chip thickness due to various limitations in the computation technology. Despite its limitations in a number of applications, it may in time give very useful information, especially when cutting experiments are extremely difficult to perform on the nanoscale (Ikawa, 1991).

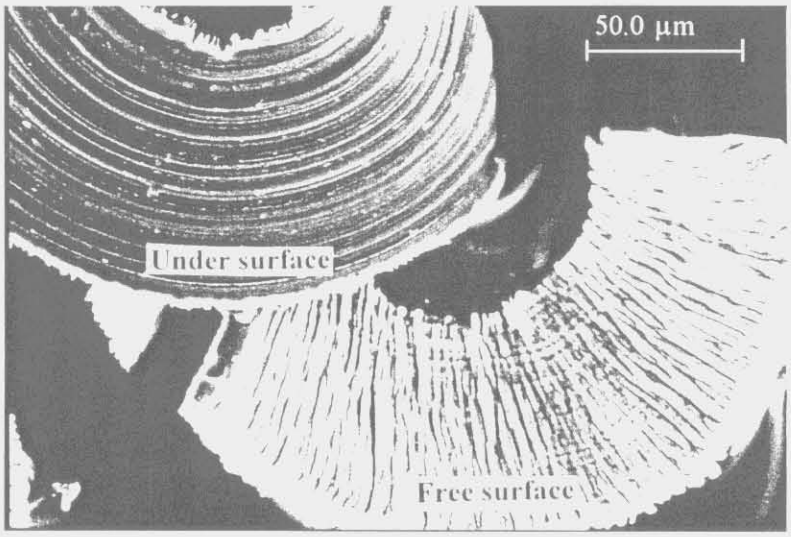

Figure 2.17 Lamella structure at the under surface and the free cutting surface of the chip (From Lee et al. 1999)

2.2.3 Cutting force and cutting model

Cutting force in diamond turning is usually of the order of sub-Newton or less which is of the same order as a single abrasive grain in grinding. Usually the cutting force in diamond turning is very difficult to measure accurately due to its small magnitude as

compared to the noise signal. During the last decades, much research work has been attempted to develop accurate tool force models for measuring the cutting force in diamond turning (Dresher and Dow, 1990). Kim, D.J. and Kim. D.S., (1995) have proposed a Round-Edge Cutting Model (RECM) for explaining the effect of plowing due to the tool edge radius on the characteristics of micro-cutting forces. Recently, Arcona and Dow (1998) developed an empirical tool force model which made use of the shear angle from micrographs of chip cross sections to characterise the material flow and the parameters on the cutting force equations.

In ultra-precision diamond turning, crystallographic orientation has been reported to have a significant influence on the micro-cutting force (Lee, 1990, Lee and Zhou, 1993, and Yuan et al., 1994). In both single crystals (Cohen et al., 1981) and in polycrystalline aggregate (Sato, 1978), the shear angles and the cutting forces have been found to vary with the crystallographic orientation of the material. Black has reported a variation in the shear front-lamellar structure at the top of the chip with grain orientation. Most researchers (Sato et al., 1983) imply that the shear planes in metal cutting are dislocation glide planes themselves. Sato (1978) has attempted to use the continuum yield theory to analyse the shear stress and shear angle with material anisotropy. However, his attempt has been deemed to be unsuccessful since the value of the shear angle was in the reverse phase to shear stress. Lee and Zhou (1993) have proposed a microplasticity model to predict the variation of shear angle with crystallographic orientation of material being cut. Although the model was found to predict well the pattern of shear angle variation for single crystal material, good correlation between the predicted and measured patterns of cutting force variations was not found in their study.

When the depth of cut becomes of the same order as the tool edge radius, the effect on the overall force system, by changes in the effective tool rake angle and resultant ploughing, can be pronounced. Recent work (Inamura et al., 1993) on diamond turning of copper has demonstrated that there is a significant fraction of mechanical energy expended in the process that is not associated with material removal but rather with the redundant plastic work caused by the plowing of the edge of the tool as well as the sliding of the flank

face which is elastically loaded at the machined surface. Lucca et al., (1991 and 1993) reported that the redundant work resulted in energy dissipation and the amount of dissipation depends on the tool edge geometry. However, most of the cutting models gained partial success in explaining the cutting mechanics in diamond turning. Clearly there is a need for developing an accurate model which works under a wide range of cutting conditions and with various materials being cut.

2.3 DYNAMICS OF THE CUTTING SYSTEM

2.3.1 Sources of vibrations

The creation of a surface in machining is a dynamic process, and the nature of the dynamics affect the geometric and dimensional quality of the surface. A large body of experimental work has been devoted in characterising and quantifying the dynamics of the cutting process. The review by Tlusty (1978) provides an overview and a large number of references to such works. An earlier work that claims evidence for the force delay model is the work of Doi and Kato (1956). There are two main types of vibrations affecting the dynamic stability of the cutting system, i.e. forced vibration and self-excited vibration. A forced vibration results when a cyclically varying external load has a frequency that is close to one of the natural frequencies of the machining system (tool-workpiece-machine). When this is the case, slightly more energy is absorbed per cycle of vibration than is given back and the net energy per cycle is available to increase the vibration amplitude. The vibration amplitude will increase until the energy dissipated per cycle just equals the net energy absorbed by the system per cycle.

The sources of forced vibration in ultra-precision machining include the imperfect coupling of machining components (e.g. spindles and their drive motors), eccentricity, manufacturing errors in machine components and also the disturbances which come from the machining environment (Ikawa et al., 1991a). The ground vibrations will cause an undesirable change in the relative position of a workpiece and the cutting tool. Many

machines require utilities such as electricity, signal wires, air, vacuum, and sometimes hydraulics and/or cooling fluid. Each of these can provide a path for vibrations to short circuit the ground isolation system. In addition, acoustic coupling from other noise sources such as fans in air conditioners, neighbouring machine tools, etc., can create disturbances on the machine which may be as significant as the ground motions.

The effect of forced vibration on the dynamic stability of the cutting system can be reduced and even eliminated by modifications in the machine tool's structure (Debra et al., 1986 and Willis-Moren, 1989) and the application of a vibration-isolation technique (Takasu et al., 1985) as discussed in the Section 2.1.3. The current available ultra-precision machines are, in general, installed in air conditioned and vibration-isolated rooms. The effect of vibrations from the machining environment can be controlled to a low amplitude and a low frequency which are less than 0.01 μm and 10 Hz, respectively.

A self-excited vibration results when the internal energy of the system varies in such a way during a cycle of vibration that more energy is stored than is released during a single cycle. It is very difficult to eliminate the effect of self-excited vibration on machined surface quality. This is because sources of the self-excited vibration are not from the external environment but have their origin in the cutting of the workpiece. The history of investigations into self-excited vibration can be dated back to the early part of this century. Many research works on this topic have been reported (Hahn, 1953, Tobias, 1958, Albrecht, 1961, and Merritt, 1965). However, little is known about the vibration induced by the changing crystallography and orientation of the slip systems of grains being cut. The vibration caused by such a variation of material properties is a kind of materials induced vibration which has a considerable effect on the machined surface quality in ultra-precision machining (Lee et al., 1999).

2.3.2 Modelling, analysis and characterisation

The dynamic characteristics of a machining system lead to the appearance of relative motion between the tool and the workpiece. Over the last three decades, substantial

research has been done in the study of machining dynamics. The dynamics of machining is governed by the dynamics of the machine tool, and the dynamics of the cutting process, as well as by the external and internal excitation caused by chip formation and properties of the material being cut. During cutting, the structural and process dynamics are intrinsically coupled, as shown in Figure 2.18. The cutting force excites the machine tool structure, which responds with a relative tool-work displacement and this in turn excites the process dynamics.

Machine tool structures are complex systems, so for the analysis of cutting dynamics, it is sufficient to consider the relationship between a pair of opposite forces applied to the cutting tool and the workpiece, respectively, and the relative displacement that they induce. This relationship has traditionally been considered linear and represented in the frequency domain by a single transfer function or a third-order receptance matrix (Koenigsberger and Tlusty, 1971, Weck, 1985). Well established methods of structural dynamics have been employed in experiments to identify the structural transfer functions (Tobias, 1965, Taylor, 1977, and Kim et al., 1984). This has been postulated and experimentally verified. However, in some cases, the structure-workpiece system exhibits intrinsic non-linearity. This is usually modelled in non-linear stiffness terms (Hanna and Tobias, 1969 and Klamecki, 1989).

The cutting process dynamics depend on the values of the machining parameters like feed rate, spindle speed, depth of cut, tool geometry and consistency, and workpiece geometry and consistency. The relationship between the shear angle and the cutting force was first analysed by Merchant (1945). The dynamic variation of the shear angle has been examined closely and used to postulate non-linear cutting force equations (Wu and Liu, 1985a, 1985b, Wu, 1988, 1989, Lin and Weng, 1990). The lack of adequate ways to measure non-linear dynamical behaviour and of appropriate signal-processing techniques has prevented in-depth experimental validation of these models. Most of the experimental studies have focused instead on empirical linear cutting force models. Methods of time-series analysis (Pandit and Wu, 1983) have been employed to estimate the parameters of transfer functions that best approximate the dynamic characteristics of a cutting system.

Non-linear equations have been combined with linear structural models to show that under certain conditions the coupled machining system may exhibit chaotic oscillations (Grabec, 1986, 1988).

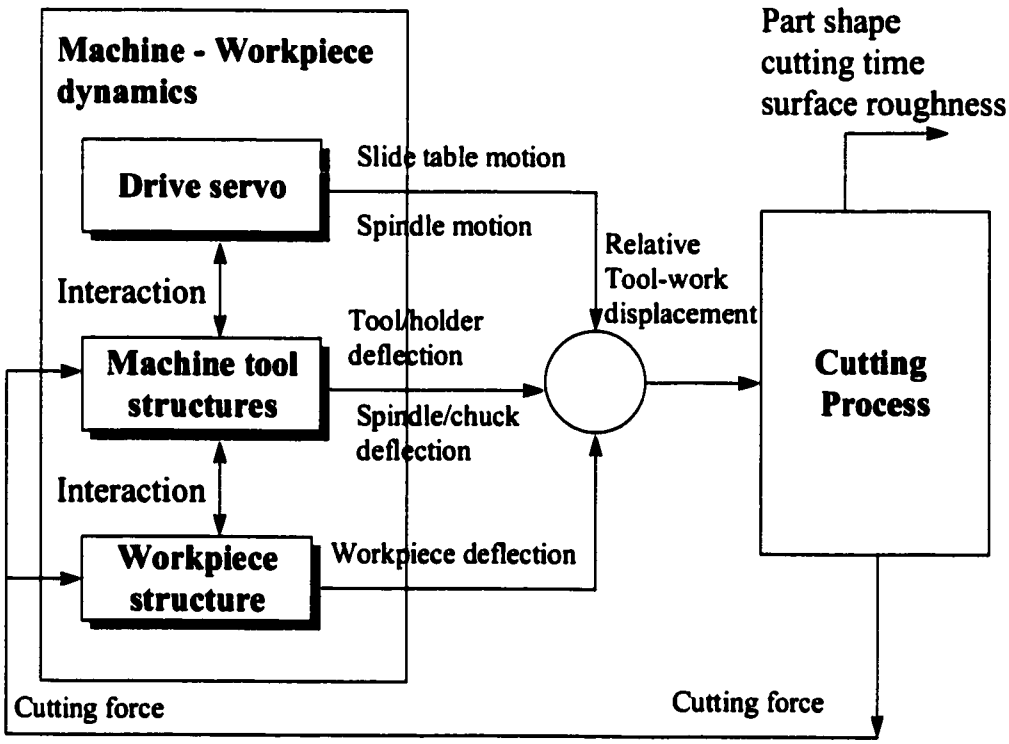

Figure 2.18 Closed-loop model for machining dynamics

Differential difference equations, or differential equations with delay, have been widely used as models for machining dynamics. The majority of the models represent the interaction between the cutting process and the machine tool-work system by a linear, closed-loop system with time delays. The use of linear differential difference equations has dominated the research literature in studies of machine tool vibrations and chatter. The book by Tobias (1965) provides numerous examples of linear constant coefficient differential difference equations used as models for chatter in milling, drilling and grinding, as well as turning. Several investigators have included friction effects between the workpiece and the tool, and the chip and the tool, in models for machine tool vibrations. Others have included cutting force models that mimic characteristics seen in

frictional oscillators. Arnold's experiments showed that the cutting force decreases with increasing cutting speed. The decline in the cutting force with relative velocity is analogous to that seen in dry friction. A friction-like model with two degrees of freedom has been proposed by Grabec (1986, 1988). This model provides some theoretical foundation for claims that machine tool vibrations can be chaotic and aperiodic.

2.4 SURFACE GENERATION

2.4.1 Factors affecting surface generation

The factors affecting the surface generation in machining operations has been studied by a number of researchers. Sata et al. (1985) reported that tool geometry, feed rate, material properties, spindle rotational errors (ANSI/ASME B89.3.4M Standard, 1985), and chatter vibration are the dominant factors which affect the surface roughness of a turned surface. Pandit (1981) made use of the Data Dependant Systems (DDS) approach to analyse the surface generation in the side turning operations. The surface roughness was found to be dominated by the relative vibration between the workpiece and the tool. Mitsui and Sato (1978) reported that the surface roughness affected by the relative vibration between the tool and the workpiece was nearly equal to the whole amplitude of the vibration. However, there is strong experimental evidence (Tai et al., 1980) that a surface finish better than the whole amplitude is often obtained in ultra-precision diamond turning. Takasu et al. (1985) explained this phenomenon by the kinematic interference of the tool in which the preceding movement of the tool removes the chip which is then cut away by some of the succeeding movements. He also emphasised that the surface roughness in the tool feed direction is more pronounced than it is in the main cutting direction since it usually has a relatively shorter wavelength and a larger peak-to-valley value than the other directions. A similar argument has been given by Bispink (1992).

Diamond turning is frequently employed for the machining of ductile materials like aluminium. The mechanism for surface generation differs from that of conventional

machining (Whitehouse, 1994). The diamond cutting process is usually carried out at very high cutting speeds so that problems associated with built-up-edge (BUE) do not arise. Under such circumstances it is possible to achieve the true theoretical surface roughness. Nowadays, most of the diamond turning machines possess extremely high loop stiffness, variation of cutting force and hence surface roughness due to regenerative charter is unusual. However, the anisotropy of the workpiece material upon surface roughness, which is neglected in conventional cutting, has a significant effect in the single-point diamond turning process. The surface roughness will not be an exact replica of the shape of the cutting tool. This is in part due to the burnishing effect on the clearance face of the cutting tool. With depth of cut less than the average grain size, cutting naturally becomes a single-crystal nature. Therefore the cutting behaviour and mechanism of chip formation depend on material factors such as the crystallographic orientation, the slip system and the dislocation that occurs. One important source of material anisotropy lies in the crystallographic nature of metallic substrate. In diamond turning of single crystal materials, the effect of crystallographic orientation was found to cause variations of cutting forces as well as surface roughness (Zhang, 1991, and Lee and Zhou, 1993). Other effects such as plastic side flow and the Spanzifel effect should also occur (Whitehouse, 1994).

2.4.2 Study of surface generation

The surface generation in machining has been studied from different approaches over the past decades. Traditionally, the generation of a machined surface was studied using models from cutting mechanics (Albrecht, 1965, Tai et al., 1980, and Kim and Kim, 1998). Such macroscopic parameters as the cutting forces and stresses were used to correlate with the surface roughness parameters (Sugano and Takeuchi, 1987 and Lo-A-Foe et al., 1988). Other approaches (Pandit and Revach, 1981 and Pandit, 1981) have been based on the analysis of the surface profile. Sata et al. (1985) made use of the spectrum analysis technique to examine the process of surface generation in turning. Some research work (Nishiguchi et al., 1988 and Masuda et al., 1989) was also found in studying the effect of tool geometry on the surface generation in diamond turning Al-Mg Alloy. In ultra-precision machining, the depth of cut is often less than the grain size of the crystallite and the effect of dislocation and of the slip

mechanism on chip formation has received much attention (Nishiguchi et al., 1988 and Masuda et al., 1989). Further work has been extended to incorporate microplasticity to correlate the shear angle with the roughness formation in cutting single crystal materials (Yuan et al., 1994 and Lee et al., 1998). Recently, molecular dynamics (Ikawa et al., 1991b and Inamura et al., 1993) has been used to analyze the mechanism of nanoscale cutting.

Most theoretical and experimental studies on the machining process were based on the measurement of cutting forces and stresses. These studies suffer from difficulties in the control of signal to noise ratio during experimentation. For example, the magnitude of the cutting force in diamond cutting is usually at sub-Newton level or less (Ikawa et al., 1991a). The accuracy of the experimental results depends very much on the signal to noise ratio in data acquisitions. The microscopic free surface morphology of the chip is not amenable to accurate measurement since chip curl, breaking, or other distortion occurs during machining. Special devices are usually needed to obtain the real chip root under certain cutting conditions (Zhang, 1991). Up to now, many advanced devices have been developed to facilitate the study of chip formation such as explosive quick-stop devices, closed-circuit television systems, high-speed cameras and the scanning electron microscope. The applications of molecular dynamic simulations have found to be useful in the simulation of the nano cutting mechanism. However, these analyses suffer from the inherent difficulties in experimental verification as well as from various limitations in the computation method (Shimada et al., 1992).

2.4.3 Characterisation of surface roughness

Surface characterization, the nature of surfaces and the measurement of surfaces cannot be separated from each other. It is taken to mean the breakdown of the surface geometry into basic components based usually on some functional requirements. These components can be of various shapes and sizes, and distribution in space and can be constrained by a multiplicity of boundaries in height and position. In general, surface roughness is the irregularities left by the tool on a surface after the manufacturing process. The roughness includes the tool traverse feed marks such as that found in turning and grinding. The term 'lay' is used to describe the

direction of the predominant surface pattern. The conventional analytical tools for the characterization of surface generation and material properties are based on macro material and surface roughness parameters. Surface roughness is generally examined in plane view with the aid of an optical or electron microscope, in cross-sections normal to the surface, with stylus instruments; and in oblique cross-sections with optical interference methods. The profile measurement based on these methods evaluates the roughness parameters for the tested length treated as a sample randomly selected from the surface.

The methodology for the characterization of surface roughness has been a subject of many theoretical and practical works (DeVries, 1979 and Nowicki, 1981). As usual, at first, assessment was dominated by the available means of measuring the surface. The stylus method of measurement has proven to be the most useful owing to its convenient output, ease of use and robustness. In many cases, the single-profile is sufficient to give an adequate idea of the surface. Examples have been found for using autoregressive time-series models (DeVries, 1979); spectrum analysis techniques (Sata et al., 1985); Data Dependent Systems method (Pandit and Revach, 1981) to extract the surface features from the roughness profile of a turned surface. However, there is strong experimental evidence that there is localized variation of surface roughness due to the crystallographic orientation and plastic anisotropy of the work material during ultra-precision diamond turning (Yuan et al, 1994). The single-profile approach for the surface roughness characterization might be inadequate. Some attempts have been made to use amplitude probability density function (APDF), autocorrelation function (ACF) (Whitehouse, 1969) and 2D Fourier Analysis (Sato and O-hori, 1981) for the characterization of surface roughness. The advantages of these methods are that they are related to the whole surface rather than to individual profiles. However, they have not yet to make an impact in industry due to the need to measure and to process an enormous amount of digital data. The complexity inherent in interpreting them makes them inconvenient for evaluation and specification purposes in practical applications.

Recently, it has been observed that some surfaces exhibit a particular type of behaviour called fractal property. Mandelbrot (1977) described structures in nature such as snowflakes, coastlines, cloud, etc. as having fractal property. The fractal property is that the geometry,

regular or random, exhibits 'self-similarity' over the whole range of the scale. This means that these structures are characterized by some dimension which is not Euclidean. The fractal property of some engineering surfaces was first investigated by Sayles and Thomas (1978) and some of the basic properties of fractals in engineering concept are given by Majundar and Bhusan (1990). Much research work show that the tendency to look for fractal behaviour is justified in the cases of the finer surfaces which tend to be manufactured by non-plastic processes and more by growth or deposition mechanisms (Whitehouse, 1994). It seems that the fractal approach to the characterization of surface roughness is in fact the spectral one with different emphasis being put on the order of the power (Mulvaney and Newland, 1986). The only real danger is that investigators try to impose fractal characteristics when they do not exist.

Although the current techniques for surface characterization are useful for solving many engineering problems, new problems keep emerging and there is a continual search for newer, perhaps better and universally acceptable parameters for industrial applications. Especially for diamond turning, there is a need for the development of newer methods and parameters for the characterization of the localized variation of material properties and hence the surface roughness that might be caused.

2.4.4 Approaches to modelling

Successful simulation of a lot of engineering problems depends on the physical models used to reduce complex systems to ones that are manageable at the appropriate level of abstraction. Some attempts have been found in developing topography models for the simulation of surface roughness in different machining processes. Bael et al. (1997), Montgomery (1991), and Ismall et al. (1993) put forward a model for the milling process. Recently, Lin and Chang (1998) have simulated a two dimensional (2-D) surface topography in lathe turning. Most of these models focused on the 2-D analysis of surface generation.

Although some attempts (Sato and O-hori, 1981 and Bispink, 1992) have been made in developing three-dimensional models for the simulation of surface topography of a machined surface, most of them focused on the synthesis of surface topography from measurement data captured by the interferometric (Sato and O-hori, 1981) or Scanning Electron Microscopic (SEM) types of instruments (Francis, 1998). Very few deterministic models (Byne, 1992, Tsai et al., 1990 and Weck et al., 1988) have been found based on machine kinematics, material science and cutting theories. Nevertheless, the influences of the properties of work materials, material crystallography and their interactions on the surface generation have been overlooked in most of the current studies.

2.5 THE STUDY OF MATERIALS INDUCED VIBRATION

Nowadays, most of the ultra-precision machines are constructed to possess extremely high loop stiffness in the order of several hundred newtons per micrometer. With a depth of cut from micrometer to sub-micrometer level, machine vibration caused by regenerative chatter is unlikely to occur in ultra-precision diamond turning of polycrystalline aggregates. In ultra-precision machining of highly anisotropic materials like single crystals, the cutting behaviour, the mechanism of chip formation and the variation of micro-cutting forces have been found to vary from the crystallographic cutting direction (Nakasuji et al., 1990). The fluctuation of the cutting forces caused by the changing crystallographic orientation of the work materials introduces vibration to the cutting process which was inferred to be materials induced vibration (Lee, 1990, K*ö* nig, W. and Spenrath, N., 1991, Lee at al., 1999). It is particularly marked in diamond turning brittle materials such as Si, SiN, etc. Over the past decades, the problem of materials induced vibration in ultra-precision machining has been investigated under two research directions (Figure 2.19), namely the avoidance direction and compensation direction, respectively.

Avoidance consists of eliminating the source or the effect of the materials induced vibration through design and manufacturing technology such as extremely high loop stiffness and accuracy in machine design, etc. There are some important principles to be

followed in the design of an adequate precision machine tool system (McKeown, 1978) and they are: stiff structure – independent of the foundation; high structural stability; the Abbe principle (Bryan, 1979b); kinematic/semi-kinematic design (Baily, 1975), the averaging principle (Astrom, 1970) as well as error budgeting (Slocum, 1992). Much research work found in the literature was working in this direction. Representative work was found at Cranfield University (Carlisle and Shore, 1991) in the designing Ultra Stiff CNC Aspheric Generating Machine Tools for single-point diamond turning and ductile regime grinding of brittle materials through its high "loop stiffness" between tool and workpiece. Other research work was also found in the design of infinite-stiffness aerostatic bearing (Mizumoto et al., 1991), considerations of optimum configuration hydrostatic or aerostatic bearings and ultra-fine infeed controller (Langenback, 1991). Most research work aims at increasing the dynamic loop stiffness of the ultra-precision machines so as to ensure "ductile mode machining". However, the cost and effort required to achieve the aim to attenuate or even eliminate the vibration might be enormous. Therefore, many of the techniques can be applied directly to the general purpose machine tool.

Compensation direction, on the other hand, is working on improving and maintaining the prescribed dimensional and form accuracy as well as surface quality by compensating the materials induced vibration through control technology (Peklenik, 1970). This approach demands quantitative analysis of the source of vibration through mathematical prediction. The compensation of errors can be realized in-process in accordance with predictions made with a mathematical model, which represents the cause-and-effect relationship between the error and the source. In other words, the compensation approach consists of prediction of the occurrence of the materials induced vibration and its effect through modelling and simulation and hence eliminates the effect using compensatory control strategy. Several authors have discussed schemes for error compensation with their pros and cons (Clark, 1974, Pfeifer and Furst, 1977, Wasiukiewiez, 1974, Eman, 1986). Recent work (Kim and Kim, 1998) was found in the design of the piezoelectric micro cutting device for waviness compensation of precision engineering.

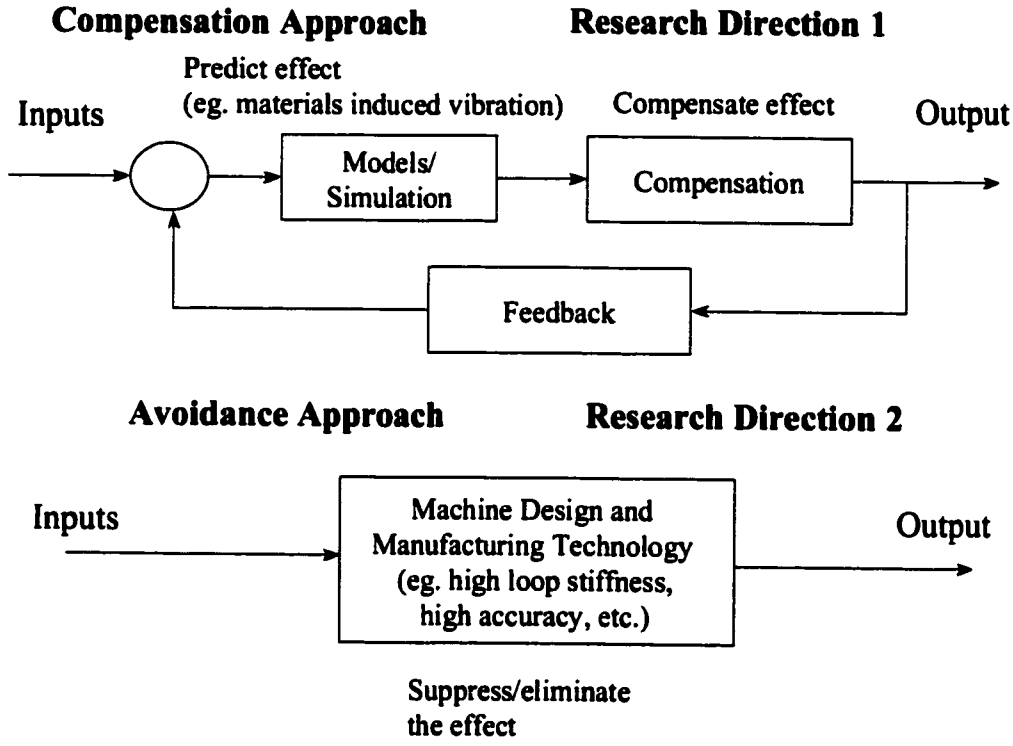

Figure 2.19 A comparsion between the avoidance and compensation approaches in studying the materials induced vibration

The compensation approach considerably departs from avoidance approach since it does not require a high precision machine tool for the achievement of high precision and high accurate results. The key postulate is the assumption that by the use of advances in computer, sensor and actuator technology along with suitable mathematical modelling techniques, high precision manufacturing can be achieved on even conventional built machines. Since the cost associated with high precision components increases exponentially, the cost associated with the addition of a compensatory system to a machine tools built with "moderate" accuracy can be readily justified based on economic considerations (Eman, 1986).

Although some research work has been found in both research directions for materials induced vibration study, the compensation direction has received relatively little attention. Moreover, the importance of materials induced vibration has not been considered

quantitatively in many studies of ultra-precision machining process (Lee et al., 1999). Most previous work was in qualitative and empirical nature. In fact, the research world is begging for quantitative models that can characterise quantitatively the materials induced vibration and its effect on the surface generation. This is vital for the development of compensation strategy for tackling the materials induced vibration problems in ultra-precision machining.

2.6 CONCLUDING REMARKS

From a practical point of view, ultra-precision machining has satisfied many of the present industrial needs in the manufacture of optical, electronic and mechanical parts for use in advanced technology. However, our scientific understanding of the micromachining process is still far from perfect. For example, the selection of optimal cutting conditions for the diamond turning process still relies on trial cutting tests, which are both time-consuming and costly. The process quality depends largely on the experience of the operator, as the optimal cutting conditions could easily drift due to any change in the machining environment such as dynamic conditions of the machine. Frequent re-calibrations are therefore needed to ensure a high level of surface finish quality. There is a need for developing deterministic models and a strategy for predicting the cutting performance as well as the optimal cutting conditions for machining a variety of materials under various cutting conditions.

Ultra-precision machining presents special phenomena like localised variation of machinability and surface quality with crystallographic orientations of work materials which are not observed in conventional machining. The conventional analytical tools for the characterisation of surface roughness and material properties based on some macro material parameters, surface roughness profiles, the surface roughness parameters and power spectrum analysis might not be sufficient. The development of new material parameters and analytical methods for the characterisation of the localised variation of material properties and surface quality is an important topic that should be addressed.

Although most diamond turning work is performed on polycrystalline aggregates, the use of single crystal materials is not uncommon. Examples include the use of single crystal silicon on a high precision infrared optical system and KDP crystals for laser applications. Single crystal materials are known to be highly anisotropic in their physical and mechanical properties. Our understanding on the machinability of these materials is still inadequate. Although some research has been done in the study of the machinability of work materials and their effect on surface quality in ultra-precision diamond turning, most of this work focused on qualitative analysis (Nakasuji et al., 1990). The development of deterministic models for quantitatively explaining some special phenomena like the localised variation of surface roughness with crystallographic orientation of work materials and the materials induced vibration have received relatively little attention. Theoretical analysis together with experimental verifications for these special phenomena needs to be done since this forms the basis for the future development of active compensation strategy for improving the accuracy of ultra-precision machine tools.

PART I

EXPERIMENTAL INVESTIGATION

Chapter 3

Experimental Investigation of The Diamond Turning Process

3.1 INTRODUCTION

The quality of a machined surface is affected by a number of factors (Sata et al., 1985) which include tool geometry, feed rate, material properties, spindle rotational errors and relative tool-work vibration as discussed in Chapter 2. Generally, these factors can be classified into process factors and material factors. The former involves the cutting conditions such spindle speed, feed rate, depth of cut and tool geometry. It also includes the relative vibration between the tool and the workpiece due to spindle error motions and machine vibration. These factors relate closely to the cutting geometry and the dynamic characteristics of a cutting system. The material factors considered are material anisotropy, swelling and the crystallographic orientation of the work materials.

A better understanding of the effect of these factors and their interactions on the surface generation are of prime importance for the further development of ultra-precision machining technology and better designs of machines to meet the needs for higher precision in the future. Some research has been found on studying the effect of tool wear (Masuda et al., 1989), cutting dynamics (Pandit and Revach, 1981) and vibration (Takasu et al., 1985) on the surface generation in diamond turning. However, most of this work focused on the study of the geometrical relationships among the process parameters (Sugano and Takeuchi, 1987), the cutting dynamics and the surface roughness. The effect of machinability (Moriwaki and Okuda, 1989), properties of the work materials (Furukawa and Moronuki, 1988), material crystallography (Yuan et al., 1994, Lee et al., 2000b) and their interactions on the surface generation have received relatively little attention. In this chapter, a comprehensive investigation into the effect of the process and material factors on surface roughness in diamond turning (Cheung and Lee, 2000a) is presented. In addition, the implications of the findings for the improvement of surface quality, are also discussed.

3.2 EXPERIMENTAL PROCEDURES

The experiments were basically divided into two groups i.e. Group 3A and Group 3B. Table 3.1 shows the specifications of the work materials being used. In Group 3A, a series of face cutting tests was conducted under different cutting conditions. Set 3A(I) and Set 3A(II) involved those cutting tests for studying the effect of spindle speed and feed rate on the surface roughness. The effect of depth of cut and tool nose radius is studied in Set 3A(III) and Set 3A(IV), respectively. Group 3B includes cutting tests for studying the effect of material anisotropy, swelling and material crystallography on surface roughness. Face cutting tests were done on copper alloy, aluminium single crystal and copper single crystal with different crystallographic orientations. Hence, the surface roughness profiles at twelve equally spaced radial sections (i.e. angle between sections is 30^{o}) were taken on a turned surface. Table 3.2 and Table 3.3 show the cutting conditions for Group 3A and Group 3B, respectively.

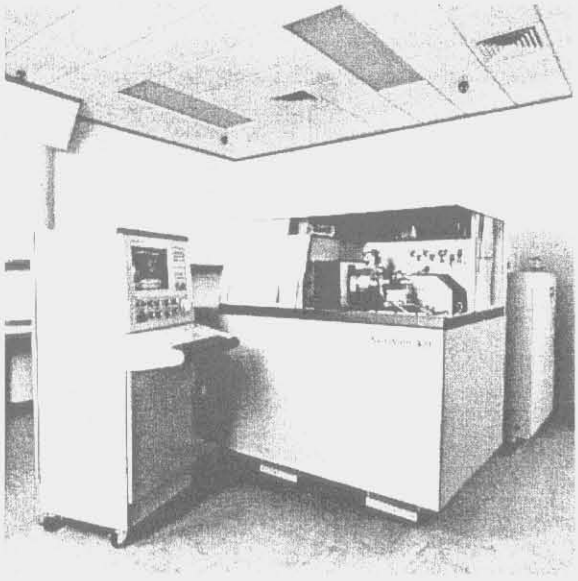

Figure 3.1 Nanoform 300 ultra-precision machine (Photo from Ultra-precision Machining Center of the Hong Kong Polytechnic University)

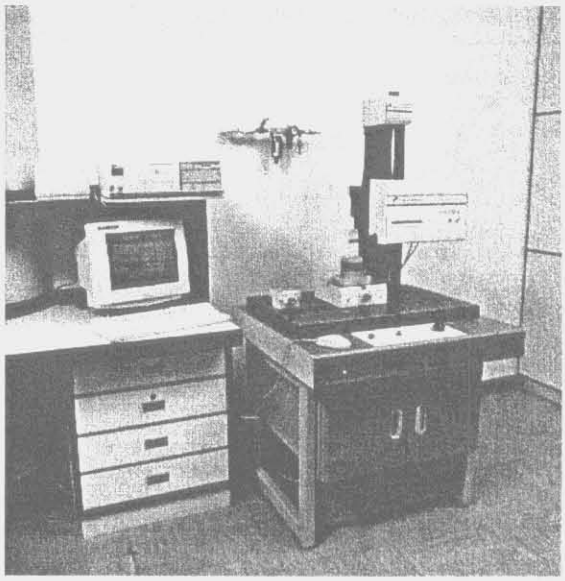

Figure 3.2 Form Talysurf system (Photo from Ultra-precision Machining Centre of the Hong Kong Polytechnic University)

Table 3.1 Specifications of the workpiece materials

Group	Set no./Specimen no.	Descriptions
3A	3A(I)	1. Aluminium alloy (6061)
	3A(II)	2. Copper alloy with chemical composition in percentage
	3A(III)	in weight of Cu. : Bal., Al:0.24, Fe:0.20, Zn:0.4., and
	3A(IV)	Pb: 0.12.
3B	3B(I)	(001) aluminium single crystal
	3B(II)	(011) aluminium single crystal
	3B(III)	Aluminium alloy (6061)
	3B(IV)	(001) copper single crystal
	3B(V)	(011) copper single crystal

Table 3.2 Cutting conditions for Group 3A

Cutting conditions	Set no.			
	3A(I)	3A(II)	3A(III)	3A(IV)
Factors under investigation	Spindle speed	Feed rate	Tool nose radius	Depth of cut
Feed rate (mm min^{-1})	15	5, 10, 15, 20 , 25	15	15
Spindle speed (rpm)	500, 1000, 1500, 2000, 3000	2000	2000	2000
Tool nose radius (mm)	1.55	1.55	0.52, 0.79, 1.17, 1.54, 2.03	1.55
Depth of cut (μm)	2	2	2	2, 5, 10, 15, 20

Table 3.3 Cutting conditions for Group 3B

Spindle rotational speed	2000 rpm.
Feed rate	20 mm min^{-1}
Depth of cut	5 μm
Front clearance angle	12.5°
Tool nose waviness	0.5 μm
Tool rake angle	0°
Tool nose radius	2.019 mm

All cutting tests were performed on a two-axis CNC ultra-precision machine (Nanoform 300 from Taylor Hobson Pneumo Co.) as shown in Figure 3.1. The crystallographic orientation of the workpiece in Group 3B was checked by a X-Ray diffractometer (Philips PW3710). The diffractometer was operated at a current of 35 mA and a tube voltage of 40kV. A copper target was used throughout the tests. The surface roughness of the machined surfaces was examined by a Form Talysurf system equipped with a rotary table with a

resolution of 0.017° (see Figure 3.2). A cut-off length of 0.25 mm and 7 cut-off per measurement were used to determine the surface roughness parameters. The surface roughness parameters under investigation are the maximum peak-to valley height R_t and the arithmetic roughness R_a, respectively. The relative vibration between the tool and the workpiece was measured with a capacitive displacement sensor on the centre line of the spindle during air cutting. As shown in Figure 3.3, a dominant mode of vibration with average amplitude of 15 nm (i.e. 30 nm peak to peak) and a frequency of 45 Hz was found to exist between the tool and the workpiece.

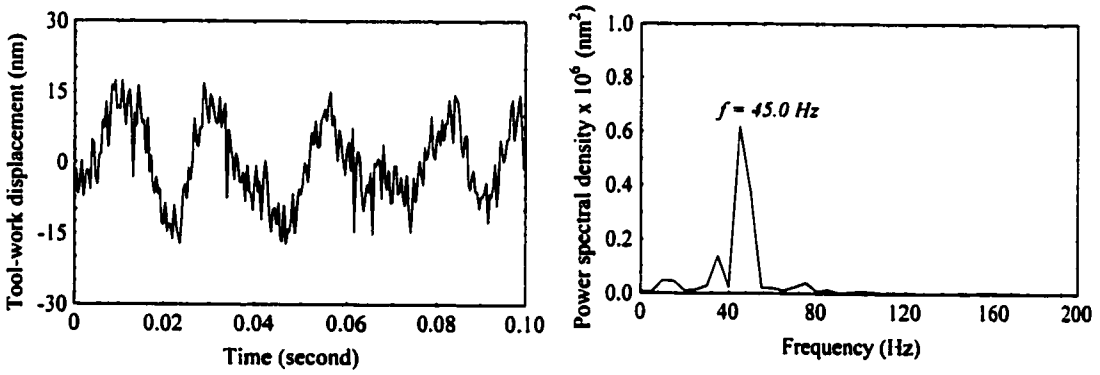

Figure 3.3 Measured (a) relative tool-work displacement and (b) its power spectrum

3.3 RESULTS AND DISCUSSION

3.3.1 Group 3A : Process factors

Under ideal conditions, the surface roughness profile is formed by the repetition of the tool tip profile at intervals of feed per workpiece revolution. The maximum peak-to-valley height, R_t, and the arithmetic roughness, R_a, of an ideal roughness profile (Whitehouse, 1994) can be derived respectively as :

$$R_t = \frac{f^2}{8rV^2} \tag{3.1}$$

$$R_a \sim \frac{0.032 f^2}{r V^2} \tag{3.2}$$

where f is the tool feed rate in mm per min, V is the spindle rotational speed in rpm, r is the tool nose radius.

The maximum peak-to-valley height R_t derived in Equation (3.1) for an ideal roughness profile is referred to as the theoretical roughness in the present study. Equations (3.1) and (3.2) provide quantitative relationships among tool feed rate, tool nose radius, spindle speed and surface roughness. They are based on the assumption that there is no relative vibration between the tool and the workpiece. However, in practice, the tool positions usually vary relative to the workpiece due to the tool-work vibration induced during machining. As vibration occurs during machining, surface modulations are formed in both the cutting and the tool feed directions. This modifies the surface roughness profile and hence significantly increases the surface roughness of a diamond turned surface.

3.3.1.1 Effect of spindle speed

Figure 3.4 shows the effect of spindle speed on surface roughness. The cutting tests were conducted under Set 3A(I) conditions. It was found that the surface roughness R_t decreases with increasing spindle speed. Similar results (Figure 3.4(b)) were observed for the arithmetic roughness R_a. Under all spindle speed conditions, copper alloy is found to have a higher surface roughness than aluminium alloy. This could be explained by the difference in the swelling property of the materials being cut (Sata, 1964, Shaw and Crowell, 1965). Such a difference seems to increase with increasing spindle speed. Equations (3.1) and (3.2) are found to make quite a good prediction under low spindle speed conditions. However, the discrepancy between the predicted and the measured roughness increases with increasing spindle rotational speed. The discrepancy can be explained by the relative vibration that exists between the tool and the workpiece at high spindle speeds.

It is considered that the dominant mode of the relative tool-work vibration determined in Section 3.2 is responsible for the additional surface roughness. It is assumed that the dominant mode of the vibration is simple harmonic with an amplitude denoted by A. A vibration adjustment curve is constructed which is defined as the sum of the theoretical roughness calculated from Equation (3.1) and the total amplitude ($2A$) of the relative tool-work vibration. The adjustment curve seems to give a far better estimate of the surface roughness. As spindle speed increases, the advantage of improved roughness tends to be overwhelmed by the influence of the tool-workpiece vibration.

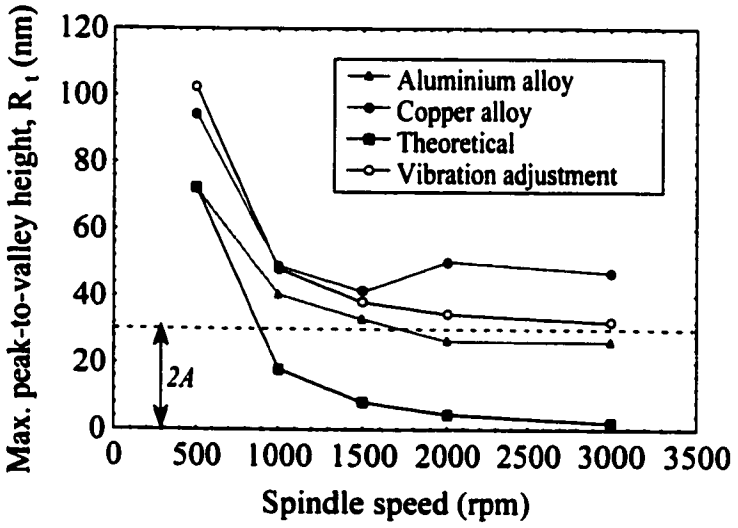

(a)

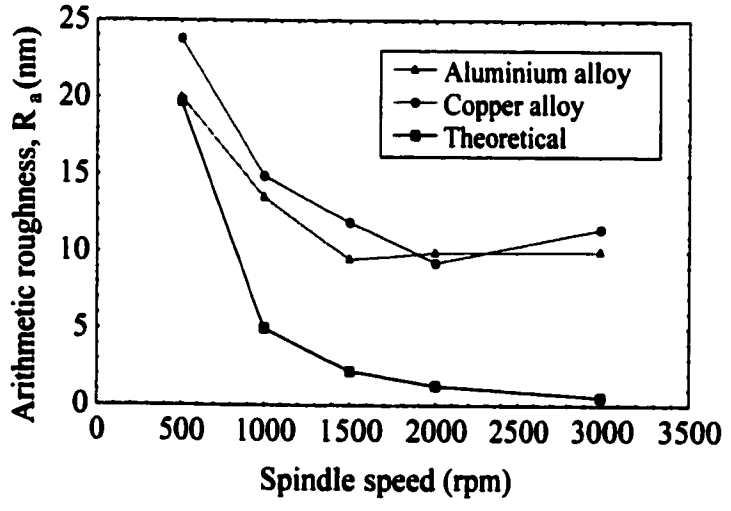

(b)

Figure 3.4 Effect of spindle speed on (a) maximum peak-to-valley height and (b) arithmetic roughness

3.3.1.2 Effect of feed rate

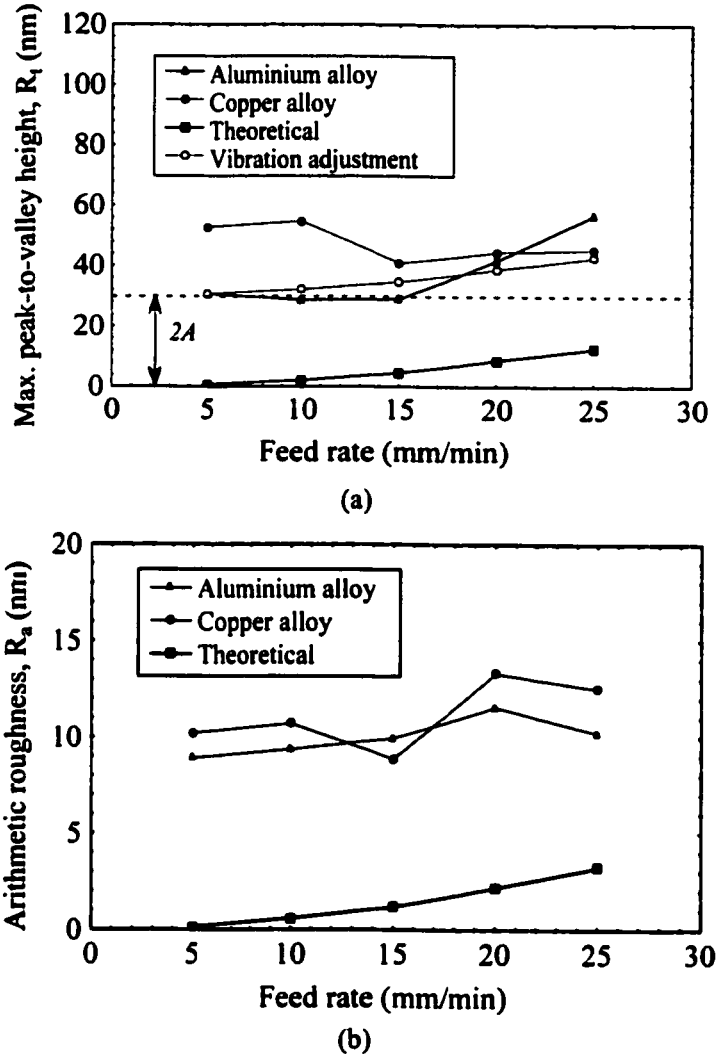

Figure 3.5 Effect of feed rate on (a) maximum peak-to-valley height and (b) arithmetic roughness

The effect of feed rate on surface roughness is shown in Figure 3.5. The surface roughness parameters (i.e. R_t and R_a) are found to increase with increasing feed rate. Similar to the spindle speed study, copper alloy seems to cause greater surface roughness than aluminium alloy. Furthermore, the vibration adjustment curve is found to give a better estimation of the R_t values than the theoretical ones determined from Equation (3.1). There is also a significant difference in the R_t values between aluminium alloy and copper alloy over the range of feed rate being investigated. However, the difference is found to decrease with increasing feed rate.

3.3.1.3 Effect of tool nose radius

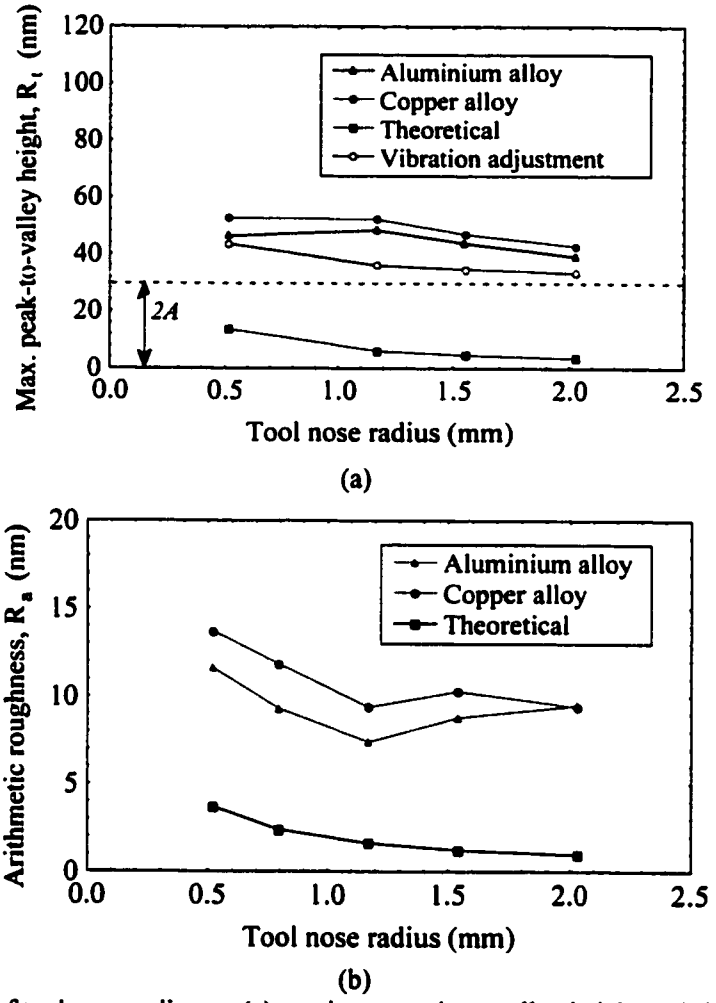

Figure 3.6 Effect of tool nose radius on (a) maximum peak-to-valley height and (b) arithmetic roughness

The relationship between the surface roughness and the tool nose radius is shown in Figure 3.6. It is found that the arithmetic roughness decreases with increasing tool nose radius at a small radius but increases at a large radius. This is different from the theoretical prediction which suggests a decrease in the surface roughness with increasing tool nose radius. The surface roughness R_t shows a similar tendency as the theoretical ones. Under identical feed rate and spindle speed conditions, the contact area between the tool and the workpiece decreases with increasing tool nose radius. This might reduce the damping of the

relative tool-work vibration which contributes to the surface roughness of the workpiece. As a result, the advantage of improved surface roughness tends to be overwhelmed by the reduced damping effect as tool nose radius increases. A difference between the maximum peak-to-valley height R_t of copper and aluminium alloys is observed throughout the study. Although the vibration adjustment curve gives a better estimate of the surface roughness R_t than the theoretical ones, the residue between the vibration adjusted values and the measured roughness values still needs other explanations.

3.3.1.4 Effect of depth of cut

Figure 3.7 shows the effect of depth of cut on surface roughness. There is no systematic relationship found between the depth of cut, the maximum peak-to-valley height and the arithmetic roughness. As the depth of cut increases, the surface roughness is found to vary unsystematically. It is different from the traditional expectation that greater depth of cut will result in greater roughness. One possible reason for this phenomenon might be the presence of voids, impurities, swelling and plastic recovery of the workpiece materials. The effect of material swelling and plastic recovery will be further discussed in the later part of the text.

3.3.1.5 Effect of tool interference

Unlike conventional machining, high spindle rotational speed together with a fine feed rate is usually adopted in ultra-precision diamond turning. Under these conditions, a phenomenon called tool interference occurs at which the preceding movement of the tool has already removed the chip which should be cut away by some of the succeeding tool movements. Better surface finish can be expected as the interference of the tool occurs. Figure 3.8 shows the simulated surface topography of a diamond turned surface generated under tool interference conditions. Takasu et al. (1985) has established a criterion for the occurrence of tool interference i.e.,

$$\frac{8R_t}{\phi^2 A} \leq 1 \tag{3.3}$$

where A is the amplitude of vibration and ϕ is the phase shift which is determined from the ratio between the frequency f_z of the relative tool-work vibration to the spindle rotational speed V in revolution per minute (rpm). Thus,

$$\frac{60 f_z}{V} = a + \varepsilon \tag{3.4}$$

where a is 0 or a positive integer and ε is a decimal fraction in the range $-0.5 \leq \varepsilon \leq 0.5$. A phase shift ϕ between subsequent undulations can be defined based on ε as:

$$\phi = 2\pi\varepsilon \tag{3.5}$$

From Equations (3.1), (3.4) and (3.5), Equation (3.3) can be rewritten as:

$$\frac{f^2}{4\pi^2 AR(60 f_z - aV)^2} < 1 \tag{3.6}$$

Equation (3.6) shows that the occurrence of tool interference depends on tool feed rate, spindle rotational speed, tool nose radius, and amplitude as well as frequency of relative tool-work vibration. Finer feed rate, larger tool radius , and higher spindle speed will be more likely to cause tool interference.

Table 3.4 summarizes the conditions of tool interference for the cutting tests in Sets 3A(I), 3A(II) and 3A(III). Referring to Figure 3.4(a) and Figure 3.5(a), it is noticed that the surface roughness is reduced down below the whole amplitude of vibration ($2A$) as tool interference occurs under various feed and spindle speed conditions. Although similar amount of roughness reduction is not explicitly observed under different tool radius conditions (Figure 3.6(a)), the gradual improvement of the arithmetic roughness together

with the reduction of the difference between the vibration adjustment curve and the maximum peak-to-valley height suggest that the influence of the tool interference exists but its extent might be overwhelmed by other factors such as material swelling (Sata et al. 1985).

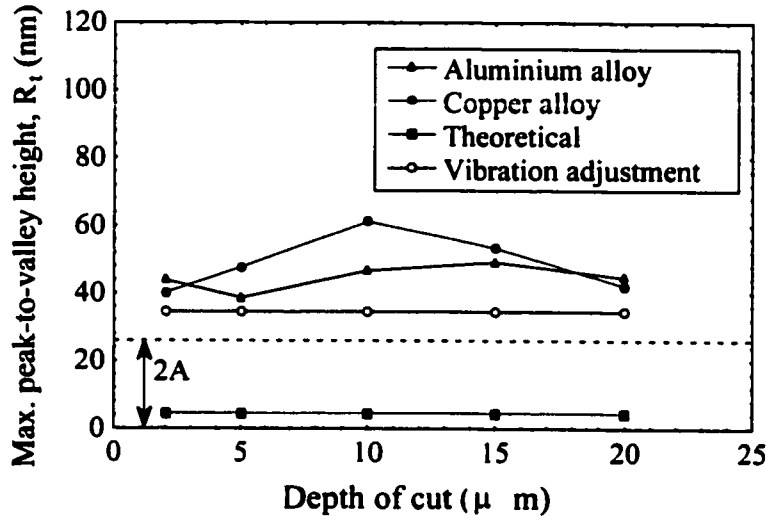

(a)

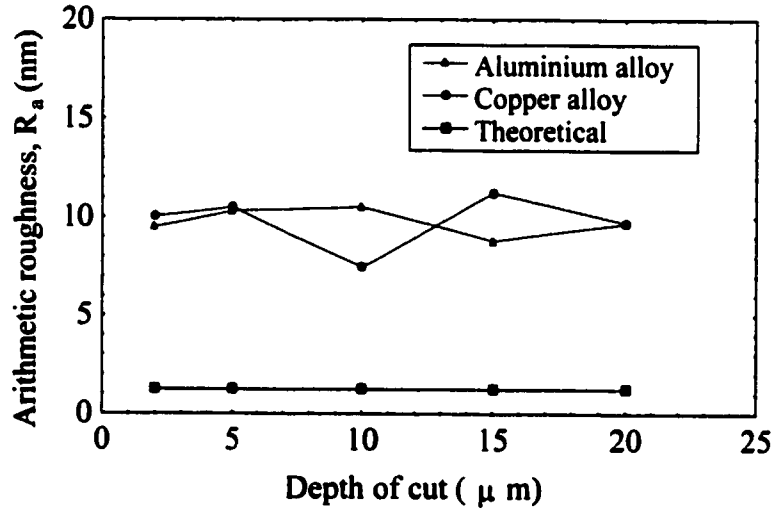

(b)

Figure 3.7 Effect of depth of cut on (a) maximum peak-to-valley height and (b) arithmetic roughness

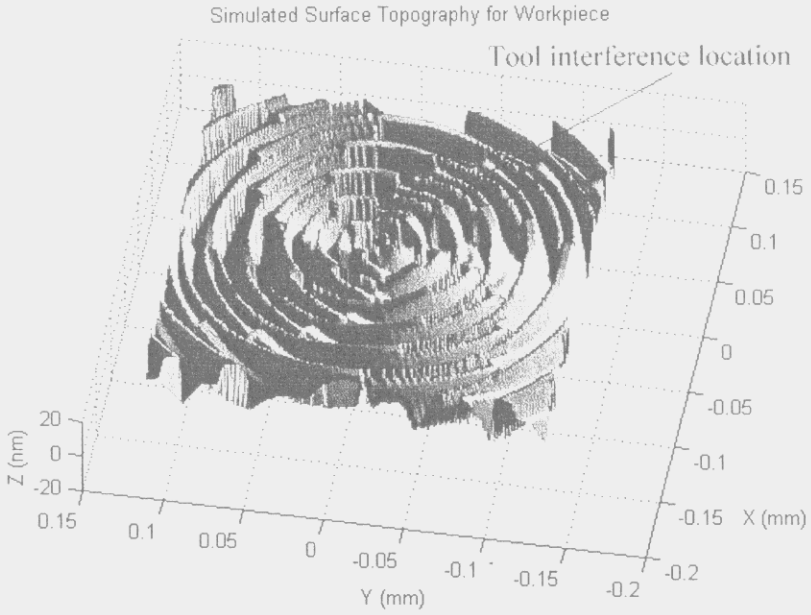

Figure 3.8 Illustration of the effect of tool interference on the surface topography of a diamond turned surface (spindle speed: 2000 rpm, feed rate: 15 mm/min; tool nose radius: 1.17 mm; depth of cut: 2 μm)

Table 3.4 Conditions of tool interference

Set no.	Feed rate, f (mm/min)	Spindle speed, V (rpm)	Tool nose radius, R (mm)	Phase shift, $\lvert\phi\rvert$	Max. peak-to-valley height R_t (nm)	Vibration amplitude A (nm)	$\frac{8R_{th}}{\phi^2 A}$	Status I : Interference N: Non-interference
3A(I)	15	500	1.55	2.513	72.40	15	6.115	N
	15	1000	1.55	1.885	18.10	15	2.717	N
	15	1500	1.55	1.257	8.04	15	2.714	N
	15	2000	1.55	2.199	4.52	15	0.498	I
	15	3000	1.55	0.628	2.01	15	2.721	N
3A(II)	5	2000	1.55	2.199	0.51	15	0.056	I
	10	2000	1.55	2.199	2.02	15	0.223	I
	15	2000	1.55	2.199	4.55	15	0.502	I
	20	2000	1.55	2.199	8.10	15	0.893	I
	25	2000	1.55	2.199	12.55	15	1.345	N
3A(III)	15	2000	0.52	2.199	13.55	15	1.494	N
	15	2000	1.17	2.199	6.01	15	0.663	I
	15	2000	1.55	2.199	4.57	15	0.564	I
	15	2000	2.03	2.199	3.46	15	0.382	I

3.3.1.6 Effect of phase shift

Theoretically, the phase shift $|\phi|$ is related to the ratio between the frequency of tool-work vibration to spindle speed as shown in Equations (3.4) and (3.5). Equation (3.4) suggests that the surface waviness in the feed direction could be eliminated by a zero phase shift which occurs as the frequency of vibration becomes equal to or becomes a multiple of the spindle rotational speed.

From Equation (3.4), it is noted that the phase shift $|\phi|$ can be adjusted by either controlling the frequency of the vibration or changing the spindle rotational speed. It is relatively easier to adjust the spindle rotational speed than to alter the dynamic characteristics of a cutting system. Figure 3.9 shows the variation of surface roughness with the phase shift characteristics. It is noted that there are optimum or sub-optimum phase shifts $|\phi|$ at which the surface roughness is significantly improved. Under a known and steady dynamic condition of a cutting system, the surface roughness of a diamond turned surface can be improved with the use of an optimum or sub-optimum phase shift $|\phi|$ which could be obtained by a proper selection of spindle rotational speed.

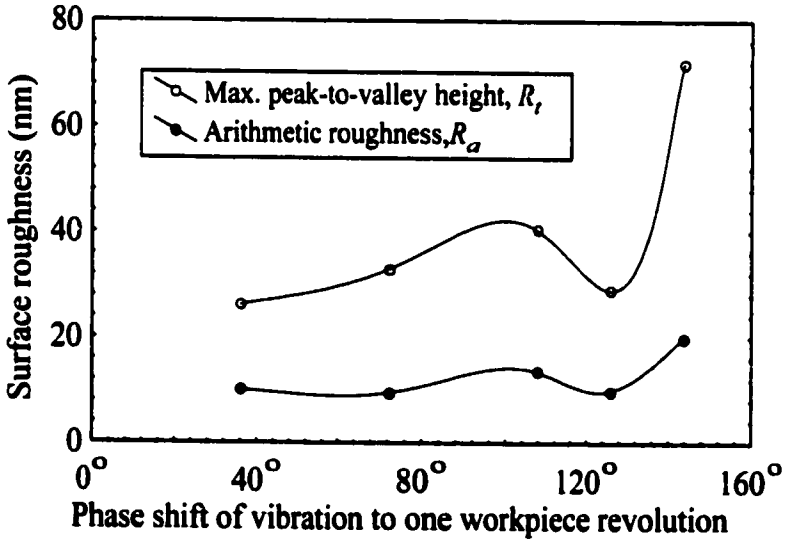

Figure 3.9 Effect of phase shift on the surface roughness parameters

3.3.2 Group 3B : Material factors

3.3.2.1 Effect of material swelling

Figures 3.4, 3.5 and 3.6 show that there is a consistent difference in the surface roughness between aluminium and copper alloys. Greater roughness is found in copper alloy than in aluminium alloy. This could be explained by the difference in the swelling properties of the materials being cut (Sata, 1964, Shaw and Crowell, 1965). As shown in Figure 3.10, the workpiece material swells at the end of the active cutting edge during machining (Sata, 1964, Shaw and Crowell, 1965). This is caused by the plastic side flow (Shaw and Crowell, 1965) in which the metal left behind on the cutting edge is subjected to pressure high enough to cause the metal to flow to the side of the active cutting edge. Moreover, the cutting force along the main cutting edge of the tool (F_z in Figure 3.10), which is required to provide two-dimensional (2D) cutting along the edge, pushes aside the work material near the tool nose causing it to flow to the free surface (Sata, 1965). In the region below the chip, complicated elastic and plastic deformation occurs (Shimada, et.al, 1993 and Whitehouse, 1994, To et al., 2000). This is caused by the indentation and/or burnishing by the cutting edge. The workpiece material left behind the front clearance of the tool springs back or recovers after burnishing. The amount of recovery is determined by the forces on the clearance face and by the crystallographic orientation of the substrate material being cut.

The combined effect of plastic side flow, burnishing and elastic recovery will cause greater and deeper tool marks to be formed on the machined surface and this is referred in the present study as the swelling effect (Cheung and Lee, 2000b). The amount of swelling depends on the properties and the crystallographic orientation of the material being cut.

Figure 3.11(a) shows the surface roughness profiles for an ideal surface, aluminium alloy and copper alloy generated under cutting conditions with a spindle speed of 500 rpm; a feed rate of 15 mm min^{-1}; a depth of cut of 2 μm and a tool nose radius of 1.55 mm. It is noticed that the surface roughness of the machined surfaces is not an exact replica of the profile of the

cutting tool. The average width of the tool marks is found to be 30.06 μm and 30.23 μm for aluminium alloy and copper alloy, respectively. It is found that copper alloy makes deeper and wider tool marks than aluminium alloy. The increased width and depth of the cutting marks illustrate the presence of the swelling effect. These findings help to explain the observed difference between the surface roughness of different materials even if the cutting tests are performed under identical cutting conditions. The influence of material swelling on the surface roughness will be studied in detail in Chapter 4.

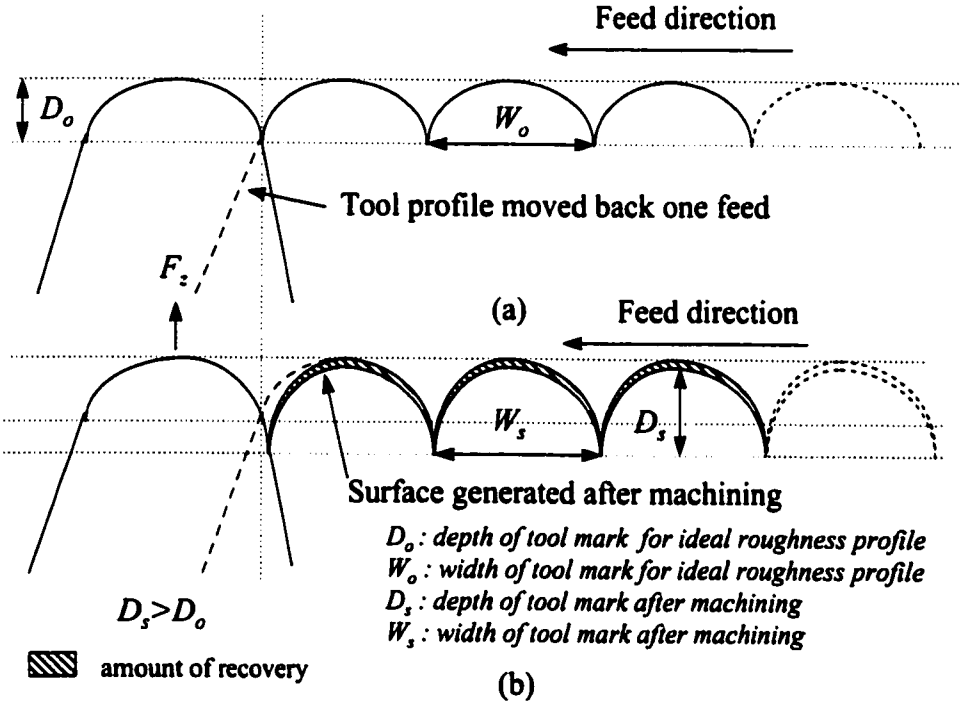

Figure 3.10 Graphical illustration of swelling effect in diamond cutting : (a) surface generated in the absence of swelling and (b) surface generated with swelling

3.3.2.2 *Effect of material anisotropy and crystallographic orientation of the work materials*

In order to measure quantitatively the localized variation of surface roughness in diamond turning, a parameter called Degree of Roughness Anisotropy (*DRA*) (Cheung and Lee, 2000a and Lee et al., 2000b) is firstly defined as the ratio of the standard deviation and

the mean of the arithmetic roughness values at a finite number of equally angular spaced radial sections of the machined surface, i.e.,

$$DRA = \frac{\sigma_{R_a}}{\overline{R}_a} = \frac{m\sqrt{\sum_{i=1}^{m} R_{a,i} - \overline{R}_a}}{\sqrt{m-1}\sum_{i=1}^{m} R_{a,i}} \tag{3.7}$$

where $R_{a,i}$ is the arithmetic roughness at i th radial section; $\overline{R}_a$ and σ_{R_a} are the mean and the standard deviation of the arithmetic roughness values for the m radial sections on the surface. The parameter (DRA) provides a measure of the normalized variation of the surface roughness over the diamond turned surface. A large value of DRA implies a high anisotropy of surface roughness.

Figure 3.12 depicts the variation of the arithmetic roughness R_a at different radial sections of the diamond turned surfaces. The surface roughness is found to vary with the crystallographic orientation of the materials being cut. Greater variation is observed for the aluminium single crystals than the copper single crystals. The observation is confirmed by the calculated DRA as shown in Table 3.5. During machining, the cutting edge of the diamond tool burnishes the machined surface (Whitehouse, 1994). The material left behind the front clearance of the tool recovers after burnishing. In anisotropic materials like single crystals, the Young's modulus is dependent on the grain orientation. Thus, a different amount of recovery is expected to occur at different crystallographic orientations of the work material (Figure 3.13). This explains the variation of the surface roughness with various crystallographic orientations of the work materials. Figure 3.14 shows a micrograph of a machined copper single crystal with (011) as cutting plane. It is clear that surface roughness varies considerably with different crystallographic cutting directions.

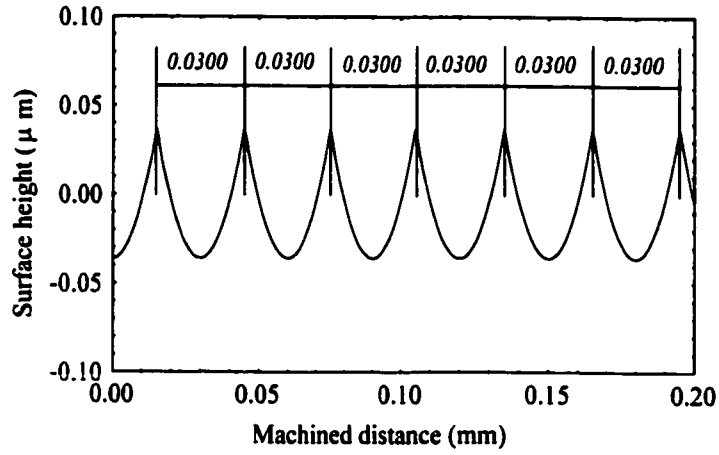

(a)

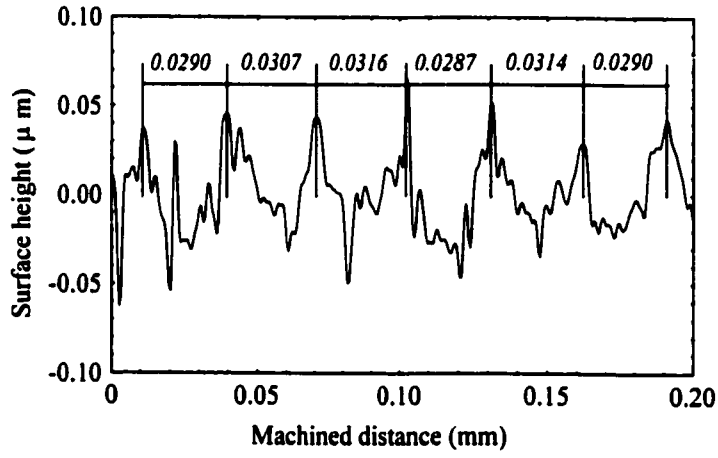

(b)

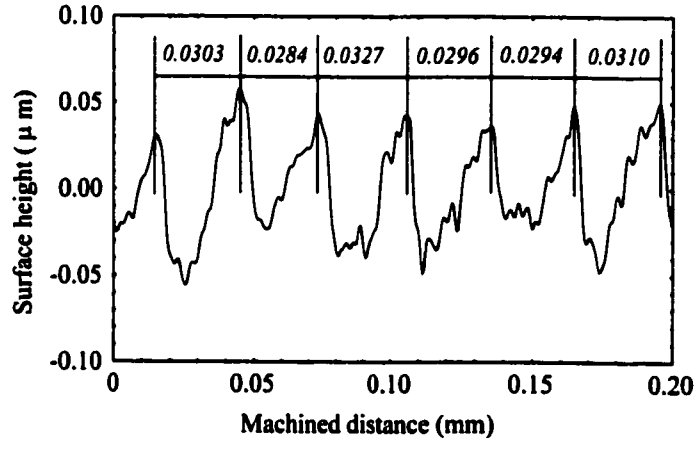

(c)

Figure 3.11 A comparison among the surface roughness profiles for (a) ideal surface; (b) aluminium alloy; (c) copper alloy

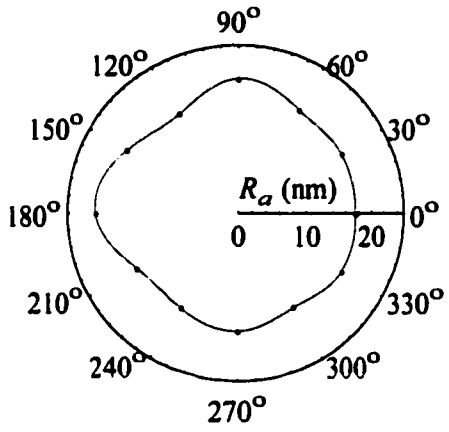

(a)

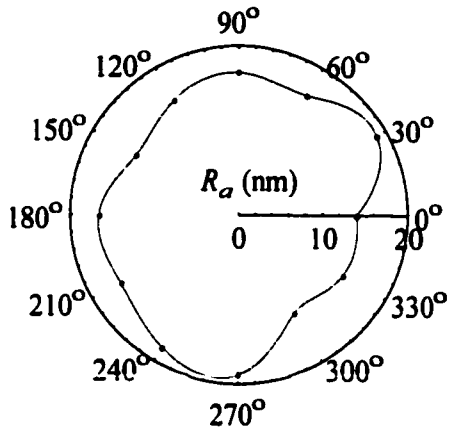

(b)

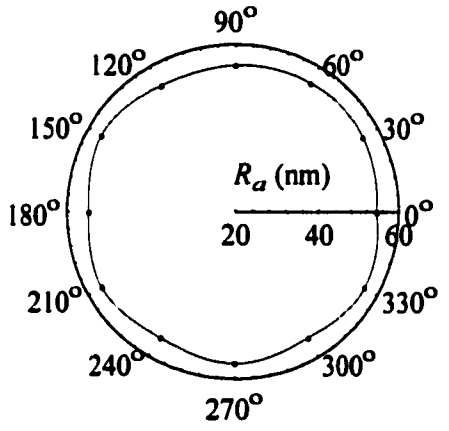

(c)

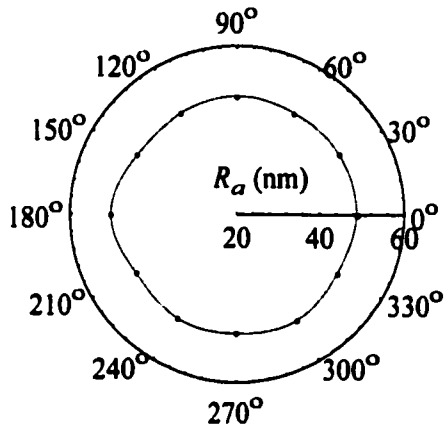

(d)

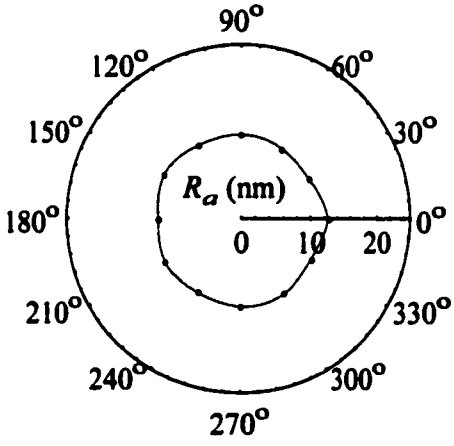

(e)

Figure 3.12 Variation of surface roughness for diamond face cutting of :

(a) (001) aluminium single crystal;

(b) (011) aluminium single crystal ;

(c) (001) copper single crystal ;

(d) (011) copper single crystal ;

(e) aluminium alloy (6061)

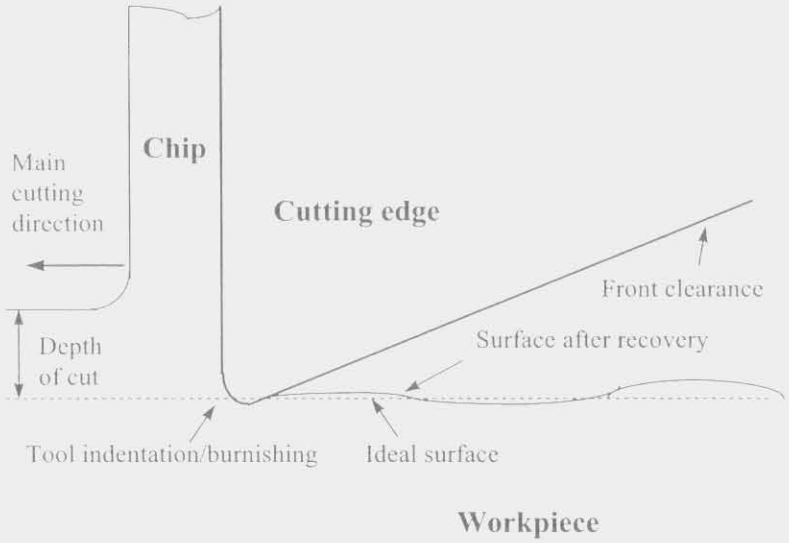

Figure 3.13 Effect of material anisotropy on recovered surface

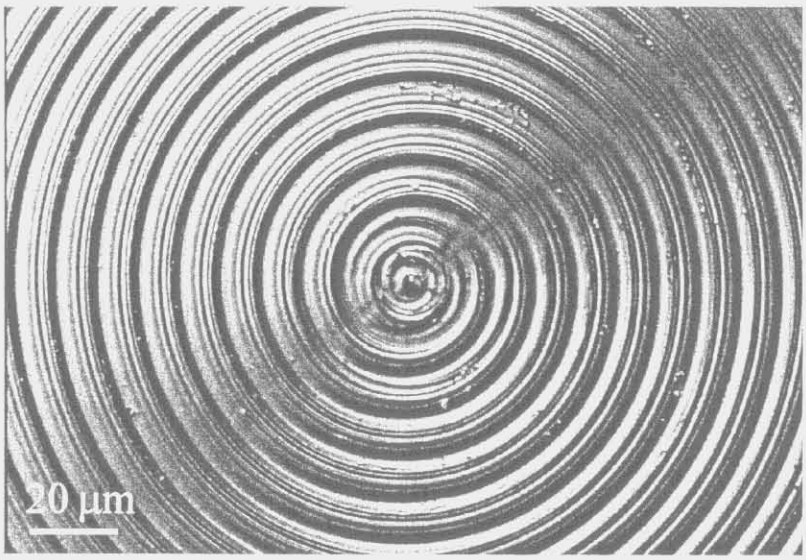

Figure 3.14 Micrograph of a turned copper single crystal with (011) as the cutting plane

A substantially small variation in surface roughness remains in Specimen 3B(III). This could be explained by the fact that the cutting is performed with a depth of cut of only a few micrometers which is less than the average grain size of a polycrystalline aggregate. Figure 3.15 shows clearly the grain distribution and grain size of aluminium alloy (6061). It is noted that the average diameter of the grains for the aluminium alloy (6061) is greater than 50 μm that is far greater than the tool feed (10 μm rev^{-1}) and the depth of cut (5 μm)

used in the experiment in Group 3B. This affords the evidence that the cutting is performed with a depth of cut that is less than the average grain size. As illustrated in Figure 3.16, the polycrystalline work material, which may be considered to be isotropic and homogeneous in the conventional analysis, should be treated as a series of single crystals which have quite random orientations and anisotropic properties (Lee, 1990). There will inevitably be imperfections (dislocations) in overall roughness due to the anisotropy in machinability on each of the crystal grains making up the machined surface. Therefore, the influence of anisotropy of materials upon surface roughness can not be neglected in diamond turning of polycrystalline materials.

Table 3.5 Results of surface roughness measurement

Specimen no.	Arithmetic roughness R_a (nm)		
	Range	Mean $\overline{R}_a$	Degree of Roughness Anisotropy , *DRA*
3B(I)	16.20-20.70	17.76	0.074
3B(II)	13.40-18.90	16.10	0.118
3B(III)	11.28-12.59	12.11	0.036
3B(IV)	54.36-56.34	55.29	0.014
3B(V)	47.53-50.26	48.39	0.015

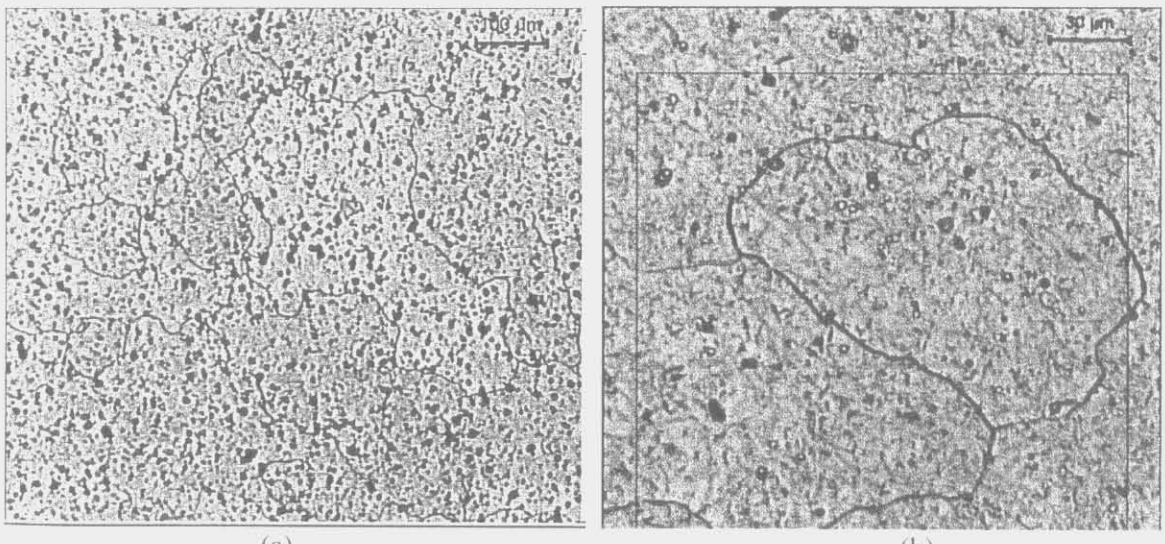

(a) (b)

Figure 3.15 (a) Grain distribution and (b) grain size of aluminium alloy (6061)

The effect of material swelling over a wide range of cutting conditions together with the anisotropic properties of the work material illustrate that the material factors are inherent in a cutting system and could not be eliminated solely by the optimization of the process factors. A possible way to minimize the material effects would be to modify the structure of the work materials by using of super fine grains or amorphous materials.

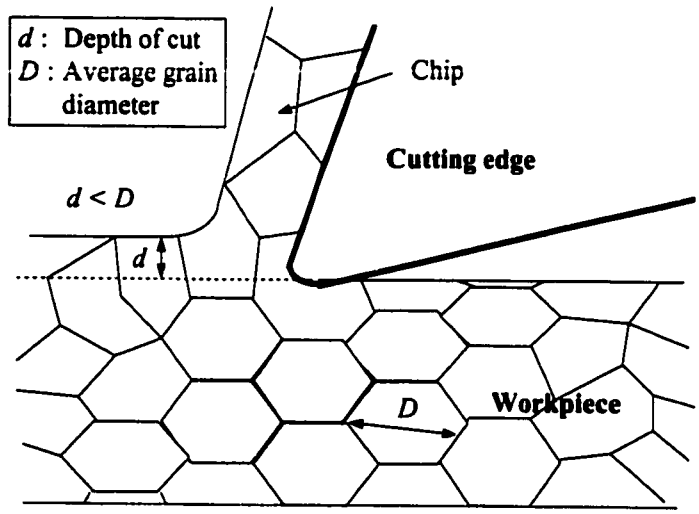

Figure 3.16 Illustration of diamond cutting on polycrystalline aggregate

3.4 SUMMARY

An investigation of the factors affecting the surface generation in ultra-precision diamond turning has been conducted. It is found that the surface roughness of a diamond turned surface is affected by both the process factors and the material factors. The results indicate that the influences due to process factors can be minimized or even eliminated through a proper selection of operational settings and a better control of the dynamic characteristics of the machine. Generally, the use of high spindle speed, fine feed rate together with a large tool nose radius is shown to be useful for the improvement of surface roughness. Under a known and steady dynamic characteristic of the cutting system, the surface roughness of a diamond turned surface can be further improved with the use of an

optimum phase shift $|\phi|$ which could be obtained by the adjustment of the spindle rotational speed. Moreover, it is shown that the surface roughness in the tool feed direction can be made much finer than the sum of the whole amplitude of the tool-work vibration and the theoretical roughness. This is achieved by the interference of the tool.

As for the material factors, it is found that the effect of material anisotropy, swelling and material crystallography plays an important role in the surface generation. Material swelling causes greater tool marks on the machined surface. This inevitably increases the surface roughness of a diamond turned surface. For anisotropic materials like single crystals, the Young's modulus is dependent on the grain orientation. Thus, different extents of swelling are found at different crystallographic orientations of the work material being cut. This results in a variation of surface roughness with the crystallographic orientation of the work material. The effect by material factors is shown to exist consistently even if cutting tests were performed under various cutting conditions. This suggests that the influence by the material factors on the surface quality could not be minimized solely by the optimization of process parameters and machine design. A proper selection of work material is of prime importance for further improvement of surface roughness.

Chapter 4

Multi-spectrum Analysis of Surface Generation

4.1 INTRODUCTION

The surface roughness profile of a machined surface provides more information about the cutting process and the variation of material properties than is provided by the chip. In addition, an imprint of all the static as well as dynamic forces, stresses, strains and material swelling during cutting is left in the surface roughness profile. Most previous research (Pandit and Revach, 1981, Pandit, 1981, and Sata, et al., 1985) relied on the surface roughness data in one cross-section of the workpiece only. However, there is strong experimental evidence as shown in Chapter 3 that there is some localized variation of surface roughness during ultra-precision diamond turning, due to the changing crystallographic orientation and plastic anisotropy of the work material. The conventional approaches to surface roughness measurement and hence the characterization of material properties might be inadequate. In this Chapter, a multi-spectrum analysis method (Cheung and Lee, 2000b) is proposed to analyze the formation of surface roughness. The use of the method to determine the effect of the properties of work material on the surface roughness is also discussed.

4.2 SPECTRUM ANALYSIS OF SURFACE ROUGHNESS PROFILE

4.2.1 Spectrum analysis

Spectrum analysis (Sata, et al., 1985) is a means to extract characteristic features of surface roughness profiles by transforming the surface roughness data into the frequency domain. The power spectrum of the roughness profile is determined by discrete Fourier transformation (DFT) computed with a fast Fourier transformation (FFT) algorithm. The surface roughness profile is denoted by $z(k)$ with $k = 0,1,2,...,N-1$, where N is the

number of positions in the roughness profile. The power spectrum of the roughness profile is defined by:

$$Z(\nu_n) = \frac{1}{N}\sum_{k=0}^{N-1} z(k)\exp(\frac{-2\pi j}{L} k\nu_n) \tag{4.1}$$

where n is an integer number, and ν_n is a frequency component of the surface roughness profile which represents the number of waves with a wavelength of λ_n within a unit length; that is,

$$\lambda_n = \frac{1}{\nu_n} = \frac{L}{n}. \tag{4.2}$$

N is the total number of samples with spacing Δl taken within the measured length L of the roughness profile; that is,

$$N = \frac{L}{\Delta l}. \tag{4.3}$$

The number N should be sufficiently large to avoid the problem of aliasing (Proakis and Manolakis, 1996). According to the Sampling Theorem (Proakis and Manolakis, 1996), the sample rate ν_{sample} chosen must be at least twice that of the highest non-zero frequency component ν_{max} contained in surface roughness data, that is,

$$\nu_{sample} \geq 2\nu_{max} \tag{4.4}$$

In terms of the sample spacing Δl, it is:

$$\Delta l \leq \frac{1}{2\nu_{max}} \tag{4.5}$$

In the present study, Δl is chosen to be 0.0005 mm which ensures an accurate representation of the surface roughness data with frequency content up to 1,000 cycles per mm.

The power spectral density (PSD) is directly determined from the DFT. The periodgram $|Z(\nu_n)|^2$ is obtained by transforming the real data. This will yield N transform points corresponding to N real data points, and this is equivalent to convoluting the desired frequency response $Z(\nu_n)$ with the frequency response of the rectangular truncation window function $W_r(\nu_n) = 1$; that is;

$$Z(\nu_n) = \frac{1}{N}\sum_{k=0}^{N-1} z(k)\exp(\frac{-2\pi j}{L} k\nu_n) W_r(\nu_n). \tag{4.6}$$

The frequency response of the wide rectangular truncation window is a narrow $\sin(x)/x$ or sinc function. The sidelobes of this sinc function result in a 'ringing' of the actual frequency response at the edges of the desired frequency response or the so-called Gibb's phenomenon (Mulgrew, et al., 1999). To minimize the distortion of the true spectrum attributable to Gibb's phenomenon, the spectral window corresponding to the Hanning lag window is used to get the PSD (Mulgrew, et al., 1999). The Hanning window is selected because it has spectral intensity concentrated at its main lobe in the frequency domain and hence provides more smoothing through convolution operation in the frequency domain; that is,

$$PSD(\nu_o) = 0.25[Z(\nu_p)]^2 + 0.50[Z(\nu_o)]^2 + 0.25[Z(\nu_s)]^2 \tag{4.7}$$

where $PSD(\nu_o)$ is the power spectral density at a particular frequency ν_o, ν_p and ν_s are the preceding and the succeeding frequencies for ν_o, respectively.

4.2.2 Factors affecting surface roughness and its spectrum

The surface roughness profile of a turned surface is composed of several periodical components (Ikawa, et al., 1991a and Sata, et. al., 1985). These include the tool feed, the relative tool-work vibration, tool geometry, rotational errors of the spindle as well as material properties. These components appear at different frequencies in the surface roughness spectrum with different intensities.

4.2.2.1 Effect of tool feed and tool nose radius

Figure 4.1 shows the ideal surface roughness profile and its spectrum generated at a tool nose radius of 2.0 mm and a feed rate of 0.01 mm per rev. The feed components appear at frequencies of $v_{Fn_f} = (n_f + 1)/s$, where s equals the feed per revolution of the workpiece and n_f denotes the number of harmonics. Since an ideal surface produced by the tool nose is periodic but not sinusoidal, its FFT spectrum would have a small but significant power spectral density at the harmonics of the feed frequency.

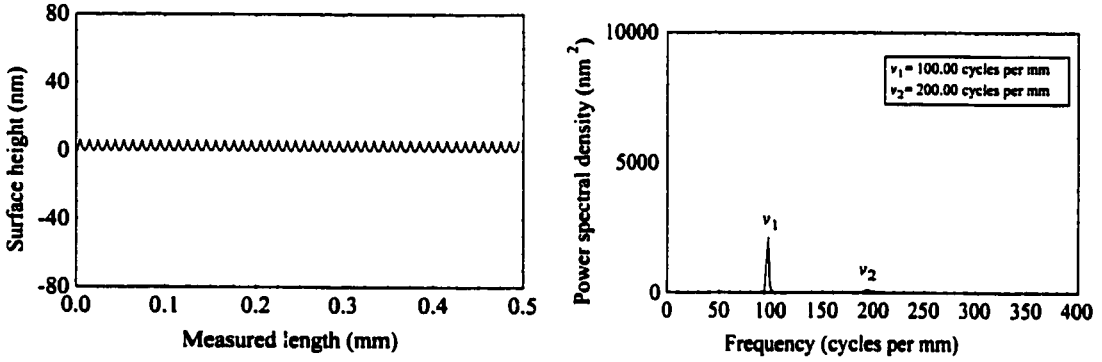

(a) (b)

Figure 4.1 (a) Ideal surface roughness profile and (b) its spectrum

Remarkable feed components are observed only when the tool nose radius is small relative to the tool feed rate. Among these feed components, the fundamental frequency of

the feed component (i.e. $n_f = 0$) is predominant and is usually used to characterize the effect of feed rate and tool geometry in the FFT spectrum analysis.

4.2.2.2 Effect of relative vibration between the tool and the workpiece

Relative vibration between the tool and the workpiece with small amplitude and low frequency (Ikawa, et al., 1991a and Takasu, et al., 1985) usually occurs in ultra-precision machine tools even if supported on air mounts and special bases. Such vibration causes the formation of surface modulations or waviness in both the cutting and the tool feed directions. Because of the long wavelength and periodicity of the surface waviness in the tool feed direction, it appears as a sharp peak in the spectrum of the surface roughness profile. The frequency of surface modulation can be deduced as follows :

Firstly, a ratio between the frequency f_z of the vibration to the rotational speed V of the workpiece in revolutions per minute (rpm) can be determined by Equation (3.4). The phase shift ϕ is then calculated by Equation (3.5). Hence, the frequency ν_{TW} of the surface waviness formed on the workpiece surface in the tool feed direction can be expressed in terms of ϕ and a tool feed s per workpiece revolution as

$$\nu_{TW} = \frac{\phi}{2\pi s} . \tag{4.8}$$

4.2.2.3 Effect of material properties

As discussed in Chapter 3, the workpiece material swells at the end of the active cutting edge during machining. This causes a greater and deeper tool mark (Sata, et al., 1985). In the region below the chip, complicated elastic and plastic deformation occurs (Shimada, et al., 1993 and Whitehouse, 1994) which is caused by the indentation and/or burnishing by the cutting edge. The workpiece material left behind the front clearance of the tool springs back or recovers after burnishing (Figure 3.13). The amount of recovery is

determined by the forces on the clearance face and by the crystallographic orientation of the substrate material being cut. These modify the surface roughness profiles on the machined surface. The effect of swelling increases the power spectral density of the feed components in the surface roughness spectrum. The amount of swelling depends on the properties and crystallographic orientation of the material being cut. The softer and more ductile the material, the greater will be the swelling effect (Sata, 1964).

To quantify the swelling effect in ultra-precision diamond turning, a local swelling ratio SR_i at the i th radial section of the machined surface (see Figure 4.2) is defined as the square root of the ratio of the power spectral density for the first feed components of the measured and of the ideal surface roughness spectrum. Thus,

$$SR_i = \sqrt{\frac{PSD_i(\nu_{FM,i})}{PSD_i(\nu_{FI,i})}} \qquad \text{for } i = 1,2,\ldots,m \tag{4.9}$$

where $\nu_{FI,i}$ and $\nu_{FM,i}$ are the frequencies of the first feed components of the ideal and of the measured surface roughness spectrum at i th radial section, respectively. $PSD_i(\nu_{FI,i})$ and $PSD_i(\nu_{FM,i})$ are the corresponding power spectral densities, respectively.

Then, the degree of swelling is determined by a swelling ratio, SR, which is defined as the average of the local swelling ratios for m radial sections. Thus,

$$SR = \frac{\sum_{i=1}^{m} SR_i}{m}. \tag{4.10}$$

The swelling ratio provides a quantitative measure for the swelling effect on a machined surface. However, as mentioned previously, the material recovers differently for different crystallographic orientations of the substrate material. In other words, the surface roughness is influenced by the plastic anisotropy of the material being cut. In such plastic

anisotropy materials like single crystals, the material properties vary with the crystallographic orientation. The swelling ratio alone might not be sufficient to explain the anisotropic properties of the work material. Some attempts have been reported in correlating the anisotropy of the material from the microscopic free surface morphology of the chips (Furukawa and Moronuki, 1988). However, because of chip curl and other distortions, an accurate analysis of the effects of swelling and plastic recovery is often difficult to make.

In the present study, a parameter, the so-called coefficient of anisotropy COA, is proposed to measure the anisotropic properties of the material. The parameter's definition is based on the local swelling ratios and the average swelling ratio as follows :

$$COA = \frac{\sigma_{SR}}{SR} = \frac{m\sqrt{\sum_{i=1}^{m}(SR_i - SR)^2}}{\sqrt{m-1}\sum_{i=1}^{m} SR_i}, \tag{4.11}$$

where σ_{SR} is the standard deviation of the local swelling ratios for the m radial sections on the surface.

For homogeneous and isotopic material, the localized swelling is constant throughout the workpiece. Therefore, its coefficient of anisotropy is zero. On the other hand, the coefficient of anisotropy for highly anisotropic materials such as single crystals would be large.

4.2.2.4 Effect of spindle error motions

The spindle of a machine tool has error motions. These error motions can be classified into two types in face turning: the axial error motions and radial error motions. Axial error motion of the spindle is a kind of relative tool-work vibration, and its effects on the surface roughness spectrum can be determined in a way similar to that described in Section 4.2.2.2.

If the spindle radial and axial error motions are synchronous, the spindle radial error contributes to the tool-work vibration at the harmonics of the spindle axial error.

4.2.2.5 Effect of materials induced vibration

The depth of cut in ultra-precision machining is usually less than the average grain size of a polycrystalline aggregate, and the chip forms in the region of a single grain. Single crystals are known to be highly anisotropic in their physical and mechanical properties. With regard to the quality of the machined surface, the elastic and plastic anisotropy of the crystalline material must be taken into account. For example, the Young's modulus of elasticity of copper single crystals varies with different crystallographic orientations by a factor of 2.9.

Because of the unchanging stiffness of the cutting system, the alternation of Young's modulus of the grains is believed to result in surface undulations of the machined substrate material. This can be observed in the machining of a polycrystalline copper substrate (Stadler, et al,1987). As cutting takes place within individual grains, the statistical distribution of crystal defects and their interaction with the stress field around the tool tip plays a dominant role in the cutting mechanism. Sato., et al. (1978) found that the shear angles and the cutting forces vary with orientation in single crystals and in polycrystalline materials. Black (1972) has reported a variation in the shear front-lamellar structure at the top of the chip with grain orientation. Most researchers infer that shear planes in metal cutting are dislocation glide planes themselves.

Any variation in the shear strength and the shear angle with respect to the crystallographic orientation of the crystal being cut causes a fluctuation of the micro-cutting force (Lee, 1990). The vibration caused by such variations is a kind of materials induced vibration (Lee, Cheung and To, 1999) which can not be eliminated by machine tool design or process control. The materials induced vibration degrades the surface quality of any diamond turned surfaces.

Although some attempts (Lo-A-Foe, et al., 1988) have been made to predict the variation of the surface roughness from a cutting force model, little quantitative work (Furukawa and Moronuki, 1988) has been done to analyze the effect of materials induced vibration. In the present study, a multi-spectrum analysis method is used to determine the characteristics of the materials induced vibration and its effects on the surface roughness of a diamond turned surface.

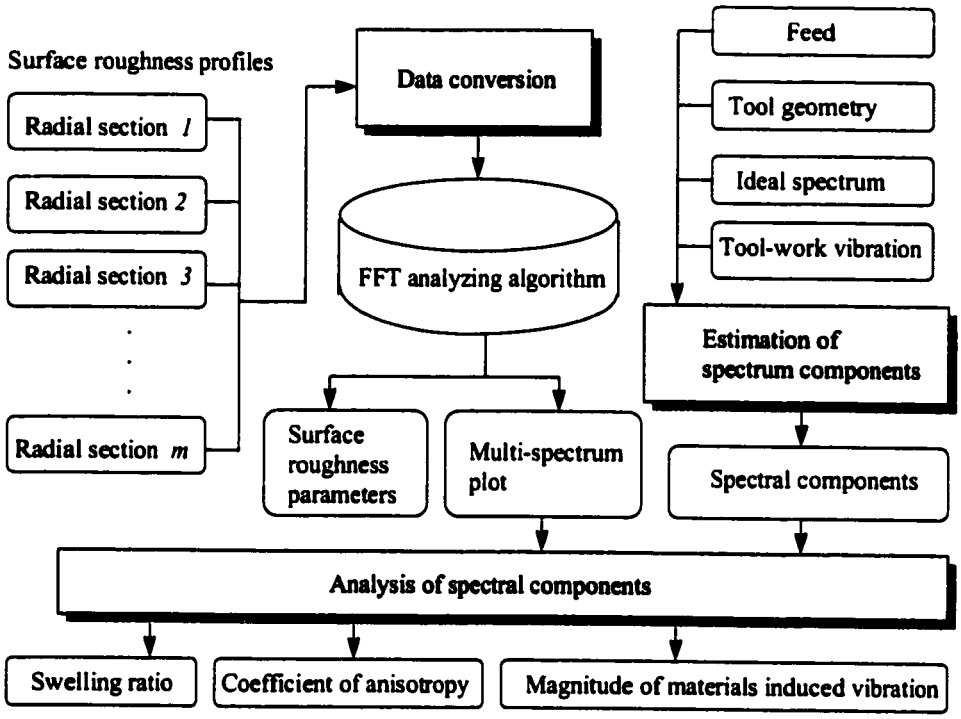

Figure 4.3 A block diagram of the multi-spectrum analysis method

4.3 MULTI-SPECTRUM ANALYSIS

Figure 4.3 shows the block diagram for the multi-spectrum analysis method. In the method, the surface roughness profiles at a finite number of equally spaced radial sections (i.e. φ is constant) of a turned surface are measured. The spectra of these surface roughness profiles are then determined using the FFT analyzing algorithm described in Section 4.2.1. Hence, a multi-spectrum plot is constructed that depicts the change of the

patterns of surface roughness spectra at different radial sections of the workpiece. The spectral components in the multi-spectrum plot are compared with those pre-determined by the analysis techniques discussed in Section 4.2.2. Since the surface roughness measurements were made on the same surface, the effects of machining conditions, i.e. dynamic conditions of the machine, the tool geometry and the other environmental factors on the surface roughness were assumed to be the same. Any variations of the spectral patterns would be attributed to the variation of the material properties and materials induced vibration. By analyzing the change of the spectral patterns in the multi-spectrum plot, it is possible to determine the effects of the material anisotropy and the materials induced vibration on the surface roughness profiles. A software package was purpose built for conducting the multi-spectrum analysis. The program is written in MATLAB language and a listing of source codes is given in Appendix I.

The following notations are defined for the subsequent analysis:

(i) $\nu_{TW,i}$ denotes the frequency of the dominant mode of tool-work vibration or spindle error motions at the i th radial section of the work surface.

(ii) $\nu_{MA,i}$ denotes the frequency of the materials induced vibration at the i th radial section of the work surface.

(iii) $\nu_{FM,i}$ denotes the fundamental frequency of the feed component at the i th radial section of the work surface.

(iv) $\nu_{FI,i}$ denotes the fundamental frequency of the feed component at the i th radial section of an ideal surface.

(v) $\nu_{Fn_f,i}$ denotes the frequency of the n_f th harmonics of the feed component at the i th radial section of the work surface.

4.4 EXPERIMENTS

Face cutting tests were conducted on aluminium single crystals and alloys using a two-axis CNC ultra-precision machine (Nanoform 300 from Taylor Hobson Pneumo Co.). Table 4.1 tabulates the specifications of the workpiece materials and the cutting conditions

being used. To remove the work deformed layer generated during the pre-machining process, the surfaces of the specimens were electropolished before the cutting tests. The specimens were firstly mechanically ground and then polished using diamond paste of 1 μm. Subsequently, they were electro-polished at room temperature in solution containing 10 vol. % perchloric acid (70%) and 90 vol % absolute ethanol for about 60 seconds. The voltage was set at 10 V by adjusting the current in about 0.02A steps. The crystallographic orientation of the workpiece was examined by a standard reflection technique with a X-Ray diffractometer. For Specimen 4A, the crystallographic orientation at radial section 1 was determined to be $(001)[0\bar{1}0]$ while that for Specimen 4B was $(110)[001]$.

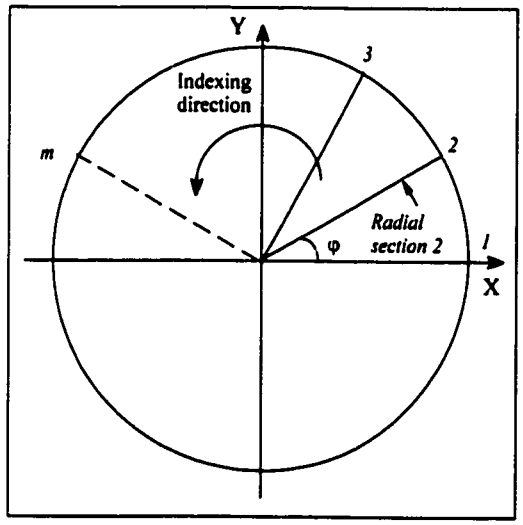

Figure 4.2 Illustration of the surface roughness measurement

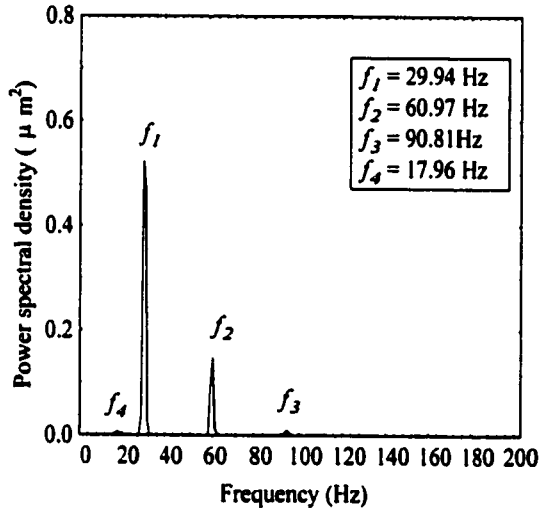

Figure 4.4 Frequency spectrum of the relative vibration between the tool and the workpiece

Table 4.1 Materials and cutting conditions

Materials	Specimen 4A : (001) aluminium single crystal Specimen 4B : (110) aluminium single crystal Specimen 4C : aluminium alloy (6061)
Spindle rotational speed	2000 rpm
Feed rate	20 mm mm^{-1}
Depth of cut	5 μm
Tool rake angle	0.0°
Front clearance angle	12.5°
Tool nose radius	2.0 mm

The vibration between the tool and the workpiece was measured on the centre line of the spindle by a capacitive displacement sensor while air cutting. Figure 4.4 shows the frequency spectrum of the displacement sensor signal. Remarkable modes of vibration at frequencies (i.e. f_1, f_2, f_3 and f_4) of 29.98 Hz, 60.97 Hz, 90.81 Hz and 17.96 Hz were observed. The first vibration mode at frequency, f_1, is close to the axial error specifications of the air bearing spindle. Modes of vibration at frequencies f_2 and f_3 seemed to be the first and the second harmonics of the frequency of the axial spindle error. These might be attributed to the radial error motion of the spindle if the spindle axial and radial errors are synchronous. The vibration mode at frequency f_4, might be due to low frequency tool-work vibration originating from the machine base. Since the spectral components at frequencies f_3 and f_4 only contribute a relatively small proportion of the overall spectrum, they can be neglected for the ease of the analysis. From Equations (3.4), (3.5) and (4.8), the vibration modes at frequencies f_1 and f_2 would form the spectrum peaks in the surface roughness spectrum at frequencies of 10.06 cycles per mm and 17.09 cycles per mm, respectively.

Surface roughness profiles at twelve radial sections (i.e. $\varphi = 30^o$) on a turned surface were measured with a Form Talysurf system equipped with a rotary table with a resolution of 0.017°. The measured length and the cut-off length were fixed at 1.75 mm and 0.25 mm respectively. For Specimens 4A and 4B, the measurements were started at the initial orientation of the workpiece. Figure 4.5 depicts a schematic diagram of the data acquisition system. The measured surface roughness data are first fed into a data conversion software and are converted to the ASCII data format. The converted data are analyzed by a multi-spectrum analysis program exclusively developed for determining the spectra of the surface roughness profiles at different radial sections of the workpiece simultaneously. The outputs of the program are the surface roughness profiles, the roughness parameters, as well as the spectrum for each of the radial sections being analyzed.

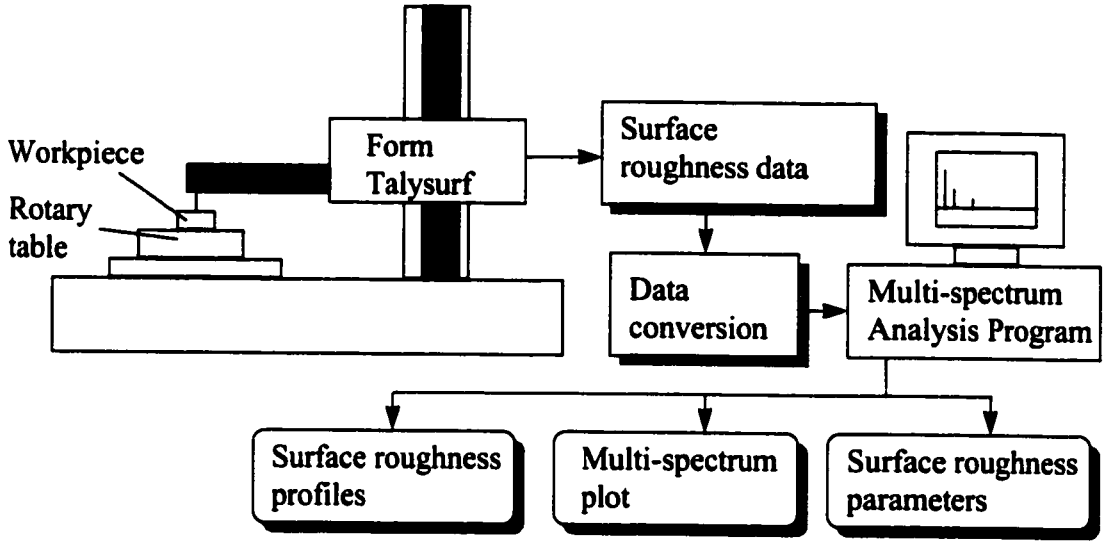

Figure 4.5 Schematic diagram of the data acquisition system

4.5 RESULTS AND DISCUSSION

4.5.1 Variation of the surface roughness profiles and parameters

Figure 4.6(a) and Figure 4.6(b) show the arithmetic roughness, R_a, of the aluminium single crystals at different radial sections as cutting is done on the (001) plane and the (110) plane, respectively. The arithmetic roughness is found to vary systematically for different crystallographic planes. It is noticed that the (110) crystal causes greater variations but smaller surface roughness than the (001) crystal. The variation of the arithmetic roughness is less for the polycrystalline material (i.e. aluminium alloy 6061) as shown in Figure 4.6(c). The results were confirmed by the calculated means and normalized standard deviations as summarized in Table 4.2. Table 4.3 tabulates the means, the standard deviations and the normalized standard deviations of five cut-off taken at radial section 1. Comparing Table 4.2 with Table 4.3, it can be seen that the natural variation within a given section is relatively smaller than that between sections. This further confirms that the variation of the surface roughness with crystallographic orientation of the work material is significant.

The surface roughness profiles and spectrum plots at the initial radial section of the specimens are shown in Figure 4.7 to Figure 4.9. Significant differences among the surface roughness profiles are observed in Figure 4.7(a), Figure 4.8(a) and Figure 4.9(a). Higher frequencies of surface modulation are found on the (110) plane as compared to the (001) plane. In the aluminium alloy, the frequency of surface modulation is the lowest.

Table 4.2 Results of surface roughness measurement at different radial sections

Specimens	Arithmetic roughness R_a (nm)		
	Mean, $\overline{R_a}$	Standard deviation , σ_{R_a}	Normalized standard deviation $\sigma_{R_a} / \overline{R_a}$
4A	17.76	1.313	0.074
4B	17.18	2.387	0.139
4C	12.11	0.440	0.036

Table 4.3 Results of surface roughness measurement for the five cut-off taken at the radial section 1

Specimens	Arithmetic roughness R_a (nm)		
	Mean, $\overline{R_a}$	Standard deviation , σ_{R_a}	Normalized standard deviation $\sigma_{R_a} / \overline{R_a}$
4A	17.85	0.653	0.037
4B	13.34	0.499	0.037
4C	11.27	0.492	0.044

Comparing the spectrum plots in Figure 4.7(b), Figure 4.8(b) and Figure 4.9(b) ,the feed rate component and its harmonics ($\nu_{FM,1}, \nu_{F1,1}, \nu_{F2,1}$) are found at almost the exact frequencies as predicted for the fundamental frequency (100 cycles per mm), the first (200 cycles per mm) and the second harmonics (300 cycles per mm), respectively. The effect of the dominant mode of tool-work vibration (29.98 Hz) is reflected at the component, $\nu_{TW,1}$,of the spectrum plots. The measured values are approximately the same as the predicted value of 10.06 cycles per mm. The spectral component at frequency $\nu_{MA,1}$, is found to vary with the material and crystallographic plane being cut. The (110) crystal causes a higher frequency at $\nu_{MA,1}$ than the (001) crystal. The frequency $\nu_{MA,1}$ is slightly higher for the

(001) crystal than for the polycrystalline aggregate. These results agree with those observed in the surface roughness profiles of Figure 4.7(a), Figure 4.8(a) and Figure 4.9(a).

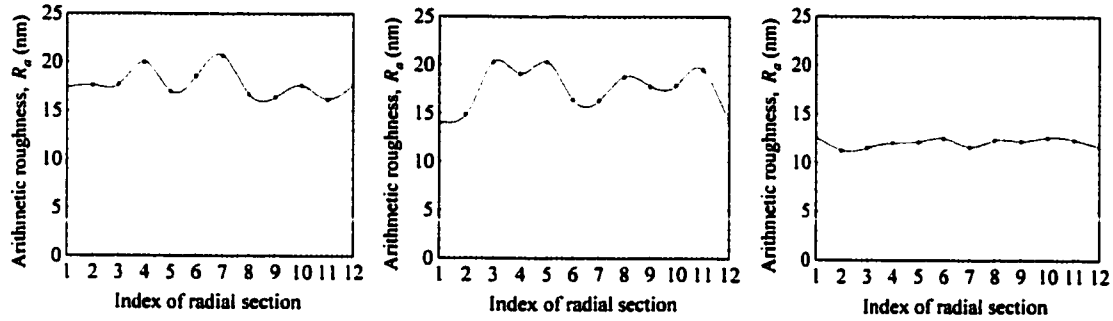

Figure 4.6 Variation of arithmetic roughness R_a at different radial sections of: (a) the (001) single crystal aluminium; (b) the (110) single crystal aluminium and (c) the aluminium alloy (6061)

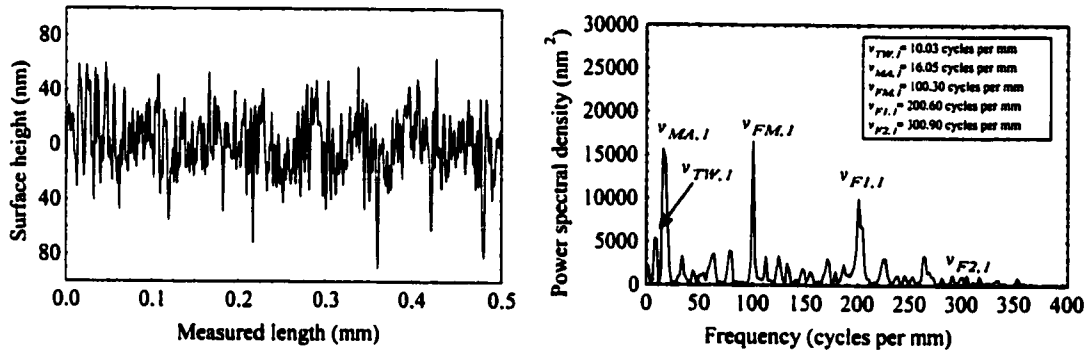

Figure 4.7 (a) Measured surface roughness profile and (b) its spectrum for the (001) aluminium single crystal at radial section 1

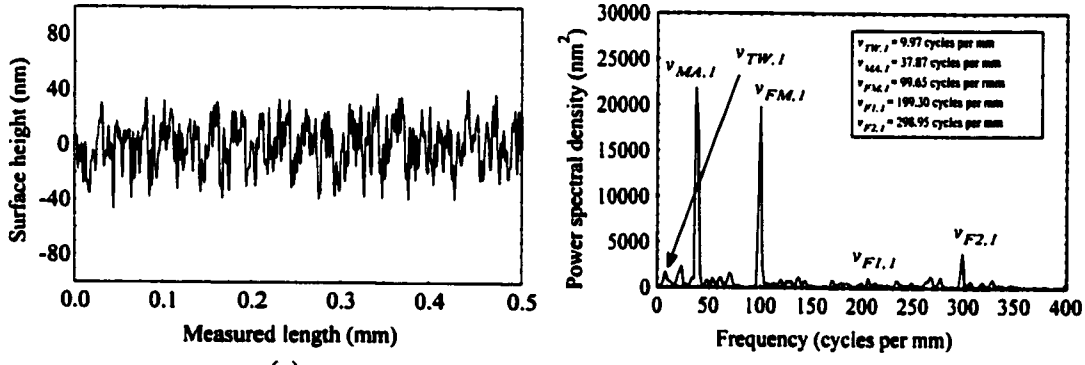

Figure 4.8 (a) Measured surface roughness profile and (b) its spectrum for the (110) aluminium single crystal at radial section 1

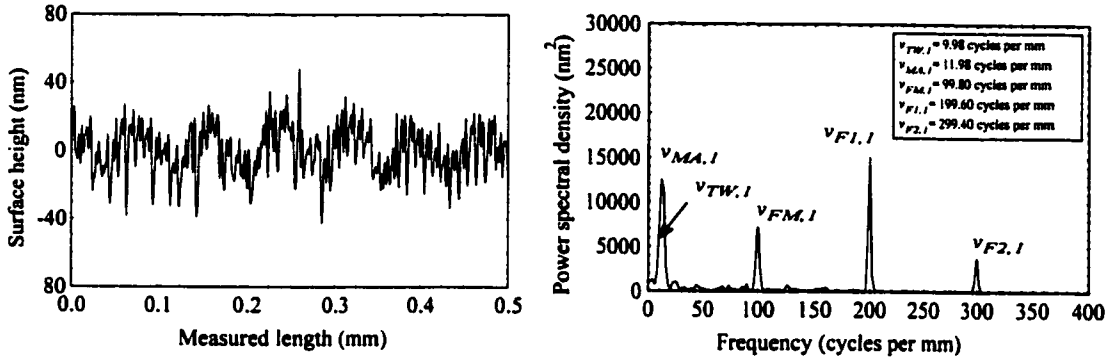

(a) (b)

Figure 4.9 (a) Measured surface roughness profile and (b) its spectrum for the aluminium alloy (6061) at radial section 1

4.5.2 Patterns of multi-spectrum plots

Figure 4.10(a) shows an ideal multi-spectrum plot simulated for an isotopic and homogeneous material being cut under vibration-free conditions. The simulation was performed with the same cutting parameters as shown in Table 4.1. It is noted that the power spectra are identical for different radial sections of the workpiece. Figures 4.10(b), 4.10(c) and 4.10(d) show the measured multi-spectrum plots for Specimen 4A, 4B, and 4C, respectively. The measured multi-spectrum plots are composed of strong feed components. For aluminium single crystals (Specimen 4A and 4B), the multi-spectrum plots exhibit a large fluctuation of the power spectral density at the first feed component for different radial sections of the workpiece. Significant low frequency components are also observed in all measured multi-spectrum plots. The distribution of these low frequency components varies with the radial sections of the work material. Greater variations are observed for the aluminium single crystals than for the polycrystalline alloy.

Table 4.4 Comparison of the swelling ratios and coefficients of anisotropy for the three specimens

Specimens	Range of local swelling ratios, SR_i	Swelling ratio SR	Coefficient of anisotropy COA
4A	1.486-4.472	3.209	0.321
4B	2.875-6.472	4.565	0.210
4C	1.358-2.582	2.028	0.146

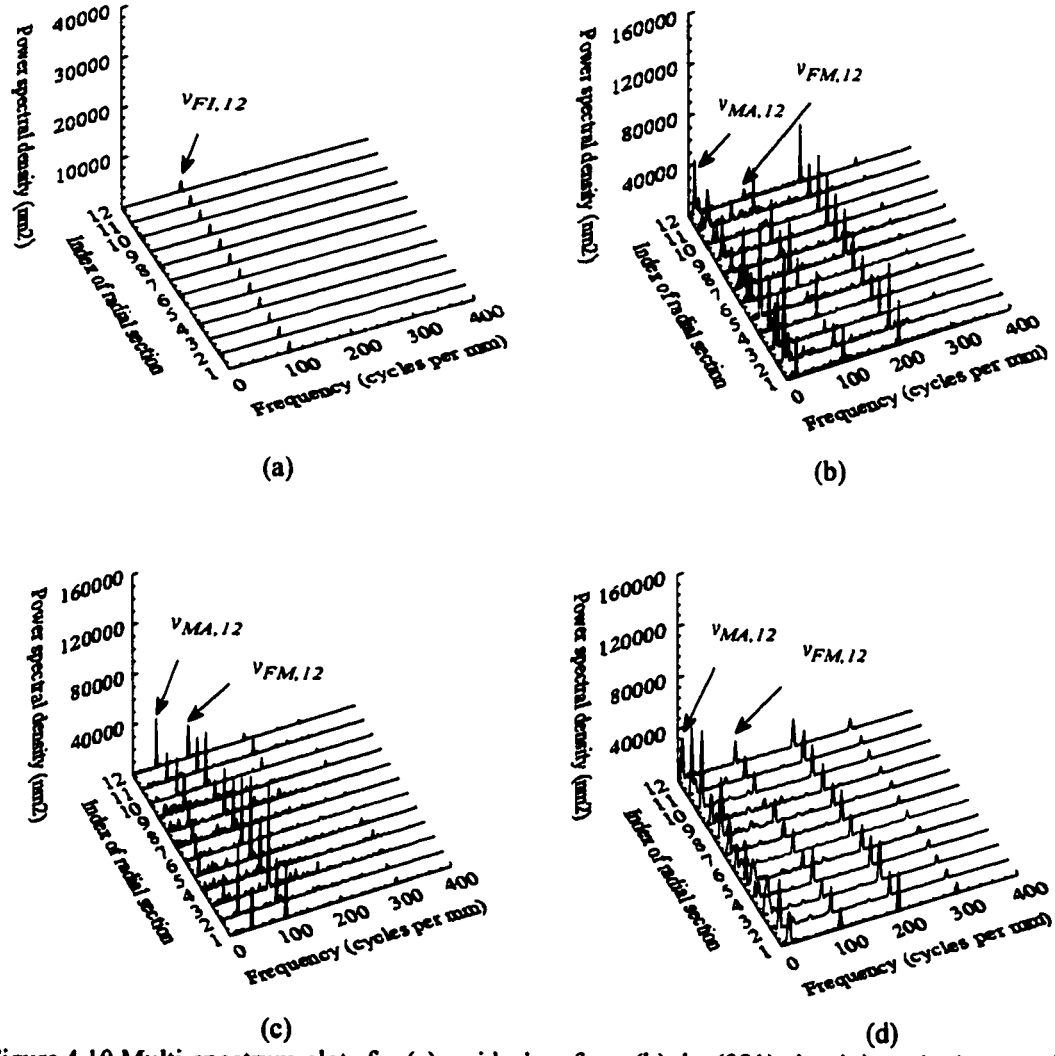

Figure 4.10 Multi-spectrum plots for (a) an ideal surface; (b) the (001) aluminium single crystal; (c) the (110) aluminium single crystal and (d) the aluminium alloy (6061)

4.5.3 Material swelling and plastic anisotropy

Comparing the measured multi-spectrum plot with the ideal ones, it is found that the spectral density of the first feed component for all specimens is significantly higher than that for the ideal ones. This implies the presence of a swelling effect for the materials being investigated. As shown in Figure 4.11, the local swelling ratios at different radial sections are found to vary differently with the materials being cut. Greater variations are observed

for the (110) crystal than for the (001) crystal. As discussed in Section 4.2.2.3, the extent of the variations indicates the degree of plastic anisotropy of the work materials. Table 4.4 summarizes the calculated swelling ratio (SR) and coefficient of anisotropy (COA). Aluminium alloy is shown to give the smallest swelling ratio and coefficient of anisotropy among the materials being investigated. In other words, the alloy swells less than the aluminium single crystals. The amount of swelling and plastic anisotropy is greater for the (110) single crystal aluminium than its (001) counterpart. Comparing Figure 4.11 with Figure 4.6, there is a fair agreement between the variation of the measured arithmetic roughness and the local swelling ratio. A larger local swelling ratio corresponds to a greater arithmetic roughness.

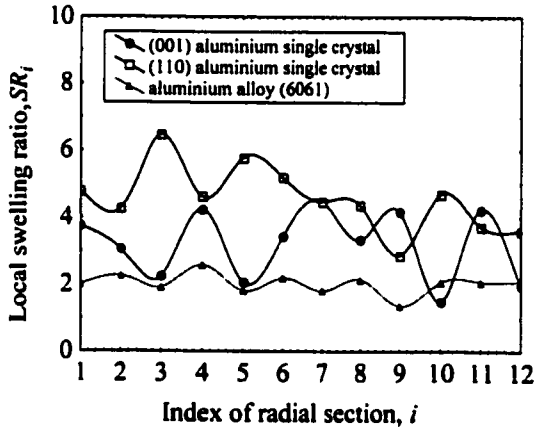

Figure 4.11 Variation of swelling ratios at different radial sections of the workpiece

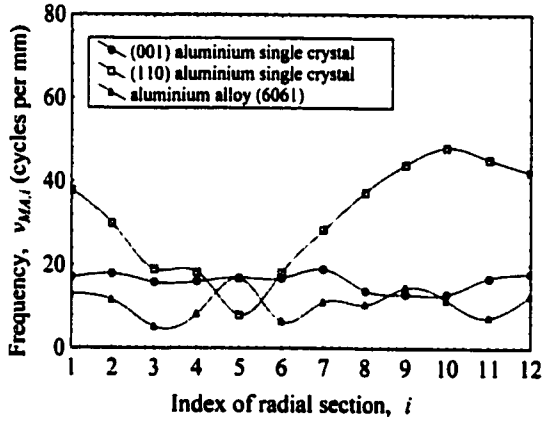

Figure 4.12 Trajectory of the variations of the natural frequency $v_{MA,i}$

4.5.4 Materials induced vibration

Figure 4.12 shows a plot of the variation of the frequency $v_{MA,i}$ at different radial sections of the specimens. Different patterns of variations are observed. Each material seems to possess its own characteristic pattern of frequency variation, which could not be explained by the machine vibration and spindle rotational errors for a number of reasons. Firstly, the specimens were machined under identical cutting conditions. Secondly, the spectral peaks for the single crystals at frequency $v_{MA,i}$ are found in a frequency range well

above the one caused by the dominant mode of the relative tool-work vibration (i.e. 10.06 cycles per mm) as determined in Section 4.4. A possible cause for such a variation is the vibration induced by the changing crystallographic orientation of the workpiece material during a revolution of cut, i.e., the materials induced vibration. The use of the multi-spectrum analysis method allows us to infer the patterns of materials induced vibration in a diamond turning process and its effect on surface roughness.

4.6 SUMMARY

The mechanism of surface generation in ultra-precision diamond turning has been investigated by using a multi-spectrum analysis method. The results indicate that the surface roughness varies systematically at different radial sections. The variations depend on the crystallographic orientations of the workpiece material. The arithmetic roughness R_a is found to be strongly correlated to the local swelling ratios determined from the feed components of the surface roughness spectrum. It is also found that the tool feed, the spindle rotational errors, the tool geometry and the relative tool-work vibration are not the only dominant components affecting the surface roughness in diamond turning. The materials induced vibration caused by the variation of crystallographic orientation is a major factor which affects the surface formation on the nanometer scale. The induced vibration results in a significant variation of the frequency of the surface modulation at different radial sections of a turned surface. With the use of the multi-spectrum analysis method, it is not only possible to evaluate the material response such as the swelling of a turned workpiece, but also to infer the patterns of materials induced variation and its effect on the surface roughness.

Chapter 5

Multiple Data Dependent Systems (MDDS) Analysis of Cutting Dynamics

5.1 INTRODUCTION

A multi-spectrum analysis method has been proposed in Chapter 4 for analyzing the surface generation in diamond turning. The method has been demonstrated to be useful for characterizing the influence of material anisotropy, swelling and materials induced vibration upon the surface generation. However, the method was incapable of determining the exact contribution of individual factors upon the overall surface roughness. In this Chapter, a multiple data dependent systems (MDDS) method (Cheung and Lee, 2000c) is proposed to overcome this shortcoming.

The MDDS method is based on a Data Dependent Systems (DDS) modelling procedure (Pandit and Wu, 1983) which provides a parsimonious mathematical model for correlating the metal cutting dynamics with their respective contributions to the total roughness of a diamond turned surface. Individual components composed of the surface roughness profiles can be studied simultaneously at different radial sections of the workpiece. The MDDS method has been shown to be effective in characterizing the effect of process parameters and material crystallography on the metal cutting dynamics and surface roughness in SPDT.

5.2 MULTIPLE DATA DEPENDENT SYSTEMS (MDDS) ANALYSIS

5.2.1 Theoretical background of Data Dependent Systems (DDS) modelling procedure

The Data Dependent Systems (DDS) modelling procedure (Pandit and Wu, 1983) is based on two theorems called the Fundamental Theorem and the Uniform Sampling Theorem (Pandit, 1981). It consists of fitting Autoregressive Moving Average ARMA

$(n, n-1)$ models into a non-linear least squares errors searching algorithm until the sum of squares of the prediction error can not be significantly reduced as judged by the F-test (Pandit and Wu, 1983). The advantage of the DDS approach over FFT is not merely in providing the parsimonious mathematical models of physical significance, but also in quantifying the power and damping ratios of all modes (Pandit, 1981). It provides statistically adequate models in the form of difference equations, directly from the measured surface roughness data as shown in Equation (5.1).

$$X_t - \phi_1 X_{t-1} - \ldots - \phi_n X_{t-n} = a_t - \theta_1 a_{t-1} - \ldots - \theta_{n-1} a_{t-n+1} \tag{5.1}$$

where X_t is the measured height of the surface roughness profile; a_t's are the independent series with variance σ_a^2 i.e. the white noise; $\phi_1, \phi_2, \ldots, \phi_n$ are the autoregressive coefficients; and $\theta_1, \theta_2, \ldots, \theta_{n-1}$ are the moving average coefficients.

The left hand side of the Equation (5.1) is the autoregressive (AR) part of the model which can be expressed by :

$$(1 - \phi_1 B - \phi_2 B^2 - \ldots - \phi_n B^n) \equiv (1 - \lambda_1 B)(1 - \lambda_2 B)\ldots(1 - \lambda_n B) \tag{5.2}$$

B is the backward shift operator defined by $BX_t = X_{t-1}$. Equation (5.2) represents a n-th order differential equation with characteristic roots $\mu_1, \mu_2, \ldots, \mu_n$ which are related to $\lambda_1, \lambda_2, \ldots, \lambda_n$ of the difference Equation (5.1) by :

$$\lambda_i = e^{\mu_i \Delta} \qquad \text{,for } i = 1,2,\ldots,n \tag{5.3}$$

where Δ is the sampling interval.

The ARMA(n,n-1) model in Equation (5.1) can be rewritten in the transfer function form by using the backward shift operator as :

$$X_t = \frac{(1-\theta_1 B-\theta_2 B^2-\ldots-\theta_{n-1}B^{n-1})}{(1-\phi_1 B-\phi_2 B^2-\ldots-\phi_n B^n)}a_t$$

$$= \sum_{j=0}^{\infty} G_j a_{t-j} \qquad \text{,for } i = 1,2,\ldots,n \tag{5.4}$$

G_j is the Green's function which can be determined by applying partial fractions to Equation (5.4) as :

$$G_j = g_1\lambda_1^j + g_2\lambda_2^j + \ldots + g_n\lambda_n^j \tag{5.5}$$

where

$$g_i = (\lambda_i^{n-1} - \theta_1\lambda_i^{n-2} - \ldots - \theta_{n-1}) / \prod_{\substack{j=1 \\ j\neq i}}^{n}(\lambda_i - \lambda_j) \tag{5.6}$$

$$d_i = \left(\frac{g_i g_1}{1-\lambda_i\lambda_1} + \frac{g_i g_2}{1-\lambda_i\lambda_2} + \ldots + \frac{g_i g_n}{1-\lambda_i\lambda_n} \right)\sigma_a^2 \qquad \text{,for } i = 1,2,\ldots,n \tag{5.7}$$

For the diamond turning process, the components g_i of the Green's function G_j are the results of inherent periodicity interacting with various process elements. Thus, the Green's function may represent a characteristic shape of the random profile and together with a_t provides a complete physically characterization of the cutting dynamics.

The variance or total power of the roughness profile is given by

$$\gamma_o = d_1 + d_2 + \ldots + d_n \tag{5.8}$$

For a pair of complex conjugate roots, λ_i, λ_{i+1}, this percentage is :

$$P = \frac{100(d_i + d_{i+1})}{\gamma_0} \tag{5.9}$$

For a real root λ_i, this percentage is given as :

$$P = \frac{100 d_i}{\gamma_0} \tag{5.10}$$

The order of the model is usually increased in an even number of step size since an odd number step size of order increment will force a root of the system to be real, not allowing for complex conjugate pairs. The statistical significance of the reduction in the sum of squares after increasing the order of the model is checked by an F-test (Pandit and Wu, 1983) at 5-percent level of significance as follows :

$$F = \frac{E_1 - E_0}{S} \Big/ \frac{E_0}{N - r} \sim F(S, N - r) \tag{5.11}$$

where N is the number of surface roughness data, E_0 is the sum of squares of the ARMA$(2n+2,2n+1)$ model, E_1 is the sum of squares of the ARMA$(2n,2n-1)$ model, and $F(S,N-r)$ denotes the F distribution with S and $N-r$ degrees of freedom. For the test of ARMA$(2n,2n-1)$ against ARMA$(2n+2,2n+1)$, the degree of freedom r and the number of additional parameters S in the higher-order model are $(2n+2)+(2n+1)=4n+3$ and $(4n+3)-[4(n-1)+3]=4$, respectively.

Should the F value exceed the value $F(S,N-r)$ at 5% level of significance, then the improvement in the residual sum of squares in going from the ARMA$(2n,2n-1)$ model to the ARMA$(2n+2,2n+1)$ model is significant. There is strong evidence to reject the hypothesis that the ARMA$(2n,2n-1)$ model is adequate. If the F value is less than the value from the F table, it can be concluded that the model is adequate at that level of significance and the modelling procedures are completed.

5.2.2 Multiple Data Dependent Systems (MDDS) method

As shown in Figure 5.1, the MDDS method makes use of a data dependent systems (DDS) model to provide component by component wavelength decomposition of the surface roughness profiles at a finite number of equally spaced radial sections (i.e. φ is a constant) of a diamond turned surface. The components of metal cutting dynamics in terms of natural frequency, damping ratio, central wavelength and contribution to total power are determined using a DDS modelling algorithm described in Section 5.2.1. According to their inherent characteristics, these components are classified into four main categories named the feed and tool nose radius, the relative tool-work vibration, the material crystallography and the machine vibration, respectively. Since the surface roughness measurements were made on the same surface, any variations of the frequency distribution and percentage contribution to the total power would be due to the variations of the material properties and materials induced vibration. By analyzing the variation of the patterns of the frequency and power distributions, it is possible to conjecture the effects of the material anisotropy and the materials induced vibration on the surface generation.

5.3 EXPERIMENTAL PROCEDURES

The cutting experiments were divided into two groups i.e. Group 5A and Group 5B. Group 5A included those cutting tests conducted on an aluminium alloy (6061) using different cutting conditions as tabulated in Table 5.1. In Group 5B, cutting tests were done on different materials (Table 5.2) using cutting conditions with the spindle speed of 2000 rpm, feed rate of 20 mm per min, tool nose radius of 2.0 mm and depth of cut of 5 μm. The surface roughness profiles at 12 radial sections on a specimen were measured as depicted in Figure 5.1. Each of the measurement was performed at an equally angular spacing φ of 30 degrees. All experiments were carried out on a two-axis CNC ultra-precision machine (Nanoform 300 from Taylor Hobson Pneumo Co.). The surface

roughness profiles and roughness parameters were measured by a Form Talysurf system equipped with a rotary table with a resolution of 0.017°. A cut-off length of 0.25 mm is used throughout the experiments. The wavelength decompositions were performed by a MDDS program exclusively developed for the investigation (see Appendix II).

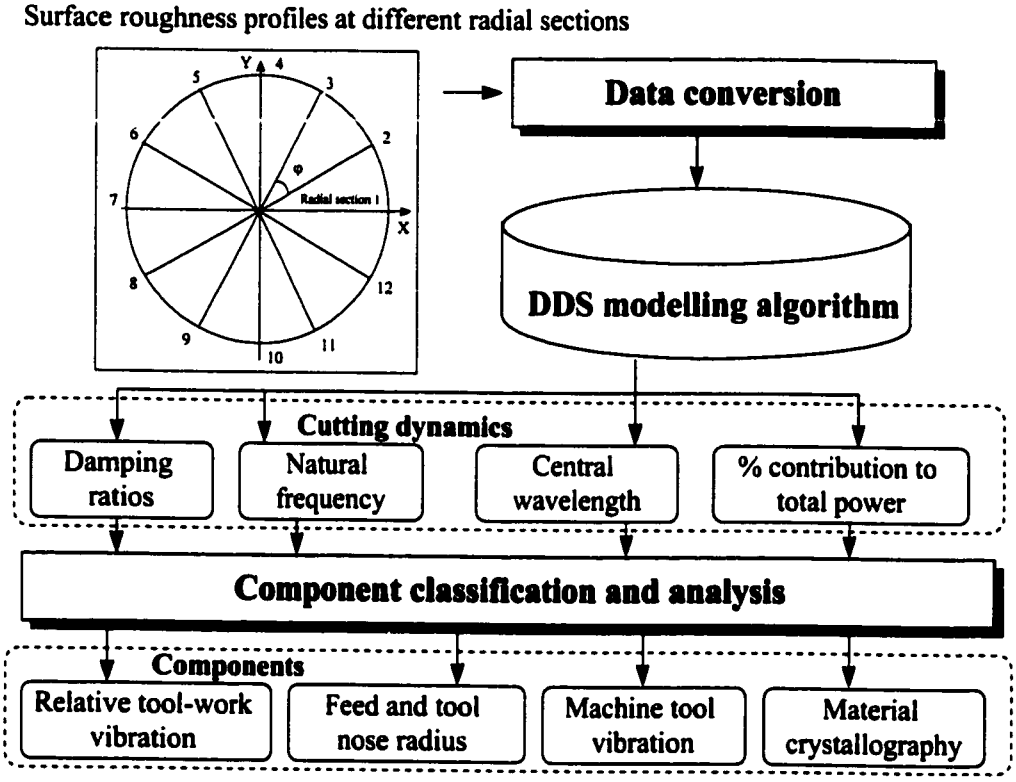

Figure 5.1 Schematic diagram of the MDDS method

Figure 5.2 depicts a schematic diagram of the data acquisition system. The surface roughness profiles of the workpiece are firstly measured by a Form Talysurf machine. The measured surface roughness data are then fed into a data conversion software which converts these into ASCII file format for the MDDS analysis. The converted data are analyzed by the MDDS program.

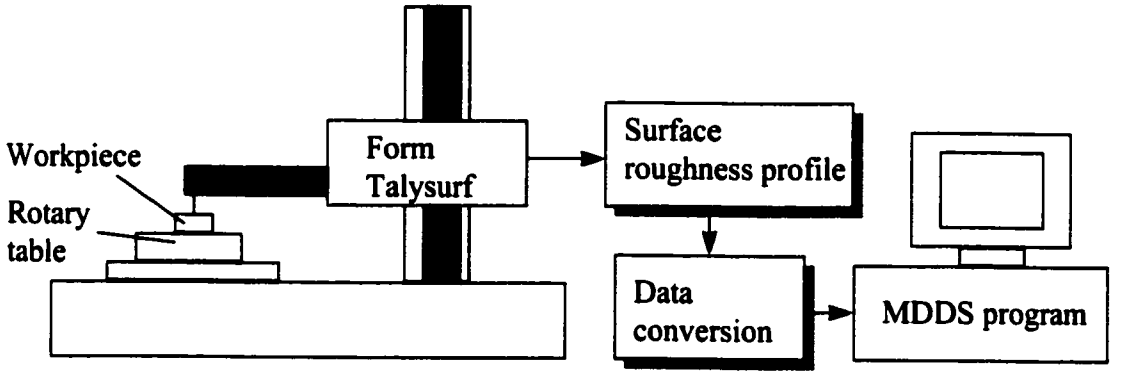

Figure 5.2 Block diagram of the data acquisition system

Table 5.1 Cutting conditions for the experiments in Group 5A

Specimen no.	Cutting conditions				
	Feed rate (mm min^{-1})	Spindle speed (rpm)	Feed rate (mm rev^{-1})	Tool nose radius (mm)	Depth of cut (μm)
5A(I)	10	2000	0.0050	0.5	2
5A(II)	20	2000	0.0100	0.5	2
5A(III)	25	2000	0.0125	0.5	2
5A(IV)	15	2000	0.0075	0.5	2
5A(V)	10	1000	0.0100	0.5	2

Table 5.2 Specimens for Group 5B experiments

Specimen no.	Descriptions
5B(I)	Aluminium single crystal with (001) as the machining plane
5B(II)	Aluminium single crystal with (011) as the machining plane
5B(III)	Aluminium alloy (6061)
5B(IV)	Copper single crystal with (001) as the machining plane
5B(V)	Copper single crystal with (011) as the machining plane

5.4 RESULTS AND DISCUSSION

5.4.1 Effect of process parameters

ARMA models of order (16,15) to (40,39) were fitted to Group 5A and were found to be adequate in providing wavelength decomposition. The results of the wavelength decomposition are summarized in Table 5.3, Table 5.4 and Table 5.5 respectively. For

detailed outputs of the MDDS program, please refer to Appendix III. In ultra-precision diamond turning, the relative vibration between the tool and the workpiece is due to spindle run-out and low frequency vibration from the machine foundation. The component of the relative tool-work vibration contributes to a strong break frequency ($\zeta = 1$) due to real roots or exponential response with high damping ratios ($\zeta > 0.5$) (Pandit and Revach, 1981) as shown in Table 5.3. Their contributions are found to vary from 42.6 to 83.80 percent of the total roughness depending on the cutting conditions being adopted. It is found to differ from conventional machining (Pandit, 1981, Pandit and Revach, 1981) in which the surface roughness is dominated by the feed rate and its harmonics caused by tool geometry.

Table 5.3 Results of MDDS analysis for the break frequency components for Group 5A

Specimen no.	Characteristic roots λ_i	Natural frequency (cycles mm^{-1})	Wavelength (mm)	Damping ratio	Percentage contribution to total power (%)
5A(I)	$51.3381 \pm i55.0903$	11.98	0.0834	0.68	65.16
5A(II)	$71.8652 \pm i73.7248$	16.39	0.0610	0.70	83.80
5A(III)	74.9920	11.94	0.0838	1.00	61.45
5A(IV)	$52.3302 \pm i70.0580$	13.92	0.0719	0.60	80.89
5A(V)	63.0597	10.04	0.0996	1.00	42.65

The feed and tool geometry components possess the characteristics of a very low damping ratio ($\zeta < 0.01$) and the periodicity at the peak frequency is almost exact. Since an ideal surface produced by the tool nose is periodic but not sinusoidal, its decomposition would make a small but significant contribution to the harmonics of the feed component. The total contribution of the feed and the tool nose radius components to the surface roughness is thus obtained by adding the power of the fundamental and its harmonics (Pandit and Revach, 1981). From Table 5.4, it is found that the contributions for these components are ranging around 10 to 35 percents of the total roughness. There is a significant drop in the percentage of contribution as compared with conventional machining in which the contributions of the feed and its harmonics components range from 40 to 90 percent of the total roughness (Pandit, 1981, Pandit and Revach, 1981). As feed rate increases, the contributions of feed and tool geometry components increase as well.

The machine vibration components are found at the high frequency range. These are due to the dynamic weak points of the machine (Weck et al., 1988). As shown in Table 5.5, these components are found to possess moderate damping ratios ($0.5 \geq \zeta \geq 0.1$) and their natural frequencies appear to be almost independent of the cutting conditions. Nevertheless, their contribution to the total roughness is moderate. These components might be responsible for the micro-waviness of a diamond turned surface (Weck et al., 1988).

Table 5.4 Results of MDDS analysis for the feed and tool geometry components for Group 5A

Specimen no.	Characteristic roots λ_i	Natural frequency (cycles mm^{-1})	Wavelength (mm)	Damping ratio	Percentage contribution to total power (%)	
					Value	Total
5A(I)	$8.1819 \pm i1225.4090$	195.03	0.0051	0.0067	1.05	1.55
	$13.9364 \pm i2492.1474$	396.64	0.0025	0.0056	0.50	
5A(II)	$0.0889 \pm i633.8583$	100.88	0.0099	0.0001	3.80	10.16
	$16.8158 \pm i1285.0968$	204.55	0.0049	0.0131	6.36	
	$3.6242 \pm i3174.1270$	505.18	00020	0.0011	0.00	
5A(III)	$0.3266 \pm i497.6971$	79.21	0.0126	0.0007	31.02	31.02
	$21.0026 \pm i3478.8064$	553.68	0.0018	0.0060	0.00	
5A(IV)	$1.0266 \pm i838.7797$	133.50	0.0075	0.0012	8.38	8.38
5A(V)	$0.1231 \pm i626.5455$	99.72	0.0100	0.0002	29.88	39.15
	$17.3548 \pm i1274.5828$	202.87	0.0049	0.0136	8.04	
	$61.7181 \pm i1910.9260$	304.29	0.0033	0.0323	1.01	
	$222.4469 \pm i2541.7769$	406.08	0.0025	0.0872	0.22	

Table 5.5 Results of MDDS analysis for the machine vibration components for Group 5A

Specimen no.	Characteristic roots λ_i	Natural frequency (cycles mm^{-1})	Wavelength (mm)	Damping ratio	Percentage contribution to total power (%)	
					Value	Total
5A(I)	$286.3702 \pm i1484.0040$	240.54	0.0042	0.19	6.701	6.702
	$430.4053 \pm i3138.0949$	504.12	0.0020	0.14	0.001	
	$670.8491 \pm i4649.0512$	747.58	0.0013	0.14	0.000	
5A(II)	$691.1212 \pm i1328.8411$	238.39	0.0042	0.46	3.530	3.611
	$460.2812 \pm i2722.1261$	439.39	0.0023	0.17	0.080	
	$343.3692 \pm i3970.0103$	634.21	00016	0.09	0.001	
5A(III)	$264.6365 \pm i14929.9593$	231.45	0.0043	0.18	5.892	5.936
	3594.0401	572.01	0.0017	1.00	0.044	
	$395.5212 \pm i4178.9480$	688.07	0.0015	0.09	0.000	
5A(IV)	$493.1178 \pm i1589.1985$	264.83	0.0038	0.30	7.478	7.761
	$598.9892 \pm i2651.3009$	432.60	0.0023	0.22	0.281	
	$216.8377 \pm i3983.2631$	634.89	0.0016	0.05	0.002	
5A(V)	$75.4770 \pm i1589.4338$	253.25	0.0039	0.05	0.138	0.195
	$120.6910 \pm i2821.4598$	449.46	0.0022	0.04	0.054	
	$554.2028 \pm i3875.3648$	623.06	0.0016	0.14	0.003	

5.4.2 Effect of material properties and crystallographic orientation of the workpiece

ARMA model of order (22,21) was fitted to the aluminium specimens (5B(I), 5B(II) and 5B(III)). For the copper specimens (5B(IV) and 5B(V)), ARMA model of order (14,13) is found adequate in providing the wavelength decomposition. The results of the wavelength decomposition are summarized in Table 5.6, Table 5.7 and Table 5.8 respectively. For detailed outputs of the MDDS program, please refer to Appendix III. The spread of the wavelength components at different radial sections is measured by the mean and the normalized standard deviation. The surface roughness profiles for each specimen at the starting radial section are depicted in Figure 5.3. Although the specimens are machined under the same cutting conditions and operational settings, significant different characteristic shapes among the surface roughness profiles are observed. Single crystal aluminium with (011) plane seems to cause higher frequency of surface modulations than that for the (001) plane crystal whereas this is the lowest for the aluminium alloy. As reflected in the order of the wavelength decomposition, the complexity of surface roughness profiles for copper single crystals (Specimens 5B(IV) and 5B(V)) is lower than that for aluminium.

From Table 5.6, it is found that the feed and the tool geometry components for aluminium specimens (5B(I), 5B(II) and 5B(III)) contribute from 21 to 26 percent of the total roughness. The exact periodicity of the feed component and its harmonics is reflected in the small values of the normalized standard deviation. For the copper specimens (5B(IV) and 5B(V)), over 97 percent of surface roughness is contributed by the feed components and its harmonics. The rest is attributed dominantly to the break frequency components. The large differences of feed contribution can be explained by the different swelling properties of materials being cut. During machining, the workpiece material swells at the end of the active cutting edge causing a greater and deeper tool mark (Sata et al., 1985) and hence a modification of the surface roughness profiles on the machined surface. The effect of swelling increases the contribution of the feed components. The amount of swelling depends on the properties and crystallographic orientation of the material being cut.

Greater feed contribution is observed for single crystal copper than that for single crystal aluminium.

On the other hand, there is a significant increase in the contribution of machine vibration components for single crystal aluminium as shown in Table 5.7. The contribution is higher for (011) crystal than for the (001) ones. However, insignificant contributions of machine vibration components are noticed for the copper specimens. The spread of these components is shown to be greater than that of the feed components.

Table 5.6 Results of MDDS analysis for the feed and tool geometry components for Group 5B

Specimen no.	Natural frequency (cycles mm^{-1})				Percentage contribution to total power (%)	
	Range ν	Mean $\bar{\nu}$	Standard deviation, σ_ν	Normalized standard deviation, $\sigma_\nu/\bar{\nu}$	Average	Total
5B(I)	99.83-100.14	99.75	0.40	0.004	8.562	21.387
	198.17-200.86	199.30	0.76	0.004	10.552	
	297.14-299.74	298.55	1.03	0.003	2.022	
	395.82-408.36	400.62	3.84	0.010	0.229	
	493.13-508.20	500.27	5.79	0.012	0.051	
	597.09-603.43	598.94	2.67	0.004	0.001	
5B(II)	99.18-101.00	100.10	0.61	0.006	15.772	25.677
	199.10-203.79	200.57	1.71	0.009	6.388	
	299.17-303.09	299.88	1.66	0.006	3.081	
	396.76-404.37	400.28	2.55	0.006	0.372	
	496.48-505.31	500.41	2.78	0.006	0.059	
	596.89-607.49	602.33	4.41	0.007	0.005	
5B(III)	97.66-100.37	99.05	0.96	0.010	11.436	24.964
	195.91-199.76	198.00	1.56	0.008	9.362	
	292.44-299.65	296.63	2.89	0.010	3.955	
	390.68-400.64	396.35	3.30	0.008	0.204	
	496.20-506.66	500.17	3.87	0.008	0.004	
	586.23-605.09	596.96	5.97	0.010	0.003	
5B(IV)	97.51-102.20	99.89	1.16	0.012	87.640	98.175
	195.53-204.41	199.91	2.15	0.011	9.508	
	294.92-306.41	300.82	3.13	0.010	0.770	
	395.51-408.02	400.43	3.20	0.008	0.237	
	497.86-507.16	500.99	3.78	0.008	0.020	
5B(V)	98.39-101.71	100.34	0.94	0.009	86.252	97.197
	197.92-203.53	200.98	1.84	0.009	10.24	
	296.86-307.15	302.04	3.08	0.010	0.587	
	396.72-407.13	401.96	4.11	0.010	0.080	
	495.92-508.54	502.00	4.20	0.008	0038	

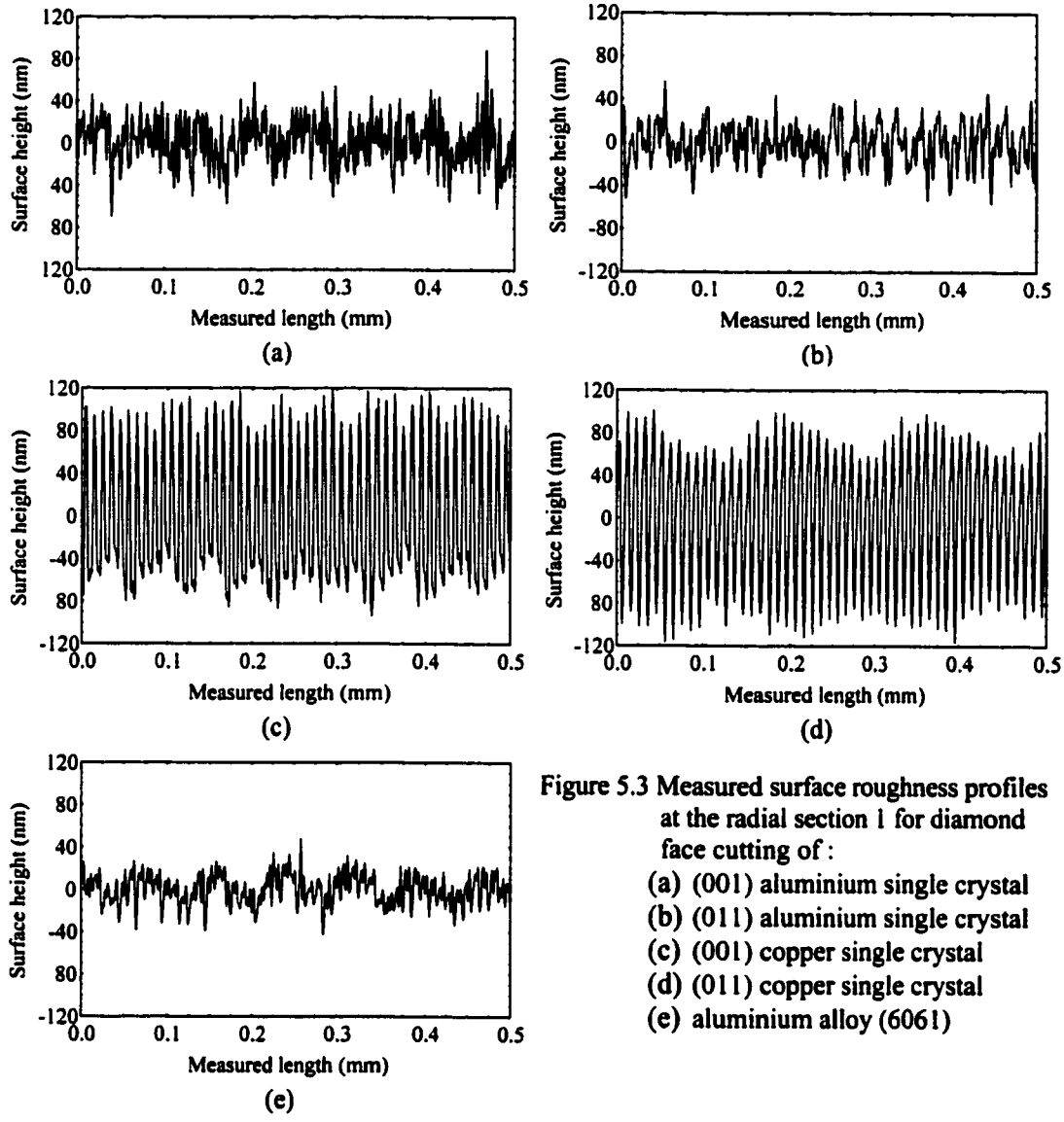

Figure 5.3 Measured surface roughness profiles at the radial section 1 for diamond face cutting of :
(a) (001) aluminium single crystal
(b) (011) aluminium single crystal
(c) (001) copper single crystal
(d) (011) copper single crystal
(e) aluminium alloy (6061)

Table 5.8 tabulates the findings for the break frequency components. The mean frequency indicates the dynamic interaction between the work material and the cutting system during machining. When comparing the normalized standard deviations among the specimens, single crystal specimens (Specimens 5B(I), 5B(II), 5B(IV) and 5B(V)) are found to cause greater variation of break frequency than the polycrystalline aggregate (Specimen 5B(III)). Single crystal aluminium and copper with (011) crystallographic plane induce greater variation in the break frequencies than those with (001) plane. Figure 5.4 depicts the variations of the break frequency with respect to different radial sections for

aluminium and copper specimens, respectively. For Specimens 5B(II) and 5B(V), distinct high break frequencies (P1, P2, P3 and P4) were detected at approximately equally spaced radial sections.

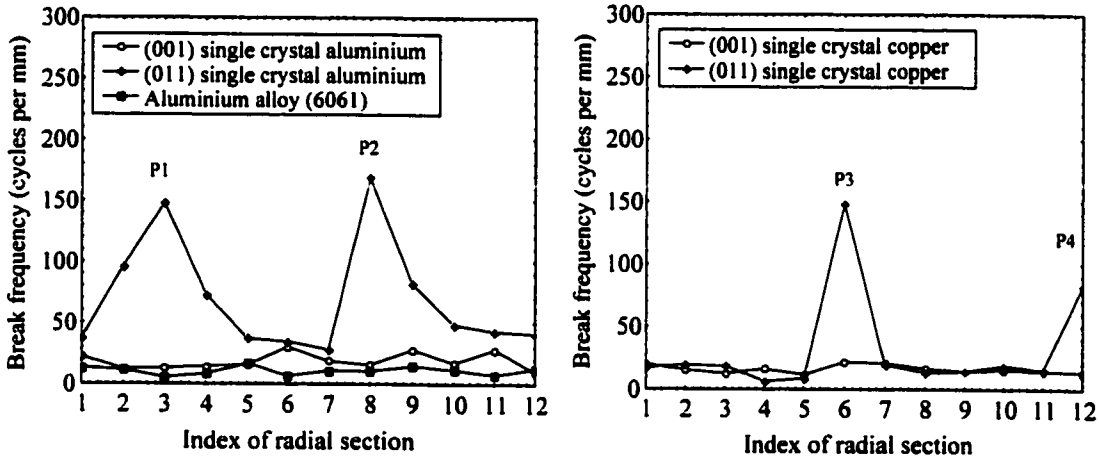

Figure 5.4 Break frequency distribution for (a) aluminium and (b) copper

Since the cuttings were conducted under the same cutting conditions, the variation of the break frequency and the machine vibration can be attributed only to the variation of the material crystallography and the anisotropy in machinability of the work material. Figure 5.5 and Figure 5.6 show the surface roughness profiles at radial sections corresponding to P1, P2, P3 and P4, respectively. As compared with those found in radial section 1 ,i.e. Figure 5.3(b) and Figure 5.3(d), significant changes of the characteristic shape are noticed. This provides additional evidence that the material crystallography alters the cutting dynamics and hence the surface roughness in diamond turning process.

Precluding the measuring instrument as a source, a comparatively small but significant variation in break frequency is also noticed for the aluminium alloy (Specimen 5B(III)). This could be explained by the fact that the depth of cut in single point diamond turning is usually in the same order as the grain sizes in a polycrystalline aggregate (Lee, 1990). A grain by its nature is crystalline and highly anisotropic. The variation of the cutting dynamics caused by changing material crystallography is inherent in the cutting system for a

work material. The magnitude of such materials induced cutting dynamics variation sets a limit to the amount of improvement in performance that an ultra-precision diamond turning machine can achieve since there is always a systematic variation of the cutting dynamics in the machining of crystalline materials.

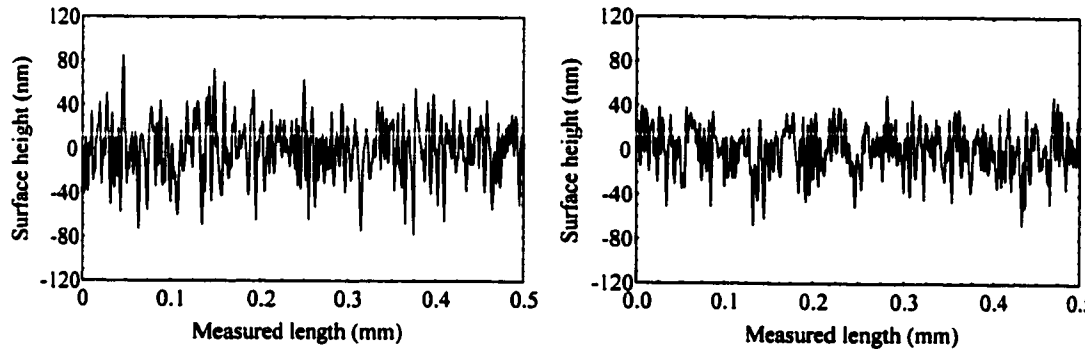

Figure 5.5 Measured surface roughness profiles for the aluminium single crystal with (011) plane at (a) radial section P1 and (b) radial section P2

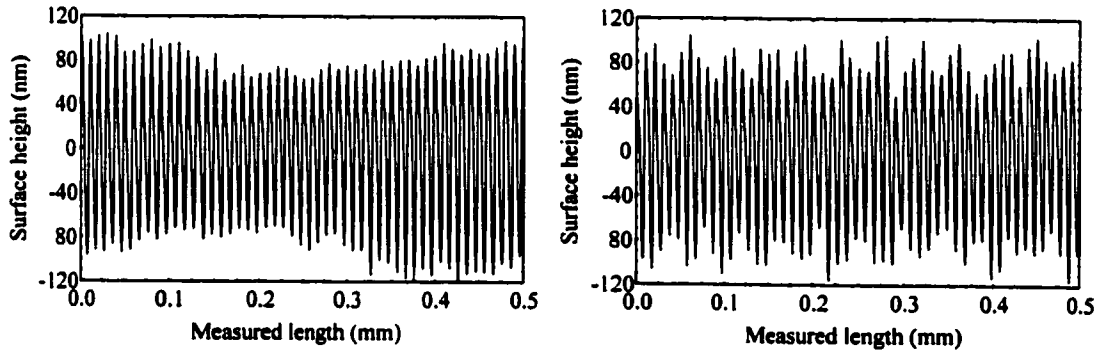

Figure 5.6 Measured surface roughness profiles for the copper single crystal with (011) plane at (a) radial section P3 and (b) radial section P4.

A surface texture analysis has been conducted for additional evidence. Figure 5.7 and Figure 5.8 show respectively the measured pole figures for (001) plane and (011) plane aluminium crystals measured at the initial orientation before and after cutting. It is found that the surface textures for the two crystals disperse significantly and differently after cutting. The dispersion of the texture components indicates high density of dislocations of the crystal lattices at the deformation layer after machining. These dislocations could introduce additional roughness on the diamond turned surface. Although no direct

quantitative correlation between the variation of surface texture and surface roughness has been established, the use of MDDS method allows us to conjecture the patterns of the variations of the cutting dynamics due to changing crystallographic orientation of the work materials and its effect on the surface roughness in the diamond turning process. In fact, the normalized standard deviation in Table 5.8 provides a proxy measure of the effect of the materials induced cutting dynamics variations on the surface roughness. A large value of the normalized standard deviation would be found for highly anisotropic material. A complete summary of the findings in the MDDS analysis is tabulated in Table 5.9.

Table 5.7 Results of MDDS analysis for the machine vibration components for Group 5B

Specimen no.	Natural frequency (cycles mm^{-1})				Percentage contribution to total power (%)	
	Range ν	Mean $\bar{\nu}$	Standard deviation, σ_ν	Normalized standard deviation, $\sigma_\nu/\bar{\nu}$	Average	Total
5B(I)	195.61-310.48	251.90	36.49	0.14	14.806	15.174
	421.03-475.99	444.52	16.02	0.04	0.365	
	593.14-695.52	646.38	34.34	0.05	0.003	
5B(II)	203.79-327.00	267.23	38.44	0.14	20.382	21.160
	413.33-518.78	454.18	27.52	0.06	0.773	
	572.59-706.04	657.48	40.82	0.06	0.005	
5B(III)	197.31-259.99	229.80	16.11	0.07	9.649	9.873
	398.19-478.10	439.13	22.73	0.05	0.222	
	571.90-755.38	687.91	77.13	0.11	0.002	
5B(IV)	390.96-517.95	482.73	46.95	0.10	0.026	0.027
	608.86-684.78	661.80	17.77	0.03	0.001	
	772.06-1401.31	1075.13	19.26	0.02	0.000	
5B(V)	405.91-429.39	417.45	8.56	0.02	0.100	0.101
	545.40-673.27	640.68	33.20	0.05	0.001	
	696.66-1159.00	1075.30	34.23	0.03	0.000	

Table 5.8 Results of MDDS analysis for the break frequency components in Group 5B

Specimen No.	Natural frequency (cycles mm^{-1})				Percentage contribution to total power (%)	
	Range ν	Mean $\bar{\nu}$	Standard deviation, σ_ν	Normalized standard deviation, $\sigma_\nu/\bar{\nu}$	Range	Average
5B(I)	9.65-30.18	18.92	6.67	0.35	40.30-74.07	59.33
5B(II)	28.20-168.96	62.04	45.75	0.74	30.77-74.36	55.51
5B(III)	5.15-16.73	10.45	2.86	0.27	43.11-81.26	65.93
5B(IV)	11.57-21.57	15.92	3.19	0.20	0.50-2.99	1.54
5B(V)	6.19-147.94	31.70	41.61	1.31	0.21-6.11	2.36

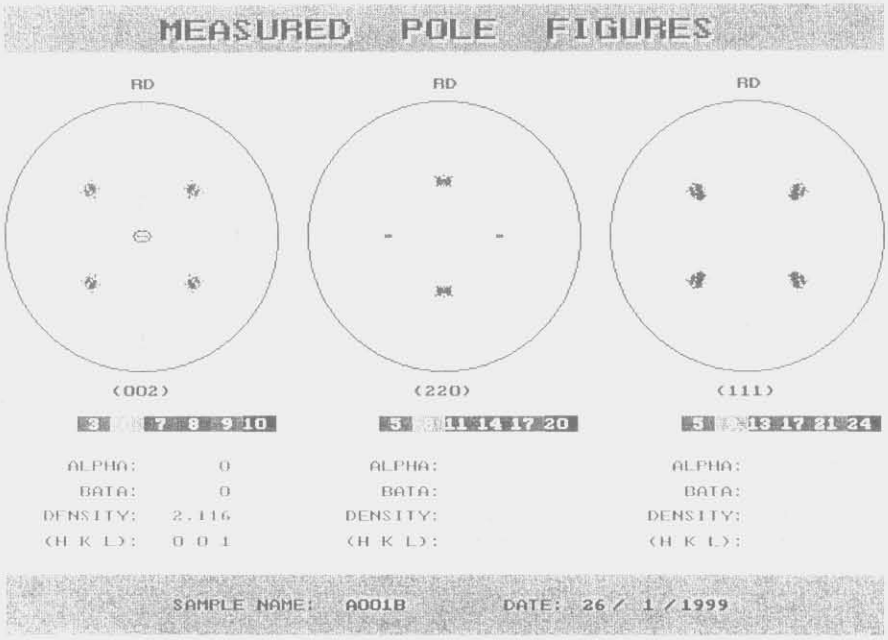

(a)

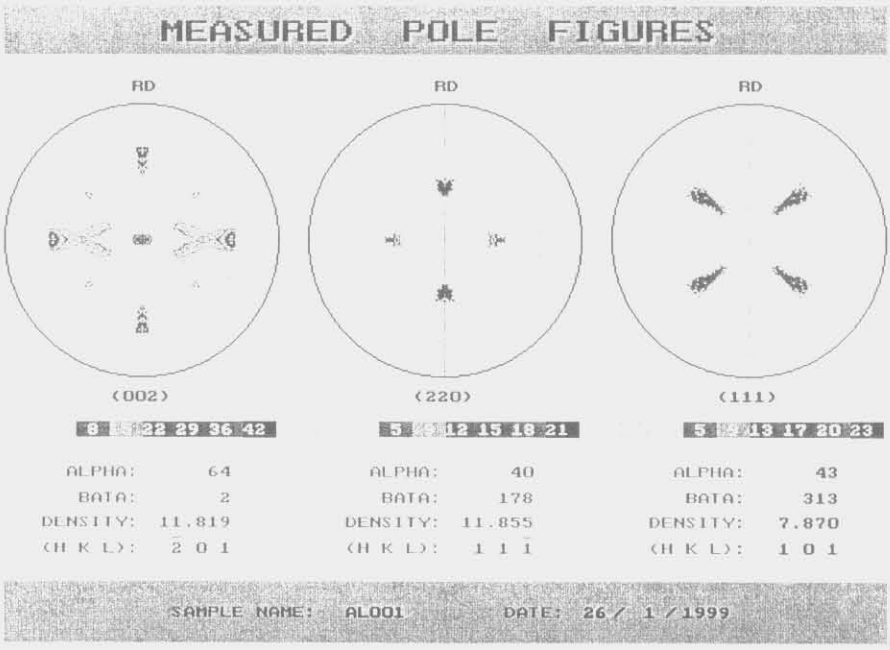

(b)

Figure 5.7 The variation of surface texture in face cutting on the (001) aluminium single crystal : (a) before and (b) after cutting.

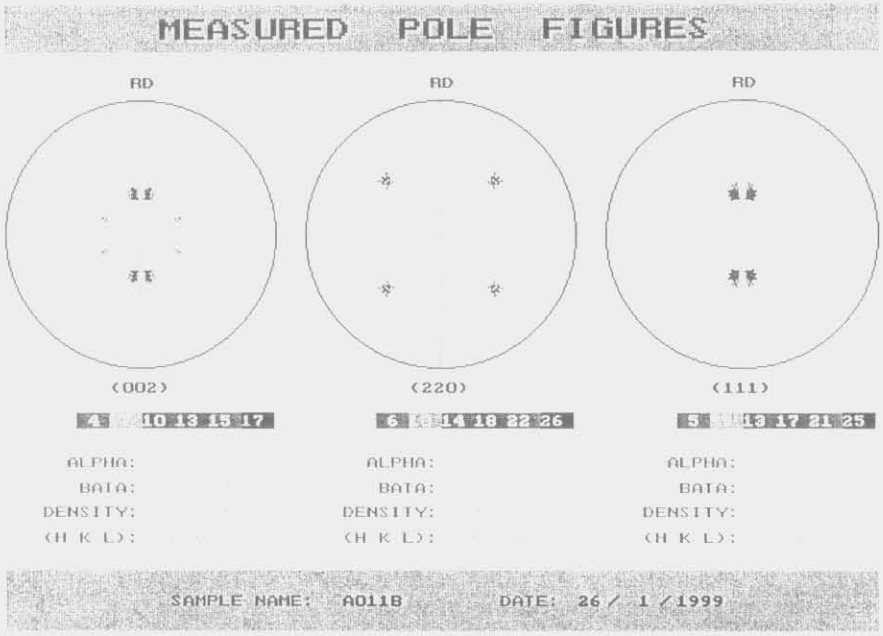

(a)

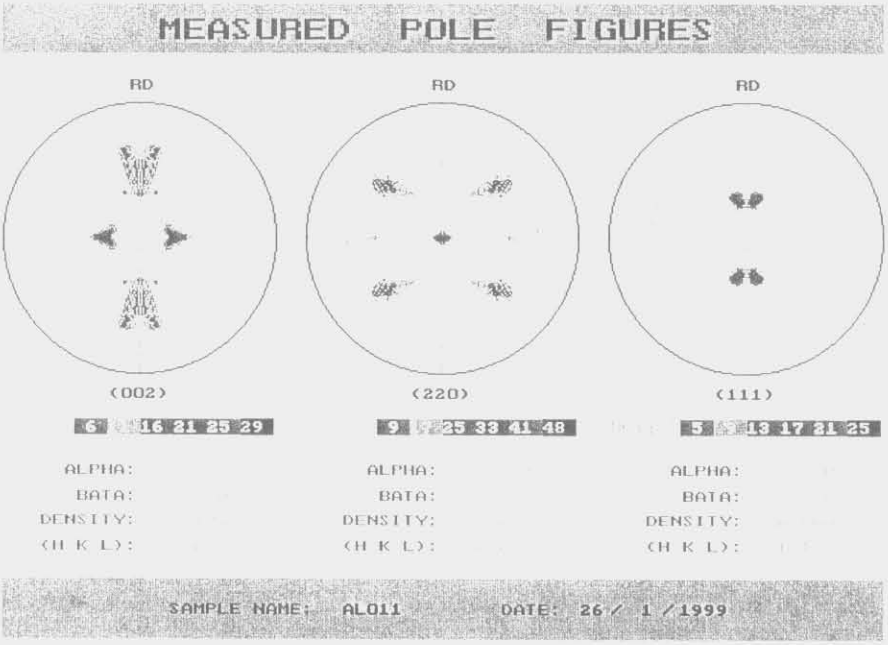

(b)

Figure 5.8 The variation of surface texture in face cutting on the (011) aluminium single crystal : (a) before and (b) after cutting

Table 5.9 Summary of the findings in MDDS analysis

Surface roughness components	Characteristic features
Feed	• Very low damping ratio ($\zeta < 0.01$) • Large contribution to the total power at the fundamental frequency • Almost exact periodicity
Tool nose radius	• Very low damping ratio ($\zeta < 0.01$) • Periodic but not sinusoidal • Possessing small but significant contribution to the total power at the harmonics of feed frequency • Almost exact periodicity
Relative tool-work vibration	• High damping ratio ($\zeta > 0.5$) • Strong break frequency ($\zeta = 1$) or exponential decaying response due to very high damping ratios • Large contribution to the total power at low frequency range
Crystallographic orientation	• High damping ratio ($\zeta > 0.5$) • Large variation of break frequencies at different radial sections of a turned surface • Strong break frequency ($\zeta = 1$) or exponential decaying response due to very high damping ratios • Contribution to the total power depends on crystallographic orientation of the workpiece • Sharp increase in break frequency at specific radial sections of a turned surface
Machine vibration	• Moderate damping ratio ($0.5 \geq \zeta \geq 0.1$) • Magnitude and frequency appear to be almost independent of the cutting conditions • Moderate contribution to the total power • High frequency in nature

5.5 SUMMARY

A Multiple Data Dependent Systems (MDDS) method is proposed which provides a component by component wavelength decomposition of the surface roughness profiles at a finite number of radial sections of the workpiece. The characteristics of these wavelength components are correlated to different surface generation mechanisms. Their relative powers are used to measure the contributions of the mechanisms to the total roughness. Since the local cutting dynamics are taken into account, the method resolves the shortcomings of conventional DDS and FFT spectrum analysis methods in characterizing

the localized variations of the material properties, cutting dynamics and surface roughness in SPDT.

Cutting experiments were conducted under different cutting conditions and materials being cut. Experimental results indicate that the cutting dynamics are dominated by the relative tool-work vibration and swelling of a work material. Compared with conventional machining, the relative contribution of feed component to the total roughness is largely diminished whereas that for the tool-work vibration is significantly increased. Under identical cutting conditions, the relative contribution of the feed and tool geometry components are shown to give a proxy measure for the swelling properties of a work material. For diamond turning of single crystal materials, the surface roughness is shown to vary with crystallographic orientation of the material being cut. The contribution and the frequency distribution of the relative tool-work vibration components are found to vary with material crystallography. Such a variation of the cutting dynamics is inherent in the cutting system of a non-amorphous material. As reflected in the normalized standard deviation of the break frequency distribution, single crystal materials are found to cause greater variation than the polycrystalline aggregate. The successful deployment of MDDS method allows the characteristics of material induced cutting dynamics to be explored and its effect on the surface roughness can be studied quantitatively in single point diamond turning.

PART II

MODEL FORMULATION AND VERIFICATION

Chapter 6

Modelling and Simulation of Surface Topography (I): Process Factors

6.1 INTRODUCTION

Based on the results in Part I, the factors affecting the surface generation in ultra-precision diamond turning can be summarised in Figure 6.1. Among various factors which affect the surface roughness of a diamond turned workpiece, the dominant factors are tool geometry, plastic anisotropy, feed rate, material swelling, and relative vibration between the tool and the workpiece. Generally, these factors can be classified into two main categories named the process factors and material factors respectively. The former involves the cutting conditions like spindle speed, feed rate, tool geometry and relative tool-work vibration. These factors are related closely to the cutting geometry and the dynamic characteristics of a cutting system. The material factors considered are material anisotropy, swelling, and crystallographic orientation of the work materials which work closely with the stress, strain and plastic deformation during cutting.

Basically, the surface roughness profile along the axial direction of a workpiece is determined by the tool geometry and the feed rate. Under ideal conditions, the surface roughness profile is generated by the repetition of the tool tip profile at intervals of feed per revolution of the spindle. The surface roughness profile is formed by successive movements of the tool tip profile at intervals of the tool feed. Surface roughness depends on the location of the succeeding cutting edges which start removing chips again from the surface profile formed by the preceding cutting edge. However, there are error motions of the spindle (i.e. axial, face, radial and tilt, etc.) as shown in Figure 6.2 (ANSI/ASME B89.3.4M Standard, 1995) as well as small amplitude and low frequency vibration remaining in ultra-precision machine tools whose cause a relative displacement between the tool and the workpiece. The relative tool-work displacement results in the formation of surface modulations and hence a modification of the surface roughness profile.

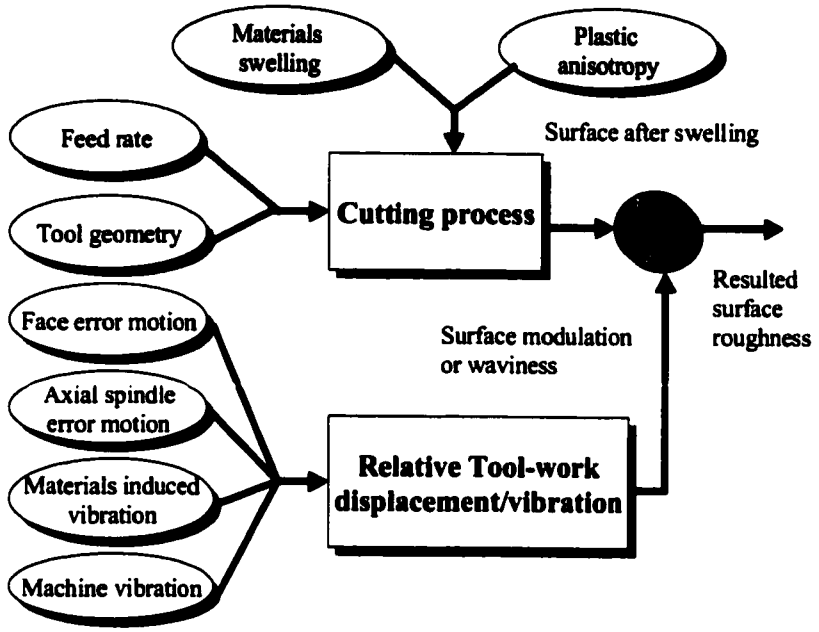

Figure 6.1 Factors affecting surface generation in ultra-precision diamond turning

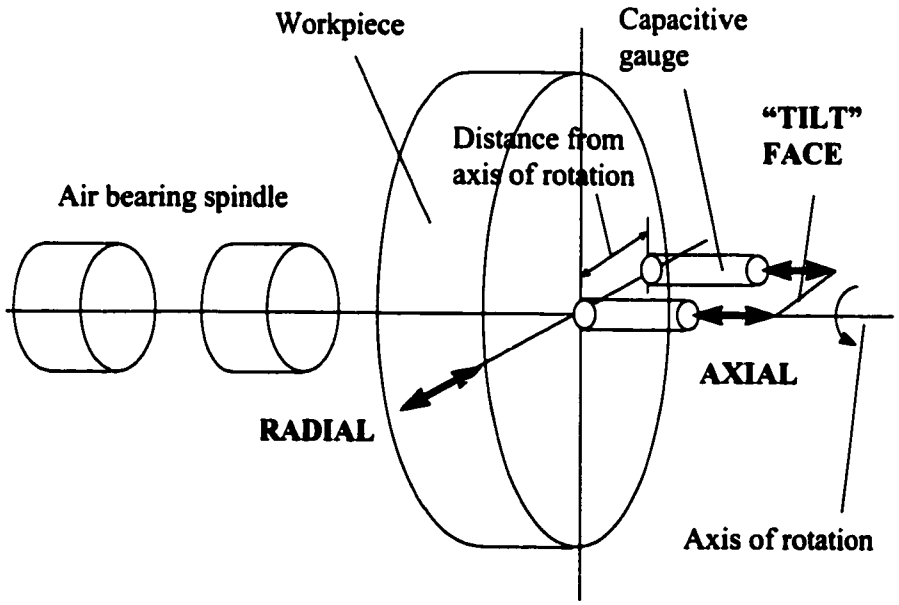

Figure 6.2 Schematic diagram showing error motions of a spindle

Apart from these, an important source of vibration in ultra-precision machining is caused by the changing crystallography and orientations of the slip systems of the grains being cut. The shear strength and the shear angle of the crystal will vary with the

crystallographic orientation. As the cutting force is a function of the shear strength and the shear angle, any variation in the shear strength and the shear angle of the crystal being cut will cause a fluctuation in the micro-cutting forces. The vibration induced by such a variation of micro-cutting forces is a kind of materials induced vibration which is difficult to eliminate by machine tool design or process control. The magnitude of such materials induced vibration limits the degree of improvement that can be achieved in the performance of an ultra-precision diamond turning machine since there is always a systematic micro-cutting force variation in ultra-precision machining of crystalline materials. The effect of materials induced vibration introduces additional relative displacement between the tool and the workpiece which further degrades the surface roughness of a diamond turned surface. There is strong experimental evidence that the surface roughness and the surface topography vary with the crystallographic orientations of the metals being cut (K*ö*ng and Spenrath, 1991, Lee and Zhou, 1993, and Yuan, et al., 1994). However, our understanding on the effect of materials induced vibration is still far from perfect.

In this Chapter, a surface topography model (Cheung and Lee, 2000d and 2000e) is proposed to account for the effect of process factors on the surface generation mechanisms in ultra-precision diamond turning. The model takes into account the static and the dynamic components of the cutting process. The former includes cutting conditions such as feed rate and tool geometry. The latter includes relative vibration between the tool and the workpiece caused by the axial error motion of the spindle and the vibration introduced by the operational settings of the machine. The topography model forms the basis for the development of a model based simulation system in Chapter 7.

6.2 MODELLING OF SURFACE TOPOGRAPHY

In the present study, it is assumed that the cutting process is orthogonal and the workpiece materials are homogeneous and isotropic. In face turning operation, the two possible error motions of the spindle which affect surface generation are axial and face error motions

(ANSI/ASME B89.3.4M Standard, 1985). For axial error motion, it is a dominant factor affecting the surface quality since it is the sensitive direction of error motion. For face error motion, it is related to the distance from the centre line of the workpiece. It will be a second order effect if the diameter of the workpiece is small (i.e. diameter less than 50 mm). In the present study, only axial error motion of the spindle is taken into account. The effect of face error is assumed to be negligible for ease of analysis. It is also assumed that the relative vibration between the tool and the workpiece is a steady simple harmonic motion with a small amplitude and a low frequency. Only the relative vibration in the infeed cutting direction is considered since its effect is significant in the surface generation. In ultra-precision machining, the depth of cut is usually in the range of a few to several ten micrometers. Under such an environment, the influence of chatter vibration induced by the regenerative effect is insignificant since chatter vibration generally develops under heavy-duty cutting. Although the fluctuation of the cutting force due to the variation of uncut chip thickness might influence the surface generation, the ratio of the amplitude of vibration to the depth of cut is usually very small in ultra-precision diamond machining. For example, the ratio used in the present study is in the order of the maximum of 0.015 (30 nm p-v /2000 nm). Such effect can be neglected for the ease of analysis.

6.2.1 Nomenclature

A = amplitude of the relative vibration between the tool and the workpiece (μm)

d = depth of cut (μm)

f_z = frequency of the relative vibration between the tool and the workpiece (Hz)

i = index for tool tip position along the feed direction

j = tool locus point index

k = index of the radial section

N = number of spindle rotations

Δr = radial increment (mm)

R_0 = radius of the workpiece (mm)

R = tool nose radius (mm)

R_t = maximum peak-to-valley height (nm)

R_a = arithmetic roughness (nm)

s = feed rate (mm per rev)

t = machining time (second)

V = spindle rotational speed (rpm)

Δt = time increment (second)

$\Delta\theta$ = rotational angle increment (radian)

ω = angular speed (radian per second)

$\lceil\ \rceil$ = operator for the next larger integer of a decimal fraction

6.2.2 Two-dimensional analysis of surface roughness profile

Under ideal conditions, the surface roughness profile as shown in Figure 6.3 is formed by the repetition of tool tip profile at intervals of feed per workpiece revolution s and hence the maximum peak-to-valley height R_t can be derived as:

$$R_t = R - \sqrt{R^2 - s^2/4} = R(1 - \sqrt{1 - s^2/4R^2}) \tag{6.1}$$

For $s << R$,

$$R_t = \frac{s^2}{8R} \tag{6.2}$$

Before the arithmetic roughness R_a can be found, the mean line has to be established. In the case of the round tool tip, the mean line is $R_t/8$ from the bottom of the trough (Whitehouse, 1994). Using the mean line, the arithmetic roughness R_a is about one-quarter of the value for R_t, i.e.,

$$R_a \sim \frac{0.032s^2}{R} \tag{6.3}$$

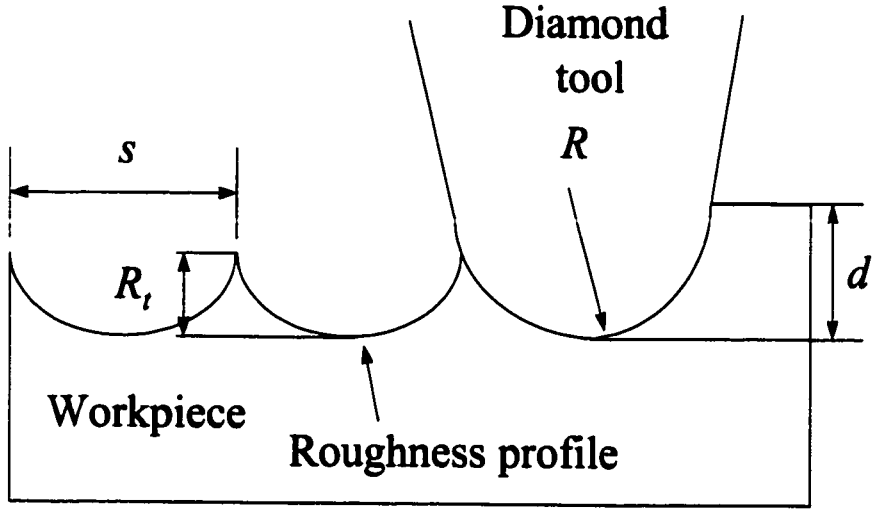

Figure 6.3 Ideal surface produced by a round cutting tool

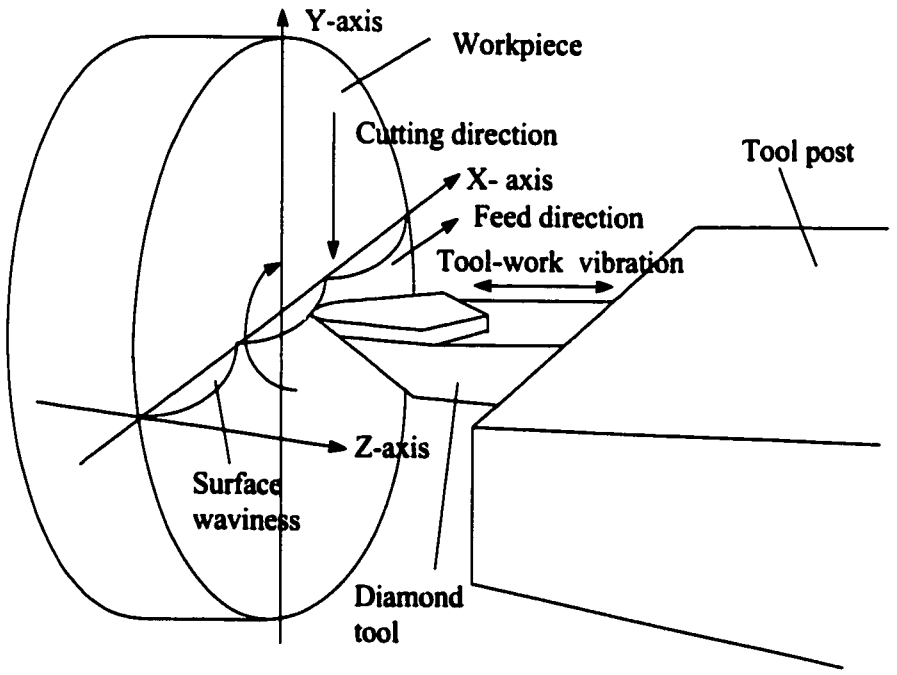

Figure 6.4 Surface waviness induced by the relative vibration between the tool and the workpiece

Equations (6.2) and (6.3) are based on the assumption that the tool is ideally positioned relative to the workpiece. The formation of a surface roughness profile can be considered as successive movements of the tool profiles at intervals of the tool feed. Surface roughness depends on the location of the succeeding cutting edges which start removing chips from the surface profile formed by the preceding cutting edges. However, in practice, the tool positions vary relative to the workpiece due to a number of factors like spindle axial error motion as well as unavoidable small amplitude and low frequency vibration of the ultra-precision machine tools (Takasu et al., 1985). This leads to the formation of surface waviness/modulations and hence a modification of the surface roughness profile as shown in Figure 6.4.

In the 2-D model (Cheung and Lee, 2000d), a ratio between the frequency f_z of the vibration to the spindle rotational speed V in revolution per minute (rpm) is determined firstly by Equation (3.4). Hence, the corresponding phase shift, ϕ, between subsequent undulations can be defined based on Equation (3.5). By taking the X-axis along the tool feed and the Z-axis along the infeed cutting direction as shown in Figure 6.3, the tool locus of discrete tool profiles projected on the $X-Z$ plane can be expressed in terms of the phase shift ϕ and the feed rate s as:

$$z_t(x) = A\left[1-\cos(\phi\frac{x}{s})\right] \tag{6.4}$$

where $z_t(x)$ is the relative vibration between the tool and the workpiece, in the tool feed direction.

As the tip of a round tool profile is taken at the origin (i.e. the perimeter of the workpiece), the cutting edge profile $z(x)$ can be expressed by:

$$z(x) = \frac{x^2}{2R} \tag{6.5}$$

As discussed previously, the surface roughness profile is formed by successive movements of the tool profiles at interval of the tool feed along the tool locus described by Equation (6.4). Surface roughness depends on the location of the succeeding cutting edges which start removing chips again from the surface profile formed by the preceding cutting edges. The points of intersection at which the tool starts to remove chips from the preceding cutting edge can be derived as follows.

It is assumed that the first tool profile starts at the lowest point, at the perimeter of the workpiece, i.e. the origin of $X-Z$ plane. The number of successive tool profiles generated in one machining cycle as measured across the radius of the workpiece is equal to R_0 / s, i.e. $N = R_0 / s$. From Equation (6.4), the locus of the tool tip at each feed position can be rewritten as:

$$z_t(i) = A\{1-\cos[(i-1)\phi]\} \qquad \text{,for } i = 1,2,\ldots,N \tag{6.6}$$

The cutting edges of the i th tool profile and the $i+1$ th tool profile counted from the first one can be determined based on Equations (6.5) and (6.6) as:

$$z_i(x_i) = A\{1-\cos[(i-1)\phi]\} + \frac{[x_i-(i-1)s]^2}{2R} \tag{6.7}$$

$$z_{i+1}(x_{i+1}) = A[1-\cos(i\phi)] + \frac{(x_{i+1}-is)^2}{2R} \tag{6.8}$$

with $i = 1,2,\ldots..N-1$.

At the intersecting location $T_{i,i+1}(x_{i,i+1}, H_{i,i+1})$ of the i th tool profile and the $i+1$ th ones, $z_i = z_{i+1}$ and $x_i = x_{i+1}$, i.e.

$$x_{i,i+1} = \frac{4RA\sin\left[(i-\frac{1}{2})\phi\right]\sin(\frac{\phi}{2}) + (2i-1)s^2}{2s} \quad \text{, for } i = 1,2,\ldots,N-1 \tag{6.9}$$

From Equations (6.8) and (6.9), the height $H_{i,i+1}$ of the intersecting location between the i th tool profile and the $i+1$ th ones, which are counted from the first tool profile is determined as:

$$H_{i,i+1} = A[1-\cos(i\phi)] + \frac{\left\{4RA\sin\left[(i-\frac{1}{2})\phi\right]\sin(\frac{\phi}{2}) - s^2\right\}^2}{8Rs^2} \quad \text{, for } i = 1,2,\ldots,N-1 \tag{6.10}$$

Since the minimum cutting edge profile below the intersecting points of each tool profile constitutes the surface roughness, a surface roughness profile can be constructed by trimming the lines above the intersecting points. A graphical illustration of the simulation process is depicted in Figure 6.5.

6.2.3 Interference of the tool

As mentioned in Chapter 3, a high spindle rotational speed together with a fine feed rate are usually adopted for improving the surface roughness quality in diamond turning. Under these conditions, interference of the tool (Takasu et al., 1985) occurs in which the preceding movement of the tool has already removed the chip which should be cut away by some of the succeeding tool movements. This results in the non-existence of intersecting points at two or more successive cutting tool profiles. In this case, there is no solution for Equations (6.9) and (6.10) at the non-existing points of intersection. Takasu et al. (1985) has established a criterion for the occurrence of the interference of tool.

However, this criterion did not determine the exact locations at which this phenomenon actually takes place. In the simulation model, the exact locations for tool interference are determined by continual checking for the existence of intersecting points at each tool feed

movement based on Equations (6.9) and (6.10). Should a tool profile not intersect with its previous and succeeding tool profiles, it will be skipped and the next closest intersection of tool profile will be used instead in the estimation of the surface roughness profile. This allows the effect of tool interference to be reflected in the simulated surface roughness profile.

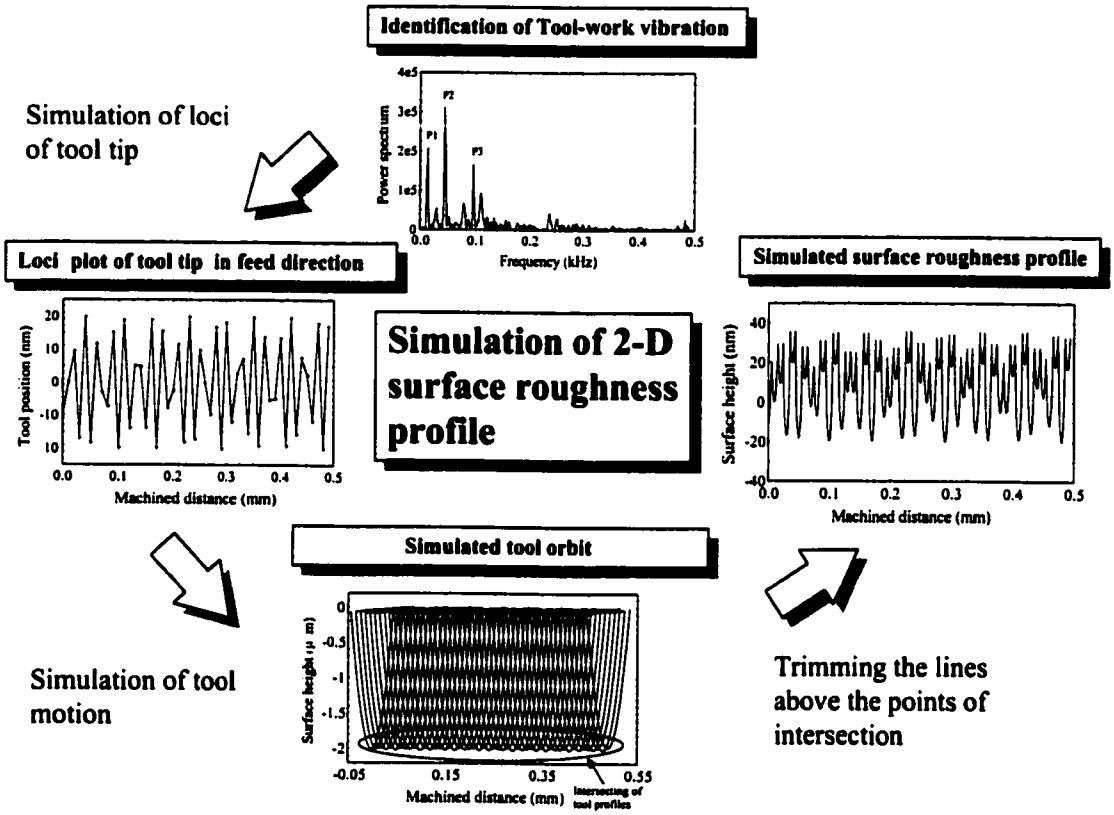

Figure 6.5 Graphical illustration of the simulation process for 2-D surface roughness profile

6.2.4 Three-dimensional (3-D) surface topography model

In the 3-D surface topography model (Cheung and Lee, 2000e), the roughness data are determined from the surface roughness profiles at a finite number of equally spaced radial sections on the workpiece (see Figure 6.6). The surface roughness profiles are predicted based on the 2-D model described in Section 6.2.2 and Section 6.2.3. The number of sections, N_p, can be expressed as:

$$N_p = \lceil 2\pi/\Delta\theta \rceil \tag{6.11}$$

where $\Delta\theta$ defines the angular resolution being adopted.

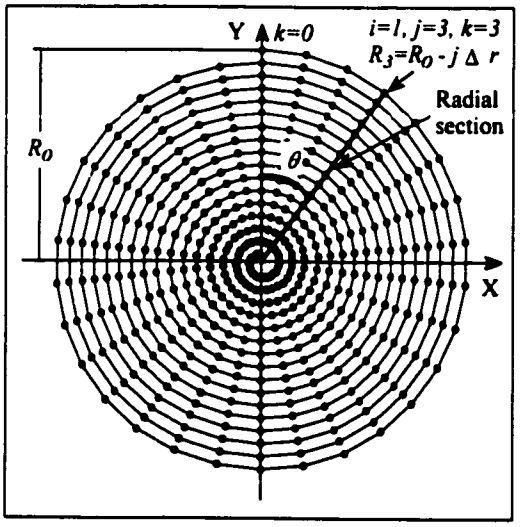

Figure 6.6 Locus of the tool positions on the X-Y plane

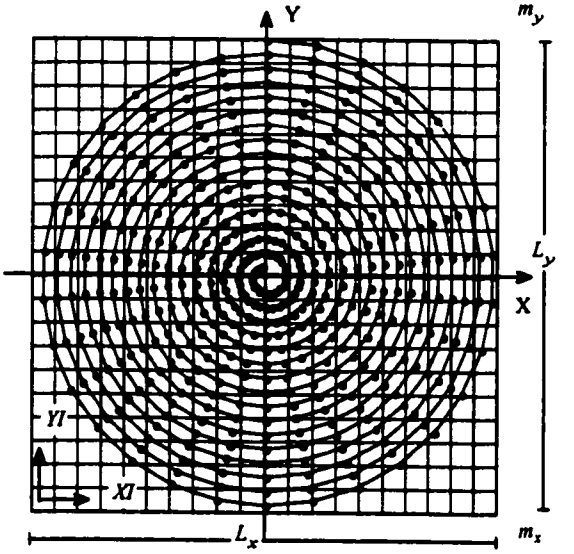

Figure 6.7 Linear mapping of predicted data on the surface elements of a cross lattice

The modelling of surface topography starts with the determination of the 3-D locus of the tool trace with respect to the workpiece. In the time domain, the relative displacement $Z_c(t)$ between the tool and the workpiece in the main cutting direction is a steady simple harmonic motion that can be expressed as:

$$Z_c(t) = A\sin(2\pi f_z t - \phi) \tag{6.12}$$

Since the spindle rotational speed and the feed rate are constant, i.e. $\omega = \Delta\theta/\Delta t$ and $N = R_0/s$ are constants, the total number of tool locus points, N_t, can be given by:

$$N_t = \frac{2\pi N}{\omega \Delta t} \tag{6.13}$$

In discrete form, the relative displacement between the tool and the workpiece can be derived based on Equations (6.12) and (6.13) as:

$$Z_c(j) = A\sin(\frac{2\pi f_z j\Delta\theta}{\omega} - \phi) \qquad \text{, for } j = 0,1,2,\ldots,N_t \tag{6.14}$$

During ultra-precision diamond turning, the cutting tool moves in a spiral locus towards the centre of the workpiece as shown in Figure 6.6. Simultaneously, the tool moves relative to the workpiece with a simple harmonic motion due to the relative vibration between the tool and the workpiece. The spiral locus of the tool on the $X-Y$ plane can be expressed in polar co-ordinates as:

$$\left.\begin{aligned} R_j &= R_0 - j\Delta r \\ \theta_j &= j\Delta\theta \end{aligned}\right\} \qquad \text{, for } j = 0,1,2,\ldots,N_t \tag{6.15}$$

Its corresponding co-ordinates on the $X-Y$ plane are given by:

$$\left.\begin{aligned} X_c(j) &= (R_0 - j\Delta r)\sin(j\Delta\theta) \\ Y_c(j) &= (R_0 - j\Delta r)\cos(j\Delta\theta) \end{aligned}\right\} \qquad \text{, for } j = 0,1,2,\ldots,N_t \tag{6.16}$$

Equations (6.15) and (6.16) describe the 3-D locus of the tool during machining. The 2-D model deduced in the Section 6.2.2 is a special case that describes the surface roughness profile at the starting radial section of the workpiece ,i.e., $k = 0$. The locus of the tool for the k th radial section can be treated as a transformation of the tool points from the $X-Y-Z$

co-ordinate system to the $R_k - Z_k$ polar plane, whereas R_k -axis is the radial axis for the k th radial section with $k = 0,1,2,\ldots,N_p$.

At the k th radial section, the co-ordinates of the tool locus on the $R_k - Z_k$ polar plane can be derived based on Equations (6.14) and (6.15) as follows:

$$\theta_t(i,k) = k\Delta\theta + 2\pi(i-1) \tag{6.17}$$

$$r_t(i,k) = R_0 - [k + (i-1)N_p]\Delta R \tag{6.18}$$

$$Z_t(i,k) = A\sin\left\{ \frac{2\pi f_z[k + (i-1)N_p]\Delta\theta}{\omega} - \phi \right\} \tag{6.19}$$

with $i = 1,2,\ldots,N$.

The cutting edges of the i th tool profile and the $i+1$ th ones, counted from the first tool profile at the k th radial section, can be derived from Equations (6.7), (6.8) and (6.19) as:

$$Z_{k,j}(r_{k,j}) = Z_t(i,k) + \frac{[r_{k,j} - (i-1)s]^2}{2R} \tag{6.20}$$

$$Z_{k,j+1}(r_{k,j+1}) = Z_t(i+1,k) + \frac{[r_{k,j+1} - is]^2}{2R} \tag{6.21}$$

where $i = 1,2,\ldots,N-1$ and $(r_{k,j},\ Z_{k,j})$ are the co-ordinates of the i th tool profile at the k th radial section of the workpiece.

At the location of intersection, $T_{k,j,j+1}(r_{k,j,j+1}, H_{k,j,j+1})$, of the i th tool profile and the $i+1$ th ones at the k th radial section, $Z_{k,j} = Z_{k,j+1}$ and $r_{k,j} = r_{k,j+1}$, i.e.,

$$r_{k,i,i+1} = \frac{4RA\cos\{\frac{C_p[2k+(2i-1)N_p]}{2} - \phi\}\sin(\frac{C_pN_p}{2}) + (2i-1)s^2}{2s}, \text{ for } i = 1,2,\ldots,N-1 \tag{6.22}$$

where $C_p = \frac{2\pi f_z \Delta\theta}{\omega}$.

From Equations (6.21) and (6.22), the height $H_{k,i,i+1}$ of the intersection between the i th and the $i+1$ th tool profiles at the k th radial section is determined as:

$$H_{k,i,i+1} = Z_t(i+1,k) + \frac{[r_{k,i,i+1} - is]^2}{2R}$$

$$= A\sin[C_p(k+iN_p) - \phi] + \frac{\left\{4RA\cos\{\frac{C_p[2k+(2i-1)N_p]}{2} - \phi\}\sin(\frac{C_pN_p}{2}) - s^2\right\}^2}{8Rs^2} \tag{6.23}$$

with $i = 1,2,\ldots,N-1$.

As mentioned in Section 6.2.2, the minimum edge profile below the intersecting points of each tool profile constitutes the surface roughness. The surface roughness profile at the k th radial section of the workpiece can be constructed by trimming the lines above the points of intersection.

Applying Equations (6.17) to (6.23) for all the radial sections, i.e. $k = 0,1,2,\ldots,N_p$, it is possible to determine the surface topography data on all $R_k - Z_k$ polar planes represented in polar co-ordinates $\{r_k, Z_k, k\Delta\theta\}$ for $k = 0,1,2,\ldots,N_p$. As shown in Figure 6.7, these data are mapped on the surface elements of a cross lattice as defined by:

$$XI = \left\lceil \frac{[\frac{L_x}{2} + r_k \sin(k\Delta\theta)]}{L_x} m_x \right\rceil \tag{6.24}$$

$$YI = \left\lceil \frac{[\frac{L_y}{2} + r_k \cos(k\Delta\theta)]}{L_y} m_y \right\rceil \tag{6.25}$$

$$ZI = Z_k \tag{6.26}$$

where $k = 0,1,2,\ldots,N_p$; m_x and m_y are the number of surface elements in the X and Y directions respectively; L_x and L_y are the length and the width of the simulated region.

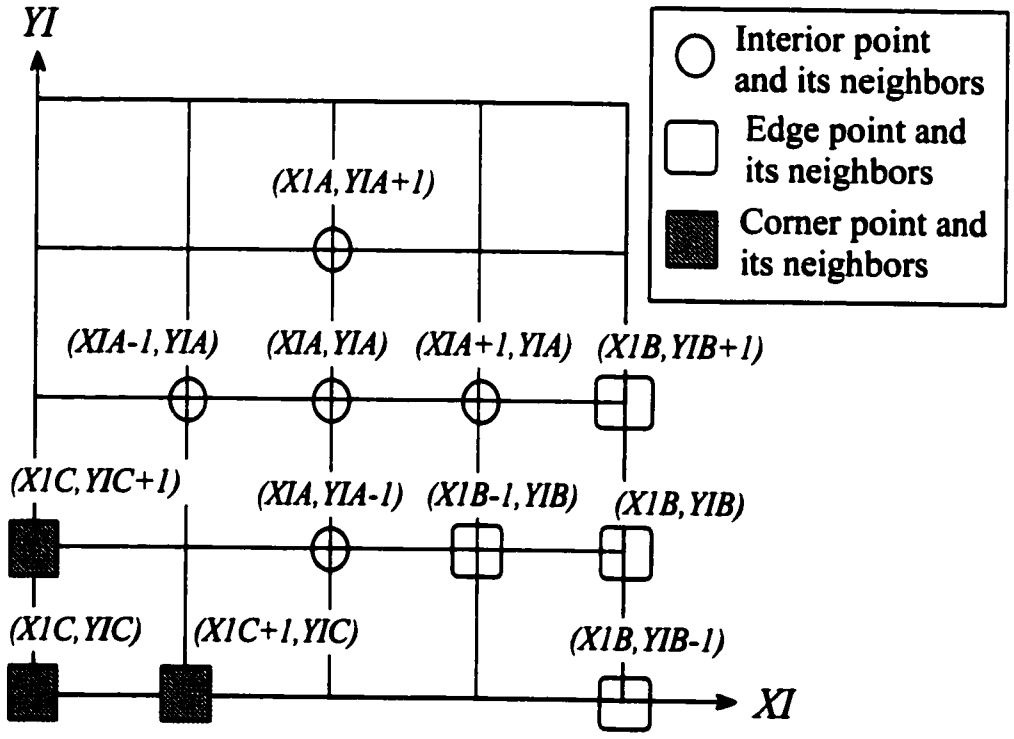

Figure 6.8 Definition of the nearest neighbours in the surface elements of a cross lattice

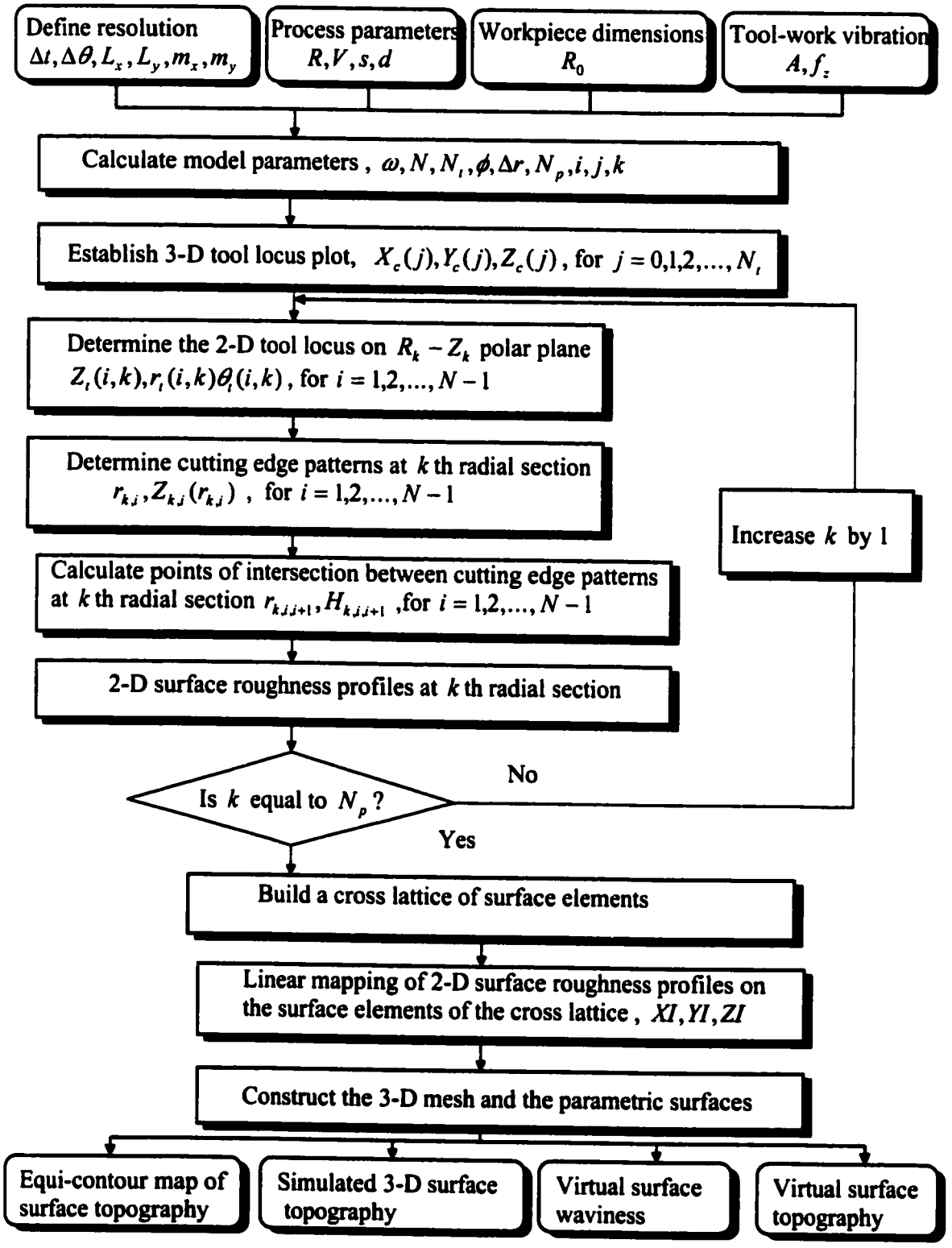

Figure 6.9 A schematic flow diagram for the 3-D simulation model

As shown in Figure 6.8, each point in the cross lattice can be thought of as being connected to its four nearest neighbours. This underlying cross lattice induces a four-sided element on the surface. Each interior point (XIA, YIA, ZIA) is connected to the four neighbours inherited. Points on the edge (XIB, YIB, ZIB) of the surface have three neighbours and those at the corners (XIC, YIC, ZIC) of the cross lattice have only two neighbours. The surface elements are used to build the mesh and the parametric surfaces which are best fitted to the surface topography data. The contour levels of the parametric surfaces are proportional to the surface height. Figure 6.9 depicts a schematic flow diagram of the 3-D surface topography model used in the generation of the surface topography. The model has been successfully implemented using MATLAB language and the program listing of it is given in Appendix IV.

6.2.5 Prediction of surface roughness parameters

In the present study, the surface roughness of the workpiece is characterised by the maximum peak-to-valley height R_t and arithmetic roughness R_a which are commonly used in assessing the surface quality in diamond turning. Assume that Set $\{Z_s\}$ contains N_s surface roughness heights Z_s predicted by the 3-D topography model over the simulated region, then the predicted maximum peak-to-valley height $\hat{R}_t$ and the predicted arithmetic roughness $\hat{R}_a$ are given as follows:

$$\hat{R}_t = \max\{Z_s\} - \min\{Z_s\}, \forall Z_s \in \{Z_s\} \tag{6.27}$$

$$\hat{R}_a = \frac{1}{N_s}\sum_{i_s=1}^{N_s}\left|Z_{s,i_s} - \overline{Z}_s\right| \tag{6.28}$$

where $Z_{s,i}$ is the i_s th predicted surface roughness height on the cross lattice

$$\bar{Z}_s = \left(\frac{1}{N_s} \sum_{i_s=1}^{N_s} Z_{s,i_s} \right) \tag{6.29}$$

6.3 EXPERIMENTAL VERIFICATIONS

The simulation model was evaluated through a series of cutting experiments. The experiments were divided into three groups, i.e., Group 6A, Group 6B and Group 6C. Group 6A included the experiments for determining the performance of the 2-D model in simulating the surface roughness profile under different modes of vibration. Group 6B involved the experiments for the verification of the performance of the 3-D model in simulating the features of the 3D surface topography. A parametric analysis of the performance of the 3-D model under different cutting conditions was done in Group 6C. All the experiments were carried out on a two-axis CNC ultra-precision machine (Nanoform 300 from Taylor Hobson Pneumo Co.). The workpiece materials are aluminium alloy (6061) and a copper alloy with chemical composition in percentage in weight of Cu. : Bal., Al:0.24, Fe:0.20, Zn:0.4, and Pb:0.12. The diameter of the workpiece is 12.7 mm.

Figure 6.10 shows the configuration of the experimental set-up used in the surface roughness analysis. The surface roughness profiles and the arithmetic roughness were measured by a Form Talysurf Laser Interferometric Profiler System. The output signal of the Form Talysurf was converted into ASCII file format and was fed into a PC computer for analysis. The power spectra of the roughness profiles were determined by a Fast Fourier Transform (FFT) routine developed based on Equations (4.1) to (4.7). The 3-D surface topography and the surface roughness parameters of the machined surfaces were measured by a WYKO TOPO-3D non-contact mircosurface measurement system (see Figure 6.11). In order to ensure compatibility and consistency between the predicted and the measured results, all simulations and measurements were made at the centre of the workpiece. All simulations were conducted at $N_p = 360$, i.e., $\Delta\theta = 0.0175$ radian, $L_x = L_y = 0.25$ mm, and $m_x = m_y = s/5$. A cut-off length of 0.25 mm was used throughout the experiments.

The cutting conditions for Group 6A and Group 6B are tabulated in Table 6.1 and Table 6.2 respectively. The relative vibration between the tool and the workpiece was measured on the centre line of the spindle by a capacitive displacement sensor with nanometer resolution during uncut conditions. Figure 6.12 shows the experimental set-up for the vibration measurement. The displacement sensor signal was first fed into an amplifier and the analogue output signal was recorded and digitised by a digitising oscilloscope (Tektronix TDS744A). Then, the digitised signal was passed on to a personal computer (PC) for analysis. The results of the vibration measurement are shown in Figure 6.13. Remarkable modes of vibration between the tool and the workpiece with an average magnitude of 15 nm and frequencies around 30 Hz and 45 Hz were found under Conditions 6A(I) and 6A(II) respectively. The second peak in Figure 6.13(a) is the first harmonic of the vibration signal. Thus, it is noted that there are some weak components in the power spectrum of the signals under both conditions. Since these components only contribute a relatively small proportion of the signals to the overall spectra, it is assumed that the vibration between the tool and the workpiece is a simple harmonic and this is the dominant mode of vibration considered in the present study.

Table 6.1 Machining conditions for Group 6A experiments

Condition no.	6A(I)	6A(II)
Spindle speed	2000 rpm	2000 rpm
Feed	25 mm min^{-1}	25 mm min^{-1}
Depth of cut	2 μm	2 μm
Rake angle of the tool	0°	0°
Tool nose radius	0.50 mm	1.55 mm
Average amplitude of relative tool-work vibration	0.015 um	0.015 um
Frequency of relative tool-work vibration	29.94 Hz	45.00 Hz

Table 6.2 Cutting conditions for Group 6B experiments

Spindle speed	500 rpm.
Feed	15 mm min^{-1}
Depth of cut	2 μm
Front clearance angle of the tool	12.5°
Rake angle of the tool	0°
Tool nose radius	1.554 mm

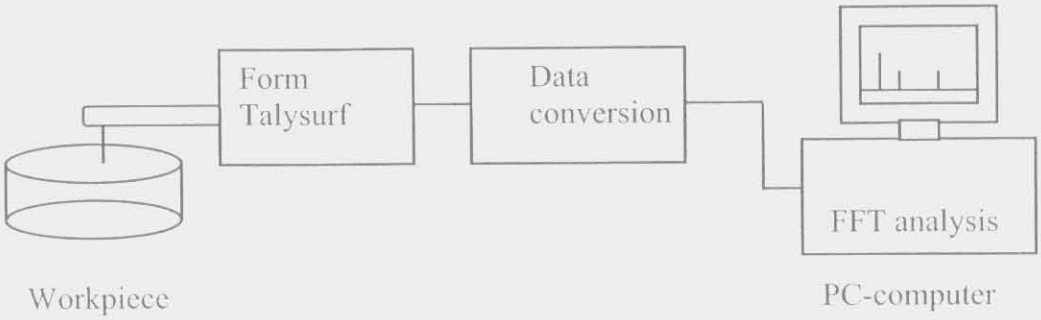

Figure 6.10 Experimental setup for surface roughness analysis

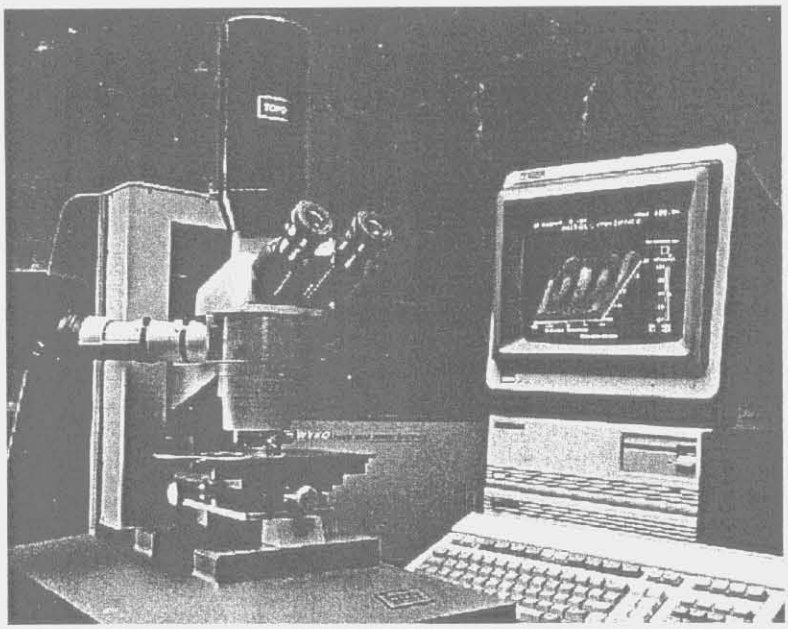

Figure 6.11 WYKO TOPO-3D non-contact microsurface measurement system

In Group 6C, a series of face cutting experiments was conducted under different cutting conditions. The experimental conditions are tabulated in Table 6.3. All the experiments in Group 6C were conducted under the same environment as in Condition 6A(II). The Set 6C(I) and Set 6C(II) experiments aimed at studying the effects of spindle speed and of feed rate on the surface roughness. The effects of depth of cut and of tool nose radius were studied in experiment set 6C(III) and 6C(IV), respectively.

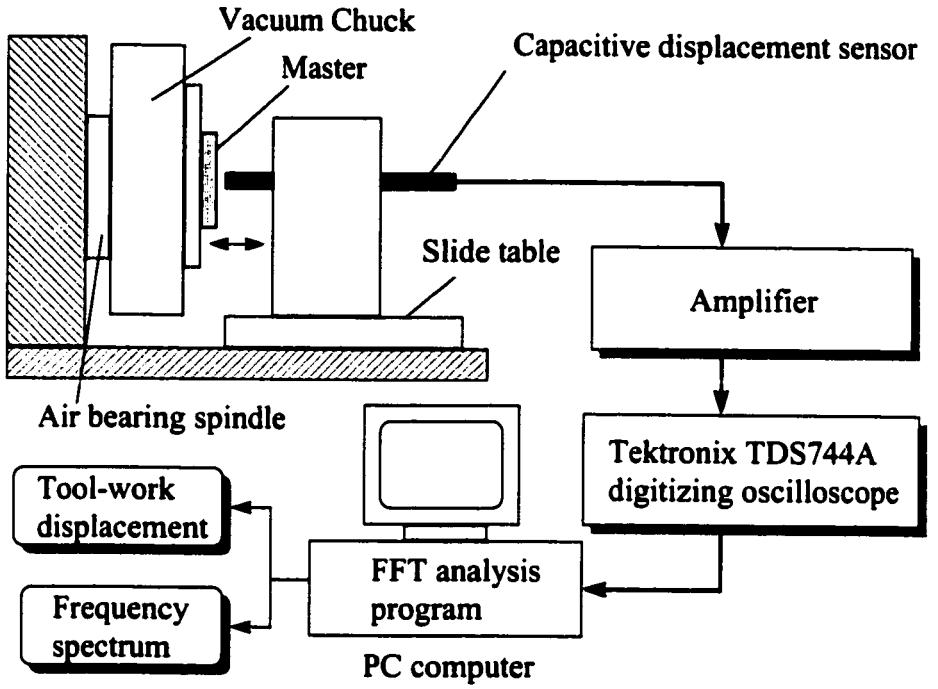

Figure 6.12 A schematic diagram for the measurement of the tool-work vibration

Table 6.3 Cutting conditions for Group 6C experiments

Set no.	Condition no.	Spindle speed (rpm)	Feed rate (mm min^{-1})	Depth of Cut (μm)	Tool nose radius (mm)
6C(I)	1	500	15	2	1.554
	2	1000	15	2	1.554
	3	1500	15	2	1.554
	4	2000	15	2	1.554
	5	2500	15	2	1.554
6C(II)	6	2000	10	2	1.554
	7	2000	15	2	1.554
	8	2000	20	2	1.554
	9	2000	25	2	1.554
6C(III)	10	2000	15	2	0.519
	11	2000	15	2	1.169
	12	2000	15	2	1.554
	13	2000	15	2	2.029
6C(IV)	14	2000	15	2	1.554
	15	2000	15	5	1.554
	16	2000	15	10	1.554
	17	2000	15	15	1.554
	18	2000	15	20	1.554

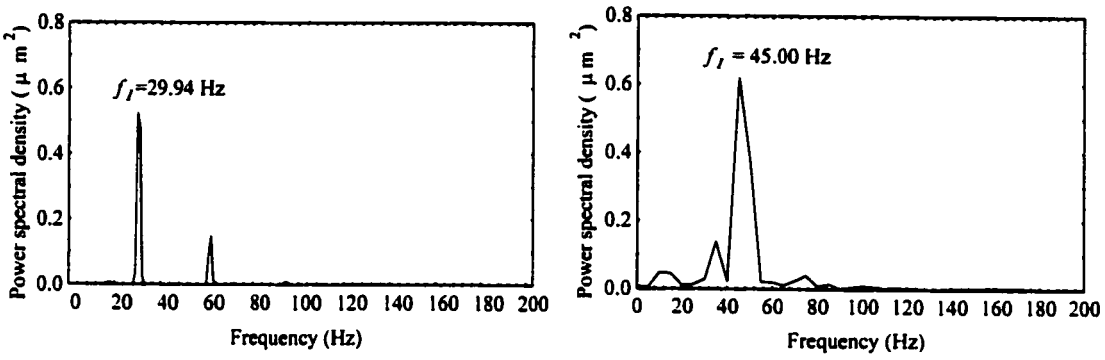

Figure 6.13 Spectrum plots of the measured relative tool-work displacement signals under (a) Condition 6A(I) and (b) Condition 6A(II)

6.4 RESULTS AND DISCUSSION

6.4.1 Performance of the 2-D model in the generation of a surface roughness profile

A simulated plot of the positions of the tool tip is shown in Figure 6.14. The plot illustrates the movement of the tool tip at each feed position across the workpiece. Such a movement can be visualised as successive movements of tool profiles across the workpiece as shown in Figure 6.15. As mentioned in Section 6.2.2, the surface roughness profile can be made by trimming the lines above the intersecting points of the minimum edge profile. Figures 6.16 and 6.17 show the simulated and measured surface roughness profiles of the workpiece generated under Condition 6A(I) and Condition 6A(II), respectively. A good agreement between the simulated and the measured profiles is observed under both machining conditions. The difference between the predicted and measured arithmetic roughness values was found to be less than 10%.

The formation of surface modulations on a diamond turned surface could be explained with the aid of the three dimensional tool locus plots. As shown in Figure 6.18, the simultaneous simple harmonic motion in the Z-axis and the kinematic spiral motion in the X-Y plane generate the surface waves in both the cutting and the feed directions. The two different patterns of tool locus illustrate that the frequency and the wavelength of the surface

waves in the feed direction are sensitive to the phase shifts $|\phi|$. As discussed in Chapter 3, the phase shift $|\phi|$ is related to the ratio between the frequency of tool-work vibration to spindle speed as shown in Equations (3.4) and (3.5). Equation (3.4) suggests that the surface waviness in the feed direction could be eliminated by a zero phase shift which occurs as the frequency of vibration becomes equal to or a multiple of the spindle rotational speed. A cutting experiment was conducted to verify the argument. The experiment was conducted under Set 6C(I) cutting conditions and dynamic conditions in Condition 6A(II). The experimental results are found to have a strong correlation with the simulated ones (see Figure 6.19). It is confirmed that there are optimum or sub-optimum phase shifts $|\phi|$ at which the surface roughness can be significantly improved. This suggests that, under a known and steady vibration environment, the surface roughness of a diamond turned surface can be improved with the use of an optimum phase shift $|\phi|$ which can be obtained by adjusting the spindle rotational speed.

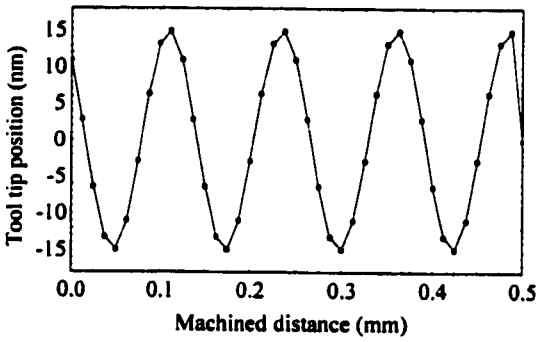

Figure 6.14 Tool nose position plot

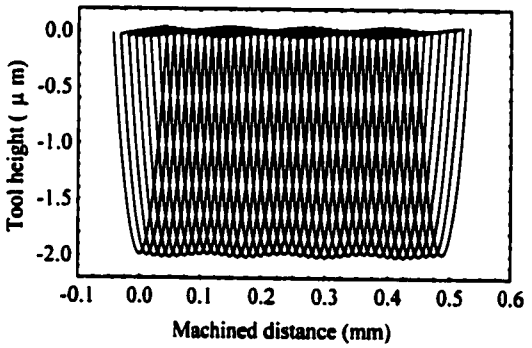

Figure 6.15 Simulated tool orbit

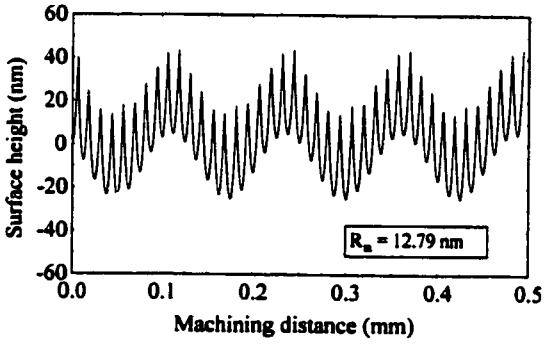

(a)

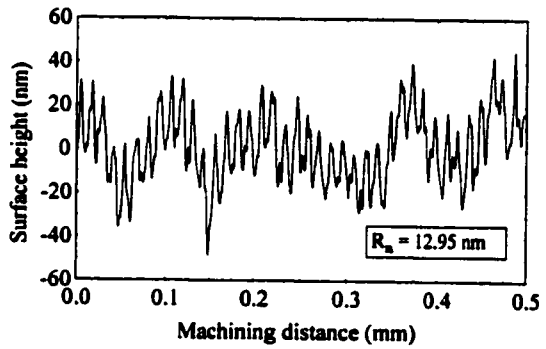

(b)

Figure 6.16 A comparison between (a) the simulated and (b) measured surface roughness profiles under Condition 6A(I)

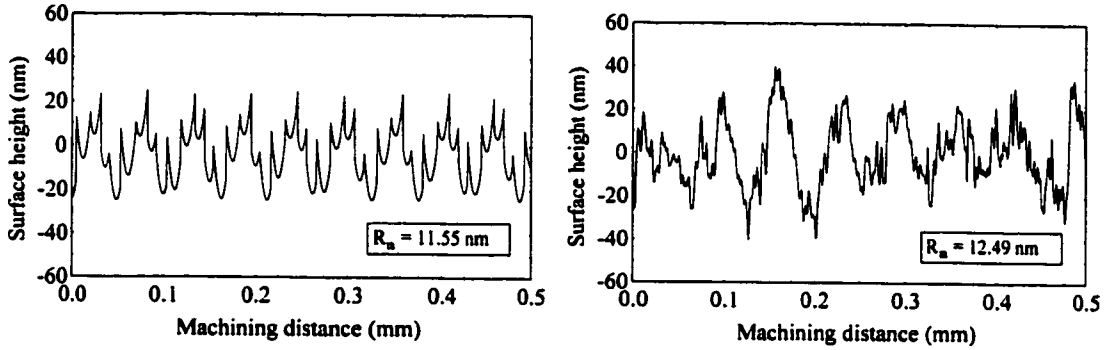

Figure 6.17 A comparison between (a) the simulated and (b) measured surface roughness profiles under Condition 6A(II)

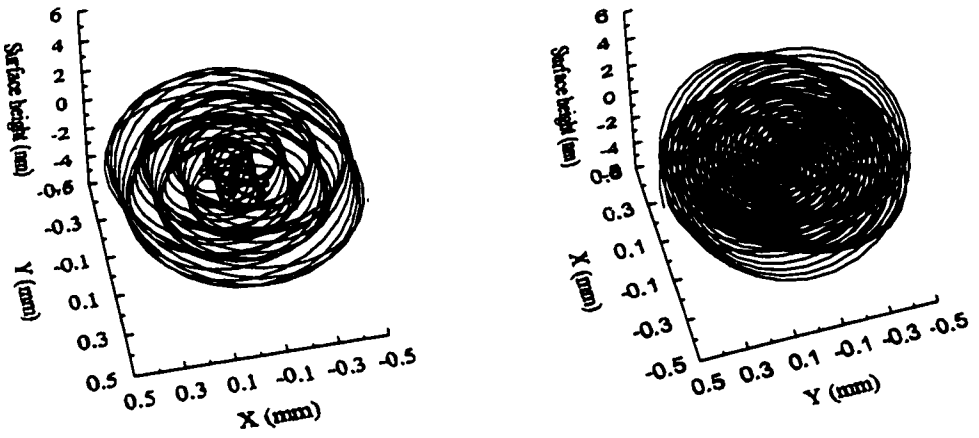

Figure 6.18 Simulated 3-D tool locus plots for diamond cutting under (a) Condition 6A(I) and (b) Condition 6A(II)

The process of the surface generation was examined in details using Fast Fourier Transform (FFT) analysis. Firstly, the ideal roughness profile and its spectrum were generated under Condition 6A(I) (Figure 6.20). The simulated and measured spectral plots generated under Condition 6A(I) are depicted in Figures 6.21(a) and 6.21(b), respectively. It is noticable that the simulated spectrum which consists of strong feed components at ν_2 and ν_3 are similar to those found in the ideal spectrum. The relative vibration between the tool and the workpiece was found to contribute to the low frequency component at ν_1. Similar components are observed in the measured spectrum. Figure 6.22 shows spectrum plots for the predicted and measured surface roughness profiles generated under Condition 6A(II). The

spectral plots are found to be composed of more complicated components. A good agreement between the predicted and measured spectral plots is observed. The components ν_4 and ν_5 are the feed component and its first harmonic respectively. The effect of the tool-work vibration is reflected in the spectral components ν_1, ν_2 and ν_3.

The use of the 2-D model together with the spectrum analysis technique allows us to generate different norm spectra under different machining conditions. Comparing the norm spectrum with the measured one, it is possible to determine any drift in the dynamic characteristics of a machine tool.

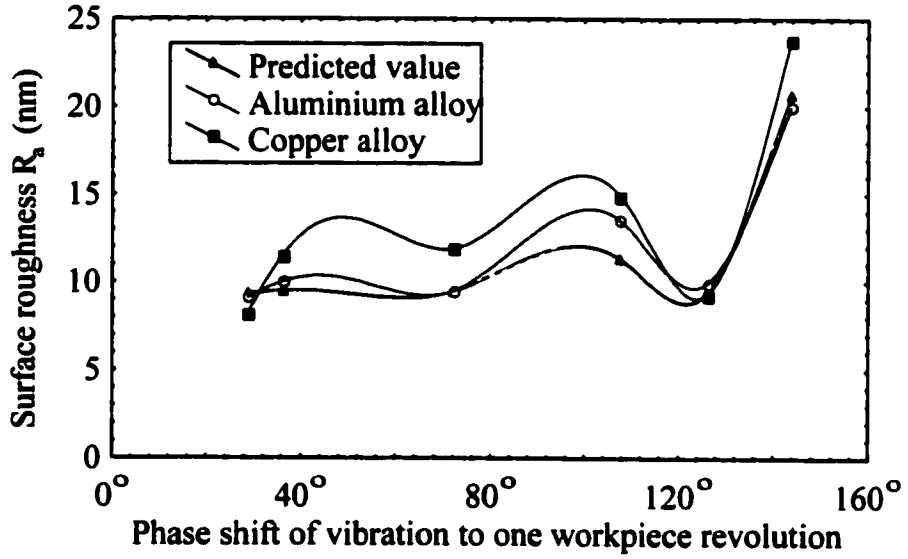

Figure 6.19 Effect of phase shift of the relative tool-work vibration on surface roughness

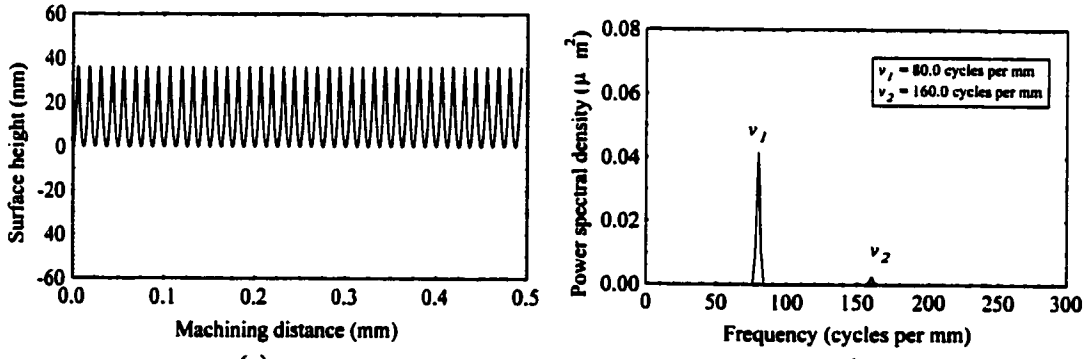

Figure 6.20 (a) Ideal surface roughness profile and (b) its power spectrum

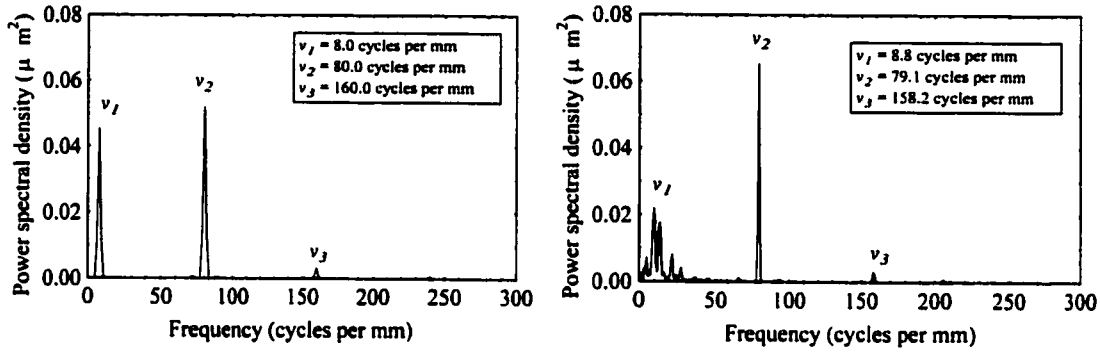

Figure 6.21 A comparison between (a) the simulated and (b) measured power spectrum density of the surface roughness profile under Condition 6A(I)

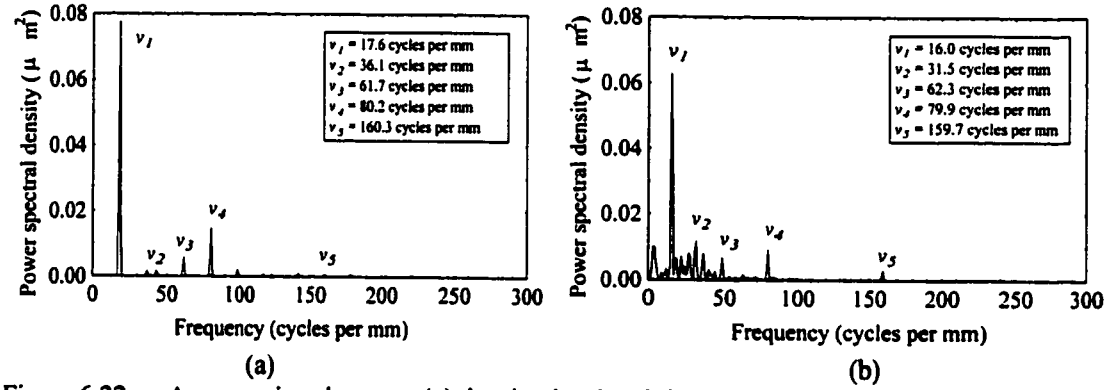

Figure 6.22 A comparison between (a) the simulated and (b) measured power spectrum density of the surface roughness profile under Condition 6A(II)

6.4.2 Visual performance of the 3-D model in the simulation of surface topography

Figure 6.23 shows the locus of the tool generated under the tool-work vibration as described in Figure 6.13(b). Based on Equations (6.16) to (6.18), the tool moves with a spiral locus on the X-Y plane towards the centre of the workpiece. Simultaneously, the tool vibrates with a simple harmonic motion in the infeed cutting direction, i.e. the Z-axis direction. The kinematics of the tool motion generates modulation/waviness on the machined surface as shown in Figure 6.24. This can be visualised in a plot of the virtual surface waviness and an equi-contour map as shown in Figure 6.25 and Figure 6.26, respectively. The equi-contour map gives a clear picture of the distribution of the surface heights attributed to the surface waviness.

By adding the tool geometry component to the model using Equations (6.19) to (6.23), a simulated 3-D surface topography of the diamond turned surface is produced. This is shown in Figure 6.27(a). The predicted surface topography is very similar to the one obtained from the interferometric microscope (see Figure 6.27(b)). In addition, the model is found to give an estimate of the surface roughness value R_t of 92.6 nm which is closet to measured value of 94.4 nm.

In order to have a close examination of the surface features such as the tool motion trace, machine marks and lay of the surface, the predicted 3-D surface topography was mapped on a 2-D equi-contour map as shown in Figure 6.28(a). When compared with the measured 2-D equi-contour map, as shown in Figure 6.28(b), a close agreement between the two is found. Most of the surface features found in the measured pattern are reflected in the simulated pattern generated by the 3-D surface topography model. These further demonstrate the capability of the model to simulate the surface topography of a diamond turned surface. Figure 6.29 shows a virtual surface topography of a diamond turned workpiece. The use of virtual surface representation allows us to visualise and examine in detail the various features of the surface topography.

6.4.3 Parametric analysis of the performance of the 3-D model under different cutting conditions

Figures 6.30 and 6.31 show the effect of the spindle speed and the feed rate on the surface roughness parameters. It is found that both of the maximum peak-to-valley height R_t and the arithmetic roughness R_a decrease with small feed rate and increase with large feed rate. As the spindle speed increases, these surface roughness parameters are found to decrease. There is a good correlation between the experimental and the simulation results.

The effect of tool nose radius and depth of cut on the surface roughness parameters (i.e., R_t and R_a) are shown in Figure 6.32 and Figure 6.33, respectively. It is found that the surface roughness decreases with increasing tool nose radius as Equations (6.2) and (6.3) suggest. On

the other hand, they are shown to vary with increasing depth of cut. As mentioned in Chapter 3, this might be due to the presence of voids or impurities as well as the plastic anisotropy of the workpiece materials. Although no systematic relationship is found between the depth of cut and the surface roughness parameters, the model seems to give a representative estimate of these parameters.

Overall, there is a good agreement between the experimental findings and the simulation results under various cutting conditions. The difference between the predicted and the measured surface roughness parameters are found to be within 15% in most cases. The average errors for the prediction of the R_t and the R_a values are 10.5% and 20.1% respectively. The discrepancies could be caused by the following factors:

(i) In the surface topography model, the relative tool-work vibration is assumed to be steady and a simple harmonic motion. Only the dominant mode of vibration is considered in this study. However, other vibration modes like low frequency vibration from the machine foundation could have entered into the cutting system during machining;

(ii) Progress of the tool wear during machining;

(iii)The swelling and recovery of the tool marks on the machined surfaces;

(iv)Only the relative tool-work vibration in the infeed cutting direction is considered in the study. The effect of the radial and face errors of the spindle as well as the vibration in the yaw direction have not been taken into account;

(v) Metallurgical properties of the workpiece material have not been included in the model. Therefore, any variations of the surface roughness due to the presence of voids and impurities have not been considered.

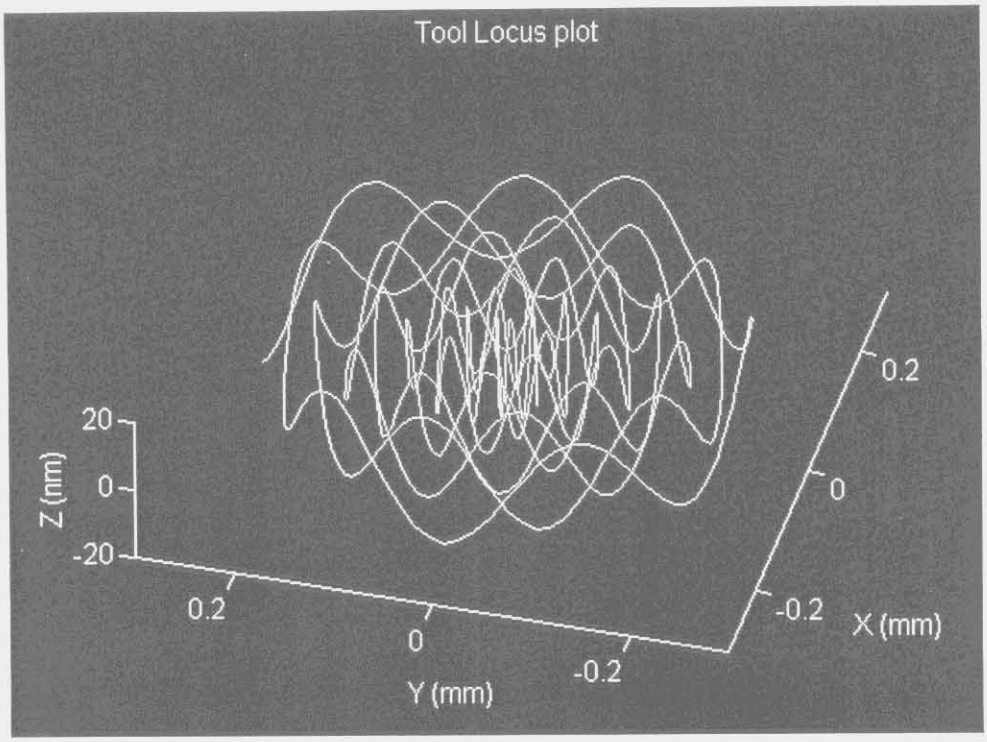

Figure 6.23 3-D plot of the tool locus

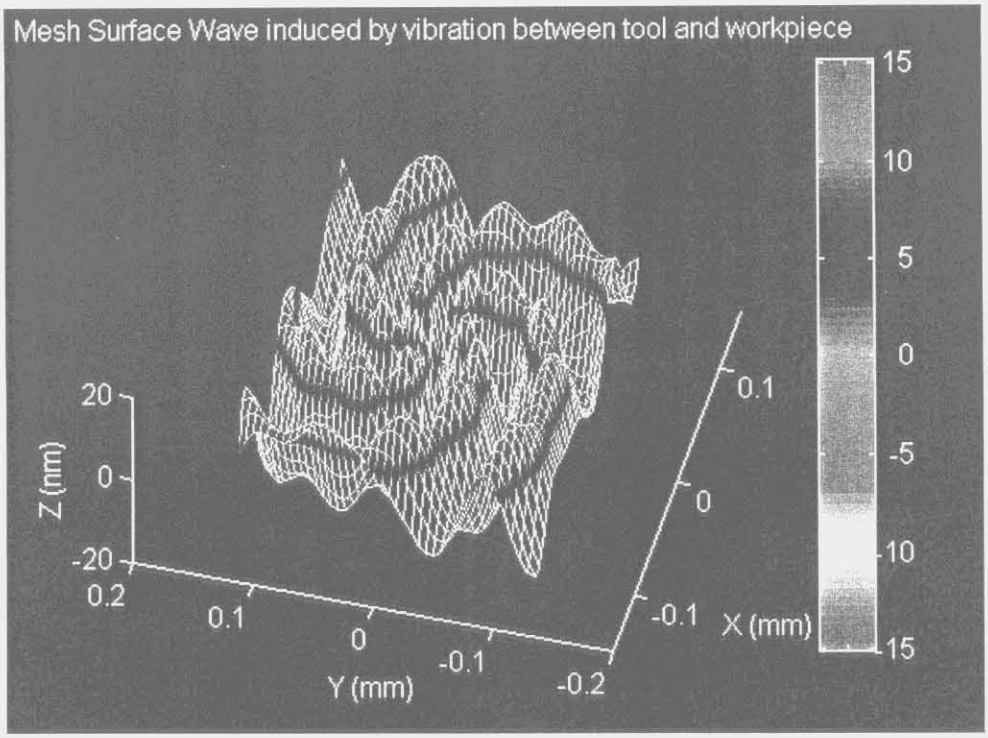

Figure 6.24 Simulated surface waviness

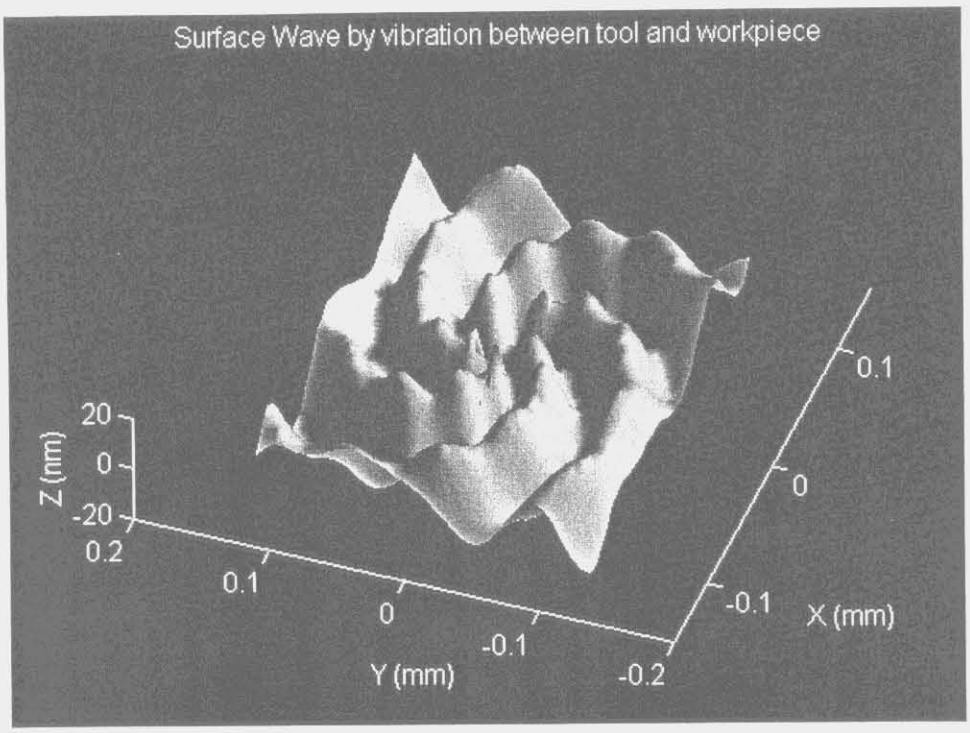

Figure 6.25 Virtual surface waviness

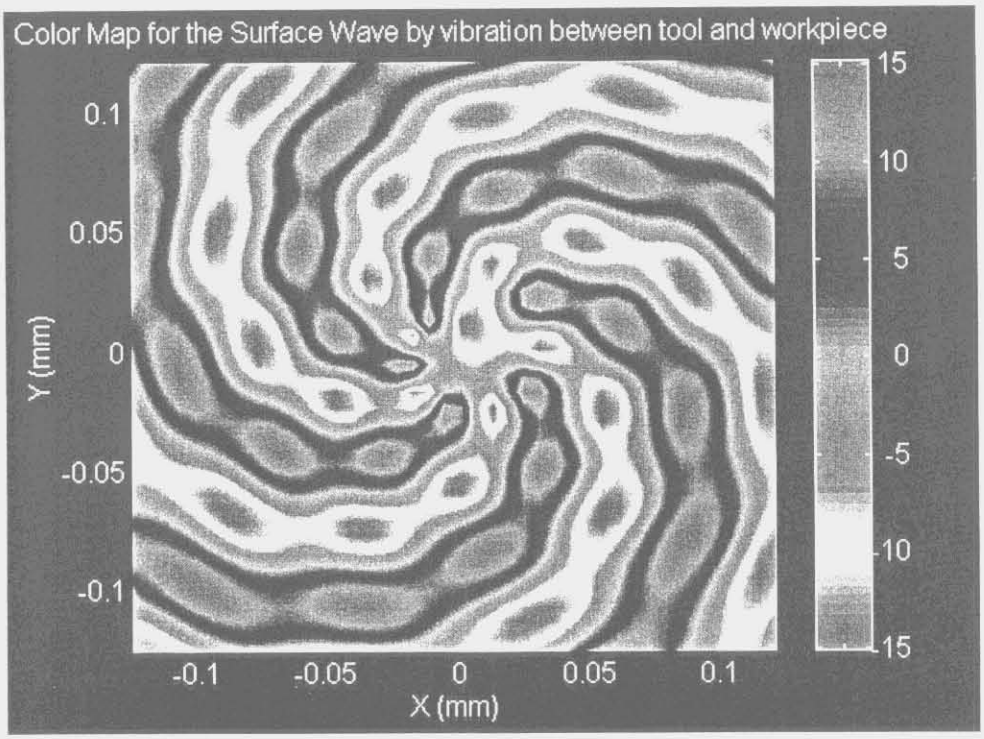

Figure 6.26 Equi-contour map for the surface waviness

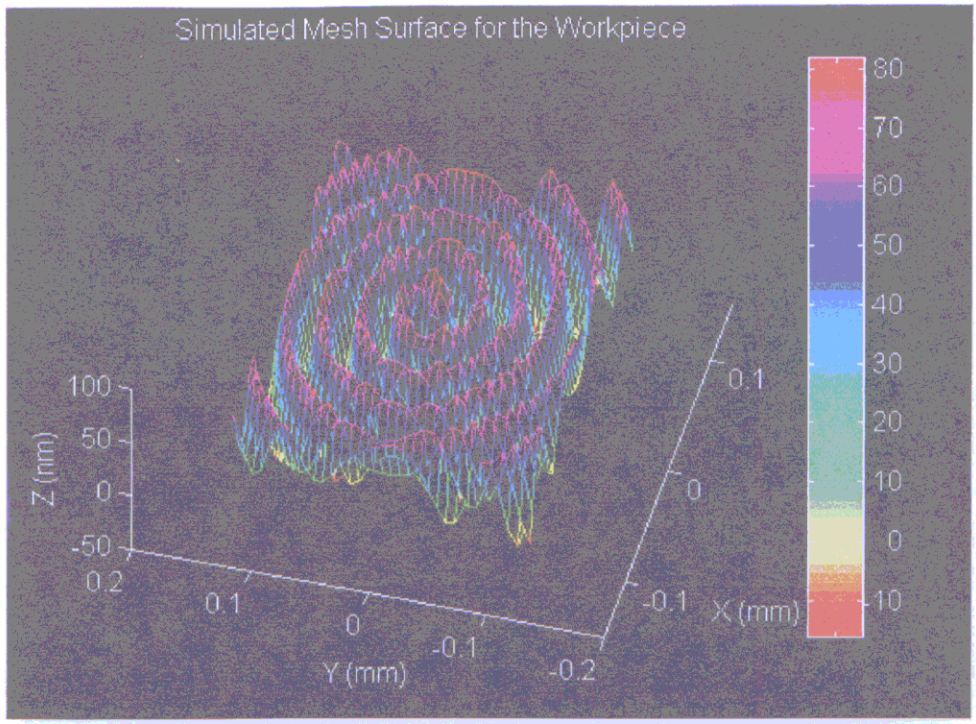

(a)

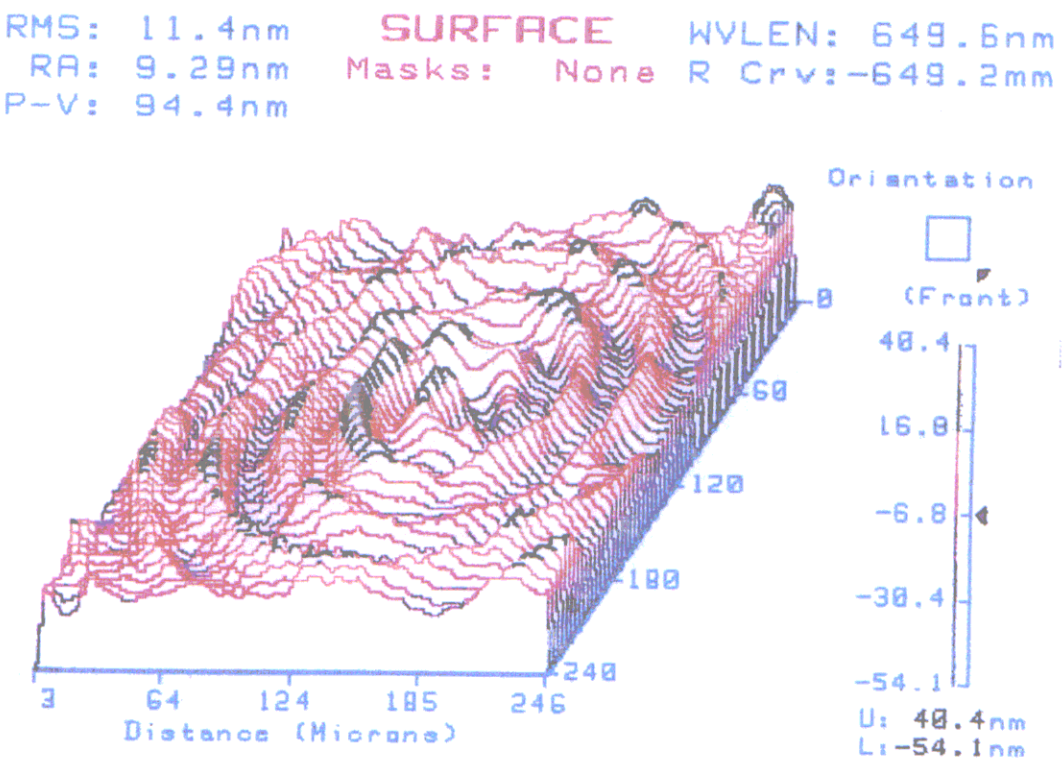

(b)

Figure 6.27 (a) Simulated and (b) measured 3-D surface topographies

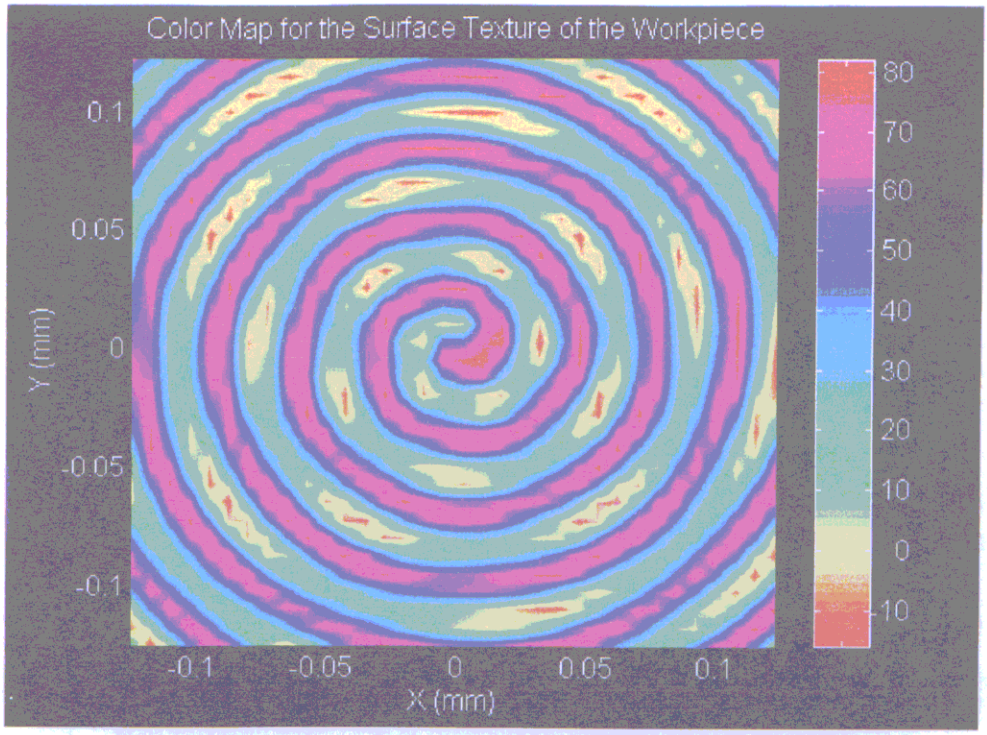

(a)

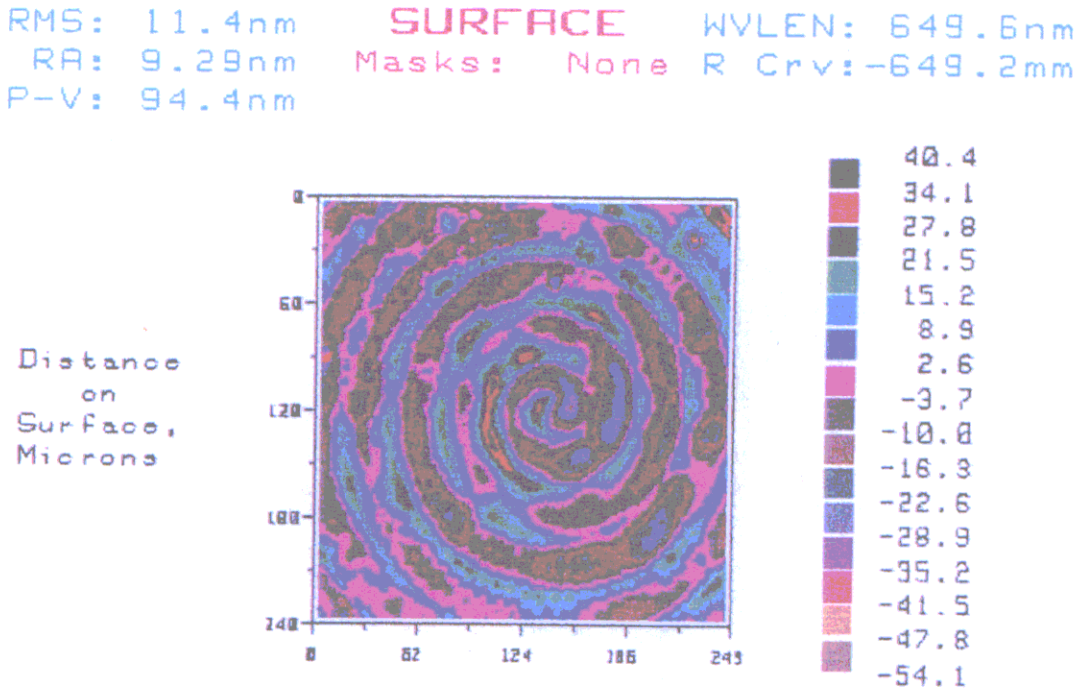

(b)

Figure 6.28 Equi-contour maps for (a) the simulated and (b) the measured surface topographies

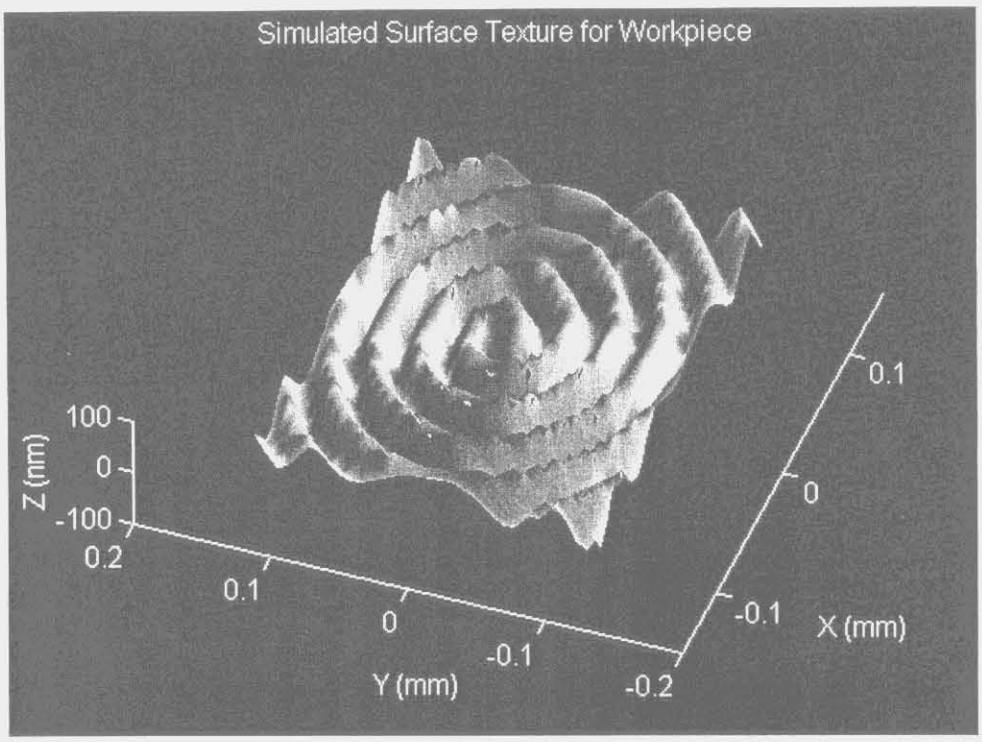

Figure 6.29 Virtual surface topography of the turned workpiece

Although the proposed model could not account for the recovery and swelling effects, it is shown to be effective in accounting for most of the process effects on the surface generation in diamond turning. As noticed in the results of DDS analysis as shown in Chapter 5, the process factors are found to contribute about 80% of the total roughness in diamond turning of polycrystalline aggregate under various cutting conditions. Therefore, the selection of an optimum cutting condition is vital for improving the surface quality. In the following section, a potential application of the model for process optimisation is discussed.

6.5 APPLICATIONS OF THE MODELS

Conventionally, the selection of set-up parameters for the diamond turning process is done with the aid of trial cutting tests, which are both time-consuming and costly. The process quality depends largely on the experience of the operator. In practice, the optimum cutting

conditions could easily drift due to any change in the machining environment. Frequent re-calibrations are therefore needed to ensure a certain level of surface quality.

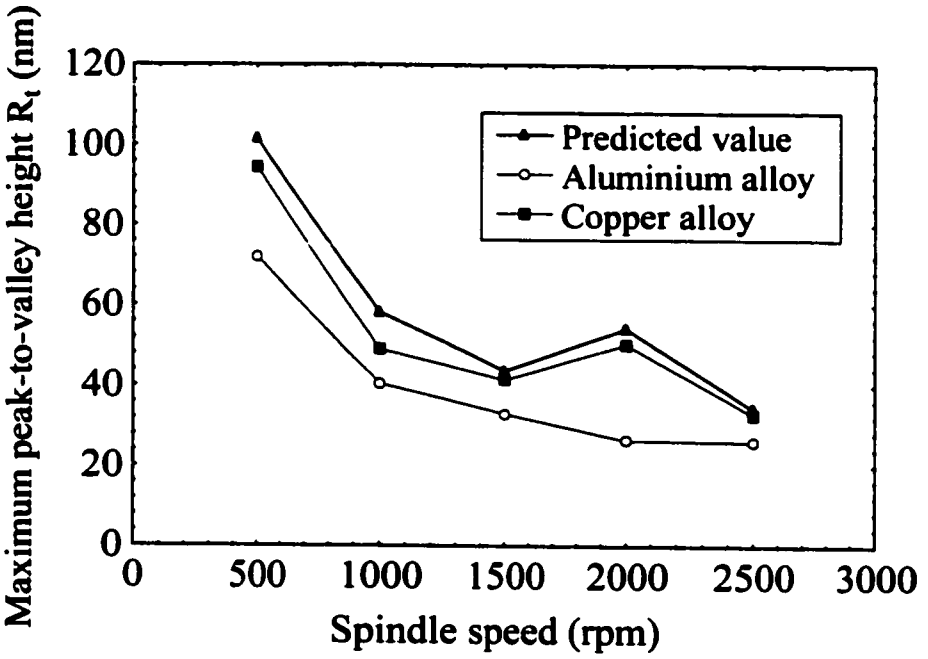

(a)

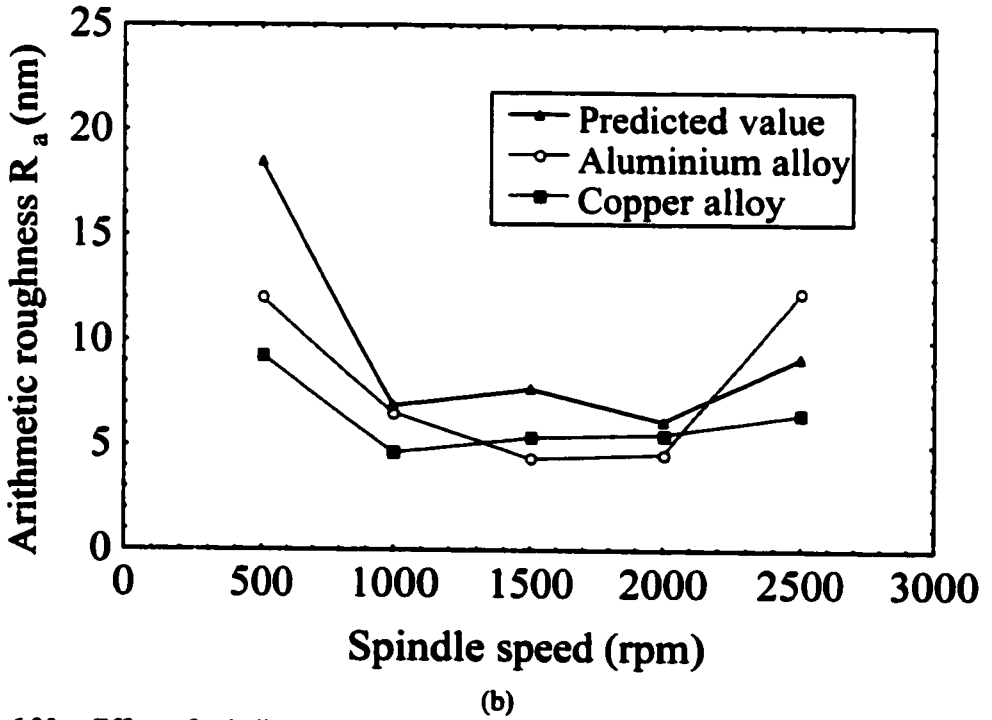

(b)

Figure 6.30 Effect of spindle speed on: (a) maximum peak-to-valley height and (b) arithmetic roughness

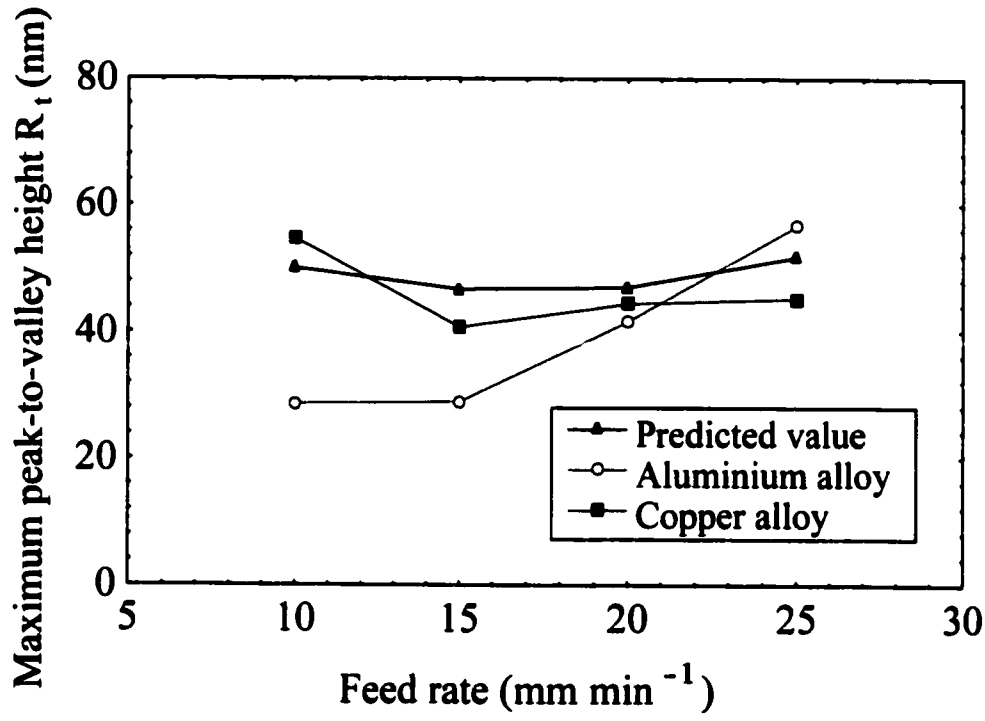

(a)

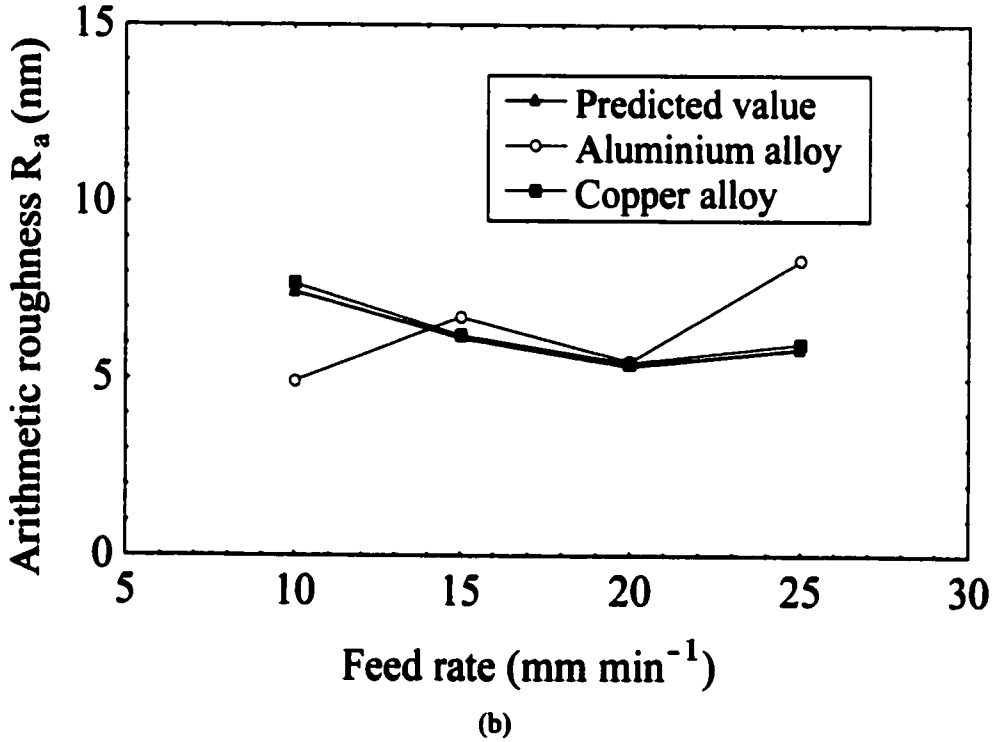

(b)

Figure 6.31 Effect of feed rate on : (a) maximum peak-to-valley height and (b) arithmetic roughness

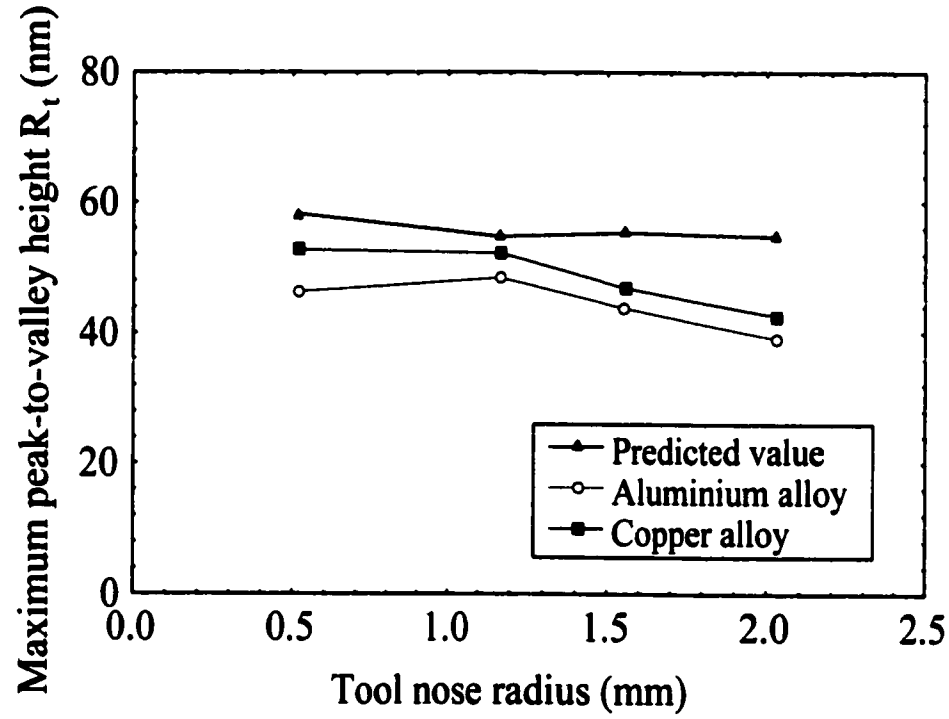

(a)

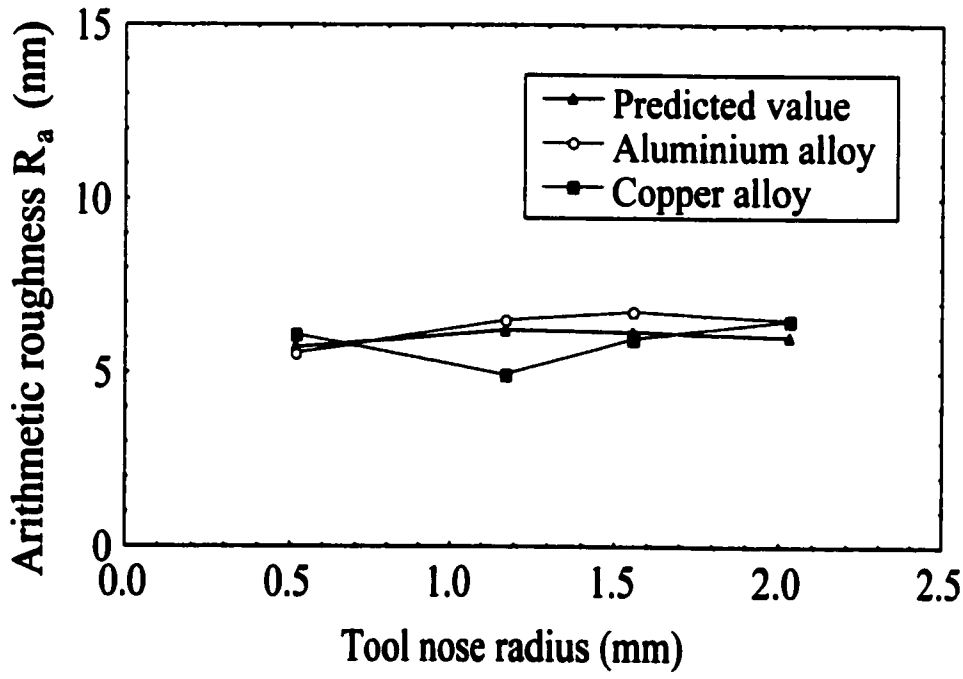

(b)

Figure 6.32 Effect of tool nose radius on : (a) maximum peak-to-valley height and (b) arithmetic roughness

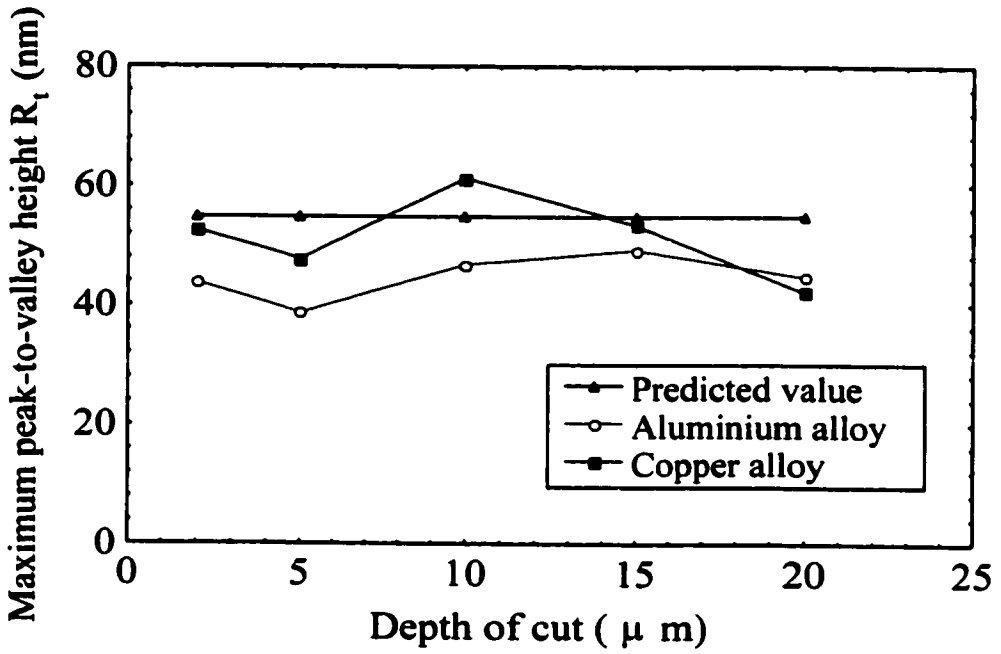

(a)

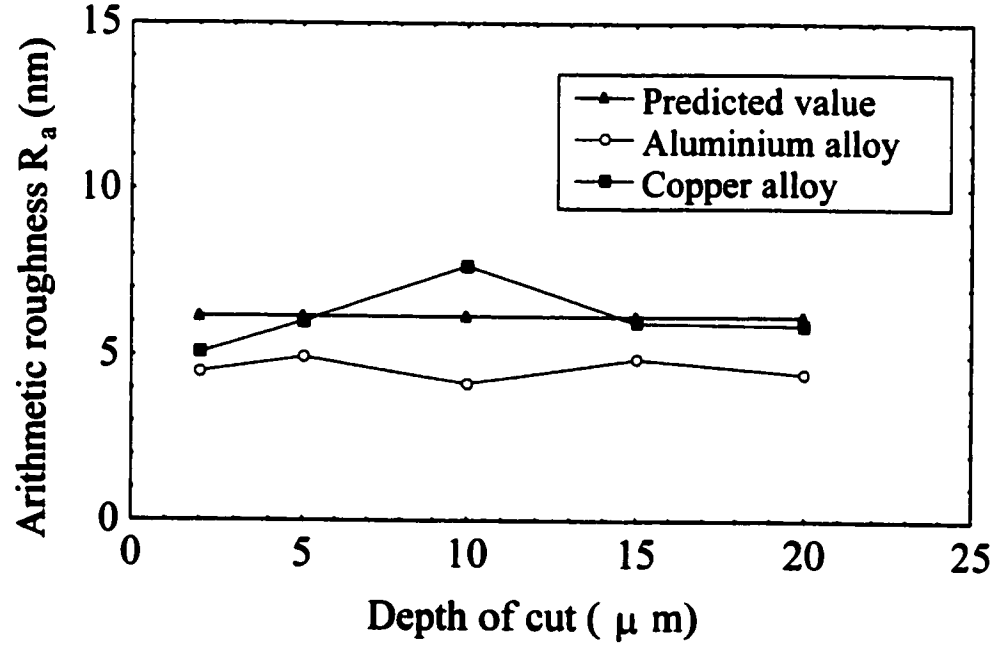

(b)

Figure 6.33 Effect of depth of cut on : (a) maximum peak-to-valley height and (b) arithmetic roughness

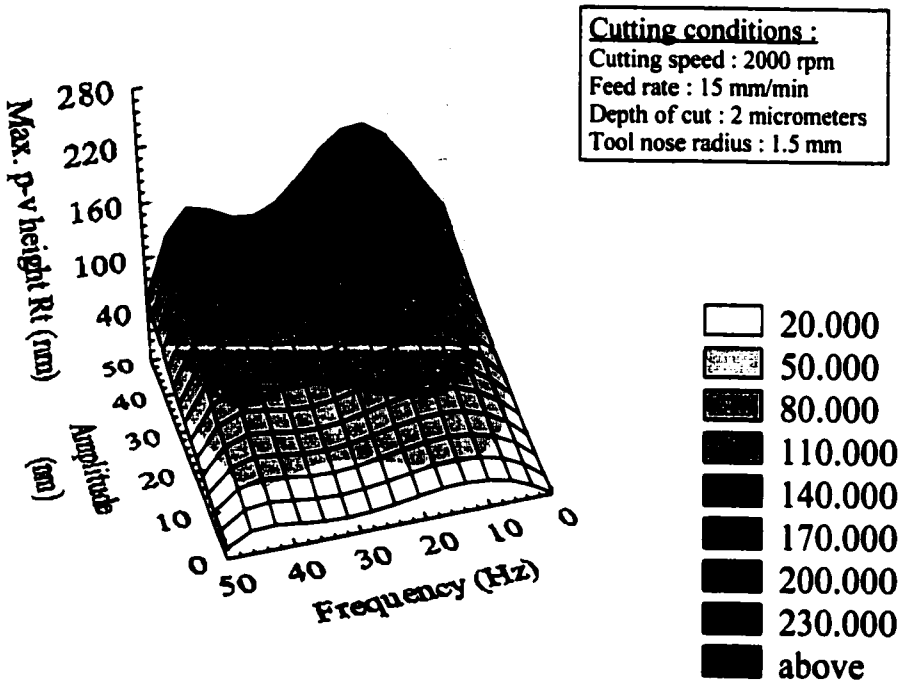

(a)

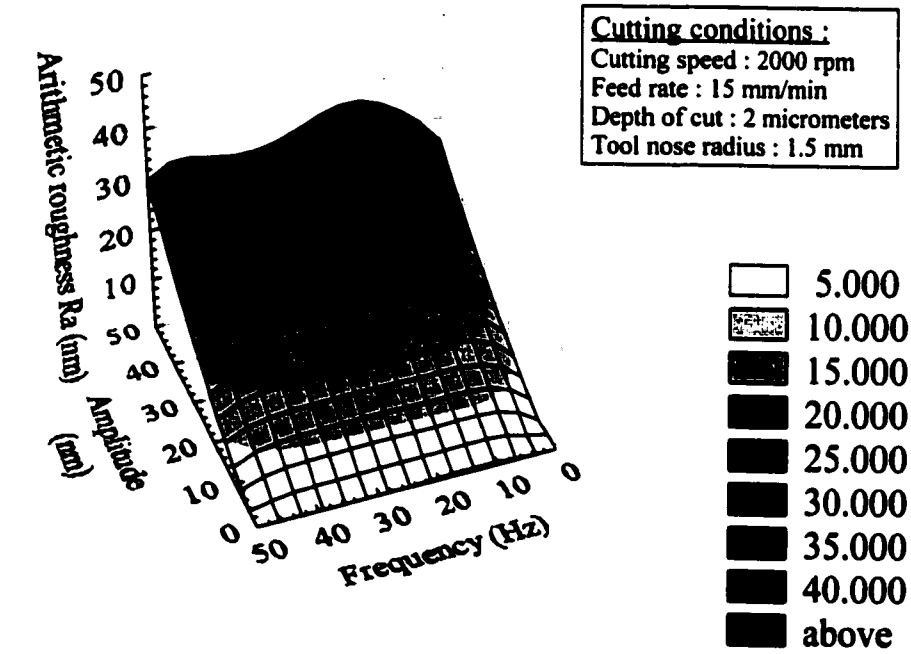

(b)

Figure 6.34 Performance characteristic diagrams showing the effect of the amplitude and frequency of the relative tool-work vibration on: (a) maximum peak-to-valley height and (b) arithmetic roughness

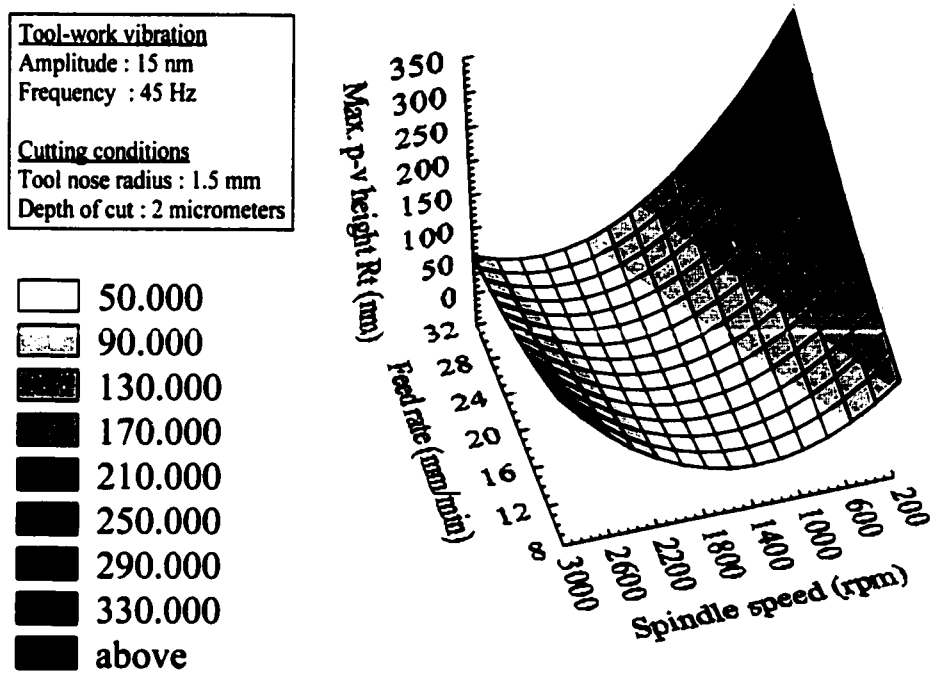

(a)

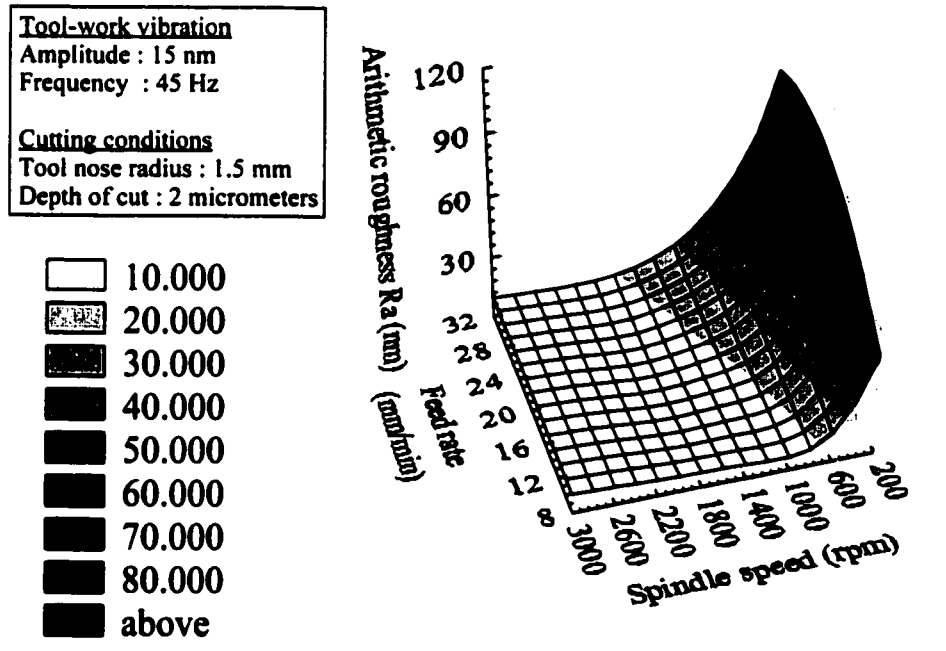

(b)

Figure 6.35 Performance characteristic diagrams showing the effect of spindle speed and feed rate on : (a) maximum peak-to-valley height and (b) arithmetic roughness

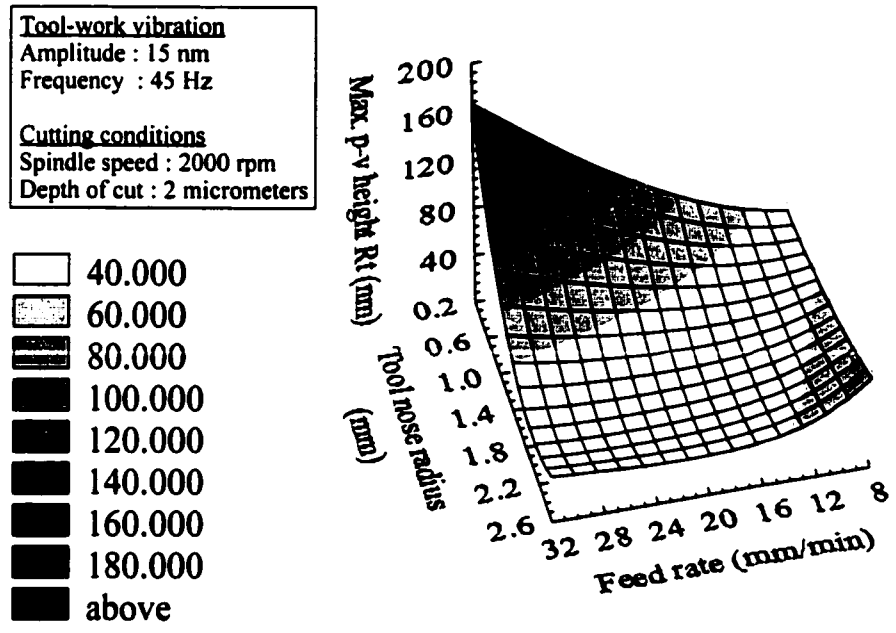

(a)

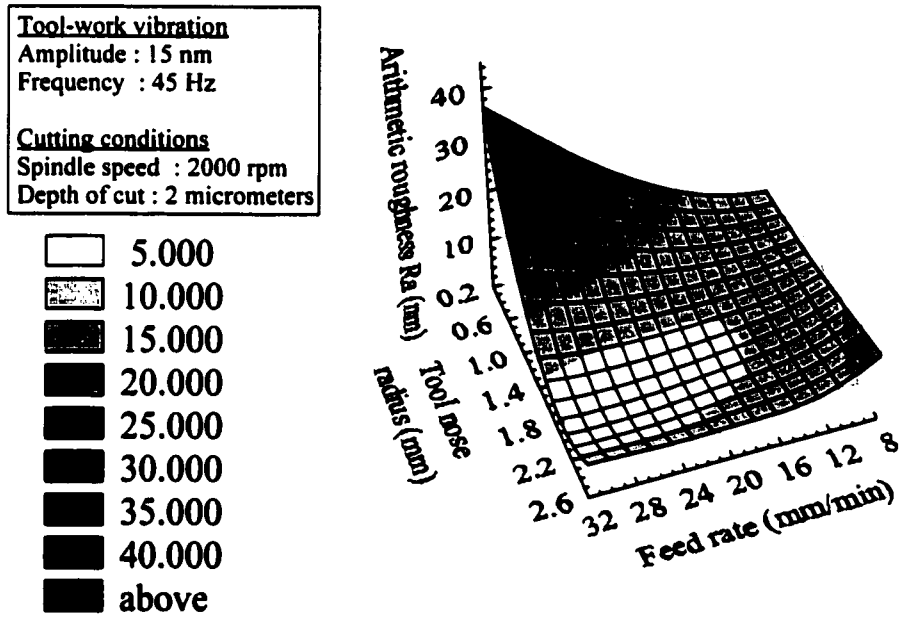

(b)

Figure 6.36 Performance characteristic diagrams showing the effect of feed rate and tool nose radius on: (a) maximum peak-to-valley height and (b) arithmetic roughness

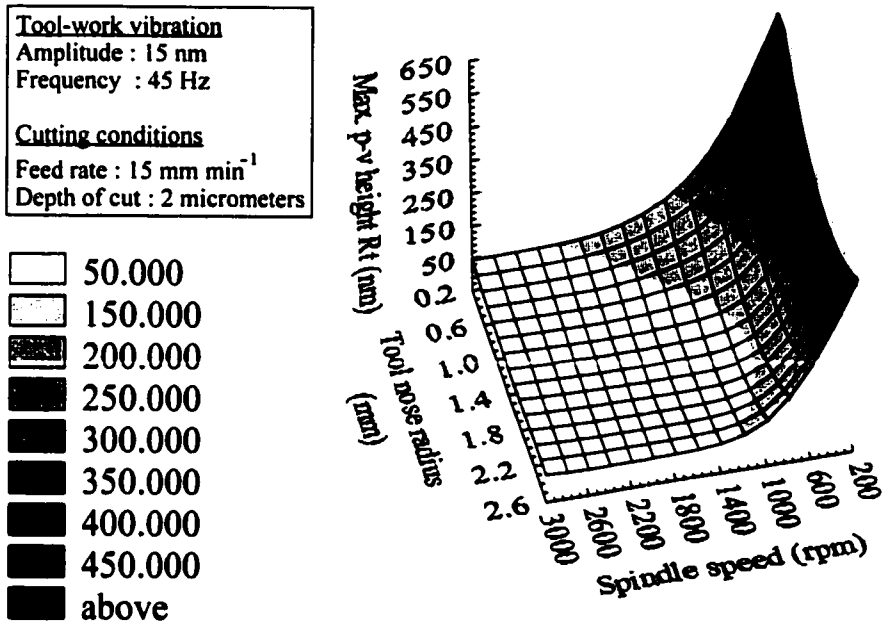

(a)

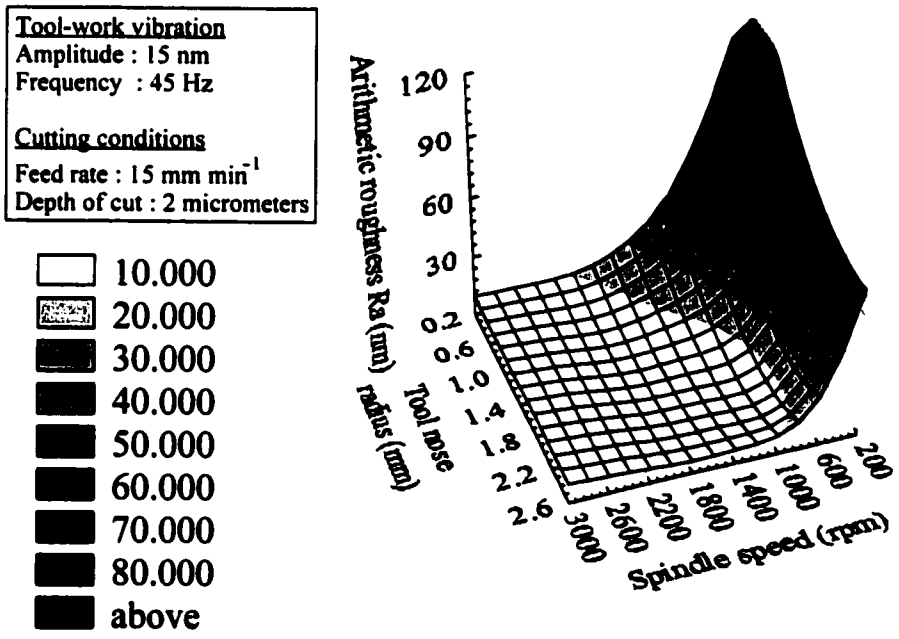

(b)

Figure 6.37 Performance characteristic diagrams showing the effect of spindle speed and tool nose radius on : (a) maximum peak-to-valley height and (b) arithmetic roughness

The proposed model contributes significantly to our understanding of the cutting process and creates a pre-condition for increased efficiency while ensuring high product quality at the same time. With the application of the surface topography model in process optimisation, an optimum cutting condition could be predicted without the need for conducting massive trial cutting tests. Figure 6.34 shows a performance characteristics diagram constructed by the simulation system under various amplitudes and frequencies of the relative tool-work vibration. The surface roughness is found to vary approximately linearly with increasing amplitude of vibration. It is also noted that the surface roughness varies periodically with increasing frequency of vibration. This can be explained by the change of phase shift with frequency as suggested by Equations (3.4) and (3.5). In fact, Figure 6.34 allows us to identify the best surface roughness quality that can be achieved under particular tool-work vibration characteristics.

The performance characteristic diagrams for different combinations of feed rate and spindle speed are illustrated in Figure 6.35. Figure 6.36 shows the performance characteristic diagrams for different combinations of feed rate and tool nose radius, while that for different combinations of spindle speed and tool nose radius are shown in Figure 6.37. In Figure 6.35, it is found that there are optimum ranges of spindle speed and feed rate that would generate preferable small surface roughness. Similar results are found in Figure 6.36 and Figure 6.37. Since the levels of the surface roughness are depicted in contour levels in the performance characteristic diagrams, the permissible combinations of process parameters could be easily identified. Indeed, the performance characteristic diagrams could provide an essential means for optimising the set-up conditions in the diamond turning process.

Other applications of the surface topography model include the simulation of virtual surfaces and surface features like those illustrated in Figure 6.25 and Figure 6.29. The construction of virtual surfaces allows us to visualise the surface quality of a machined surface. The possible factors affecting surface quality can be identified and studied individually.

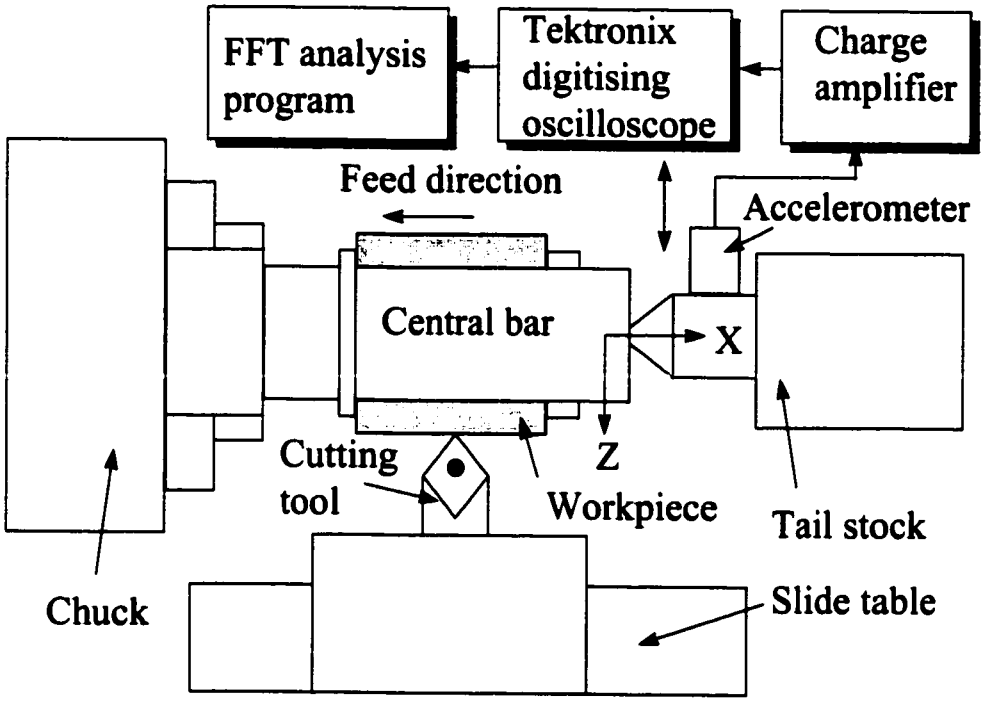

Figure 6.38 Proposed setup configuration for the side turning process

The modelling techniques used in the present study could be extended to other machining processes, tool and workpiece combinations. With a modification of the setup configuration (Lin and Chang, 1997) as proposed in Figure 6.38, the 2-D model described in Section 2.1 could be applied to the prediction of the surface roughness profile and hence the surface roughness parameters for the side turning process.

Fly cutting is another ultra-precision machining technique which is usually employed in machining flat or off-axis mirror finished surfaces. The fly-cutting operation is performed by a fly-cutter tool mounted directly on the air bearing spindle while the workpiece is fixed at the hydrostatic slide. The 3-D modelling techniques used in the present study could be extended to the fly-cutting operation provided that the workpiece could be cut perpendicular to the fly-cutter feed and if the diameter of the fly-cutter is much larger than the width of the workpiece.

6.6 SUMMARY

The establishment of a 3-D surface topography simulation model for ultra-precision diamond turning is presented. The model takes into account the effects of tool geometry, machining conditions as well as relative tool-work vibration. It makes use of the surface roughness profiles predicted at a finite number of radial sections of the workpiece to construct the surface topography of a diamond turned surface. A series of cutting experiments has been conducted to verify the performance of the model. The results indicate that the model can predict well the surface roughness parameters as well as the 3-D surface topography. With the use of equi-contour mapping techniques, it is possible to abstract the surface features like the trace of tool motion, characteristics of the 3-D surface texture as well as the presence of the surface marks caused by vibration.

Ultra-precision diamond turning is an expensive process. With the development of the topography model, it is now feasible to determine the optimum cutting conditions without the need for costly trial and error cutting tests. It also helps to establish the best surface finish that can be achieved under a particular machining condition. The performance characteristic diagrams generated by the simulation model provide an essential means for determining the optimum set-up conditions in diamond turning. With appropriate modifications of the setup configurations, the modelling technique could also be extended to other processes and, tool and workpiece combinations.

Chapter 7

Modelling and Simulation of Surface Topography (II) : Materials Induced Vibration

7.1 INTRODUCTION

As discussed in the previous Chapters, the surface roughness of a diamond turned surface is not only affected by the process factors such as tool feed rate, spindle rotational error and tool geometry but also the material factors like material swelling, plastic anisotropy and materials induced vibration. The topography simulation model established in Chapter 7 is shown to be capable of accounting for most of the process effects on the surface roughness. The optimisation of the cutting conditions to minimise adverse process effects has also been proposed. However, in machining anisotropic materials like single crystals, experimental results show clearly that the surface roughness varies with the changing crystallographic orientation of the substrate being cut. The captioned topography simulation model alone will not be able to explain this phenomenon.

Although most of the materials used in diamond turning are polycrystalline in nature, the use of single crystal materials is not uncommon. Examples include the use of KDP single crystal in laser systems and single crystal silicon for high precision infrared optical systems. Single crystal materials are known to be highly anisotropic in their physical and mechanical properties. The local variation of machinability due to the variation of the crystallographic orientation induces a local variation in the surface qualities (Nakasuji, 1990). On the other hand, as shown in Chapter 3, there is strong experimental evidence of a small but significant variation in local surface roughness in diamond turned aluminium alloy. Such local variation of surface quality has been attributed to the anisotropy of each grain which make up the surface to be machined. Although there is research work studying the effect of crystallographic orientation on surface roughness in ultra-precision diamond turning, most of this work focused on qualitative analysis (Nakasuji et al., 1990). Only a limited number of studies (Yuan et al., 1994, and Lee and Zhou, 1993) have been found on

the development of a quantitative model for explaining the effect of crystallographic orientation on the surface roughness (Lee et al., 1999).

In this Chapter, the development of a model-based simulation system for determining quantitatively the variation of local surface roughness due to the effect of crystallographic orientation of the work material is presented. The system is based on several model elements which include a microplasticity model, a dynamic model and an enhanced surface topography model. The microplasticity model is used for predicting the variation of micro-cutting forces with the changing crystallography of the materials being cut. A dynamic model is built to determine the relative vibration induced by the variation of micro-cutting forces. The surface roughness and the topography of the machined surface are predicted by an enhanced surface topography model developed based on the one described in Chapter 6.

7.2 MICROPLASTICITY THEORY FOR MICRO-CUTTING FORCE PREDICTION

In ultra-precision machining, the cutting is performed with a depth of cut less than the average grain size of a polycrystalline aggregate. The polycrystalline work material, which may be considered to be an isotropic and homogeneous continuum in conventional analysis, is treated as a series of single crystals. Thus, the crystallographic orientation of the material being cut exerts a significant influence on the cutting mechanism and hence on the surface quality.

When cutting is performed within a grain, the statistical distribution of crystal defects and their interaction with the stress field of the cutting tip plays a dominant role in the cutting mechanism. As most of the ultra-precision machine is dimensionally stable and mechanically rigid, the fluctuation in the cutting forces could not be due to the machine tool chatter. Sato, et. al. (1978) found that the shear angles and the cutting forces vary with

the orientation of both single crystal and polycrystalline materials. Black (1972) has reported a variation in the shear front-lamellar structure at the top of the chip with the grain orientation. Most researchers imply that the shear planes in metal cutting are dislocation glide planes themselves. Lee (1990), and Lee and Zhou (1993) have proposed a microplasticity model to predict the fluctuation of the shear angle based on the change in shear strength of the crystallites being cut. In the present study, the analysis for cutting force variation is based on the work of Lee and Zhou (1993). The microplasticity model is further developed to predict the pattern of the cyclic variation of cutting forces in diamond face turning. In addition, power spectrum analysis is used to extract the features of the cycle cutting force patterns.

7.2.1 Review of microplasticity model for shear angle prediction

Many studies of metal cutting have been based on the concept of a shear zone in the formation of the chip. In the machining of ductile metals, the magnitude of the shear plane angle indicates the machinability of the work materials and the efficiency of the cutting process. The shear angle has been found to vary with the work material, the tool geometry, and the cutting conditions. Various shear angle equations (Merchant, 1945, Lee and Shaffer, 1951) have been derived in the past but have met with only partial success (Shaw, 1984).

One of the drawbacks in the existing theories is that they are post facto in nature. Metal cutting experiments are necessary to obtain important material parameters prior to the prediction of the shear angle. Another shortcoming of existing theories is that most studies of the cutting mechanism are performed under the assumption that the material is isotropic and is a homogeneous continuum. The effect of material anisotropy is often not included in the theories of analysis. One important source of material anisotropy, which lies in the crystallographic orientation, has drawn a lot of attention from researchers (Lee, 1990, K*ö* nig and Spenrath, 1991, Yuan et al., 1994).

As discussed in Chapter 3, ultra-precision diamond cutting is usually performed with a depth of cut of less than the average grain size of a polycrystalline aggregate. Single crystals are known to be highly anisotropic in their physical and mechanical properties. The surface quality and the cutting forces are affected by the crystallographic structure of the substrate material. There is strong experimental evidence that the shear angles and the cutting forces vary with the crystallographic orientation of the metals being cut (Sato, 1978, Lee and Zhou, 1993). Although the shear direction has been shown to be very sensitive to the crystallographic orientation, no simple analytical relationship between shear direction and the crystallography has been established, and the past attempts to correlate the shear stress and the shear angle based on Hill's macroscopic anisotropic function have been unsuccessful (Sato, 1978). Lee and Zhou (1993) have proposed a microplasticity model to explain the effect of crystallographic orientation on the shear angle in ultra-precision machining.

The analysis of cutting force variation proposed in this study is based on the previous work of Lee and Zhou (1993). Plane-strain orthogonal cutting is assumed in the model and a cutting tool of zero rake angle is used. The effect of plowing and sliding due to tool edge radius is ignored. The deformation is considered to be accomplished by the crystallographic slip only. Equal hardening of the slip systems is assumed. A large plastic deformation in the shear zone is treated as a succession of incremental plastic strains and the workpiece material is assumed to be rigidly plastic and uncompressible.

In the microplasticity model, the basic cutting mechanism that occurs in ultra-precision diamond turning of a polycrystalline aggregate is considered to be similar to that in the machining of a single crystal. During machining, the tool tip acts as a strong source of dislocations. Fine cracks are produced near the vicinity of the tool tip and trigger the primary shearing process. As the tool advances, the material ahead of the tool is compressed in the cutting direction and a shear band joining the top of the tool and the surface of the work material develops.

Referring to the workpiece coordinate system (CD-CP-OD) as shown in Figure 7.1, the symmetric strain tensor in the shear band, ε_w, is given by:

$$\varepsilon_w = d\tau/2\begin{bmatrix} \sin 2\Phi & 0 & \cos 2\Phi \\ 0 & 0 & 0 \\ \cos 2\Phi & 0 & -\sin 2\Phi \end{bmatrix} \tag{7.1}$$

where $d\tau$ is the shear strain in the shear band.

The crystallographic orientation of the crystal is represented by the Miller indices such that (hkl) is parallel to the cutting direction and $[uvw]$ is parallel to the normal of the cutting plane. The imposed strain tensor, ε_w, is transformed from the workpiece coordinate system (CD-CP-OD) to the crystallographic axis of the crystal where the crystallographic slip system are based, i.e.,

$$\varepsilon_c = \mathbf{P}\varepsilon_w\mathbf{P}^T \tag{7.2}$$

where ε_c is the strain tensor referred to the cube axes of the crystal , $\mathbf{P}$ is the transformation matrix and $\mathbf{P}^T$ is its transpose.

$$\mathbf{P} = \begin{bmatrix} r_1 & u_1 & n_1 \\ r_2 & u_2 & n_2 \\ r_3 & u_3 & n_3 \end{bmatrix} \tag{7.3}$$

where

$$r_1 = \frac{u}{\sqrt{u^2+v^2+w^2}},\ r_2 = \frac{v}{\sqrt{u^2+v^2+w^2}},\ r_3 = \frac{w}{\sqrt{u^2+v^2+w^2}} \tag{7.4}$$

$$n_1 = \frac{h}{\sqrt{h^2+k^2+l^2}},\ n_2 = \frac{k}{\sqrt{h^2+k^2+l^2}},\ n_3 = \frac{l}{\sqrt{h^2+k^2+l^2}} \tag{7.5}$$

$$u_1 = n_2 r_3 - n_3 r_2,\ u_2 = n_3 r_1 - n_1 r_3,\ u_3 = n_1 r_2 - n_2 r_1 \tag{7.6}$$

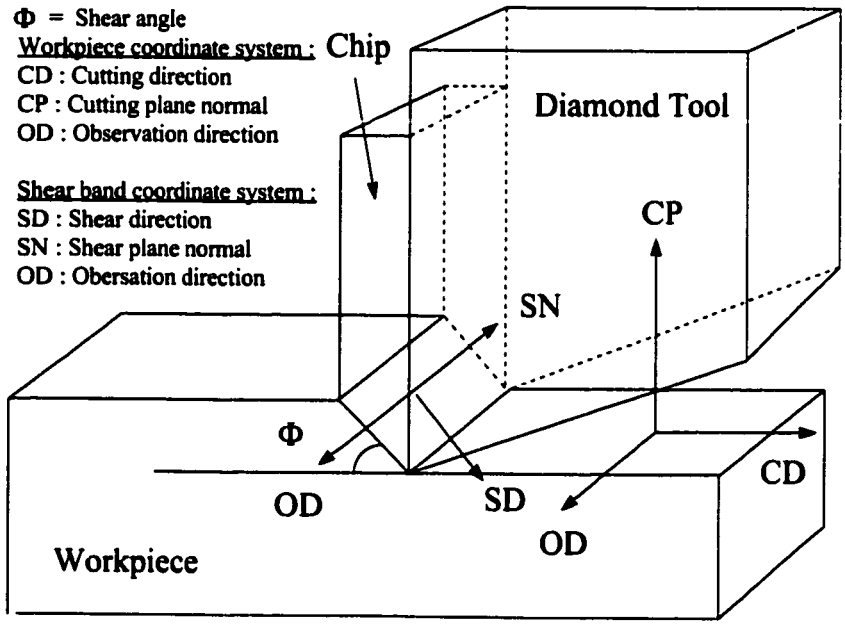

Figure 7.1 The co-ordinate systems for the cutting geometry

The increment of plastic work done during deformation dW is given by:

$$dW = \sigma d\varepsilon_w \tag{7.7}$$

where σ is the equivalent stress or the plastic work per unit volume and strain ,and $d\varepsilon_w$ is the macroscopic effective strain. Φ coincides with the direction of the maximum shear stress and makes an angle 45° with the cutting direction. If the shear angle deviates from 45° by an angle of ψ, the shear strain in the band will be increased by a factor of $1/\cos 2\psi$ in order to produce the same amount of macroscopic deformation. The shear band will

occur at an angle Φ such that the plastic work done in deforming the metal will be the minimum. It must be noted that the shear band is macroscopic in nature and the shear band may not be parallel to a particular crystallographic slip plane of the crystal. However, the shear in the band has to be accomplished by homogeneously distributed slip, i.e. all alternative slip systems co-operate in the shear band development. Hence the Taylor model of polycrystalline plasticity can be applied for the analysis of the shear band formation.

The virtual work equation for deforming a single crystal can be written as:

$$\sigma d\varepsilon_w = \tau_c d\Gamma \tag{7.8}$$

where $d\Gamma$ is the total dislocation shear strain accumulated in the crystal and τ_c is the critical resolved shear stress on the active slip systems.

The effect strain $d\varepsilon_w$ is related to the total dislocation shear strain by the Taylor-factor M, i.e.,

$$M = \frac{d\Gamma}{d\varepsilon_w} \tag{7.9}$$

and

$$\sigma = M\tau_c \tag{7.10}$$

The Taylor factor M is a dimensionless number that is sensitive to the crystallographic orientation. It is often used as an index of plastic anisotropy - the extent to

which the strength σ of a crystal varies with orientation for a given critical shear stress τ_c. A large value of M indicates a large shear strength of crystal being cut and hence the cutting force. Any variation in shear strength will cause the fluctuation in cutting force. M is calculated according to the maximum work principle of Bishop and Hill (1951) which states that the state of actual stress σ_{ij} required to cause a given increment of strain $d\varepsilon_{ij}$ is the one that maximises the work done during deformation dW.

Referring the stress and the strain to the cubic axes, the plastic work done, dW, during deformation is given by:

$$dW = -Bd\varepsilon_{11(c)} + Ad\varepsilon_{22(c)} + 2Fd\varepsilon_{23(c)} + 2Gd\varepsilon_{13(c)} + 2Hd\varepsilon_{12(c)} \tag{7.11}$$

where

$$A = (\sigma_{22(c)} - \sigma_{33(c)})/\sqrt{6}\tau_c, B = (\sigma_{33(c)} - \sigma_{11(c)})/\sqrt{6}\tau_c, F = \sigma_{23(c)}/\sqrt{6}\tau_c, G = \sigma_{13(c)}/\sqrt{6}\tau_c$$

$$, H = \sigma_{12(c)}/\sqrt{6}\tau_c.$$

The work done is calculated for all fifty-six possible stress states and the one whose work done value is the highest becomes the yielding stress state. Appendix V tabulates the positive twenty-eight states while the remaining twenty-eight are simply the negatives of these. The Taylor factor M can be determined by substituting the calculated value of maximum work done dW into the following equation:

$$M = \frac{dW}{(\tau_c d\varepsilon_{ij(c)})} \tag{7.12}$$

Since the resolved shear stress on the inclined plane varies as $1/\cos 2\psi$ from a 45° plane, an effective Taylor factor M' is defined as $M/\cos 2\psi$. Based on the minimum work principle, a shear band will be formed at such a direction along which the effective Taylor factor gets its minimal value. Very often the variation of $M/\cos 2\psi$ with shear angle is associated with a plateau and a range of shear angles is then possible based on the principle of minimum work alone. This uncertainty can be removed if the load instability criterion is imposed. A shear band will be formed as:

$$\frac{1}{\sigma}\frac{d\sigma}{d\varepsilon_w} = \frac{1}{M}\frac{dM}{d\varepsilon_w} + \frac{M}{\tau_c}\frac{d\tau_c}{d\Gamma} \le 0 \tag{7.13}$$

$(1/M)(dM/d\varepsilon_w)$ depends on the rate of change of the crystallographic orientation of the material with strain, and is called the texture softening factor S if it is negative or the texture hardening factor if it is positive. The second term $(M/\tau_c)(d\tau_c/d\Gamma)$ represents the slip plane hardening contribution which is usually positive. Therefore, a shear band will develop when $(1/M)(dM/d\varepsilon_w)$ is the most negative.

7.2.2 Texture softening factor

7.2.2.1 Selection of active set of slip systems

In the previous section, it is mentioned that the shear in the band has to be accomplished by the slip systems co-operating in the development of the shear band. For a crystal to undergo an arbitrary plastic strain or deformation by slip, five independent slip systems (represented in terms of the slip direction **b** and a slip plane normal **n**) are needed. In face-centred cubic (F.C.C.) crystals, the (111)[110] family of slip systems is dominant. The labels of the slip systems for the (111)[110] family of slip systems are

tabulated in Table 7.1. Taking the system a_1 as an example, the slip plane normal and the slip direction are $\mathbf{n} = 1/\sqrt{3},1/\sqrt{3},1/\sqrt{3}$ and $\mathbf{b} = 0,1/\sqrt{2},-1/\sqrt{2}$ respectively. The possible slip systems for the stress states of the (111)[110] family are summarised in Appendix V.

For faced-centred-cubic (F.C.C.) crystal structures, there are many ways of choosing an active set of five independent systems from the total number of possible slip systems. Taylor postulates that the preferred set of slip systems will be that for which the sum of the shears on each system is a minimum. As a slip system is operating, it is assumed that the shear stress acting on the system is equal to the critical resolved shear stress τ_c for slip. In order to simplify the calculation, the critical resolved shear stress τ_c is assumed to be $1/\sqrt{6}$ arbitrary units. Suppose that a small increment of strain represented by $[\varepsilon]$ is imposed on a crystal, this is related to the shears $[\gamma]$ that would be required for a given set of five independent slip systems to accomplish the strain as follows:

$$[\varepsilon] = [E][\gamma] \tag{7.14}$$

where $[E]$ is the direction cosines of the five slip systems. Equation (7.14) can be written in full as:

$$\begin{pmatrix} \varepsilon_{22(c)} \\ \varepsilon_{33(c)} \\ 2\varepsilon_{23(c)} \\ 2\varepsilon_{13(c)} \\ 2\varepsilon_{12(c)} \end{pmatrix} = \begin{pmatrix} (n_2^1 b_2^1) & (n_2^2 b_2^2) & (n_2^3 b_2^3) & (n_2^4 b_2^4) & (n_2^5 b_2^5) \\ (n_3^1 b_3^1) & (n_3^2 b_3^2) & (n_3^3 b_3^3) & (n_3^4 b_3^4) & (n_3^5 b_3^5) \\ (n_2^1 b_3^1 + n_3^1 b_2^1) & (n_2^2 b_3^2 + n_3^2 b_2^2) & (n_2^3 b_3^3 + n_3^3 b_2^3) & (n_2^4 b_3^4 + n_3^4 b_2^4) & (n_2^5 b_3^5 + n_3^5 b_2^5) \\ (n_1^1 b_3^1 + n_3^1 b_1^1) & (n_1^2 b_3^2 + n_3^2 b_1^2) & (n_1^3 b_3^3 + n_3^3 b_1^3) & (n_1^4 b_3^4 + n_3^4 b_1^4) & (n_1^5 b_3^5 + n_3^5 b_1^5) \\ (n_1^1 b_2^1 + n_2^1 b_1^1) & (n_1^2 b_2^2 + n_2^2 b_1^2) & (n_1^3 b_2^3 + n_2^3 b_1^3) & (n_1^4 b_2^4 + n_2^4 b_1^4) & (n_1^5 b_2^5 + n_2^5 b_1^5) \end{pmatrix} \begin{pmatrix} \gamma_1 \\ \gamma_2 \\ \gamma_3 \\ \gamma_4 \\ \gamma_5 \end{pmatrix} \tag{7.15}$$

In the notation used, the superscript indicates the referred slip system and it is not a power. In order to have the five slip systems to be independent, the inverse of $[E]$ or $[E^{-1}]$ must exist ,and this requires the determinant of $[E]$ or $|E|$ to be non-zero. Equation (7.15) can be uniquely solved for the shears as:

$$[\gamma] = [E^{-1}][\varepsilon] \tag{7.16}$$

Table 7.1 Labels for the slip systems

Slip plane, **n**	111			$\bar{1}\bar{1}1$			$\bar{1}11$			$1\bar{1}1$		
Slip direction, **b**	$01\bar{1}$	$\bar{1}01$	$1\bar{1}0$	$0\bar{1}\bar{1}$	101	$\bar{1}10$	$01\bar{1}$	101	$\bar{1}\bar{1}0$	$0\bar{1}\bar{1}$	$\bar{1}01$	110
Slip system	a_1	a_2	a_3	b_1	b_2	b_3	c_1	c_2	c_3	d_1	d_2	d_3

According to the Taylor criterion (Reid, C.N., 1973), the work done δw in activating the preferred set of slip systems is less than that of all other sets of systems that could geometrically accomplish the strain. i.e.,

$$\delta w = \tau_c \sum \delta\gamma \tag{7.17}$$

where the summation sign denotes the sum of the incremental shears, on each of the five independent systems of a set. In other words, the sum of the total shears $\sum\gamma$ as determined by Equation (7.16) should be the minimum. The Taylor criterion provides one possible way to predict the set of slip systems which will actually operate while the strain is imposed.

Bishop and Hill have proposed another principle for the prediction of the active slip system. It is stated that in the deformation of a single crystal, the actual stress corresponding to a given strain is not less than any other stress that satisfies the yielding conditions. In other words, the state of stress giving the maximum value of dW in Equation (7.11) will actually motivate the strain. The Bishop and Hill's Principle of Maximum Work criterion has been reported as giving the same results as the Taylor criterion in the prediction of active set of slip systems (Reid, C.N., 1973). When considering (111)[110] slip, the Bishop and Hill criterion has the advantage that the maximum of only fifty-six stress states is sought whereas the minimum of 384 stress states is required in the Taylor criterion.

However, ambiguities still exist in the selection of active slip systems based on the Bishop and Hill criterion since the selected stress states give either five out of six or five out of eight possible combinations of slip systems for accomplishing a given strain. The ambiguity in identifying the set of five slip systems is resolved in the present study by selecting the set of active slip systems which minimises the second order plastic work as proposed (Lee and Chan, 1991). In this method, an infinitesimal strain is applied to each possible set of the slip systems. This leads to a small crystal rotation. For a given imposed strain state, the second order plastic work dW' for each possible combination of slip system can be determined from:

$$dW' = \sigma'_{ij} d\varepsilon'_{ij} \tag{7.18}$$

where σ'_{ij} and $d\varepsilon'_{ij}$ are the new stress and strain components respectively due to the rotation and the strain hardening of the crystal. The set of active slip systems which corresponds to the minimum second order plastic work will then be selected.

7.2.2.2 Determination of texture softening factor

The texture softening factor S is computed numerically by determining the rate of lattice rotation ($d\Omega / d\varepsilon_w$) and the associated change in Taylor factor ($dM / d\Omega$) as follows:

$$S = \frac{1}{M}\frac{d\Omega}{d\varepsilon_w}\frac{dM}{d\Omega} \tag{7.19}$$

Suppose an infinitesimal strain $[\varepsilon']$ is applied to the active set of slip systems determined in the previous section. The strain components of $[\varepsilon']$ are related to the active set of five independent slip systems by

$$[\varepsilon'] = [E'][\gamma] \tag{7.20}$$

$$\begin{pmatrix} \dot{\varepsilon}_{22} \\ \dot{\varepsilon}_{33} \\ 2\dot{\varepsilon}_{23} \\ 2\dot{\varepsilon}_{13} \\ 2\dot{\varepsilon}_{12} \end{pmatrix} = [E'] \begin{pmatrix} \gamma^1 \\ \gamma^2 \\ \gamma^3 \\ \gamma^4 \\ \gamma^5 \end{pmatrix} \tag{7.21}$$

where $[E']$ is a square matrix that denotes the direction cosines of the selected active slip systems with respect to the cube axes of the crystal. The value of the shears on each slip system can be obtained by rewriting Equation (7.20) as:

$$[\gamma] = [E'^{-1}][\varepsilon'] \tag{7.22}$$

The shear $[\gamma]$ will cause the lattice rotation and the lattice rotation tensor **W** is given by:

$$\mathbf{W} = \begin{pmatrix} \omega_{11} & \omega_{12} & \omega_{13} \\ \omega_{21} & \omega_{22} & \omega_{23} \\ \omega_{31} & \omega_{32} & \omega_{33} \end{pmatrix}$$

$$= \frac{1}{2}\sum_{s=1}^{5} \begin{pmatrix} 0 & (b_1^s n_2^s - b_2^s n_1^s)\gamma^s & (b_1^s n_3^s - b_3^s n_1^s)\gamma^s \\ (b_2^s n_1^s - b_1^s n_2^s)\gamma & 0 & (b_2^s n_3^s - b_3^s n_2^s)\gamma^s \\ (b_3^s n_1^s - b_1^s n_3^s)\gamma^s & (b_3^s n_2^s - b_2^s n_3^s)\gamma^s & 0 \end{pmatrix} \tag{7.23}$$

Assume the initial orientation of the lattice to be **P** as given in Equation (7.3) and the shears will cause the crystal to rotate to a new orientation **P'** given by:

$$\mathbf{P'} = (\mathbf{I} - \mathbf{W})\mathbf{P} \tag{7.24}$$

where **I** is the unit matrix.

The net rotation $d\Omega$ can be determined by:

$$d\Omega = \sqrt{\omega_{12}^2 + \omega_{13}^2 + \omega_{23}^2} \tag{7.25}$$

Referring the stress and the strain to the cubic axes, the plastic work done, dW', during this deformation is given by:

$$dW' = -Bd\dot{\varepsilon}_{11(c)} + Ad\dot{\varepsilon}_{22(c)} + 2Fd\dot{\varepsilon}_{23(c)} + 2Gd\dot{\varepsilon}_{13(c)} + 2Hd\dot{\varepsilon}_{12(c)} \tag{7.26}$$

The corresponding change in Taylor factor dM can be determined by substituting the calculated value of maximum work done dW' into the following equation:

$$dM = \frac{dW'}{(\tau_c d\dot{\varepsilon}_{ij(c)})} \tag{7.27}$$

Hence, the Texture Softening Factor S can be determined by Equations (7.12), (7.19), (7.25) and (7.27).

7.2.3 Criterion for shear angle prediction

The criterion for predicting the shear angle is based on the combination of the effective Taylor factor M', the number of slip systems and the texture softening factor in sequence until a unique solution is obtained (Lee and Chan, 1991). In order to predict the most likely shear angles, the minimum M' is calculated first. Should a range of shear angles all possess the same minimum M', then the one with both minimum M' and the smallest number of slip systems will be selected. If there is still no unique shear angle, the one with the minimum M', the smallest number of slip systems and with the smallest Taylor Softening Factor S will be the most likely shear angle.

7.2.4 Variation of micro-cutting forces

Based on the shear angle calculated from the microplasticity model, the corresponding cutting force, $F_c(t)$, and the thrust force, $F_t(t)$, can be determined by Equations (7.28) and (7.29), respectively.

$$F_c(t) = \frac{\tau A \cos(\beta - \alpha)}{\sin[\Phi(t)]\cos[\Phi(t) + \beta - \alpha]} \tag{7.28}$$

$$F_t(t) = \frac{\tau A \sin(\beta - \alpha)}{\sin[\Phi(t)]\cos[\Phi(t) + \beta - \alpha]} \tag{7.29}$$

where A is the area of the undeformed chip section, $\Phi(t)$ is the shear angle determined by the microplasticity model, α is the rake angle of the diamond tool (i.e. $\alpha = 0^o$ as assumed in the model), τ is the shear stress of the single crystal, β is the friction angle between the tool and the chip material which is determined by the Merchant equation (Merchant, 1945):

$$\Phi = 45^o - \beta/2 + \alpha/2 \tag{7.30}$$

By substituting Equation (7.30) for Equation (7.28) and Equation (7.29), the cutting force $F_c(t)$ and the thrust force $F_t(t)$ can be derived as:

$$F_c(t) = \tau A \cot \Phi(t) \tag{7.31}$$

$$F_t(t) = \tau A[2 - 1/\sin^2 \Phi(t)] \tag{7.32}$$

7.3 DYNAMIC MODEL FOR THE CUTTING SYSTEM

A dynamic cutting system can be subdivided into two major components: the machine tool and the cutting process itself. The machine tool can be considered as a mechanism performing an oscillatory motion with certain mass, rigidity, and damping characteristics. In the cutting process, forces are required to separate and to form the chip. A machine tool

subjected to cutting forces can be considered as an oscillator subjected to a fluctuating load. As a result, the fluctuation of cutting forces may result in vibration of the system.

7.3.1 Formulation of second order autoregressive model A(2) for a vibration system

A dynamic vibration system can be represented as a spring-mass-dashpot system with the equivalent mass M_e being subjected to a forcing function $F(t)$, the motion caused by $F(t)$ opposed by a spring with a spring constant K and the dashpot with dashpot constant C. The spring constant and the dashpot provide a measure for the stiffness of the system. Let $X(t)$ denote the distance of the equivalent mass of the cutting system from the equilibrium position. By Newton's law, the equation of motion of the vibration system can be expressed as:

$$\frac{d^2X(t)}{dt^2} + 2\zeta\omega_n \frac{dX(t)}{dt} + \omega_n^2 X(t) = \frac{1}{M_e} F(t) \tag{7.33}$$

or

$$(D^2 + 2\zeta\omega_n D + \omega_n^2) X(t) = \frac{1}{M_e} F(t) \tag{7.34}$$

where

$$\omega_n = \sqrt{\frac{K}{M_e}} \text{ , denotes the natural frequency of the system} \tag{7.35}$$

$$\zeta = \frac{C}{2\sqrt{KM_e}} \text{ ,denotes the damping ratio of the system} \tag{7.36}$$

Equation (7.34) is ,in fact, equivalent to a continuous time second order autoregressive stochastic system A(2). Assuming,

$\alpha_1 = 2\zeta\omega_n = \frac{C}{M_e}$, being the system damping force per unit mass per unit velocity. (7.37)

and

$\alpha_0 = \omega_n^2 = \frac{K}{M_e}$, being the restoring force per unit mass per unit displacement. (7.38)

The second order autoregressive stochastic system A(2) described by Equation (7.34) can be expressed as:

$$(D^2 + \alpha_1 D + \alpha_0)X(t) = \frac{1}{M_e}F(t) \tag{7.39}$$

7.3.1.1 The Green's function of the A(2) system

The solution of the nonhomogeneous Equation (7.39) can be symbolically written as:

$$\begin{aligned} X(t) &= (D^2 + \alpha_1 D + \alpha_0)^{-1}\left(\frac{F(t)}{M_e}\right) \\ &= \int_0^\infty G(v)\frac{F(t-v)}{M_e}dv \\ &= \int_{-\infty}^{t} G(t-v)\frac{F(v)}{M_e}dv \end{aligned} \tag{7.40}$$

with the Green's Function $G(t)$ of the system being expressed as:

$$G(t) = \frac{e^{\mu_1 t} - e^{\mu_2 t}}{\mu_1 - \mu_2}, \quad \text{for } t \geq 0 \tag{7.41a}$$

and

$$G(t) = 0, \text{ for } t < 0 \tag{7.41b}$$

The characteristic roots μ_1 and μ_2 for the system are given by:

$$\mu_1 = 1/2(-\alpha_1 + \sqrt{\alpha_1^2 - 4\alpha_0}) = \omega_n(-\zeta + \sqrt{\zeta^2 - 1}) \tag{7.42a}$$

and

$$\mu_2 = 1/2(-\alpha_1 - \sqrt{\alpha_1^2 - 4\alpha_0}) = \omega_n(-\zeta - \sqrt{\zeta^2 - 1}) \tag{7.42b}$$

This integral may be viewed as a superposition or summation of impulse responses generated by the impulse force $F(t)$. In fact, the Green's function $G(t)$ allows the non-homogeneous equation to be solved with an arbitrary forcing function by expressing the solution as a convolution.

7.3.2 Model for the vibration system

The differential Equation (7.39) is a continuous representation of an one-degree-freedom vibration system subjected to a forced function $F(t)$. In the continuous model, in the form of differential equation, a live description of the system is provided in the sense that the coefficients in the equation can be related to known characteristics of the system. It is sometimes possible to get a plot of digitised data. Because of high degree of accuracy of observation and the ease of data processing on a digital computer, it is advantageous to use discrete data obtained at uniform sampling intervals to determine a discrete equivalent representation of the continuous model.

In the present study, the time-series and system analysis approach based on the previous work of Pandit and Wu (1983) was used to determine the dynamic characteristics of the cutting system. This approach bypasses the element of trial and error and provides models in the form of difference/differential equations directly from the observed data that was outlined with requisite mathematical foundation. In addition, the approach has been successfully applied in the determination of dynamic characteristics of different machining systems such as face milling (Baek et al., 1997).

The continuous model for the vibration system is obtained from a discrete set of observed data taken at uniform sampling intervals during machining. This can be treated as a discrete model developed from the relations between the differential equation representing the continuous model and the difference equation representing the uniformly sampled discrete model. Such an approach allows both the continuous and the discrete models to be obtained simultaneously from the discrete data. The discrete model for the uniformly sampled system turns out to be a second order autoregressive moving average ARMA(2,1) model. With appropriate modifications in the estimation procedure to incorporate the parametric relationships between the continuous model and the discrete model, the discrete model can be utilised for predicting the system performance and incorporated into for determining the parametric relations between the continuous and the discrete representations; whereas the continuous model is useful for system characterisation and system analysis.

7.3.3 Uniformly sampled second order autoregressive moving average ARMA(2,1) system

As mentioned in Section 7.3.2, it is required to obtain an A(2) model from a discrete set of data measured during machining. To estimate the A(2) model parameters, a discrete model for the sampled data is needed. Such a model can be obtained either by reparameterizing Equation (7.40) or by requiring that the discrete model be an ARMA model and that its covariance function coincide at all the sampled points $s_s = k\Delta$, with $k = 0,1,2,...,N$. The autocovariance $\gamma(s_s)$ takes the form:

$$\gamma_k = \gamma(k\Delta)$$

$$= \frac{\sigma_z^2}{2\mu_1\mu_2(\mu_1^2 - \mu_2^2)}(\mu_2 e^{\mu_1 k\Delta} - \mu_1 e^{\mu_2 k\Delta}) \tag{7.43}$$

$$\gamma_k = d_1\lambda_1^k + d_2\lambda_2^k \tag{7.44}$$

where

$$d_1 = \frac{\sigma_z^2}{2\mu_1(\mu_1^2 - \mu_2^2)} \tag{7.45}$$

$$d_2 = \frac{-\sigma_z^2}{2\mu_2(\mu_1^2 - \mu_2^2)} \tag{7.46}$$

and

$$\lambda_1 = e^{\mu_1\Delta} \tag{7.47}$$

$$\lambda_2 = e^{\mu_2\Delta} \tag{7.48}$$

To estimate the A(2) model parameters, a covariance equivalent ARMA(2,1) model is employed which is in the form of a difference equation with:

$$X_t - \phi_1 X_{t-1} - \phi_2 X_{t-2} = a_t - \theta_1 a_{t-1} \tag{7.49}$$

where

$$\phi_1 = \lambda_1 + \lambda_2 = e^{\mu_1\Delta} + e^{\mu_2\Delta} \tag{7.50}$$

$$\phi_2 = -\lambda_1\lambda_2 = -e^{(\mu_1+\mu_2)\Delta} \tag{7.51}$$

Δ is the sampling interval.

a_t is the disturbance affecting the system at time interval t

$$\theta_1 = -P \pm \sqrt{P^2 - 1} \tag{7.52}$$

$$\text{with } P = \frac{-\mu_1(1+\lambda_1^2)(1-\lambda_2^2) + \mu_2(1+\lambda_2^2)(1-\lambda_1^2)}{2\mu_1\lambda_1(1-\lambda_2^2) - \mu_2\lambda_2(1-\lambda_1^2)} \tag{7.53}$$

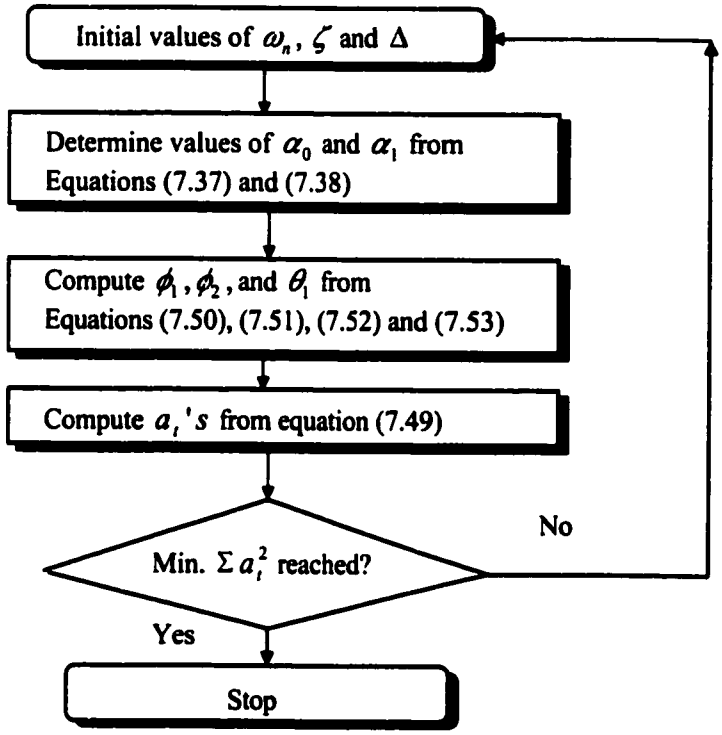

Figure 7.2 Flowchart of the estimation of the covariance equivalent ARMA(2,1) model

7.3.4 Estimation of covariance equivalent ARMA(2,1) model

The estimation of the discrete covariance equivalent ARMA(2,1) model cannot be separated from that of the A(2) model since θ_1 cannot be determined unless μ_1 and μ_2 or

their implicit functions are known. The estimation of the A(2) model can be done by a least-squares-error search algorithm which minimises the sum of squares of a_t's in the model. The flowchart of the algorithm is depicted in Figure 7.2. The parameters to be estimated are α_1 and α_0. The procedure starts with initial values for α_1 and α_0. Then, the values of ϕ_1, ϕ_2 and θ_1 can be computed using Equations (7.50), (7.51), (7.52) and (7.53) and the sum of squares of a_t's is computed using Equation (7.49). The values of α_1 and α_0 are adjusted until the minimum sum of squares of a_t's is reached. The optimum values of ϕ_1, ϕ_2, θ_1, α_1 and α_0 are used to construct the covariance equivalent ARMA(2,1) discrete model and the A(2) continuous model as well.

7.3.4.1 Effect of sampling interval, natural frequency, and damping ratio

The choice of a sampling interval for digitising a given continuous A(2) system, may affect the final form of the discrete model. When the sampling interval is too large or too small, the information extracted from the sampled data might be misleading. In the case of continuous signals with high frequency, the smaller sampling interval may be appropriate to represent the original signal. A larger sampling interval may be needed to obtain a continuous signal with a low frequency. The sampling theorem discussed in Chapter 4 provides a guideline for the choice of the sampling interval for digitisation.

7.3.5 Representation of the cutting system

The influence of vibration on the surface roughness machined with a single point tool has been previously discussed in some papers (Tai et al., 1980, Sata et al., 1985, and Takasu et al., 1985). Mitsui (1978) concluded that the surface roughness affected by the vibration was nearly equal to the whole amplitude of the vibration. Surface finish better than the whole amplitude of vibration, however, is often obtained in ultra-precision machining. In considering that some of chatter marks were removed by the following cuts, Tai et al.,(1980) emphasised the fact that the height of chatter marks in the cutting direction became smaller than the whole amplitude of chatter vibration. The machined surface roughness in the

transverse direction, however, is more dominant than it is in the cutting direction, because of the very low frequency vibration present in ultra-precision machining. In other words, the machined surface roughness in the infeed cutting direction is more dominant than it is in the Cutting direction, as the relative displacement of the tool in the Cutting direction does not engage in the generation of surface roughness (Baek et al, 1997). In the present study, only the relative displacement between the workpiece and the tool in the infeed direction is considered.

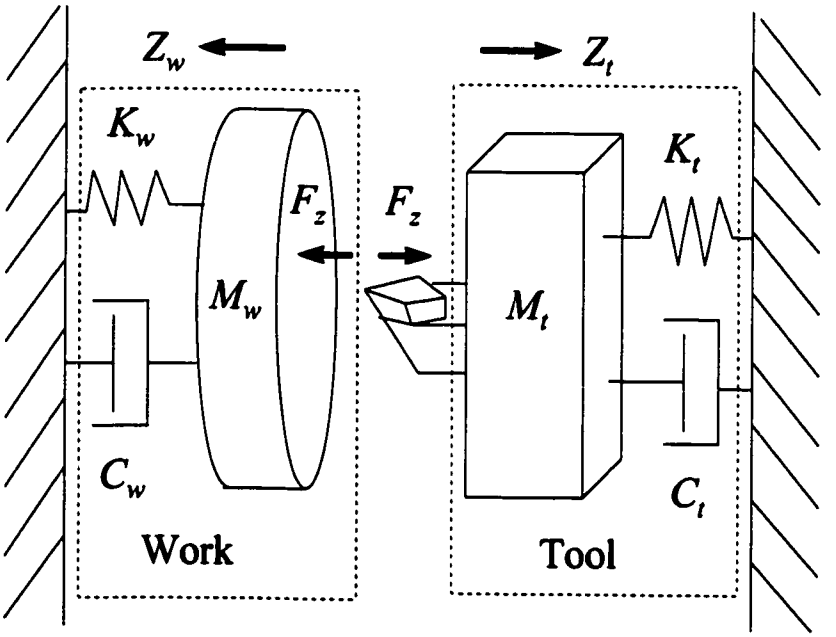

Figure 7.3 Lumped-parameter representation of the dynamic cutting system

As shown in Figure 7.3, the cutting system is modelled with one degree of freedom in the consideration of the cutting tool and the workpiece. The complexity of the machine structure is represented in terms of a lumped-parameter for the purpose of the analytical study. The lumped parameters in such a representation will be the equivalent mass, the rigidity and the damping for one of the modes of oscillation of the machine structure. The tool and the work systems are represented by springs and dashpots connected in parallel. The tool and the workpiece are acted upon by the variation of the thrust force, $F_z(t)$ which is induced by the change in the crystallographic orientation of the workpiece. Thus, the tool and work cutting systems can be separately modelled as follows:

Tool system

$$\frac{d^2Z_t(t)}{dt^2}+\frac{C_t}{M_t}\frac{dZ_t(t)}{dt}+\frac{K_t}{M_t}Z_t(t)=\frac{F_z(t)}{M_t} \tag{7.54}$$

Work system

$$\frac{d^2Z_w(t)}{dt^2}+\frac{C_w}{M_w}\frac{dZ_w(t)}{dt}+\frac{K_w}{M_w}Z_w(t)=\frac{F_z(t)}{M_w} \tag{7.55}$$

Where M_t and M_w are the equivalent masses of the tool and the workpiece respectively. The dashpot constant for the tool is C_t and that of the workpiece is C_w. K_t is the spring constant for the tool and K_w for the workpiece. The displacement of the tool and the workpiece are represented by Z_t and Z_w respectively.

From Equations (7.54) and (7.55), let

$$\omega_{nt}=\sqrt{\frac{K_t}{M_t}}\ ,\ \omega_{nw}=\sqrt{\frac{K_w}{M_w}} \tag{7.56}$$

and

$$\zeta_t=\frac{C_t}{2\sqrt{K_tM_t}},\ \zeta_w=\frac{C_w}{2\sqrt{K_wM_w}} \tag{7.57}$$

where ω_{nt} and ω_{nw} are the natural frequencies of the tool system and the work system ,respectively. ζ_t denotes the damping ratio of the tool system while ζ_w denotes that of the work system. Hence, Equations (7.54) and (7.55) can be rewritten in matrix form as:

$$\begin{bmatrix} \frac{d^2Z_t(t)}{dt^2} \\ \frac{d^2Z_w(t)}{dt^2} \end{bmatrix} + \begin{bmatrix} 2\zeta_t\omega_{nt} & 0 \\ 0 & 2\zeta_w\omega_{nw} \end{bmatrix} \begin{bmatrix} \frac{dZ_t(t)}{dt} \\ \frac{dZ_w(t)}{dt} \end{bmatrix} + \begin{bmatrix} \omega_{nt}^2 & 0 \\ 0 & \omega_{nw}^2 \end{bmatrix} \begin{bmatrix} Z_t(t) \\ Z_w(t) \end{bmatrix} = \begin{bmatrix} \frac{F_z(t)}{M_t} \\ \frac{F_z(t)}{M_w} \end{bmatrix} \tag{7.58}$$

The relative displacement between the tool and the workpiece can be simulated from Equation (7.58) under the steady-state cutting condition. Equation (7.58) is the second order autoregressive A(2) representation of the dynamic system while the discrete covariance equivalent ARMA(2,1) representation is given by:

$$\begin{bmatrix} Z_{T,t} \\ Z_{W,t} \end{bmatrix} - \begin{bmatrix} \phi_{T,1} & 0 \\ 0 & \phi_{W,1} \end{bmatrix} \begin{bmatrix} Z_{T,t-1} \\ Z_{W,t-1} \end{bmatrix} - \begin{bmatrix} \phi_{T,2} & 0 \\ 0 & \phi_{W,2} \end{bmatrix} \begin{bmatrix} Z_{T,t-2} \\ Z_{W,t-2} \end{bmatrix} = \begin{bmatrix} a_{T,t} \\ a_{W,t} \end{bmatrix} - \begin{bmatrix} \theta_{T,1} & 0 \\ 0 & \theta_{W,1} \end{bmatrix} \begin{bmatrix} a_{T,t-1} \\ a_{W,t-1} \end{bmatrix} \tag{7.59}$$

7.3.6 Determination of the relative tool-work displacement

The cutting system represented by Equation (7.58) is a system of nonhomogeneous second order differential equations. The solution of the system of equations can be expressed as the convolution of the Green's functions and the force functions of the tool and the work system respectively (Pandit S.M. and Wu, S.M., 1983).

The Green's functions for the tool system and work system are defined as follows:

$$G_t(\nu) = \frac{(e^{\mu_{t1}\nu} - e^{\mu_{t2}\nu})}{(\mu_{t1} - \mu_{t2})} \qquad \text{for } \nu \geq 0 \text{ and 0 otherwise} \tag{7.60}$$

$$G_w(\nu) = \frac{(e^{\mu_{w1}\nu} - e^{\mu_{w2}\nu})}{(\mu_{w1} - \mu_{w2})} \qquad \text{for } \nu \geq 0 \text{ and 0 otherwise} \tag{7.61}$$

where $\mu_{t1},\mu_{t2} = \omega_{nt}(-\zeta_t \pm \sqrt{\zeta_t^2 - 1})$ and $\mu_{w1},\mu_{w2} = \omega_{nw}(-\zeta_w \pm \sqrt{\zeta_w^2 - 1})$ are the characteristic roots of the homogeneous parts of the solutions for the tool and the work systems ,respectively. Thus,

$$\begin{bmatrix} Z_t(t) \\ Z_w(t) \end{bmatrix} = \begin{bmatrix} \int_0^\infty \frac{(e^{\mu_{t1}\nu} - e^{\mu_{t2}\nu})}{(\mu_{t1} - \mu_{t2})} \frac{F_z(t-\nu)}{M_t} d\nu \\ \int_0^\infty \frac{(e^{\mu_{w1}\nu} - e^{\mu_{w2}\nu})}{(\mu_{w1} - \mu_{w2})} \frac{F_z(t-\nu)}{M_w} d\nu \end{bmatrix} \tag{7.62}$$

$$\begin{bmatrix} Z_t(t) \\ Z_w(t) \end{bmatrix} = \begin{bmatrix} \int_{-\infty} \frac{(e^{\mu_{t1}(t-\nu)} - e^{\mu_{t2}(t-\nu)})}{(\mu_{t1} - \mu_{t2})} \frac{F_z(\nu)}{M_t} d\nu \\ \int_{-\infty} \frac{(e^{\mu_{w1}(t-\nu)} - e^{\mu_{w2}(t-\nu)})}{(\mu_{w1} - \mu_{w2})} \frac{F_z(\nu)}{M_w} d\nu \end{bmatrix} \tag{7.63}$$

The integral may be viewed as a superposition or summation of impulse responses generated by impulses $Z_t(t)$ and $Z_w(t)$. From Equation (7.63), the relative displacement $Z_m(t)$ between the tool and the workpiece can be determined as:

$$Z_m(t) = Z_w(t) - Z_t(t) \tag{7.64}$$

7.4 ENHANCED SURFACE TOPOGRAPHY MODEL

Referring to the surface topography model in Chapter 6, it is assumed that only the dominant mode of relative tool-work vibration is considered. As the effect of material anisotropy caused by the changing crystallographic orientation of the work material is taken into account, an additional tool-work displacement will be introduced into the cutting system. Since the force function $F_z(t)$ in Section 7.2 varies with the crystallographic orientation of the workpiece, the patterns of the variation of cutting force is not a simple harmonic function but can be treated as an arbitrary function which varies with the crystallographic

orientation of the work materials. The resultant tool-work displacement determined from Equation (7.63) and Equation (7.64) will be an arbitrary function which varies with the crystallographic orientation of the work material being cut. As a result, the assumption of a simple harmonic vibration might not hold in such a case. There is a need to modify the topography model to accomplish the additional displacement due to the changes induced by the crystallography of the material being cut.

In the enhanced surface topography model, the vibration is assumed to be an arbitrary function instead of a simple harmonic existing between the tool and the workpiece. The modelling of the surface topography starts with the determination of the 3-D locus of the tool trace with respect to the workpiece. In the time domain, the relative displacement $Z_c(t)$ between the tool and the workpiece in the Cutting direction can be expressed as:

$$Z_c(t) = Z_m(t) + A\sin(2\pi f_z t - \phi) \tag{7.65}$$

In discrete form, the relative displacement between the tool and the workpiece can be derived based on Equation (7.65) and Equation (6.13) as:

$$Z_c(j) = Z_m(\frac{j\Delta\theta}{\omega}) + A\sin\left\{ \frac{2\pi f_z j\Delta\theta}{\omega} - \phi \right\} \qquad \text{, for } j = 0,1,2,\ldots,N_t \tag{7.66}$$

As explained in Section 6.2.4, Equations (6.15) and (6.16) describe the 3-D spiral locus of the tool during machining (see Figure 6.6). The locus of the tool for the k th radial section can be treated as a transformation of the tool points from the $X-Y-Z$ co-ordinate system to the $R_k - Z_k$ polar plane, whereas R_k -axis is the radial axis for the k th radial section with $k = 0,1,2,\ldots,N_p$.

At the k th radial section, the co-ordinates of the tool locus on the $R_k - Z_k$ polar plane can be derived from Equations (7.66) and (6.15) as follows:

$$\theta_t(i,k) = k\Delta\theta + 2\pi(i-1) \tag{7.67}$$

$$r_t(i,k) = R_0 - [k + (i-1)N_p]\Delta R \tag{7.68}$$

$$Z_t(i,k) = Z_m\left\{ \frac{[k+(i-1)N_p]\Delta\theta}{\omega} \right\} + A\sin\left\{ \frac{2\pi f_z[k+(i-1)N_p]\Delta\theta}{\omega} - \phi \right\} \tag{7.69}$$

with $i = 1,2,\ldots,N$. Letting

$$Z_m(i,k) = Z_m\left\{ \frac{[k+(i-1)N_p]\Delta\theta}{\omega} \right\} \quad \text{, for } i = 1,2,\ldots,N \tag{7.70}$$

$$Z_v(i,k) = A\sin\left\{ \frac{2\pi f_z[k+(i-1)N_p]\Delta\theta}{\omega} - \phi \right\} \quad \text{, for } i = 1,2,\ldots,N \tag{7.71}$$

where $Z_m(i,k)$ and $Z_v(i,k)$ denote the tool-work displacement due to material anisotropy and the machine vibration respectively.

Hence, Equation (7.69) can be rewritten as:

$$Z_t(i,k) = Z_m(i,k) + Z_v(i,k) \tag{7.72}$$

The cutting edges of the i th tool profile and the $i+1$ th ones counted from the first tool profile at the k th radial section can be derived from Equations (6.5), (6.6), (6.7), (6.8) and (7.72) as:

$$Z_{k,i}(r_{k,i}) = Z_t(i,k) + \frac{[r_{k,i} - (i-1)s]^2}{2R} \tag{7.73}$$

$$Z_{k,j+1}(r_{k,j+1}) = Z_t(i+1,k) + \frac{[r_{k,j+1} - is]^2}{2R} \tag{7.74}$$

where $i = 1,2,\ldots, N-1$ and $(r_{k,j},\ Z_{k,j})$ are the co-ordinates of the i th tool profile at the k th radial section of the workpiece.

At the location of intersection, $T_{k,j,j+1}(r_{k,j,j+1}, H_{k,j,j+1})$, of the i th tool profile and the $i+1$ th ones at the k th radial section, $Z_{k,j} = Z_{k,j+1}$ and $r_{k,j} = r_{k,j+1}$, i.e.,

$$r_{k,j,j+1} = \frac{R[Z_t(i+1,k) - Z_t(i,k)] + (i - \frac{1}{2})s^2}{s} \qquad \text{, for } i = 1,2,\ldots, N-1 \tag{7.75}$$

From Equations (7.74) and (7.75), the height $H_{k,j,j+1}$ of the intersection between the i th and the $i+1$ th tool profiles at the k th radial section is determined as:

$$H_{k,j,j+1} = Z_t(i+1,k) + \frac{[r_{k,j,j+1} - is]^2}{2R}$$

$$= Z_t(i+1,k) + \frac{\{2R[Z_t(i+1,k) - Z_t(i,k)] - s^2\}^2}{8Rs^2} \tag{7.76}$$

with $i = 1,2,\ldots, N-1$.

As mentioned in Section 6.2.4, the minimum edge profile below the intersecting points of each tool profile constitutes the surface roughness. The surface roughness profile at the k th radial section of the workpiece can be constructed by trimming the lines above the points of intersection. By applying Equations (7.75) and (7.76) for all radial sections, i.e. $k = 0,1,2,\ldots.. N_p$, and mapping them on the surface elements of a cross lattice as defined by Equations (6.24), (6.25) and (6.26), it is possible to construct the 3-D surface topography

of the diamond turned surface. Similar to Section 6.2.5, the maximum peak-to-valley height $\hat{R}_t$ and the arithmetic roughness $\hat{R}_a$ can be predicted by Equation (6.27) and Equation (6.28), respectively.

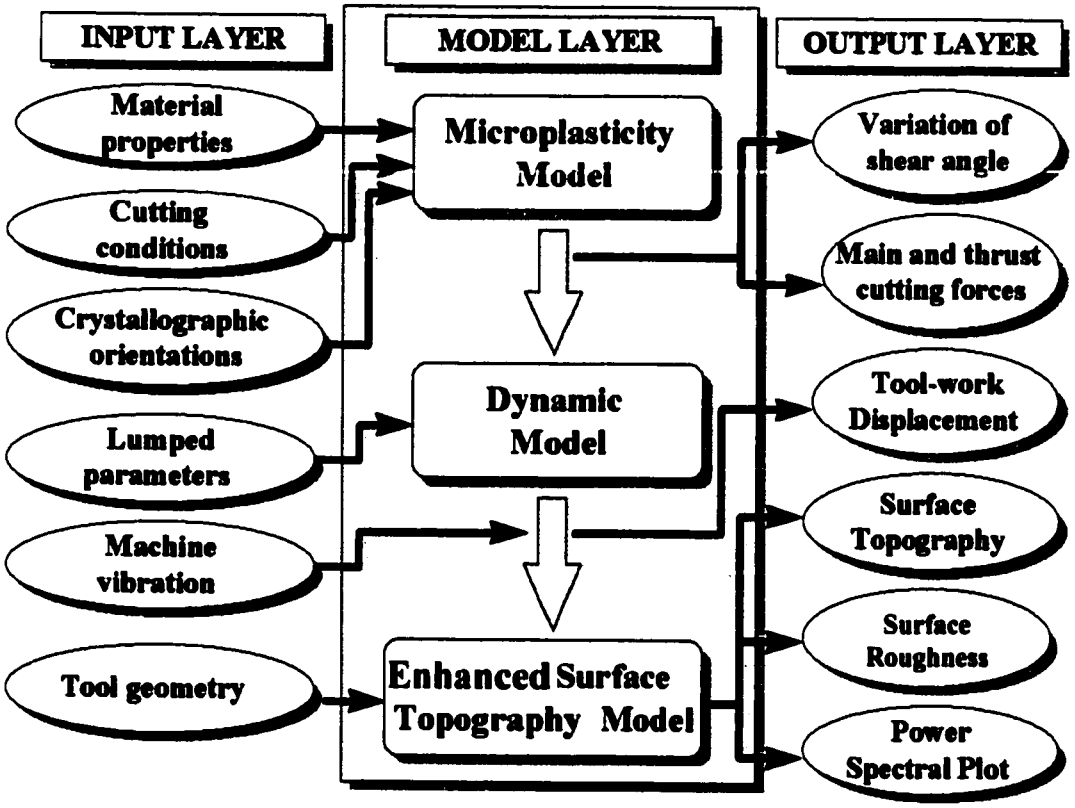

Figure 7.4 An architecture of the model-based simulation system

7.5 MODEL-BASED SIMULATION SYSTEM

As shown in Figure 7.4, the model-based simulation system (Lee and Cheung, 2000) is composed of several model elements which include a microplasticity model, a dynamic model and an enhanced surface topography model. The microplasticity model as discussed in Section 7.2 is used for predicting the variation of cutting forces when a highly anisotropic workpiece substrate is machined. The dynamic model established in Section 7.3 is used for determining the vibration induced by the variation of the cutting forces. The influence of the

induced vibration on surface roughness of the workpiece is estimated by the enhanced surface topography model described in Section 7.4.

A software package has been developed to implement the captioned system. Appendix VI shows the program structure and the program listing for the package. The inputs into the package are tool geometry, machine settings such as feed rate, lumped-parameter which identifies the dynamics of the machine, as well as the material properties such as the crystallographic orientation of the workpiece. The outputs of the software are simulated tool locus, 3-D surface topography, predicted roughness parameters and spectrum of the surface roughness profile.

7.6 EXPERIMENTAL PROCEDURES

The captioned system was evaluated through a series of cutting experiments. They were divided into three groups, i.e. Group 7A, Group 7B and Group 7C. Group 7A included those experiments for the investigation of micro-cutting forces. In Group 7B, the dynamic characteristics of the cutting system were identified based on the dynamic model developed in Section 7.3. The final group (Group 7C) of experiments was carried out to verify the performance of the model-based simulation system. The experiments in Group 7A were performed on a two-axis CNC ultra-precision lathe (Optoform 30 from Taylor Hobson Pneumo Co.) whereas those for Group 7B and Group 7C were conducted on a two-axis CNC ultra-precision machine (Nanoform 300 from Taylor Hobson Pneumo Co.).

In Group 7A, two sets of face cutting tests were conducted on aluminium single crystals with different crystallographic axes, i.e. Set 7A(I) and Set 7A(II). The diameter of the workpiece is 12.7 mm. Table 7.2 and Table 7.3 tabulate the specifications of the workpiece and the cutting conditions being used respectively. The cutting and thrust forces were captured approximately at the mid-point of the tool's travel between the periphery and the centre of the workpiece. Since the captured length (0.2 second) is relatively small as compared with the overall cutting cycle (19 seconds), it is assumed that the mean cutting

forces are quasi-static in the measuring range. Figure 7.5 and Figure 7.6 show respectively a picture of the machine setup and a schematic diagram of the signal flow in the micro-cutting force experiments. The cutting and thrust forces were measured respectively by a Kistler 9252A piezoelectric force transducer mounted directly under the tool post. The force signal captured from the transducer was first pre-amplified by a charge amplifier (Kistler 5011A) and the analogue voltage output was recorded and digitised by a digitising oscilloscope (Tektronix TDS744A). Then, the digitised signal was passed to a personal computer for analysing.

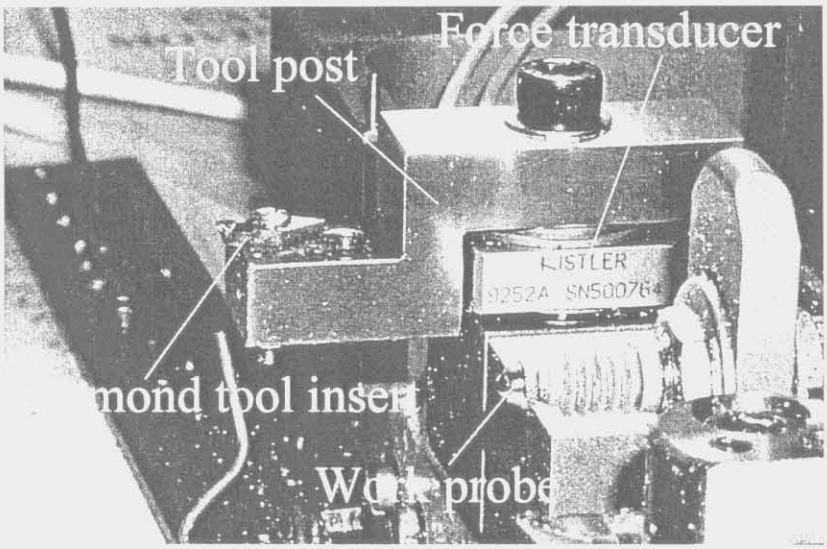

Figure 7.5 Experimental setup for the cutting force measurement

In Group 7B, the parameters in Equations (7.58), (7.59) and (7.63) were estimated by the covariance equivalent ARMA (2,1) model described in Section 7.3.5. Figure 7.7 depicts the configuration of the experimental setup used for cutting system characterisation. The displacements of the tool and the workpiece due to machine vibration were measured separately by a capacitive displacement sensor with nanometer resolution. The measured displacement signals for the tool and the work systems were fed respectively into an optimisation program purposely made for the study. A list of program source codes is given in Appendix VI. The program works on a least-squares-error searching algorithm which changes the parameters one by one within the predetermined iteration ranges for each parameter. The optimum set of parameters is identified based on the criterion of minimum

sum of square of errors between the measured displacement data and the predicted values from the ARMA(2,1) model. Table 7.4 shows the searching ranges used in the present study.

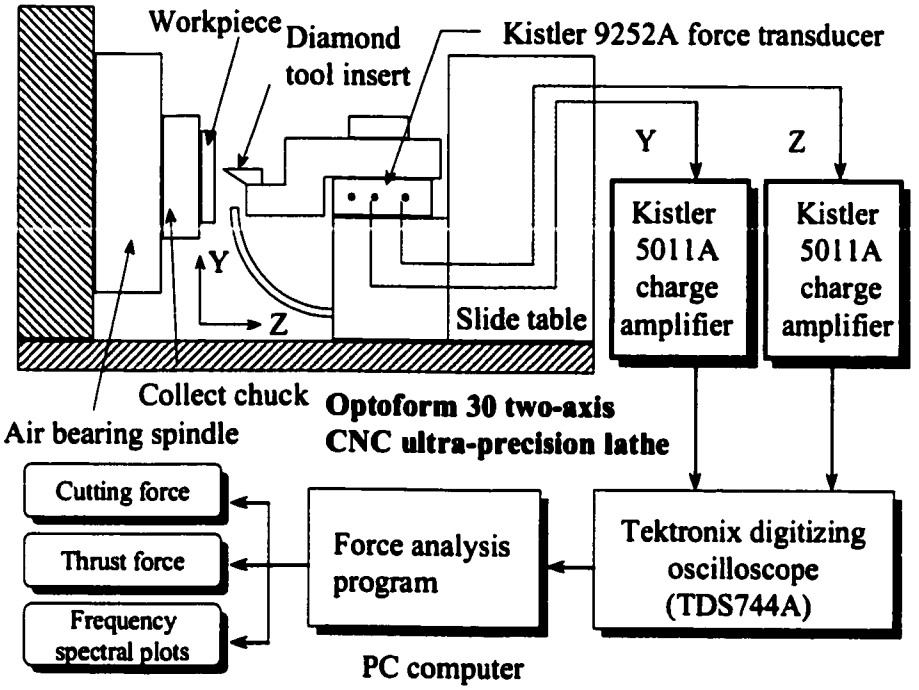

Figure 7.6 Schematic diagram of the signal flow in cutting force measurement

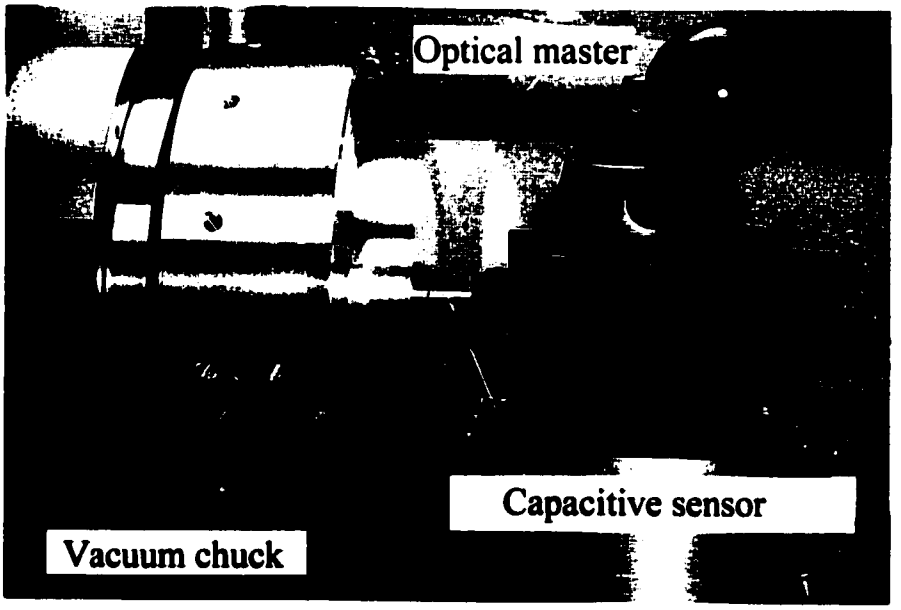

Figure 7.7 Experimental setup for the dynamic system characterization

Group 7C experiments involve those cutting tests for evaluating the performance of the model-based simulation system in surface roughness prediction. Aluminium single crystals were diamond turned under cutting conditions as tabulated in Table 7.5. Table 7.6 gives the specifications of the work materials being used. The initial crystallographic orientation (i.e. at radial section 1) of the specimens were checked by a standard reflection technique on a X-Ray Diffractometer. To remove the work deformed layer generated during the pre-machining process, the surfaces of the specimens were electropolished prior to the cutting tests using similar procedures as described in Section 4.4. To ensure an ideal depth of cut (5 μm), a fine cutting of 1 μm was done on the tested specimen prior to the actual cutting test. The surface topographies of the machined surfaces were measured by a WYKO TOPO-3D non-contact microsurface measurement system. In order to ensure the compatibility and the consistency between the predicted and the measured results, all simulations and measurements were made at the centre of the workpiece. A simulation of the 3-D surface topography was conducted at $N_p = 360$, i.e., $\Delta\theta = 0.0175$ radian, $L_x = L_y = 0.25$ mm, and $m_x = m_y = s/5$, the values of which are the same as those used in Chapter 6. The localised variation of surface roughness of the specimens was examined using similar methodologies and experimental setup as described in Chapter 4. A cut-off length of 0.25 mm was used throughout the surface roughness experiments.

Table 7.2 Specifications of work materials in Group 7A

Specimen no.	Specifications of materials
7A(1)	Aluminium single crystal with (001) as the cutting plane
7A(2)	Aluminium single crystal with (110) as the cutting plane
7A(3)	Aluminium single crystal with (111) as the cutting plane

Table 7.3 Cutting conditions for the cutting tests in Group 7A

Set no.	7A(I)	7A(II)
Spindle speed (rpm)	3000	3000
Feed (mm min^{-1})	20	20
Depth of cut (μm)	15	10, 20, 30
Tool rake angle	0°	0°
Tool front clearance angle	12.5°	12.5°
Tool nose radius (mm)	0.7740	0.7740

Table 7.4 Searching conditions used in the characterisation of the cutting system in Group 7B

	Damping ratio		Natural frequency (rad s^{-1})		Sample rate
	Range	Step size	Range	Step size	
Tool system	0.1 to 0.9	0.01	100 to 2000	10	0.01
Work system	0.1 to 0.9	0.01	100 to 1000	10	0.01

Table 7.5 Conditions of the cutting tests in Group 7C

Spindle rotational speed	2000 rpm
Feed rate	20 mm min^{-1}
Depth of cut	5 μm
Tool rake angle	0°
Tool front clearance angle	12.5°
Tool nose radius	2.019 mm
Amplitude of relative tool-work vibration	0.015 μm
Frequency of relative tool-work vibration	29.94 Hz

Table 7.6 Specifications of work materials in Group 7C

Specimen no.	Specifications of materials
7C(1)	Aluminium single crystal with (001) as the cutting plane and the initial crystallographic orientation as (001)[0 $\bar{1}$ 0] at radial section 1
7C(2)	Aluminium single crystal with (110) as the cutting plane and the initial crystallographic orientation as (110)[001] at radial section 1
7C(3)	Aluminium single crystal with (111) as the cutting plane and the initial crystallographic orientation as (111)[1 $\bar{1}$ 0] at radial section 1

7.7 RESULTS AND DISCUSSION

7.7.1 Investigation of the micro-cutting forces

7.7.1.1 Variation of cutting forces with crystallographic orientation of the workpiece

Figure 7.8 shows the predicted shear angle variation in diamond turning aluminium single crystals under Set 7A(I) conditions. The cutting tests were done on (001), (110) and (111) planes, respectively. The corresponding variation of the cutting and thrust forces are shown in Figure 7.9 and Figure 7.10, respectively. It is observed that the shear angle varies

with the crystallographic orientation of the material being cut. The patterns of shear angle variation are found to be different for different crystals. There seems to exist a fundamental cyclic frequency of variation of the cutting force for each workpiece revolution. As observed in Figure 7.9 and Figure 7.10, the fundamental cyclic frequencies are found to be four for (001) crystal, two for (110) crystal and three for the (111) crystal respectively. These relate closely to the crystallographic orientation of the crystals being investigated. To verify these findings, the spectrum analysis is employed to extract the features of the cutting force patterns as discussed below.

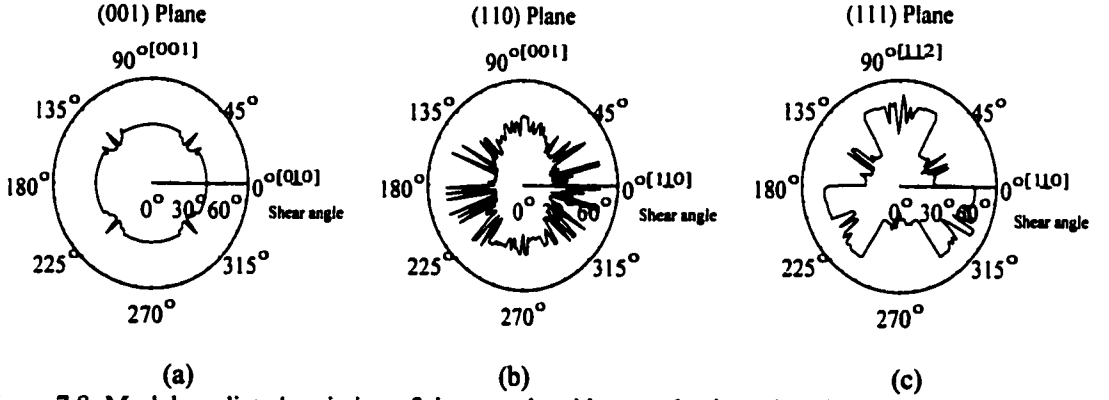

Figure 7.8 Model predicted variation of shear angle with crystal orientations in cutting aluminium single crystals on (a) (001) plane, (b) (110) plane and (c) (111) plane.

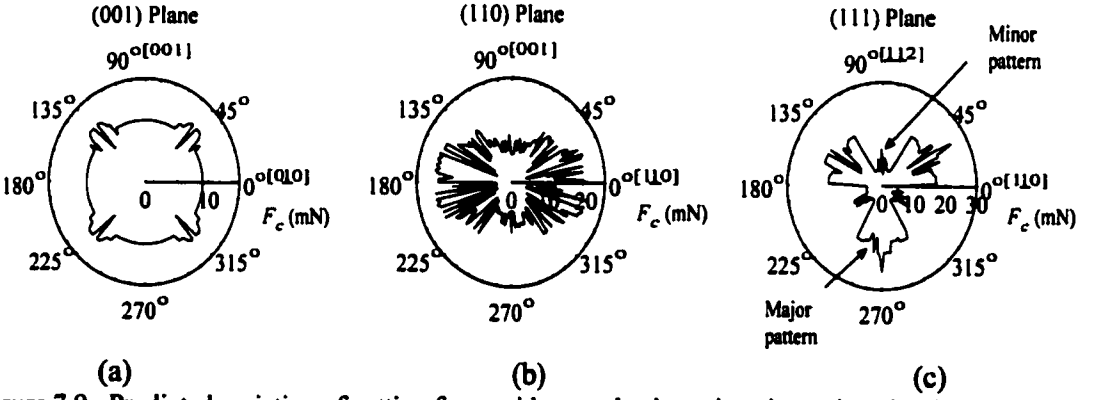

Figure 7.9 Predicted variation of cutting force with crystal orientations in cutting aluminium single crystals on (a) (001) plane, (b) (110) plane and (c) (111) plane.

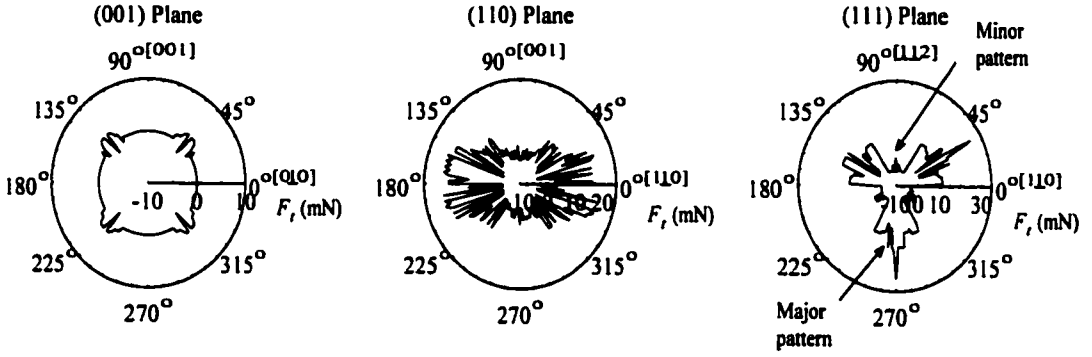

(a) (b) (c)

Figure 7.10 Predicted variation of thrust force with crystal orientations in cutting aluminium single crystals on (a) (001) plane, (b) (110) plane and (c) (111) plane.

Table 7.7 A comparison between the predicted and measured dominant frequency components for the variation of the cutting forces

Specimen no.	Dominant frequency component f_2 (Hz)			
	Cutting force		Thrust force	
	Predicted	Measured	Predicted	Measured
7A(I)	200	200	200	200
7A(II)	100	95	100	100
7A(III)	150	300	150	300
7A(III)*	297	150	297	140

Note : * Frequency component at f_3

Table 7.8 A comparison between the predicted and measured fundamental cyclic frequency of cutting forces variation

Specimen no.	Fundamental cyclic frequency of cutting forces variation (cycles per workpiece revolution)			
	Cutting force		Thrust force	
	Predicted	Measured	Predicted	Measured
7A(I)	4.0	4.0	4.0	4.0
7A(II)	2.0	1.9	2.0	2.0
7A(III)	3.0	6.0	3.0	6.0
7A(III)*	5.94	3.0	5.94	2.8

Note : * Frequency component at f_3

The background spectral plots for the cutting and thrust force signals were first obtained in air cutting. The results are depicted in Figure 7.11. It is noticed that the background spectra are composed of random frequency components with a low power spectral density (*PSD*) in nature. These could be attributed to the spray of coolant and fine

vibration of the machine. Figure 7.12, Figure 7.13 and Figure 7.14 show the predicted and the measured spectral plots for the variation of cutting forces in diamond turning of (001), (110) and (111) crystals ,respectively. The predicted spectra are found to agree well with the measured spectra.

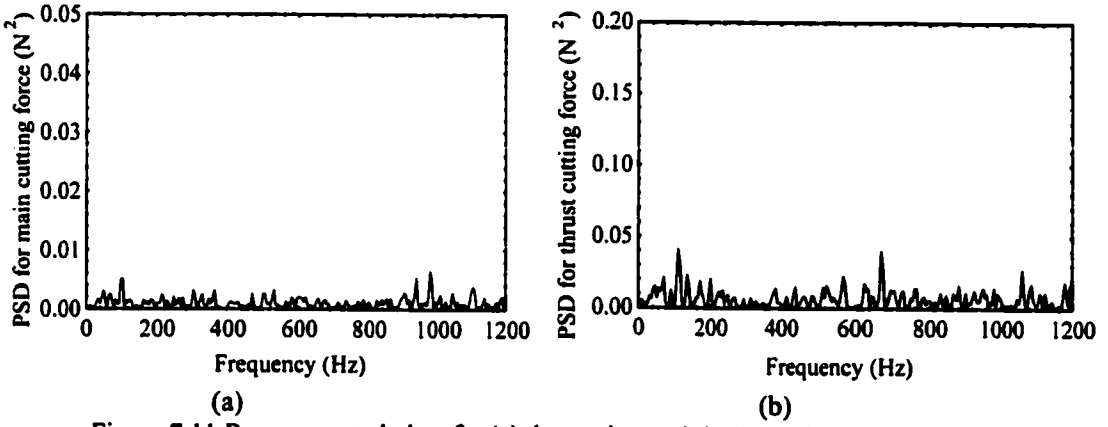

Figure 7.11 Power spectral plots for (a) the cutting and (b) thrust forces in air cutting

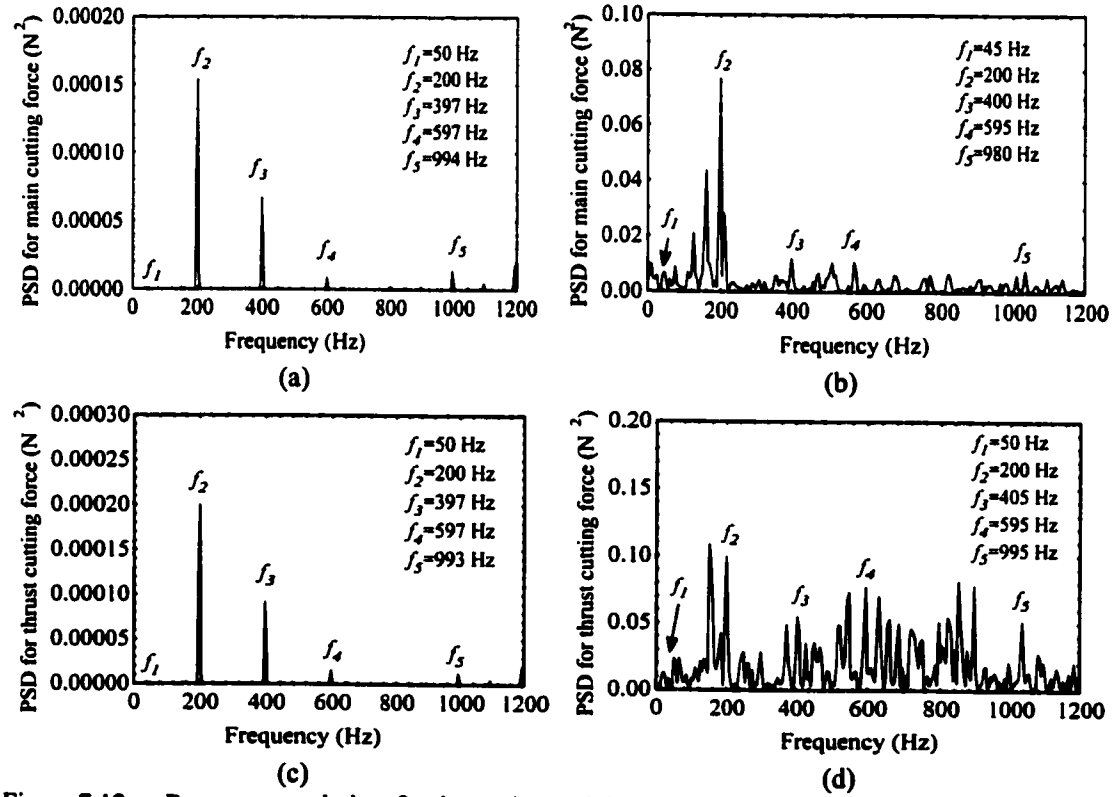

Figure 7.12 Power spectral plots for the cutting and the thrust forces for face turning of aluminium single crystal with (001) as the cutting plane : (a) and (c) are as predicted; (b) and (d) are as measured

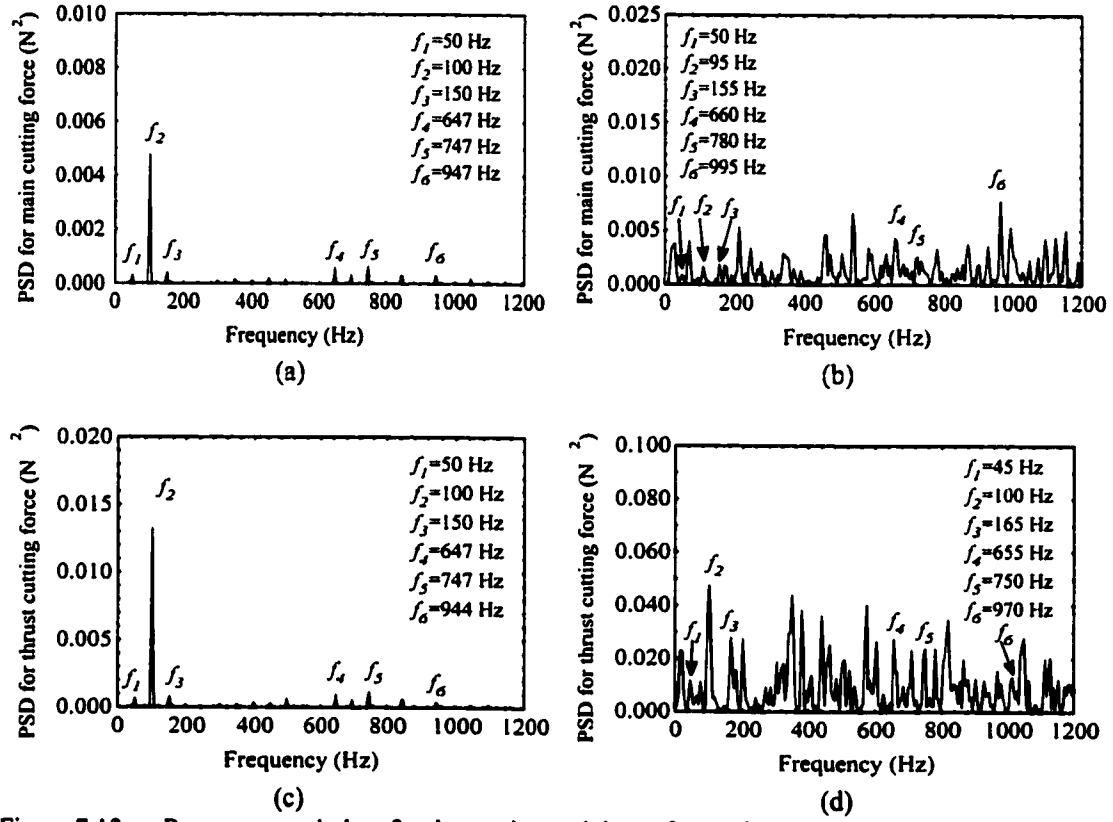

Figure 7.13 Power spectral plots for the cutting and thrust forces for face turning of aluminium single crystal with (110) as the cutting plane : (a) and (c) are as predicted; (b) and (d) are as measured

Remarkable frequency components (f_1, f_2, f_3, f_4, f_5 and f_6) are observed in the predicted spectra for cutting forces and they are also reflected in the measured spectra. The first frequency, f_1, is found to be close to the rotational frequency of the spindle (i.e. 50 Hz). When comparing Figures 7.12 to 7.14, distinctive patterns of frequency distributions are observed for different crystals. Both the predicted and the measured spectra exhibit a dominant frequency component (f_2) which can be correlated to the crystallographic orientation of the work material being cut. As shown in Table 7.7 and Table 7.8, the captioned component appears at almost the exact fundamental cyclic frequency of each of the crystals except for the one with (111) axis. From Figure 7.14, the measured dominant frequency component (300 Hz) for the (111) crystal plane appears almost double that of the predicted dominant frequency component (150 Hz) and is almost identical to its first harmonic (297 Hz). In Figure 7.9(c) and Figure 7.10(c), the cyclic cutting forces are shown to

be made up of two patterns hereby referred to as the major pattern, with a higher amplitude, and a minor pattern, with a lower amplitude. The presence of six peaks is well predicted except that there is a discrepancy in the amplitude of the peak. This suggests that the (111) single crystal might possess two fundamental cyclic frequencies which are three for the major pattern of the cutting force variation as well as six for both of the major and the minor patterns of the cutting force variation. The overall results support the argument that the variation of the cutting forces is related closely to the crystallographic orientation of the crystals being investigated.

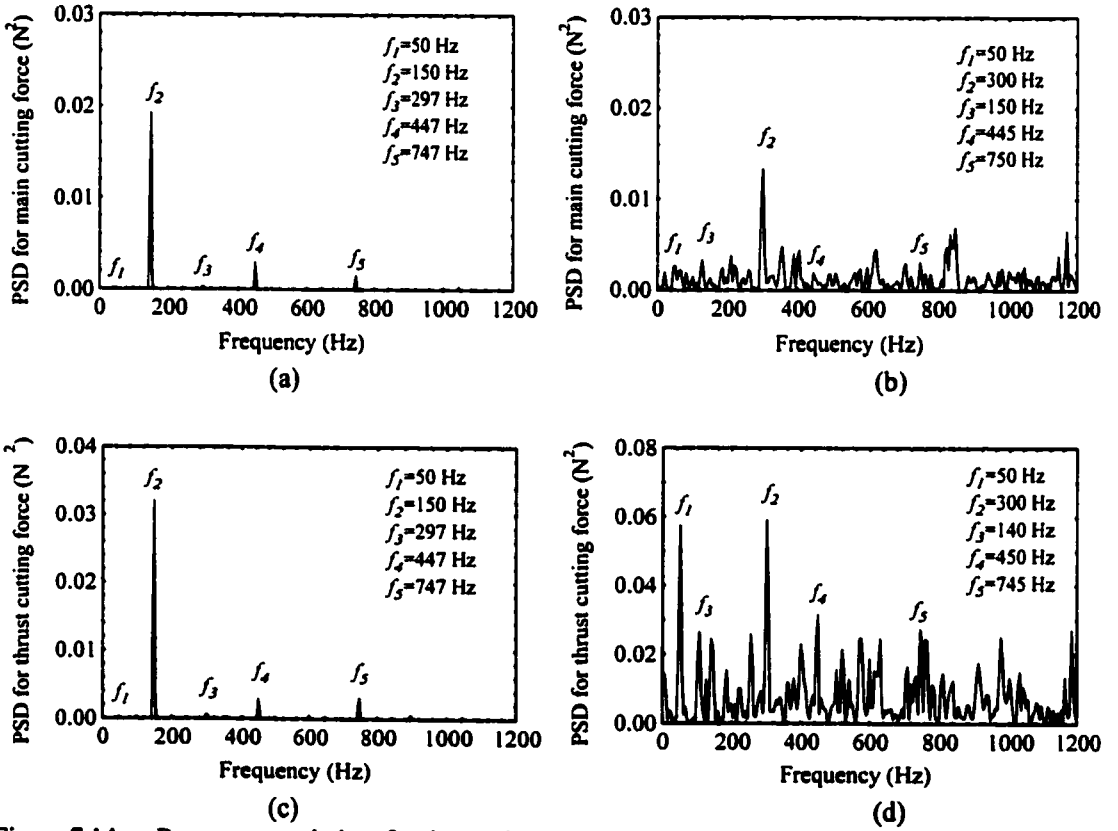

Figure 7.14 Power spectral plots for the cutting and thrust forces for face turning of aluminium single crystal with (111) as the cutting plane : (a) and (c) are as predicted; (b) and (d) are as measured

7.7.1.2 Influence of depth of cut on the variation of cutting forces

Figure 7.15, Figure 7.16 and Figure 7.17 show the variation of power spectral densities (*PSD*) with depth of cut in diamond turning of (001), (110) and (111) aluminium single crystals under Set 7A(II) conditions. As depth of cut increases, the predicted power spectral densities (*PSD*) are found to increase accordingly. The findings agree well with the measured *PSD* for all materials being investigated. The remarkable increase in the *PSD* of the dominant frequency component, f_2, with depth of cut illustrates that the influences of the crystallographic orientation of single crystal materials could be pronounced at large depth of cut.

Overall, the microplasticity model is demonstrated to be helpful in explaining the variation of micro-cutting forces in diamond turning crystalline materials. The main features of the cutting forces patterns are well predicted and confirmed by the cutting tests. There is a good agreement between the experimental findings and the predicted results. The discrepancy in the power spectral densities (*PSD*) between the predicted and the measured spectra could have been due to the following reasons:

(i) The spray of coolant which will introduce disturbances to the cutting force signals and hence the frequency spectrum at the high frequency range;

(ii) The progress of tool wear during machining;

(iii)Fine vibration between the tool and the workpiece which might affect the uncut chip thickness and hence the cutting forces;

(iv) The effect of friction between the tool and the workpiece which is not taken into consideration.

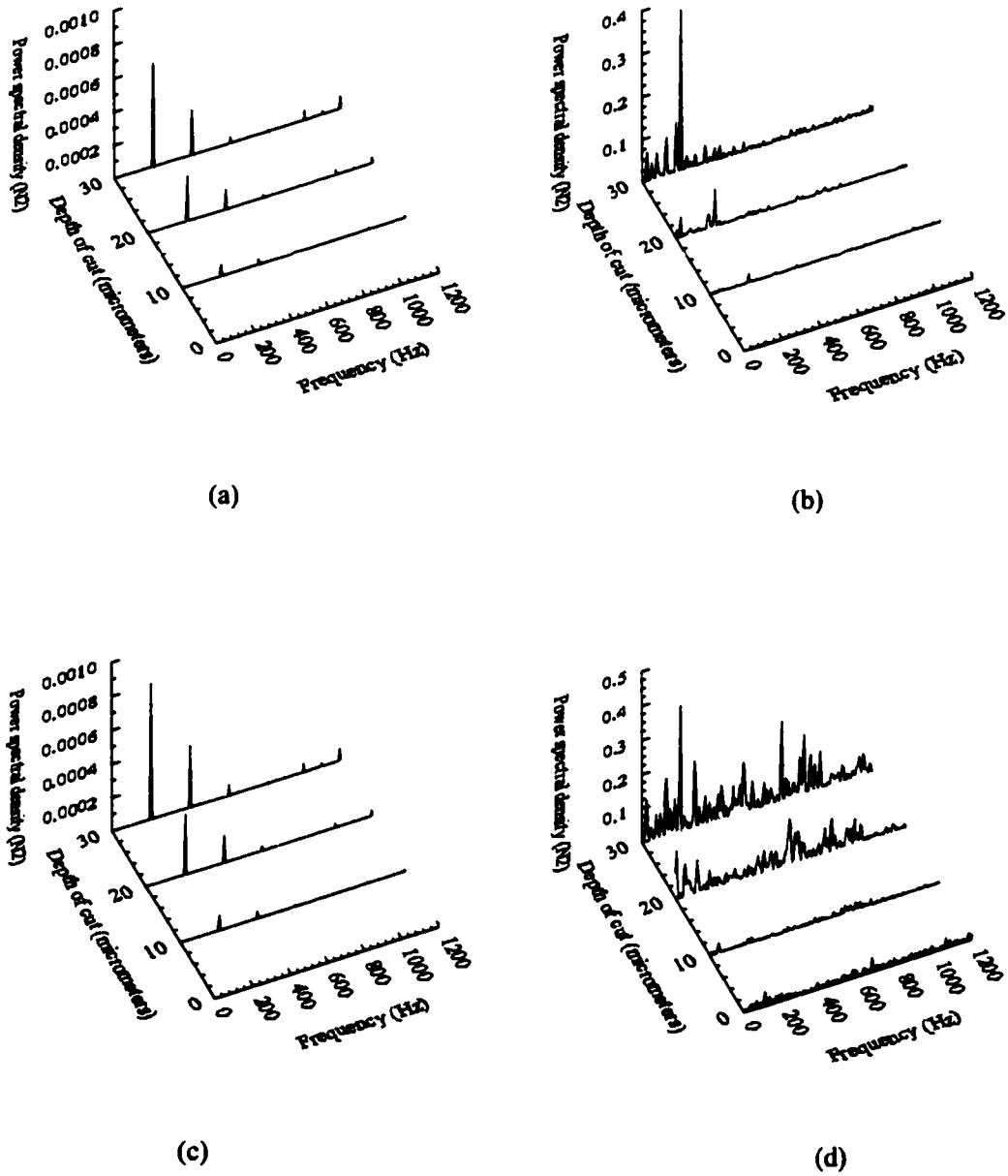

Figure 7.15 Effect of depth of cut on the power spectral densities (PSD) of the cutting forces in diamond turning aluminium single crystal with (001) cutting plane: (a) and (b) are as the predicted and the measured PSD for the cutting force; (c) and (d) are as the predicted and the measured PSD for the thrust force

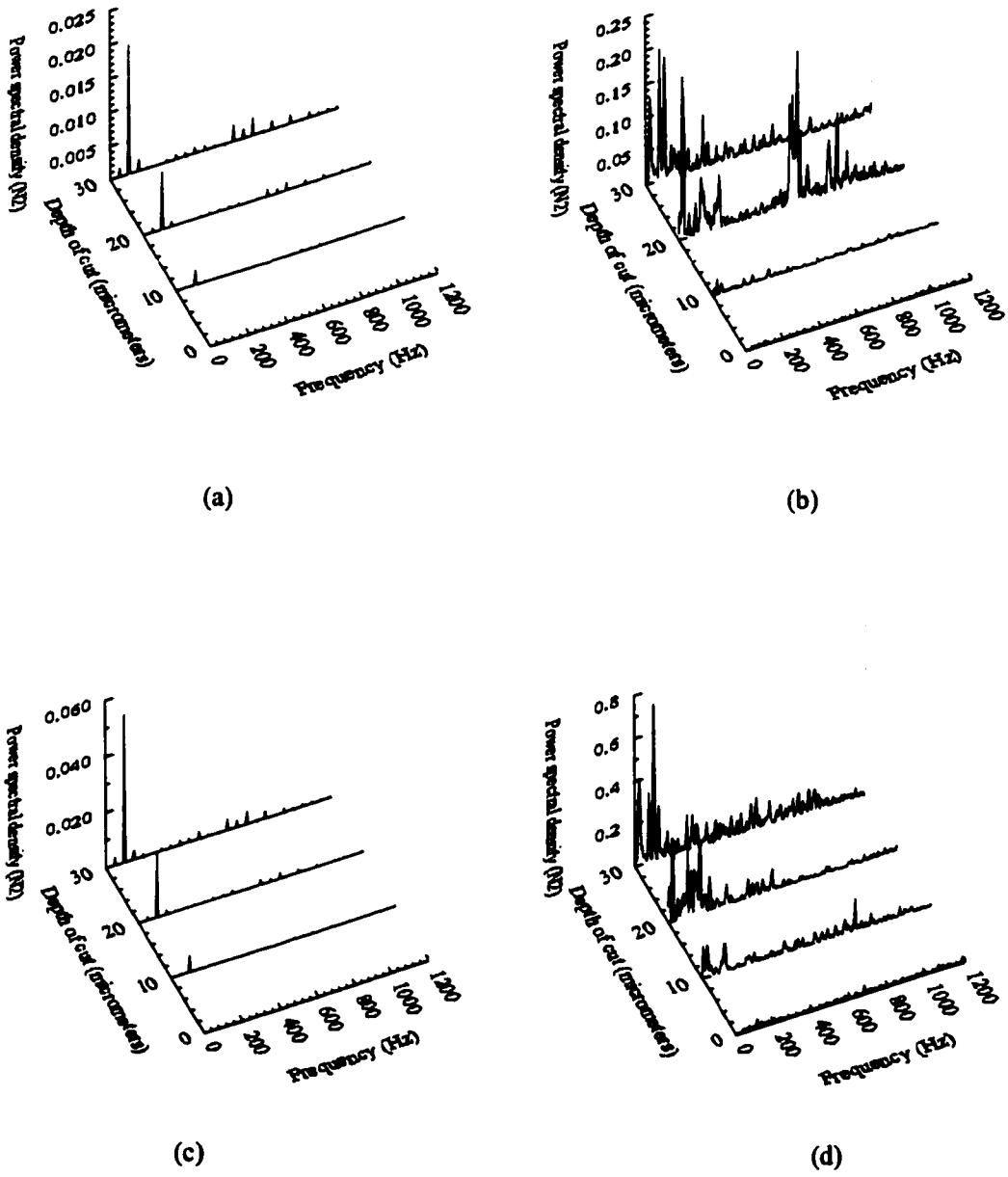

Figure 7.16 Effect of depth of cut on the power spectral densities (PSD) of the cutting forces in diamond turning aluminium single crystal with (110) cutting plane: (a) and (b) are as the predicted and the measured PSD for the cutting force; (c) and (d) are as the predicted and the measured PSD for the thrust force

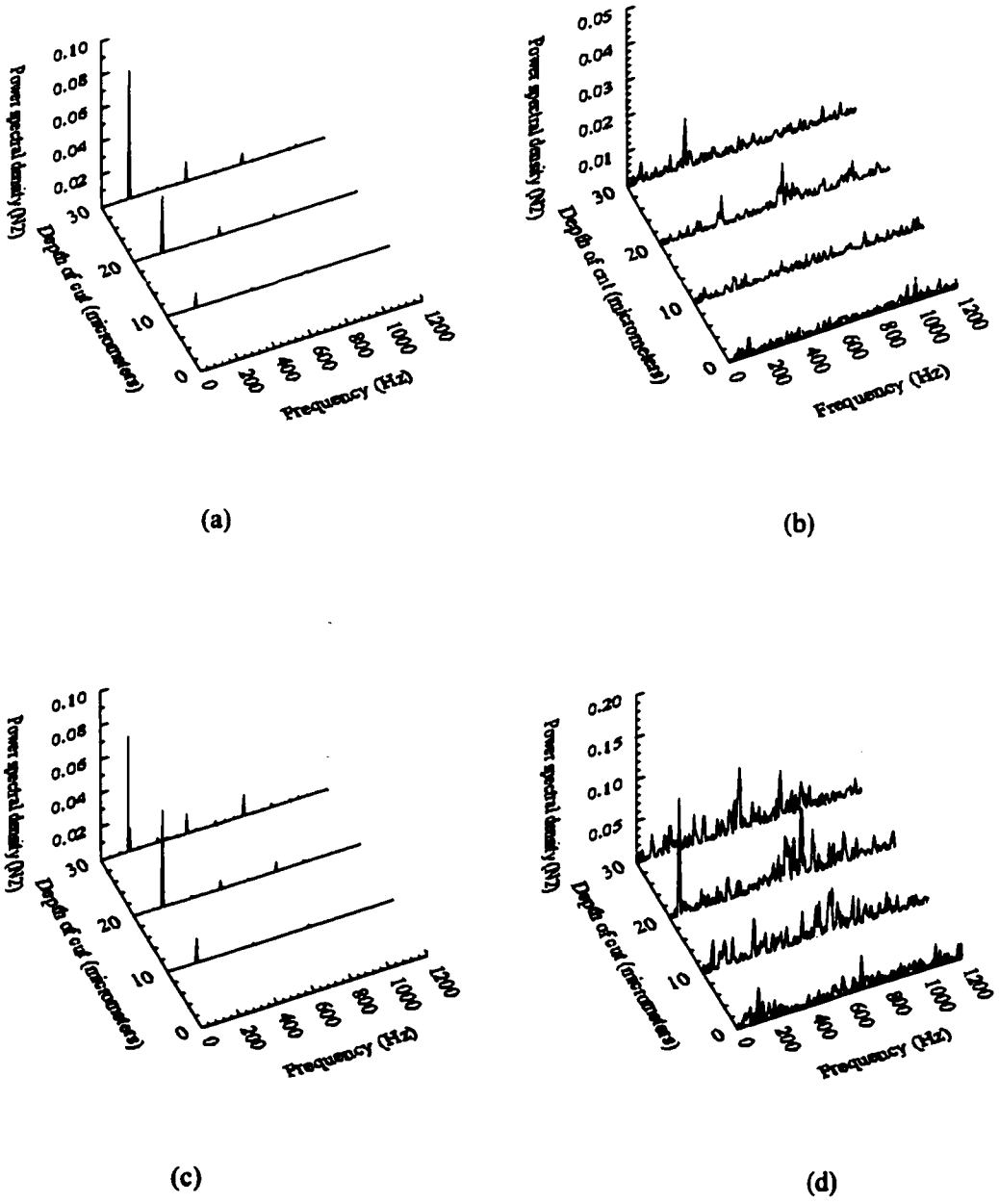

Figure 7.17 Effect of depth of cut on the power spectral densities (PSD) of the cutting forces in diamond turning aluminium single crystal with (111) cutting plane: (a) and (b) are as the predicted and the measured PSD for the cutting force; (c) and (d) are as the predicted and the measured PSD for the thrust force

7.7.2 Characterisation of the dynamics cutting system

Figure 7.18 and Figure 7.19 depict the dependence of the sum of square errors on the natural frequencies and the damping ratios for the tool and the work systems, respectively. The error performance surfaces suggest that there exist optimum values for the natural frequency and the damping ratio which could minimize the sum of square errors between the predicted and the measured displacement signals for the tool and the work systems, respectively. These optimum values identify the dynamic characteristics of the cutting systems. Tables 7.9 and 7.10 tabulate the determined parameters for the A(2) dynamic systems and their covariance equivalent ARMA(2,1) models, respectively. Based on these findings, the cutting system can be derived using Equations (7.56) to (7.59) as follows:

For the A(2) representation,

$$\begin{bmatrix} \frac{d^2Z_t(t)}{dt^2} \\ \frac{d^2Z_w(t)}{dt^2} \end{bmatrix} + \begin{bmatrix} 2519.87 & 0 \\ 0 & 489.97 \end{bmatrix} \begin{bmatrix} \frac{dZ_t(t)}{dt} \\ \frac{dZ_w(t)}{dt} \end{bmatrix} + \begin{bmatrix} 1.9598x10^6 & 0 \\ 0 & 1.2249x10^6 \end{bmatrix} \begin{bmatrix} Z_t(t) \\ Z_w(t) \end{bmatrix} = \begin{bmatrix} \frac{F_z(t)}{89.04} \\ \frac{F_z(t)}{1193.20} \end{bmatrix} \tag{7.77}$$

For the covariance equivalent ARMA(2,1) representation,

$$\begin{bmatrix} Z_{T,t} \\ Z_{W,t} \end{bmatrix} - \begin{bmatrix} 0.4649 & 0 \\ 0 & 1.0753 \end{bmatrix} \begin{bmatrix} Z_{T,t-1} \\ Z_{W,t-1} \end{bmatrix} - \begin{bmatrix} -0.0805 & 0 \\ 0 & -0.3753 \end{bmatrix} \begin{bmatrix} Z_{T,t-2} \\ Z_{W,t-2} \end{bmatrix}$$

$$= \begin{bmatrix} a_{T,t} \\ a_{W,t} \end{bmatrix} - \begin{bmatrix} -0.2300 & 0 \\ 0 & -0.2678 \end{bmatrix} \begin{bmatrix} a_{T,t-1} \\ a_{W,t-1} \end{bmatrix} \tag{7.78}$$

As shown in Figure 7.20, the predicted displacement values based on Equation (7.78) conform well to the measured values. With the identification of the system parameters, it is possible to construct the Green's functions which determine the response of the dynamic systems to vibration. Figure 7.21(a) and Figure 7.21(b) depicts the Green's function for the

tool and work systems, respectively. It is noticed that both the tool and the work systems exhibit heavy damped sinusoidal characteristics which are due to the high stiffness of the machine structure. The tool system is shown to possess higher damping characteristics than that of the work system. In other words, the tool system is stiffer than the work system.

Table 7.9 Estimated parameters for the A(2) dynamic systems

Constants	Tool system	Work system
Equivalent Mass (kg)	89.04	1193.20
Stiffness (MNm^{-1})	174.50	146.15
Damping ratios	0.9	0.7
Natural frequency (Hz)	8796	2199

Table 7.10 Estimated constants for the equivalent ARMA(2,1) model coefficients

Constants	Tool system	Work system
Coefficient, ϕ_1	0.4649	1.0753
Coefficient, ϕ_2	-0.0805	-0.3753
Coefficient, θ_1	-0.2300	-0.2678

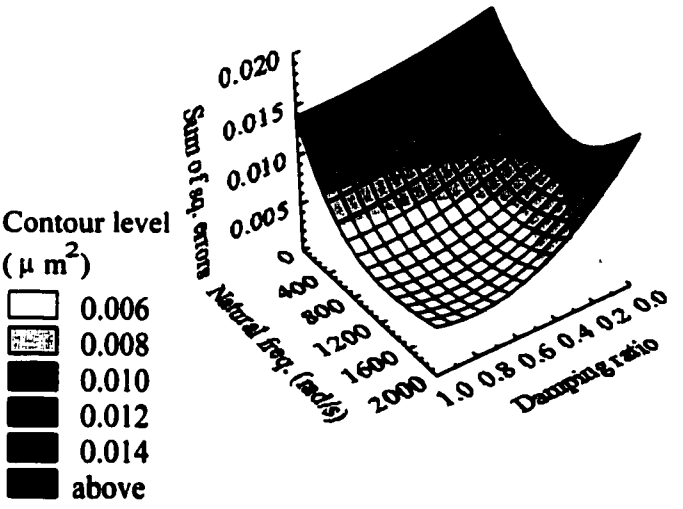

Figure 7.18 Dependence of sum of square errors on the damping ratio and the natural frequency of the tool system

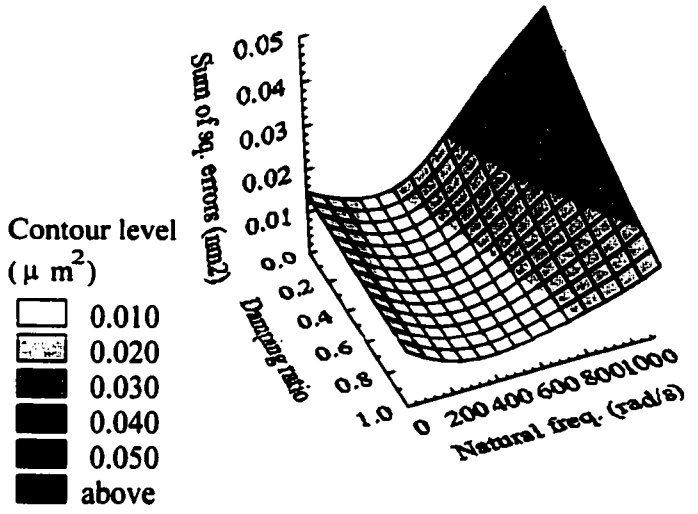

Figure 7.19 Dependence of sum of square errors on the damping ratio and the natural frequency of the work system

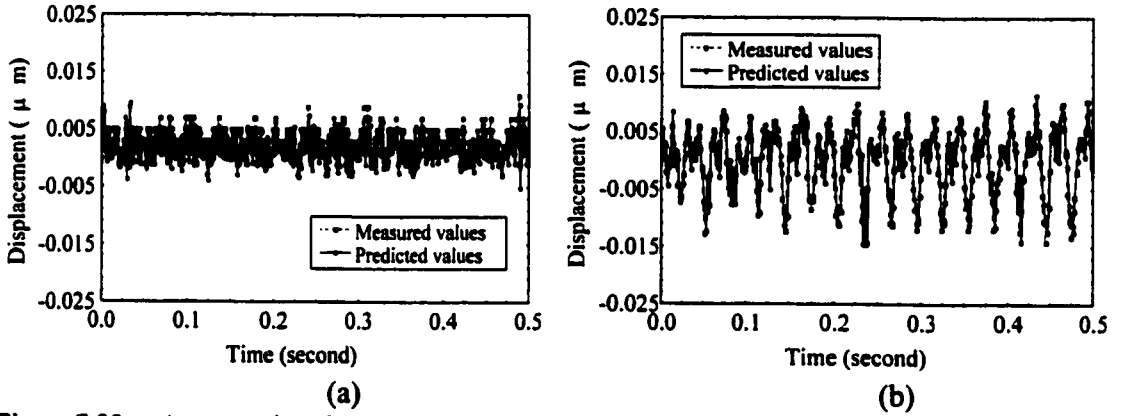

Figure 7.20 A comparison between the measured and the predicted displacement values for (a) the tool and (b) the work systems respectively

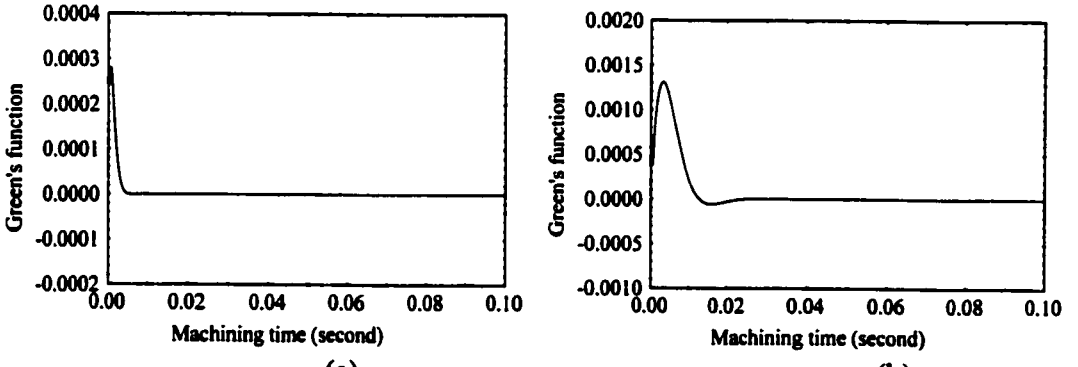

Figure 7.21 Green's functions for (a) the tool and (b) the work systems

7.7.3 Performance of the surface roughness prediction

7.7.3.1 Simulation of materials induced vibration and its effect on the surface generation

Figure 7.22, Figure 7.23 and Figure 7.24 show the predicted materials induced vibration and the corresponding power spectra in diamond turning of (001), (110) and (111) aluminium signal crystals, respectively. It is observed that the vibration induced by the change of crystallographic orientation of work materials is not a simple harmonic. Each crystal has a distinctive vibration pattern. As shown in the spectral plots of the vibration in Figure 7.22(b), Figure 7.23(b) and Figure 7.24(b), the spectra are composed mainly of the harmonics of the rotational frequency of the spindle, i.e. 33.3 Hz. However, the dominant frequency components ($f_{v,2}$) are shown to vary with the crystallographic orientation of the work materials. They are found to be 130.0 Hz, 66.7 Hz and 100.0 Hz for the (001), (110) and (111) crystals respectively. These components are equivalent to the third harmonic, the first harmonic and the second harmonic of the rotational frequency of the spindle. Also, the locations of these components closely match the fundamental cyclic frequency of the variation of the cutting forces as discussed in Section 7.7.1.

The effect of materials induced vibration on the tool loci is simulated in Figure 7.25. The captioned vibration induces surface waviness with different wavelengths as shown in Figure 7.26. The number of surface waves formed on the surface is found to agree well with the fundamental cyclic frequency of the variation of the micro-cutting force. Figure 7.27 shows the virtual surface topographies simulated for different crystals. Their corresponding equi-contour maps are shown in Figure 7.28 which provide clear pictures of the variation of surface height. A different pattern is observed in each crystal. The high and low surface heights represent the bright and dark sectors, respectively.

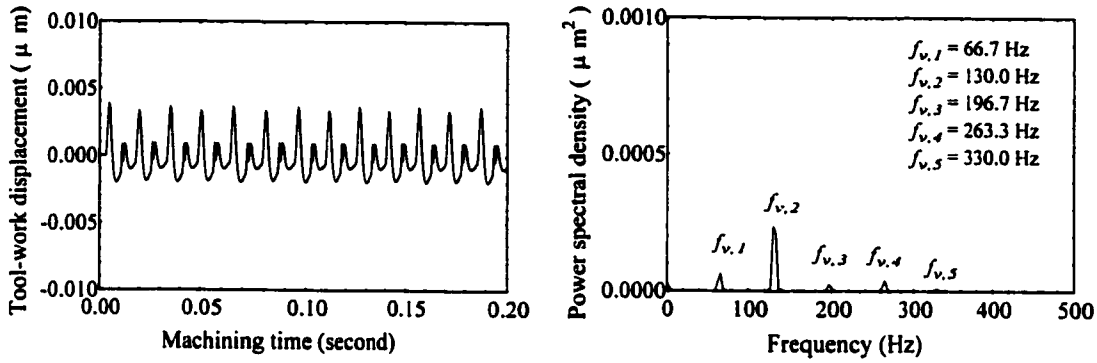

(a) (b)

Figure 7.22 (a) Predicted materials induced vibration and (b) its power spectrum for machining aluminium single crystal with (001) as cutting plane

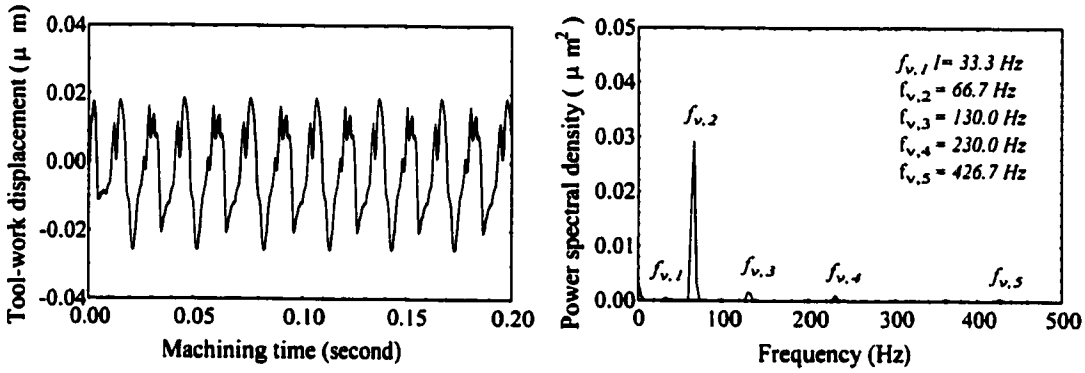

(a) (b)

Figure 7.23 (a) Predicted materials induced vibration and (b) its power spectrum for machining aluminium single crystal with (110) as cutting plane

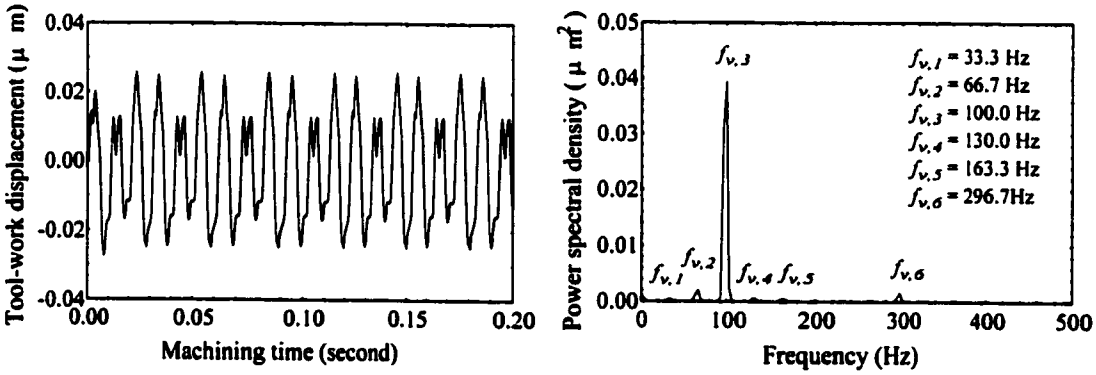

(a) (b)

Figure 7.24 (a) Predicted materials induced vibration and (b) its power spectrum for machining aluminium single crystal with (111) as cutting plane

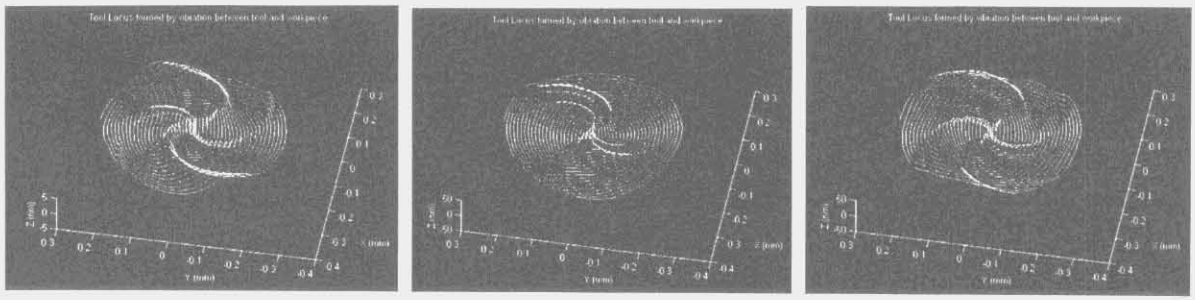

(a) (b) (c)

Figure 7.25 Simulated tool loci for face cutting of aluminium single crystals on: (a) (001) plane, (b) (110) plane and (c) (111) plane

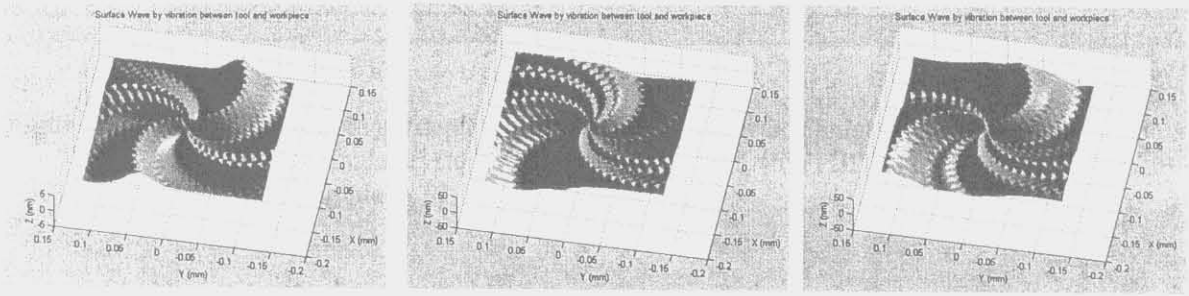

(a) (b) (c)

Figure 7.26 Visualization of surface modulation for face cutting aluminium single crystals on: (a) (001) plane, (b) (110) plane and (c) (111) plane

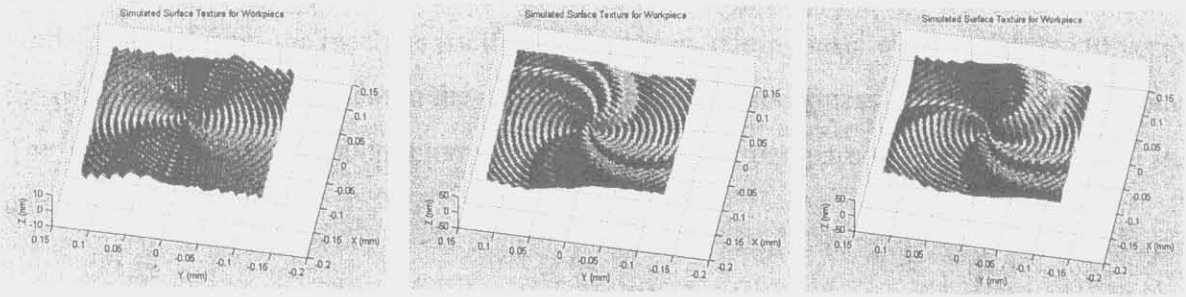

(a) (b) (c)

Figure 7.27 Visualization of the effect of materials induced vibration on surface generation in diamond turning of aluminium single crystals on: (a) (001) plane; (b) (110) plane and (c) (111) plane

There is a difference between the frequency of surface modulation induced by the materials induced vibration and that by the relative tool-work vibration as discussed in Chapter 6. The former depends on the crystallographic orientation of the work material and is thus independent on the phase relationships described in Equations (3.4) and (3.5). The

machine tool vibration, on the other hand, induces surface modulation with a frequency which depends on the ratio of frequency of vibration to the spindle rotational speed. In other words, the former is material dependent whereas the latter is machine dependent.

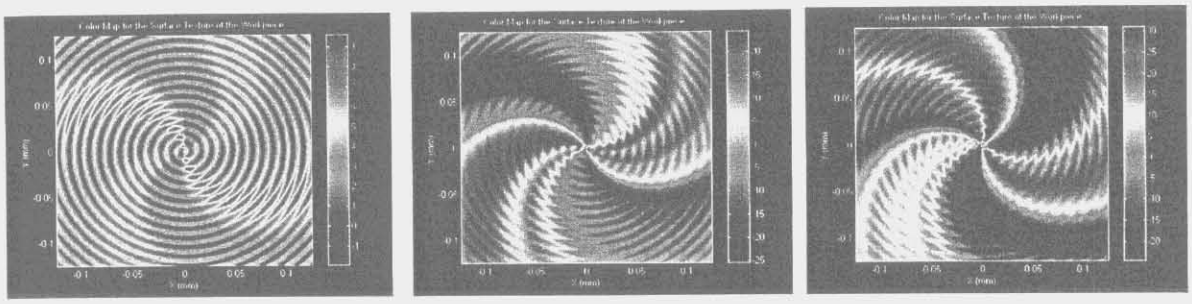

(a) (b) (c)

Figure 7.28 Equi-contour maps depicting the variation of surface height in face cutting of aluminium single crystals with : (a) (001) plane, (b) (110) plane and (c) (111) plane as the cutting plane

7.7.3.2 Experimental verification

As discussed in Section 7.4, the formation of surface topography in diamond turning is affected by the crystallographic orientation of the work materials as well as the relative tool-work vibration from the machine itself. In this section, cutting tests were performed to verify the performance of the system in the prediction of surface roughness and surface topography. The predicted results for aluminium single crystals were compared with those found in the cutting tests.

Figure 7.29, Figure 7.30 and Figure 7.31 show the simulated and the measured surface topographies for the diamond turned (001) plane, (110) plane and (111) plane, respectively. Overall, the simulated surface topographies are similar to those obtained from the WYKO interferometric microscope for the work materials being investigated. The observed difference at the central region of the predicted and the measured topographies is mainly due to tool decentering errors (Lee, Cheung and Chiu, 1999) introduced in tool setting. The topographies exhibit combined features of surface modulation caused by the materials induced vibration and the relative tool-work vibration. The observed surface modulations due

to materials induced vibration in Figure 7.27 are shown to merge with those caused by the machine vibration. For (001) crystal, the features induced by the variation of the crystallographic orientation of the work material are found to be overwhelmed by machine vibration. However, for the (110) plane and (111) crystals, the influences of materials induced vibration on the surface generation are shown to be significant. Such findings are further supported by comparing the predicted and the measured equi-contour maps of the crystals as shown in Figure 7.32, Figure 7.33 and Figure 7.34. Most of the surface features found in the measured patterns are reflected in the simulated patterns. These further demonstrate the capability of the system to simulate the combined effects of the machine and the materials induced vibration.

Table 7.11 tabulates the predicted and the measured arithmetic roughness R_a values of the machined surfaces. It is found that the predicted values are systematically smaller than the measured values. The discrepancy could have been caused by the effect of swelling, as discussed in Chapter 3 and Chapter 4, which have not considered in the enhanced surface topography model. Figures 7.35, Figure 7.36 and Figure 7.37 show the predicted and the measured variation of arithmetic roughness R_a at different radial sections of the turned crystals. It is noticed that the predicted patterns of surface roughness variation conform well to the measured patterns. (110) crystal is shown to have a larger variation of surface roughness than the (111) crystal whereas that for (001) crystal is the smallest. Since the experiments were conducted under the same cutting conditions, the variation of the surface roughness were attributed to the changing crystallographic orientation of the work materials and the vibration induced, as predicted, by the system. As shown in Table 7.10, the argument is further supported by the agreement of the predicted and the measured values for degree of roughness anisotropy (DRA) which is defined in Section 3.3.2.

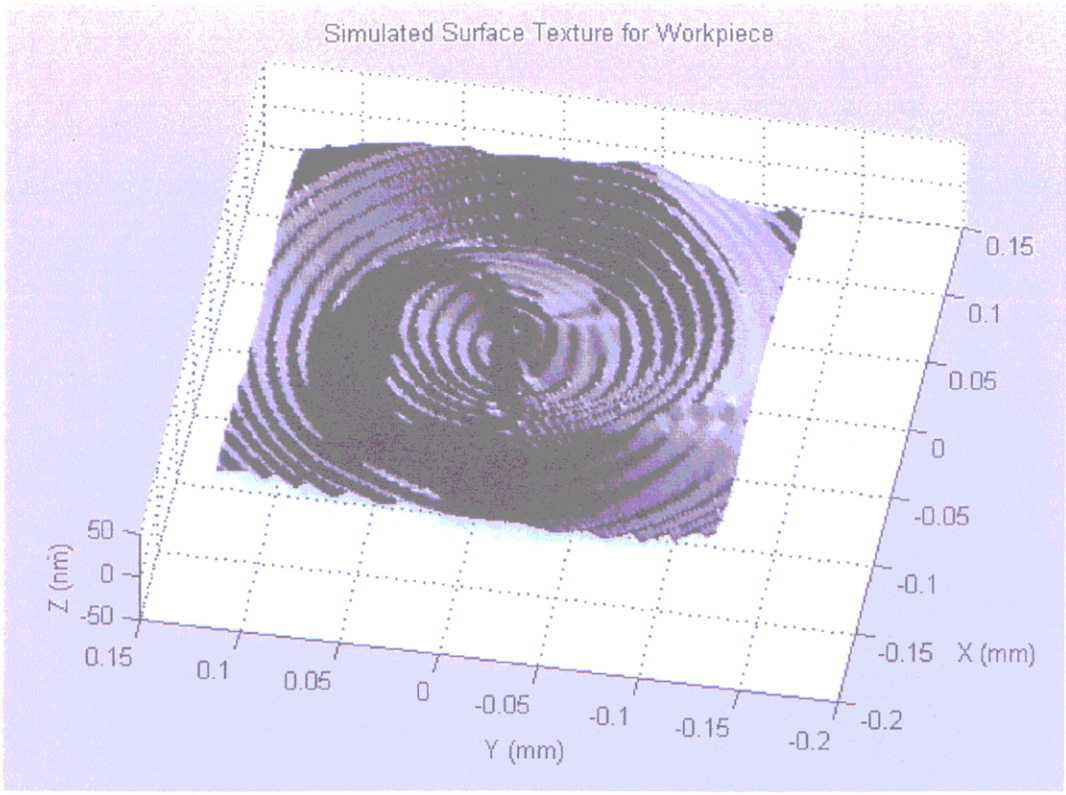

(a)

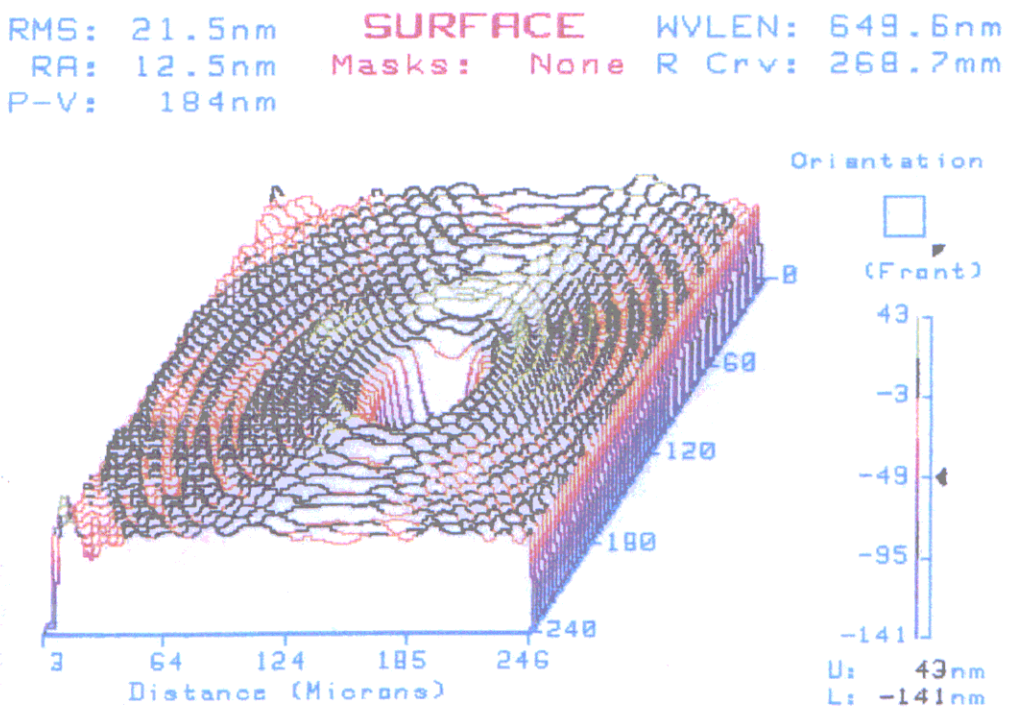

(b)

Figure 7.29 (a) Simulated and (b) measured surface topographies for face cutting of aluminium single crystal with (001) plane (combined effects)

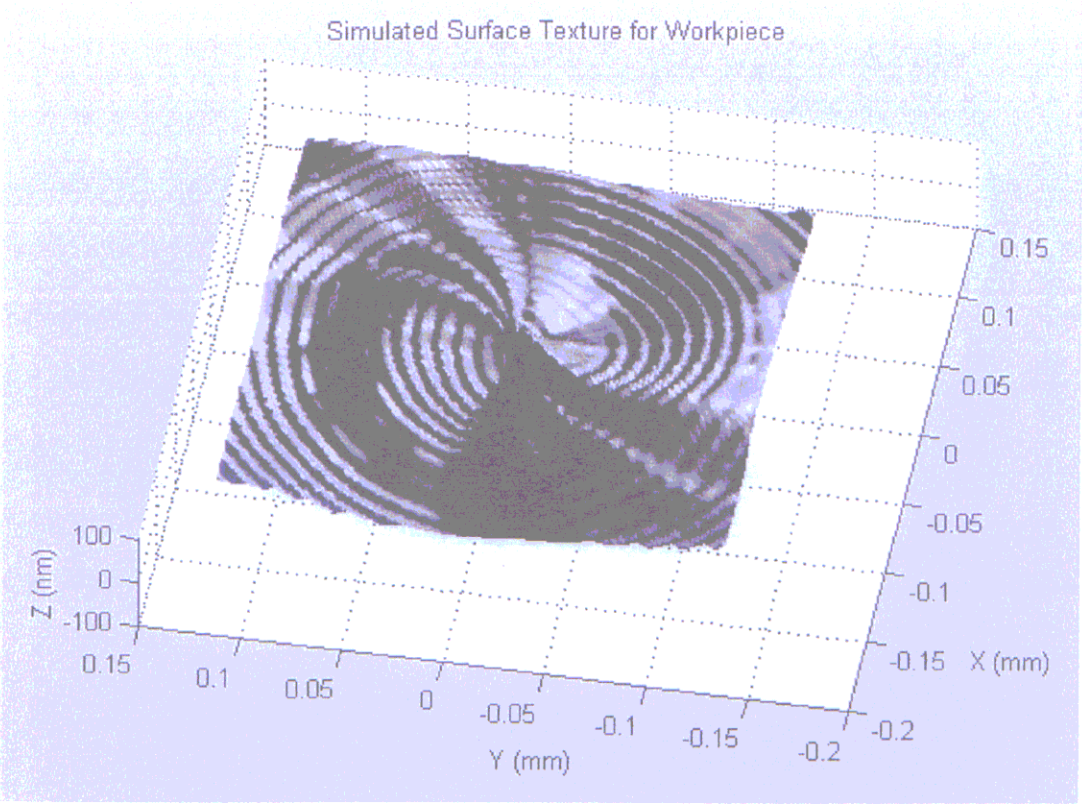

(a)

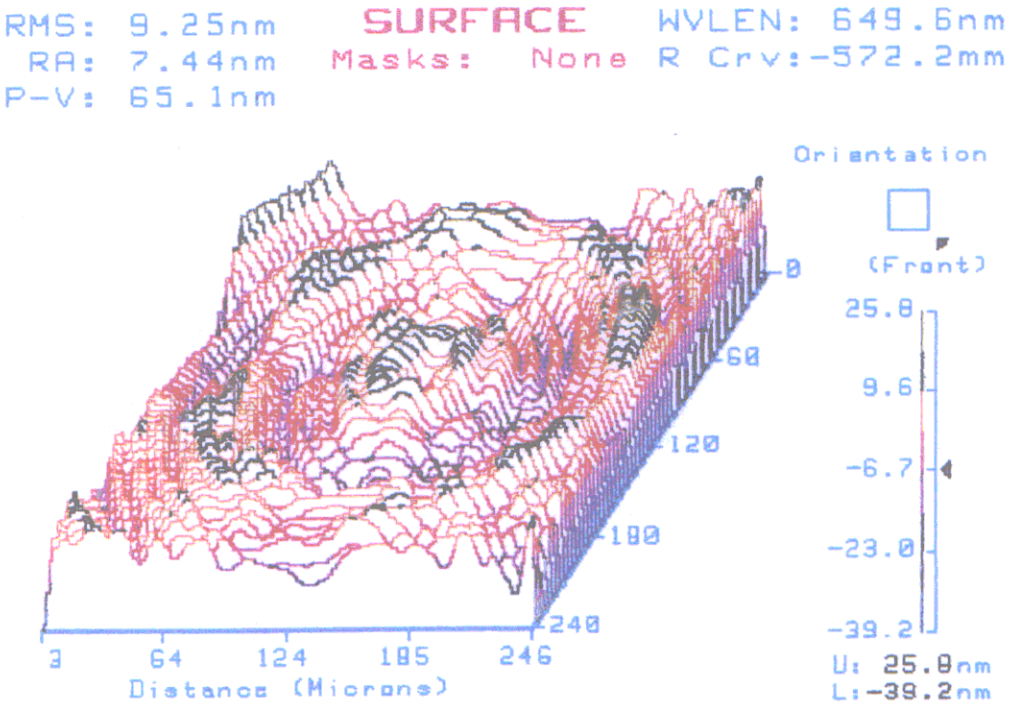

(b)

Figure 7.30 (a) Simulated and (b) measured surface topographies for face cutting of aluminium single crystal with (110) plane (combined effects)

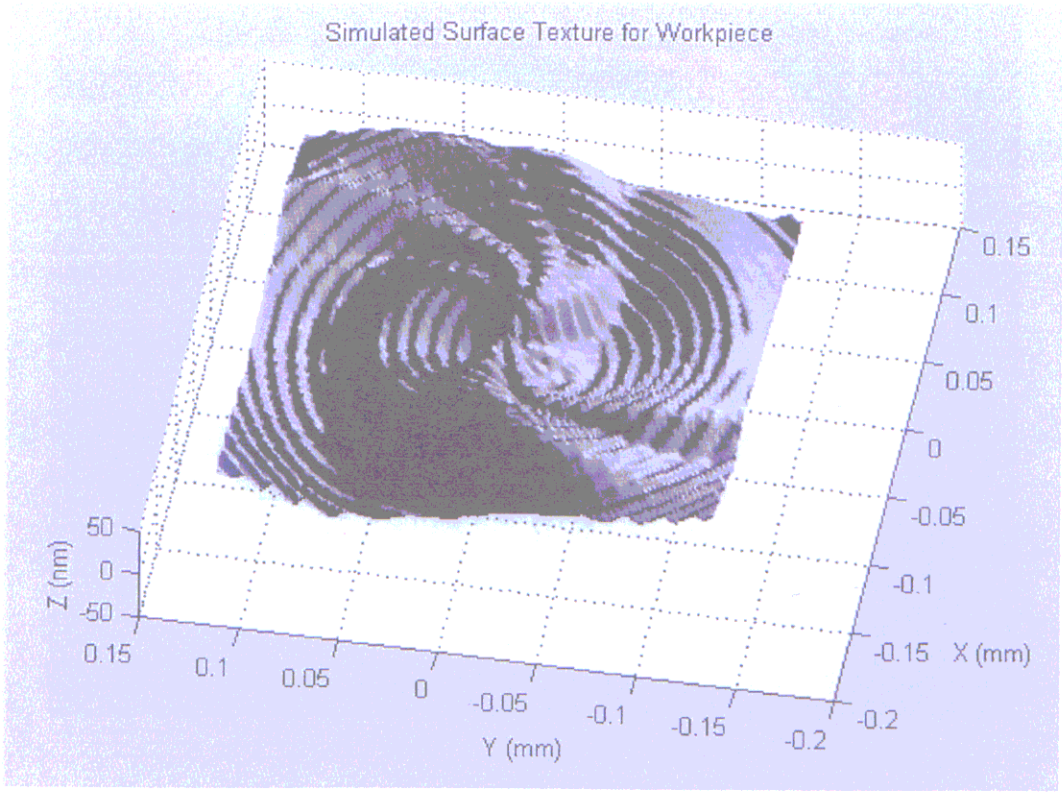

(a)

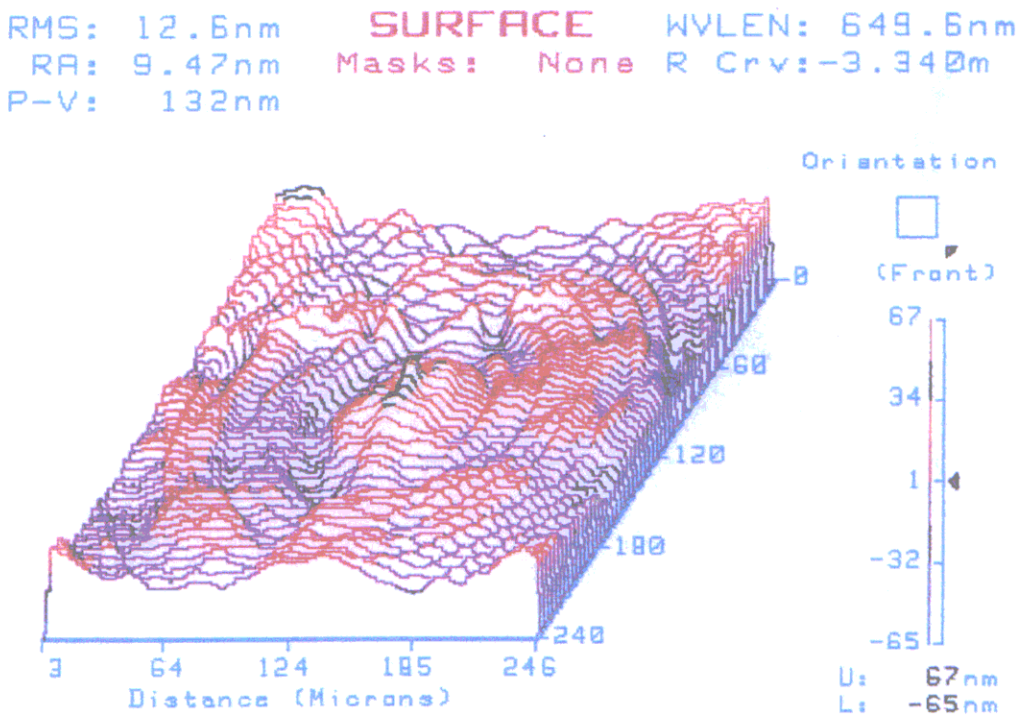

(b)

Figure 7.31 (a) Simulated and (b) measured surface topographies for face cutting of aluminium single crystal with (111) plane (combined effects)

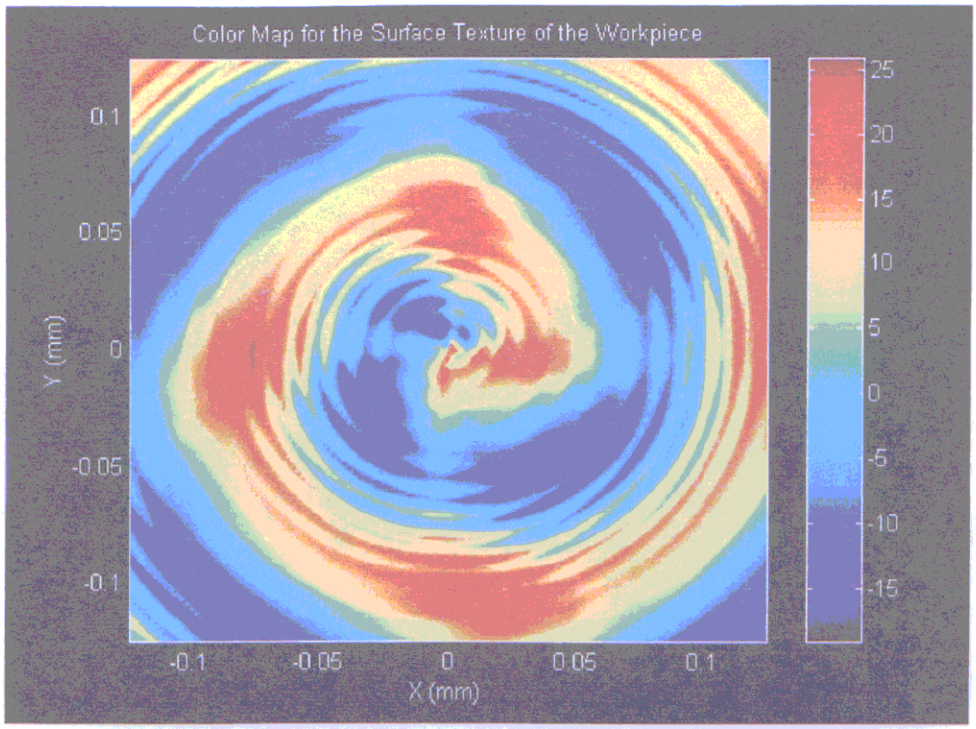

(a)

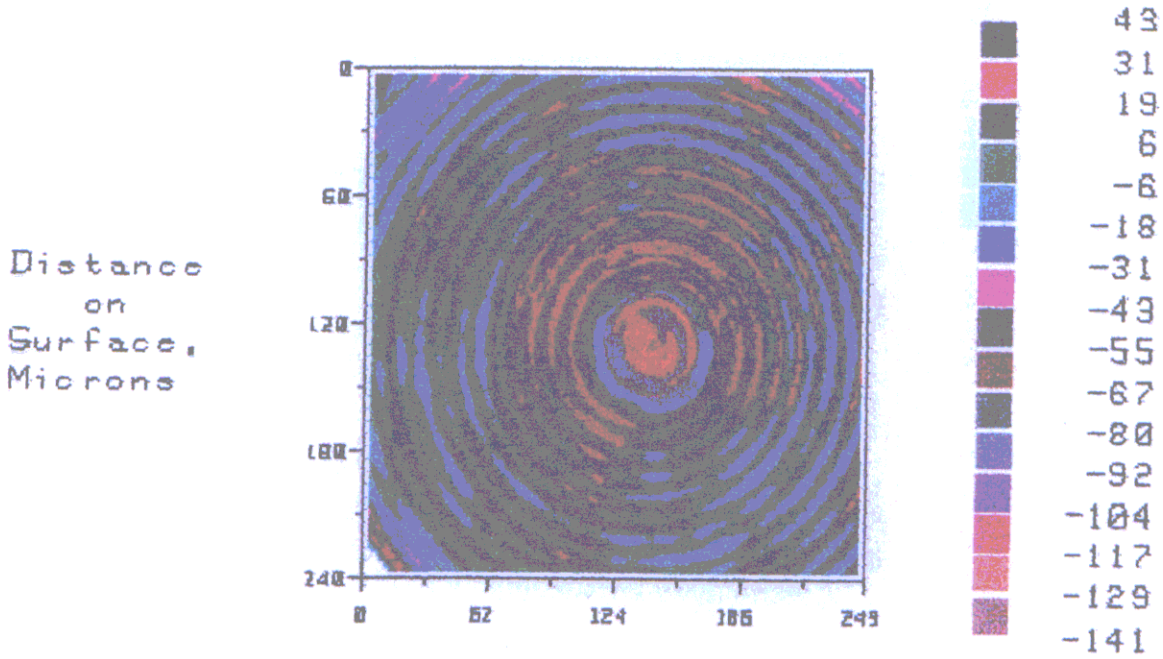

(b)

Figure 7.32 (a) Simulated and (b) measured equi-contour maps for face cutting of aluminium single crystal with (001) plane (combined effects)

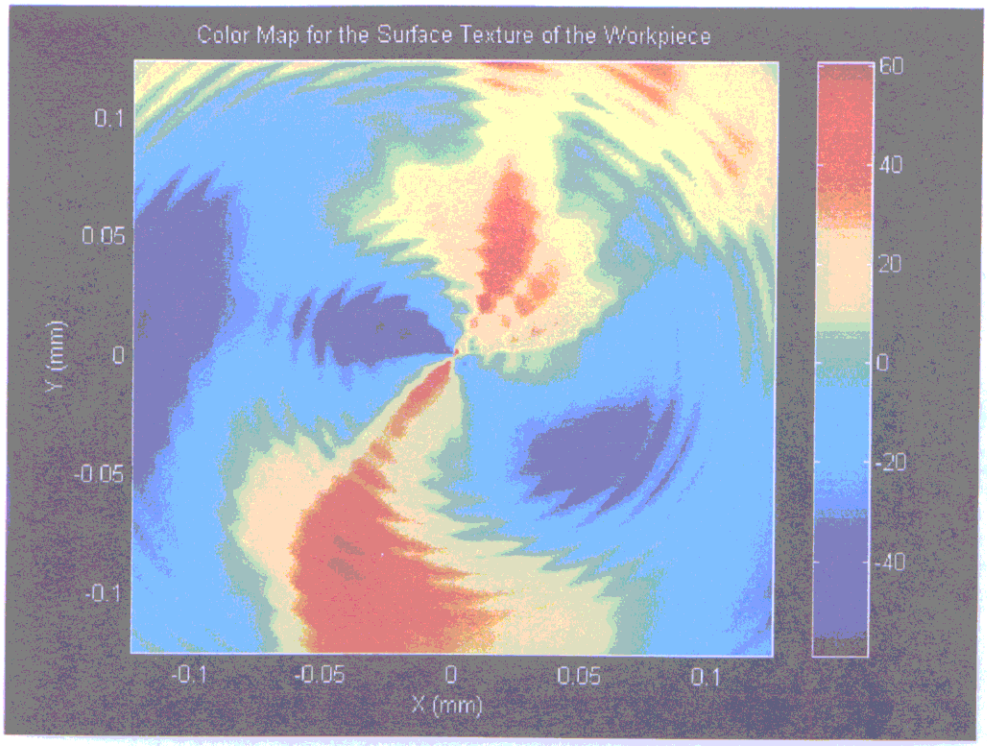

(a)

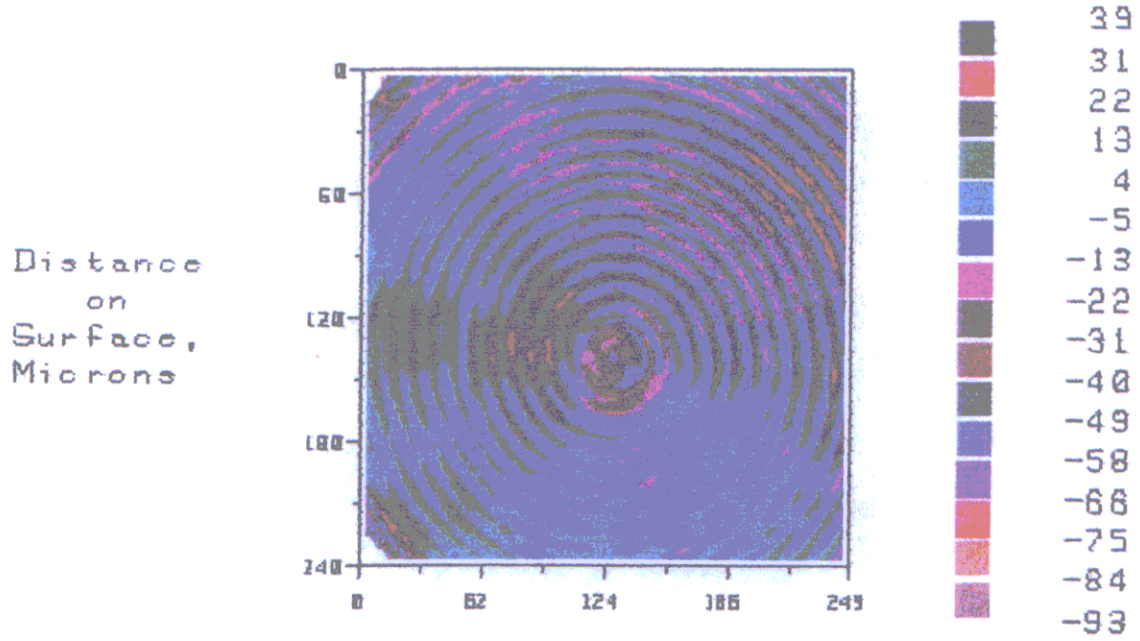

(b)

Figure 7.33 (a) Simulated and (b) measured equi-contour maps for face cutting of aluminium single crystal with (110) plane (combined effects)

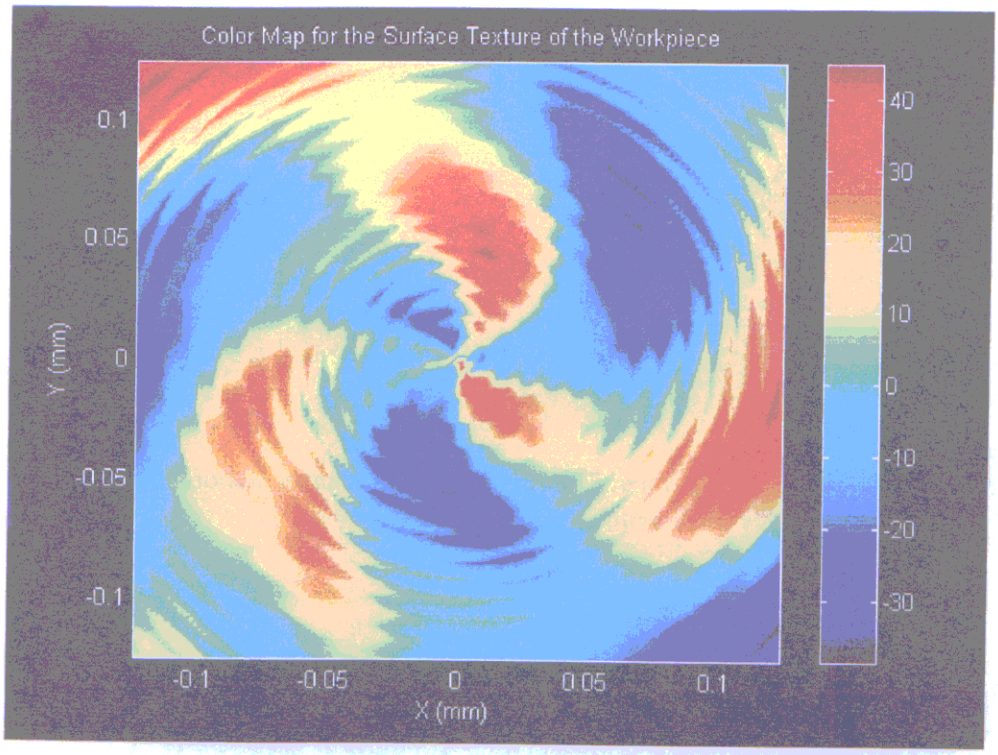

(a)

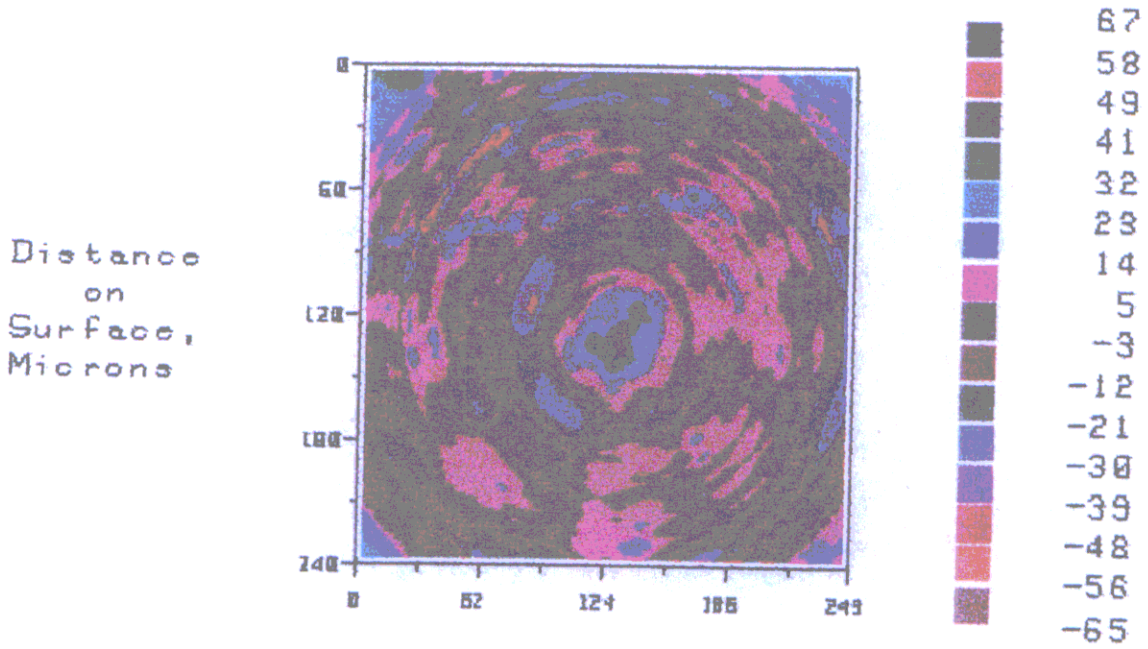

(b)

Figure 7.34 (a) Simulated and (b) measured equi-contour maps for face cutting of aluminium single crystal with (111) plane (combined effects)

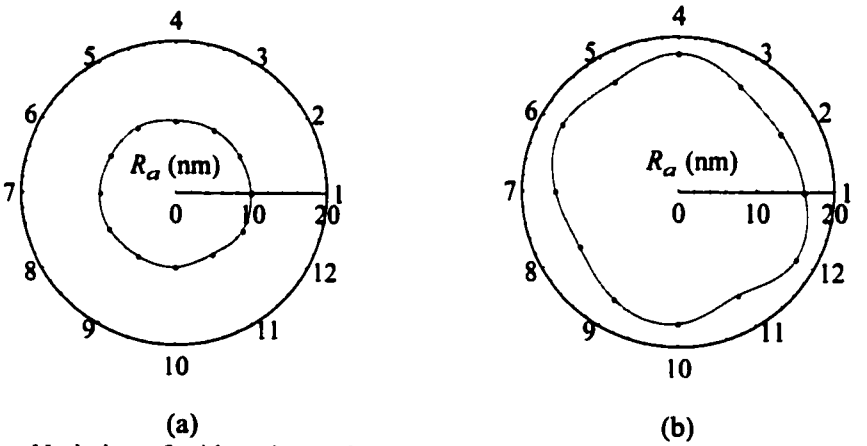

Figure 7.35 Variation of arithmetic roughness at different radial sections of (001) aluminium single crystal: (a) as predicted and (b) as measured.

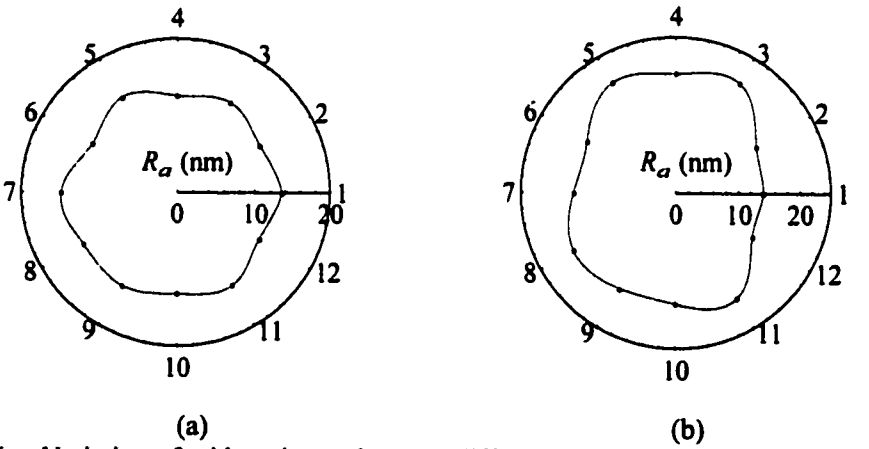

Figure 7.36 Variation of arithmetic roughness at different radial sections of (110) aluminium single crystal: (a) as predicted and (b) as measured.

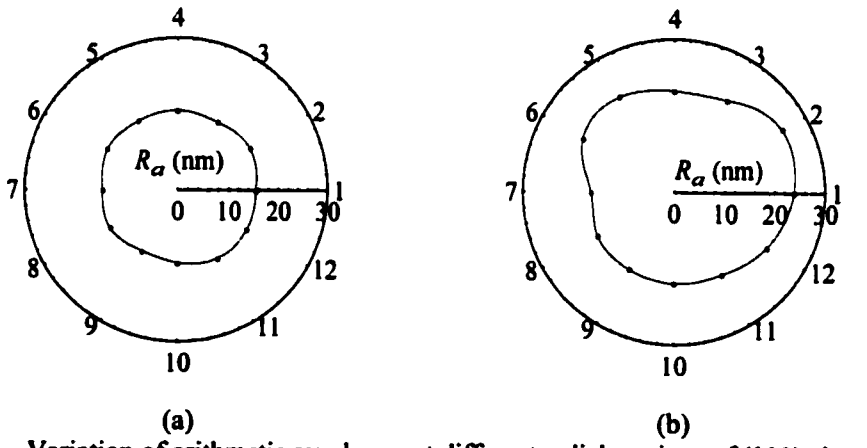

Figure 7.37 Variation of arithmetic roughness at different radial sections of (111) aluminium single crystal: (a) as predicted and (b) as measured.

Table 7.11 A comparison between the predicted and the measured arithmetic roughness and degree of roughness anisotropy

Specimen no.	Arithmetic roughness R_a (nm)			
	Predicted		Measured	
	Mean $\overline{R}_a$	Degree of Roughness Anisotropy, *DRA*	Mean $\overline{R}_a$	Degree of Roughness Anisotropy, *DRA*
7C(1)	9.70	0.020	16.16	0.062
7C(2)	13.38	0.063	17.18	0.139
7C(3)	15.28	0.044	19.99	0.130

Overall, the model based simulation system is demonstrated to be helpful in explaining the additional roughness due to the variation of crystallographic orientation of the workpiece. There is a good agreement between the experimental findings and the simulation results. The discrepancy could have been caused by the following factors:

(i) The effect of material swelling was not taken into account;

(ii) Tool decentering errors (Lee et al., 2000a) in tool setting;

(iii) Progress of tool wear during machining;

(iv) Only relative tool-work vibration in the infeed cutting direction was considered in the study. The influence caused by the spindle radial error motion and the vibration in the yaw direction were not taken into account.

7.8 SUMMARY

In this Chapter, a model-based simulation system for determining quantitatively the variation of local surface roughness due to materials induced vibration in diamond turning is presented. The system is based on several model elements which include a microplasticity model, a dynamic model and an enhanced surface topography model. The microplasticity model is used for predicting the variation of micro-cutting forces caused by

the changing crystallographic orientation of the workpiece materials during cutting. A dynamic model has been built for assessing the vibration induced by the variation of micro-cutting forces. The surface roughness and the topography of the machined surface are predicted by an enhanced surface topography model developed based on the one described in Chapter 6. A software package was developed to implement the simulation system, and the performance of the system has been evaluated through a series of cutting experiments. Experimental results indicate that the variation of the cutting forces and the surface roughness are related closely to the crystallographic orientation of the crystals being cut. As the depth of cut increases, the influences of the crystallographic orientation of the single crystal materials on micro-cutting forces could be pronounced. Overall, the simulation results are found to agree well with the experimental ones.

This study is the first attempt in which the microplasticity theory, theory of system dynamics and machining theory are integrated to tackle the materials induced vibration problems encountered in ultra-precision machining. Indeed, this is a new attempt to link up the microplasticity theory to macro-mechanisms in metal cutting. The successful development of the model-based system will allow the prediction of the magnitude and the effect of materials induced vibration. It also helps to explain quantitatively the additional roughness caused by the variation of the crystallographic properties of the workpiece, and leads us to a better understanding of the "limit of performance" of ultra-precision machining systems.

Chapter 8

Overall Conclusion

A comprehensive investigation of the factors affecting the surface generation in ultra-precision diamond turning has been conducted. The quality of a diamond turned surface is found to be affected by both process factors and material factors. The former involves cutting conditions such as spindle speed, feed rate, tool geometry and relative vibration between the tool and the workpiece. These factors are related closely to the cutting geometry and dynamic characteristics of the cutting system. The material factors include the swelling, the anisotropy and the crystallographic properties of the work materials.

The results show that the influences due to process factors can be minimized or even eliminated through a proper selection of operational settings and control of the dynamic characteristics of the machine. Generally, the use of a high spindle speed, a fine feed rate together with a large tool nose radius are found to be useful for the improvement of surface finish. Under a known and steady vibration characteristic of the cutting system, the surface roughness can be further reduced with the use of an optimum phase shift $|\phi|$ that can be obtained by an adjustment of the spindle rotational speed. Furthermore, it is shown that the surface roughness in the tool feed direction can be made much finer than the sum of the whole amplitude of the tool-work vibration and the theoretical roughness due to the interference of the tool.

As for the material factors, the effect of anisotropy, swelling and crystallographic orientation of the work materials play an essential role on the surface generation. Material swelling causes greater tool marks on the machined surface. This inevitably increases the surface roughness. However, this effect has been overlooked in many studies of surface generation. For anisotropic materials like single crystals, the Young's modulus is dependent on the grain orientation. Thus, the extent of swelling is different for different crystallographic orientations of the work materials and this results in a variation of local

surface roughness. The influences of these material factors are shown to exist consistently even if the cutting is performed under various cutting conditions. This suggests that the influences of the material factors on the surface quality could not be minimized solely by the optimization of process parameters and machine design. A proper selection of work material is of prime importance for further reduction of the surface roughness.

A Multi-spectrum Analysis Method was purposely built for measuring quantitatively the effect of material swelling, anisotropy and materials induced vibration on the surface generation. In the proposed method, the surface features on a diamond turned surface are extracted and analyzed by the FFT spectrum analysis of its surface roughness profiles measured at a finite number of radial sections of the workpiece. The properties of swelling and plastic anisotropy are characterized respectively by a swelling ratio (SR) and a coefficient of anisotropy (COA) which are defined based on the power spectral density (PSD) of the feed components in the surface roughness spectrum. A parameter called the degree of roughness anisotropy (DRA) is also defined to measure the extent of localized variation of surface roughness. The results indicate that the surface roughness varies systematically at different radial sections. Such a variation depends on the crystallographic orientation of the work materials being cut. The arithmetic roughness R_a is found to be strongly correlated to the local swelling ratios. It is also shown that tool feed rate, spindle rotational errors, tool geometry and relative tool-work vibration are not the only dominant components affecting the surface roughness. The vibration caused by the variation of crystallographic orientation of work material or so-called materials induced vibration is another major factor. This vibration results in a significant variation of the frequency distribution of the surface modulation at different radial sections of the turned surface. With the use of the multi-spectrum analysis method is possible to construct the patterns of such variation.

However, one of the shortcomings of the multi-spectrum analysis method is that it is incapable of determining the exact contribution of individual factors upon the overall surface roughness. To overcome this shortcoming, a Multiple Data Dependent Systems

(MDDS) analysis method is proposed. The method provides a component by component wavelength decomposition of the surface roughness profiles at different radial sections of the work surface. The cutting dynamics are characterized by the natural frequency of the central wavelength and the damping ratio of these wavelength components. The relative contribution of each component to the total surface roughness is determined from the variance of the profile. A series of cutting tests was carried out under different cutting conditions and on different materials. Experimental results indicate that the surface roughness profile of a diamond turned surface can be decomposed into four main categories of components which include the components of the feed and the tool geometry, the relative tool-work vibration, the machine vibration and the material crystallography, respectively. It is further confirmed that the surface roughness is dominated by the relative vibration between the tool and the workpiece. Compared with conventional machining, the contribution of feed component to the total roughness is much less, whereas the effect of tool-work vibration is prominent. Besides, the frequency of the relative tool-work vibration components is shown to vary with the crystallographic orientation of the materials being cut. Such a variation of cutting dynamics is inherent in the cutting response of an anisotropic material. Single crystal materials are more prone to this effect than polycrystalline materials. The results agree well with those found in the multi-spectrum analysis.

Based on the results of the experimental findings and the quantitative analysis, a 3-D surface topography simulation model is established for ultra-precision diamond turning. The model takes into the account of the effect of tool geometry, machining conditions and relative tool-work vibration. It makes use of the surface roughness profiles predicted at a finite number of radial sections of the workpiece to construct the surface topography of a diamond turned surface. The performance of the model has been verified through a series of cutting experiments. The results indicate that the model can predict well the surface roughness parameters and the 3-D surface topography. With the use of equi-contour mapping techniques, it is possible to abstract the surface features such as the trace of tool motion, characteristics of the 3-D surface texture and the presence of the surface marks caused by vibration. Although the proposed model could not fully account for the swelling

effect, it is shown to be effective in accounting for most of the process effect in diamond turning of a polycrystalline aggregate. With appropriate modification of the setup configurations, the modelling technique could also be extended to other processes, tool and workpiece combinations.

To account for the influence of the crystallographic orientation of a work material on surface generation, a model-based simulation system has been developed. The system consists of several model elements which include a microplasticity model, a dynamic model and an enhanced surface topography model. The microplasticity model is used for the prediction of the variation of micro-cutting force caused by the changing crystallographic orientation of workpiece material during cutting. A dynamic model is built to determine the vibration induced by the variation of the cutting forces. The influence of such vibration on the surface roughness is considered in an enhanced model developed based on the above mentioned surface topography model. The model-based simulation system has been successfully implemented and evaluated through a series of cutting experiments. Experimental results indicate that the variation of the cutting forces and the surface roughness are related closely to the crystallographic orientation of the crystals being cut. As the depth of cut increases, the influences of the crystallographic orientation of the work materials on the cutting forces can be pronounced. Very distinctive patterns of cutting force variation, power spectra of the cutting forces, and surface topographies are displayed when cutting is performed on different crystallographic planes. Good agreement is found between the simulation results and the experimental findings.

This is the first of its kind in which a model-based simulation system is developed to tackle the materials induced vibration problems in diamond turning of anisotropic materials like single crystal metals. The successful development of the model-based cutting system allow the prediction of the magnitude and the effect of materials induced vibration on the surface generation. It helps to explain quantitatively the localized variation of the surface roughness due to changing crystallography of the workpiece in diamond turning. This is essential for better understanding of the performance of ultra-precision machines.

Ultra-precision diamond turning is an expensive process. Nowadays, the achievement of a super mirror finish in many industrial applications still depends much on the experience and skills of a machine operator through an expensive trial and error approach when new materials or new machine tools are used. The development of the surface topography model together with the model-based simulation system does contribute to the identification of the optimum cutting conditions for diamond turning of different materials without the need for costly trial and error cutting tests. It also helps to establish the best surface quality that can be achieved under a particular dynamic condition of an ultra-precision machine.

Chapter 9

Suggestions for Further Work

From a practical point of view, ultra-precision machining has fulfilled the industrial needs in the manufacture of optical, electronic and mechanical parts for use in advanced technology. However, our understanding of many of the basic phenomena in the generation of new surfaces in ultra-precision machining is still far from perfect. The machine tool-workpiece forms a complex system and very often a multi-disciplinary approach is needed for its study. Some further topics for research are suggested as follows:

(i) To establish a deterministic model for predicting quantitatively the influence of material swelling in surface generation

As shown in Part I of the investigation, material swelling causes greater tool marks and additional surface roughness in diamond turning. The effects have been found to depend on the properties and the crystallographic orientation of the work materials. The multi-spectrum analysis method and the MDDS method provide a powerful quantitative tool for measuring the magnitude and contributions of these effects on the surface quality. However, our scientific understanding of the causes of this phenomenon is still inadequate. More quantitative work has to be done to establish a deterministic model for the prediction of material swelling and its effect on surface generation.

(ii) To develop modified surface topography models for diamond face turning of large workpiece

As discussed in Section 6.2, the surface topography of a diamond turned surface can be affected by the face error motion of the spindle as the size of the workpiece is large (eg. radius of workpiece > 100 mm). The surface topography models developed in the thesis might not be adequate enough to account for the effect due to face error motion of the spindle. Further work has to be done to incorporate the face error factor in the surface topography models.

(iii) To develop quantitative relationships for predicting the surface crystallographic texture after cutting

In Chapter 5, it is pointed out that there is a change in the crystallographic textures of the single crystal aluminium after diamond cutting. The change in the crystallographic texture not only gives clues as to how the plastic deformation has occurred in the deformed layer but also affect the physical properties of the machined surface. Our understanding of the crystallographic texture in machining is still far from perfect. Research on exploring direct quantitative relationships between the microscopic changes and the macroscopic surface roughness parameters has to be done.

(iv) Establishing active control strategy for compensating the effect of materials induced vibration in ultra-precision machining

As mentioned in Section 2.7, the compensation approach consists of prediction of the occurrence of the materials induced vibration and its effect through modelling and simulation and hence eliminates the effect using compensatory control strategy. The model-based simulation system established in Chapter 7 contributes to the prediction of the magnitude of materials induced vibration and its effect on the surface generation in ultra-precision machining. This forms the basis for further development of active compensation strategy for attenuating the materials induced vibration.

(v) To apply established theories to virtual manufacturing

Virtual Manufacturing (VM) is an emerging technology that summarizes computerized manufacturing activities with models, simulations and artificial intelligence instead of objects and their operations in the real world (Onosato and Iwata, 1993, and Ehmann, et al., 1997). This provides a digital tool for the optimization of the production efficiency through simulations prior to the start of actual production. A virtual manufacturing package in ultra-precision machining is being developed (Cheung and Lee, 1999). The package will

allow manufacturers to evaluate the feasibility of a manufacturing plan and optimize the allocation of production resources prior to the actual production. It will also be helpful for conducting training on the use of ultra-precision machines.

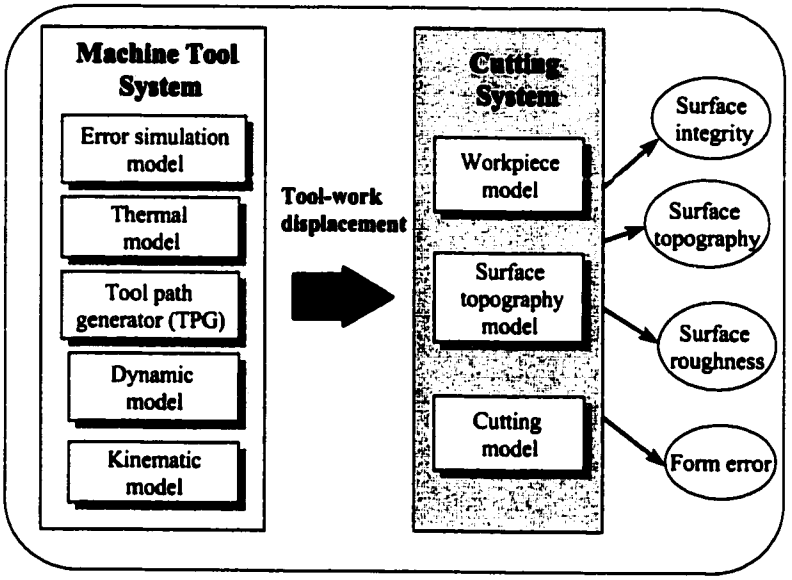

Figure 9.1 A framework of a virtual ultra-precision machining package

Figure 9.1 shows a framework of the virtual ultra-precision machining package, which is divided into two parts, i.e., the machine tool system and the cutting system. Figure 9.2 depicts the functions of the surface topography model or the model-based simulation system on the conceptual virtual machining package. In the machine tool system, the thermal model, the kinematic model and the dynamic model are used to simulate the error motions caused by the thermal effect, the kinematic and the dynamic characteristics of the machine, respectively. A tool path generator is incorporated to simulate the ideal tool path for machining (Lee et al. 2000). An error simulation model, a workpiece model and a cutting model will be incorporated so as to simulate the machine's actual behaviour resulting from the various error motions and the change in work material properties. The surface topography of the workpiece will be simulated by the surface topography model (Cheung and Lee, 2000d and 2000e). The package will be ideal for training designers and engineers in the operation of ultra-precision machines and in the design of optical products.

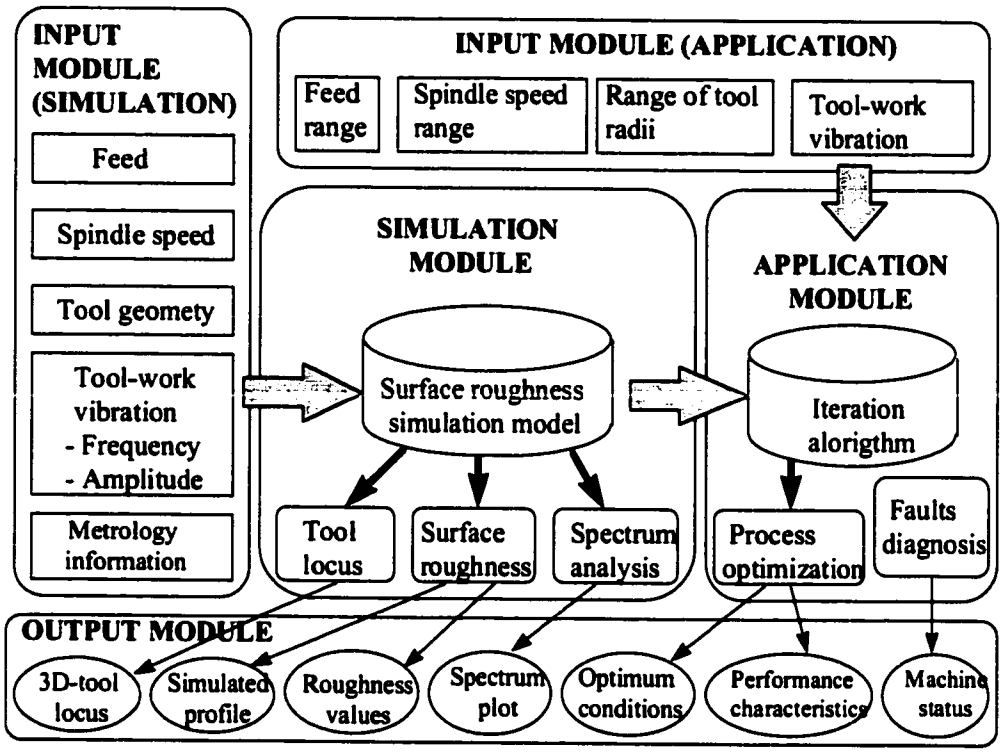

Figure 9.2 Functions of the surface topography model

(vi) To develop cutting force and surface topography models for brittle materials

Mirror finishing of brittle materials is an important research topic in diamond turning. Brittle materials like glass and silicon are widely used for a variety of devices which are used in electronic, optical and some laser optical products. However, brittle materials present some different characteristics which are not encountered in machining ductile materials. For instance, the ductile-brittle transitions and discontinuous chip formation in brittle materials affect the surface generation. Although there are many researches on the cutting mechanics and the surface generation in machining brittle materials, most of the work is empirical and relative few quantitative studies have been reported. The crystal structure of brittle materials is different from a F.C.C. structure. Different microplasticity and surface topography models have to be developed for brittle materials.

References

Albrecht, P. "New Developments in the Theory of the Metal-cutting Process: Part II, The Theory of Chip Formation," *Journal of Engineering for Industry*, Vol. 83, p.557 (1961)

Albrecht, P. "Dynamics of the Metal-Cutting Process," *Journal of Engineering for Industry*, Vol. 87, p.429 (1965)

ANSI/ASME B89.3.4M Standard, *Axes of Rotation, Methods for Specifying and Testing* (1985)

Arcona, C. and Dow, Th. A. "An Empirical Tool Force Model for Precision Machining," *Journal of Manufacturing Science and Engineering*, Vol. 120, p.700 (1998)

Astrom, K.J. *Stochastic Control Theory*, New York, Academic Press (1970)

Bael, D.K., Ko, T.J. and Kim, H.S. "A Dynamic Surface Roughness Model for Face Milling," *Precision Engineering*, Vol. 20, p.171 (1997)

Baily, W. "The Tribology of Precision Machines," *Tribology*, June, p.131 (1975)

Black, J.T. "On the Fundamental Mechanism of Large Strain Plastic Deformation-electron Microscopy and Metal Cutting Chips," *Journal of Engineering for Industry*, No.5, p.507 (1971)

Black, J.T. "Shear Front-lamella Structures in Large Strain Plastic Deformation Processes," *Journal of Engineering for Industry*, No.2, p.307 (1972)

Black, J.T. "Flow Stress Model in Metal Cutting," *Journal of Engineering for Industry*, Vol.101B, p.403 (1979)

Bishop, J.F.W. and Hill, R. "A Theory of the Plastic Distortion of a Polycrystalline Aggregate Under Combined Stresses," *Phil. Mag.*, Vol. 42, p. 414 (1951)

Bispink, T. "Performance Analysis of Feed-Drive Systems in Diamond Turning by Machining Specified Test Samples," *Annals of the CIRP*, Vol. 41, No. 1, p.601 (1992)

Bryan, J.B. "Design and Construction of an Ultraprecision 84 inch Diamond Turning Machine," *Precision Engineering*, Vol.1, p.13 (1979a)

Bryan, J.B. "The Abbe Principle Revisited; an Updated Interpretation," *Precision Engineering*, Vol. 1, p.129 (1979b)

Bryan, J.B., et al. "A Simple Method for Testing Measuring Machines and Machine Tools," Part I: Principle and Applications, *Precision Engineering*, Vol. 4, No. 2, Butterworth, London (1982)

Byne, G. "New Approach to the Theoretical Analysis of Surface Generation Mechanisms in Machining," *Annals of CIRP*, Vol.41, No.1, p.67 (1992)

Carlisle, K. and Shore, P. "Experiences in the Development of Ultra Stiff CNC Aspheric Generating Machine Tools for Ductile Regime Grinding of Brittle Materials," *Proc. 6th Int. Precision Engng. Seminar, Braunscheweig*, Germany, p.85 (1991)

Casstevens, J.M. "Diamond Turning of Steel in Carbon-Saturated Atmosphere," Precision Engineering, Vol. 5, No. 1, p.9 (1983)

Chan, K.C., Ramesh, M.V., Lee, W.B. and Cheung, C.F. "A Parametric Analysis of Surface Quality in Diamond Turning of an Al6061/SiC_p Metal Matrix Composite," *Key Engineering Materials*, accepted for publication, Vol. 177-180, p.369 (2000)

Cheung, C.F. "The Process Chain for The Design and The Manufacture of Plastic Optical Products," *Plastics Newsletter Special Issue: Optical Products*, p.25 (1998)

Cheung, C.F., Chan, K.C., Lee, W.B., Ramesh, M.V. and To, S. "An Investigation of Surface Roughness Formation in Ultra-precision Machining of Al6061/SiC_p Metal Matrix Composites," *Key Engineering Materials*, Vol. 177-180, p.375 (2000)

Cheung, C.F. and Lee, W.B. "A Framework of a Virtual Machining and Inspection System for Diamond Turning of Precision Optics," *Proceedings of the International Conference on Advances in Materials and Processing Technologies, AMPT'99 and 16th Annual Conference of the Irish Manufacturing Committee, IMC16*, 3-6 August, Dublin, Ireland, Vol. III, p.1675 (1999)

Cheung, C.F. and Lee, W.B., "Study of Factors Affecting the Surface Quality in Ultra-precision Diamond Turning," *Materials and Manufacturing Processes*, Vol. 15, No. 4, in print (2000a)

Cheung, C.F. and Lee, W.B. "A Multi-spectrum Analysis of Surface Roughness Formation in Ultra-precision Machining," *Precision Engineering*, Vol. 24, No.1, p.77 (2000b)

Cheung, C.F. and Lee, W.B., "An Investigation of Cutting Dynamics in Single Point Diamond Turning," *JSME International Journal-Series C: Mechanical Systems, Machine Elements and Manufacturing*, Vol. 43, No. 1, p.116 (2000c)

Cheung, C.F. and Lee, W.B. "A Theoretical and Experimental Investigation of Surface Roughness Formation in Ultra-precision Diamond Turning," *International Journal of Machine Tools and Manufacture*, Vol. 40, No. 7, p. 979 (2000d)

Cheung, C.F. and Lee, W.B. "Modelling and Simulation of Surface Topography in Ultra-precision Diamond Turning," *Journal of Engineering Manufacture, Proceedings of The Institute of Mechanical Engineers Part B*, accepted for publication (2000e)

Cheung, C.F., Lee, W.B. Chiu, W.M. and Leung, T.P. "The Manufacturing of High Quality Aspheric Surfaces for Optical Products," *CIRP International Symposium-Advanced Design and Manufacture in Global Manufacturing Era*, August 21-22, Hong Kong, p.37 (1997)

Cheung, C.F. and To, S. "Aspheric CCD Camera Lenses-A profitable Product for CCTV and Multimedia Applications," *Plastics Newsletter Special Issue: Optical Products*, p.7 (1998)

Childs, T.H.C. and Mahdi, M.I. "On the Stress Distribution Between the Chip and Tool During Metal Turning," *Annals of the CIRP*, Vol. 38, No.1, p.55 (1989)

Chiu, W.M., Lee, W.B., Leung, T.P. and Cheung, C.F. "Diamond Turning and Precision Grinding with Submicron Precision," *Asian Industrial Technology Congress (AITC) 1997, AITC Technology Digest : Manufacturing Technology*, p.197 (1997)

Clark, W.N. "In-process or post-process metrology?," *Proceedings of the 15th International MTDR Conference*, Birmingham, U.K., p.163 (1974)

Debra, D.B., Victor, R.A., Bryan, J.B. "Shower and High Pressure Oil Temperature Control," *Annals of the CIRP*, Vol. 35, No.1, p.359 (1986)

DeVries, W.R. "Autoregressive Time Series Models for Surface Profile Characterization," *Annals of the CIRP*, Vol. 28, No.1, p.437 (1979)

Doi, S. and Kato, S. "Chatter Vibration of Lathe Tools," *Journal of Engineering for Industry Trans. ASME*, Vol.78, p.1127 (1956)

Donaldson, R.R. and Patterson, S.R. "Design and Construction of a Large Vertical Axis Diamond Turning Machine," *Proc. SPIE 433*, p.62 (1983)

Drescher, J.D. and Dow, T.A. "Tool Force Model Development for Diamond Turning," *Precision Engineering*, Vol. 12, No. 1, p.29 (1990)

Drucker, D.C. "Material Response and Continuum Relations; or From Microscales to Macroscale," *ASME Annual Winter Meeting*, New Orleans (1984)

Drucker, D.C. "Plasticity Today: Modelling, Methods and Applications," *A. Sawczuk and G. Bianchi, Eds., Elsevier*, London, p.47 (1985)

Duggan, B.J., Hather, M., Huchison, W.B. and Wakefield, P.T. "Deformation Structure and Texture in Cold-rolled 70:30 Brass," *Met. Sci.*, Vol. 12, p.293 (1978)

Ehmann, K.F., et al. "A Framework for a Virtual Machine Tool (VMT)," *Technical Papers of the North American Manufacturing*, Research Institute of SEM, USA, p.143 (1997)

Eman, K.F. "A New Approach to Form Accuracy Control in Machining," *Int. J. Prod. Res.*, Vol. 24, No. 4, p. 825 (1986).

Eshelby, J.D. "Uniformly Moving Dislocations," *Proc. Phys. Soc.*, A62, p.307 (1949)

Evans, C. *Precision Engineering: an Evolutionary View*, Cranfield Press (1989).

Evans, C. "Cryogenic Diamond Turning of Stainless Steel," *Annals of the CIRP*, Vol. 40, No.1, p.571 (1991)

Franks, A. "Nanotechnology at the National Physical Laboratory," Ultra-precision Manufacturing Engineering, *Proceedings of the International Congress for Ultra-precision Technology*, Springer-Verag, p.255 (1988)

Franks, F.C. "On the Equation of Motion of Crystal Dislocations," *Proc. Phys. Soc.*, A62, p.131 (1949)

Furukawa, Y. and Moronuki, N. "Effect of Material Properties on Ultra Precise Cutting Processes," *Annals of the CIRP*, Vol.37, No.1, p.113 (1988)

Gilman, J.J. "Mechanical Behaviour of Metallic Glasses," *J. of App. Phys.*, Vol.46, No.4, p.1625 (1975)

Grabec, I. "Chaos Generated by the Cutting Process," *Phys. Lett. A*, Vol. 117, p.384 (1986)

Grabec, I. "Exploration of Random Vibration in Cutting on Grounds of Deterministic Chaos," *Roboti. Comp.-Integrated Manuf.*, Vol. 4, p.129 (1988)

Hahn, R.S. "Metal-cutting Chatter and Its Elimination," *Trans. ASME*, Vol. 75, 1073 (1953)

Hanna, N.H. and Tobias, S.A. "The Non-linear Dynamic Behaviour of A Machine Structure," *Int. J. Mach. Tool Des. Res.*, Vol. 9, p.293 (1969)

Hara, Y., Motonishi, S. ,and Yoshida, K. "A New Micro-Cutting Device with High Stiffness and Resolution," *Annals of the CIRP*, Vol. 39, No.1, p.375 (1990)

Honeycombe, R.W.K., *The Plastic Deformation of Metals*, 2nd Edition, Edward Arnold (1984)

Horne, D.F., "Testing time for aspherics (Comment)," Precision Engineering, Vol. 3, No. 2, p. 59 (1981).

Ikawa, N., Donaldson, R.R., Komanduri, R., K$\ddot{o}$nig, W., Aachen, T.H., McKeown, P.A., Moriwaki, T., and Stowers, I.F. "Ultra-precision Metal Cutting - The Past, the Present and the Future," *Annals of the CIRP*, Vol. 40, No.1, p.587 (1991a)

Ikawa, N, Shimada, S., and Ohmori, G. "Recent Trends in Diamond Tool Technology," *Ultra-precision Manufacturing Engineering, Proceedings of the International Congress for Ultra-precision Technology*, Springer-Verag, p.126 (1988)

Ikawa, N., Shimada, S., Tanaka, H. and Ohmori, G. "An Atomistic Analysis of Nanometric Chip Removal as Affected by Tool-Work Interaction in Diamond Turning," *Annals of the CIRP*, Vol. 40, No.1, p.551 (1991b)

Inamura, T. and Takezawa, N. "Cutting Experiment in a Computer Using Atomic Models of a Copper Crystal and a Diamond Tool," *Proc. 6 th Int. Prec. Engng. Seminar*, Braunschweig, Germany, p.231 (1991)

Inamura, T., et al. "Mechanics and Energy Dissipation in Nanoscale Cutting," *Annals of the CIRP*, Vol. 42, No. 1, p.79 (1993)

Ismall, F., Elbestawi, M.A., Du, R. and Urbasik, K. "Generation of Milled Surfaces Including Tool Dynamic and Wear," *Journal of Engineering for Industry*, Vol.115, p.245 (1993)

Iwata, K., Osakada, K. and Terasaka, Y. "Process Modeling of Orthogonal Cutting by the Rigid-plastic Finite Element Method," *J. Engng. Mater. Technol.*, Vol. 106, p.132 (1984)

Kanai, A. "Nanometer Positioning Characteristics of Closed Looped Differential Hydro or Aerostatic Actuator," *Annals of the CIRP*, Vol.32, No.1, p.287 (1983)

Kanji, U. and Keiji, M. "Chip Formation Mechanism in Microcutting of an Amorphous Metal," *Annals of the CIRP*, Vol. 41, No.1, p.129 (1992)

Kim, J.D. and Kim, D.S. "Theoretical Analysis of Micro-cutting Characteristics in Ultra-precision Machining," *Journal of Materials Processing Technology*, Vol. 49, p.387 (1995)

Kim, J.D. and Kim, D.S. "Waviness Compensation of Precision Machining by Piezoelectric Micro Cutting Device," *International Journal of Machine Tools and Manufacture*, Vol. 38, 1305 (1998)

Kim, K.J., Eman, E.F. and Wu, S.M. "Identification of Natural Frequencies and Damping Ratios of Machine Tool Structure by the Dynamic Data System Approach," *Int. J. Mach. Tool Des. Res.*, Vol. 24, p.161 (1984)

Klamecki, B.E. "On the Effects of Process Asymmetry on Process Dynamics," *Journal of Engineering for Industry*, Vol. 111, p.193 (1989)

Knapp, W. "Circular Test for Three-coordinate Measuring Machines and Machine Tools," *Precision Engineering*, Vol. 5, No. 3, p.115 (1983)

Kobayashi, A., Hoshina, N., Tsukada, T., and Ueda, K. "High Precision Cutting with a New Ultra Precision Spindle," *Annals of the CIRP*, Vol. 27, No.1, p.283 (1978)

Koenigsberger, I. and Tlusty, J. *Structures of Machine Tools*, Pergamon Press, Manchester (1971)

Komanduri, R. and Shaw, M.C. "Wear of Synthetic Diamond When Grinding Ferrous Materials," *Nature*, Vol. 255, p.211 (1975)

König, W. and Spenrath, N. "The Influence of the Crystallographic Structure of the Substrate Material on Surface Quality and Cutting Forces in Micromachining," *Proc. 6th Int. Precision Engng. Seminar, Braunscheweig*, Germany, p.141 (1991)

Langenbeck, P. "An Ultra-fine Infeed Controller," *Proc. 6th Int. Precision Engng. Seminar, Braunscheweig*, Germany, p.342 (1991)

Lee, K.I., and Noh, S.D. "Virtual Manufacturing System - a Test-Bed of Engineering Activities," *Annals of the CIRP*, Vol. 46, No. 1, p.347 (1997)

Lee, E.H. and Shaffer, B.W. "The Theory of Plasticity Applied on a Problem of Machining," *ASME Journal of Applied Mechanics*, Vol. 73, p.405 (1951)

Lee, W.B. "Prediction of Microcutting Force Variation in Ultra-precision Machining," *Precision Engineering*, Vol.12, No.1, p.25 (1990)

Lee, W.B. and Chan, K.C. "A Criterion for the Formation of Shear Band Angles in f.c.c. Metals," *Acta Metallurgica et Materialia*, Vol.39, No.3, p. 411 (1991)

Lee, W.B. and Cheung, C.F. "A Dynamic Surface Topography Model for the Prediction of Nano-surface Generation in Ultra-precision Machining," *International Journal of Mechanical Sciences*, reviewed and revised (2000).

Lee, W.B., Cheung, C.F., Chiu, W.M. and Leung, T.P. "An Investigation of Residual Form Error Compensation in the Ultra-precision Machining of Aspheric Surfaces," *Journal of Materials Processing Technology*, Vol. 99, No.1-3, p.129 (2000a)

Lee, W.B., Cheung, C.F., and To, S. "An Analysis of Nano-surface Generation in Ultra-precision Diamond Turning," *Proceedings of Symposium on Nano-metrology in Precision Engineering*, 24-25 November, Hong Kong, p. 81 (1998)

Lee, W.B., Cheung, C.F., and To, S. "Materials Induced Vibration in Ultra-precision Machining," *Journal of Materials Processing Technology*, Vol. 89-90, p.318 (1999)

Lee, W.B., To, S. and Cheung, C.F. "Effect of Crystallographic Orientation in Diamond Turning of Copper Single Crystals," *Scripta Materialia*, accepted for publication (2000b)

Lee, W.B. and Zhou, M. "A Theoretical Analysis of the Effect of Crystallographic Orientation on Chip Formation in Micro-machining," *Int. J. Mach. Tools Manufact.*, Vol. 33, No. 3, 439 (1993)

Leamy, H.J., Chen, H.S. and Wan, T.T. "Plastic Flow and Fracture of Metallic Glass," *Met. Trans.*, Vol.3, p.699 (1972)

Lin, S.C. and Chang, M.F. "A Study on The Effects of Vibrations on the Surface Finish Using a Surface Topography Simulation Model for Turning," *Int. J. Mach. Tools and Manuf.*, Vol. 38, p.763 (1998)

Lin, J.S. and Weng, C.I. "A Nonlinear Dynamic Model of Cutting," *Int. J. Mach. Tools Manuf.*, Vol. 30, p. 53 (1990)

Lo-A-Foe, T.C.G., Dautzenberg, J.H. and van der Wolf, A.C.H. "Cutting Forces and Their Influences Upon the Surface Integrity in Single-Point Diamond Turning," *Ultra-precision Manufacturing Engineering, Proceedings of the International Congress for Ultra-precision Technology*, Springer-Verag, p.110 (1988)

Lucca, D.A., Rhorer, R.L., and Komanduri, R. "Energy Dissipation in the Ultraprecision Machining of Copper," *Annals of the CIRP*, Vol. 40, No.1, p.69 (1991)

Lucca, D.A. and Seo, Y.W. "Effect of Tool Edge Geometry on Energy Dissipation in Ultraprecision Machining," *Annals of the CIRP*, Vol. 42, No.1, p.83 (1993)

Majundar, A. and Bhusan, B. "Role of Fractual Geometry in Roughness Characterization and Contact Mechanics of Surface," *ASME J. Tribology*, Vol.112, p.205 (1990)

Mandelbrot, B.B. *The Fractal Geometry of Nature*, New York: Freeman (1977)

Masuda, M., Maeda, Y., Nishiguchi, T., Sawa, M., and Ito, R. "A Study on Diamond Turning of Al-Mg Alloy - Generation Mechanism of Surface Machined with Worn Tool," *Annals of the CIRP*, Vol. 38, No.1, p.111 (1989)

Masumoto, T., and Maddin, R. "The Mechanical Properties of Palladium 20 a/o Silicon Alloy Quenched From Liquid State," *Acta. Met.*, Vol.19, p.725 (1971)

McKeown, P.A. "Structural Design for High Precision Measurement and Control," *SPIE*, Vol. 153, p.101 (1978)

McKeown, P.A. "The role of Precision Engineering in Manufacturing of the Future," *Annals of the CIRP*, Vol.36, No.2, p.496 (1987)

McKeown, P.A. "Nanotechnology," *Symposium of Nano-metrology in Precision Engineering*, 24-25 November, Hong Kong, p.5 (1998)

McKeown, P.A., Carlisle, K., Shore, P., and Read, R.F.J. "Ultraprecision High Stiffness CNC Grinding Machines for Ductile Mode Grinding of Brittle Materials," *SPIE*, Vol. 1320 Infrared Technology & Application, p.301 (1990)

McKeown, P.A., Wills-Moren, W.J., and Read, R.F.J. "In-situ Metrology and Machine Based Interferometry for Shape Determination," *SPIE*, Vol. 802, In-Process Optical Metrology for Precision Machining, p.42 (1987)

Merchant, M.E. "Mechanics of the Metal Cutting Process. I: Orthogonal Cutting and A Type 2 Chip," *J. App. Phys.*, Vol. 16, p.267 (1945)

Merritt, H.E. "Theory of Self-excited Machine-tool Chatter," *Journal of Engineering for Industry*, Vol.87, p.447 (1965)

Mitsui, K. and Sato, H. "Frequency Characteristic of Cutting Process Identified by a In-Process Measurement of Surface Roughness," *Annals of the CIRP*, Vol. 27, No. 1, p.67 (1978)

Mizumoto, H., Matsubara, T., Yamamoto, H., Okuno, K. and Yabuya, M. "An Infinite-stiffness Aerostatic Bearing with an Exhaust-control Restrictor," *Proc. 6th Int. Precision Engng. Seminar, Braunscheweig*, Germany, p.315 (1991)

Montgomery, M. and Altintas, Y. "Mechanism of Cutting Force and Surface Generation in Dynamic Milling," *Journal of Engineering for Industry*, Vol. 113, p.160 (1991)

Moon, F.C. *Dynamics and Chaos in Manufacturing Processes*, Wiley, New York (1998)

Moriwaki, T. "Ultra-precision Ductile Cutting of Glass by Applying Ultrasonic Vibration," *Annals of the CIRP*, Vol. 41, No.1, p.141 (1992)

Moriwaki, T. and Okuda, K. "Machinability of Copper in Ultra-Precision Micro Diamond Cutting," *Annals of the CIRP*, Vol. 38, No.1, p.115 (1989)

Moriwaki, T. and Shamoto, E. "Ultraprecision Diamond Turning of Stainless Steel by Applying Ultrasonic Vibration," *Annals of the CIRP*, Vol. 40, No.1, p.559 (1991)

Mulgrew, B., Grant, P. and Thompson, J. *Digital Signal Processing : Concepts & Applications*, Macmillan Press Ltd (1999)

Mulvaney, D.J. and Newland, D.E., "A Characterization of Surface Texture Profiles," *Proc. IMechE*, Vol. 200, p.167 (1986)

Nabarro, F.R.N. "Dislocations in a Simple Cubic Lattice," *Proc. Phys. Soc.*, Vol. 59, p.256 (1947)

Nakasuji, T., Kodera, S., Hara, S., and Matsunaga, H. "Diamond Turning of Brittle Materials for Optical Components," *Annals of the CIRP*, Vol. 39. No.1, p.89 (1990)

Nakayama, K. and Arai, M. "Comphensive Chip Form Classification Based on the Cutting Mechanism," *Annals of the CIRP*, Vol. 41, No.1, p.71 (1992)

Nishiguchi, T., Maeda, Y., Masuda, M., and Sawa, M. "Mechanism of Micro Chip Formation in Diamond Turning of Al-Mg Alloy," *Annals of the CIRP*, Vol. 37, No. 1, p.117 (1988)

Nowicki, B. "Investigation of the Surface Roughness Range," *Annals of the CIRP*, Vol. 30, No.1, p.493 (1981)

Onosato, M. and Iwata, K. "Development of a Virtual Manufacturing System by Integrating Product Models and Factory Models," *Annuals of the CIRP*, Vol. 42, No.1, p.475 (1993)

Ostafiev, V., Ostafiev, D., and Mukhmudov, K. "Distribution of Cutting Tool Contact Loads along Rake and Flank Surfaces," *Annals of the CIRP*, Vol. 43, No.1, p.55 (1994)

Pandit, S.M. "Characteristic Shapes and Wavelength Decomposition of Surfaces in Machining," *Annals of the CIRP*, Vol. 30, No. 1, p.487 (1981)

Pandit, S.M. and Revach, S. "A Data Dependent Systems Approach to Dynamics of Surface Generation in Turning," *Journal of Engineering for Industry*, Vol. 103, p.437 (1981)

Pandit, S.M. and Wu, S.M. *Time Series and System Analysis with Applications*, New York, Wiley (1983)

Peklemik, J. "Geometrical Adaptive Control of Manufacturing Systems," *Annals of the CIRP*, Vol. 18, p.265 (1970).

Pfeifer, T. and Furst, A. "Advantages and Conditions for a Direct Measurement of the Workpiece Geometry on NC-machine Tools," *Proceedings of the IFEC International Symposium on Information Control Problems in Manufacturing Technology*, Tokyo, Japan, p.165 (1977).

Proakis, J.G. and Manolakis, D.G. *Digital Signal Processing: Principles, Algorithm, and Applications*, 3rd Edition, Prentice Hall (1996)

Puttick, K.E., Rudman, M.R., Smith, K.J. and Franks, A. " Single-Point Diamond Machining of Glasses," *Proc. R. Soc. Lond. A426*, p.19 (1989)

Ramalingam, S. "Deformation in Orthogonal Cutting," J. of Engineering for Industry, Trans. ASME, Vol. 92, p.93 (1970)

Reid, C.N. *Deformation Geometry for Material Scientists*, Pergamon Press (1973)

Sata, T. "Surface Finish in Metal Cutting," *Annals of the CIRP*, Vol. 12, p.190 (1964)

Sata,T., Li, M., Takata, S., Hiraoka, H., Li, C.Q., Xing, X.Z. and Xiao, X.G. "Analysis of Surface Roughness Generation in Turning Operation and Its Applications," *Annals of the CIRP*, Vol. 34, No.1, p.473 (1985)

Sato, H. and O-hori, M. "Characteristics of Two Dimensional Surface Roughness - Taking Self-Excited Chatter Marks as Objective," *Annals of CIRP*, Vol. 30, No. 1, p.481 (1981)

Sato, M., Kato, Y. and Aoki, S. "Effect of Crystallographic Orientation on the Cutting Mechanism of the Aluminium Single Crystal," *Bulletin of the JSME*, Vol. 26, p.890 (1983)

Sato, M., Kato, K., and Tuchiya,K. "Effect of Material and Anisotropy Upon the Cutting Mechanism," *Trans. JIM.*, Vol. 9, p.530 (1978)

Sayles, R. and Thomas, T.R. "Surface Topography as a Non-stationary Random Process," *Nature*, Vol. 271, 431 (1978)

Shaw, M.C. "A Quantized Effect of Strain-hardening as Applied to Cutting of Metals," *Journal of Applied Physics*, Vol. 21, p.599 (1950)

Shaw, M.C. *Metal Cutting Principles*, Clarendon Press, Oxford, p.529 (1984)

Shaw, M.S. and Crowell, J.A. "Finish Machining," *Annals of the CIRP*, Vol. 13, p.5 (1965)

Shimada, S., Ikawa, N., Ohmori, G., Tanaka, H. and Uchikoshi, U. "Molecular Dynamics Analysis as Compared with Experimental Results of Micromachining," *Annals of the CIRP*, Vol. 41, No. 1, p.117 (1992)

Shimada, S., et al. "Feasibility Study of Ultimate Accuracy in Microcutting Using Molecular Dynamics Simulation," *Annals of the CIRP*, Vol. 42, No.1, p.91 (1993)

Shimada, S., Yoshinaga, H., Ohmori, G., Uchikoshi, J. "The Scientific Qualification of Diamond as Applied to a Highly Reliable Cutting Tool," Preprints, *5th IPES*, Monterey, p.75 (1989)

Shimokohbe, A., Horikawa, O., and Sato, K. "An Active Air Journal Bearing with Ultra-precision Infinite Static Stiffness, High Damping Capability and New Functions," *Annals of CIRP*, Vol.40, No.1, p.563 (1991)

Stadler, H., Freisleben, B. and Heubeck, C. "Response of metallic material to micromachining," *Proc. 4th International Precision Engineering Seminar*, Cranfield, UK, p.11 (1987)

Stowers, I.F., Belak, J.F., Lucca, D.A. and Komanduri, R. "Molecular Dynamics Simulation of the Chip Forming Process in Single Crystal Copper and Comparison with Experimental Data," *Proc. Of the ASPE Annual Meeting*, USA, p.13 (1991)

Sugano, T. and Takeuchi, K. "Diamond Turning of an Aluminium Alloy for Mirror," *Annals of the CIRP*, Vol.36, No.1, p.17 (1987)

Syn, C.K., Taylor, J.S., Donaldson, R.R. and Shimada, S. "Ductile-brittle Transition of Cutting Behaviour in Diamond Turning of Single Crystal Si," *Preprint of Japan Soc. Prec. Engng.*, p.73 (1988)

Tai, T.P., Yang, Y.C., Hwong, Y.C. and Ku, C.H. "A New Concept of Cutting Marks Formation in Metal Cutting Vibration," *Proceedings of 20th MTDR*, p.449 (1980)

Takasu, S., Masuda, M. and Nishiguchi, T. "Influence of Study Vibration with Small Amplitude Upon Surface Roughness in Diamond Machining," *Annals of the CIRP*, Vol. 34, No.1, p.463 (1985)

Taylor, G.I. "The Mechanism of Plastic Deformation of Crystals," *Proc. R. Soc., A145*, p.362 (1934)

Taylor, H.R. "A Comparison of Methods for Measuring The Frequency Response of Mechanical Structures With Particular Reference to Machine Tools," *Proc. Inst. Mech. Eng.*, Vol. 191, p.257 (1977)

Tlusty, J. "Analysis of the State of Research in Cutting Dynamics," *Annals of the CIRP*, Vol. 27, No.1, p.583 (1978)

To, S., Cheung, C.F. and Lee, W.B. "Influence of Material Swelling Upon Surface Roughness in Diamond Turning of Single Crystals," *Materials Science and Technology*, accepted for publication (2000).

To, S., Lee, W.B. and Chan, C.Y. "Ultraprecision Diamond Turning of Aluminium Single Crystals," *Journal of Materials Processing Technology*, Vol. 63, p.157 (1997)

Tobias, S.A. *Machine Tool Vibration*, Wiley, New York (1965)

Tobias, S.A. and Fishwick, W. "The Chatter of Lathe Tools Under Orthogonal Cutting Conditions," *Journal of Engineering for Industry, Trans. ASME*, Vol. 80, p.1079 (1958)

Tsai, M.D., Takata, S., Inui, M., Kimura, F. and Sata, T. "Prediction of Chatter Vibration by Means of a Model-Based Cutting Simulation System," *Annals of CIRP*, Vol. 39, No. 1, p.447 (1990)

Ueda, K. and Iwata, K. "Chip Formation Mechanism in Single Crystal Cutting of β-brass," *Annals of the CIRP*, Vol. 28, p.41 (1980)

Ueda, K. and Manabe, K. "Chip Formation Mechanism in Microcutting of an Amorphous Metal," *Annals of the CIRP*, Vol.41, No.1, p.129 (1992)

Von Turkovich, B.F. and Black, J.T. "Micro-machining of Copper and Aluminium Crystals," *Journal of Engineering for Industry, Trans. ASME.*, Vol. 92, p.130 (1970)

Wasiukiewicz, I. "The Improvement in Accuracy of High Precision Machine Tool by Means of Adaptive Control," *Proceedings of the 15th International MTDR Conference*, Birmingham, U.K., p.79 (1974).

Weck, M. *Handbook of Machine Tools*, Vol. 4, Wiley, New York (1985)

Weck, M., Hartel, R., and Bispink,T. "Limits of Workpiece Accuracy Caused by the Geometrical and Dynamical Behaviour of Ultraprecision Diamond Turning Machines," *Ultra-precision Manufacturing Engineering, Proceedings of the International Congress for Ultra-precision Technology*, Springer-Verag, p.153 (1988)

Weck, M., Hartel, R., and Modemann, K. "Performance Assessment in Ultra-precision Micromachining," *Annals of the CIRP*, Vol. 37, No. 1, p.499 (1988)

Whitehouse, D.J. *Handbook of Surface Metrology*, Bristol, Philadelphia: Institute of Physics Pub. (1994)

Whitehouse, D.J. and Archard, J.F. "Properties of Random Processes of Significance in Their Contact," *ASME Conf. on Surface Mechanics*, Los Angeles, p.36 (1969)

Wills, E.M., Wiks, J. "The Mechanical Strength and Reliability of Natural Diamonds," *Diamond Research*, p.2 (1978)

Wills-Moren, W.J., Modjarrad, H., and Read, R.F.J. "Some Aspects of the Design and Development of a Large High Precision CNC Diamond Turning Machine," *Annals of the CIRP*, Vol. 31, No.1, p.409 (1982)

Wills-Moren, W.J. and Wilson, T. "The Design and Manufacture of a Large CNC Grinding Machine for Off-Axis Mirror Segments," *Annals of the CIRP*, Vol. 38, No.1, p.529 (1989)

Wu, D.W. "Comprehensive Dynamic Cutting Force Model and Its Application to Wave-removing Processes," *Journal of Engineering for Industry*, Vol. 110, p.153 (1988)

Wu, D.W. "A New Approach to Formulating the Transfer Function for Dynamic Cutting Processes," *Journal of Engineering for Industry*, Vol.111, p.37 (1989)

Wu, D.W. and Liu, C.R. "An Analytical Model of Cutting Dynamics I: Model Building," *Journal of Engineering for Industry*, Vol. 107, p.107 (1985a)

Wu, D.W. and Liu, C.R. "An Analytical Model of Cutting Dynamics II," *Journal of Engineering for Industry*, Vol. 107, p.112 (1985b)

Xie, J.Q., Bayoumi, A.E., and Zbib, H.M. "FEA Modelling and Simulation of Shear Localized Chip Formation in Metal Cutting," *International Journal of Machine Tools and Manufacture*, Vol. 38, p.10670 (1998)

Yang, W. and Lee, W.B., *Mesoplasticity and Its Applications*, Springer-Verlag (1993)

Yuan, Z.J., Geng, L., and Dong, S. "Ultraprecision Machining of SiCw/Al Composites," *Annals of the CIRP*, Vol. 42, No.1, p.107 (1993)

Yuan, Z.J., He, J.C., and Yao, Y.X. "The Optimum Crystal Plane of Natural Diamond Tool for Precision Machining," *Annals of the CIRP*, Vol. 4, No.1, p.605 (1992)

Yuan, Z.J., Lee, W.B., Yao, Y.X., and Zhou, M. "Effect of Crystallographic Orientation on Cutting Forces and Surface Quality in Diamond Cutting of Single Crystal," *Annals of the CIRP*, Vol. 43, No.1, p.39 (1994)

Zhang, B. and Bagchi, A. "Finite Element Simulation of Chip Formation and Comparison with Machining Experiment," *Journal of Engineering for Industry*, Vol. 116, p.289 (1994)

Zhang, J.H. *Theory and Technique of Precision Cutting*, Pergamon Press (1991)

APPENDICES

Appendix I

Program Listing for Multi-spectrum Analysis Software

The multi-spectrum analysis software is composed of two portions which are (a) data conversion and (b) multi-spectrum analysis. It should be run by MATLAB 4.2c or above. The data conversion is conducted by the routine MRPCONV1.M which converts surface roughness profiles at a maximum of 12 radial sections of the workpiece. The converted data file will be analyzed by the routine MSPPROG2.M. The output will be the multi-spectrum plots, the surface roughness and the frequency spectrum for individual surface roughness profile.

MRPCONV1.M

```
%Conversion of surface roughness profile data for multi-spectrum analysis and MDDS analysis

n_p=2000;                                   %no. of points
CVF = zeros(2*n_p, 12);                     %buffer for the data

%A maximum of 12 orientations

[fname1, pname1]=uigetfile('*.dat', 'Select file of the 1st orientation to be processed');

fid1 = fopen(fname1);
G1 = fscanf(fid1, '%g', [1,inf]);
fclose(fid1);

[n1,m1] = size(G1);

A1=zeros(m1,1);

for i=1:m1
   A1(i,1)=G1(1,i);
end

Y1=zeros(m1/2,1);
T1=zeros(m1/2,1);
B1=zeros(2*n_p,1);

Xmin1 = A1(1,1);

for i=1:n_p
   T1(i,1)=A1(i,1)-Xmin1;
   B1(i,1)=T1(i,1);
end

for j=(m1/2+1):(m1/2+n_p)
   Y1((j-(m1/2)),1)=1000*A1(j,1);
   B1((j-(m1/2))+n_p,1)=Y1((j-(m1/2)),1);
end

for k=1:2*n_p
            CVF(k,1)=B1(k,1);
end

[fname2, pname2]=uigetfile('*.dat', 'Select file of the 2nd orientation to be processed');

fid2 = fopen(fname2);
G2 = fscanf(fid2, '%g', [1,inf]);
fclose(fid2);
[n2,m2] = size(G2);

A2=zeros(m2,1);

for i=1:m2
   A2(i,1)=G2(1,i);
end

Y2=zeros(m2/2,1);
T2=zeros(m2/2,1);
B2=zeros(2*n_p,1);
```

```
Xmin2 = A2(1,1);

for i=1:n_p
   T2(i,1)=A2(i,1)-Xmin2;
   B2(i,1)=T2(i,1);
end

for j=(m2/2+1):(m2/2+n_p)
   Y2((j-(m2/2)),1)=1000*A2(j,1);
   B2((j-(m2/2))+n_p,1)=Y2((j-(m2/2)),1);
end

for k=1:2*n_p
            CVF(k,2)=B2(k,1);
end

[fname3, pname3]=uigetfile('*.dat', 'Select file of the 3rd orientation to be processed');

fid3 = fopen(fname3);
G3 = fscanf(fid3, '%g', [1,inf]);
fclose(fid3);

[n3,m3] = size(G3);

A3=zeros(m3,1);

for i=1:m3
   A3(i,1)=G3(1,i);
end

Y3=zeros(m3/2,1);
T3=zeros(m3/2,1);
B3=zeros(2*n_p,1);

Xmin3 = A3(1,1);

for i=1:n_p
   T3(i,1)=A3(i,1)-Xmin3;
   B3(i,1)=T3(i,1);
end

for j=(m3/2+1):(m3/2+n_p)
   Y3((j-(m3/2)),1)=1000*A3(j,1);
   B3((j-(m3/2))+n_p,1)=Y3((j-(m3/2)),1);
end

for k=1:2*n_p
            CVF(k,3)=B3(k,1);
end


[fname4, pname4]=uigetfile('*.dat', 'Select file of the 4th orientation to be processed');

fid4 = fopen(fname4);
G4 = fscanf(fid4, '%g', [1,inf]);
fclose(fid4);

[n4,m4] = size(G4);

A4=zeros(m4,1);

for i=1:m4
   A4(i,1)=G4(1,i);
end

Y4=zeros(m4/2,1);
T4=zeros(m4/2,1);
B4=zeros(2*n_p,1);

Xmin4 = A4(1,1);

for i=1:n_p
   T4(i,1)=A4(i,1)-Xmin4;
   B4(i,1)=T4(i,1);
end

for j=(m4/2+1):(m4/2+n_p)
   Y4((j-(m4/2)),1)=1000*A4(j,1);
   B4((j-(m4/2))+n_p,1)=Y4((j-(m4/2)),1);
end

for k=1:2*n_p
            CVF(k,4)=B4(k,1);
end


[fname5, pname5]=uigetfile('*.dat', 'Select file of the 5th orientation to be processed');

fid5 = fopen(fname5);
G5 = fscanf(fid5, '%g', [1,inf]);
fclose(fid5);
```

```
[n5,m5] = size(G5);

A5=zeros(m5,1);

for i=1:m5
   A5(i,1)=G5(1,i);
end

Y5=zeros(m5/2,1);
T5=zeros(m5/2,1);
B5=zeros(2*n_p,1);

Xmin5 = A5(1,1);

for i=1:n_p
   T5(i,1)=A5(i,1)-Xmin5;
   B5(i,1)=T5(i,1);
end

for j=(m5/2+1):(m5/2+n_p)
   Y5((j-(m5/2)),1)=1000*A5(j,1);
   B5((j-(m3/2))+n_p,1)=Y5((j-(m5/2)),1);
end

for k=1:2*n_p
            CVF(k,5)=B5(k,1);
end

[fname6, pname6]=uigetfile('*.dat', 'Select file of the 6th orientation to be processed');

fid6 = fopen(fname6);
G6 = fscanf(fid6, '%g', [1,inf]);
fclose(fid6);

[n6,m6] = size(G6);

A6=zeros(m6,1);

for i=1:m6
   A6(i,1)=G6(1,i);
end

Y6=zeros(m6/2,1);
T6=zeros(m6/2,1);
B6=zeros(2*n_p,1);

Xmin6 = A6(1,1);

for i=1:n_p
   T6(i,1)=A6(i,1)-Xmin6;
   B6(i,1)=T6(i,1);
end

for j=(m6/2+1):(m6/2+n_p)
   Y6((j-(m6/2)),1)=1000*A6(j,1);
   B6((j-(m6/2))+n_p,1)=Y6((j-(m6/2)),1);
end

for k=1:2*n_p
            CVF(k,6)=B6(k,1);
end

[fname7, pname7]=uigetfile('*.dat', 'Select file of the 7th orientation to be processed');

fid7 = fopen(fname7);
G7 = fscanf(fid7, '%g', [1,inf]);
fclose(fid7);

[n7,m7] = size(G7);

A7=zeros(m7,1);

for i=1:m7
   A7(i,1)=G7(1,i);
end

Y7=zeros(m7/2,1);
T7=zeros(m7/2,1);
B7=zeros(2*n_p,1);

Xmin7 = A7(1,1);

for i=1:n_p
   T7(i,1)=A7(i,1)-Xmin7;
   B7(i,1)=T7(i,1);
end

for j=(m7/2+1):(m7/2+n_p)
   Y7((j-(m7/2)),1)=1000*A7(j,1);
   B7((j-(m7/2))+n_p,1)=Y7((j-(m7/2)),1);
end
```

```
for k=1:2*n_p
                CVF(k,7)=B7(k,1);
end

[fname8, pname8]=uigetfile('*.dat', 'Select file of the 8th orientation to be processed');

fid8 = fopen(fname8);
G8 = fscanf(fid8, '%g', [1,inf]);
fclose(fid8);

[n8,m8] = size(G8);

A8=zeros(m8,1);

for i=1:m8
   A8(i,1)=G8(1,i);
end

Y8=zeros(m8/2,1);
T8=zeros(m8/2,1);
B8=zeros(2*n_p,1);

Xmin8 = A8(1,1);

for i=1:n_p
   T8(i,1)=A8(i,1)-Xmin8;
   B8(i,1)=T8(i,1);
end

for j=(m8/2+1):(m8/2+n_p)
   Y8((j-(m8/2)),1)=1000*A8(j,1);
   B8((j-(m8/2))+n_p,1)=Y8((j-(m8/2)),1);
end

for k=1:2*n_p
                CVF(k,8)=B8(k,1);
end

[fname9, pname9]=uigetfile('*.dat', 'Select file of the 9th orientation to be processed');

fid9 = fopen(fname9);
G9 = fscanf(fid9, '%g', [1,inf]);
fclose(fid9);

[n9,m9] = size(G9);

A9=zeros(m9,1);

for i=1:m9
   A9(i,1)=G9(1,i);
end

Y9=zeros(m9/2,1);
T9=zeros(m9/2,1);
B9=zeros(2*n_p,1);

Xmin9 = A9(1,1);

for i=1:n_p
   T9(i,1)=A9(i,1)-Xmin9;
   B9(i,1)=T9(i,1);
end

for j=(m9/2+1):(m9/2+n_p)
   Y9((j-(m9/2)),1)=1000*A9(j,1);
   B9((j-(m9/2))+n_p,1)=Y9((j-(m9/2)),1);
end

for k=1:2*n_p
                CVF(k,9)=B9(k,1);
end

[fname10, pname10]=uigetfile('*.dat', 'Select file of the 10th orientation to be processed');

fid10 = fopen(fname10);
G10 = fscanf(fid10, '%g', [1,inf]);
fclose(fid10);

[n10,m10] = size(G10);

A10=zeros(m10,1);

for i=1:m10
   A10(i,1)=G10(1,i);
end

Y10=zeros(m10/2,1);
T10=zeros(m10/2,1);
B10=zeros(2*n_p,1);

Xmin10 = A10(1,1);
```

```
for i=1:n_p
   T10(i,1)=A10(i,1)-Xmin10;
   B10(i,1)=T10(i,1);
end

for j=(m10/2+1):(m10/2+n_p)
   Y10((j-(m10/2)),1)=1000*A10(j,1);
   B10((j-(m10/2))+n_p,1)=Y10((j-(m10/2)),1);
end

for k=1:2*n_p
            CVF(k,10)=B10(k,1);
end

[fname11, pname11]=uigetfile('*.dat', 'Select file of the 11th orientation to be processed');

fid11 = fopen(fname11);
G11 = fscanf(fid11, '%g', [1,inf]);
fclose(fid11);

[n11,m11] = size(G11);

A11=zeros(m11,1);

for i=1:m11
   A11(i,1)=G11(1,i);
end

Y11=zeros(m11/2,1);
T11=zeros(m11/2,1);
B11=zeros(2*n_p,1);

Xmin11 = A11(1,1);

for i=1:n_p
   T11(i,1)=A11(i,1)-Xmin11;
   B11(i,1)=T11(i,1);
end

for j=(m11/2+1):(m11/2+n_p)
   Y11((j-(m11/2)),1)=1000*A11(j,1);
   B11((j-(m11/2))+n_p,1)=Y11((j-(m11/2)),1);
end

for k=1:2*n_p
            CVF(k,11)=B11(k,1);
end

[fname12, pname12]=uigetfile('*.dat', 'Select file of the 12th orientation to be processed');

fid12 = fopen(fname12);
G12 = fscanf(fid12, '%g', [1,inf]);
fclose(fid12);

[n12,m12] = size(G12);

A12=zeros(m12,1);

for i=1:m12
   A12(i,1)=G12(1,i);
end

Y12=zeros(m12/2,1);
T12=zeros(m12/2,1);
B12=zeros(2*n_p,1);

Xmin12 = A12(1,1);

for i=1:n_p
   T12(i,1)=A12(i,1)-Xmin12;
   B12(i,1)=T12(i,1);
end

for j=(m12/2+1):(m12/2+n_p)
   Y12((j-(m12/2)),1)=1000*A12(j,1);
   B12((j-(m12/2))+n_p,1)=Y12((j-(m12/2)),1);
end

for k=1:2*n_p
            CVF(k,12)=B12(k,1);
end

save tmpmrp.dat CVF -ascii;  %save the roughness values
```

MSPPROG2.M

```
%Mult-spectrum Analysis of the roughness profile from Talysurf (Multiple Profile)

[fname, pname]=uigetfile('m*.dat', 'Select file to be processed');

fid = fopen(fname);
```

```
G = fscanf(fid, '%g', [12,inf]);
fclose(fid);

[n,m] = size(G);
MRTA = zeros(n,3);
AN = zeros(n+1,1);
rot_step = 360/n;
rot_a=zeros(n,1);
VRA=zeros(n+1,1);
VRT=zeros(n+1,1);

for k=1:n
        A=zeros(m,1);

        for i=1:m
                A(i,1)=G(k,i);
        end

        Y=zeros(m/2,1);
        T=zeros(m/2,1);
        B=zeros(m/2,2);

        Xmin = A(1,1);
        s_rate = fix(1/(A(2,1)-A(1,1)))                 %sample rate for FFT
        %s_rate = m/2

        for i=1:m/2
                T(i,1)=A(i,1)-Xmin;
                B(i,1)=T(i,1);
        end

        for j=(m/2+1):m
                Y((j-(m/2)),1)=1000*A(j,1);
                B((j-(m/2)),2)=Y((j-(m/2)),1);
        end

        Rx=zeros(m/2,1);
        Ry=zeros(m/2,1);
        sumR=0;
        sumP=0;

        for i=1:m/2
                Rx(i,1)=B(i,1);
                Ry(i,1)=B(i,2);
                sumR =sumR+B(i,2);
        end

        %Surface roughness determination - Ra
        RAV=sumR/(m/2);

        for j=1:m/2
                sumP=sumP+abs(B(j,2)-RAV);
        end

        Ra=(sumP/(m/2));                        %Ra in nanometre

        %Geometrical Surface Roughness Determination - Rt

        Rmax = max(Ry);
        Rmin = min(Ry);

        Rt=Rmax-Rmin;                                   %geometrical roughness (P-V value)

        Rth = Rt                                        %unit conversion for Rth (nanometre)

        rot_a(k,1) = rot_step*(k-1);
        AN(k,1) = rot_a(k,1)*(pi/180);
        VRT(k,1) = Rth;
        VRA(k,1) = Ra;

        %Save Roughness data
        MRTA(k,1)=Rth;
        MRTA(k,2)=Ra;
        MRTA(k,3)=rot_a(k,1);

        save rartval.dat MRTA -ascii;           %save the roughness values

        Rt_hd = uicontrol(gcf,'Style', 'text', ...
                                'Position', [5 4 25 20],...
                                'BackgroundColor', 'g',...
                                'String', 'Rt :');

        Rt_cur = uicontrol(gcf,'Style', 'text', ...
                                'Position', [30 4 50 20],...
                                'BackgroundColor', 'g',...
                                'String', num2str(Rth));

        Rt_unit = uicontrol(gcf,'Style', 'text', ...
                                'Position', [80 4 17 20],...
                                'BackgroundColor', 'g',...
                                'String', 'nm');
```

```
Ra_hd = uicontrol(gcf,'Style', 'text', ...
                                'Position', [105 4 25 20],...
                                'BackgroundColor', 'c',...
                                'String', 'Ra :');

Ra_cur = uicontrol(gcf,'Style', 'text', ...
                                'Position', [130 4 50 20],...
                                'BackgroundColor', 'c',...
                                'String', num2str(Ra));

Ra_unit = uicontrol(gcf,'Style', 'text', ...
                                'Position', [180 4 17 20],...
                                'BackgroundColor', 'c',...
                                'String', 'nm');

plot(Rx,Ry);
grid;
title('Roughness profile');
xlabel('Distance travel (mm)');
ylabel('Surface height (nm)');
pause;
clf;

%Spectrum Analysis of the roughness profile

[Pxx, fss]=psd(Y,n/2,s_rate);
[fssm, fssn]=size(fss);
fsw=zeros(fssm-1,1);
Pxw=zeros(fssm-1,1);

for i=1:fssm-1
        fsw(i,1)=(1000/fss(i+1,1));
        Pxw(i,1)=Pxx(i+1,1);
end;

if k==1
        FF1=fss(2:fssm);
        PF1=Pxx(2:fssm);
        AN1=zeros(fssm-1,1);
        for i=1:fssm-1
                AN1(i,1)=rot_a(k,1);
        end
end

if k==2
        FF2=fss(2:fssm);
        PF2=Pxx(2:fssm);
        AN2=zeros(fssm-1,1);
        for i=1:fssm-1
                AN2(i,1)=rot_a(k,1);
        end
end

if k==3
        FF3=fss(2:fssm);
        PF3=Pxx(2:fssm);
        AN3=zeros(fssm-1,1);
        for i=1:fssm-1
                AN3(i,1)=rot_a(k,1);
        end
end

if k==4
        FF4=fss(2:fssm);
        PF4=Pxx(2:fssm);
        AN4=zeros(fssm-1,1);
        for i=1:fssm-1
                AN4(i,1)=rot_a(k,1);
        end
end

if k==5
        FF5=fss(2:fssm);
        PF5=Pxx(2:fssm);
        AN5=zeros(fssm-1,1);
        for i=1:fssm-1
                AN5(i,1)=rot_a(k,1);
        end
end

if k==6
        FF6=fss(2:fssm);
        PF6=Pxx(2:fssm);
        AN6=zeros(fssm-1,1);
        for i=1:fssm-1
                AN6(i,1)=rot_a(k,1);
        end
end

if k==7
        FF7=fss(2:fssm);
        PF7=Pxx(2:fssm);
```

```
                    AN7=zeros(fssm-1,1);
                    for i=1:fssm-1
                            AN7(i,1)=rot_a(k,1);
                    end
            end
            if k==8
                    FF8=fss(2:fssm);
                    PF8=Pxx(2:fssm);
                    AN8=zeros(fssm-1,1);
                    for i=1:fssm-1
                            AN8(i,1)=rot_a(k,1);
                    end
            end

            if k==9
                    FF9=fss(2:fssm);
                    PF9=Pxx(2:fssm);
                    AN9=zeros(fssm-1,1);
                    for i=1:fssm-1
                            AN9(i,1)=rot_a(k,1);
                    end
            end

            if k==10
                    FF10=fss(2:fssm);
                    PF10=Pxx(2:fssm);
                    AN10=zeros(fssm-1,1);
                    for i=1:fssm-1
                            AN10(i,1)=rot_a(k,1);
                    end
            end

            if k==11
                    FF11=fss(2:fssm);
                    PF11=Pxx(2:fssm);
                    AN11=zeros(fssm-1,1);
                    for i=1:fssm-1
                            AN11(i,1)=rot_a(k,1);
                    end
            end

            if k==12
                    FF12=fss(2:fssm);
                    PF12=Pxx(2:fssm);
                    AN12=zeros(fssm-1,1);
                    for i=1:fssm-1
                            AN12(i,1)=rot_a(k,1);
                    end
            end

end

AN(n+1,1)=360*(pi/180);
VRT(n+1,1)=VRT(1,1);
VRA(n+1,1)=VRA(1,1);

polar(AN, VRT);
grid;
title('Variation of Rt values with crystallographic orientation');
pause;

polar(AN, VRA);
grid;
title('Variation of Ra values with crystallographic orientation');
pause;

v_az = uicontrol(gcf,'Style', 'slider',...
            'Position', [220 395 100 20],...
            'BackgroundColor', 'g',...
            'Min', 0, 'Max', 360, 'Value', vw(1),...
            'CallBack', [...
            'set(az_cur, "String", num2str(get(v_az, "Value")));'...
            'plot3(FF1,AN1,PF1,FF2,AN2,PF2,FF3,AN3,PF3,FF4,AN4,PF4,FF5,AN5,PF5,FF6,AN6,PF6,FF7,AN7,P

F7,FF8,AN8,PF8,FF9,AN9,PF9,FF10,AN10,PF10,FF11,AN11,PF11,FF12,AN12,PF12);,'...
            'AZ1=get(v_az, "Value");EL1=get(v_el, "Value");,'...
            'XC1=0.5+sqrt(3)/2*[cos(EL1)*sin(AZ1),-cos(EL1)*cos(AZ1), sin(EL1)];,'...
            'T1=viewmtx(AZ1, EL1, 0, XC1);view(T1);,'...
            'xlabel("Frequency (cycle/mm)");zlabel("Power spectral density");ylabel("Angle (degree)");']);

az_head = uicontrol(gcf,'Style', 'text', ...
            'Position', [100 395 100 20],...
            'BackgroundColor', 'c',...
            'String', 'Rotation (deg.):');

az_min = uicontrol(gcf,'Style', 'text', ...
            'Position', [200 395 20 20],...
            'BackgroundColor', 'c',...
            'String', num2str(get(v_az, 'Min')));

az_max = uicontrol(gcf,'Style', 'text', ...
            'Position', [320 395 50 20],...
```

```
                'BackgroundColor', 'c',...
                'String', num2str(get(v_az, 'Max')));

az_vhd = uicontrol(gcf,'Style', 'text', ...
                'Position', [380 395 45 20],...
                'BackgroundColor', 'g',...
                'String', 'Value :');

az_cur = uicontrol(gcf,'Style', 'text', ...
                'Position', [425 395 60 20],...
                'BackgroundColor', 'g',...
                'String', num2str(get(v_az, 'Value')));

v_el = uicontrol(gcf,'Style', 'slider',...
                'Position', [220 370 100 20],...
                'BackgroundColor', 'g',...
                'Min', 0, 'Max', 180, 'Value', vw(1),...
                'CallBack', [...
                'set(el_cur, "String", num2str(get(v_el, "Value")));,'...
                'plot3(FF1,AN1,PF1,FF2,AN2,PF2,FF3,AN3,PF3,FF4,AN4,PF4,FF5,AN5,PF5,FF6,AN6,PF6,FF7,AN7,P

F7,FF8,AN8,PF8,FF9,AN9,PF9,FF10,AN10,PF10,FF11,AN11,PF11,FF12,AN12,PF12);,'...
                'EL1=get(v_el, "Value");AZ1 = get(v_az, "Value");'...
                'XC1 = 0.5+sqrt(3)/2*[cos(EL1)*sin(AZ1),-cos(EL1)*cos(AZ1), sin(EL1)];,'...
                'T1=viewmtx(AZ1, EL1, 0, XC1);view(T1);,'...
                'xlabel("Frequency (cycle/mm)");zlabel("Power spectral density");ylabel("Angle (degree)");']);

el_head = uicontrol(gcf,'Style', 'text', ...
                'Position', [100 370 100 20],...
                'BackgroundColor', 'c',...
                'String', 'Elevation (deg.) :');

el_min = uicontrol(gcf,'Style', 'text', ...
                'Position', [200 370 20 20],...
                'BackgroundColor', 'c',...
                'String', num2str(get(v_el, 'Min')));

el_max = uicontrol(gcf,'Style', 'text', ...
                'Position', [320 370 50 20],...
                'BackgroundColor', 'c',...
                'String', num2str(get(v_el, 'Max')));

el_vhd = uicontrol(gcf,'Style', 'text', ...
                'Position', [380 370 45 20],...
                'BackgroundColor', 'g',...
                'String', 'Value :');

el_cur = uicontrol(gcf,'Style', 'text', ...
                'Position', [425 370 60 20],...
                'BackgroundColor', 'g',...
                'String', num2str(get(v_el, 'Value')));

plot3(FF1,AN1,PF1,FF2,AN2,PF2,FF3,AN3,PF3,FF4,AN4,PF4,FF5,AN5,PF5,FF6,AN6,PF6,FF7,AN7,PF7,FF8,AN8,PF8,FF9,AN9,PF9,FF10,AN10,PF10,FF11,AN11,PF11,FF12,
AN12,PF12);
EL2 = 120;
AZ2 = 173;
XC2 = 0.5+sqrt(3)/2*[cos(EL2)*sin(AZ2),-cos(EL2)*cos(AZ2), sin(EL2)];
T1=viewmtx(AZ2, EL2, 0, XC2);view(T1);
xlabel('Frequency (cycle/mm)');
zlabel('Power spectral density');
ylabel('Angle (degree)');
pause;
clg;

plot3(FF1,AN1,PF1,FF2,AN2,PF2,FF3,AN3,PF3,FF4,AN4,PF4,FF5,AN5,PF5,FF6,AN6,PF6,FF7,AN7,PF7,FF8,AN8,PF8,FF9,AN9,PF9,FF10,AN10,PF10,FF11,AN11,PF11,FF12,
AN12,PF12);
EL2 = 104;
AZ2 = 173;
XC2 = 0.5+sqrt(3)/2*[cos(EL2)*sin(AZ2),-cos(EL2)*cos(AZ2), sin(EL2)];
T1=viewmtx(AZ2, EL2, 0, XC2);view(T1);
title('Variations of power spectrum density with crystallographic orientation');
xlabel('Frequency (cycle/mm)');
zlabel('Power spectral density');
ylabel('Angle (degree)');
pause;

MSSP
=[FF1,AN1,PF1,FF2,AN2,PF2,FF3,AN3,PF3,FF4,AN4,PF4,FF5,AN5,PF5,FF6,AN6,PF6,FF7,AN7,PF7,FF8,AN8,PF8,FF9,AN9,PF9,FF10,AN10,PF10,FF11,AN11,PF11,FF12,AN1
2,PF12];
save msptmp.dat MSSP -ascii

Hc_quit = uicontrol(gcf, 'Style', 'push', ...
                'Position', [160 3 70 20],...
                'String', 'Quit',...
                'CallBack','clg; fftsgs1;');

Hc_close = uicontrol(gcf, 'Style', 'push', ...
                'Position', [5 3 70 20],...
                'String', 'Close',...
                'CallBack','fftsavea; clg; fftsgs1;');
```

Appendix II

Program Listing for Multiple Data Dependent Systems Analysis Software

The Multiple Data Dependent Systems (MDDS) analysis software is composed of two portions which are (a) data conversion and (b) multiple data dependent systems (MDDS) analysis. The program should be run by MATLAB 4.2c or above. The data conversion is conducted by the routine MRPCONV1.M (see Appendix I) which converts surface roughness profiles at a maximum of 12 radial sections of the workpiece. The converted data file will be analyzed by the routine MDDSPRO1.M. The output will be spreadsheets of decomposed wavelength components for the roughness profiles at the 12 radial sections of the workpieces.

MDDSPRO1.M

```
%Multiple Data Dependent Systems (MDDS) Analysis of the roughness profile from Talysurf
%(Variable Order)

[fname, pname]=uigetfile('m*.dat', 'Select file to be processed');

fid = fopen(fname);
G = fscanf(fid, '%g', [12,inf]);
fclose(fid);

[n,m] = size(G);
MRTA = zeros(n,3);
AN = zeros(n+1,1);
rot_step = 360/n;
rot_a=zeros(n,1);
VRA=zeros(n+1,1);
VRT=zeros(n+1,1);

for n_k=1:n
        A=zeros(m,1);

        for i=1:m
                A(i,1)=G(n_k,i);
        end

        Y=zeros(m/2,1);
        T=zeros(m/2,1);
        B=zeros(m/2,2);

        Xmin = A(1,1);
        s_rate = (A(2,1)-A(1,1))                %sample rate for DDS
        %s_rate = m/2

        for i=1:m/2
                T(i,1)=A(i,1)-Xmin;
                B(i,1)=T(i,1);
        end

        for j=(m/2+1):m
                Y((j-(m/2)),1)=1000*A(j,1);
                B((j-(m/2)),2)=Y((j-(m/2)),1);
        end

        Rx=zeros(m/2,1);
        Ry=zeros(m/2,1);
        sumR=0;
        sumP=0;

        for i=1:m/2
                Rx(i,1)=B(i,1);
                Ry(i,1)=B(i,2);
                sumR =sumR+B(i,2);
        end
```

```
%Surface roughness determination - Ra
RAV=sumR/(m/2);

for j=1:m/2
        sumP=sumP+abs(B(j,2)-RAV);
end

Ra=(sumP/(m/2));                        %Ra in nanometre

%Geometrical Surface Roughness Determination - Rt

Rmax = max(Ry);
Rmin = min(Ry);

Rt=Rmax-Rmin;                           %geometrical roughness (P-V value)

Rth = Rt                        %unit conversion for Rth (nanometre)

rot_a(k,1) = rot_step*(k-1);
AN(k,1) = rot_a(k,1)*(pi/180);
VRT(k,1) = Rth;
VRA(k,1) = Ra;

%Save Roughness data
MRTA(k,1)=Rth;
MRTA(k,2)=Ra;
MRTA(k,3)=rot_a(k,1);

save rartval.dat MRTA -ascii;           %save the roughness values

Rt_hd = uicontrol(gcf,'Style', 'text', ...
                        'Position', [5 4 25 20],...
                        'BackgroundColor', 'g',...
                        'String', 'Rt :');

Rt_cur = uicontrol(gcf,'Style', 'text', ...
                        'Position', [30 4 50 20],...
                        'BackgroundColor', 'g',...
                        'String', num2str(Rth));

Rt_unit = uicontrol(gcf,'Style', 'text', ...
                        'Position', [80 4 17 20],...
                        'BackgroundColor', 'g',...
                        'String', 'nm');

Ra_hd = uicontrol(gcf,'Style', 'text', ...
                        'Position', [105 4 25 20],...
                        'BackgroundColor', 'c',...
                        'String', 'Ra :');

Ra_cur = uicontrol(gcf,'Style', 'text', ...
                        'Position', [130 4 50 20],...
                        'BackgroundColor', 'c',...
                        'String', num2str(Ra));

Ra_unit = uicontrol(gcf,'Style', 'text', ...
                        'Position', [180 4 17 20],...
                        'BackgroundColor', 'c',...
                        'String', 'nm');

plot(Rx,Ry);
grid;
title('Roughness profile');
xlabel('Distance travel (mm)');
ylabel('Surface height (nm)');
pause;
clf;


%DDS analysis

F_pass=0;
mt=10;

TH = armax(Ry, [mt,mt-1], 10000, 0.01,1.6, 4096, s_rate);
[MC, CM, LAMC] =th2par(TH);

OFI=zeros(mt,1);
OTI=zeros(mt-1,1);
atm =zeros(mt-1,1);
Xtp =zeros(m/2,1);
Xtm = zeros(mt,1);
Xtmp=zeros(mt,1);
atmp = zeros(mt-1,1);
perr = zeros(m/2,1);

sumsqerr = 0;

for i=1:mt
        OFI(i,1)=MC(1,i);
end
```

```
for i=mt+1:2*mt-1
        OTI(i-mt,1)=MC(1,i);
end

for j=1:m/2

        Xtp(j,1)=-dot(OFI',Xtm')+dot(atm',OTI');

        perr(j,1)=Ry(j,1)-Xtp(j,1);
        sumsqerr = sumsqerr+perr(j,1)*perr(j,1);

        %Reset the Xt vector by shift regrister
        for i=2:mt
                Xtmp(i,1)=Xtm(i-1,1);
        end

        Xtmp(1,1)=Ry(j,1);
        Xtm=Xtmp;

        %Reset the atm vector by shift regrister
        for k=2:mt-1
                atmp(k,1)=atm(k-1,1);
        end

        atmp(mt-1,1)=perr(j,1);
        atm=atmp;
end

plot(Rx(2*mt:m/2), Ry(2*mt:m/2), Rx(2*mt:m/2), Xtp(2*mt:m/2));
title('Comparing the model performance at optimum conditions');
xlabel('distance (mm)');
ylabel('Y (nm)');
pause(1);

plot(Rx(2*mt:m/2), perr(2*mt:m/2));
title('Prediction error at optimum conditions');
xlabel('distance (mm)');
ylabel('Y (nm)');
pause(1);

newsqerr=sumsqerr;

while (F_pass==0)

        mt=mt+2
        f_r = 2*mt-1;
        f_s = 2;

        TH = armax(Ry, [mt,mt-1], 10000, 0.01,1.6, 4096, s_rate);
        [MC, CM, LAMC] =th2par(TH);

        OFI=zeros(mt,1);
        OTI=zeros(mt-1,1);
        atm =zeros(mt-1,1);
        Xtp =zeros(m/2,1);
        Xtm = zeros(mt,1);
        Xtmp=zeros(mt,1);
        atmp = zeros(mt-1,1);
        perr = zeros(m/2,1);

        sumsqerr = 0;

        for i=1:mt
                OFI(i,1)=MC(1,i);
        end

        for i=mt+1:2*mt-1
                OTI(i-mt,1)=MC(1,i);
        end

        for j=1:m/2

                Xtp(j,1)=-dot(OFI',Xtm')+dot(atm',OTI');

                perr(j,1)=Ry(j,1)-Xtp(j,1);
                sumsqerr = sumsqerr+perr(j,1)*perr(j,1);

                %Reset the Xt vector by shift regrister
                for i=2:mt
                        Xtmp(i,1)=Xtm(i-1,1);
                end

                Xtmp(1,1)=Ry(j,1);
                Xtm=Xtmp;

                %Reset the atm vector by shift regrister
                for k=2:mt-1
                        atmp(k,1)=atm(k-1,1);
                end

                atmp(mt-1,1)=perr(j,1);
```

```
                        atm=atmp;
                end

                plot(Rx(2*mt:m/2), Ry(2*mt:m/2), Rx(2*mt:m/2), Xtp(2*mt:m/2));
                title('Comparing the model performance at optimum conditions');
                xlabel('distance (mm)');
                ylabel('Y (nm)');
                pause(1);

                plot(Rx(2*mt:m/2), perr(2*mt:m/2));
                title('Prediction error at optimum conditions');
                xlabel('distance (mm)');
                ylabel('Y (nm)');
                pause(1);

                %F-test for the adquency
                oldsqerr = newsqerr;
                newsqerr = sumsqerr;

                FV = ((newsqerr-oldsqerr)/f_s)/(oldsqerr/((m/2)-f_r))

                if FV>=2.99                             % 0.05 level of significant
                        F_pass = 0;
                else
                        F_pass = 1;
                end
end

OPFI = OFI;
OPTI = OTI;

[om, on] = size(OPFI);

BP = zeros(om,1);
AP = zeros(om+1,1);

BP(1,1)=1;

for i=2:om
                BP(i,1)=OPTI(i-1,1);
end

AP(1,1)=1;

for j=2:om+1
                AP(j,1)=OPFI(j-1,1);
end

crts = roots(AP);                       %roots of the characteristic equation
[orm, orn]=size(crts);

mcrts = zeros(om, om);

for k=1:om
                for j=om:-1:1
                        mcrts(k,(om-j+1))=crts(k,1).^(j-1); %matrix for root multiplication
                end
end

gu = mcrts*BP;

gl = zeros(om,1);

for k=1:om
                mdifrts = 1;

                for j=1:om
                        if k~=j
                                mdifrts = mdifrts*(crts(k,1)-crts(j,1));
                        end
                end

                gl(k,1)=mdifrts;
end

gt = zeros(om,1);

for i=1:om
                gt(i,1)=gu(i,1)/gl(i,1);
end

dc = zeros(om,1);

for i=1:om

                sumdc = 0;

                for j=1:om
                        sumdc=sumdc+((gt(i,1)*gt(j,1))/(1-crts(i,1)*crts(j,1)));
                end

                dc(i,1)=sumdc;
```

```
end

pres = zeros(om,5);

urt = (1/s_rate)*log(crts);

rurt=real(urt);
iurt=imag(urt);
rdc=real(dc);

d_tot = 0;

for i=1:om
        d_tot = d_tot + abs(rdc(i,1));
end

cdc = (100/d_tot)*abs(rdc);

for i=1:om
        pres(i,1)=urt(i,1);
        pres(i,2)=(1/(2*pi))*sqrt(rurt(i,1)*rurt(i,1)+iurt(i,1)*iurt(i,1));
        pres(i,3)=1/pres(i,2);                                  %wavelength
        pres(i,4)=rurt(i,1)/(2*pi*pres(i,2)); %damping ratio
        pres(i,5)=cdc(i,1);                                     %contribution
end

%Sorting top 10 contribution roots
ptop = zeros(10,4);
[CDY,CDI]=sort(abs(cdc));

for i=1:10
        ptop(i,1)=pres(CDI(om-i+1,1),1);
        ptop(i,2)=pres(CDI(om-i+1,1),2);
        ptop(i,3)=pres(CDI(om-i+1,1),3);
        ptop(i,4)=pres(CDI(om-i+1,1),5);
end

rpres=zeros(om,6);

for i=1:om
        rpres(i,1)=rurt(i,1);                   %reak part of roots
        rpres(i,2)=iurt(i,1);                   %imaginary part of roots
        rpres(i,3)=pres(i,2);                   %frequency
        rpres(i,4)=pres(i,3);                   %wavelength
        rpres(i,5)=pres(i,4);                   %damping ratio
        rpres(i,6)=pres(i,5);                   %percentage contribution
end
clf;

%save the results of the MDDS analysis
if n_k==1
        save mddsrp1.dat rpres -ascii;
end

if n_k==2
        save mddsrp2.dat rpres -ascii;
end

if n_k==3
        save mddsrp3.dat rpres -ascii;
end

if n_k==4
        save mddsrp4.dat rpres -ascii;
end

if n_k==5
        save mddsrp5.dat rpres -ascii;
end

if n_k==6
        save mddsrp6.dat rpres -ascii;
end

if n_k==7
        save mddsrp7.dat rpres -ascii;
end

if n_k==8
        save mddsrp8.dat rpres -ascii;
end

if n_k==9
        save mddsrp9.dat rpres -ascii;
end

if n_k==10
        save mddsrp10.dat rpres -ascii;
end

if n_k==11
        save mddsrp11.dat rpres -ascii;
```

```
end

if n_k==12
        save mddsrp12.dat rpres -ascii;
end

t_frame = uicontrol(gcf, 'Style', 'frame','BackgroundColor', 'm',...
        'HorizontalAlignment','Center','Position', [20 15 520 395]);

t1_head = uicontrol(gcf,'Style', 'text',...
        'Position', [80 375 430 20],...
        'String', 'THE HONG KONG POLYTECHNIC UNIVERSITY',...
        'BackgroundColor', 'm','HorizontalAlignment', 'Center');

t2_head = uicontrol(gcf,'Style', 'text',...
        'Position', [80 355 430 20],...
        'String', 'Department of Manufacturing Engineering',...
        'BackgroundColor', 'm','HorizontalAlignment', 'Center');

Hc_frame = uicontrol(gcf, 'Style', 'frame','BackgroundColor', 'b',...
        'HorizontalAlignment','Center','Position', [20 15 460 340]);

M_label = uicontrol(gcf, 'Style', 'text',...
        'Position', [25 320 355 20],'BackgroundColor', 'c',...
        'HorizontalAlignment','Center',...
        'String', 'RESULTS OF THE DDS ANALYSIS');

root_label = uicontrol(gcf, 'Style', 'text',...
        'Position', [25 290 100 15],...
        'BackgroundColor', 'y',...
        'HorizontalAlignment','Center',...
        'String', 'Roots');

frqc_label = uicontrol(gcf, 'Style', 'text',...
        'Position', [135 290 100 15],...
        'BackgroundColor', 'y',...
        'HorizontalAlignment','Center',...
        'String', 'Wn (cycle/mm)');

wl_label = uicontrol(gcf, 'Style', 'text',...
        'Position', [245 290 100 15],...
        'BackgroundColor', 'y',...
        'HorizontalAlignment','Center',...
        'String', 'Wavelength (mm)');

con_label = uicontrol(gcf, 'Style', 'text',...
        'Position', [355 290 100 15],...
        'BackgroundColor', 'y',...
        'HorizontalAlignment','Center',...
        'String', 'Power (%)');

Hc_r1 = uicontrol(gcf, 'Style', 'edit',...
        'Position', [25 270 100 15],...
        'BackgroundColor', 'w',...
        'HorizontalAlignment','Center',...
        'String', num2str(ptop(1,1)),...
        'Callback', 'get(Hc_r1, "String");');

Hc_f1 = uicontrol(gcf, 'Style', 'edit',...
        'Position', [135 270 100 15],...
        'BackgroundColor', 'w',...
        'HorizontalAlignment','Center',...
        'String', num2str(ptop(1,2)),...
        'Callback', 'get(Hc_f1, "String");');

Hc_w1 = uicontrol(gcf, 'Style', 'edit',...
        'Position', [245 270 100 15],...
        'BackgroundColor', 'w',...
        'HorizontalAlignment','Center',...
        'String', num2str(ptop(1,3)),...
        'Callback', 'get(Hc_w1, "String");');

Hc_c1 = uicontrol(gcf, 'Style', 'edit',...
        'Position', [355 270 100 15],...
        'BackgroundColor', 'w',...
        'HorizontalAlignment','Center',...
        'String', num2str(ptop(1,4)),...
        'Callback', 'get(Hc_c1, "String");');

Hc_r2 = uicontrol(gcf, 'Style', 'edit',...
        'Position', [25 250 100 15],...
        'BackgroundColor', 'w',...
        'HorizontalAlignment','Center',...
        'String', num2str(ptop(2,1)),...
        'Callback', 'get(Hc_r2, "String");');

Hc_f2 = uicontrol(gcf, 'Style', 'edit',...
        'Position', [135 250 100 15],...
        'BackgroundColor', 'w',...
        'HorizontalAlignment','Center',...
        'String', num2str(ptop(2,2)),...
        'Callback', 'get(Hc_f2, "String");');
```

```
Hc_w2 = uicontrol(gcf, 'Style', 'edit',...
                'Position', [245 250 100 15],...
                'BackgroundColor', 'w',...
                'HorizontalAlignment','Center',...
                'String', num2str(ptop(2,3)),...
                'Callback', 'get(Hc_w2, "String");');

Hc_c2 = uicontrol(gcf, 'Style', 'edit',...
                'Position', [355 250 100 15],...
                'BackgroundColor', 'w',...
                'HorizontalAlignment','Center',...
                'String', num2str(ptop(2,4)),...
                'Callback', 'get(Hc_c2, "String");');

Hc_r3 = uicontrol(gcf, 'Style', 'edit',...
                'Position', [25 230 100 15],...
                'BackgroundColor', 'w',...
                'HorizontalAlignment','Center',...
                'String', num2str(ptop(3,1)),...
                'Callback', 'get(Hc_r3, "String");');

Hc_f3 = uicontrol(gcf, 'Style', 'edit',...
                'Position', [135 230 100 15],...
                'BackgroundColor', 'w',...
                'HorizontalAlignment','Center',...
                'String', num2str(ptop(3,2)),...
                'Callback', 'get(Hc_f3, "String");');

Hc_w3 = uicontrol(gcf, 'Style', 'edit',...
                'Position', [245 230 100 15],...
                'BackgroundColor', 'w',...
                'HorizontalAlignment','Center',...
                'String', num2str(ptop(3,3)),...
                'Callback', 'get(Hc_w3, "String");');

Hc_c3 = uicontrol(gcf, 'Style', 'edit',...
                'Position', [355 230 100 15],...
                'BackgroundColor', 'w',...
                'HorizontalAlignment','Center',...
                'String', num2str(ptop(3,4)),...
                'Callback', 'get(Hc_c3, "String");');

Hc_r4 = uicontrol(gcf, 'Style', 'edit',...
                'Position', [25 210 100 15],...
                'BackgroundColor', 'w',...
                'HorizontalAlignment','Center',...
                'String', num2str(ptop(4,1)),...
                'Callback', 'get(Hc_r4, "String");');

Hc_f4 = uicontrol(gcf, 'Style', 'edit',...
                'Position', [135 210 100 15],...
                'BackgroundColor', 'w',...
                'HorizontalAlignment','Center',...
                'String', num2str(ptop(4,2)),...
                'Callback', 'get(Hc_f4, "String");');

Hc_w4 = uicontrol(gcf, 'Style', 'edit',...
                'Position', [245 210 100 15],...
                'BackgroundColor', 'w',...
                'HorizontalAlignment','Center',...
                'String', num2str(ptop(4,3)),...
                'Callback', 'get(Hc_w4, "String");');

Hc_c4 = uicontrol(gcf, 'Style', 'edit',...
                'Position', [355 210 100 15],...
                'BackgroundColor', 'w',...
                'HorizontalAlignment','Center',...
                'String', num2str(ptop(4,4)),...
                'Callback', 'get(Hc_c4, "String");');

Hc_r5 = uicontrol(gcf, 'Style', 'edit',...
                'Position', [25 190 100 15],...
                'BackgroundColor', 'w',...
                'HorizontalAlignment','Center',...
                'String', num2str(ptop(5,1)),...
                'Callback', 'get(Hc_r5, "String");');

Hc_f5 = uicontrol(gcf, 'Style', 'edit',...
                'Position', [135 190 100 15],...
                'BackgroundColor', 'w',...
                'HorizontalAlignment','Center',...
                'String', num2str(ptop(5,2)),...
                'Callback', 'get(Hc_f5, "String");');

Hc_w5 = uicontrol(gcf, 'Style', 'edit',...
                'Position', [245 190 100 15],...
                'BackgroundColor', 'w',...
                'HorizontalAlignment','Center',...
                'String', num2str(ptop(5,3)),...
                'Callback', 'get(Hc_w5, "String");');
```

```
Hc_c5 = uicontrol(gcf, 'Style', 'edit',...
                'Position', [355 190 100 15],...
                'BackgroundColor', 'w',...
                'HorizontalAlignment','Center',...
                'String', num2str(ptop(5,4)),...
                'Callback', 'get(Hc_c5, "String");');

Hc_r6 = uicontrol(gcf, 'Style', 'edit',...
                'Position', [25 170 100 15],...
                'BackgroundColor', 'w',...
                'HorizontalAlignment','Center',...
                'String', num2str(ptop(6,1)),...
                'Callback', 'get(Hc_r6, "String");');

Hc_f6 = uicontrol(gcf, 'Style', 'edit',...
                'Position', [135 170 100 15],...
                'BackgroundColor', 'w',...
                'HorizontalAlignment','Center',...
                'String', num2str(ptop(6,2)),...
                'Callback', 'get(Hc_f6, "String");');

Hc_w6 = uicontrol(gcf, 'Style', 'edit',...
                'Position', [245 170 100 15],...
                'BackgroundColor', 'w',...
                'HorizontalAlignment','Center',...
                'String', num2str(ptop(6,3)),...
                'Callback', 'get(Hc_w6, "String");');

Hc_c6 = uicontrol(gcf, 'Style', 'edit',...
                'Position', [355 170 100 15],...
                'BackgroundColor', 'w',...
                'HorizontalAlignment','Center',...
                'String', num2str(ptop(6,4)),...
                'Callback', 'get(Hc_c6, "String");');

Hc_r7 = uicontrol(gcf, 'Style', 'edit',...
                'Position', [25 150 100 15],...
                'BackgroundColor', 'w',...
                'HorizontalAlignment','Center',...
                'String', num2str(ptop(7,1)),...
                'Callback', 'get(Hc_r7, "String");');

Hc_f7 = uicontrol(gcf, 'Style', 'edit',...
                'Position', [135 150 100 15],...
                'BackgroundColor', 'w',...
                'HorizontalAlignment','Center',...
                'String', num2str(ptop(7,2)),...
                'Callback', 'get(Hc_f7, "String");');

Hc_w7 = uicontrol(gcf, 'Style', 'edit',...
                'Position', [245 150 100 15],...
                'BackgroundColor', 'w',...
                'HorizontalAlignment','Center',...
                'String', num2str(ptop(7,3)),...
                'Callback', 'get(Hc_w7, "String");');

Hc_c7 = uicontrol(gcf, 'Style', 'edit',...
                'Position', [355 150 100 15],...
                'BackgroundColor', 'w',...
                'HorizontalAlignment','Center',...
                'String', num2str(ptop(7,4)),...
                'Callback', 'get(Hc_c7, "String");');

Hc_r8 = uicontrol(gcf, 'Style', 'edit',...
                'Position', [25 130 100 15],...
                'BackgroundColor', 'w',...
                'HorizontalAlignment','Center',...
                'String', num2str(ptop(8,1)),...
                'Callback', 'get(Hc_r8, "String");');

Hc_f8 = uicontrol(gcf, 'Style', 'edit',...
                'Position', [135 130 100 15],...
                'BackgroundColor', 'w',...
                'HorizontalAlignment','Center',...
                'String', num2str(ptop(8,2)),...
                'Callback', 'get(Hc_f8, "String");');

Hc_w8 = uicontrol(gcf, 'Style', 'edit',...
                'Position', [245 130 100 15],...
                'BackgroundColor', 'w',...
                'HorizontalAlignment','Center',...
                'String', num2str(ptop(8,3)),...
                'Callback', 'get(Hc_w8, "String");');

Hc_c8 = uicontrol(gcf, 'Style', 'edit',...
                'Position', [355 130 100 15],...
                'BackgroundColor', 'w',...
                'HorizontalAlignment','Center',...
                'String', num2str(ptop(8,4)),...
                'Callback', 'get(Hc_c8, "String");');

Hc_r9 = uicontrol(gcf, 'Style', 'edit',...
```

```
                'Position', [25 110 100 15],...
                'BackgroundColor', 'w',...
                'HorizontalAlignment','Center',...
                'String', num2str(ptop(9,1)),...
                'Callback', 'get(Hc_r9, "String");');

Hc_f9 = uicontrol(gcf, 'Style', 'edit',...
                'Position', [135 110 100 15],...
                'BackgroundColor', 'w',...
                'HorizontalAlignment','Center',...
                'String', num2str(ptop(9,2)),...
                'Callback', 'get(Hc_f9, "String");');

Hc_w9 = uicontrol(gcf, 'Style', 'edit',...
                'Position', [245 110 100 15],...
                'BackgroundColor', 'w',...
                'HorizontalAlignment','Center',...
                'String', num2str(ptop(9,3)),...
                'Callback', 'get(Hc_w9, "String");');

Hc_c9 = uicontrol(gcf, 'Style', 'edit',...
                'Position', [355 110 100 15],...
                'BackgroundColor', 'w',...
                'HorizontalAlignment','Center',...
                'String', num2str(ptop(9,4)),...
                'Callback', 'get(Hc_c9, "String");');

Hc_r10 = uicontrol(gcf, 'Style', 'edit',...
                'Position', [25 90 100 15],...
                'BackgroundColor', 'w',...
                'HorizontalAlignment','Center',...
                'String', num2str(ptop(10,1)),...
                'Callback', 'get(Hc_r10, "String");');

Hc_f10 = uicontrol(gcf, 'Style', 'edit',...
                'Position', [135 90 100 15],...
                'BackgroundColor', 'w',...
                'HorizontalAlignment','Center',...
                'String', num2str(ptop(10,2)),...
                'Callback', 'get(Hc_f10, "String");');

Hc_w10 = uicontrol(gcf, 'Style', 'edit',...
                'Position', [245 90 100 15],...
                'BackgroundColor', 'w',...
                'HorizontalAlignment','Center',...
                'String', num2str(ptop(10,3)),...
                'Callback', 'get(Hc_w10, "String");');

Hc_c10 = uicontrol(gcf, 'Style', 'edit',...
                'Position', [355 90 100 15],...
                'BackgroundColor', 'w',...
                'HorizontalAlignment','Center',...
                'String', num2str(ptop(10,4)),...
                'Callback', 'get(Hc_c10, "String");');

AP_label = uicontrol(gcf, 'Style', 'text',...
                'Position', [25 60 355 20],...
                'BackgroundColor', 'c',...
                'HorizontalAlignment','Center',...
                'String', 'Information of ARMA (n,n-1) Model');

or_label = uicontrol(gcf, 'Style', 'text',...
                'Position', [50 40 220 15],...
                'BackgroundColor', 'g',...
                'HorizontalAlignment','Left',...
                'String', 'Order of ARMA(n,n-1) :');

Hc_order = uicontrol(gcf, 'Style', 'edit',...
                'Position', [290 40 100 15],...
                'BackgroundColor', 'w',...
                'HorizontalAlignment','Center',...
                'String', num2str(om),...
                'Callback', 'get(Hc_order, "String");');

Sqerr_label = uicontrol(gcf, 'Style', 'text',...
                'Position', [50 20 220 15],...
                'BackgroundColor', 'g',...
                'HorizontalAlignment','Left',...
                'String', 'Sum of square error (sq. nm) :');

Hc_sqerr = uicontrol(gcf, 'Style', 'edit',...
                'Position', [290 20 100 15],...
                'BackgroundColor', 'w',...
                'HorizontalAlignment','Center',...
                'String', num2str(sumsqerr),...
                'Callback', 'get(Hc_sqerr, "String");');

pause;
clf;

plot(Rx(2*mt:m/2), Ry(2*mt:m/2), Rx(2*mt:m/2), Xtp(2*mt:m/2));
title('Comparing the model performance at optimum conditions');
```

```
                xlabel('distance (mm)');
                ylabel('Y (nm)');
                pause;
end

AN(n+1,1)=360*(pi/180);
VRT(n+1,1)=VRT(1,1);
VRA(n+1,1)=VRA(1,1);

polar(AN, VRT);
grid;
title('Variation of Rt values with crystallographic orientation');
pause;

polar(AN, VRA);
grid;
title('Variation of Ra values with crystallographic orientation');
pause;


Hc_close = uicontrol(gcf, 'Style', 'push', ...
                'Position', [160 3 70 20],...
                'String', 'Close',...
                'CallBack','clg; fftsgs1;');
```

Appendix III

Outputs of Multiple Data Dependent Systems (MDDS) Program

Part 5A

Specimens 5A(I) to 5A(V)

Real (λ)	Imag. (λ)	Freq. (cycles/mm)	Wavelength (mm)	Damping ratio	Contribution %	
-51.33805200	55.09034300	11.98484400	0.08343871	-0.68175310	32.57957300	Specimen 5A(I)
-51.33805200	-55.09034300	11.98484400	0.08343871	-0.68175310	32.57957300	Al 6061
-20.69950500	1257.00230000	200.08525000	0.00499787	-0.01646513	9.28686690	Order 38
-20.69950500	-1257.00230000	200.08525000	0.00499787	-0.01646513	9.28686690	
-26.72764300	401.92068000	64.10894700	0.01559845	-0.06635324	3.36393040	
-26.72764300	-401.92068000	64.10894700	0.01559845	-0.06635324	3.36393040	
-286.37020000	1484.00410000	240.54395000	0.00415724	-0.18947570	3.35042310	
-286.37020000	-1484.00410000	240.54395000	0.00415724	-0.18947570	3.35042310	
-8.18186290	1225.40900000	195.03425000	0.00512730	-0.00667669	0.52344933	
-8.18186290	-1225.40900000	195.03425000	0.00512730	-0.00667669	0.52344933	
-30.77130900	2061.01490000	328.05727000	0.00304825	-0.01492851	0.39291577	
-30.77130900	-2061.01490000	328.05727000	0.00304825	-0.01492851	0.39291577	
-13.93638300	2492.14740000	396.64377000	0.00252115	-0.00559203	0.24858343	
-13.93638300	-2492.14740000	396.64377000	0.00252115	-0.00559203	0.24858343	
-79.68399400	1670.62300000	266.19019000	0.00375671	-0.04764301	0.10829376	
-79.68399400	-1670.62300000	266.19019000	0.00375671	-0.04764301	0.10829376	
-43.89529100	875.64141000	139.53765000	0.00716652	-0.05006643	0.10507797	
-43.89529100	-875.64141000	139.53765000	0.00716652	-0.05006643	0.10507797	
-58.90291900	2622.26710000	417.45204000	0.00239548	-0.02245693	0.03911307	
-58.90291900	-2622.26710000	417.45204000	0.00239548	-0.02245693	0.03911307	
-138.17065000	3641.48200000	579.97690000	0.00172421	-0.03791624	0.00123776	
-138.17065000	-3641.48200000	579.97690000	0.00172421	-0.03791624	0.00123776	
-430.40530000	3138.09490000	504.11907000	0.00198366	-0.13588284	0.00032951	
-430.40530000	-3138.09490000	504.11907000	0.00198366	-0.13588284	0.00032951	
-9.22079800	3484.16780000	554.52447000	0.00180335	-0.00264648	0.00014889	
-9.22079800	-3484.16780000	554.52447000	0.00180335	-0.00264648	0.00014889	
-12.00800000	3343.83620000	532.19149000	0.00187902	-0.00359106	0.00003243	
-12.00800000	-3343.83620000	532.19149000	0.00187902	-0.00359106	0.00003243	
-670.84907000	4649.05120000	747.58307000	0.00133764	-0.14281884	0.00000913	
-670.84907000	-4649.05120000	747.58307000	0.00133764	-0.14281884	0.00000913	
-9.85114170	4259.46730000	677.91708000	0.00147511	-0.00231276	0.00000796	
-9.85114170	-4259.46730000	677.91708000	0.00147511	-0.00231276	0.00000796	
-113.23780000	4388.82970000	698.73640000	0.00143115	-0.02579278	0.00000771	
-113.23780000	-4388.82970000	698.73640000	0.00143115	-0.02579278	0.00000771	
-84.35853700	4915.03830000	782.36784000	0.00127817	-0.01716083	0.00000000	
-84.35853700	-4915.03830000	782.36784000	0.00127817	-0.01716083	0.00000000	
-94.43333600	5287.15130000	841.61048000	0.00118820	-0.01785806	0.00000000	
-94.43333600	-5287.15130000	841.61048000	0.00118820	-0.01785806	0.00000000	

Real (λ)	Imag. (λ)	Freq. (cycles/mm)	Wavelength (mm)	Damping ratio	Contribution %	
-71.8652090	73.7247970	16.3859690	0.0610278	-0.6980181	41.8979980	Specimen 5A(II)
-71.8652090	-73.7247970	16.3859690	0.0610278	-0.6980181	41.8979980	Al 6061
-16.8158320	1285.0968000	204.5470200	0.0048889	-0.0130841	3.1807750	Order 18
-16.8158320	-1285.0968000	204.5470200	0.0048889	-0.0130841	3.1807750	
-0.0888704	633.8582900	100.8816800	0.0099126	-0.0001402	1.8990952	
-0.0888704	-633.8582900	100.8816800	0.0099126	-0.0001402	1.8990952	
-691.1211600	1328.8411000	238.3855800	0.0041949	-0.4614178	1.7651081	
-691.1211600	-1328.8411000	238.3855800	0.0041949	-0.4614178	1.7651081	
-44.6757060	2090.1691000	332.7367300	0.0030054	-0.0213693	1.2160712	
-44.6757060	-2090.1691000	332.7367300	0.0030054	-0.0213693	1.2160712	
-460.2812000	2722.1261000	439.3895600	0.0022759	-0.1667223	0.0400994	
-460.2812000	-2722.1261000	439.3895600	0.0022759	-0.1667223	0.0400994	
-343.3691600	3970.0103000	634.2056600	0.0015768	-0.0861690	0.0006606	
-343.3691600	-3970.0103000	634.2056600	0.0015768	-0.0861690	0.0006606	
-3.6242277	3174.1270000	505.1783300	0.0019795	-0.0011418	0.0001654	
-3.6242277	-3174.1270000	505.1783300	0.0019795	-0.0011418	0.0001654	
-166.6966700	4345.8864000	692.1779300	0.0014447	-0.0383292	0.0000276	
-166.6966700	-4345.8864000	692.1779300	0.0014447	-0.0383292	0.0000276	

Real (λ)	Imag. (λ)	Freq. (cycles/mm)	Wavelength (mm)	Damping ratio	Contribution %	
-74.9919770	0.0000000	11.9353440	0.0837848	-1.0000000	61.4458910	Specimen 5A(III)
-0.3266261	497.6970500	79.2109630	0.0126245	-0.0006563	15.5091250	Al 6061
-0.3266261	-497.6970500	79.2109630	0.0126245	-0.0006563	15.5091250	Order 16
-264.6365400	1429.9593000	231.4496100	0.0043206	-0.1819757	2.9463245	
-264.6365400	-1429.9593000	231.4496100	0.0043206	-0.1819757	2.9463245	
-59.1464120	1420.9092000	226.3405600	0.0044181	-0.0415897	0.6565248	
-59.1464120	-1420.9092000	226.3405600	0.0044181	-0.0415897	0.6565248	
-90.2036180	2037.0128000	324.5183600	0.0030815	-0.0442390	0.1396283	
-90.2036180	-2037.0128000	324.5183600	0.0030815	-0.0442390	0.1396283	
-3594.0401000	0.0000000	572.0092500	0.0017482	-1.0000000	0.0436236	
-342.0266300	3167.9311000	507.1219300	0.0019719	-0.1073415	0.0035369	
-342.0266300	-3167.9311000	507.1219300	0.0019719	-0.1073415	0.0035369	
-395.5212000	4178.9480000	668.0725300	0.0014968	-0.0942250	0.0000873	
-395.5212000	-4178.9480000	668.0725300	0.0014968	-0.0942250	0.0000873	
-21.0026040	3478.8064000	553.6793300	0.0018061	-0.0060372	0.0000156	
-21.0026040	-3478.8064000	553.6793300	0.0018061	-0.0060372	0.0000156	

Real (λ)	Imag. (λ)	Freq. (cycles/mm)	Wavelength (mm)	Damping ratio	Contribution %	
-52.330170	70.058025	13.917254	0.071853	-0.598437	40.446891	Specimen 5A(IV)
-52.330170	-70.058025	13.917254	0.071853	-0.598437	40.446891	Al 6061
-1.026570	838.779670	133.496030	0.007491	-0.001224	4.187629	Order 16
-1.026570	-838.779670	133.496030	0.007491	-0.001224	4.187629	
-493.117750	1589.198500	264.825260	0.003776	-0.296354	3.739385	
-493.117750	-1589.198500	264.825260	0.003776	-0.296354	3.739385	
-14.766670	1304.354800	207.607810	0.004817	-0.011320	1.476644	
-14.766670	-1304.354800	207.607810	0.004817	-0.011320	1.476644	
-598.989210	2651.300900	432.602470	0.002312	-0.220369	0.140595	

-598.989210	-2651.300900	432.602470	0.002312	-0.220369	0.140595
-14.604965	2706.420600	430.746490	0.002322	-0.005396	0.006650
-14.604965	-2706.420600	430.746490	0.002322	-0.005396	0.006650
-103.880760	3847.871300	612.630870	0.001632	-0.026987	0.001288
-103.880760	-3847.871300	612.630870	0.001632	-0.026987	0.001288
-216.837690	3983.263100	634.894650	0.001575	-0.054357	0.000918
-216.837690	-3983.263100	634.894650	0.001575	-0.054357	0.000918

Real (λ)	Imag. (λ)	Freq. (cycles/mm)	Wavelength (mm)	Damping ratio	Contribution %	
-63.05972900	0.00000000	10.03626800	0.09963863	-1.00000000	42.65133800	Specimen 5A(V)
-0.12305165	626.54553000	99.71782100	0.01002830	-0.00019640	14.93918500	Al 6061
-0.12305165	-626.54553000	99.71782100	0.01002830	-0.00019640	14.93918500	Order 40
-514.68611000	339.14722000	98.09970800	0.01019371	-0.83501613	6.23308450	
-514.68611000	-339.14722000	98.09970800	0.01019371	-0.83501613	6.23308450	
-17.35481800	1274.58280000	202.87495000	0.00492914	-0.01361482	4.01751950	
-17.35481800	-1274.58280000	202.87495000	0.00492914	-0.01361482	4.01751950	
-3.88953600	64.16911700	10.23157600	0.09773665	-0.06050279	2.30857360	
-3.88953600	-64.16911700	10.23157600	0.09773665	-0.06050279	2.30857360	
-61.71811700	1910.92600000	304.29191000	0.00328632	-0.03228066	0.50609354	
-61.71811700	-1910.92600000	304.29191000	0.00328632	-0.03228066	0.50609354	
-54.02366800	2063.00660000	328.45026000	0.00304460	-0.02617789	0.44275908	
-54.02366800	-2063.00660000	328.45026000	0.00304460	-0.02617789	0.44275908	
-222.44688000	2541.77690000	406.08260000	0.00246255	-0.08718305	0.10976765	
-222.44688000	-2541.77690000	406.08260000	0.00246255	-0.08718305	0.10976765	
-75.47703900	1589.43380000	253.25130000	0.00394865	-0.04743330	0.06947484	
-75.47703900	-1589.43380000	253.25130000	0.00394865	-0.04743330	0.06947484	
-120.69095000	2821.45980000	449.45991000	0.00222489	-0.04273699	0.02737564	
-120.69095000	-2821.45980000	449.45991000	0.00222489	-0.04273699	0.02737564	
-8.70833520	976.60180000	155.43718000	0.00643347	-0.00891662	0.01429844	
-8.70833520	-976.60180000	155.43718000	0.00643347	-0.00891662	0.01429844	
-1706.53460000	3352.75530000	598.75325000	0.00167014	-0.45361493	0.00277022	
-1706.53460000	-3352.75530000	598.75325000	0.00167014	-0.45361493	0.00277022	
-554.20277000	3875.36480000	623.05844000	0.00160499	-0.14156635	0.00158428	
-554.20277000	-3875.36480000	623.05844000	0.00160499	-0.14156635	0.00158428	
-40.84332500	3126.03540000	497.56644000	0.00200978	-0.01306442	0.00136439	
-40.84332500	-3126.03540000	497.56644000	0.00200978	-0.01306442	0.00136439	
-4375.10030000	6283.18530000	1218.54830000	0.00082065	-0.57143311	0.00056391	
-59.68383000	3850.87990000	612.96018000	0.00163143	-0.01549689	0.00010220	
-59.68383000	-3850.87990000	612.96018000	0.00163143	-0.01549689	0.00010220	
-5.34420670	3465.17250000	551.49998000	0.00181324	-0.00154226	0.00009397	
-5.34420670	-3465.17250000	551.49998000	0.00181324	-0.00154226	0.00009397	
-24.75134300	4255.65000000	677.31920000	0.00147641	-0.00581602	0.00000190	
-24.75134300	-4255.65000000	677.31920000	0.00147641	-0.00581602	0.00000190	
-28.06466700	4672.26730000	743.62786000	0.00134476	-0.00600654	0.00000004	
-28.06466700	-4672.26730000	743.62786000	0.00134476	-0.00600654	0.00000004	
-84.67511800	5015.34020000	798.32993000	0.00125261	-0.01688082	0.00000000	
-84.67511800	-5015.34020000	798.32993000	0.00125261	-0.01688082	0.00000000	
-53.83002700	5294.63590000	842.71103000	0.00118665	-0.01016637	0.00000000	
-53.83002700	-5294.63590000	842.71103000	0.00118665	-0.01016637	0.00000000	

Part 5B

Specimen 5B(I)

Real (λ)	Imag. (λ)	Freq. (cycles/mm)	Wavelength (mm)	Damping ratio	Contribution %	
-138.81824000	0.00000000	22.09360800	0.04526196	-1.00000000	28.36992600	Remark : al001
-443.95976000	937.67788000	165.11818000	0.00605627	-0.42792618	15.93459200	orientation 1
-443.95976000	-937.67788000	165.11818000	0.00605627	-0.42792618	15.93459200	order 22
-0.25910964	1262.04930000	200.86139000	0.00497856	-0.00020531	9.24725460	rotation : 0
-0.25910964	-1262.04930000	200.86139000	0.00497856	-0.00020531	9.24725460	
-382.13087000	1913.03340000	310.48355000	0.00322078	-0.19588161	6.36522190	
-382.13087000	-1913.03340000	310.48355000	0.00322078	-0.19588161	6.36522190	
-19.88967700	0.00000000	3.16554040	0.31590183	-1.00000000	3.99397760	
-1.07413360	630.74752000	100.38673000	0.00996148	-0.00170295	2.14079900	
-1.07413360	-630.74752000	100.38673000	0.00996148	-0.00170295	2.14079900	
-439.15187000	2659.92510000	429.07110000	0.00233062	-0.16289419	0.06829490	
-439.15187000	-2659.92510000	429.07110000	0.00233062	-0.16289419	0.06829490	
1.07224810	2524.43090000	401.77570000	0.00248895	0.00042475	0.04965831	
1.07224810	-2524.43090000	401.77570000	0.00248895	0.00042475	0.04965831	
-290.64517000	3179.89010000	508.20482000	0.00196771	-0.09102160	0.01025767	
-290.64517000	-3179.89010000	508.20482000	0.00196771	-0.09102160	0.01025767	
-40.01724100	3791.28630000	603.43557000	0.00165718	-0.01055447	0.00178521	
-40.01724100	-3791.28630000	603.43557000	0.00165718	-0.01055447	0.00178521	
-442.69939000	4298.93920000	687.81569000	0.00145388	-0.10243703	0.00018314	
-442.69939000	-4298.93920000	687.81569000	0.00145388	-0.10243703	0.00018314	
-88.14117300	4382.36390000	697.61593000	0.00143345	-0.02010863	0.00000122	
-88.14117300	-4382.36390000	697.61593000	0.00143345	-0.02010863	0.00000122	

Real (λ)	Imag. (λ)	Freq. (cycles/mm)	Wavelength (mm)	Damping ratio	Contribution %	
-10.30415900	74.98098900	12.04575300	0.08301681	-0.13614408	25.75479100	Remark : al001
-10.30415900	-74.98098900	12.04575300	0.08301681	-0.13614408	25.75479100	orientation 2
-571.01429000	781.50279000	154.04389000	0.00649166	-0.58996008	17.20208800	order 22
-571.01429000	-781.50279000	154.04389000	0.00649166	-0.58996008	17.20208800	rotation : 30
-409.92188000	1790.95500000	292.41037000	0.00341985	-0.22311484	5.40093600	
-409.92188000	-1790.95500000	292.41037000	0.00341985	-0.22311484	5.40093600	
-5.83939940	624.04384000	99.32401000	0.01006806	-0.00935694	1.42052560	
-5.83939940	-624.04384000	99.32401000	0.01006806	-0.00935694	1.42052560	
-1.59209380	2498.72080000	397.68385000	0.00251456	-0.00063716	0.11318089	
-1.59209380	-2498.72080000	397.68385000	0.00251456	-0.00063716	0.11318089	
-578.48969000	2934.23710000	475.98765000	0.00210089	-0.19342832	0.08080154	
-578.48969000	-2934.23710000	475.98765000	0.00210089	-0.19342832	0.08080154	
0.32430933	1249.49390000	198.86313000	0.00502858	0.00025955	0.01602547	
0.32430933	-1249.49390000	198.86313000	0.00502858	0.00025955	0.01602547	
-555.88945000	3685.14410000	593.14424000	0.00168593	-0.14915858	0.00685495	
-555.88945000	-3685.14410000	593.14424000	0.00168593	-0.14915858	0.00685495	
-28.32333200	3142.84220000	500.21918000	0.00199912	-0.00901165	0.00432286	
-28.32333200	-3142.84220000	500.21918000	0.00199912	-0.00901165	0.00432286	
-52.29762000	3687.57790000	586.95527000	0.00170371	-0.01418068	0.00047348	
-52.29762000	-3687.57790000	586.95527000	0.00170371	-0.01418068	0.00047348	

-45.59062400	4558.72600000	725.58006000	0.00137821	-0.01000024	0.00000050
-45.59062400	-4558.72600000	725.58006000	0.00137821	-0.01000024	0.00000050

Real (λ)	Imag. (λ)	Freq. (cycles/mm)	Wavelength (mm)	Damping ratio	Contribution %	
-39.2015710	70.7103900	12.8676770	0.0777141	-0.4848679	28.1274970	Remark : al001
-39.2015710	-70.7103900	12.8676770	0.0777141	-0.4848679	28.1274970	orientation 3
-98.7365210	564.8689400	91.2647540	0.0109571	-0.1721848	7.8721983	order 22
-98.7365210	-564.8689400	91.2647540	0.0109571	-0.1721848	7.8721983	rotation : 60
-416.3292700	1584.6474000	260.7634800	0.0038349	-0.2541033	6.8866779	
-416.3292700	-1584.6474000	260.7634800	0.0038349	-0.2541033	6.8866779	
-0.9806152	1245.1365000	198.1697000	0.0050462	-0.0007876	4.0791529	
-0.9806152	-1245.1365000	198.1697000	0.0050462	-0.0007876	4.0791529	
0.1523059	1866.9740000	297.1381300	0.0033654	0.0000816	2.7396474	
0.1523059	-1866.9740000	297.1381300	0.0033654	0.0000816	2.7396474	
-0.5051278	2487.0118000	395.8202300	0.0025264	-0.0002031	0.1923660	
-0.5051278	-2487.0118000	395.8202300	0.0025264	-0.0002031	0.1923660	
-470.9587100	2711.1078000	437.9482300	0.0022834	-0.1711513	0.0795762	
-470.9587100	-2711.1078000	437.9482300	0.0022834	-0.1711513	0.0795762	
-73.1068990	3146.8733000	500.9755800	0.0019961	-0.0232253	0.0214218	
-73.1068990	-3146.8733000	500.9755800	0.0019961	-0.0232253	0.0214218	
-22.3619150	3752.0985000	597.1756300	0.0016745	-0.0059597	0.0007592	
-22.3619150	-3752.0985000	597.1756300	0.0016745	-0.0059597	0.0007592	
-593.9466300	4039.4565000	649.8119400	0.0015389	-0.1454722	0.0006990	
-593.9466300	-4039.4565000	649.8119400	0.0015389	-0.1454722	0.0006990	
-76.9964670	4435.6193000	706.0570900	0.0014163	-0.0173561	0.0000044	
-76.9964670	-4435.6193000	706.0570900	0.0014163	-0.0173561	0.0000044	

Real (λ)	Imag. (λ)	Freq. (cycles/mm)	Wavelength (mm)	Damping ratio	Contribution %	
-46.4305920	76.9960940	14.3099660	0.0698814	-0.5163994	28.7479280	Remark : al001
-46.4305920	-76.9960940	14.3099660	0.0698814	-0.5163994	28.7479280	orientation 4
-16.2502810	628.9822200	100.1390300	0.0099861	-0.0258272	7.5399099	order :22
-16.2502810	-628.9822200	100.1390300	0.0099861	-0.0258272	7.5399099	rotation : 90
-307.1219900	1391.4502000	226.7864400	0.0044094	-0.2155331	7.0085420	
-307.1219900	-1391.4502000	226.7864400	0.0044094	-0.2155331	7.0085420	
-1.9862200	1257.8987000	200.2010500	0.0049950	-0.0015790	5.7546474	
-1.9862200	-1257.8987000	200.2010500	0.0049950	-0.0015790	5.7546474	
-216.9848200	2074.9649000	332.0416800	0.0030117	-0.1040056	0.8890252	
-216.9848200	-2074.9649000	332.0416800	0.0030117	-0.1040056	0.8890252	
-417.6851100	2734.1752000	440.2058500	0.0022717	-0.1510126	0.0218432	
-417.6851100	-2734.1752000	440.2058500	0.0022717	-0.1510126	0.0218432	
-138.0989900	3125.9359000	497.9934200	0.0020081	-0.0441354	0.0191836	
-138.0989900	-3125.9359000	497.9934200	0.0020081	-0.0441354	0.0191836	
-101.9825100	2823.1484000	449.6111000	0.0022241	-0.0361001	0.0175918	
-101.9825100	-2823.1484000	449.6111000	0.0022241	-0.0361001	0.0175918	
-594.9083000	3933.8412000	633.2091400	0.0015793	-0.1495282	0.0013024	
-594.9083000	-3933.8412000	633.2091400	0.0015793	-0.1495282	0.0013024	
-6.2803652	3951.2419000	628.8604700	0.0015902	-0.0015895	0.0000175	
-6.2803652	-3951.2419000	628.8604700	0.0015902	-0.0015895	0.0000175	
-149.3708300	4396.0602000	700.0584800	0.0014285	-0.0339587	0.0000087	

-149.3708300	-4396.0602000	700.0584800	0.0014285	-0.0339587	0.0000087

Real (λ)	Imag. (λ)	Freq. (cycles/mm)	Wavelength (mm)	Damping ratio	Contribution %	
-67.055576	70.278179	15.459732	0.064684	-0.690324	30.313724	Remark : al001
-67.055576	-70.278179	15.459732	0.064684	-0.690324	30.313724	orientation 5
-342.070900	1342.283900	220.459100	0.004536	-0.246950	9.268359	order :22
-342.070900	-1342.283900	220.459100	0.004536	-0.246950	9.268359	rotation : 120
-46.226783	626.735090	100.018950	0.009998	-0.073558	5.547376	
-46.226783	-626.735090	100.018950	0.009998	-0.073558	5.547376	
-0.204954	1254.654500	199.684460	0.005008	-0.000163	3.769756	
-0.204954	-1254.654500	199.684460	0.005008	-0.000163	3.769756	
-41.008182	1882.931100	299.748860	0.003336	-0.021774	0.902515	
-41.008182	-1882.931100	299.748860	0.003336	-0.021774	0.902515	
-432.883650	2769.860300	446.188100	0.002241	-0.154409	0.160105	
-432.883650	-2769.860300	446.188100	0.002241	-0.154409	0.160105	
-45.958690	2549.248100	405.791370	0.002464	-0.018025	0.034458	
-45.958690	-2549.248100	405.791370	0.002464	-0.018025	0.034458	
-415.459180	3820.796200	611.682990	0.001635	-0.108099	0.002954	
-415.459180	-3820.796200	611.682990	0.001635	-0.108099	0.002954	
-32.632760	3239.385400	515.590360	0.001940	-0.010073	0.000739	
-32.632760	-3239.385400	515.590360	0.001940	-0.010073	0.000739	
-32.422660	4372.116000	695.863010	0.001437	-0.007416	0.000011	
-32.422660	-4372.116000	695.863010	0.001437	-0.007416	0.000011	
-431.011260	4276.773100	684.117460	0.001462	-0.100272	0.000003	
-431.011260	-4276.773100	684.117460	0.001462	-0.100272	0.000003	

Real (λ)	Imag. (λ)	Freq. (cycles/mm)	Wavelength (mm)	Damping ratio	Contribution %	
-189.599730	0.000000	30.175734	0.033139	-1.000000	58.032090	Remark : al001
-396.447610	1496.954400	246.461240	0.004057	-0.256010	10.160717	orientation 6
-396.447610	-1496.954400	246.461240	0.004057	-0.256010	10.160717	order :22
-14.545400	0.000000	2.314972	0.431971	-1.000000	4.582150	rotation : 150
-2.327998	623.122270	99.173681	0.010083	-0.003736	3.654328	
-2.327998	-623.122270	99.173681	0.010083	-0.003736	3.654328	
0.523156	1245.567300	198.238220	0.005044	0.000420	3.551890	
0.523156	-1245.567300	198.238220	0.005044	0.000420	3.551890	
-2.471674	1867.369100	297.201280	0.003365	-0.001324	0.810111	
-2.471674	-1867.369100	297.201280	0.003365	-0.001324	0.810111	
-280.795950	2810.751400	449.571720	0.002224	-0.099406	0.282022	
-280.795950	-2810.751400	449.571720	0.002224	-0.099406	0.282022	
-228.842070	2658.786100	424.723460	0.002354	-0.085753	0.189617	
-228.842070	-2658.786100	424.723460	0.002354	-0.085753	0.189617	
-51.516747	3097.967800	493.125050	0.002028	-0.016627	0.042708	
-51.516747	-3097.967800	493.125050	0.002028	-0.016627	0.042708	
-39.723000	3755.584700	597.753300	0.001673	-0.010576	0.000978	
-39.723000	-3755.584700	597.753300	0.001673	-0.010576	0.000978	
-442.384580	4181.697200	669.251660	0.001494	-0.105204	0.000496	
-442.384580	-4181.697200	669.251660	0.001494	-0.105204	0.000496	
-132.632490	4403.020100	701.080280	0.001426	-0.030109	0.000013	
-132.632490	-4403.020100	701.080280	0.001426	-0.030109	0.000013	

Real (λ)	Imag. (λ)	Freq. (cycles/mm)	Wavelength (mm)	Damping ratio	Contribution %	
-118.1316500	0.0000000	18.8012360	0.0531880	-1.0000000	30.5208850	Remark : al001
-749.7904300	0.0000000	119.3328500	0.0083799	-1.0000000	16.9430160	orientation 7
-527.0379100	1350.5256000	230.7301200	0.0043341	-0.3635446	12.3525000	order :22
-527.0379100	-1350.5256000	230.7301200	0.0043341	-0.3635446	12.3525000	rotation : 180
-0.2908013	1250.8189000	199.0740200	0.0050233	-0.0002325	10.5808900	
-0.2908013	-1250.8189000	199.0740200	0.0050233	-0.0002325	10.5808900	
-102.7011600	1877.7770000	299.3041400	0.0033411	-0.0546113	1.7681703	
-102.7011600	-1877.7770000	299.3041400	0.0033411	-0.0546113	1.7681703	
-1.7451041	625.6312500	99.5726940	0.0100429	-0.0027893	0.9024746	
-1.7451041	-625.6312500	99.5726940	0.0100429	-0.0027893	0.9024746	
-336.9388900	2623.8351000	421.0254000	0.0023752	-0.1273688	0.5488963	
-336.9388900	-2623.8351000	421.0254000	0.0023752	-0.1273688	0.5488963	
-26.4628220	2565.6541000	408.3582500	0.0024488	-0.0103137	0.0650952	
-26.4628220	-2565.6541000	408.3582500	0.0024488	-0.0103137	0.0650952	
-75.0650340	3020.2363000	480.8339800	0.0020797	-0.0248464	0.0457183	
-75.0650340	-3020.2363000	480.8339800	0.0020797	-0.0248464	0.0457183	
-653.8965100	3766.6021000	608.4398300	0.0016435	-0.1710455	0.0038783	
-653.8965100	-3766.6021000	608.4398300	0.0016435	-0.1710455	0.0038783	
-2.9319602	3751.6368000	597.0917200	0.0016748	-0.0007815	0.0004253	
-2.9319602	-3751.6368000	597.0917200	0.0016748	-0.0007815	0.0004253	
-169.4371500	4498.8789000	716.5264500	0.0013956	-0.0376354	0.0000010	
-169.4371500	-4498.8789000	716.5264500	0.0013956	-0.0376354	0.0000010	

Real (λ)	Imag. (λ)	Freq. (cycles/mm)	Wavelength (mm)	Damping ratio	Contribution %	
-86.64851200	44.15397800	15.47779800	0.06460867	-0.89098841	20.15164000	Remark : al001
-86.64851200	-44.15397800	15.47779800	0.06460867	-0.89098841	20.15164000	orientation 8
-373.79425000	1239.86160000	206.10282000	0.00485195	-0.28864818	14.12185700	order :22
-373.79425000	-1239.86160000	206.10282000	0.00485195	-0.28864818	14.12185700	rotation : 210
-6.09011800	624.81137000	99.44654200	0.01005565	-0.00974667	5.62421210	
-6.09011800	-624.81137000	99.44654200	0.01005565	-0.00974667	5.62421210	
-303.47085000	1949.35240000	313.98610000	0.00318485	-0.15382492	4.94838230	
-303.47085000	-1949.35240000	313.98610000	0.00318485	-0.15382492	4.94838230	
-1.57222060	1249.68950000	198.89442000	0.00502779	-0.00125809	4.58910460	
-1.57222060	-1249.68950000	198.89442000	0.00502779	-0.00125809	4.58910460	
-5.27106710	2500.82850000	398.02011000	0.00251244	-0.00210772	0.32018610	
-5.27106710	-2500.82850000	398.02011000	0.00251244	-0.00210772	0.32018610	
-281.83327000	2755.03240000	440.76534000	0.00226878	-0.10176653	0.19931494	
-281.83327000	-2755.03240000	440.76534000	0.00226878	-0.10176653	0.19931494	
-42.19280700	3105.16810000	494.24848000	0.00202327	-0.01358668	0.04379376	
-42.19280700	-3105.16810000	494.24848000	0.00202327	-0.01358668	0.04379376	
-294.83409000	3837.35080000	612.53336000	0.00163256	-0.07660693	0.00148803	
-294.83409000	-3837.35080000	612.53336000	0.00163256	-0.07660693	0.00148803	
-28.74596500	4007.65420000	637.85438000	0.00156776	-0.00717258	0.00002047	
-28.74596500	-4007.65420000	637.85438000	0.00156776	-0.00717258	0.00002047	
-173.21504000	4606.57550000	733.67738000	0.00136300	-0.03757514	0.00000085	
-173.21504000	-4606.57550000	733.67738000	0.00136300	-0.03757514	0.00000085	

Real (λ)	Imag. (λ)	Freq. (cycles/mm)	Wavelength (mm)	Damping ratio	Contribution %	
0.0008913	1253.9964000	199.5797300	0.0050105	0.0000007	48.4076940	Remark : al001
0.0008913	-1253.9964000	199.5797300	0.0050105	0.0000007	48.4076940	orientation 9
-175.9362900	0.0000000	28.0011310	0.0357128	-1.0000000	2.0234473	order :22
-53.0328950	0.0000000	8.4404473	0.1184771	-1.0000000	0.5622886	rotation : 240
-404.1543400	1504.1621000	247.8857700	0.0040341	-0.2594871	0.2365307	
-404.1543400	-1504.1621000	247.8857700	0.0040341	-0.2594871	0.2365307	
-1.1180537	627.2658000	99.8326110	0.0100168	-0.0017824	0.0306376	
-1.1180537	-627.2658000	99.8326110	0.0100168	-0.0017824	0.0306376	
-10.1959570	1879.2179000	299.0912200	0.0033435	-0.0054256	0.0240436	
-10.1959570	-1879.2179000	299.0912200	0.0033435	-0.0054256	0.0240436	
-6.4810348	2509.6169000	399.4192700	0.0025036	-0.0025825	0.0049206	
-6.4810348	-2509.6169000	399.4192700	0.0025036	-0.0025825	0.0049206	
-580.9914700	2846.8191000	462.4246800	0.0021625	-0.1999627	0.0032470	
-580.9914700	-2846.8191000	462.4246800	0.0021625	-0.1999627	0.0032470	
-242.2986800	3829.1293000	610.6437300	0.0016376	-0.0631514	0.0000429	
-242.2986800	-3829.1293000	610.6437300	0.0016376	-0.0631514	0.0000429	
-641.6162700	4214.5181000	678.4899400	0.0014739	-0.1505054	0.0000093	
-641.6162700	-4214.5181000	678.4899400	0.0014739	-0.1505054	0.0000093	
-9.1906198	3197.7722000	508.9433600	0.0019649	-0.0028741	0.0000058	
-9.1906198	-3197.7722000	508.9433600	0.0019649	-0.0028741	0.0000058	
-42.1955200	4434.2129000	705.7588500	0.0014169	-0.0095155	0.0000000	
-42.1955200	-4434.2129000	705.7588500	0.0014169	-0.0095155	0.0000000	

Real (λ)	Imag. (λ)	Freq. (cycles/mm)	Wavelength (mm)	Damping ratio	Contribution %	
-27.6081320	102.6556300	16.9186930	0.0591062	-0.2597110	21.9022380	Remark : al001
-27.6081320	-102.6556300	16.9186930	0.0591062	-0.2597110	21.9022380	orientation 10
-200.0317500	550.7097700	93.2509370	0.0107238	-0.3414018	12.9697670	order :22
-200.0317500	-550.7097700	93.2509370	0.0107238	-0.3414018	12.9697670	rotation : 270
-3.7197738	1252.7663000	199.3848200	0.0050154	-0.0029692	7.2767800	
-3.7197738	-1252.7663000	199.3848200	0.0050154	-0.0029692	7.2767800	
-378.8169700	1169.2193000	195.6101700	0.0051122	-0.3082181	5.0897889	
-378.8169700	-1169.2193000	195.6101700	0.0051122	-0.3082181	5.0897889	
-193.2580100	1900.9765000	304.1092500	0.0032883	-0.1011412	2.5420774	
-193.2580100	-1900.9765000	304.1092500	0.0032883	-0.1011412	2.5420774	
-10.0064590	2509.6707000	399.4296700	0.0025036	-0.0039871	0.1403576	
-10.0064590	-2509.6707000	399.4296700	0.0025036	-0.0039871	0.1403576	
-285.5922000	2828.3842000	452.4403000	0.0022102	-0.1004628	0.0421111	
-285.5922000	-2828.3842000	452.4403000	0.0022102	-0.1004628	0.0421111	
-160.5130600	3127.6724000	498.4396100	0.0020063	-0.0512528	0.0365127	
-160.5130600	-3127.6724000	498.4396100	0.0020063	-0.0512528	0.0365127	
-45.1331560	3747.9418000	596.5467100	0.0016763	-0.0120412	0.0002545	
-45.1331560	-3747.9418000	596.5467100	0.0016763	-0.0120412	0.0002545	
-589.1229200	4330.1989000	695.5214600	0.0014378	-0.1348080	0.0001106	
-589.1229200	-4330.1989000	695.5214600	0.0014378	-0.1348080	0.0001106	
-84.0556440	4511.6929000	718.1828400	0.0013924	-0.0186274	0.0000031	
-84.0556440	-4511.6929000	718.1828400	0.0013924	-0.0186274	0.0000031	

Real (λ)	Imag. (λ)	Freq. (cycles/mm)	Wavelength (mm)	Damping ratio	Contribution %	
-176.52986000	0.00000000	28.09560100	0.03559276	-1.00000000	56.27313600	Remark : al001
-59.46821100	0.00000000	9.46465970	0.10565620	-1.00000000	17.80240100	orientation 11
-391.73090000	1443.43670000	238.03975000	0.00420098	-0.26191386	6.68529300	order :22
-391.73090000	-1443.43670000	238.03975000	0.00420098	-0.26191386	6.68529300	rotation : 300
-1.50394790	627.28405000	99.83564400	0.01001646	-0.00239755	3.88982570	
-1.50394790	-627.28405000	99.83564400	0.01001646	-0.00239755	3.88982570	
0.29094377	1252.87340000	199.40101000	0.00501502	0.00023222	2.16001330	
0.29094377	-1252.87340000	199.40101000	0.00501502	0.00023222	2.16001330	
-576.59245000	2801.00590000	455.14120000	0.00219712	-0.20162433	0.08641778	
-576.59245000	-2801.00590000	455.14120000	0.00219712	-0.20162433	0.08641778	
-1.74521530	2505.59300000	398.77761000	0.00250766	-0.00069653	0.07916780	
-1.74521530	-2505.59300000	398.77761000	0.00250766	-0.00069653	0.07916780	
-1.24508360	1878.97890000	299.04884000	0.00334394	-0.00066264	0.06057621	
-1.24508360	-1878.97890000	299.04884000	0.00334394	-0.00066264	0.06057621	
-850.20637000	3985.45250000	648.57705000	0.00154184	-0.20863296	0.00047697	
-850.20637000	-3985.45250000	648.57705000	0.00154184	-0.20863296	0.00047697	
-16.95530600	3381.81590000	538.23949000	0.00185791	-0.00501361	0.00025076	
-16.95530600	-3381.81590000	538.23949000	0.00185791	-0.00501361	0.00025076	
-28.69106500	3761.39100000	598.66138000	0.00167039	-0.00762756	0.00020962	
-28.69106500	-3761.39100000	598.66138000	0.00167039	-0.00762756	0.00020962	
-144.99007000	4523.78760000	720.35286000	0.00138821	-0.03203414	0.00000001	
-144.99007000	-4523.78760000	720.35286000	0.00138821	-0.03203414	0.00000001	

Real (λ)	Imag. (λ)	Freq. (cycles/mm)	Wavelength (mm)	Damping ratio	Contribution %	
-29.1678340	53.1554930	9.6499213	0.1036278	-0.4810614	26.3386150	Remark : al001
-29.1678340	-53.1554930	9.6499213	0.1036278	-0.4810614	26.3386150	orientation 12
-83.1039270	599.4056200	96.3108830	0.0103830	-0.1373303	7.8117695	order :22
-83.1039270	-599.4056200	96.3108830	0.0103830	-0.1373303	7.8117695	rotation : 330
-330.1896300	1465.7580000	239.1284700	0.0041819	-0.2197618	7.2794974	
-330.1896300	-1465.7580000	239.1284700	0.0041819	-0.2197618	7.2794974	
-1.5323012	1252.2533000	199.3024500	0.0050175	-0.0012236	7.0160039	
-1.5323012	-1252.2533000	199.3024500	0.0050175	-0.0012236	7.0160039	
-2.5641651	1874.5756000	298.3482600	0.0033518	-0.0013679	0.7726977	
-2.5641651	-1874.5756000	298.3482600	0.0033518	-0.0013679	0.7726977	
-326.9342100	2640.6877000	423.4872700	0.0023613	-0.1228684	0.6189460	
-326.9342100	-2640.6877000	423.4872700	0.0023613	-0.1228684	0.6189460	
-21.8964890	2519.9394000	401.0759500	0.0024933	-0.0086890	0.1466425	
-21.8964890	-2519.9394000	401.0759500	0.0024933	-0.0086890	0.1466425	
-392.2953300	3333.0736000	534.1367800	0.0018722	-0.1168909	0.0151870	
-392.2953300	-3333.0736000	534.1367800	0.0018722	-0.1168909	0.0151870	
-463.8255100	4171.6719000	668.0334300	0.0014969	-0.1105036	0.0003871	
-463.8255100	-4171.6719000	668.0334300	0.0014969	-0.1105036	0.0003871	
-7.2760574	3782.0517000	601.9333400	0.0016613	-0.0019238	0.0002509	
-7.2760574	-3782.0517000	601.9333400	0.0016613	-0.0019238	0.0002509	
-100.5669500	4427.8741000	704.8997900	0.0014186	-0.0227064	0.0000029	
-100.5669500	-4427.8741000	704.8997900	0.0014186	-0.0227064	0.0000029	

Specimen 5B(II)

Real (λ)	Imag. (λ)	Freq. (cycles/mm)	Wavelength (mm)	Damping ratio	Contribution %	
-86.50861300	216.89771000	37.16476100	0.02690721	-0.37046581	25.64648400	order 22
-86.50861300	-216.89771000	37.16476100	0.02690721	-0.37046581	25.64648400	rotation : 0
-3.41065900	623.14755000	99.17849800	0.01008283	-0.00547319	13.44822400	Remark : al011
-3.41065900	-623.14755000	99.17849800	0.01008283	-0.00547319	13.44822400	orientation 1
-403.15078000	1836.05560000	299.17873000	0.00334248	-0.21446524	7.55827500	
-403.15078000	-1836.05560000	299.17873000	0.00334248	-0.21446524	7.55827500	
-21.64501500	1251.33090000	199.18528000	0.00502045	-0.01729501	2.28307420	
-21.64501500	-1251.33090000	199.18528000	0.00502045	-0.01729501	2.28307420	
-3.47035300	1878.11060000	298.91109000	0.00334548	-0.00184779	0.75712433	
-3.47035300	-1878.11060000	298.91109000	0.00334548	-0.00184779	0.75712433	
-549.03266000	2894.49940000	468.88796000	0.00213271	-0.18635851	0.27117035	
-549.03266000	-2894.49940000	468.88796000	0.00213271	-0.18635851	0.27117035	
-4.91358620	3124.24850000	497.24021000	0.00201110	-0.00157272	0.02326355	
-4.91358620	-3124.24850000	497.24021000	0.00201110	-0.00157272	0.02326355	
0.64364781	2501.91830000	398.19267000	0.00251135	0.00025726	0.01229401	
0.64364781	-2501.91830000	398.19267000	0.00251135	0.00025726	0.01229401	
-683.74809000	4275.98360000	689.18955000	0.00145098	-0.15789834	0.00004686	
-683.74809000	-4275.98360000	689.18955000	0.00145098	-0.15789834	0.00004686	
3.00442820	3750.37650000	596.89115000	0.00167535	0.00080110	0.00004313	
3.00442820	-3750.37650000	596.89115000	0.00167535	0.00080110	0.00004313	
-142.38114000	4590.40880000	730.93761000	0.00136811	-0.03100218	0.00000080	
-142.38114000	-4590.40880000	730.93761000	0.00136811	-0.03100218	0.00000080	

Real (λ)	Imag. (λ)	Freq. (cycles/mm)	Wavelength (mm)	Damping ratio	Contribution %	
-0.72321023	185.64920000	29.54721300	0.03384414	-0.00389554	20.55036900	Remark : al011
-0.72321023	-185.64920000	29.54721300	0.03384414	-0.00389554	20.55036900	orientation 2
-447.05005000	403.72286000	95.86967100	0.01043083	-0.74215572	14.41959600	order 22
-447.05005000	-403.72286000	95.86967100	0.01043083	-0.74215572	14.41959600	rotation : 30
-486.36952000	1530.38800000	255.57344000	0.00391277	-0.30288012	11.62423700	
-486.36952000	-1530.38800000	255.57344000	0.00391277	-0.30288012	11.62423700	
-0.87997699	624.10963000	99.33023100	0.01006743	-0.00140997	2.83299970	
-0.87997699	-624.10963000	99.33023100	0.01006743	-0.00140997	2.83299970	
-629.89402000	2742.51970000	447.85027000	0.00223289	-0.22384880	0.40887483	
-629.89402000	-2742.51970000	447.85027000	0.00223289	-0.22384880	0.40887483	
-3.53457540	2492.91710000	396.76048000	0.00252041	-0.00141785	0.09914574	
-3.53457540	-2492.91710000	396.76048000	0.00252041	-0.00141785	0.09914574	
-14.67329700	1766.72920000	281.19339000	0.00355627	-0.00830506	0.03976711	
-14.67329700	-1766.72920000	281.19339000	0.00355627	-0.00830506	0.03976711	
-4.39090970	3119.47140000	496.47978000	0.00201418	-0.00140758	0.02273889	
-4.39090970	-3119.47140000	496.47978000	0.00201418	-0.00140758	0.02273889	
-668.23736000	3916.14340000	632.28236000	0.00158157	-0.16820536	0.00209643	
-668.23736000	-3916.14340000	632.28236000	0.00158157	-0.16820536	0.00209643	
-80.98291800	3896.32210000	620.25285000	0.00161225	-0.02077996	0.00017495	
-80.98291800	-3896.32210000	620.25285000	0.00161225	-0.02077996	0.00017495	
-24.16457200	4569.38120000	727.24977000	0.00137504	-0.00528829	0.00000026	
-24.16457200	-4569.38120000	727.24977000	0.00137504	-0.00528829	0.00000026	

Real (λ)	Imag. (λ)	Freq. (cycles/mm)	Wavelength (mm)	Damping ratio	Contribution %	
-367.82434000	852.04072000	147.70300000	0.00677034	-0.39634308	23.01986700	Remark : al011
-367.82434000	-852.04072000	147.70300000	0.00677034	-0.39634308	23.01986700	orientation 3
-1.71302170	628.53995000	100.03561000	0.00999644	-0.00272539	9.22014110	order 22
-1.71302170	-628.53995000	100.03561000	0.00999644	-0.00272539	9.22014110	rotation : 60
-495.99286000	1993.83570000	327.00007000	0.00305810	-0.24140581	9.05373850	
-495.99286000	-1993.83570000	327.00007000	0.00305810	-0.24140581	9.05373850	
-25.22875400	129.16825000	20.94622200	0.04774131	-0.19169476	5.81471160	
-25.22875400	-129.16825000	20.94622200	0.04774131	-0.19169476	5.81471160	
-909.76531000	2432.49000000	413.33371000	0.00241935	-0.35030689	1.45718860	
-909.76531000	-2432.49000000	413.33371000	0.00241935	-0.35030689	1.45718860	
-67.74443500	1622.88590000	258.51525000	0.00386824	-0.04170687	0.96524066	
-67.74443500	-1622.88590000	258.51525000	0.00386824	-0.04170687	0.96524066	
-50.04217300	2293.46180000	365.10267000	0.00273896	-0.02181430	0.42755568	
-50.04217300	-2293.46180000	365.10267000	0.00273896	-0.02181430	0.42755568	
-2.99572020	3145.68150000	500.65098000	0.00199740	-0.00095233	0.03025444	
-2.99572020	-3145.68150000	500.65098000	0.00199740	-0.00095233	0.03025444	
-419.02929000	3715.35600000	595.06617000	0.00168049	-0.11207255	0.01098761	
-419.02929000	-3715.35600000	595.06617000	0.00168049	-0.11207255	0.01098761	
-39.13773300	3842.53240000	611.58974000	0.00163508	-0.01018487	0.00031418	
-39.13773300	-3842.53240000	611.58974000	0.00163508	-0.01018487	0.00031418	
-47.00896900	4624.85170000	736.10604000	0.00135850	-0.01016390	0.00000021	
-47.00896900	-4624.85170000	736.10604000	0.00135850	-0.01016390	0.00000021	

Real (λ)	Imag. (λ)	Freq. (cycles/mm)	Wavelength (mm)	Damping ratio	Contribution %	
-457.3449800	0.0000000	72.7887150	0.0137384	-1.0000000	29.1504240	Remark : al011
-291.2861200	1576.5198000	255.1578000	0.0039191	-0.1816900	21.5213960	orientation 4
-291.2861200	-1576.5198000	255.1578000	0.0039191	-0.1816900	21.5213960	order :22
-213.4803600	1472.0240000	236.7308000	0.0042242	-0.1435236	10.5594850	rotation : 90
-213.4803600	-1472.0240000	236.7308000	0.0042242	-0.1435236	10.5594850	
-40.0275160	0.0000000	6.3705771	0.1569717	-1.0000000	1.6226903	
-0.2734915	634.0075700	100.9054500	0.0099103	-0.0004314	1.2598692	
-0.2734915	-634.0075700	100.9054500	0.0099103	-0.0004314	1.2598692	
-733.7952400	2594.4790000	429.1218900	0.0023303	-0.2721538	0.5968983	
-733.7952400	-2594.4790000	429.1218900	0.0023303	-0.2721538	0.5968983	
-2.1269678	1904.3530000	303.0873800	0.0032994	-0.0011169	0.5657498	
-2.1269678	-1904.3530000	303.0873800	0.0032994	-0.0011169	0.5657498	
-3.8272640	2540.7221000	404.3689400	0.0024730	-0.0015064	0.0909547	
-3.8272640	-2540.7221000	404.3689400	0.0024730	-0.0015064	0.0909547	
-0.2605244	3174.9524000	505.3093700	0.0019790	-0.0000821	0.0163205	
-0.2605244	-3174.9524000	505.3093700	0.0019790	-0.0000821	0.0163205	
-222.6632900	3960.4525000	631.3209900	0.0015840	-0.0561330	0.0016320	
-222.6632900	-3960.4525000	631.3209900	0.0015840	-0.0561330	0.0016320	
-442.8158000	4058.9340000	649.8324000	0.0015389	-0.1084531	0.0011356	
-442.8158000	-4058.9340000	649.8324000	0.0015389	-0.1084531	0.0011356	
-166.5038800	4603.6265000	733.1689800	0.0013639	-0.0361443	0.0000010	
-166.5038800	-4603.6265000	733.1689800	0.0013639	-0.0361443	0.0000010	

Real (λ)	Imag. (λ)	Freq. (cycles/mm)	Wavelength (mm)	Damping ratio	Contribution %	
-230.9765300	0.0000000	36.7610560	0.0272027	-1.0000000	49.6620260	Remark : al011
-363.0803200	1650.0171000	268.8910200	0.0037190	-0.2149050	9.8592456	orientation 5
-363.0803200	-1650.0171000	268.8910200	0.0037190	-0.2149050	9.8592456	order :22
-3.3064156	627.5823800	99.8842240	0.0100116	-0.0052684	7.0771411	rotation : 120
-3.3064156	-627.5823800	99.8842240	0.0100116	-0.0052684	7.0771411	
-23.8003720	0.0000000	3.7879468	0.2639953	-1.0000000	4.6502367	
-55.5325860	1279.2533000	203.7912400	0.0049070	-0.0433693	3.8990616	
-55.5325860	-1279.2533000	203.7912400	0.0049070	-0.0433693	3.8990616	
-9.4407308	1883.1757000	299.7204800	0.0033364	-0.0050131	1.2725269	
-9.4407308	-1883.1757000	299.7204800	0.0033364	-0.0050131	1.2725269	
-716.7968900	2774.7080000	456.1060400	0.0021925	-0.2501212	0.3659750	
-716.7968900	-2774.7080000	456.1060400	0.0021925	-0.2501212	0.3659750	
-48.2279240	2511.3119000	399.7613900	0.0025015	-0.0192007	0.3639019	
-48.2279240	-2511.3119000	399.7613900	0.0025015	-0.0192007	0.3639019	
-1.9488540	3158.0607000	502.6210600	0.0019896	-0.0006171	0.0037942	
-1.9488540	-3158.0607000	502.6210600	0.0019896	-0.0006171	0.0037942	
-518.3654200	4040.4924000	648.3348400	0.0015424	-0.1272497	0.0020466	
-518.3654200	-4040.4924000	648.3348400	0.0015424	-0.1272497	0.0020466	
-37.0360680	3816.7950000	607.4903900	0.0016461	-0.0097030	0.0001753	
-37.0360680	-3816.7950000	607.4903900	0.0016461	-0.0097030	0.0001753	
-128.0746800	4627.2257000	736.7278800	0.0013574	-0.0276679	0.0000007	
-128.0746800	-4627.2257000	736.7278800	0.0013574	-0.0276679	0.0000007	

Real (λ)	Imag. (λ)	Freq. (cycles/mm)	Wavelength (mm)	Damping ratio	Contribution %	
-216.1788300	0.0000000	34.4059290	0.0290648	-1.0000000	48.1633530	Remark : al011
-209.9022600	1263.7741000	203.8913300	0.0049046	-0.1638470	10.0326680	orientation 6
-209.9022600	-1263.7741000	203.8913300	0.0049046	-0.1638470	10.0326680	order :22
-43.0429060	0.0000000	6.8504913	0.1459749	-1.0000000	9.9313382	rotation : 150
-187.8674500	1880.6072000	300.7976900	0.0033245	-0.0994025	6.0607006	
-187.8674500	-1880.6072000	300.7976900	0.0033245	-0.0994025	6.0607006	
-2.8390977	631.7089400	100.5406200	0.0099462	-0.0044943	4.3202296	
-2.8390977	-631.7089400	100.5406200	0.0099462	-0.0044943	4.3202296	
-36.6475180	1696.7503000	270.1091800	0.0037022	-0.0215936	0.3041673	
-36.6475180	-1696.7503000	270.1091800	0.0037022	-0.0215936	0.3041673	
-567.7398700	2844.5559000	461.6543400	0.0021661	-0.1957278	0.1623858	
-567.7398700	-2844.5559000	461.6543400	0.0021661	-0.1957278	0.1623858	
-2.2164429	2518.9620000	400.9054100	0.0024944	-0.0008799	0.0523227	
-2.2164429	-2518.9620000	400.9054100	0.0024944	-0.0008799	0.0523227	
-11.5220780	3157.1898000	502.4857200	0.0019901	-0.0036494	0.0190551	
-11.5220780	-3157.1898000	502.4857200	0.0019901	-0.0036494	0.0190551	
-58.8384980	3809.9072000	606.4378700	0.0016490	-0.0154417	0.0008297	
-58.8384980	-3809.9072000	606.4378700	0.0016490	-0.0154417	0.0008297	
-420.8588200	4294.6391000	686.7871800	0.0014561	-0.0975291	0.0002945	
-420.8588200	-4294.6391000	686.7871800	0.0014561	-0.0975291	0.0002945	
-115.0268500	4559.5958000	725.9130900	0.0013776	-0.0252194	0.0000006	
-115.0268500	-4559.5958000	725.9130900	0.0013776	-0.0252194	0.0000006	

Real (λ)	Imag. (λ)	Freq. (cycles/mm)	Wavelength (mm)	Damping ratio	Contribution %	
-80.0053150	158.1094800	28.2020840	0.0354584	-0.4515000	15.5295090	Remark : al011
-80.0053150	-158.1094800	28.2020840	0.0354584	-0.4515000	15.5295090	orientation 7
-413.6627100	795.4355900	142.6932700	0.0070080	-0.4613845	15.2137890	order :22
-413.6627100	-795.4355900	142.6932700	0.0070080	-0.4613845	15.2137890	rotation : 180
-293.2343800	1623.9581000	262.6406900	0.0038075	-0.1776941	9.3421567	
-293.2343800	-1623.9581000	262.6406900	0.0038075	-0.1776941	9.3421567	
-0.3594351	634.6202400	101.0029600	0.0099007	-0.0005664	9.2954634	
-0.3594351	-634.6202400	101.0029600	0.0099007	-0.0005664	9.2954634	
-102.9405500	1780.6886000	283.8785600	0.0035226	-0.0577130	0.3235516	
-102.9405500	-1780.6886000	283.8785600	0.0035226	-0.0577130	0.3235516	
-5.4096603	2538.8779000	404.0758900	0.0024748	-0.0021307	0.1684367	
-5.4096603	-2538.8779000	404.0758900	0.0024748	-0.0021307	0.1684367	
-354.7536500	2794.1540000	448.2733000	0.0022308	-0.1259517	0.0942598	
-354.7536500	-2794.1540000	448.2733000	0.0022308	-0.1259517	0.0942598	
-42.0828870	3150.8134000	501.5122600	0.0019940	-0.0133550	0.0306790	
-42.0828870	-3150.8134000	501.5122600	0.0019940	-0.0133550	0.0306790	
-26.4231980	3810.0505000	606.4029600	0.0016491	-0.0069350	0.0015078	
-26.4231980	-3810.0505000	606.4029600	0.0016491	-0.0069350	0.0015078	
-437.7959700	4161.0639000	665.9092700	0.0015017	-0.1046350	0.0006444	
-437.7959700	-4161.0639000	665.9092700	0.0015017	-0.1046350	0.0006444	
-118.7613600	4576.0554000	728.5470700	0.0013726	-0.0259440	0.0000031	
-118.7613600	-4576.0554000	728.5470700	0.0013726	-0.0259440	0.0000031	

Real (λ)	Imag. (λ)	Freq. (cycles/mm)	Wavelength (mm)	Damping ratio	Contribution %	
-407.6204400	980.2458900	168.9620300	0.0059185	-0.3839609	28.8456710	Remark : al011
-407.6204400	-980.2458900	168.9620300	0.0059185	-0.3839609	28.8456710	orientation 8
-0.9642509	633.5376700	100.8307700	0.0099176	-0.0015220	8.3790613	order :22
-0.9642509	-633.5376700	100.8307700	0.0099176	-0.0015220	8.3790613	rotation : 210
-49.0152460	247.1537400	40.1018240	0.0249365	-0.1945303	8.3337327	
-49.0152460	-247.1537400	40.1018240	0.0249365	-0.1945303	8.3337327	
-418.0629600	2011.6890000	327.0109100	0.0030580	-0.2034696	4.1010090	
-418.0629600	-2011.6890000	327.0109100	0.0030580	-0.2034696	4.1010090	
-555.2980600	3211.9565000	518.7821400	0.0019276	-0.1703575	0.1158034	
-555.2980600	-3211.9565000	518.7821400	0.0019276	-0.1703575	0.1158034	
-2.7167125	1498.1204000	238.4336700	0.0041940	-0.0018134	0.1157635	
-2.7167125	-1498.1204000	238.4336700	0.0041940	-0.0018134	0.1157635	
-50.2692020	2196.2048000	349.6284100	0.0028602	-0.0228831	0.0691469	
-50.2692020	-2196.2048000	349.6284100	0.0028602	-0.0228831	0.0691469	
-3.5473983	3162.8909000	503.3900400	0.0019865	-0.0011216	0.0292930	
-3.5473983	-3162.8909000	503.3900400	0.0019865	-0.0011216	0.0292930	
-0.1348029	3796.7886000	604.2776700	0.0016549	-0.0000355	0.0103688	
-0.1348029	-3796.7886000	604.2776700	0.0016549	-0.0000355	0.0103688	
-621.3408700	4182.7538000	673.0107900	0.0014859	-0.1469359	0.0001451	
-621.3408700	-4182.7538000	673.0107900	0.0014859	-0.1469359	0.0001451	
-6.0331751	4423.7525000	704.0627400	0.0014203	-0.0013638	0.0000052	
-6.0331751	-4423.7525000	704.0627400	0.0014203	-0.0013638	0.0000052	

Real (λ)	Imag. (λ)	Freq. (cycles/mm)	Wavelength (mm)	Damping ratio	Contribution %	
-513.2322700	0.0000000	81.6834520	0.0122424	-1.0000000	60.7423760	Remark : al011
-1310.0622000	0.0000000	208.5028800	0.0047961	-1.0000000	19.6424320	orientation 9
-75.7268070	0.0000000	12.0522960	0.0829717	-1.0000000	6.4487829	order :22
-2.3834886	627.2098000	99.8242610	0.0100176	-0.0038001	3.5826220	rotation : 240
-2.3834886	-627.2098000	99.8242610	0.0100176	-0.0038001	3.5826220	
-21.5263950	1251.7538000	199.2522700	0.0050188	-0.0171944	1.2925322	
-21.5263950	-1251.7538000	199.2522700	0.0050188	-0.0171944	1.2925322	
-433.1423400	2067.6804000	336.2245500	0.0029742	-0.2050319	0.9301290	
-433.1423400	-2067.6804000	336.2245500	0.0029742	-0.2050319	0.9301290	
-3020.3666000	0.0000000	480.7062700	0.0020803	-1.0000000	0.4915272	
-2.0244167	1881.9967000	299.5292600	0.0033386	-0.0010757	0.4488980	
-2.0244167	-1881.9967000	299.5292600	0.0033386	-0.0010757	0.4488980	
-63.1913810	2420.3966000	385.3493400	0.0025950	-0.0260990	0.0612191	
-63.1913810	-2420.3966000	385.3493400	0.0025950	-0.0260990	0.0612191	
-5.8225161	3134.6269000	498.8922200	0.0020044	-0.0018575	0.0126904	
-5.8225161	-3134.6269000	498.8922200	0.0020044	-0.0018575	0.0126904	
-547.9338000	3555.7082000	572.5883500	0.0017465	-0.1523020	0.0093341	
-547.9338000	-3555.7082000	572.5883500	0.0017465	-0.1523020	0.0093341	
-177.3311200	4312.6275000	686.9560000	0.0014557	-0.0410843	0.0000082	
-177.3311200	-4312.6275000	686.9560000	0.0014557	-0.0410843	0.0000082	
-94.8393590	4383.4551000	697.8118100	0.0014331	-0.0216307	0.0000075	
-94.8393590	-4383.4551000	697.8118100	0.0014331	-0.0216307	0.0000075	

Real (λ)	Imag. (λ)	Freq. (cycles/mm)	Wavelength (mm)	Damping ratio	Contribution %	
-129.7268800	274.8225900	48.3675310	0.0206750	-0.4268706	21.4646840	Remark : al011
-129.7268800	-274.8225900	48.3675310	0.0206750	-0.4268706	21.4646840	orientation 10
-0.4322518	626.5656300	99.7210410	0.0100280	-0.0006899	14.3277800	order :22
-0.4322518	-626.5656300	99.7210410	0.0100280	-0.0006899	14.3277800	rotation : 270
-315.8950800	1618.5554000	262.4614700	0.0038101	-0.1915567	8.8073726	
-315.8950800	-1618.5554000	262.4614700	0.0038101	-0.1915567	8.8073726	
-25.9892760	1262.2175000	200.9307400	0.0049768	-0.0205858	3.6627605	
-25.9892760	-1262.2175000	200.9307400	0.0049768	-0.0205858	3.6627605	
-17.4421340	1872.3893000	298.0129400	0.0033556	-0.0093150	1.3259352	
-17.4421340	-1872.3893000	298.0129400	0.0033556	-0.0093150	1.3259352	
-307.3588400	2684.1921000	429.9940300	0.0023256	-0.1137636	0.3549967	
-307.3588400	-2684.1921000	429.9940300	0.0023256	-0.1137636	0.3549967	
-17.1392400	3130.5845000	498.2554600	0.0020070	-0.0054747	0.0466492	
-17.1392400	-3130.5845000	498.2554600	0.0020070	-0.0054747	0.0466492	
-0.2157622	2506.6257000	398.9418700	0.0025066	-0.0000861	0.0083697	
-0.2157622	-2506.6257000	398.9418700	0.0025066	-0.0000861	0.0083697	
-35.3323050	3754.3305000	597.5467100	0.0016735	-0.0094107	0.0013677	
-35.3323050	-3754.3305000	597.5467100	0.0016735	-0.0094107	0.0013677	
-745.3186000	4155.7612000	671.9628600	0.0014882	-0.1765293	0.0000840	
-745.3186000	-4155.7612000	671.9628600	0.0014882	-0.1765293	0.0000840	
-70.0505720	4569.2358000	727.3019200	0.0013749	-0.0153291	0.0000004	
-70.0505720	-4569.2358000	727.3019200	0.0013749	-0.0153291	0.0000004	

Real (λ)	Imag. (λ)	Freq. (cycles/mm)	Wavelength (mm)	Damping ratio	Contribution %	
-213.1078200	164.1464100	42.8120850	0.0233579	-0.7922334	28.9739880	Remark : al011
-213.1078200	-164.1464100	42.8120850	0.0233579	-0.7922334	28.9739880	orientation 11
-490.1321800	1692.8576000	280.4920800	0.0035652	-0.2781075	13.6802810	order :22
-490.1321800	-1692.8576000	280.4920800	0.0035652	-0.2781075	13.6802810	rotation : 300
-4.1426134	1257.8401000	200.1925600	0.0049952	-0.0032934	5.2871455	
-4.1426134	-1257.8401000	200.1925600	0.0049952	-0.0032934	5.2871455	
-5.8670781	1889.9714000	300.7997300	0.0033245	-0.0031043	0.8815940	
-5.8670781	-1889.9714000	300.7997300	0.0033245	-0.0031043	0.8815940	
-2.0157280	2516.5792000	400.5261500	0.0024967	-0.0008010	0.6519947	
-2.0157280	-2516.5792000	400.5261500	0.0024967	-0.0008010	0.6519947	
-497.9759200	2716.1094000	439.4875800	0.0022754	-0.1803358	0.4030529	
-497.9759200	-2716.1094000	439.4875800	0.0022754	-0.1803358	0.4030529	
-1.8025058	3146.0189000	500.7045400	0.0019972	-0.0005729	0.0634964	
-1.8025058	-3146.0189000	500.7045400	0.0019972	-0.0005729	0.0634964	
-0.2400855	629.8296100	100.2405000	0.0099760	-0.0003812	0.0544130	
-0.2400855	-629.8296100	100.2405000	0.0099760	-0.0003812	0.0544130	
-26.9054340	3780.2181000	601.6556300	0.0016621	-0.0071172	0.0037584	
-26.9054340	-3780.2181000	601.6556300	0.0016621	-0.0071172	0.0037584	
-591.0667600	4350.5527000	698.7730100	0.0014311	-0.1346234	0.0002678	
-591.0667600	-4350.5527000	698.7730100	0.0014311	-0.1346234	0.0002678	
-54.0784510	4411.9719000	702.2398800	0.0014240	-0.0122563	0.0000077	
-54.0784510	-4411.9719000	702.2398800	0.0014240	-0.0122563	0.0000077	

Real (λ)	Imag. (λ)	Freq. (cycles/mm)	Wavelength (mm)	Damping ratio	Contribution %	
-99.1258870	237.4781600	40.9562970	0.0244163	-0.3852002	25.9122150	Remark : al011
-99.1258870	-237.4781600	40.9562970	0.0244163	-0.3852002	25.9122150	orientation 12
-0.7318770	626.3301200	99.6836030	0.0100317	-0.0011685	13.0007120	order :22
-0.7318770	-626.3301200	99.6836030	0.0100317	-0.0011685	13.0007120	rotation : 330
-314.0594700	1577.5659000	256.0044500	0.0039062	-0.1952471	6.8919020	
-314.0594700	-1577.5659000	256.0044500	0.0039062	-0.1952471	6.8919020	
-6.3026469	1256.8847000	200.0419300	0.0049990	-0.0050144	2.7386566	
-6.3026469	-1256.8847000	200.0419300	0.0049990	-0.0050144	2.7386566	
-10.3699050	1873.5816000	298.1943400	0.0033535	-0.0055347	1.0096975	
-10.3699050	-1873.5816000	298.1943400	0.0033535	-0.0055347	1.0096975	
-4.9481174	2506.7829000	398.9676700	0.0025065	-0.0019739	0.2261240	
-4.9481174	-2506.7829000	398.9676700	0.0025065	-0.0019739	0.2261240	
-306.5924300	2848.2488000	455.9315600	0.0021933	-0.1070242	0.1620780	
-306.5924300	-2848.2488000	455.9315600	0.0021933	-0.1070242	0.1620780	
-9.5636742	3125.4378000	497.4312000	0.0020103	-0.0030599	0.0555562	
-9.5636742	-3125.4378000	497.4312000	0.0020103	-0.0030599	0.0555562	
-20.6842510	3756.8951000	597.9374900	0.0016724	-0.0055056	0.0029221	
-20.6842510	-3756.8951000	597.9374900	0.0016724	-0.0055056	0.0029221	
-355.1424400	4421.9417000	706.0400000	0.0014164	-0.0800559	0.0001361	
-355.1424400	-4421.9417000	706.0400000	0.0014164	-0.0800559	0.0001361	
-148.8646800	4600.2557000	732.5366800	0.0013651	-0.0323432	0.0000013	
-148.8646800	-4600.2557000	732.5366800	0.0013651	-0.0323432	0.0000013	

Specimen 5B(III)

Real (λ)	Imag. (λ)	Freq. (cycles/mm)	Wavelength (mm)	Damping ratio	Contribution %	
-56.88316500	60.63122600	13.23174000	0.07557585	-0.68420606	40.62846500	Remark : al6061
-56.88316500	-60.63122600	13.23174000	0.07557585	-0.68420606	40.62846500	orientation 1
-566.77831000	1532.09570000	259.99093000	0.00384629	-0.34695660	4.36303940	order 22
-566.77831000	-1532.09570000	259.99093000	0.00384629	-0.34695660	4.36303940	rotation : 0
-6.19241350	629.01875000	100.11629000	0.00998838	-0.00984408	3.62452320	
-6.19241350	-629.01875000	100.11629000	0.00998838	-0.00984408	3.62452320	
-0.64838677	1253.27570000	199.46505000	0.00501341	-0.00051735	1.09905540	
-0.64838677	-1253.27570000	199.46505000	0.00501341	-0.00051735	1.09905540	
0.71620940	1881.43720000	299.44005000	0.00333957	0.00038067	0.17869601	
0.71620940	-1881.43720000	299.44005000	0.00333957	0.00038067	0.17869601	
-545.33238000	2739.47250000	444.55531000	0.00224944	-0.19523407	0.08656366	
-545.33238000	-2739.47250000	444.55531000	0.00224944	-0.19523407	0.08656366	
0.88602964	2508.05280000	399.16903000	0.00250520	0.00035327	0.01707077	
0.88602964	-2508.05280000	399.16903000	0.00250520	0.00035327	0.01707077	
-98.48079400	3749.81240000	597.00695000	0.00167502	-0.02625381	0.00210170	
-98.48079400	-3749.81240000	597.00695000	0.00167502	-0.02625381	0.00210170	
-440.75551000	4302.29340000	688.31512000	0.00145282	-0.10191323	0.00027660	
-440.75551000	-4302.29340000	688.31512000	0.00145282	-0.10191323	0.00027660	
-37.29996600	3117.61630000	496.21956000	0.00201524	-0.01196340	0.00020781	
-37.29996600	-3117.61630000	496.21956000	0.00201524	-0.01196340	0.00020781	
-22.84641100	4598.75940000	731.92432000	0.00136626	-0.00496789	0.00000070	
-22.84641100	-4598.75940000	731.92432000	0.00136626	-0.00496789	0.00000070	

Real (λ)	Imag. (λ)	Freq. (cycles/mm)	Wavelength (mm)	Damping ratio	Contribution %	
-60.0775890	40.4185940	11.5241580	0.0867742	-0.8297044	28.7768400	Remark : al6061
-60.0775890	-40.4185940	11.5241580	0.0867742	-0.8297044	28.7768400	orientation 2
-4.2341480	630.6686400	100.3762900	0.0099625	-0.0067136	7.7802074	order 22
-4.2341480	-630.6686400	100.3762900	0.0099625	-0.0067136	7.7802074	rotation : 30
-407.1625300	1374.0774000	228.0901900	0.0043842	-0.2841066	6.3098258	
-407.1625300	-1374.0774000	228.0901900	0.0043842	-0.2841066	6.3098258	
-2.7123997	1255.1460000	199.7631500	0.0050059	-0.0021610	5.4228985	
-2.7123997	-1255.1460000	199.7631500	0.0050059	-0.0021610	5.4228985	
-1.3336331	1881.7067000	299.4830100	0.0033391	-0.0007087	1.3437300	
-1.3336331	-1881.7067000	299.4830100	0.0033391	-0.0007087	1.3437300	
-4.6912770	2507.7166000	399.1161900	0.0025055	-0.0018707	0.1904454	
-4.6912770	-2507.7166000	399.1161900	0.0025055	-0.0018707	0.1904454	
-529.1274300	2584.1290000	419.8101600	0.0023820	-0.2005984	0.1653669	
-529.1274300	-2584.1290000	419.8101600	0.0023820	-0.2005984	0.1653669	
-393.1595000	3571.7594000	571.8966500	0.0017486	-0.1094136	0.0103374	
-393.1595000	-3571.7594000	571.8966500	0.0017486	-0.1094136	0.0103374	
-48.2369450	3682.8216000	586.1895300	0.0017059	-0.0130967	0.0003302	
-48.2369450	-3682.8216000	586.1895300	0.0017059	-0.0130967	0.0003302	
-54.7575300	4171.1019000	663.9086800	0.0015062	-0.0131267	0.0000167	
-54.7575300	-4171.1019000	663.9086800	0.0015062	-0.0131267	0.0000167	
-215.6600900	4627.8768000	737.3487700	0.0013562	-0.0465497	0.0000018	
-215.6600900	-4627.8768000	737.3487700	0.0013562	-0.0465497	0.0000018	

Real (λ)	Imag. (λ)	Freq. (cycles/mm)	Wavelength (mm)	Damping ratio	Contribution %	
-32.3426660	0.0000000	5.1474952	0.1942692	-1.0000000	36.3380660	Remark : al6061
-281.8630600	0.0000000	44.8598990	0.0222916	-1.0000000	26.8322210	orientation 3
-0.5734924	1869.5252000	297.5441900	0.0033608	-0.0003068	7.1173932	order 22
-0.5734924	-1869.5252000	297.5441900	0.0033608	-0.0003068	7.1173932	rotation : 60
-413.3136500	1365.4469000	227.0552400	0.0044042	-0.2897133	6.3969324	
-413.3136500	-1365.4469000	227.0552400	0.0044042	-0.2897133	6.3969324	
0.5066724	621.8228000	98.9662060	0.0101045	0.0008148	4.6919076	
0.5066724	-621.8228000	98.9662060	0.0101045	0.0008148	4.6919076	
-373.8726900	2757.7973000	442.9321400	0.0022577	-0.1343404	0.1552479	
-373.8726900	-2757.7973000	442.9321400	0.0022577	-0.1343404	0.1552479	
-2.8522989	2489.5988000	396.2322200	0.0025238	-0.0011457	0.0272250	
-2.8522989	-2489.5988000	396.2322200	0.0025238	-0.0011457	0.0272250	
0.1190952	1245.9866000	198.3049300	0.0050427	0.0000956	0.0248086	
0.1190952	-1245.9866000	198.3049300	0.0050427	0.0000956	0.0248086	
-106.1136300	3793.1475000	603.9343600	0.0016558	-0.0279641	0.0007944	
-106.1136300	-3793.1475000	603.9343600	0.0016558	-0.0279641	0.0007944	
-16.0940060	3250.8672000	517.3979200	0.0019327	-0.0049506	0.0005085	
-16.0940060	-3250.8672000	517.3979200	0.0019327	-0.0049506	0.0005085	
-226.1565900	4281.4388000	682.3621300	0.0014655	-0.0527490	0.0000338	
-226.1565900	-4281.4388000	682.3621300	0.0014655	-0.0527490	0.0000338	
-99.4861390	4575.5210000	728.3889000	0.0013729	-0.0217380	0.0000052	
-99.4861390	-4575.5210000	728.3889000	0.0013729	-0.0217380	0.0000052	

Real (λ)	Imag. (λ)	Freq. (cycles/mm)	Wavelength (mm)	Damping ratio	Contribution %	
-254.1432000	0.0000000	40.4481470	0.0247230	-1.0000000	54.3791620	Remark : al6061
-51.9207610	0.0000000	8.2634458	0.1210149	-1.0000000	20.9994930	orientation 4
-547.9355800	1384.9276000	237.0424500	0.0042187	-0.3678947	5.9756305	order :22
-547.9355800	-1384.9276000	237.0424500	0.0042187	-0.3678947	5.9756305	rotation : 90
-3.1609429	626.3660400	99.6905210	0.0100310	-0.0050464	4.8009376	
-3.1609429	-626.3660400	99.6905210	0.0100310	-0.0050464	4.8009376	
0.4647700	1253.3978000	199.4844700	0.0050129	0.0003708	1.0767621	
0.4647700	-1253.3978000	199.4844700	0.0050129	0.0003708	1.0767621	
0.3178204	1881.6693000	299.4769800	0.0033392	0.0001689	0.3518450	
0.3178204	-1881.6693000	299.4769800	0.0033392	0.0001689	0.3518450	
-8.4345065	2517.2990000	400.6428300	0.0024960	-0.0033506	0.0657878	
-8.4345065	-2517.2990000	400.6428300	0.0024960	-0.0033506	0.0657878	
-411.8242000	2809.9839000	452.0002700	0.0022124	-0.1450084	0.0347607	
-411.8242000	-2809.9839000	452.0002700	0.0022124	-0.1450084	0.0347607	
-32.8792240	3137.5466000	499.3834700	0.0020025	-0.0104787	0.0038924	
-32.8792240	-3137.5466000	499.3834700	0.0020025	-0.0104787	0.0038924	
-24.1732470	3763.0934000	598.9272700	0.0016697	-0.0064236	0.0009265	
-24.1732470	-3763.0934000	598.9272700	0.0016697	-0.0064236	0.0009265	
-466.5239500	4394.4836000	703.3339600	0.0014218	-0.1055681	0.0001286	
-466.5239500	-4394.4836000	703.3339600	0.0014218	-0.1055681	0.0001286	
-65.8837300	4603.7692000	732.7876500	0.0013647	-0.0143094	0.0000010	
-65.8837300	-4603.7692000	732.7876500	0.0013647	-0.0143094	0.0000010	

Real (λ)	Imag. (λ)	Freq. (cycles/mm)	Wavelength (mm)	Damping ratio	Contribution %	
-105.1281400	0.0000000	16.7316630	0.0597669	-1.0000000	63.7525580	Remark : al6061
-0.9669118	1254.7451000	199.6989400	0.0050075	-0.0007706	7.4440606	orientation 5
-0.9669118	-1254.7451000	199.6989400	0.0050075	-0.0007706	7.4440606	order :22
-64.7781640	0.0000000	10.3097650	0.0969954	-1.0000000	6.8810747	rotation : 120
-453.3719100	1424.8058000	237.9681800	0.0042022	-0.3032186	4.0192764	
-453.3719100	-1424.8058000	237.9681800	0.0042022	-0.3032186	4.0192764	
-0.9719962	629.2734800	100.1521000	0.0099848	-0.0015446	1.6689841	
-0.9719962	-629.2734800	100.1521000	0.0099848	-0.0015446	1.6689841	
-3.0717528	1882.2451000	299.5690100	0.0033381	-0.0016320	1.3619493	
-3.0717528	-1882.2451000	299.5690100	0.0033381	-0.0016320	1.3619493	
-4.9416290	2509.5582000	399.4093700	0.0025037	-0.0019691	0.1086668	
-4.9416290	-2509.5582000	399.4093700	0.0025037	-0.0019691	0.1086668	
-323.9837300	2899.2476000	464.3017100	0.0021538	-0.1110563	0.0739204	
-323.9837300	-2899.2476000	464.3017100	0.0021538	-0.1110563	0.0739204	
-32.2298510	3229.9100000	514.0817400	0.0019452	-0.0099781	0.0057177	
-32.2298510	-3229.9100000	514.0817400	0.0019452	-0.0099781	0.0057177	
-6.2602138	3766.4784000	599.4544800	0.0016682	-0.0016621	0.0005707	
-6.2602138	-3766.4784000	599.4544800	0.0016682	-0.0016621	0.0005707	
-461.0933200	4590.0365000	734.2037100	0.0013620	-0.0999522	0.0000349	
-461.0933200	-4590.0365000	734.2037100	0.0013620	-0.0999522	0.0000349	
-29.1643090	4424.8425000	704.2508500	0.0014199	-0.0065909	0.0000029	
-29.1643090	-4424.8425000	704.2508500	0.0014199	-0.0065909	0.0000029	

Real (λ)	Imag. (λ)	Freq. (cycles/mm)	Wavelength (mm)	Damping ratio	Contribution %	
-226.850350	0.000000	36.104355	0.027697	-1.000000	51.817907	Remark : al6061
-40.237437	0.000000	6.403987	0.156153	-1.000000	20.266097	orientation 6
-0.803017	1240.671300	197.459010	0.005064	-0.000647	4.602883	order :22
-0.803017	-1240.671300	197.459010	0.005064	-0.000647	4.602883	rotation : 150
-591.445140	1390.284800	240.460910	0.004159	-0.391462	4.355143	
-591.445140	-1390.284800	240.460910	0.004159	-0.391462	4.355143	
-2.212763	620.077440	98.689018	0.010133	-0.003569	3.303028	
-2.212763	-620.077440	98.689018	0.010133	-0.003569	3.303028	
-2.963902	1861.075900	296.199810	0.003376	-0.001593	1.489494	
-2.963902	-1861.075900	296.199810	0.003376	-0.001593	1.489494	
-1.351207	2482.575700	395.114250	0.002531	-0.000544	0.120353	
-1.351207	-2482.575700	395.114250	0.002531	-0.000544	0.120353	
-552.925400	2746.856900	445.944920	0.002242	-0.197336	0.085659	
-552.925400	-2746.856900	445.944920	0.002242	-0.197336	0.085659	
-55.426908	3751.837800	597.188680	0.001675	-0.014772	0.000943	
-55.426908	-3751.837800	597.188680	0.001675	-0.014772	0.000943	
-2.313602	3139.256300	499.628290	0.002001	-0.000737	0.000261	
-2.313602	-3139.256300	499.628290	0.002001	-0.000737	0.000261	
-438.822370	4316.256300	690.494660	0.001448	-0.101146	0.000219	
-438.822370	-4316.256300	690.494660	0.001448	-0.101146	0.000219	
-102.853570	4427.883900	704.909710	0.001419	-0.023222	0.000015	
-102.853570	-4427.883900	704.909710	0.001419	-0.023222	0.000015	

Real (λ)	Imag. (λ)	Freq. (cycles/mm)	Wavelength (mm)	Damping ratio	Contribution %	
-69.8417430	0.0000000	11.1156590	0.0899632	-1.0000000	52.4943870	Remark : al6061
-50.7978830	0.0000000	8.0847341	0.1236899	-1.0000000	37.7971240	orientation 7
-5.4048591	1235.0577000	196.5674200	0.0050873	-0.0043762	2.1491894	order :22
-5.4048591	-1235.0577000	196.5674200	0.0050873	-0.0043762	2.1491894	rotation : 180
-317.1313600	1456.7599000	237.2808400	0.0042144	-0.2127143	1.2612632	
-317.1313600	-1456.7599000	237.2808400	0.0042144	-0.2127143	1.2612632	
-1.9039608	618.5617900	98.4476330	0.0101577	-0.0030780	0.7502349	
-1.9039608	-618.5617900	98.4476330	0.0101577	-0.0030780	0.7502349	
-8.7558766	1845.6611000	293.7494000	0.0034043	-0.0047440	0.6604157	
-8.7558766	-1845.6611000	293.7494000	0.0034043	-0.0047440	0.6604157	
-7.9386594	2479.3024000	394.5952600	0.0025342	-0.0032020	0.0267707	
-7.9386594	-2479.3024000	394.5952600	0.0025342	-0.0032020	0.0267707	
-433.9111500	2972.4960000	478.1013300	0.0020916	-0.1444445	0.0054014	
-433.9111500	-2972.4960000	478.1013300	0.0020916	-0.1444445	0.0054014	
-21.9711040	3135.1056000	498.9798000	0.0020041	-0.0070079	0.0007473	
-21.9711040	-3135.1056000	498.9798000	0.0020041	-0.0070079	0.0007473	
-123.5192400	3737.5284000	595.1708700	0.0016802	-0.0330303	0.0002149	
-123.5192400	-3737.5284000	595.1708700	0.0016802	-0.0330303	0.0002149	
-481.3677900	4599.6212000	736.0504100	0.0013586	-0.1040854	0.0000059	
-481.3677900	-4599.6212000	736.0504100	0.0013586	-0.1040854	0.0000059	
-90.4988550	4410.0302000	702.0258800	0.0014244	-0.0205168	0.0000014	
-90.4988550	-4410.0302000	702.0258800	0.0014244	-0.0205168	0.0000014	

Real (λ)	Imag. (λ)	Freq. (cycles/mm)	Wavelength (mm)	Damping ratio	Contribution %	
-57.6049520	31.5113090	10.4501830	0.0956921	-0.8773160	21.5575880	Remark : al6061
-57.6049520	-31.5113090	10.4501830	0.0956921	-0.8773160	21.5575880	orientation 8
-0.1801425	628.0512200	99.9574600	0.0100043	-0.0002868	16.8350270	order :22
-0.1801425	-628.0512200	99.9574600	0.0100043	-0.0002868	16.8350270	rotation : 210
-490.9333700	1138.3586000	197.3056600	0.0050683	-0.3960073	5.1109696	
-490.9333700	-1138.3586000	197.3056600	0.0050683	-0.3960073	5.1109696	
-1.6995211	1254.6449000	199.6831200	0.0050079	-0.0013546	4.6044217	
-1.6995211	-1254.6449000	199.6831200	0.0050079	-0.0013546	4.6044217	
-1.6728212	1882.7478000	299.6487300	0.0033372	-0.0008885	1.6252325	
-1.6728212	-1882.7478000	299.6487300	0.0033372	-0.0008885	1.6252325	
-816.4885500	2364.9113000	398.1883300	0.0025114	-0.3263486	0.1682806	
-816.4885500	-2364.9113000	398.1883300	0.0025114	-0.3263486	0.1682806	
-2.8284125	2511.1288000	399.6588100	0.0025021	-0.0011264	0.0748624	
-2.8284125	-2511.1288000	399.6588100	0.0025021	-0.0011264	0.0748624	
-509.9417200	3339.6932000	537.6891600	0.0018598	-0.1509418	0.0228891	
-509.9417200	-3339.6932000	537.6891600	0.0018598	-0.1509418	0.0228891	
-2.5576984	3759.4083000	598.3285600	0.0016713	-0.0006803	0.0006671	
-2.5576984	-3759.4083000	598.3285600	0.0016713	-0.0006803	0.0006671	
-446.0357400	4387.3023000	701.8601100	0.0014248	-0.1011438	0.0000616	
-446.0357400	-4387.3023000	701.8601100	0.0014248	-0.1011438	0.0000616	
-20.6077360	4424.5253000	704.1927200	0.0014201	-0.0046576	0.0000004	
-20.6077360	-4424.5253000	704.1927200	0.0014201	-0.0046576	0.0000004	

Real (λ)	Imag. (λ)	Freq. (cycles/mm)	Wavelength (mm)	Damping ratio	Contribution %	
-91.344433	0.000000	14.537918	0.068786	-1.000000	28.111313	Remark : al6061
-226.862720	0.000000	36.106323	0.027696	-1.000000	27.560990	orientation 9
-1.390359	1236.352700	196.771760	0.005082	-0.001125	9.023886	order :22
-1.390359	-1236.352700	196.771760	0.005082	-0.001125	9.023886	rotation : 240
-375.431310	1268.006900	210.469410	0.004751	-0.283898	5.843999	
-375.431310	-1268.006900	210.469410	0.004751	-0.283898	5.843999	
-0.862221	618.264970	98.400022	0.010163	-0.001395	4.581435	
-0.862221	-618.264970	98.400022	0.010163	-0.001395	4.581435	
-4.382477	1852.774400	294.879030	0.003391	-0.002365	2.504086	
-4.382477	-1852.774400	294.879030	0.003391	-0.002365	2.504086	
-7.448200	2479.873700	394.685930	0.002534	-0.003003	0.126726	
-7.448200	-2479.873700	394.685930	0.002534	-0.003003	0.126726	
-390.060340	2819.276500	452.975970	0.002208	-0.137049	0.082162	
-390.060340	-2819.276500	452.975970	0.002208	-0.137049	0.082162	
-180.133470	3797.634400	605.091840	0.001653	-0.047380	0.000842	
-180.133470	-3797.634400	605.091840	0.001653	-0.047380	0.000842	
-8.176624	3213.682000	511.475030	0.001955	-0.002544	0.000694	
-8.176624	-3213.682000	511.475030	0.001955	-0.002544	0.000694	
-3.683143	4338.469000	690.489030	0.001448	-0.000849	0.000015	
-3.683143	-4338.469000	690.489030	0.001448	-0.000849	0.000015	
-312.602240	4735.917700	755.384910	0.001324	-0.065863	0.000003	
-312.602240	-4735.917700	755.384910	0.001324	-0.065863	0.000003	

Real (λ)	Imag. (λ)	Freq. (cycles/mm)	Wavelength (mm)	Damping ratio	Contribution %	
-67.0027170	27.4274920	11.5226770	0.0867854	-0.9254633	28.5427250	Remark : al6061
-67.0027170	-27.4274920	11.5226770	0.0867854	-0.9254633	28.5427250	orientation 10
-2.5385075	1237.1612000	196.9007400	0.0050787	-0.0020519	9.3944008	order :22
-2.5385075	-1237.1612000	196.9007400	0.0050787	-0.0020519	9.3944008	rotation : 270
-3.1536936	616.7369900	98.1580230	0.0101877	-0.0051134	5.1152886	
-3.1536936	-616.7369900	98.1580230	0.0101877	-0.0051134	5.1152886	
-474.6757700	1422.1436000	238.6161700	0.0041908	-0.3166047	3.9742038	
-474.6757700	-1422.1436000	238.6161700	0.0041908	-0.3166047	3.9742038	
-4.7778694	1848.9687000	294.2734900	0.0033982	-0.0025841	2.4785156	
-4.7778694	-1848.9687000	294.2734900	0.0033982	-0.0025841	2.4785156	
-880.2052200	2431.2512000	411.5238300	0.0024300	-0.3404153	0.2638690	
-880.2052200	-2431.2512000	411.5238300	0.0024300	-0.3404153	0.2638690	
-45.4116890	2458.1037000	391.2861100	0.0025557	-0.0184711	0.2251793	
-45.4116890	-2458.1037000	391.2861100	0.0025557	-0.0184711	0.2251793	
-306.4774500	3168.6247000	506.6557200	0.0019737	-0.0962733	0.0043632	
-306.4774500	-3168.6247000	506.6557200	0.0019737	-0.0962733	0.0043632	
-27.9092420	3711.0872000	590.6545800	0.0016930	-0.0075203	0.0013187	
-27.9092420	-3711.0872000	590.6545800	0.0016930	-0.0075203	0.0013187	
-440.5540000	4340.4336000	694.3507500	0.0014402	-0.1009812	0.0001280	
-440.5540000	-4340.4336000	694.3507500	0.0014402	-0.1009812	0.0001280	
-73.5070910	4410.3542000	702.0271600	0.0014244	-0.0166646	0.0000082	
-73.5070910	-4410.3542000	702.0271600	0.0014244	-0.0166646	0.0000082	

Real (λ)	Imag. (λ)	Freq. (cycles/mm)	Wavelength (mm)	Damping ratio	Contribution %	
-46.7947760	0.0000000	7.4476199	0.1342711	-1.0000000	45.1068420	Remark : al6061
-365.0783200	0.0000000	58.1040190	0.0172105	-1.0000000	14.0002330	orientation 11
-3.6755858	1230.9662000	195.9152400	0.0051042	-0.0029859	8.1324813	order :22
-3.6755858	-1230.9662000	195.9152400	0.0051042	-0.0029859	8.1324813	rotation : 300
-2.4961816	613.5928200	97.6571380	0.0102399	-0.0040681	4.7653109	
-2.4961816	-613.5928200	97.6571380	0.0102399	-0.0040681	4.7653109	
-454.7766200	1306.9259000	220.2371500	0.0045406	-0.3286455	4.1360467	
-454.7766200	-1306.9259000	220.2371500	0.0045406	-0.3286455	4.1360467	
-7.9617715	1837.4625000	292.4439800	0.0034195	-0.0043330	3.1126169	
-7.9617715	-1837.4625000	292.4439800	0.0034195	-0.0043330	3.1126169	
-38.6363350	2485.5672000	395.6381000	0.0025276	-0.0155424	0.1455994	
-38.6363350	-2485.5672000	395.6381000	0.0025276	-0.0155424	0.1455994	
-275.9197100	2727.8468000	436.3655900	0.0022917	-0.1006358	0.1343827	
-275.9197100	-2727.8468000	436.3655900	0.0022917	-0.1006358	0.1343827	
-178.1128100	3225.6629000	514.1622400	0.0019449	-0.0551334	0.0187985	
-178.1128100	-3225.6629000	514.1622400	0.0019449	-0.0551334	0.0187985	
-25.8287190	3695.9222000	588.2386600	0.0017000	-0.0069883	0.0012177	
-25.8287190	-3695.9222000	588.2386600	0.0017000	-0.0069883	0.0012177	
-125.8681600	4319.6673000	687.7882000	0.0014539	-0.0291260	0.0000064	
-125.8681600	-4319.6673000	687.7882000	0.0014539	-0.0291260	0.0000064	
-229.7091100	4633.4916000	738.3487600	0.0013544	-0.0495150	0.0000020	
-229.7091100	-4633.4916000	738.3487600	0.0013544	-0.0495150	0.0000020	

Real (λ)	Imag. (λ)	Freq. (cycles/mm)	Wavelength (mm)	Damping ratio	Contribution %	
-79.06882300	0.00000000	12.58419400	0.07946476	-1.00000000	57.68055400	Remark : al6061
-101.57054000	0.00000000	16.16545400	0.06186031	-1.00000000	8.13350290	orientation 12
-1.85617360	1231.15880000	195.94524000	0.00510347	-0.00150766	6.80570010	order :22
-1.85617360	-1231.15880000	195.94524000	0.00510347	-0.00150766	6.80570010	rotation : 330
-3.60601150	615.49218000	97.96030400	0.01020822	-0.00585864	5.72992670	
-3.60601150	-615.49218000	97.96030400	0.01020822	-0.00585864	5.72992670	
-355.60408000	1355.80950000	223.08242000	0.00448265	-0.25370061	2.87065040	
-355.60408000	-1355.80950000	223.08242000	0.00448265	-0.25370061	2.87065040	
-7.43937560	1839.84550000	292.82291000	0.00341503	-0.00404345	1.50944660	
-7.43937560	-1839.84550000	292.82291000	0.00341503	-0.00404345	1.50944660	
-8.36296160	2454.71080000	390.68162000	0.00255963	-0.00340688	0.09796587	
-8.36296160	-2454.71080000	390.68162000	0.00255963	-0.00340688	0.09796587	
-375.60269000	2630.44740000	422.89510000	0.00236465	-0.14135663	0.07483567	
-375.60269000	-2630.44740000	422.89510000	0.00236465	-0.14135663	0.07483567	
-169.92417000	3419.25490000	544.86290000	0.00183532	-0.04963500	0.00332487	
-169.92417000	-3419.25490000	544.86290000	0.00183532	-0.04963500	0.00332487	
-28.64680900	3683.29180000	586.23182000	0.00170581	-0.00777727	0.00110212	
-28.64680900	-3683.29180000	586.23182000	0.00170581	-0.00777727	0.00110212	
-69.02843500	4330.44290000	689.29894000	0.00145075	-0.01593825	0.00001878	
-69.02843500	-4330.44290000	689.29894000	0.00145075	-0.01593825	0.00001878	
-235.18000000	4660.55670000	742.69443000	0.00134645	-0.05039766	0.00000020	
-235.18000000	-4660.55670000	742.69443000	0.00134645	-0.05039766	0.00000020	

Specimen 5B(IV)

Real (λ)	Imag. (λ)	Freq. (cycles/mm)	Wavelength (mm)	Damping ratio	Contribution %	
-1.766053	627.245370	99.829596	0.010017	-0.002816	44.262525	order 22
-1.766053	-627.245370	99.829596	0.010017	-0.002816	44.262525	rotation : 0
-5.265369	1253.660800	199.528080	0.005012	-0.004200	4.506383	Remark : Cu001
-5.265369	-1253.660800	199.528080	0.005012	-0.004200	4.506383	orientation 1
-124.474980	0.000000	19.810809	0.050477	-1.000000	1.196633	
-71.752041	1882.715800	299.861050	0.003335	-0.038083	0.488985	
-71.752041	-1882.715800	299.861050	0.003335	-0.038083	0.488985	
-6.138781	2508.185000	399.191240	0.002505	-0.002447	0.135015	
-6.138781	-2508.185000	399.191240	0.002505	-0.002447	0.135015	
-121.332170	3180.119500	506.499990	0.001974	-0.038126	0.008704	
-121.332170	-3180.119500	506.499990	0.001974	-0.038126	0.008704	
-121.035040	4104.791600	653.581810	0.001530	-0.029473	0.000070	
-121.035040	-4104.791600	653.581810	0.001530	-0.029473	0.000070	
-2607.547400	6263.143200	1079.749500	0.000926	-0.384352	0.000006	

Real (λ)	Imag. (λ)	Freq. (cycles/mm)	Wavelength (mm)	Damping ratio	Contribution %	
-6.549862	625.054870	99.486035	0.010052	-0.010478	44.582098	Remark : Cu001
-6.549862	-625.054870	99.486035	0.010052	-0.010478	44.582098	orientation 2
-3.824825	1253.336000	199.475550	0.005013	-0.003052	4.929736	order 22
-3.824825	-1253.336000	199.475550	0.005013	-0.003052	4.929736	rotation : 30
-30.889756	1876.238500	298.653100	0.003348	-0.016461	0.410527	
-30.889756	-1876.238500	298.653100	0.003348	-0.016461	0.410527	
-0.702816	2508.311300	399.210160	0.002505	-0.000280	0.053567	
-0.702816	-2508.311300	399.210160	0.002505	-0.000280	0.053567	
-1134.034500	2572.765800	447.481830	0.002235	-0.403340	0.020928	
-1134.034500	-2572.765800	447.481830	0.002235	-0.403340	0.020928	
-424.187260	3384.746500	542.913030	0.001842	-0.124350	0.002929	
-424.187260	-3384.746500	542.913030	0.001842	-0.124350	0.002929	
-272.580010	3815.865100	608.861290	0.001642	-0.071252	0.000214	
-272.580010	-3815.865100	608.861290	0.001642	-0.071252	0.000214	

Real (λ)	Imag. (λ)	Freq. (cycles/mm)	Wavelength (mm)	Damping ratio	Contribution %	
-2.16096	642.16634	102.20453	0.00978	-0.00337	43.205559	Remark : Cu001
-2.16096	-642.16634	102.20453	0.00978	-0.00337	43.205559	orientation 3
-3.85439	1284.31190	204.40550	0.00489	-0.00300	5.468482	order 22
-3.85439	-1284.31190	204.40550	0.00489	-0.00300	5.468482	rotation : 60
-78.38851	0.00000	12.47592	0.08015	-1.00000	1.511804	
-34.54951	1924.89430	306.40579	0.00326	-0.01795	0.407581	
-34.54951	-1924.89430	306.40579	0.00326	-0.01795	0.407581	
-10.06431	2563.66430	408.02298	0.00245	-0.00393	0.154681	
-10.06431	-2563.66430	408.02298	0.00245	-0.00393	0.154681	
-77.53112	3185.63520	507.15973	0.00197	-0.02433	0.007685	
-77.53112	-3185.63520	507.15973	0.00197	-0.02433	0.007685	
-76.03671	4253.04060	677.00061	0.00148	-0.01788	0.000109	
-76.03671	-4253.04060	677.00061	0.00148	-0.01788	0.000109	
-2524.68210	6404.87800	1095.70380	0.00091	-0.36672	0.000002	

Real (λ)	Imag. (λ)	Freq. (cycles/mm)	Wavelength (mm)	Damping ratio	Contribution %	
-3.548164	617.817360	98.330308	0.010170	-0.005743	40.557555	Remark : Cu001
-3.548164	-617.817360	98.330308	0.010170	-0.005743	40.557555	orientation 4
-4.649239	1238.864600	197.172820	0.005072	-0.003753	6.985002	order :22
-4.649239	-1238.864600	197.172820	0.005072	-0.003753	6.985002	rotation : 90
-100.334310	0.000000	15.968702	0.062622	-1.000000	2.822121	
-21.884716	1862.434000	296.436040	0.003373	-0.011750	0.745155	
-21.884716	-1862.434000	296.436040	0.003373	-0.011750	0.745155	
-7.683405	2485.036600	395.507740	0.002528	-0.003092	0.293012	
-7.683405	-2485.036600	395.507740	0.002528	-0.003092	0.293012	
-121.583390	3125.766600	497.857410	0.002009	-0.038868	0.008132	
-121.583390	-3125.766600	497.857410	0.002009	-0.038868	0.008132	
-6647.180100	6197.657600	1446.437100	0.000691	-0.731405	0.000097	
-103.719540	4236.586600	674.475730	0.001483	-0.024475	0.000035	
-103.719540	-4236.586600	674.475730	0.001483	-0.024475	0.000035	

Real (λ)	Imag. (λ)	Freq. (cycles/mm)	Wavelength (mm)	Damping ratio	Contribution %	
-1.829917	630.628880	100.368130	0.009963	-0.002902	43.8324740	Remark : Cu001
-1.829917	-630.628880	100.368130	0.009963	-0.002902	43.8324740	orientation 5
-4.595075	1260.405100	200.601030	0.004985	-0.003646	4.8070201	order :22
-4.595075	-1260.405100	200.601030	0.004985	-0.003646	4.8070201	rotation : 120
-72.715347	0.000000	11.573007	0.086408	-1.000000	1.8060975	
-65.354285	1891.005500	301.142570	0.003321	-0.034540	0.3600472	
-65.354285	-1891.005500	301.142570	0.003321	-0.034540	0.3600472	
-6.167991	2517.064500	400.604460	0.002496	-0.002450	0.0888284	
-6.167991	-2517.064500	400.604460	0.002496	-0.002450	0.0888284	
-131.046580	3107.172800	494.961540	0.002020	-0.042138	0.0085673	
-131.046580	-3107.172800	494.961540	0.002020	-0.042138	0.0085673	
-4578.054900	6283.185300	1237.290300	0.000808	-0.588884	0.0000120	
-191.831760	4251.386000	677.317550	0.001476	-0.045076	0.0000082	
-191.831760	-4251.386000	677.317550	0.001476	-0.045076	0.0000082	

Real (λ)	Imag. (λ)	Freq. (cycles/mm)	Wavelength (mm)	Damping ratio	Contribution %	
0.512702	632.714380	100.699650	0.009931	0.000810	47.705663	Remark : Cu001
0.512702	-632.714380	100.699650	0.009931	0.000810	47.705663	orientation 6
-3.942144	1264.897700	201.315690	0.004967	-0.003117	1.858321	order :22
-3.942144	-1264.897700	201.315690	0.004967	-0.003117	1.858321	rotation : 150
-135.507850	0.000000	21.566744	0.046368	-1.000000	0.527616	
-33.824497	1906.358300	303.454110	0.003295	-0.017740	0.139275	
-33.824497	-1906.358300	303.454110	0.003295	-0.017740	0.139275	
-13.252392	2529.368200	402.566980	0.002484	-0.005239	0.031918	
-13.252392	-2529.368200	402.566980	0.002484	-0.005239	0.031918	
-170.936580	3249.888500	517.950800	0.001931	-0.052525	0.000966	
-170.936580	-3249.888500	517.950800	0.001931	-0.052525	0.000966	
-4855.701100	0.000000	772.808840	0.001294	-1.000000	0.000088	
-97.373332	4296.744600	684.023730	0.001462	-0.022656	0.000005	
-97.373332	-4296.744600	684.023730	0.001462	-0.022656	0.000005	

Real (λ)	Imag. (λ)	Freq. (cycles/mm)	Wavelength (mm)	Damping ratio	Contribution %	
-1.593096	631.130170	100.447810	0.009955	-0.002524	45.3417980	Remark : Cu001
-1.593096	-631.130170	100.447810	0.009955	-0.002524	45.3417980	orientation 7
-4.377967	1259.270700	200.420370	0.004990	-0.003477	3.6078834	order :22
-4.377967	-1259.270700	200.420370	0.004990	-0.003477	3.6078834	rotation : 180
-129.703350	0.000000	20.642929	0.048443	-1.000000	1.1727730	
-77.616653	1895.926500	301.998820	0.003311	-0.040904	0.3723657	
-77.616653	-1895.926500	301.998820	0.003311	-0.040904	0.3723657	
-9.174674	2516.366300	400.494800	0.002497	-0.003646	0.0851885	
-9.174674	-2516.366300	400.494800	0.002497	-0.003646	0.0851885	
-115.351710	3192.206700	508.387070	0.001967	-0.036112	0.0062959	
-115.351710	-3192.206700	508.387070	0.001967	-0.036112	0.0062959	
-147.993390	4035.976300	642.777270	0.001556	-0.036644	0.0000788	
-147.993390	-4035.976300	642.777270	0.001556	-0.036644	0.0000788	
-2486.394600	6283.185300	1075.451500	0.000930	-0.367959	0.0000059	

Real (λ)	Imag. (λ)	Freq. (cycles/mm)	Wavelength (mm)	Damping ratio	Contribution %	
-1.627620	627.689360	99.900199	0.010010	-0.002593	44.294117	Remark : Cu001
-1.627620	-627.689360	99.900199	0.010010	-0.002593	44.294117	orientation 8
-4.068826	1256.985700	200.056540	0.004999	-0.003237	4.272425	order :22
-4.068826	-1256.985700	200.056540	0.004999	-0.003237	4.272425	rotation : 210
-102.052260	0.000000	16.242122	0.061568	-1.000000	1.984425	
-49.471570	1892.978700	301.379790	0.003318	-0.026125	0.362571	
-49.471570	-1892.978700	301.379790	0.003318	-0.026125	0.362571	
-7.519266	2513.733500	400.074900	0.002500	-0.002991	0.074855	
-7.519266	-2513.733500	400.074900	0.002500	-0.002991	0.074855	
-152.154620	3200.742900	509.989310	0.001961	-0.047484	0.003736	
-152.154620	-3200.742900	509.989310	0.001961	-0.047484	0.003736	
-6174.405800	6276.908400	1401.312600	0.000714	-0.701262	0.000133	
-137.824350	4212.079700	670.732090	0.001491	-0.032704	0.000016	
-137.824350	-4212.079700	670.732090	0.001491	-0.032704	0.000016	

Real (λ)	Imag. (λ)	Freq. (cycles/mm)	Wavelength (mm)	Damping ratio	Contribution %	
-1.8547374	628.9811200	100.1058900	0.0099894	-0.0029488	41.2540730	Remark : Cu001
-1.8547374	-628.9811200	100.1058900	0.0099894	-0.0029488	41.2540730	orientation 9
-3.3054435	1261.1043000	200.7116600	0.0049823	-0.0026211	6.9009046	order :22
-3.3054435	-1261.1043000	200.7116600	0.0049823	-0.0026211	6.9009046	rotation : 240
-88.8584020	0.0000000	14.1422540	0.0707101	-1.0000000	2.9905186	
-23.5512930	1909.4716000	303.9249600	0.0032903	-0.0123330	0.3016666	
-23.5512930	-1909.4716000	303.9249600	0.0032903	-0.0123330	0.3016666	
-86.9448710	2583.3511000	411.3858900	0.0024308	-0.0336368	0.0355136	
-86.9448710	-2583.3511000	411.3858900	0.0024308	-0.0336368	0.0355136	
-20.9780970	3151.4350000	501.5775600	0.0019937	-0.0066565	0.0124352	
-20.9780970	-3151.4350000	501.5775600	0.0019937	-0.0066565	0.0124352	
-109.3424600	4088.1122000	650.8759400	0.0015364	-0.0267369	0.0001468	
-109.3424600	-4088.1122000	650.8759400	0.0015364	-0.0267369	0.0001468	
-2410.9468000	6283.1853000	1071.0913000	0.0009336	-0.3582459	0.0000014	

Real (λ)	Imag. (λ)	Freq. (cycles/mm)	Wavelength (mm)	Damping ratio	Contribution %	
-2.5750159	625.0712900	99.4840300	0.0100519	-0.0041195	41.7266870	Remark : Cu001
-2.5750159	-625.0712900	99.4840300	0.0100519	-0.0041195	41.7266870	orientation 10
-3.1224561	1252.9080000	199.4071300	0.0050149	-0.0024922	6.6176539	order :22
-3.1224561	-1252.9080000	199.4071300	0.0050149	-0.0024922	6.6176539	rotation : 270
-98.2922330	0.0000000	15.6436950	0.0639235	-1.0000000	1.3698342	
-38.9302020	1892.0992000	301.2006800	0.0033200	-0.0205708	0.7258475	
-38.9302020	-1892.0992000	301.2006800	0.0033200	-0.0205708	0.7258475	
-5.1424465	2511.1212000	399.6581800	0.0025021	-0.0020479	0.2340343	
-5.1424465	-2511.1212000	399.6581800	0.0025021	-0.0020479	0.2340343	
-132.4564000	3152.6762000	502.2066500	0.0019912	-0.0419769	0.0108270	
-132.4564000	-3152.6762000	502.2066500	0.0019912	-0.0419769	0.0108270	
-98.6928930	4287.1093000	682.4954100	0.0014652	-0.0230148	0.0000320	
-98.6928930	-4287.1093000	682.4954100	0.0014652	-0.0230148	0.0000320	
-2911.0695000	6283.1853000	1102.1149000	0.0009073	-0.4203837	0.0000023	

Real (λ)	Imag. (λ)	Freq. (cycles/mm)	Wavelength (mm)	Damping ratio	Contribution %	
-0.50639531	628.10154000	99.96549800	0.01000345	-0.00080623	42.89359300	Remark : Cu001
-0.50639531	-628.10154000	99.96549800	0.01000345	-0.00080623	42.89359300	orientation 11
-1.95161370	1257.02280000	200.06163000	0.00499846	-0.00155257	6.51965640	order :22
-1.95161370	-1257.02280000	200.06163000	0.00499846	-0.00155257	6.51965640	rotation : 300
-89.40983600	0.00000000	14.23001700	0.07027398	-1.00000000	0.49504703	
-23.13567400	1882.70950000	299.66515000	0.00333706	-0.01228757	0.26122223	
-23.13567400	-1882.70950000	299.66515000	0.00333706	-0.01228757	0.26122223	
-10.74949100	2506.45940000	398.91908000	0.00250677	-0.00428868	0.07276549	
-10.74949100	-2506.45940000	398.91908000	0.00250677	-0.00428868	0.07276549	
-72.37275500	3129.00990000	498.13059000	0.00200751	-0.02312342	0.00520878	
-72.37275500	-3129.00990000	498.13059000	0.00200751	-0.02312342	0.00520878	
-124.54812000	4159.76530000	662.34389000	0.00150979	-0.02992773	0.00003056	
-124.54812000	-4159.76530000	662.34389000	0.00150979	-0.02992773	0.00003056	
-1997.48960000	6276.90840000	1048.36540000	0.00095387	-0.30324384	0.00000022	

Real (λ)	Imag. (λ)	Freq. (cycles/mm)	Wavelength (mm)	Damping ratio	Contribution %	
-0.2351871	612.6482000	97.5059970	0.0102558	-0.0003839	47.3080230	Remark : Cu001
-0.2351871	-612.6482000	97.5059970	0.0102558	-0.0003839	47.3080230	orientation 12
-2.3122672	1228.5738000	195.5339400	0.0051142	-0.0018821	2.3750788	order :22
-2.3122672	-1228.5738000	195.5339400	0.0051142	-0.0018821	2.3750788	rotation : 330
-85.7417770	0.0000000	13.6462280	0.0732803	-1.0000000	0.2772843	
-21.0174880	1852.8978000	294.9168200	0.0033908	-0.0113423	0.1368090	
-21.0174880	-1852.8978000	294.9168200	0.0033908	-0.0113423	0.1368090	
-11.9010900	2456.4501000	390.9607700	0.0025578	-0.0048448	0.0399800	
-11.9010900	-2456.4501000	390.9607700	0.0025578	-0.0048448	0.0399800	
-110.8116200	3140.9116000	500.2026100	0.0019992	-0.0352581	0.0014574	
-110.8116200	-3140.9116000	500.2026100	0.0019992	-0.0352581	0.0014574	
-144.7425300	4104.2258000	653.6139100	0.0015300	-0.0352448	0.0000099	
-144.7425300	-4104.2258000	653.6139100	0.0015300	-0.0352448	0.0000099	
-2375.8925000	6149.1342000	1049.1766000	0.0009531	-0.3604113	0.0000004	

Specimen 5B(V)

Real (λ)	Imag. (λ)	Freq. (cycles/mm)	Wavelength (mm)	Damping ratio	Contribution %	
-0.9390642	630.9243400	100.4148400	0.0099587	-0.0014884	39.4592270	order 22
-0.9390642	-630.9243400	100.4148400	0.0099587	-0.0014884	39.4592270	rotation : 0
-6.9798271	1262.0747000	200.8684900	0.0049784	-0.0055304	8.8357011	Remark : Cu011
-6.9798271	-1262.0747000	200.8684900	0.0049784	-0.0055304	8.8357011	orientation 1
-110.1641400	0.0000000	17.5331670	0.0570348	-1.0000000	2.0532732	
-5.8105075	1890.9419000	300.9541600	0.0033228	-0.0030728	0.5044092	
-5.8105075	-1890.9419000	300.9541600	0.0033228	-0.0030728	0.5044092	
-0.0649234	3155.5098000	502.2149900	0.0019912	-0.0000206	0.1002990	
-0.0649234	-3155.5098000	502.2149900	0.0019912	-0.0000206	0.1002990	
-144.5639900	2633.6175000	419.7842500	0.0023822	-0.0548093	0.0732794	
-144.5639900	-2633.6175000	419.7842500	0.0023822	-0.0548093	0.0732794	
-100.7392900	4057.2740000	645.9342300	0.0015481	-0.0248217	0.0004466	
-100.7392900	-4057.2740000	645.9342300	0.0015481	-0.0248217	0.0004466	
-2044.9174000	6295.7769000	1053.5347000	0.0009492	-0.3089207	0.0000015	

Real (λ)	Imag. (λ)	Freq. (cycles/mm)	Wavelength (mm)	Damping ratio	Contribution %	
-0.2474857	625.9668700	99.6257290	0.0100376	-0.0003954	45.7110760	Remark : Cu011
-0.2474857	-625.9668700	99.6257290	0.0100376	-0.0003954	45.7110760	orientation 2
-15.0358060	1255.5046000	199.8341000	0.0050042	-0.0119750	3.3231223	order 22
-15.0358060	-1255.5046000	199.8341000	0.0050042	-0.0119750	3.3231223	rotation : 30
-120.5798000	0.0000000	19.1908710	0.0521081	-1.0000000	1.5071995	
-8.6181422	1885.2886000	300.0561400	0.0033327	-0.0045712	0.1653608	
-8.6181422	-1885.2886000	300.0561400	0.0033327	-0.0045712	0.1653608	
-153.4038100	2626.5670000	418.7434900	0.0023881	-0.0583053	0.0365354	
-153.4038100	-2626.5670000	418.7434900	0.0023881	-0.0583053	0.0365354	
-0.4730989	3129.8259000	498.1272600	0.0020075	-0.0001512	0.0101831	
-0.4730989	-3129.8259000	498.1272600	0.0020075	-0.0001512	0.0101831	
-161.2034600	4003.3150000	637.6637200	0.0015682	-0.0402349	0.0001218	
-161.2034600	-4003.3150000	637.6637200	0.0015682	-0.0402349	0.0001218	
-2295.5852000	6245.7110000	1059.0517000	0.0009442	-0.3449820	0.0000014	

Real (λ)	Imag. (λ)	Freq. (cycles/mm)	Wavelength (mm)	Damping ratio	Contribution %	
-0.695410	634.203620	100.936700	0.009907	-0.001097	41.905965	Remark : Cu011
-0.695410	-634.203620	100.936700	0.009907	-0.001097	41.905965	orientation 3
-9.612414	1266.604100	201.592110	0.004961	-0.007589	6.238754	order 22
-9.612414	-1266.604100	201.592110	0.004961	-0.007589	6.238754	rotation : 60
-114.149340	0.000000	18.167432	0.055044	-1.000000	2.761397	
-90.642986	1906.473900	303.767500	0.003292	-0.047491	0.422933	
-90.642986	-1906.473900	303.767500	0.003292	-0.047491	0.422933	
-162.154100	2672.499900	426.123800	0.002347	-0.060564	0.037305	
-162.154100	-2672.499900	426.123800	0.002347	-0.060564	0.037305	
-5.443666	3169.030000	504.367530	0.001983	-0.001718	0.014015	
-5.443666	-3169.030000	504.367530	0.001983	-0.001718	0.014015	
-183.079130	3929.010300	625.999900	0.001597	-0.046546	0.000323	
-183.079130	-3929.010300	625.999900	0.001597	-0.046546	0.000323	
-2549.513000	6321.112000	1084.783900	0.000922	-0.374054	0.000015	

Real (λ)	Imag. (λ)	Freq. (cycles/mm)	Wavelength (mm)	Damping ratio	Contribution %	
-0.1107652	638.1397400	101.5631000	0.0098461	-0.0001736	45.2990340	Remark : Cu011
-0.1107652	-638.1397400	101.5631000	0.0098461	-0.0001736	45.2990340	orientation 4
-2.8335408	1278.8668000	203.5384700	0.0049131	-0.0022157	3.9201806	order :22
-2.8335408	-1278.8668000	203.5384700	0.0049131	-0.0022157	3.9201806	rotation : 90
-38.9157330	0.0000000	6.1936312	0.1614562	-1.0000000	1.1117719	
-14.7423450	1917.5452000	305.1958100	0.0032766	-0.0076879	0.1814555	
-14.7423450	-1917.5452000	305.1958100	0.0032766	-0.0076879	0.1814555	
-29.0803120	2550.2592000	405.9127500	0.0024636	-0.0114021	0.0361080	
-29.0803120	-2550.2592000	405.9127500	0.0024636	-0.0114021	0.0361080	
-18.4045530	3182.0072000	506.4406400	0.0019746	-0.0057838	0.0072570	
-18.4045530	-3182.0072000	506.4406400	0.0019746	-0.0057838	0.0072570	
-96.9877540	4119.5512000	655.8286200	0.0015248	-0.0235368	0.0000792	
-96.9877540	-4119.5512000	655.8286200	0.0015248	-0.0235368	0.0000792	
-1839.9666000	6372.3989000	1055.6298000	0.0009473	-0.2774076	0.0000003	

Real (λ)	Imag. (λ)	Freq. (cycles/mm)	Wavelength (mm)	Damping ratio	Contribution %	
-0.02541189	633.66436000	100.85081000	0.00991564	-0.00004010	48.96490300	Remark : Cu011
-0.02541189	-633.66436000	100.85081000	0.00991564	-0.00004010	48.96490300	orientation 5
-2.76592970	1266.27470000	201.53436000	0.00496193	-0.00218430	0.84534114	order :22
-2.76592970	-1266.27470000	201.53436000	0.00496193	-0.00218430	0.84534114	rotation : 120
-53.67895400	0.00000000	8.54327090	0.11705119	-1.00000000	0.21431423	
-10.41445400	1900.86480000	302.53657000	0.00330539	-0.00547872	0.06845731	
-10.41445400	-1900.86480000	302.53657000	0.00330539	-0.00547872	0.06845731	
-22.73389300	2543.88120000	404.88744000	0.00246982	-0.00893634	0.01159218	
-22.73389300	-2543.88120000	404.88744000	0.00246982	-0.00893634	0.01159218	
-12.06965200	3169.49050000	504.44374000	0.00198238	-0.00380805	0.00252576	
-12.06965200	-3169.49050000	504.44374000	0.00198238	-0.00380805	0.00252576	
-103.42075000	4229.03020000	673.27230000	0.00148528	-0.02444765	0.00002343	
-103.42075000	-4229.03020000	673.27230000	0.00148528	-0.02444765	0.00002343	
-1965.15710000	6321.11200000	1053.53240000	0.00094919	-0.29687219	0.00000042	

Real (λ)	Imag. (λ)	Freq. (cycles/mm)	Wavelength (mm)	Damping ratio	Contribution %	
-1.4328214	639.0619900	101.7101300	0.0098319	-0.0022421	42.3154620	Remark : Cu011
-1.4328214	-639.0619900	101.7101300	0.0098319	-0.0022421	42.3154620	orientation 6
-1.0601178	1278.2454000	203.4391500	0.0049155	-0.0008294	7.1749394	order :22
-1.0601178	-1278.2454000	203.4391500	0.0049155	-0.0008294	7.1749394	rotation : 150
-36.0653030	1929.5269000	307.1473800	0.0032558	-0.0186880	0.3027189	
-36.0653030	-1929.5269000	307.1473800	0.0032558	-0.0186880	0.3027189	
-929.5163300	0.0000000	147.9371200	0.0067596	-1.0000000	0.2549658	
-4.8599604	2558.0728000	407.1306600	0.0024562	-0.0018998	0.0655255	
-4.8599604	-2558.0728000	407.1306600	0.0024562	-0.0018998	0.0655255	
-2.2715380	3195.2278000	508.5364300	0.0019664	-0.0007109	0.0130056	
-2.2715380	-3195.2278000	508.5364300	0.0019664	-0.0007109	0.0130056	
-78.9150540	4014.2218000	639.0066800	0.0015649	-0.0196551	0.0008641	
-78.9150540	-4014.2218000	639.0066800	0.0015649	-0.0196551	0.0008641	
-1869.0822000	6372.3989000	1056.9247000	0.0009461	-0.2814521	0.0000038	

Real (λ)	Imag. (λ)	Freq. (cycles/mm)	Wavelength (mm)	Damping ratio	Contribution %	
-1.7331952	633.9529800	100.8971300	0.0099111	-0.0027339	38.3289630	Remark : Cu011
-1.7331952	-633.9529800	100.8971300	0.0099111	-0.0027339	38.3289630	orientation 7
-21.1577400	1277.8167000	203.3987200	0.0049165	-0.0165555	8.0217235	order :22
-21.1577400	-1277.8167000	203.3987200	0.0049165	-0.0165555	8.0217235	rotation : 180
-124.3163000	0.0000000	19.7855540	0.0505419	-1.0000000	6.1127335	
-16.2519400	1917.2242000	305.1466700	0.0032771	-0.0084765	0.4929403	
-16.2519400	-1917.2242000	305.1466700	0.0032771	-0.0084765	0.4929403	
-183.3037100	2691.7099000	429.3911400	0.0023289	-0.0679420	0.0826036	
-183.3037100	-2691.7099000	429.3911400	0.0023289	-0.0679420	0.0826036	
-4.8434124	3185.8800000	507.0491300	0.0019722	-0.0015203	0.0172860	
-4.8434124	-3185.8800000	507.0491300	0.0019722	-0.0015203	0.0172860	
-187.3348700	4162.2924000	663.1200300	0.0015080	-0.0449621	0.0001161	
-187.3348700	-4162.2924000	663.1200300	0.0015080	-0.0449621	0.0001161	
-3547.9295000	6359.4993000	1159.0047000	0.0008628	-0.4872030	0.0000010	

Real (λ)	Imag. (λ)	Freq. (cycles/mm)	Wavelength (mm)	Damping ratio	Contribution %	
-1.1754573	627.1582800	99.8155160	0.0100185	-0.0018743	40.1516740	Remark : Cu011
-1.1754573	-627.1582800	99.8155160	0.0100185	-0.0018743	40.1516740	orientation 8
-12.4620100	1255.6769000	199.8570300	0.0050036	-0.0099240	6.7611764	order :22
-12.4620100	-1255.6769000	199.8570300	0.0050036	-0.0099240	6.7611764	rotation : 210
-81.9770170	0.0000000	13.0470470	0.0766457	-1.0000000	5.4561567	
-11.0664510	1875.0935000	298.4356000	0.0033508	-0.0059017	0.2685401	
-11.0664510	-1875.0935000	298.4356000	0.0033508	-0.0059017	0.2685401	
-130.1413200	2577.7193000	410.7792900	0.0024344	-0.0504228	0.0775902	
-130.1413200	-2577.7193000	410.7792900	0.0024344	-0.0504228	0.0775902	
-2.3303145	3133.5129000	498.7142100	0.0020052	-0.0007437	0.0127977	
-2.3303145	-3133.5129000	498.7142100	0.0020052	-0.0007437	0.0127977	
-183.3089500	3998.9694000	637.1240700	0.0015696	-0.0457910	0.0001385	
-183.3089500	-3998.9694000	637.1240700	0.0015696	-0.0457910	0.0001385	
-2745.9939000	6258.1527000	1087.6812000	0.0009194	-0.4018075	0.0000086	

Real (λ)	Imag. (λ)	Freq. (cycles/mm)	Wavelength (mm)	Damping ratio	Contribution %	
-1.8547374	628.9811200	100.1058900	0.0099894	-0.0029488	41.2540730	Remark : Cu011
-1.8547374	-628.9811200	100.1058900	0.0099894	-0.0029488	41.2540730	orientation 9
-3.3054435	1261.1043000	200.7116600	0.0049823	-0.0026211	6.9009046	order :22
-3.3054435	-1261.1043000	200.7116600	0.0049823	-0.0026211	6.9009046	rotation : 240
-88.8584020	0.0000000	14.1422540	0.0707101	-1.0000000	2.9905186	
-23.5512930	1909.4716000	303.9249600	0.0032903	-0.0123330	0.3016666	
-23.5512930	-1909.4716000	303.9249600	0.0032903	-0.0123330	0.3016666	
-86.9448710	2583.3511000	411.3858900	0.0024308	-0.0336368	0.0355136	
-86.9448710	-2583.3511000	411.3858900	0.0024308	-0.0336368	0.0355136	
-20.9780970	3151.4350000	501.5775600	0.0019937	-0.0066565	0.0124352	
-20.9780970	-3151.4350000	501.5775600	0.0019937	-0.0066565	0.0124352	
-109.3424600	4088.1122000	650.8759400	0.0015364	-0.0267369	0.0001468	
-109.3424600	-4088.1122000	650.8759400	0.0015364	-0.0267369	0.0001468	
-2410.9468000	6283.1853000	1071.0913000	0.0009336	-0.3582459	0.0000014	

Real (λ)	Imag. (λ)	Freq. (cycles/mm)	Wavelength (mm)	Damping ratio	Contribution %	
-2.0046799	625.1704900	99.4994860	0.0100503	-0.0032066	44.0563370	Remark : Cu011
-2.0046799	-625.1704900	99.4994860	0.0100503	-0.0032066	44.0563370	orientation 10
-6.3636048	1247.3831000	198.5297700	0.0050370	-0.0051015	4.6722275	order :22
-6.3636048	-1247.3831000	198.5297700	0.0050370	-0.0051015	4.6722275	rotation : 270
-117.4695600	0.0000000	18.6958620	0.0534878	-1.0000000	1.7643698	
-40.8716400	1873.8811000	298.3083800	0.0033522	-0.0218060	0.2973318	
-40.8716400	-1873.8811000	298.3083800	0.0033522	-0.0218060	0.2973318	
-46.6368810	2512.4854000	399.9433500	0.0025004	-0.0185589	0.0721499	
-46.6368810	-2512.4854000	399.9433500	0.0025004	-0.0185589	0.0721499	
-16.6697260	3121.2277000	496.7659000	0.0020130	-0.0053407	0.0196226	
-16.6697260	-3121.2277000	496.7659000	0.0020130	-0.0053407	0.0196226	
-149.6299600	4042.1574000	643.7699600	0.0015533	-0.0369920	0.0001455	
-149.6299600	-4042.1574000	643.7699600	0.0015533	-0.0369920	0.0001455	
-2124.2525000	6245.7110000	1049.9566000	0.0009524	-0.3219993	0.0000025	

Real (λ)	Imag. (λ)	Freq. (cycles/mm)	Wavelength (mm)	Damping ratio	Contribution %	
-4.156519	630.022890	100.273440	0.009973	-0.006597	45.302526	Remark : Cu011
-4.156519	-630.022890	100.273440	0.009973	-0.006597	45.302526	orientation 11
-0.454562	1260.317500	200.585780	0.004985	-0.000361	3.296162	order :22
-0.454562	-1260.317500	200.585780	0.004985	-0.000361	3.296162	rotation : 300
-93.091399	0.000000	14.815956	0.067495	-1.000000	1.921150	
-83.706446	1892.130300	301.436430	0.003317	-0.044196	0.391574	
-83.706446	-1892.130300	301.436430	0.003317	-0.044196	0.391574	
-1.544038	2520.149300	401.094290	0.002493	-0.000613	0.031534	
-1.544038	-2520.149300	401.094290	0.002493	-0.000613	0.031534	
-72.117657	3139.581500	499.811730	0.002001	-0.022964	0.017578	
-72.117657	-3139.581500	499.811730	0.002001	-0.022964	0.017578	
-4151.580900	6308.419000	1201.928300	0.000832	-0.549737	0.000042	
-186.519100	4206.544100	670.150090	0.001492	-0.044297	0.000030	
-186.519100	-4206.544100	670.150090	0.001492	-0.044297	0.000030	

Real (λ)	Imag. (λ)	Freq. (cycles/mm)	Wavelength (mm)	Damping ratio	Contribution %	
-9.400321	618.139380	98.391313	0.010163	-0.015206	42.891598	Remark : Cu011
-9.400321	-618.139380	98.391313	0.010163	-0.015206	42.891598	orientation 12
-1.748721	1243.556700	197.918390	0.005053	-0.001406	6.744643	order :22
-1.748721	-1243.556700	197.918390	0.005053	-0.001406	6.744643	rotation : 330
-1.890024	1865.234000	296.861360	0.003369	-0.001013	0.291052	
-1.890024	-1865.234000	296.861360	0.003369	-0.001013	0.291052	
-120.029430	2503.405900	398.887130	0.002507	-0.047891	0.051411	
-120.029430	-2503.405900	398.887130	0.002507	-0.047891	0.051411	
-0.940614	3116.015100	495.929230	0.002016	-0.000302	0.016350	
-0.940614	-3116.015100	495.929230	0.002016	-0.000302	0.016350	
-3045.898700	2021.219900	581.794130	0.001719	-0.833233	0.004798	
-3045.898700	-2021.219900	581.794130	0.001719	-0.833233	0.004798	
-196.630920	3903.282600	622.014470	0.001608	-0.050312	0.000147	
-196.630920	-3903.282600	622.014470	0.001608	-0.050312	0.000147	

Appendix IV

Program Listing for the Surface Topography Model

Basically, the program is composed of two subroutines with the first routine (INPS3D4.M) for the input of cutting conditions and dynamic conditions of between the tool and the workpiece. The former include the feed rate, the tool nose radius, the spindle speed, the depth of cut and the workpiece diameter. The later include the amplitude and the frequency of the tool-work vibration in the thrust and the main cutting directions. Based on the input data, the second routine (SIM3D4.m) performs the simulation of the surface topography and the calculation of the surface roughness parameters. The program is capable of simulating the 3-D tool path and surface topography of a diamond turned surface. Besides, it can determine the arithmetic roughness R_a and the maximum peak-to-valley height R_t values under different cutting conditions. It should be run by MATLAB 5.2 or above.

INPS3D4.M

```
%input for the 3D surface simulation program

load s3dpara.dat;

SP=s3dpara;
dia = SP(1,1);
f = SP(2,1);
v = SP(3,1);
d = SP(4,1);
trad = SP(5,1);
ampz = SP(6,1);
frz = SP(7,1);
ampx = SP(8,1);
frx = SP(9,1);

t_frame = uicontrol(gcf, 'Style', 'frame','BackgroundColor', 'm',...
        'HorizontalAlignment','Center','Position', [20 15 520 395]);

t1_head = uicontrol(gcf,'Style', 'text',...
        'Position', [80 375 430 20],...
        'String', 'THE HONG KONG POLYTECHNIC UNIVERSITY',...
        'BackgroundColor', 'm','HorizontalAlignment', 'Center');

t2_head = uicontrol(gcf,'Style', 'text',...
        'Position', [80 355 430 20],...
        'String', 'Department of Manufacturing Engineering',...
        'BackgroundColor', 'm','HorizontalAlignment', 'Center');

Hc_frame = uicontrol(gcf, 'Style', 'frame','BackgroundColor', 'b',...
        'HorizontalAlignment','Center','Position', [20 15 460 340]);

M_label = uicontrol(gcf, 'Style', 'text',...
                'Position', [50 320 390 20],'BackgroundColor', 'c',...
                'HorizontalAlignment','Center',...
                'String', 'MACHINE PARAMETERS SETTING for 3D SGS');

dia_label = uicontrol(gcf, 'Style', 'text',...
                'Position', [50 290 230 20],...
                'BackgroundColor', 'g',...
                'HorizontalAlignment','Left',...
                'String', 'Part diameter (mm) :');

Hc_dia = uicontrol(gcf, 'Style', 'edit',...
                'Position', [300 290 100 20],...
                'BackgroundColor', 'w',...
                'HorizontalAlignment','Center',...
                'String', num2str(dia),...
```

```
                'Callback', 'get(Hc_dia, "String");');

f_label = uicontrol(gcf, 'Style', 'text',...
                'Position', [50 260 230 20],...
                'BackgroundColor', 'g',...
                'HorizontalAlignment','Left',...
                'String', 'Feed Rate (mm/min) :');

Hc_feed = uicontrol(gcf, 'Style', 'edit',...
                'Position', [300 260 100 20],...
                'BackgroundColor', 'w',...
                'HorizontalAlignment','Center',...
                'String', num2str(f),...
                'Callback', 'get(Hc_feed, "String");');

s_label = uicontrol(gcf, 'Style', 'text',...
                'Position', [50 230 230 20],...
                'BackgroundColor', 'g',...
                'HorizontalAlignment','Left',...
                'String', 'Spindle speed (rpm) :');

Hc_sspeed = uicontrol(gcf, 'Style', 'edit',...
                'Position', [300 230 100 20],...
                'BackgroundColor', 'w',...
                'HorizontalAlignment','Center',...
                'String', num2str(v),...
                'Callback', 'get(Hc_sspeed, "String");');

d_label = uicontrol(gcf, 'Style', 'text',...
                'Position', [50 200 230 20],...
                'BackgroundColor', 'g',...
                'HorizontalAlignment','Left',...
                'String', 'Depth of cut (micrometre) :');

Hc_dcut = uicontrol(gcf, 'Style', 'edit',...
                'Position', [300 200 100 20],...
                'BackgroundColor', 'w',...
                'HorizontalAlignment','Center',...
                'String', num2str(d),...
                'Callback', 'get(Hc_dcut, "String");');

trad_label = uicontrol(gcf, 'Style', 'text',...
                'Position', [50 170 230 20],...
                'BackgroundColor', 'g',...
                'HorizontalAlignment','Left',...
                'String', 'Tool radius (mm) :');

Hc_trad = uicontrol(gcf, 'Style', 'edit',...
                'Position', [300 170 100 20],...
                'BackgroundColor', 'w',...
                'HorizontalAlignment','Center',...
                'String', num2str(trad),...
                'Callback', 'get(Hc_trad, "String");');

V_label = uicontrol(gcf, 'Style', 'text',...
                'Position', [50 140 400 20],...
                'BackgroundColor', 'c',...
                'HorizontalAlignment','Center',...
                'String','VIBRATION PARAMETERS SETTING');

Vz_label = uicontrol(gcf, 'Style', 'text',...
                'Position', [320 110 60 20],...
                'BackgroundColor', 'g',...
                'HorizontalAlignment','Center',...
                'String', 'Z-axis');

Vx_label = uicontrol(gcf, 'Style', 'text',...
                'Position', [390 110 60 20],...
                'BackgroundColor', 'g',...
                'HorizontalAlignment','Center',...
                'String', 'X-axis');

vaz_label = uicontrol(gcf, 'Style', 'text',...
                'Position', [50 80 260 20],...
                'BackgroundColor', 'g',...
                'HorizontalAlignment','Left',...
                'String', 'Amplitude of vibration (micrometers) :');

Hc_zvam = uicontrol(gcf, 'Style', 'edit',...
                'Position', [320 80 60 20],...
                'BackgroundColor', 'w',...
                'HorizontalAlignment','Center',...
                'String', num2str(ampz),...
                'Callback', 'get(Hc_zvam, "String");');

Hc_xvam = uicontrol(gcf, 'Style', 'edit',...
                'Position', [390 80 60 20],...
                'BackgroundColor', 'w',...
                'HorizontalAlignment','Center',...
                'String', num2str(ampx),...
                'Callback', 'get(Hc_xvam, "String");');
```

```
vfz_label = uicontrol(gcf, 'Style', 'text',...
                'Position', [50 50 260 20],...
                'BackgroundColor', 'g',...
                'HorizontalAlignment','Left',...
                'String', 'Frequency of vibration (Hz) :');

Hc_frz = uicontrol(gcf, 'Style', 'edit',...
                'Position', [320 50 60 20],...
                'BackgroundColor', 'w',...
                'HorizontalAlignment','Center',...
                'String', num2str(frz),...
                'Callback', 'get(Hc_frz, "String");');

Hc_frx = uicontrol(gcf, 'Style', 'edit',...
                'Position', [390 50 60 20],...
                'BackgroundColor', 'w',...
                'HorizontalAlignment','Center',...
                'String', num2str(frx),...
                'Callback', 'get(Hc_frx, "String");');

Hc_proceed = uicontrol(gcf, 'Style', 'push', ...
        'Position', [390 20 80 20],...
        'String', 'Proceed',...
        'CallBack',[...
        'P = zeros(9,1); P(1,1)=eval(get(Hc_dia, "String"));',...
        'P(2,1)=eval(get(Hc_feed, "String"));',...
        'P(3,1)=eval(get(Hc_aspeed, "String"));',...
        'P(4,1)=eval(get(Hc_dcut, "String"));',...
        'P(5,1)=eval(get(Hc_trad, "String"));',...
        'P(6,1)=eval(get(Hc_zvam, "String"));',...
        'P(7,1)=eval(get(Hc_frz, "String"));',...
        'P(8,1)=eval(get(Hc_xvam, "String"));',...
        'P(9,1)=eval(get(Hc_frx, "String"));',...
        'save s3dpara.dat P -ascii;clf;sim3d4']);

Hc_close = uicontrol(gcf, 'Style', 'push', ...
        'Position', [485 25 50 45],...
        'String', 'Exit',...
        'CallBack',[...
        'P = zeros(9,1); P(1,1)=eval(get(Hc_dia, "String"));',...
        'P(2,1)=eval(get(Hc_feed, "String"));',...
        'P(3,1)=eval(get(Hc_aspeed, "String"));',...
        'P(4,1)=eval(get(Hc_dcut, "String"));',...
        'P(5,1)=eval(get(Hc_trad, "String"));',...
        'P(6,1)=eval(get(Hc_zvam, "String"));',...
        'P(7,1)=eval(get(Hc_frz, "String"));',...
        'P(8,1)=eval(get(Hc_xvam, "String"));',...
        'P(9,1)=eval(get(Hc_frx, "String"));',...
        'save s3dpara.dat P -ascii;clf;fftsgs1']);
```

SIM3D4.M

```
%3D SURFACE Topography Generation Simulation (SGS)

%Define machining parameters.

load s3dpara.dat;

SP = s3dpara;

dia = SP(1,1);          %part diameter (mm)
f = SP(2,1);            %feed rate (mm/min)
v = SP(3,1);            %spindle speed (rpm)
d = SP(4,1);            %depth of cut (micrometre)
trad = SP(5,1);     %tool radius (mm)
ampz = SP(6,1);         %amplitude of Z-axis vibration (micrometers)
frz = SP(7,1);          %frequency of Z-axis vibration (Hz)
ampx = SP(8,1);         %amplitude of X-axis vibration (micrometers)
frx = SP(9,1);          %frequency of X-axis vibration (Hz)

ampz = 0.001*ampz;      %unit conversion for amplitude of Z-axis vibration (mm)
ampx = 0.001*ampx;      %unit conversion for amplitude of X-axis vibration (mm)

s = f/v                 %feed rate (mm/rev)
r = dia/2;              %Part radius (mm)
d = 0.001*d;            %unit conversion for depth of cut (mm)

c_mark = (60*frz)/v     %number of cut marks per revolution of the work

N = fix(r/s)            %no. of revolutions

a_res = 360;

a_step = (2*pi)/a_res;  %step size of angular rotation

%phase shift angle for z-axis vibration

pcon = (c_mark-fix(c_mark))
```

```
if pcon>0.5
  psz = 2*pi*(1-pcon)
else
        psz=2*pi*pcon
end

psx=a_step/100;                         %phase shift for x-axis vibration

r_step = (s*a_step)/(2*pi);     %step size of radial movement

t_rot = 2*N*pi;                         %total angular rotation

%m = fix(t_rot/a_step)                  %number of steps
m = N*a_res

t_tot = (60*N)/v                        %total machine time (second)

t_step = (60/(v*a_res))                 %time step (second)

t_res = 0.0005;                         %tool resolution

s_rate= 1/t_res;                        %sample frequency for the roughness data (Hz)

nt = round(sqrt(2*trad*d)/(t_res));     %number of tool points
ts = nt*(t_res);                        %tool span

%initiation
v_a = zeros(m,1);                       %angle vector
v_r = zeros(m,1);                       %radial vector
t_vector = zeros(m,1);
XS = zeros(m,1);
ZS = zeros(m,1);
YS = zeros(m,1);
XP = zeros(m,1);
ZP = zeros(m,1);
YP = zeros(m,1);
YEP = zeros(m,1);
TX = zeros(2*nt,1);
TY = zeros(2*nt,1);
RX = zeros(N*2*nt,1);
RY = zeros(N*2*nt,1);
RX = zeros(2*nt,1);
RY = zeros(2*nt,1);
PV = zeros(N,1);
RIX = zeros(N,1);
RIY = zeros(N,1);
RRX = zeros(N*2*nt,1);
RRY = zeros(N*2*nt,1);
fj = 0;
k = 0;
s_i = 0;
eia = 80;
ava = -80;

%Tool path under vibration

%Tool geometry plot
for q=1:nt
   TX(q,1) = q*t_res-ts;
   TY(q,1) = (TX(q,1)*TX(q,1))/(2*trad);
   TX(nt+q,1) = q*t_res;
   TY(nt+q,1) = (TX(nt+q,1)*TX(nt+q,1))/(2*trad);
end

plot(TX, TY);
title('Tool geometry');
xlabel('Tool span (mm)');
ylabel('Tool height (mm)');
grid;
pause;

%Tool positions under vibration
r_angle =-a_step;

for i=1:m
        %vibration data
        v_a(i,1) = (i-1)*a_step;
        v_r(i,1) = r-r_step*(i-1);
        v_angle=(ampx/r)*sin(2*pi*frx*i*t_step);
        r_angle=r_angle+a_step+v_angle;
        v_r_diff = ((abs(r_angle-v_a(i,1))*s)/(2*pi));
        t_diff = (60*v_r_diff)/f;

        %vibration conditions
        if r_angle>v_a(i,1)
                s_i=s_i+1;
                XS(s_i,1)=v_r(i,1)*sin(v_a(i,1));
                YS(s_i,1)=v_r(i,1)*cos(v_a(i,1));
                YEP(s_i,1)=v_r(i,1);
                ZS(s_i,1)=1e6*ampz*sin((2*pi*frz*(i*t_step-t_diff))-psz); %unit convert from mm to nm
                t_vector(s_i,1)=i*t_step-t_diff;
        end
```

```
        if r_angle<v_a(i,1)
                s_i=s_i+1;
                XS(s_i,1)=v_r(i,1)*sin(v_a(i,1));
                YS(s_i,1)=v_r(i,1)*cos(v_a(i,1));
                YEP(s_i,1)=v_r(i,1);
                ZS(s_i,1)=1e6*ampz*sin((2*pi*frz*(i*t_step+t_diff))-psz); %unit covert from mm to nm
                t_vector(s_i,1)=i*t_step+t_diff;
        end

        if r_angle==v_a(i,1)
                s_i=s_i+1;
                XS(s_i,1)=v_r(i,1)*sin(v_a(i,1));
                YS(s_i,1)=v_r(i,1)*cos(v_a(i,1));
                YEP(s_i,1)=v_r(i,1);
                ZS(s_i,1)=1e6*ampz*sin((2*pi*frz*i*t_step)-psz); %unit convert from mm to nm
                t_vector(s_i,1)=i*t_step;
        end

        if rem(i-1,a_res)==0
          fj=fj+1
          YP(fj,1)=YS(i,1);
          ZP(fj,1)=ZS(i,1);
        end
end


%axis([-dia/4, dia/4, -dia/4, dia/4]);
%grid off;
%hold on;

%Tool Locus Plot
vw=get(gca, 'View');
plot3(XS,YS,ZS);
EL1 = ela;
AZ1 = ava;
XC1 = 0.5+sqrt(3)/2*[cos(EL1)*sin(AZ1),-cos(EL1)*cos(AZ1), sin(EL1)];
T1=viewmtx(AZ1, EL1, 0, XC1);view(T1);
title('Tool Locus plot');
xlabel('X (mm)');
ylabel('Y (mm)');
zlabel('Z (nm)');
SD=[XS, YS, ZS];
pause;

axis([-dia/4, dia/4, -dia/4, dia/4]);
axis(axis);

%Simulation of Surface Wave
%gs_n=30;
%gs=0.25/gs_n;
gs=s/5;

for g_is=1:1
        g_i=-(dia/(4*g_is)):gs:(dia/(4*g_is));
        [XGI, YGI]=meshgrid(g_i, g_i);
        ZGI=griddata(XS, YS, ZS, XGI, YGI);
        GWS = ZGI;
        save gridwave.dat GWS -ascii;
        [DX, DY]=gradient(ZGI, g_i, g_i);
        mesh(XGI, YGI, ZGI);
        EL1 = ela;
        AZ1 = ava;
        XC1 = 0.5+sqrt(3)/2*[cos(EL1)*sin(AZ1),-cos(EL1)*cos(AZ1), sin(EL1)];
        T1=viewmtx(AZ1, EL1, 0, XC1);view(T1);
        caxis auto;
        colorbar('vert');
        %surfl(XGI,YGI,ZGI);
        title('Mesh Surface Wave induced by vibration between tool and workpiece');
        xlabel('X (mm)');
        ylabel('Y (mm)');
        zlabel('Z (nm)');
        shading interp;
        pause;
end

%plot3(XS, YS, ZS, 'o')
%hold off
pause;
surfl(XGI,YGI,ZGI)
EL1 = ela;
AZ1 = ava;
XC1 = 0.5+sqrt(3)/2*[cos(EL1)*sin(AZ1),-cos(EL1)*cos(AZ1), sin(EL1)];
T1=viewmtx(AZ1, EL1, 0, XC1);view(T1);
colormap(gray);
shading interp;
title('Surface Wave by vibration between tool and workpiece');
xlabel('X (mm)');
ylabel('Y (mm)');
zlabel('Z (nm)');
pause;
clf;
```

```
colormap('default');
%contour(XGI,YGI,ZGI, 10);
%hold on;
%quiver(XGI, YGI, DX, DY);
%hold off;
%title('Gradient field for the Surface Waviness');
%xlabel('X (mm)');
%ylabel('Y (mm)');
%zlabel('Z (nm)');
%caxis auto;
%colorbar('vert');
%pause;

caxis auto;
pcolor(XGI,YGI,ZGI);
title('Color Map for the Surface Wave by vibration between tool and workpiece');
xlabel('X (mm)');
ylabel('Y (mm)');
zlabel('Z (nm)');
colorbar('vert');
shading interp;
pause;
clf;

%Generation of Real Surface

SYTP = zeros(N,a_res);
SZTP = zeros(N,a_res);
SYTPM = zeros(N,a_res);
SZTPM = zeros(N,a_res);
SXSP = zeros(3*m, 1);
SYSP = zeros(3*m, 1);
SZSP = zeros(3*m, 1);
SYIP = zeros(N, 1);
SZIP = zeros(N, 1);

%plot(YP, ZP);
%pause;

i_p=0;

%determine the initial intercept point
for j=1:a_res

    if j==1
        i_i=1;
        SYIP(i_i,1)=-s/2;
        SZIP(i_i,1)=((s*s)/(8*trad));
    end

    for i=1:N

        SYTP(i,j)=YEP((i-1)*a_res+j,1);
        SZTP(i,j)=(1e-6*ZS((i-1)*a_res+j,1));        %unit convert nm to mm
        i_p=i_p+1;
        SXSP(i_p,1)=(SYTP(i,j))*sin((j-1)*a_step);
        SYSP(i_p,1)=(SYTP(i,j))*cos((j-1)*a_step);
        SZSP(i_p,1)=SZTP(i,j);

        i_i=i_i+1;
        if i==1
            Top = (2*SZTP(i,j)*trad)+(s*s)*(2*i-1);     %determine the intercept points
        else
            Top = (2*(SZTP(i,j)-SZTP(i-1,j))*trad)+(s*s)*(2*i-1);     %determine the intercept points
        end

        SYIP(i_i,1)=Top/(2*s);
        SZIP(i_i,1)=SZTP(i,j)+(((SYIP(i_i,1)-i*s)*(SYIP(i_i,1)-i*s))/(2*trad));

        i_p=i_p+1;
        SXSP(i_p,1)=(r-SYIP(i_i,1)-(j-1)*r_step)*sin((j-1)*a_step);
        SYSP(i_p,1)=(r-SYIP(i_i,1)-(j-1)*r_step)*cos((j-1)*a_step);
        SZSP(i_p,1)=SZIP(i_i,1);

        if (i==N)
            SYIP(1,1)=-s/2;
            SZIP(1,1)=((s*s)/(8*trad));
            i_i=1;

            i_p=i_p+1;
            SXSP(i_p,1)=(r-SYIP(1,1)-j*r_step)*sin(j*a_step);
            SYSP(i_p,1)=(r-SYIP(1,1)-j*r_step)*cos(j*a_step);
            SZSP(i_p,1)=SZIP(1,1);
        end

    end

    %plot(SYIP, SZIP);
    %pause;
end
```

```
SZPP = zeros(i_p,1);
SYPP = zeros(i_p,1);
SXPP = zeros(i_p,1);

for i=1:i_p;
        SXPP(i,1)=SXSP(i,1);
        SYPP(i,1)=SYSP(i,1);
        SZPP(i,1)=1e6*SZSP(i,1);    %unit convert from mm to nm
end

%plot3(SXPP,SYPP,SZPP,'y.');
%pause;

%Real Surface Generation
%sgs_n = 30;
%sgs=0.25/sgs_n;

sgs = s/5;

for sg_is=1:1
        sg_i=-(dia/(4*sg_is)):sgs:(dia/(4*sg_is));
        [SXGI, SYGI]=meshgrid(sg_i, sg_i);
        SZGI=griddata(SXPP, SYPP, SZPP, SXGI, SYGI);
        [DXI, DYI]=gradient(SZGI, sg_i, sg_i);
        mesh(SXGI, SYGI, SZGI);
        caxis auto;
        colorbar('vert');
        %surfl(SXGI,SYGI,SZGI);
        EL1 = ela;
        AZ1 = ava;
        XC1 = 0.5+sqrt(3)/2*[cos(EL1)*sin(AZ1),-cos(EL1)*cos(AZ1), sin(EL1)];
        T1=viewmtx(AZ1, EL1, 0, XC1);view(T1);
        title('Simulated Mesh Surface for the Workpiece');
        xlabel('X (mm)');
        ylabel('Y (mm)');
        zlabel('Z (nm)');
        shading interp;
end

%Determination of surface roughness values
[orx, ory]=size(SZGI);
sumR=0;
sumP=0;

for i=1:orx
        for j=1:ory
          sumR =sumR+SZGI(i,j);
        end
end

%Surface roughness determination - Ra
RAV=sumR/(orx*ory);

for i=1:orx
        for j=1:ory
          sumP=sumP+abs(SZGI(i,j)-RAV);
        end
end

Ra=sumP/(orx*ory);          %Ra in nanometre

%Geometrical Surface Roughness Determination - Rt

Rmax=-1000*d;
Rmin=-1000*d;

for i=1:orx
        for j=1:ory
                if SZGI(i,j)>Rmax
                        Rmax=SZGI(i,j);
                end

                if SZGI(i,j)<Rmin
                        Rmin=SZGI(i,j);
                end
        end
end

Rt=Rmax-Rmin;                       %geometrical roughness (P-V value)

Rth = Rt;                           %unit conversion for Rth (micrometre to nanometre)

Rt_hdM = uicontrol(gcf,'Style', 'text', ...
        'Position', [5 4 25 20],...
        'BackgroundColor', 'g',...
        'String', 'Rt :');

Rt_curM = uicontrol(gcf,'Style', 'text', ...
        'Position', [30 4 50 20],...
        'BackgroundColor', 'g',...
        'String', num2str(Rth));
```

```
Rt_unitM = uicontrol(gcf,'Style', 'text', ...
        'Position', [80 4 17 20],...
        'BackgroundColor', 'g',...
        'String', 'nm');

Ra_hdM = uicontrol(gcf,'Style', 'text', ...
        'Position', [105 4 25 20],...
        'BackgroundColor', 'c',...
        'String', 'Ra :');

Ra_curM = uicontrol(gcf,'Style', 'text', ...
        'Position', [130 4 50 20],...
        'BackgroundColor', 'c',...
        'String', num2str(Ra));

Ra_unitM = uicontrol(gcf,'Style', 'text', ...
        'Position', [180 4 17 20],...
        'BackgroundColor', 'c',...
        'String', 'nm');

MRTA = [Ra, Rth];

save r3dval.dat MRTA -ascii;          %save the roughness values

%plot3(XS, YS, ZS, 'o')
%hold off
pause;

surf(SXGI,SYGI,SZGI)
colorbar('vert');
EL1 = ela;
AZ1 = ava;
XC1 = 0.5+sqrt(3)/2*[cos(EL1)*sin(AZ1),-cos(EL1)*cos(AZ1), sin(EL1)];
T1=viewmtx(AZ1, EL1, 0, XC1);view(T1);
title('Simulated Surface Topograpgy for Workpiece');
xlabel('X (mm)');
ylabel('Y (mm)');
zlabel('Z (nm)');
pause;
clf;

surfl(SXGI,SYGI,SZGI)
shading interp;
colormap(gray);
shading interp;
EL1 = ela;
AZ1 = ava;
XC1 = 0.5+sqrt(3)/2*[cos(EL1)*sin(AZ1),-cos(EL1)*cos(AZ1), sin(EL1)];
T1=viewmtx(AZ1, EL1, 0, XC1);view(T1);
title('Simulated Surface Topography for Workpiece');
xlabel('X (mm)');
ylabel('Y (mm)');
zlabel('Z (nm)');
pause;
clf;

colormap('default');
contour(SXGI,SYGI,SZGI, 10);
title('Contour Map for the Surface Topography of the Workpiece');
xlabel('X (mm)');
ylabel('Y (mm)');
caxis auto;
colorbar('vert');
pause;

caxis auto;
colormap('default');
pcolor(SXGI,SYGI,SZGI);
title('Color Map for the Surface Topography of the Workpiece');
xlabel('X (mm)');
ylabel('Y (mm)');
zlabel('Z (nm)');
colorbar('vert');
shading interp;
pause;

caxis auto;
colormap('gray');
pcolor(SXGI,SYGI,SZGI);
title('Color Map for the Surface Topography of the Workpiece');
xlabel('X (mm)');
ylabel('Y (mm)');
zlabel('Z (nm)');
colorbar('vert');
shading interp;
pause;


%contour(SXGI,SYGI,SZGI);
%colormap('default');
%hold on;
%quiver(SXGI, SYGI, DXI, DYI);
```

```
%hold off;
%title('Gradient field for the Surface Texture of the Workpiece');
%xlabel('X (mm)');
%ylabel('Y (mm)');
%zlabel('Z (nm)');
%colorbar('vert');
%shading interp;
%pause;

Hm_ex=uimenu(gcf, 'Label','Option');

Hm_exview = uimenu(Hm_ex, 'Label', 'View');

Hm_zoom = uimenu(Hm_ex, 'Label', 'Zoom', 'CallBack', 'zoom');

Hm_zoomon = uimenu(Hm_zoom, 'Label', 'On', 'CallBack', 'zoom on');

Hm_zoomoff = uimenu(Hm  zoom, 'Label', 'Off', 'CallBack', 'zoom off');

set(Hm_exview, 'Separator', 'on');

Hm_exv2d = uimenu(Hm_exview, 'Label', '2-D', 'CallBack', 'view(2)');

Hm_exv3d = uimenu(Hm_exview, 'Label', '3-D', 'CallBack', 'view(3)');

Hm_close = uimenu(gcf, 'Label', 'Close');

Hm_clfig = uimenu(Hm_close, 'Label', 'Close Figure', 'CallBack', 'clf; fftsgs1;');

Hm_clmenu = uimenu(Hm_close, 'Label', 'Remove Menu', ...
        'CallBack', 'delete(Hm_ex); delete(Hm_close); drawnow');

vw=get(gca, 'View');

Hc_zoom = uicontrol(gcf, 'Style', 'push', ...
        'Position', [400 3 70 20],...
        'String', 'Zoom','CallBack', 'zoom on');

Hc_quit = uicontrol(gcf, 'Style', 'push', ...
        'Position', [5 3 70 20],...
        'String', 'Quit',...
        'CallBack','clf; fftsgs1;');

Hc_close = uicontrol(gcf, 'Style', 'push', ...
        'Position', [80 3 70 20],...
        'String', 'Exit',...
        'CallBack','clf; fftsgs1;');
```

Appendix V

Stress States For (111)[110] or (110)[111] Slip

Table A5.1 Stress states for (111)[110] or (110)[111] slip (From Reid, 1973)

Number of stress state	A	B	C	F	G	H	a_1	a_2	a_3	b_1	b_2	b_3	c_1	c_2	c_3	d_1	d_2	d_3	Number of active slip systems
1	1	−1	0	0	0	0	÷	−		÷	−		÷	−		÷	−		8
2	0	1	−1	0	0	0		÷	−		÷	−		÷	−		÷	−	8
3	−1	0	1	0	0	0	−		÷	−		÷	−		÷	−		÷	8
4	0	0	0	1	0	0		÷	−		−	÷		÷	−		−	÷	8
5	0	0	0	0	1	0	−		÷	÷		−	÷		−	−		÷	8
6	0	0	0	0	0	1	÷	−		÷	−		−	÷		−	÷		8
7	½	−1	½	0	½	0		−	÷	÷	−		÷	−			−	÷	8
8	½	−1	½	0	−½	0	÷	−			−	÷		−	÷	÷	−		8
9	−1	½	½	½	0	0	−	÷		−		÷	−	÷		−		÷	8
10	−1	½	½	−½	0	0	−		÷	−	÷		−		÷	−	÷		8
11	½	½	−1	0	0	½	÷		−	÷		−		÷	−		÷	−	8
12	½	½	−1	0	0	−½		÷	−		÷	−	÷		−	÷		−	8
13	½	0	−½	½	0	½	÷		−	÷	−			÷	−				6
14	½	0	−½	−½	0	½	÷	−		÷		−					÷	−	6
15	½	0	−½	½	0	−½		÷	−				÷		−	÷	−		6
16	½	0	−½	−½	0	−½				÷	−	÷	−			÷		−	6
17	0	−½	½	0	½	½		−	÷	÷	−					−		÷	6
18	0	−½	½	0	−½	½	÷	−			−	÷	−		÷				6
19	0	−½	½	0	½	−½	−		÷				÷	−			−	÷	6
20	0	−½	½	0	−½	−½				−		÷		−	÷	÷	−		6
21	−½	½	0	½	½	0	−	÷						÷	−	−		÷	6
22	−½	½	0	−½	½	0	−		÷		÷	−				−	÷		6
23	−½	½	0	½	−½	0		÷	−	−		÷	−	÷					6
24	−½	½	0	−½	−½	0				−	÷		−		÷		÷	−	6
25	0	0	0	½	½	−½	−	÷					÷		−		−	÷	6
26	0	0	0	½	−½	½	÷		−		−	÷	−	÷					6
27	0	0	0	−½	½	½		−	÷	÷		−				−	÷		6
28	0	0	0	½	½	½				÷	−		+	−	−			÷	6

Appendix VI

Program Listing for The Model-based Simulation System

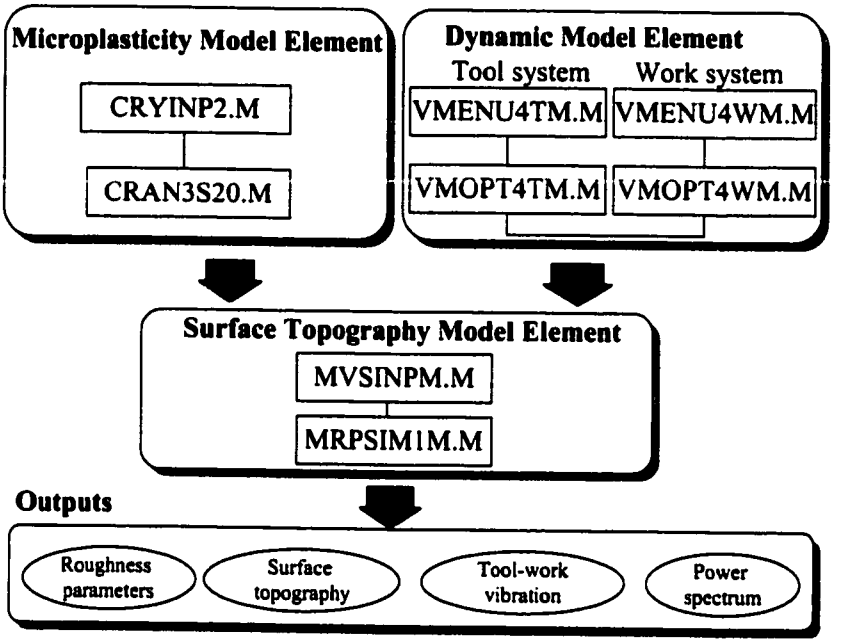

Figure A6.1 The program structure of the Model-based Simulation System

The software package for the model-based simulation system was developed by MATLAB 5.2. As shown in Figure A6.1, the structure of the package is basically divided into three parts which are the microplasticity model element, the dynamic model element and the surface topography model element respectively. The microplasticity model element is composed of the input routine (CRYINP2.M) which provide an user inference for the input of the machining conditions, material properties, the crystallographic orientation of the workpiece and the resolution of the simulation being adopted. The simulation of the variation of the shear angle and the microcutting forces are carried out by the routine named CRAN3S20.M. The output of the element is the variation of microcutting forces which are used as the input for the dynamic model element.

The dynamic model element performs the tasks of identifying the dynamics parameters for the tool and the work systems respectively. The user is allowed to input the iteration ranges and resolution for least square searching for the optimal dynamic

conditions for the work and the tool system based on the displacement signals captured by the capacitive displacement sensor. These are accomplished by the routines VMENU4TM.M and VMENU4WM.M for the tool and the work system respectively. The identification of the dynamic characteristics of the tool and work systems is done by the routines VMOPT4TM.M and VMOPT4WM.M respectively.

Hence, the surface topography model elements makes use of the predicted cutting force patterns in the microplasticity model together with the predetermined dynamic characteristics of the machine to determine the relative tool-work vibration and hence the 3D surface topography of the work surface. These are accomplished by the routines MVSINPM.M and MVIBS3DM.M. The output will be the 3-D tool locus, the simulated surface topography and the predicted surface roughness parameters.

CRYINP2.M

```
Input for the Crystallographic Analysis (Shear angle determination)

load crypara.dat;

CRP=crypara;
mh = CRP(1,1);
mk = CRP(2,1);
ml = CRP(3,1);
rot_au = CRP(4,1);
rot_al = CRP(5,1);
rot_as = CRP(6,1);
feed = CRP(7,1);
sspeed = CRP(8,1);
d_cut = CRP(9,1);
ts = CRP(10,1);        %shear stress (N/sq. m)

t_frame = uicontrol(gcf, 'Style', 'frame','BackgroundColor', 'm',...
        'HorizontalAlignment','Center','Position', [20 15 520 395]);

t1_head = uicontrol(gcf,'Style', 'text',...
        'Position', [80 375 430 20],...
        'String', 'THE HONG KONG POLYTECHNIC UNIVERSITY',...
        'BackgroundColor', 'm','HorizontalAlignment', 'Center');

t2_head = uicontrol(gcf,'Style', 'text',...
        'Position', [80 355 430 20],...
        'String', 'Department of Manufacturing Engineering',...
        'BackgroundColor', 'm','HorizontalAlignment', 'Center');

Hc_frame = uicontrol(gcf, 'Style', 'frame','BackgroundColor', 'b',...
        'HorizontalAlignment','Center','Position', [20 15 460 340]);

M_label = uicontrol(gcf, 'Style', 'text',...
                'Position', [30 320 440 20],'BackgroundColor', 'c',...
                'HorizontalAlignment','Center',...
                'String', 'PARAMETERS SETTING FOR SHEAR ANGLE DETERMINATION');

miller_i = uicontrol(gcf, 'Style', 'text',...
                'Position', [50 295 340 20],...
                'BackgroundColor', 'y',...
                'HorizontalAlignment','Center',...
                'String', 'Miller index for the crystal plane');

h_label = uicontrol(gcf, 'Style', 'text',...
                'Position', [50 270 100 20],...
                'BackgroundColor', 'g',...
                'HorizontalAlignment','Center',...
                'String', 'h');

k_label = uicontrol(gcf, 'Style', 'text',...
                'Position', [170 270 100 20],...
                'BackgroundColor', 'g',...
```

```
                'HorizontalAlignment','Center',...
                'String', 'k');

l_label = uicontrol(gcf, 'Style', 'text',...
                'Position', [290 270 100 20],...
                'BackgroundColor', 'g',...
                'HorizontalAlignment','Center',...
                'String', 'l');

Hc_h = uicontrol(gcf, 'Style', 'edit',...
                'Position', [50 245 100 20],...
                'BackgroundColor', 'w',...
                'HorizontalAlignment','Center',...
                'String', num2str(mh),...
                'Callback', 'get(Hc_h, "String");');

Hc_k = uicontrol(gcf, 'Style', 'edit',...
                'Position', [170 245 100 20],...
                'BackgroundColor', 'w',...
                'HorizontalAlignment','Center',...
                'String', num2str(mk),...
                'Callback', 'get(Hc_k, "String");');

Hc_l = uicontrol(gcf, 'Style', 'edit',...
                'Position', [290 245 100 20],...
                'BackgroundColor', 'w',...
                'HorizontalAlignment','Center',...
                'String', num2str(ml),...
                'Callback', 'get(Hc_l, "String");');

u_label = uicontrol(gcf, 'Style', 'text',...
                'Position', [50 220 250 20],...
                'BackgroundColor', 'g',...
                'HorizontalAlignment','Center',...
                'String', 'Upper limit for the crystal rotation (degree)');

l_label = uicontrol(gcf, 'Style', 'text',...
                'Position', [50 195 250 20],...
                'BackgroundColor', 'g',...
                'HorizontalAlignment','Center',...
                'String', 'Lower limit for the crystal rotation (degree)');

s_label = uicontrol(gcf, 'Style', 'text',...
                'Position', [50 170 250 20],...
                'BackgroundColor', 'g',...
                'HorizontalAlignment','Center',...
                'String', 'Step size for the crystal rotation (degree)');

Hcu_rot = uicontrol(gcf, 'Style', 'edit',...
                'Position', [320 220 100 20],...
                'BackgroundColor', 'w',...
                'HorizontalAlignment','Center',...
                'String', num2str(rot_au),...
                'Callback', 'get(Hcu_rot, "String");');

Hcl_rot = uicontrol(gcf, 'Style', 'edit',...
                'Position', [320 195 100 20],...
                'BackgroundColor', 'w',...
                'HorizontalAlignment','Center',...
                'String', num2str(rot_al),...
                'Callback', 'get(Hcl_rot, "String");');

Hcs_rot = uicontrol(gcf, 'Style', 'edit',...
                'Position', [320 170 100 20],...
                'BackgroundColor', 'w',...
                'HorizontalAlignment','Center',...
                'String', num2str(rot_as),...
                'Callback', 'get(Hcs_rot, "String");');

f_label = uicontrol(gcf, 'Style', 'text',...
                'Position', [50 140 260 20],...
                'BackgroundColor', 'y',...
                'HorizontalAlignment','Left',...
                'String','Feed rate (mm/min) : ');

Hc_feed = uicontrol(gcf, 'Style', 'edit',...
                'Position', [320 140 100 20],...
                'BackgroundColor', 'w',...
                'HorizontalAlignment','Center',...
                'String', num2str(feed),...
                'Callback', 'get(Hc_feed, "String");');

v_label = uicontrol(gcf, 'Style', 'text',...
                'Position', [50 110 260 20],...
                'BackgroundColor', 'y',...
                'HorizontalAlignment','Left',...
                'String', 'Spindle speed (rpm) : ');

Hc_speed = uicontrol(gcf, 'Style', 'edit',...
                'Position', [320 110 100 20],...
                'BackgroundColor', 'w',...
                'HorizontalAlignment','Center',...
```

```
                'String', num2str(sspeed),...
                'Callback', 'get(Hc_sspeed, "String");');

d_label = uicontrol(gcf, 'Style', 'text',...
                'Position', [50 80 260 20],...
                'BackgroundColor', 'y',...
                'HorizontalAlignment','Left',...
                'String', 'Depth of cut (micrometer) : ');

Hc_d = uicontrol(gcf, 'Style', 'edit',...
                'Position', [320 80 100 20],...
                'BackgroundColor', 'w',...
                'HorizontalAlignment','Center',...
                'String', num2str(d_cut),...
                'Callback', 'get(Hc_d, "String");');

ts_label = uicontrol(gcf, 'Style', 'text',...
                'Position', [50 50 260 20],...
                'BackgroundColor', 'y',...
                'HorizontalAlignment','Left',...
                'String', 'shear stress (N/sq. 2): ');

Hc_ts = uicontrol(gcf, 'Style', 'edit',...
                'Position', [320 50 100 20],...
                'BackgroundColor', 'w',...
                'HorizontalAlignment','Center',...
                'String', num2str(ts),...
                'Callback', 'get(Hc_ts, "String");');

Hc_proceed = uicontrol(gcf, 'Style', 'push', ...
        'Position', [390 20 80 20],...
        'String', 'Proceed',...
        'CallBack',[...
        'CRP = zeros(10,1); CRP(1,1)=eval(get(Hc_h, "String"));...
        'CRP(2,1)=eval(get(Hc_k, "String"));...
        'CRP(3,1)=eval(get(Hc_l, "String"));...
        'CRP(4,1)=eval(get(Hcu_rot, "String"));...
        'CRP(5,1)=eval(get(Hcl_rot, "String"));...
        'CRP(6,1)=eval(get(Hcs_rot, "String"));...
        'CRP(7,1)=eval(get(Hc_feed, "String"));...
        'CRP(8,1)=eval(get(Hc_sspeed, "String"));...
         'CRP(9,1)=eval(get(Hc_d, "String"));...
         'CRP(10,1)=eval(get(Hc_ts, "String"));...
        'save crypara.dat CRP -ascii;clf;cran3s20']);

Hc_close = uicontrol(gcf, 'Style', 'push', ...
        'Position', [485 25 50 45],...
        'String', 'Exit',...
        'CallBack',[...
        'CRP = zeros(10,1); CRP(1,1)=eval(get(Hc_h, "String"));...
        'CRP(2,1)=eval(get(Hc_k, "String"));...
        'CRP(3,1)=eval(get(Hc_l, "String"));...
        'CRP(4,1)=eval(get(Hcu_rot, "String"));...
        'CRP(5,1)=eval(get(Hcl_rot, "String"));...
        'CRP(6,1)=eval(get(Hcs_rot, "String"));...
        'CRP(7,1)=eval(get(Hc_feed, "String"));...
        'CRP(8,1)=eval(get(Hc_sspeed, "String"));...
         'CRP(9,1)=eval(get(Hc_d, "String"));...
         'CRP(10,1)=eval(get(Hc_ts, "String"));...
        'save crypara.dat CRP -ascii;clf;cutfmenu']);
```

CRAN3S20.M

```
%Shear angle analysis based on Microplasticity Model

%Define crystallographic data.

TS = CRP(10,1);              %shear stress N/sq. m

%pause off;
load crypara.dat;

CRP = crypara;

mh = CRP(1,1);                          %define crystal plane (hkl)
mk = CRP(2,1);
ml = CRP(3,1);

rot_au = pi*(CRP(4,1)/180);  %define rotational angle for the crystal in radian
rot_al = pi*(CRP(5,1)/180);
rot_as = pi*(CRP(6,1)/180);

infinity = 1000000000000;

f = CRP(7,1);                           %feed (mm/min)
v = CRP(8,1);                           %spindle speed (rpm)
d_cut = CRP(9,1);                       %depth of cut (micrometer)
s = f/v;                                %calculate feed (mm/rev)
a_v = (2*pi*v)/60;                      %angular velocity (radian per second)
t_s = rot_as/a_v;                       %calculate unit time (second)
```

```
d_cut = d_cut*0.000001;                    %unit conversion (um to m)
w_cut = s*0.001;                           %unit conversion (mm to m)

rp = sqrt(mh*mh+mk*mk+ml*ml);

%Calculate Euler angles
cos_ap = ml/rp;
sin_ap = sqrt(mh*mh+mk*mk)/rp;
cos_af = mk/sqrt(mh*mh+mk*mk);
sin_af = mh/sqrt(mh*mh+mk*mk);
%pause;

str_w = zeros(3,3);                        %define strain tensor in shear band
rv = zeros(3,1);
uv = zeros(3,1);
nv = zeros(3,1);

%define the positive 28 stress states (A B F G H)
pst = [ 1     -1     0     0     0
        0      1     0     0     0
       -1      0     0     0     0
        0      0     1     0     0
        0      0     0     1     0
        0      0     0     0     1
        0.5   -1     0     0.5   0
        0.5   -1     0    -0.5   0
       -1      0.5   0.5   0     0
       -1      0.5  -0.5   0     0
        0.5    0.5   0     0     0.5
        0.5    0.5   0     0    -0.5
        0.5    0     0.5   0     0.5
        0.5    0    -0.5   0     0.5
        0.5    0     0.5   0    -0.5
        0.5    0    -0.5   0    -0.5
        0     -0.5   0     0.5   0.5
        0     -0.5   0    -0.5   0.5
        0     -0.5   0     0.5  -0.5
        0     -0.5   0    -0.5  -0.5
       -0.5    0.5   0.5   0.5   0
       -0.5    0.5  -0.5   0.5   0
       -0.5    0.5   0.5  -0.5   0
       -0.5    0.5  -0.5  -0.5   0
        0      0     0.5   0.5  -0.5
        0      0     0.5  -0.5   0.5
        0      0    -0.5  0.5    0.5
        0      0     0.5   0.5   0.5];

pstpr = pst;
pstnr = -pst;

pstr = zeros(56, 8);

for i=1:28
  for j=1:5
    pstr(i,j)=pstpr(i,j);
    pstr(i+28,j)=pstnr(i,j);
  end
end

%Define Slip system matrices

%sign matrix

%define slip system id (28 positive state)
s_idp = [1     -2     4     -5     7     -8     10     -11
         2     -3     5     -6     8     -9     11     -12
        -1      3    -4      6    -7      9    -10      12
         2     -3    -5      6     8     -9     -11      12
        -1      3     4     -6     7     -9     -10      12
         1     -2     4     -5    -7      8     -10      11
        -2      3     4     -5     7     -8     -11      12
         1     -2    -5      6    -8      9      10     -11
        -1      2    -4      6    -7      8     -10      12
        -1      3    -4      5    -7      9     -10      11
         1     -3     4     -6     8     -9      11     -12
         2     -3     5     -6     7     -9      10     -12
         1     -3     4     -5     8     -9       0       0
         1     -2     4     -6     11    -12      0       0
         2     -3     7     -9     10    -11      0       0
         5     -6     7     -8     10    -12      0       0
        -2      3     4     -5    -10     12      0       0
         1     -2    -5      6     -7      9      0       0
        -1      3     7     -8    -11     12      0       0
        -4      6    -8      9     10    -11      0       0
        -1      2     8     -9    -10     12      0       0
        -1      3     5     -6    -10     11      0       0
         2     -3    -4      6     -7      8      0       0
        -4      5    -7      9     11    -12      0       0
        -1      2     7     -9    -11     12      0       0
         1     -3    -5      6     -7      8      0       0
        -2      3     4     -6    -10     11      0       0
         4     -5     8     -9    -10     12      0       0];
```

```
s_idn = -s_idp;
s_id = zeros(56, 8);

for i=1:28
  for j=1:8
    s_id(i,j)=s_idp(i,j);
    s_id(i+28,j)=s_idn(i,j);
  end
end

%define slip system vectors
n = zeros(3,5);
b = zeros(3,5);
ns = zeros(3,5);
bs = zeros(3,5);
E = zeros(5,5);
Es = zeros(5,5);

pss = zeros(56,1),                          %possible stress state

for i=1:12
        pss(i,1)=8;
        pss(i+28,1)=8;
end

for i=1:16
        pss(i+12,1)=6;
        pss(i+40,1)=6;
end

pss;

sh_as = (pi)/180;                           %step size of shear angle
sh_al = (10*pi)/180;                        %lower limint shear angle
sh_au = (80*pi)/180;                        %upper limit shear angle
n_a = (sh_au-sh_al)/sh_as;                  %number of shear angle step

n_rot = (rot_au-rot_al)/rot_as;             %number of angle rotation step
vtime = zeros(1,n_rot);                     %initiate the time vector

vpsh_a = zeros(1,n_rot);                    %initiate the possible shear angle vector
vpsh_ap = zeros(1,n_rot);                   %initiate the possible shear angle vector (polar)

v_rot = zeros(1,n_rot);                     %initiate the crystal rotation vector (degree)
v_rotr = zeros(1,n_rot);                    %initiate the crystal rotation vector (radian)

vforce = zeros(1,n_rot);                    %initiate the vertical cutting force vector
hforce = zeros(1,n_rot);                    %initiate the horizontal cutting force vector
rforce = zeros(1,n_rot);                    %initiate the cutting force ratio (vertical/horizontal)
t_i = 0;
sa_i = 0;

%Determining effective Taylor factor M' for different crystallographic orientations

dW = zeros(56,1);                           %initiate the work vector
dWp = zeros(28,1);
dWn = zeros(28,1);
dWm = zeros(56,1);
dWmw = zeros(56,1);
M = zeros(1,n_a);                           %initiate Taylor factor vector
Mf = zeros(1,n_a);                          %initiate Effect Taylor factor vector
vsh_a = zeros(1,n_a);                       %initiate shear angle vector
vsh_as = zeros(1,n_a);                      %initiate no. of slip system vector
Tsoft = zeros(1,n_a);                       %initiate Taylor softening vector
orient_v = zeros(n_rot, 6);                 %orientation vector

count_c1=0;
count_c2=0;
count_c3=0;
orient_i=0;

rmu=rmh;
rmv=rmk;
rmw=rml;

for rot_a=rot_al:rot_as:rot_au

 %crystal orientation
 rmh = cos(rot_a)*cos_af-sin(rot_a)*sin_af*cos_ap;
 rmk =-cos(rot_a)*sin_af-sin(rot_a)*cos_af*cos_ap;
 rml = sin(rot_a)*sin_ap;
 %pause;

 %debug
 %rmh = 1
       %rmk = 0
 %rml = 0

 chc = (rmh*rmu+rmk*rmv+rml*rmw)            %check for perpendicularity
       %pause;

 orient_i=orient_i+1;
```

```
orient_v(orient_i,1)=rmh;
orient_v(orient_i,2)=rmk;
orient_v(orient_i,3)=rml;
orient_v(orient_i,4)=rmu;
orient_v(orient_i,5)=rmv;
orient_v(orient_i,6)=rmw;

Ir = [1     0     0
      0     1     0
            0     0     1];

    m_i = 0;

    for sh_a=sh_al:sh_as:sh_au

 %transformation from workpiece to cystrallographic axes
    rd = sqrt(rmu*rmu+rmv*rmv+rmw*rmw);
     nd = sqrt(rmh*rmh+rmk*rmk+rml*rml);
     rv1=rmu/rd;
     rv2=rmv/rd;
     rv3=rmw/rd;
     nv1=rmh/nd;
     nv2=rmk/nd;
     nv3=rml/nd;

          uv1=nv2*rv3-nv3*rv2;
          uv2=nv3*rv1-nv1*rv3;
          uv3=nv1*rv2-nv2*rv1;

     P = [ rv1 uv1 nv1
           rv2 uv2 nv2
           rv3 uv3 nv3];

     ds = 0.025;                                    %assume shear strain at shear band (arbitary)
     tc = ds/2;

 strw =[   tc*sin(2*sh_a)      0      tc*cos(2*sh_a)
             0                 0            0
           tc*cos(2*sh_a)      0      -tc*sin(2*sh_a)];

          %strain tensor refer to the crystallographic axes
     sc = P*strw*(P');

     v_sc = [     sc(2,2)
                  -sc(1,1)
                  2*sc(2,3)
                  2*sc(1,3)
                  2*sc(1,2)];

   dWp = pst*v_sc;
          dWn = -pst*v_sc;
          i_dw = 0;

          for i=1:28
               dW(i,1)=dWp(i,1);
               dW(i+28,1)=dWn(i,1);
          end

   dW_max=max(dW);

   m_i = m_i+1

     tsc = 1/sqrt(6);                                   %define the critical shear stress
     M(1,m_i)= dW_max/(tsc*ds);                         %calculating Taylor factor
     s_a = 2*(sh_a-(pi/4));
     Mf(1,m_i) = M(1,m_i)/cos(s_a);   %calculating effective Taylor factor
     vsh_a(1,m_i)=(sh_a/pi)*180;

%permissible angles based on the min. M'
no_max=0;
dW_i=zeros(56,1);
dW_s=zeros(56,1);

   for j=1:56
               if dW(j,1)==dW_max
   no_max = no_max+1

   dW_i(no_max,1)=j;
   dW_s(no_max,1)=pss(j,1);
   end
end

dW_ss=dW_s(1:no_max,1);
dW_is=dW_i(1:no_max,1);

%angles with min. no. of slip systems
min_slip=min(dW_ss);

vsh_as(1,m_i)=min_slip;

no_wp=0;
Min_Mi=zeros(no_max,1);
```

```
for k=1:no_max
  if dW_ss(k,1) == min_slip
    no_wp=no_wp+1;
    Min_Mi(no_wp,1)=dW_ss(k,1);
  end
end

M_index=Min_Mi(1:no_wp,1)

          %Selection of active slip system
sort_slip = zeros(no_wp,1);                          %initiate sort slip
          asl_id = zeros(no_wp,5);                   %initiate active slip system id
no_aslip = zeros(no_wp,1);                           %store no_aslip

for k=1:no_wp
          %Generation of possible slip systems combinations
    s8_v=zeros(8,1);
  s6_v=zeros(6,1);

    W_index = M_index(k,1);

    if (W_index>28) & (W_index<=40)
    for i=1:8                                        %Type I : 8 slip system
          s8_v(i,1) = s_id(W_index,i);
                end

    no_aslip(k,1)=8;
    scom = nchoosek(s8_v, 5);
    no_com = nchoosek(8,5);
  end

  if (W_index<=12)
    for i=1:8                                        %Type I : 8 slip system
          s8_v(i,1) = s_id(W_index,i);
                end

    no_aslip(k,1)=8;
    scom = nchoosek(s8_v, 5);
    no_com = nchoosek(8,5);
  end

  if (W_index>12) & (W_index<=28)
    for i=1:6                                        %Type II : 6 slip plane system
          s6_v(i,1) = s_id(W_index,i);
    end

    no_aslip(k,1)=6;
    scom = nchoosek(s6_v, 5);
    no_com = nchoosek(6,5);
          end

  if (W_index>40)
    for i=1:6                                        %Type II : 6 slip plane system
      s6_v(i,1) = s_id(W_index,i);
    end

    no_aslip(k,1)=6;
    scom = nchoosek(s6_v, 5);
    no_com = nchoosek(6,5);
          end

  tot_work = zeros(no_com,1);

    %Mapping of the slip system
    for j=1:no_com
          for m=1:5
      if scom(j,m)==1
        n(1,m)=1/sqrt(3);
        n(2,m)=1/sqrt(3);
        n(3,m)=1/sqrt(3);
        b(1,m)=0;
        b(2,m)=1/sqrt(2);
        b(3,m)=-1/sqrt(2);
      end

      if scom(j,m)==2
        n(1,m)=1/sqrt(3);
        n(2,m)=1/sqrt(3);
        n(3,m)=1/sqrt(3);
        b(1,m)=-1/sqrt(2);
        b(2,m)=0;
        b(3,m)=1/sqrt(2);
      end

      if scom(j,m)==3
        n(1,m)=1/sqrt(3);
        n(2,m)=1/sqrt(3);
        n(3,m)=1/sqrt(3);
        b(1,m)=1/sqrt(2);
        b(2,m)=-1/sqrt(2);
        b(3,m)=0;
      end
```

```
 if scom(j,m)==4
   n(1,m)=-1/sqrt(3);
   n(2,m)=-1/sqrt(3);
   n(3,m)=1/sqrt(3);
   b(1,m)=0;
   b(2,m)=-1/sqrt(2);
   b(3,m)=-1/sqrt(2);
 end

 if scom(j,m)==5
   n(1,m)=-1/sqrt(3);
   n(2,m)=-1/sqrt(3);
   n(3,m)=1/sqrt(3);
   b(1,m)=1/sqrt(2);
   b(2,m)=0;
   b(3,m)=1/sqrt(2);
 end

 if scom(j,m)==6
   n(1,m)=-1/sqrt(3);
   n(2,m)=-1/sqrt(3);
   n(3,m)=1/sqrt(3);
   b(1,m)=-1/sqrt(2);
   b(2,m)=1/sqrt(2);
   b(3,m)=0;
 end

if scom(j,m)==7
   n(1,m)=-1/sqrt(3);
   n(2,m)=1/sqrt(3);
   n(3,m)=1/sqrt(3);
   b(1,m)=0;
   b(2,m)=1/sqrt(2);
   b(3,m)=-1/sqrt(2);
 end

 if scom(j,m)==8
   n(1,m)=-1/sqrt(3);
   n(2,m)=1/sqrt(3);
   n(3,m)=1/sqrt(3);
   b(1,m)=1/sqrt(2);
   b(2,m)=0;
   b(3,m)=1/sqrt(2);
 end

 if scom(j,m)==9
   n(1,m)=-1/sqrt(3);
   n(2,m)=1/sqrt(3);
   n(3,m)=1/sqrt(3);
   b(1,m)=-1/sqrt(2);
   b(2,m)=-1/sqrt(2);
   b(3,m)=0;
 end

 if scom(j,m)==10
   n(1,m)=1/sqrt(3);
   n(2,m)=-1/sqrt(3);
   n(3,m)=1/sqrt(3);
   b(1,m)=0;
   b(2,m)=-1/sqrt(2);
   b(3,m)=-1/sqrt(2);
 end

if scom(j,m)==11
   n(1,m)=1/sqrt(3);
   n(2,m)=-1/sqrt(3);
   n(3,m)=1/sqrt(3);
   b(1,m)=-1/sqrt(2);
   b(2,m)=0;
   b(3,m)=1/sqrt(2);
 end

 if scom(j,m)==12
   n(1,m)=1/sqrt(3);
   n(2,m)=-1/sqrt(3);
   n(3,m)=1/sqrt(3);
   b(1,m)=1/sqrt(2);
   b(2,m)=1/sqrt(2);
   b(3,m)=0;
 end

 if scom(j,m)==-1
   n(1,m)=-1/sqrt(3);
   n(2,m)=-1/sqrt(3);
   n(3,m)=-1/sqrt(3);
   b(1,m)=0;
   b(2,m)=-1/sqrt(2);
   b(3,m)=1/sqrt(2);
 end

 if scom(j,m)==-2
   n(1,m)=-1/sqrt(3);
```

```
    n(2,m)=-1/sqrt(3);
    n(3,m)=-1/sqrt(3);
    b(1,m)=1/sqrt(2);
    b(2,m)=0;
    b(3,m)=-1/sqrt(2);
   end

   if scom(j,m)==-3
    n(1,m)=-1/sqrt(3);
    n(2,m)=-1/sqrt(3);
    n(3,m)=-1/sqrt(3);
    b(1,m)=-1/sqrt(2);
    b(2,m)=1/sqrt(2);
    b(3,m)=0;
   end

   if scom(j,m)==-4
    n(1,m)=1/sqrt(3);
    n(2,m)=1/sqrt(3);
    n(3,m)=-1/sqrt(3);
    b(1,m)=0;
    b(2,m)=1/sqrt(2);
    b(3,m)=1/sqrt(2);
   end

   if scom(j,m)==-5
    n(1,m)=1/sqrt(3);
    n(2,m)=1/sqrt(3);
    n(3,m)=-1/sqrt(3);
    b(1,m)=-1/sqrt(2);
    b(2,m)=0;
    b(3,m)=-1/sqrt(2);
   end

   if scom(j,m)==-6
    n(1,m)=1/sqrt(3);
    n(2,m)=1/sqrt(3);
    n(3,m)=-1/sqrt(3);
    b(1,m)=1/sqrt(2);
    b(2,m)=-1/sqrt(2);
    b(3,m)=0;
   end

  if scom(j,m)==-7
    n(1,m)=1/sqrt(3);
    n(2,m)=-1/sqrt(3);
    n(3,m)=-1/sqrt(3);
    b(1,m)=0;
    b(2,m)=-1/sqrt(2);
    b(3,m)=1/sqrt(2);
   end

   if scom(j,m)==-8
    n(1,m)=1/sqrt(3);
    n(2,m)=-1/sqrt(3);
    n(3,m)=-1/sqrt(3);
    b(1,m)=-1/sqrt(2);
    b(2,m)=0;
    b(3,m)=-1/sqrt(2);
   end

   if scom(j,m)==-9
    n(1,m)=1/sqrt(3);
    n(2,m)=-1/sqrt(3);
    n(3,m)=-1/sqrt(3);
    b(1,m)=1/sqrt(2);
    b(2,m)=1/sqrt(2);
    b(3,m)=0;
   end

   if scom(j,m)==-10
    n(1,m)=-1/sqrt(3);
    n(2,m)=1/sqrt(3);
    n(3,m)=-1/sqrt(3);
    b(1,m)=0;
    b(2,m)=1/sqrt(2);
    b(3,m)=1/sqrt(2);
   end

  if scom(j,m)==-11
    n(1,m)=-1/sqrt(3);
    n(2,m)=1/sqrt(3);
    n(3,m)=-1/sqrt(3);
    b(1,m)=1/sqrt(2);
    b(2,m)=0;
    b(3,m)=-1/sqrt(2);
   end

   if scom(j,m)==-12
    n(1,m)=-1/sqrt(3);
    n(2,m)=1/sqrt(3);
    n(3,m)=-1/sqrt(3);
```

```
    b(1,m)=-1/sqrt(2);
    b(2,m)=-1/sqrt(2);
    b(3,m)=0;
  end
end

      E(1,1)=n(2,1)*b(2,1);
      E(1,2)=n(2,2)*b(2,2);
      E(1,3)=n(2,3)*b(2,3);
      E(1,4)=n(2,4)*b(2,4);
      E(1,5)=n(2,5)*b(2,5);
      E(2,1)=n(3,1)*b(3,1);
      E(2,2)=n(3,2)*b(3,2);
      E(2,3)=n(3,3)*b(3,3);
      E(2,4)=n(3,4)*b(3,4);
      E(2,5)=n(3,5)*b(3,5);
      E(3,1)=n(2,1)*b(3,1)+n(3,1)*b(2,1);
      E(3,2)=n(2,2)*b(3,2)+n(3,2)*b(2,2);
      E(3,3)=n(2,3)*b(3,3)+n(3,3)*b(2,3);
      E(3,4)=n(2,4)*b(3,4)+n(3,4)*b(2,4);
      E(3,5)=n(2,5)*b(3,5)+n(3,5)*b(2,5);
      E(4,1)=n(1,1)*b(3,1)+n(3,1)*b(1,1);
      E(4,2)=n(1,2)*b(3,2)+n(3,2)*b(1,2);
      E(4,3)=n(1,3)*b(3,3)+n(3,3)*b(1,3);
      E(4,4)=n(1,4)*b(3,4)+n(3,4)*b(1,4);
      E(4,5)=n(1,5)*b(3,5)+n(3,5)*b(1,5);
      E(5,1)=n(1,1)*b(2,1)+n(2,1)*b(1,1);
      E(5,2)=n(1,2)*b(2,2)+n(2,2)*b(1,2);
      E(5,3)=n(1,3)*b(2,3)+n(2,3)*b(1,3);
      E(5,4)=n(1,4)*b(2,4)+n(2,4)*b(1,4);
      E(5,5)=n(1,5)*b(2,5)+n(2,5)*b(1,5);

if det(E)>=1e-10                    %check for singularity

      strain_v=[ sc(2,2)
                 sc(3,3)
                   2*sc(2,3)
                 2*sc(1,3)
                 2*sc(1,2)];

                    shear_v = inv(E)*strain_v;

                    %crystal rotation
                     w12r = 0;
                    w13r = 0;
                    w23r = 0;
                    w21r = 0;
                    w31r = 0;
                    w32r = 0;
                    w11r = 0;
                    w22r = 0;
                    w33r = 0;

                          for i=1:5
                          w12r = w12r+0.5*(b(1,i)*n(2,i)-b(2,i)*n(1,i))*shear_v(i,1);
                          w13r = w13r+0.5*(b(1,i)*n(3,i)-b(3,i)*n(1,i))*shear_v(i,1);
                          w23r = w23r+0.5*(b(2,i)*n(3,i)-b(3,i)*n(2,i))*shear_v(i,1);
                          w21r = w21r+0.5*(b(2,i)*n(1,i)-b(1,i)*n(2,i))*shear_v(i,1);
                          w31r = w31r+0.5*(b(3,i)*n(1,i)-b(1,i)*n(3,i))*shear_v(i,1);
                          w32r = w32r+0.5*(b(3,i)*n(2,i)-b(2,i)*n(3,i))*shear_v(i,1);
                          end

                    %Lattice rotation tensor
                    L_rotr =[w11r w12r   w13r
                             w21r   w22r   w23r
                             w31r   w32r   w33r];

                    %new orientation of the crystal
                    Pnwr=(Ir-L_rotr)*P;

                    danwr = 0.0001;

                          tcnwr = danwr/2;

      strwnwr =[tcnwr*sin(2*sh_a)        0              tcnwr*cos(2*sh_a)
                        0                0                      0
                tcnwr*cos(2*sh_a)        0              -tcnwr*sin(2*sh_a)];

  %strain tensor refer to the crystallographic axes
  scnwr = Pnwr*strwnwr*(Pnwr');

  strain_vr = [scnwr(2,2)
               scnwr(3,3)
               2*scnwr(2,3)
               2*scnwr(1,3)
               2*scnwr(1,2)];

  shear_vr = inv(E)*strain_vr;

%crystal rotation
                    w12rn = 0;
                   w13rn = 0;
```

```
                    w23ra = 0;
                    w21ra = 0;
                    w31ra = 0;
                    w32ra = 0;
                    w11ra = 0;
                    w22ra = 0;
                    w33ra = 0;

                        for i=1:5
                        w12ra = w12ra+0.5*(b(1,i)*n(2,i)-b(2,i)*n(1,i))*shear_vr(i,1);
                        w13ra = w13ra+0.5*(b(1,i)*n(3,i)-b(3,i)*n(1,i))*shear_vr(i,1);
                        w23ra = w23ra+0.5*(b(2,i)*n(3,i)-b(3,i)*n(2,i))*shear_vr(i,1);
                        w21ra = w21ra+0.5*(b(2,i)*n(1,i)-b(1,i)*n(2,i))*shear_vr(i,1);
                        w31ra = w31ra+0.5*(b(3,i)*n(1,i)-b(1,i)*n(3,i))*shear_vr(i,1);
                        w32ra = w32ra+0.5*(b(3,i)*n(2,i)-b(2,i)*n(3,i))*shear_vr(i,1);
                        end

                    %Lattice rotation tensor
                    L_rotra =[    w11ra w12ra w13ra
                                  w21ra  w22ra  w23ra
                                  w31ra  w32ra  w33ra];

                    %new orientation of the crystal
                    Pnwra=(Ir-L_rotra)*Pnwr;

                    scnwra = Pnwra*strwnwr*(Pnwra');

                    v_scnwra = [scnwra(2,2)
                                -scnwra(1,1)
                                2*scnwra(2,3)
                                2*scnwra(1,3)
                                2*scnwra(1,2)];

            pstrv = zeros(1,5);

            for i=1:5
            pstrv(1,i) = pstr(W_index,i);
            end

        tot_work(j,1)= pstrv*(v_scnwra);

        else
            tot_work(j,1)=infinity;
        end
    end

    %2nd order plastic work criteria
    [sort_min,s_index]=sort(tot_work);
    %pause;

    sort_slip(k,1) = sort_min(1,1);
    %pause;

    for i=1:5
    asl_id(k,i) = scom(s_index(1,1),i);
    end
end

[sort2_min, s2_index]=sort(sort_slip);
%pause;

            %Determine the active slip system
            for m=1:5
            if asl_id(s2_index(1,1),m)==1
            ns(1,m)=1/sqrt(3);
            ns(2,m)=1/sqrt(3);
            ns(3,m)=1/sqrt(3);
            bs(1,m)=0;
            bs(2,m)=1/sqrt(2);
            bs(3,m)=-1/sqrt(2);
            end

            if asl_id(s2_index(1,1),m)==2
            ns(1,m)=1/sqrt(3);
            ns(2,m)=1/sqrt(3);
            ns(3,m)=1/sqrt(3);
            bs(1,m)=-1/sqrt(2);
            bs(2,m)=0;
            bs(3,m)=1/sqrt(2);
            end

            if asl_id(s2_index(1,1),m)==3
            ns(1,m)=1/sqrt(3);
            ns(2,m)=1/sqrt(3);
            ns(3,m)=1/sqrt(3);
            bs(1,m)=1/sqrt(2);
            bs(2,m)=-1/sqrt(2);
            bs(3,m)=0;
            end

            if asl_id(s2_index(1,1),m)==4
            ns(1,m)=-1/sqrt(3);
```

```
ns(2,m)=-1/sqrt(3);
ns(3,m)=1/sqrt(3);
bs(1,m)=0;
bs(2,m)=-1/sqrt(2);
bs(3,m)=-1/sqrt(2);
end

if asl_id(s2_index(1,1),m)==5
ns(1,m)=-1/sqrt(3);
ns(2,m)=-1/sqrt(3);
ns(3,m)=1/sqrt(3);
bs(1,m)=1/sqrt(2);
bs(2,m)=0;
bs(3,m)=1/sqrt(2);
end

if asl_id(s2_index(1,1),m)==6
ns(1,m)=-1/sqrt(3);
ns(2,m)=-1/sqrt(3);
ns(3,m)=1/sqrt(3);
bs(1,m)=-1/sqrt(2);
bs(2,m)=1/sqrt(2);
bs(3,m)=0;
end

if asl_id(s2_index(1,1),m)==7
ns(1,m)=-1/sqrt(3);
ns(2,m)=1/sqrt(3);
ns(3,m)=1/sqrt(3);
bs(1,m)=0;
bs(2,m)=1/sqrt(2);
bs(3,m)=-1/sqrt(2);
end

if asl_id(s2_index(1,1),m)==8
ns(1,m)=-1/sqrt(3);
ns(2,m)=1/sqrt(3);
ns(3,m)=1/sqrt(3);
bs(1,m)=1/sqrt(2);
bs(2,m)=0;
bs(3,m)=1/sqrt(2);
end

if asl_id(s2_index(1,1),m)==9
ns(1,m)=-1/sqrt(3);
ns(2,m)=1/sqrt(3);
ns(3,m)=1/sqrt(3);
bs(1,m)=-1/sqrt(2);
bs(2,m)=-1/sqrt(2);
bs(3,m)=0;
end

if asl_id(s2_index(1,1),m)==10
ns(1,m)=1/sqrt(3);
ns(2,m)=-1/sqrt(3);
ns(3,m)=1/sqrt(3);
bs(1,m)=0;
bs(2,m)=-1/sqrt(2);
bs(3,m)=-1/sqrt(2);
end

if asl_id(s2_index(1,1),m)==11
ns(1,m)=1/sqrt(3);
ns(2,m)=-1/sqrt(3);
ns(3,m)=1/sqrt(3);
bs(1,m)=-1/sqrt(2);
bs(2,m)=0;
bs(3,m)=1/sqrt(2);
end

if asl_id(s2_index(1,1),m)==12
ns(1,m)=1/sqrt(3);
ns(2,m)=-1/sqrt(3);
ns(3,m)=1/sqrt(3);
bs(1,m)=1/sqrt(2);
bs(2,m)=1/sqrt(2);
bs(3,m)=0;
end

if asl_id(s2_index(1,1),m)==-1
ns(1,m)=-1/sqrt(3);
ns(2,m)=-1/sqrt(3);
ns(3,m)=-1/sqrt(3);
bs(1,m)=0;
bs(2,m)=-1/sqrt(2);
bs(3,m)=1/sqrt(2);
end

if asl_id(s2_index(1,1),m)==-2
ns(1,m)=-1/sqrt(3);
ns(2,m)=-1/sqrt(3);
ns(3,m)=-1/sqrt(3);
```

```
bs(1,m)=1/sqrt(2);
bs(2,m)=0;
bs(3,m)=-1/sqrt(2);
end

if asl_id(s2_index(1,1),m)==-3
ns(1,m)=-1/sqrt(3);
ns(2,m)=-1/sqrt(3);
ns(3,m)=-1/sqrt(3);
bs(1,m)=-1/sqrt(2);
bs(2,m)=1/sqrt(2);
bs(3,m)=0;
end

if asl_id(s2_index(1,1),m)==-4
ns(1,m)=1/sqrt(3);
ns(2,m)=1/sqrt(3);
ns(3,m)=-1/sqrt(3);
bs(1,m)=0;
bs(2,m)=1/sqrt(2);
bs(3,m)=1/sqrt(2);
end

if asl_id(s2_index(1,1),m)==-5
ns(1,m)=1/sqrt(3);
ns(2,m)=1/sqrt(3);
ns(3,m)=-1/sqrt(3);
bs(1,m)=-1/sqrt(2);
bs(2,m)=0;
bs(3,m)=-1/sqrt(2);
end

if asl_id(s2_index(1,1),m)==-6
ns(1,m)=1/sqrt(3);
ns(2,m)=1/sqrt(3);
ns(3,m)=-1/sqrt(3);
bs(1,m)=1/sqrt(2);
bs(2,m)=-1/sqrt(2);
bs(3,m)=0;
end

if asl_id(s2_index(1,1),m)==-7
ns(1,m)=1/sqrt(3);
ns(2,m)=-1/sqrt(3);
ns(3,m)=-1/sqrt(3);
bs(1,m)=0;
bs(2,m)=-1/sqrt(2);
bs(3,m)=1/sqrt(2);
end

if asl_id(s2_index(1,1),m)==-8
ns(1,m)=1/sqrt(3);
ns(2,m)=-1/sqrt(3);
ns(3,m)=-1/sqrt(3);
bs(1,m)=-1/sqrt(2);
bs(2,m)=0;
bs(3,m)=-1/sqrt(2);
end

if asl_id(s2_index(1,1),m)==-9
ns(1,m)=1/sqrt(3);
ns(2,m)=-1/sqrt(3);
ns(3,m)=-1/sqrt(3);
bs(1,m)=1/sqrt(2);
bs(2,m)=1/sqrt(2);
bs(3,m)=0;
end

if asl_id(s2_index(1,1),m)==-10
ns(1,m)=-1/sqrt(3);
ns(2,m)=1/sqrt(3);
ns(3,m)=-1/sqrt(3);
bs(1,m)=0;
bs(2,m)=1/sqrt(2);
bs(3,m)=1/sqrt(2);
end

if asl_id(s2_index(1,1),m)==-11
ns(1,m)=-1/sqrt(3);
ns(2,m)=1/sqrt(3);
ns(3,m)=-1/sqrt(3);
bs(1,m)=1/sqrt(2);
bs(2,m)=0;
bs(3,m)=-1/sqrt(2);
end

if asl_id(s2_index(1,1),m)==-12
ns(1,m)=-1/sqrt(3);
ns(2,m)=1/sqrt(3);
ns(3,m)=-1/sqrt(3);
bs(1,m)=-1/sqrt(2);
bs(2,m)=-1/sqrt(2);
```

```
            bs(3,m)=0;
            end
end

      Es(1,1)=ns(2,1)*bs(2,1);
      Es(1,2)=ns(2,2)*bs(2,2);
      Es(1,3)=ns(2,3)*bs(2,3);
      Es(1,4)=ns(2,4)*bs(2,4);
      Es(1,5)=ns(2,5)*bs(2,5);
      Es(2,1)=ns(3,1)*bs(3,1);
      Es(2,2)=ns(3,2)*bs(3,2);
      Es(2,3)=ns(3,3)*bs(3,3);
      Es(2,4)=ns(3,4)*bs(3,4);
      Es(2,5)=ns(3,5)*bs(3,5);
      Es(3,1)=ns(2,1)*bs(3,1)+ns(3,1)*bs(2,1);
      Es(3,2)=ns(2,2)*bs(3,2)+ns(3,2)*bs(2,2);
      Es(3,3)=ns(2,3)*bs(3,3)+ns(3,3)*bs(2,3);
      Es(3,4)=ns(2,4)*bs(3,4)+ns(3,4)*bs(2,4);
      Es(3,5)=ns(2,5)*bs(3,5)+ns(3,5)*bs(2,5);
      Es(4,1)=ns(1,1)*bs(3,1)+ns(3,1)*bs(1,1);
      Es(4,2)=ns(1,2)*bs(3,2)+ns(3,2)*bs(1,2);
      Es(4,3)=ns(1,3)*bs(3,3)+ns(3,3)*bs(1,3);
      Es(4,4)=ns(1,4)*bs(3,4)+ns(3,4)*bs(1,4);
      Es(4,5)=ns(1,5)*bs(3,5)+ns(3,5)*bs(1,5);
      Es(5,1)=ns(1,1)*bs(2,1)+ns(2,1)*bs(1,1);
      Es(5,2)=ns(1,2)*bs(2,2)+ns(2,2)*bs(1,2);
      Es(5,3)=ns(1,3)*bs(2,3)+ns(2,3)*bs(1,3);
      Es(5,4)=ns(1,4)*bs(2,4)+ns(2,4)*bs(1,4);
      Es(5,5)=ns(1,5)*bs(2,5)+ns(2,5)*bs(1,5);

      shear_va = inv(Es)*strain_v;

      %crystal rotation
      w12a = 0;
      w13a = 0;
      w23a = 0;
      w21a = 0;
      w31a = 0;
       w32a = 0;
      w11a = 0;
       w22a = 0;
      w33a = 0;

      for i=1:5
      w12a = w12a+0.5*(bs(1,i)*ns(2,i)-bs(2,i)*ns(1,i))*shear_va(i,1);
      w13a = w13a+0.5*(bs(1,i)*ns(3,i)-bs(3,i)*ns(1,i))*shear_va(i,1);
      w23a = w23a+0.5*(bs(2,i)*ns(3,i)-bs(3,i)*ns(2,i))*shear_va(i,1);
       w21a = w21a+0.5*(bs(2,i)*ns(1,i)-bs(1,i)*ns(2,i))*shear_va(i,1);
      w31a = w31a+0.5*(bs(3,i)*ns(1,i)-bs(1,i)*ns(3,i))*shear_va(i,1);
       w32a = w32a+0.5*(bs(3,i)*ns(2,i)-bs(2,i)*ns(3,i))*shear_va(i,1);
      end

%Lattice rotation tensor
L_rota =[    w11a  w12a  w13a
             w21a  w22a  w23a
             w31a  w32a  w33a];

%Net rotation dw
      net_rot = sqrt(w12a*w12a+w13a*w13a+w23a*w23a);

%new orientation of the crystal
Pnwa=(Ir-L_rota)*P;

%strain tensor refer to the crystallographic axes
scnwa = Pnwa*strw*(Pnwa');

      v_scnwa = [    scnwa(2,2)
                              -scnwa(1,1)

        2*scnwa(2,3)
                    2*scnwa(1,3)
        2*scnwa(1,2)];

dWnp = pst*(v_scnwa);
      dWnn = -pst*(v_scnwa);
      i_dwn = 0;

      for i=1:28
            dWm(i,1)=dWnp(i,1);
            dWm(i+28,1)=dWnn(i,1);
      end

      %macroscopic strain
      d_st=(sqrt(2)/3)*sqrt(power((scnwa(1,1)-scnwa(2,2)),2)+power((scnwa(2,2)-scnwa(3,3)),2)+power((scnwa(3,3)-
      scnwa(1,1)),2)+6*(power(scnwa(1,2),2)+power(scnwa(2,3),2)+power(scnwa(1,3),2)))

      %dWn_max=dWn(M_index(s2_index(1,1),1),1);
      dWm_max=max(dWm);
      Mm = dWm_max/(tsc*d_st);
       Mmf = Mm/cos(2*s_a);

%strain vector
```

```
dsnw = 0.0001;

      tcnw = dsnw/2;

      strwnw =[      tcnw*sin(2*sh_a)          0      tcnw*cos(2*sh_a)
                           0                   0            0
                     tcnw*cos(2*sh_a)          0      -tcnw*sin(2*sh_a)];

scnw = Pnwa*strwnw*inv(Pnwa);

v_scnw = [  scnw(2,2)
            -scnw(1,1)
            2*scnw(2,3)
           2*scnw(1,3)
            2*scnw(1,2)];

strain_vs=[  scnw(2,2)
           scnw(3,3)
           2*scnw(2,3)
           2*scnw(1,3)
           2*scnw(1,2)];

      %Determine Taylor Softening Factor

shear_vs = inv(Es)*strain_vs        %shear on the slip system
%pause;

      %crystal rotation
      w12 = 0;
      w13 = 0;
      w23 = 0;
      w21 = 0;
      w31 = 0;
      w32 = 0;
       w11 = 0;
      w22 = 0;
      w33 = 0;

      for i=1:5
      w12 = w12+0.5*(bs(1,i)*ns(2,i)-bs(2,i)*ns(1,i))*shear_vs(i,1);
      w13 = w13+0.5*(bs(1,i)*ns(3,i)-bs(3,i)*ns(1,i))*shear_vs(i,1);
       w23 = w23+0.5*(bs(2,i)*ns(3,i)-bs(3,i)*ns(2,i))*shear_vs(i,1);
        w21 = w21+0.5*(bs(2,i)*ns(1,i)-bs(1,i)*ns(2,i))*shear_vs(i,1);
      w31 = w31+0.5*(bs(3,i)*ns(1,i)-bs(1,i)*ns(3,i))*shear_vs(i,1);
       w32 = w32+0.5*(bs(3,i)*ns(2,i)-bs(2,i)*ns(3,i))*shear_vs(i,1);
      end

%Lattice rotation tensor
L_rot = [w11      w12    w13
      w21    w22    w23
      w31    w32    w33];

%Net rotation dw
      net_rotnw = sqrt(w12*w12+w13*w13+w23*w23);

%new orientation of the crystal
Pnw=(I+L_rot)*Pnwa ;

      %strain tensor refer to the crystallographic axes
      scnwn = Pnw*strwnw*(Pnw');

      v_scnwn = [   scnwn(2,2)
                        -scnwn(1,1)
                        2*scnwn(2,3)
                  2*scnwn(1,3)
        2*scnwn(1,2)];

      strain_vn=[    scnwn(2,2)
        scnwn(3,3)
        2*scnwn(2,3)
        2*scnwn(1,3)
             2*scnwn(1,2)];

      dWpnw = pst*(v_scnwn);
      dWnnw = -pst*(v_scnwn);
      i_dwnw = 0;

      for i=1:28
            dWmw(i,1)=dWpnw(i,1);
            dWmw(i+28,1)=dWnnw(i,1);
      end

 d_stnw=(sqrt(2)/3)*sqrt(power((scnwn(1,1)-scnwn(2,2)),2)+power((scnwn(2,2)-scnwn(3,3)),2)+power((scnwn(3,3)-
scnwn(1,1)),2)+6*(power(scnwn(1,2),2)+power(scnwn(2,3),2)+power(scnwn(1,3),2)))

 %dWnw_max=dWnw(M_index(s2_index(1,1),1),1);
      dWmw_max=max(dWmw);
 Mmw = dWmw_max/(tsc*(d_stnw));                    %calculating new Taylor factor
 Mmwf = Mmw/cos(a_a);

 %Change in Taylor factor dM
 dM = Mmw-Mm;
```

```
  dnet_rot=net_rotnw-net_rot;

  %Calculate Taylor softening factor
  Tsoft(1,m_i)=(1/Mm)*(dM/d_stnw)
  %Tsoft(1,m_i)=(1/Mm)*(dM/dsnw)

  %pause;
end

%Shear angle selection (1st criterion)

plot(vsh_a, Tsoft);
%pause;

plot(vsh_a, M);
grid;
title('Variation of Taylor factor with Shear Angle');
xlabel('Shear angle (degree)');
ylabel('Taylor factor');

plot(vsh_a, Mf);
grid;
title('Variation of Effective Taylor factor with Shear Angle');
xlabel('Shear angle (degree)');
ylabel('Effective Taylor factor');
%pause;

psh_a1 = zeros(1, m_i);
psh_a1s = zeros(1,m_i);

%Mff = Mf;
Mf_min=min(Mf);
psh_c1=0;

for k=1:m_i
%Minimum Effective Taylor Factor (1st criterion)
        if Mf(1,k)==Mf_min
                        psh_c1=psh_c1+1;
                        psh_a1(1,psh_c1)=vsh_a(1,k);
                        psh_a1s(1,psh_c1)=vsh_as(1,k);
         end
end

lps1 = psh_a1(1:psh_c1)
lps1s = psh_a1s(1:psh_c1);

if psh_c1>1
        %shear angle selection (2nd criterion)
        psh_a2 = zeros(1,psh_c1);
        psh_c2 = 0;

        Min_s = min(lps1s);

        for j=1:psh_c1
                if lps1s(1,j)==Min_s
                        psh_c2=psh_c2+1;
                        psh_a2(1,psh_c2)=lps1(1,j);
                end
        end

        lps2=psh_a2(1:psh_c2);

 %Taylor Softening Factor(3rd criterion)
  if psh_c2>1
    psh_a3 = zeros(1,psh_c2);
        s_tsoft = zeros(1,psh_c2);
    psh_c3 = 0;

    for i=1:psh_c2
      for j=1:n_a
                if vsh_a(1,j)==lps2(1,i)
          psh_c3=psh_c3+1;
          psh_a3(1,psh_c3)=vsh_a(1,j);
                        s_tsoft(1,psh_c3) = Tsoft(1,j);
        end
        end
    end

        [min_tsoft, tsoft_i]=sort(s_tsoft);
        psh_a=psh_a3(1,tsoft_i(1,1))
        count_c3 = count_c3+1;
  else
        psh_a=psh_a2(1,psh_c2)
        count_c2 = count_c2+1;
  end
end

if psh_c1==1
  psh_a=psh_a1(1,psh_c1)
  count_c1=count_c1+1;
end
```

```
        sa_i = sa_i+1;
        vpsh_a(1,sa_i) = psh_a;
        psh_ar=(psh_a*pi)/180;
        v_rotr(1,sa_i) = rot_a;
        v_rot(1,sa_i) = rot_a*(180/pi);

        hforce(1,sa_i) = TS*d_cut*w_cut*2*cot(psh_ar);
        vforce(1,sa_i) = TS*d_cut*w_cut*((1/(sin(psh_ar)*sin(psh_ar)))-2);
        rforce(1,sa_i) = vforce(1,sa_i)/hforce(1,sa_i);

        t_i = t_i+t_s;
        vtime(1,sa_i) = t_i;
end

%statistic of each criterion
c1_ratio = (count_c1*100)/sa_i
c2_ratio = (count_c2*100)/sa_i
c3_ratio = (count_c3*100)/sa_i

MSH = [v_rot',vpsh_a'];
MCF = [v_rot',vforce'];
MTC = [v_rot',hforce'];
MCRY = [vpsh_a'];

pause on;

plot(v_rot, vpsh_a);
grid;
title('Variation of shear angle with crystallographic orientation');
xlabel('Angle of rotation of the crystal');
ylabel('Possible shear angle (degree)');
pause;

plot(vtime, vpsh_a);
grid;
title('Variation of shear angle with time');
xlabel('Time (ms)');
ylabel('Possible shear angle (degree)');
pause;

polar(v_rotr, vpsh_a);
grid;
title('Variation of shear angle with crystallographic orientation');
pause;

plot(v_rot, hforce);
grid;
title('Variation of cutting force (X-axis) with crystallographic orientation');
xlabel('Angle of rotation of the crystal');
ylabel('Cutting force number');
pause;

plot(v_rot, vforce);
grid;
title('Variation of cutting force (Z-axis) with crystallographic orientation');
xlabel('Angle of rotation of the crystal');
ylabel('Cutting force number');
pause;

plot(v_rot, rforce);
grid;
title('Variation of cutting force ratio with crystallographic orientation');
xlabel('Angle of rotation of the crystal');
ylabel('Cutting force ratio');
pause;

polar(v_rotr, hforce);
grid;
title('Variation of cutting force (X-axis) with crystallographic orientation');
pause;

polar(v_rotr, vforce+1);
grid;
title('Variation of cutting force (Z-axis) with crystallographic orientation');
pause;

polar(v_rotr, rforce+1);
grid;
title('Variation of cutting force ratio with crystallographic orientation');
pause;

[mx, nx] = size(hforce);
s_rate = nx;

%Spectrum analysis
[Pxx, fxx]=psd(hforce', nx, s_rate);
[Pyy, fxy]=psd(vforce', nx, s_rate);

subplot(2,1,1);
plot(fxx, Pxx);
xlabel('Frequency of X-axis cutting force variation (Hz)');
ylabel('Power spectral density');
```

```
grid;
pause;

subplot(2,1,2);
plot(fxy, Pyy)
xlabel('Frequency of Z-axis cutting force variation (Hz)');
ylabel('Power spectral density');
grid;

save orient.dat orient_v -ascii;        %save orientation data

Hc_close = uicontrol(gcf, 'Style', 'push', ...
        'Position', [480 3 70 20],...
        'String', 'Close',...
         'CallBack','clf; fftsave4; fftsgs1;');

Hc_quit = uicontrol(gcf, 'Style', 'push', ...
        'Position', [80 3 70 20],...
        'String', 'Quit',
        'CallBack','clf; fftsgs1;');

Hc_zoom = uicontrol(gcf, 'Style', 'push', ...
        'Position', [5 3 70 20],...
        'String', 'Zoom','CallBack', 'zoom on');


VMENU4TM.M

%Input for vibration model parameters (Tool)

clf;

load vmtpara.dat;

SP=vmtpara;

a0_u = SP(1,1);
a0_l = SP(2,1);
a0_s = SP(3,1);
a1_u = SP(4,1);
a1_l = SP(5,1);
a1_s = SP(6,1);
s_rate = SP(7,1);

t_frame = uicontrol(gcf, 'Style', 'frame','BackgroundColor', 'm',...
                'HorizontalAlignment','Center','Position', [20 15 520 395]);

t1_head = uicontrol(gcf,'Style', 'text',...
                'Position', [80 375 430 20],...
                'String', 'THE HONG KONG POLYTECHNIC UNIVERSITY',...
                'BackgroundColor', 'm','HorizontalAlignment', 'Center');

t2_head = uicontrol(gcf,'Style', 'text',...
                'Position', [80 355 430 20],...
                'String', 'Department of Manufacturing Engineering',...
                'BackgroundColor', 'm','HorizontalAlignment', 'Center');

Hc_frame = uicontrol(gcf, 'Style', 'frame','BackgroundColor', 'b',...
                'HorizontalAlignment','Center','Position', [20 15 460 340]);

M_label = uicontrol(gcf, 'Style', 'text',...
                                'Position', [30 320 440 30],'BackgroundColor', 'c',...
                                'HorizontalAlignment','Center',...
                                'String', 'VIBRATION MODEL PARAMETERS DETERMINATION (TOOL)');

cl_label = uicontrol(gcf, 'Style', 'text',...
                                'Position', [30 290 400 20],...
                                'BackgroundColor', 'g',...
                                'HorizontalAlignment','Center',...
                                'String', 'Pleas input 95% confidence interval for the parameters');

dr_label = uicontrol(gcf, 'Style', 'text',...
                                'Position', [150 250 100 30],...
                                'BackgroundColor', 'g',...
                                'HorizontalAlignment','Center',...
                                'String', 'Damping ratio');

fn_label = uicontrol(gcf, 'Style', 'text',...
                                'Position', [270 250 100 30],...
                                'BackgroundColor', 'g',...
                                'HorizontalAlignment','Center',...
                                'String', 'Natural freq (Wn)');

u_label = uicontrol(gcf, 'Style', 'text',...
                                'Position', [30 210 100 30],...
                                'BackgroundColor', 'g',...
                                'HorizontalAlignment','Center',...
                                'String', 'Upper limit');

l_label = uicontrol(gcf, 'Style', 'text',...
                                'Position', [30 170 100 30],...
```

```
                    'BackgroundColor', 'g',...
                    'HorizontalAlignment','Center',...
                    'String', 'Lower limit');

s_label = uicontrol(gcf, 'Style', 'text',...
                    'Position', [30 130 100 30],...
                    'BackgroundColor', 'g',...
                    'HorizontalAlignment','Center',...
                    'String', 'Step size');

Hcu_a0 = uicontrol(gcf, 'Style', 'edit',...
                    'Position', [150 210 100 30],...
                    'BackgroundColor', 'w',...
                    'HorizontalAlignment','Center',...
                    'String', num2str(a0_u),...
                    'Callback', 'get(Hcu_a0, "String");');

Hcl_a0 = uicontrol(gcf, 'Style', 'edit',...
                    'Position', [150 170 100 30],...
                    'BackgroundColor', 'w',...
                    'HorizontalAlignment','Center',...
                    'String', num2str(a0_l),...
                    'Callback', 'get(Hcl_a0, "String");');

Hcs_a0 = uicontrol(gcf, 'Style', 'edit',...
                    'Position', [150 130 100 30],...
                    'BackgroundColor', 'w',...
                    'HorizontalAlignment','Center',...
                    'String', num2str(a0_s),...
                    'Callback', 'get(Hcs_a0, "String");');

Hcu_a1 = uicontrol(gcf, 'Style', 'edit',...
                    'Position', [270 210 100 30],...
                    'BackgroundColor', 'w',...
                    'HorizontalAlignment','Center',...
                    'String', num2str(a1_u),...
                    'Callback', 'get(Hcu_a1, "String");');

Hcl_a1 = uicontrol(gcf, 'Style', 'edit',...
                    'Position', [270 170 100 30],...
                    'BackgroundColor', 'w',...
                    'HorizontalAlignment','Center',...
                    'String', num2str(a1_l),...
                    'Callback', 'get(Hcl_a1, "String");');

Hcs_a1 = uicontrol(gcf, 'Style', 'edit',...
                    'Position', [270 130 100 30],...
                    'BackgroundColor', 'w',...
                    'HorizontalAlignment','Center',...
                    'String', num2str(a1_s),...
                    'Callback', 'get(Hcs_a1, "String");');

srate_label = uicontrol(gcf, 'Style', 'text',...
                    'Position', [30 80 200 30],...
                    'BackgroundColor', 'y',...
                    'HorizontalAlignment','Left',...
                    'String', 'Sample rate :');

Hc_srate = uicontrol(gcf, 'Style', 'edit',...
                    'Position', [250 80 150 30],...
                    'BackgroundColor', 'w',...
                    'HorizontalAlignment','Center',...
                    'String', num2str(s_rate),...
                    'Callback', 'get(Hc_srate, "String");');

Hc_proceed = uicontrol(gcf, 'Style', 'push', ...
                'Position', [390 20 80 20],...
                'String', 'Proceed',...
                'CallBack',[...
                'P=zeros(6,1); P(1,1)=eval(get(Hcu_a0, "String"));,'...
                'P(2,1)=eval(get(Hcl_a0, "String"));,'...
                'P(3,1)=eval(get(Hcs_a0, "String"));,'...
                'P(4,1)=eval(get(Hcu_a1, "String"));,'...
                'P(5,1)=eval(get(Hcl_a1, "String"));,'...
                'P(6,1)=eval(get(Hcs_a1, "String"));,'...
                'P(7,1)=eval(get(Hc_srate, "String"));,'...
                'save vmtpara.dat P -ascii;clg;vmopt4tm']);

Hc_close = uicontrol(gcf, 'Style', 'push', ...
                'Position', [485 25 50 45],...
                'String', 'Exit',...
                'CallBack',[...
                'P=zeros(6,1); P(1,1)=eval(get(Hcu_a0, "String"));,'...
                'P(2,1)=eval(get(Hcl_a0, "String"));,'...
                'P(3,1)=eval(get(Hcs_a0, "String"));,'...
                'P(4,1)=eval(get(Hcu_a1, "String"));,'...
                'P(5,1)=eval(get(Hcl_a1, "String"));,'...
                'P(6,1)=eval(get(Hcs_a1, "String"));,'...
                'P(7,1)=eval(get(Hc_srate, "String"));,'...
                'save vmtpara.dat P -ascii;clg; fftsgs1']);
```

VOPT4TM.M

```
%Determination of vibration model parameters for the tool

load vmtpara.dat;

SP=vmtpara;

dr_u = SP(1,1);
dr_l = SP(2,1);
dr_s = SP(3,1);

fn_u = SP(4,1);
fn_l = SP(5,1);
fn_s = SP(6,1);
s = SP(7,1);

[fname, pname]=uigetfile('*.dat', 'Select tool vibration file to process');

fid = fopen(fname);
G = fscanf(fid, '%g', [1,inf]);
fclose(fid);

A=G';

[m,n] = size(A);

Y=zeros(m/2,1);
T=zeros(m/2,1);
B=zeros(m/2,2);

Xmin = A(1,1);
t_step = A(2,1)-A(1,1);
%s = t_step;

for i=1:m/2
   T(i,1)=A(i,1)-Xmin;
   B(i,1)=T(i,1);
end

for j=(m/2+1):m
   Y((j-(m/2)),1)= A(j,1);                    % unit in um
   B((j-(m/2)),2)=Y((j-(m/2)),1);
end

plot(T,Y);
Title('Profile plot');
xlabel('time (second) ');
ylabel('Displacement (micrometres)');
grid;
pause;

no_fn = fix((fn_u-fn_l)/fn_s)+1;
no_dr = fix((dr_u-dr_l)/dr_s)+1;
no_s = no_dr*no_fn
pause;

optf1 = zeros(no_s, 1);
optf2 = zeros(no_s, 1);
optap = zeros(no_s, 1);
opterr = zeros(no_s,1);
optfn = zeros(no_s,1);
optdr = zeros(no_s,1);

optm =zeros(1,8);
i_s = 0;

pause off;

for dr_i=dr_l:dr_s:dr_u
  for fn_i=fn_l:fn_s:fn_u

                a1 = 2*dr_i*fn_i;
                a0 = fn_i*fn_i;

                u1=0.5*(-a1+sqrt(a1*a1-4*a0));
                u2=0.5*(-a1-sqrt(a1*a1-4*a0));

                L1=exp(u1*t_step);
                L2=exp(u2*t_step);

                f1=L1+L2;
                f2=-L1*L2;

                PU = -u1*(1+L1*L1)*(1-L2*L2)+u2*(1+L2*L2)*(1-L1*L1);
                PL = 2*(u1*L1*(1-L2*L2)-u2*L2*(1-L1*L1));
                P= PU/PL

                ap1=-P+sqrt(P*P-1)
                ap2=-P-sqrt(P*P-1)

                if (abs(ap1)<=1)&(abs(ap2)>1)
```

```
                ap = ap1
        end

        if (abs(ap1)>1)&(abs(ap2)<=1)
                ap = ap2
        end

        mt=2;

        OFI=zeros(mt,1);
        OTI=zeros(mt-1,1);
        atm =zeros(mt-1,1);
        Xtp =zeros(m/2,1);
        Xtm = zeros(mt,1);
        Xtmp=zeros(mt,1);
        atmp = zeros(mt-1,1);
        Ep = zeros(m/2,1);
        sumsqerr=0;

        OFI(1,1)=f1;
        OFI(2,1)=f2;

        OTI(1,1)=ap;

        for j=1:m/2

                Xtp(j,1)=dot(OFI',Xtm')-dot(atm',OTI');

                perr=Y(j,1)-Xtp(j,1);
                Ep(j,1)=perr;

                %Reset the Xt vector by shift regrister
                for i=2:mt
                        Xtmp(i,1)=Xtm(i-1,1);
                end

                Xtmp(1,1)=Y(j,1);
                Xtm=Xtmp;

                %Reset the atm vector by shift regrister
                for k=2:mt-1
                        atmp(k,1)=atm(k-1,1);
                end

                atmp(mt-1,1)=perr;
                atm=atmp;

                sqerr = perr*perr;
                sumsqerr=sumsqerr+sqerr;
        end

        plot(T(10:m/2), Y(10:m/2), T(10:m/2), Xtp(10:m/2));
        pause;

        i_s = i_s+1
        opta0(i_s,1)=a0;
        opta1(i_s,1)=a1;
        optf1(i_s,1)=f1;
        optf2(i_s,1)=f2;
        optap(i_s,1)=ap;
        optfn(i_s,1)=fn_i;
        optdr(i_s,1)=dr_i;
        opterr(i_s,1)=sumsqerr;
  end
end

pause on;

plot3(optdr, optfn, opterr);
title('Error Performance Surface');
ylabel('Natural freq (rad/s)');
xlabel('Damping ratio');
zlabel('Sum of square errors');
grid;
pause;

MOPT = [optdr, optfn, opterr];

min_err=10e12;

for i=1:i_s
  if    opterr(i,1)<min_err
        min_err=opterr(i,1);
        optm(1,1)=opta0(i,1);
        optm(1,2)=opta1(i,1);
        optm(1,3)=optf1(i,1);
        optm(1,4)=optf2(i,1);
        optm(1,5)=optap(i,1);
        optm(1,6)=optfn(i,1);
        optm(1,7)=optdr(i,1);
        optm(1,8)=min_err;
  end
```

```
end

oa0 = optm(1,1);
oa1 = optm(1,2);
of1 = optm(1,3);
of2 = optm(1,4);
oap = optm(1,5);
ofn = optm(1,6);
odr = optm(1,7);

n_freq = ofn
n_freqc = 2*pi*n_freq
d_ratio = odr
clf;

t_frame = uicontrol(gcf, 'Style', 'frame','BackgroundColor', 'm',...
                'HorizontalAlignment','Center','Position', [20 15 520 395]);

t1_head = uicontrol(gcf,'Style', 'text',...
                'Position', [80 375 430 20],...
                'String', 'THE HONG KONG POLYTECHNIC UNIVERSITY',...
                'BackgroundColor', 'm','HorizontalAlignment', 'Center');

t2_head = uicontrol(gcf,'Style', 'text',...
                'Position', [80 355 430 20],...
                'String', 'Department of Manufacturing Engineering',...
                'BackgroundColor', 'm','HorizontalAlignment', 'Center');

Hc_frame = uicontrol(gcf, 'Style', 'frame','BackgroundColor', 'b',...
                'HorizontalAlignment','Center','Position', [20 15 460 340]);

M_label = uicontrol(gcf, 'Style', 'text',...
                                'Position', [50 320 340 20],'BackgroundColor', 'c',...
                                'HorizontalAlignment','Center',...
                                'String', 'VIBRATION SYSTEM PARAMETERS (Tool)');

ARMA_label = uicontrol(gcf, 'Style', 'text',...
                                'Position', [50 290 340 20],...
                                'BackgroundColor', 'y',...
                                'HorizontalAlignment','Center',...
                                'String', 'Parameters for ARMA(2,1) difference equation ');

ARMAEQN_label = uicontrol(gcf, 'Style', 'text',...
                                'Position', [50 260 340 20],...
                                'BackgroundColor', 'c',...
                                'HorizontalAlignment','Center',...
                                'String', 'X(t) = f1*X(t-1) - f2*X(t-2) = e(t) - ap*e(t-1)');

f1_label = uicontrol(gcf, 'Style', 'text',...
                                'Position', [50 230 220 20],...
                                'BackgroundColor', 'g',...
                                'HorizontalAlignment','Left',...
                                'String', 'Optimum value of f1 :');

Hc_opf1 = uicontrol(gcf, 'Style', 'edit',...
                                'Position', [290 230 100 20],...
                                'BackgroundColor', 'w',...
                                'HorizontalAlignment','Center',...
                                'String', num2str(of1),...
                                'Callback', 'get(Hc_opf1, "String");');

f2_label = uicontrol(gcf, 'Style', 'text',...
                                'Position', [50 200 220 20],...
                                'BackgroundColor', 'g',...
                                'HorizontalAlignment','Left',...
                                'String', 'Optimum value of f2 :');

Hc_opf2 = uicontrol(gcf, 'Style', 'edit',...
                                'Position', [290 200 100 20],...
                                'BackgroundColor', 'w',...
                                'HorizontalAlignment','Center',...
                                'String', num2str(of2),...
                                'Callback', 'get(Hc_opf2, "String");');

oap_label = uicontrol(gcf, 'Style', 'text',...
                                'Position', [50 170 220 20],...
                                'BackgroundColor', 'g',...
                                'HorizontalAlignment','Left',...
                                'String', 'Optimum value of ap :');

Hc_opap = uicontrol(gcf, 'Style', 'edit',...
                                'Position', [290 170 100 20],...
                                'BackgroundColor', 'w',...
                                'HorizontalAlignment','Center',...
                                'String', num2str(oap),...
                                'Callback', 'get(Hc_opap, "String");');

Sqerr_label = uicontrol(gcf, 'Style', 'text',...
                                'Position', [50 140 220 20],...
                                'BackgroundColor', 'g',...
                                'HorizontalAlignment','Left',...
                                'String', 'Sum of square error :');
```

```
Hc_sqerr = uicontrol(gcf, 'Style', 'edit',...
                                'Position', [290 140 100 20],...
                                'BackgroundColor', 'w',...
                                'HorizontalAlignment','Center',...
                                'String', num2str(min_err),...
                                'Callback', 'get(Hc_sqerr, "String");');

A2_label = uicontrol(gcf, 'Style', 'text',...
                                'Position', [50 110 340 20],...
                                'BackgroundColor', 'y',...
                                'HorizontalAlignment','Center',...
                                'String', 'Parameters for autoregressive system A(2)');

dr_label = uicontrol(gcf, 'Style', 'text',...
                                'Position', [50 80 220 20],...
                                'BackgroundColor', 'g',...
                                'HorizontalAlignment','Left',...
                                'String', 'Damping ratio : ');

Hc_dr = uicontrol(gcf, 'Style', 'edit',...
                                'Position', [290 80 100 20],...
                                'BackgroundColor', 'w',...
                                'HorizontalAlignment','Center',...
                                'String', num2str(d_ratio),...
                                'Callback', 'get(Hc_dr, "String");');

nfreq_label = uicontrol(gcf, 'Style', 'text',...
                                'Position', [50 50 220 20],...
                                'BackgroundColor', 'g',...
                                'HorizontalAlignment','Left',...
                                'String', 'Natural frequency (Hz) :');

Hc_nfreq = uicontrol(gcf, 'Style', 'edit',...
                                'Position', [290 50 100 20],...
                                'BackgroundColor', 'w',...
                                'HorizontalAlignment','Center',...
                                'String', num2str(n_freqc),...
                                'Callback', 'get(Hc_nfreq, "String");');

pause;
clf;

%display the optimum conditions
ou1=0.5*(-oa1+sqrt(oa1*oa1-4*oa0));
ou2=0.5*(-oa1-sqrt(oa1*oa1-4*oa0));

oL1=exp(ou1*t_step);
oL2=exp(ou2*t_step);

of1=oL1+oL2;
of2=-oL1*oL2;

oPU = -ou1*(1+oL1*oL1)*(1-oL2*oL2)+ou2*(1+oL2*oL2)*(1-oL1*oL1);
oPL = 2*(ou1*oL1*(1-oL2*oL2)-ou2*oL2*(1-oL1*oL1));
oP= oPU/oPL;

oap1=-oP+sqrt(oP*oP-1)
oap2=-oP-sqrt(oP*oP-1)

if (abs(oap1)<=1)&(abs(oap2)>=1)
        oap = oap1
end

if (abs(oap1)>1)&(abs(oap2)<1)
        oap = oap2
end

        mt=2;

        OF=zeros(mt,1);
        OT=zeros(mt-1,1);
        oatm =zeros(mt-1,1);
        oXtp =zeros(m/2,1);
        oXtm = zeros(mt,1);
        oXtmp=zeros(mt,1);
        oatmp = zeros(mt-1,1);
        oEp = zeros(m/2,1);
        osumsqerr=0;

        OF(1,1)=of1;
        OF(2,1)=of2;

        OT(1,1)=oap;

        for j=1:m/2

                oXtp(j,1)=dot(OF',oXtm')-dot(oatm',OT');

                operr=Y(j,1)-oXtp(j,1);
                oEp(j,1)=operr;
```

```
                %Reset the Xt vector by shift regrister
                for i=2:mt
                        oXtmp(i,1)=oXtm(i-1,1);
                end

                oXtmp(1,1)=Y(j,1);
                oXtm=oXtmp;

                %Reset the atm vector by shift regrister
                for k=2:mt-1
                        oatmp(k,1)=oatm(k-1,1);
                end

                oatmp(mt-1,1)=operr;
                oatm=oatmp;

                osqerr = operr*operr;
                sumsqerr=sumsqerr+sqerr;
        end

plot(T(10:m/2), Y(10:m/2), T(10:m/2), oXtp(10:m/2));
title('Comparing the model performance at optimum conditions');
xlabel('time');
ylabel('Y (micrometers)');
pause;

plot(T(10:m/2), oEp(10:m/2));
title('Prediction error plot at optimum conditions');
xlabel('time');
ylabel('Error (micrometers)');

MET = [T, oXtp, Y, oEp];

save errvmpt.dat MET -ascii  %save the error signal data
save optvmpt.dat optm -ascii  %save the vibration model parameters
save errsurft.dat MOPT -ascii %save the square error data

Hc_proceed = uicontrol(gcf, 'Style', 'push', ...
                'Position', [80 3 70 20],...
                'String', 'proceed',...
                'CallBack','clg; savevt1; fftsgs1;');

Hc_zoom = uicontrol(gcf, 'Style', 'push', ...
                'Position', [5 3 70 20],...
                'String', 'Zoom','CallBack', 'zoom on');
```

VMENU4WM.M

```
%Input for vibration model parameters (Work)

clf;

load vmwpara.dat;

SP=vmwpara;

a0_u = SP(1,1);
a0_l = SP(2,1);
a0_s = SP(3,1);
a1_u = SP(4,1);
a1_l = SP(5,1);
a1_s = SP(6,1);
s_rate = SP(7,1);

t_frame = uicontrol(gcf, 'Style', 'frame','BackgroundColor', 'm',...
                'HorizontalAlignment','Center','Position', [20 15 520 395]);

t1_head = uicontrol(gcf,'Style', 'text',...
                'Position', [80 375 430 20],...
                'String', 'THE HONG KONG POLYTECHNIC UNIVERSITY',...
                'BackgroundColor', 'm','HorizontalAlignment', 'Center');

t2_head = uicontrol(gcf,'Style', 'text',...
                'Position', [80 355 430 20],...
                'String', 'Department of Manufacturing Engineering',...
                'BackgroundColor', 'm','HorizontalAlignment', 'Center');

Hc_frame = uicontrol(gcf, 'Style', 'frame','BackgroundColor', 'b',...
                'HorizontalAlignment','Center','Position', [20 15 460 340]);

M_label = uicontrol(gcf, 'Style', 'text',...
                        'Position', [30 320 440 30],'BackgroundColor', 'c',...
                        'HorizontalAlignment','Center',...
                        'String', 'VIBRATION MODEL PARAMETERS DETERMINATION (Work)');

c1_label = uicontrol(gcf, 'Style', 'text',...
                        'Position', [30 290 400 20],...
                        'BackgroundColor', 'g',...
                        'HorizontalAlignment','Center',...
                        'String', 'Pleas input 95% confidence interval for the parameters');
```

```
dr_label = uicontrol(gcf, 'Style', 'text',...
                                'Position', [150 250 100 30],...
                                'BackgroundColor', 'g',...
                                'HorizontalAlignment','Center',...
                                'String', 'Damping ratio');

fn_label = uicontrol(gcf, 'Style', 'text',...
                                'Position', [270 250 100 30],...
                                'BackgroundColor', 'g',...
                                'HorizontalAlignment','Center',...
                                'String', 'Natural freq (Wn)');

u_label = uicontrol(gcf, 'Style', 'text',...
                                'Position', [30 210 100 30],...
                                'BackgroundColor', 'g',...
                                'HorizontalAlignment','Center',...
                                'String', 'Upper limit');

l_label = uicontrol(gcf, 'Style', 'text',...
                                'Position', [30 170 100 30],...
                                'BackgroundColor', 'g',...
                                'HorizontalAlignment','Center',...
                                'String', 'Lower limit');

s_label = uicontrol(gcf, 'Style', 'text',...
                                'Position', [30 130 100 30],...
                                'BackgroundColor', 'g',...
                                'HorizontalAlignment','Center',...
                                'String', 'Step size');

Hcu_a0 = uicontrol(gcf, 'Style', 'edit',...
                                'Position', [150 210 100 30],...
                                'BackgroundColor', 'w',...
                                'HorizontalAlignment','Center',...
                                'String', num2str(a0_u),...
                                'Callback', 'get(Hcu_a0, "String");');

Hcl_a0 = uicontrol(gcf, 'Style', 'edit',...
                                'Position', [150 170 100 30],...
                                'BackgroundColor', 'w',...
                                'HorizontalAlignment','Center',...
                                'String', num2str(a0_l),...
                                'Callback', 'get(Hcl_a0, "String");');

Hcs_a0 = uicontrol(gcf, 'Style', 'edit',...
                                'Position', [150 130 100 30],...
                                'BackgroundColor', 'w',...
                                'HorizontalAlignment','Center',...
                                'String', num2str(a0_s),...
                                'Callback', 'get(Hcs_a0, "String");');

Hcu_a1 = uicontrol(gcf, 'Style', 'edit',...
                                'Position', [270 210 100 30],...
                                'BackgroundColor', 'w',...
                                'HorizontalAlignment','Center',...
                                'String', num2str(a1_u),...
                                'Callback', 'get(Hcu_a1, "String");');

Hcl_a1 = uicontrol(gcf, 'Style', 'edit',...
                                'Position', [270 170 100 30],...
                                'BackgroundColor', 'w',...
                                'HorizontalAlignment','Center',...
                                'String', num2str(a1_l),...
                                'Callback', 'get(Hcl_a1, "String");');

Hcs_a1 = uicontrol(gcf, 'Style', 'edit',...
                                'Position', [270 130 100 30],...
                                'BackgroundColor', 'w',...
                                'HorizontalAlignment','Center',...
                                'String', num2str(a1_s),...
                                'Callback', 'get(Hcs_a1, "String");');

srate_label = uicontrol(gcf, 'Style', 'text',...
                                'Position', [30 80 200 30],...
                                'BackgroundColor', 'y',...
                                'HorizontalAlignment','Left',...
                                'String', 'Sample rate :');

Hc_srate = uicontrol(gcf, 'Style', 'edit',...
                                'Position', [250 80 150 30],...
                                'BackgroundColor', 'w',...
                                'HorizontalAlignment','Center',...
                                'String', num2str(s_rate),...
                                'Callback', 'get(Hc_srate, "String");');

Hc_proceed = uicontrol(gcf, 'Style', 'push', ...
                'Position', [390 20 80 20],...
                'String', 'Proceed',...
                'CallBack',[...
                'P=zeros(6,1); P(1,1)=eval(get(Hcu_a0, "String"));',...
                'P(2,1)=eval(get(Hcl_a0, "String"));',...
                'P(3,1)=eval(get(Hcs_a0, "String"));',...
```

```
                'P(4,1)=eval(get(Hcu_a1, "String"));,'...
                'P(5,1)=eval(get(Hcl_a1, "String"));,'...
                'P(6,1)=eval(get(Hcs_a1, "String"));,'...
                'P(7,1)=eval(get(Hc_srate, "String"));,'...
                'save vmwpara.dat P -ascii;clg;vmopt4wm']);

Hc_close = uicontrol(gcf, 'Style', 'push', ...
                'Position', [485 25 50 45],...
                'String', 'Exit',...
                'CallBack',[...
                'P=zeros(6,1); P(1,1)=eval(get(Hcu_a0, "String"));,'...
                'P(2,1)=eval(get(Hcl_a0, "String"));,'...
                'P(3,1)=eval(get(Hcs_a0, "String"));,'...
                'P(4,1)=eval(get(Hcu_a1, "String"));,'...
                'P(5,1)=eval(get(Hcl_a1, "String"));,'...
                'P(6,1)=eval(get(Hcs_a1, "String"));,'...
                'P(7,1)=eval(get(Hc_srate, "String"));,'...
                'save vmwpara.dat P -ascii;clg; fftsgs1']);
```

VOPT4WM.M

```
%Determination of vibration model parameters for the work

load vmwpara.dat;

SP=vmwpara;

dr_u = SP(1,1);
dr_l = SP(2,1);
dr_s = SP(3,1);

fn_u = SP(4,1);
fn_l = SP(5,1);
fn_s = SP(6,1);
s = SP(7,1);

[fname, pname]=uigetfile('*.dat', 'Select work vibration file to process');

fid = fopen(fname);
G = fscanf(fid, '%g', [1,inf]);
fclose(fid);

A=G';

[m,n] = size(A);

Y=zeros(m/2,1);
T=zeros(m/2,1);
B=zeros(m/2,2);

Xmin = A(1,1);
t_step = A(2,1)-A(1,1);
%t_step=s;

for i=1:m/2
   T(i,1)=A(i,1)-Xmin;
   B(i,1)=T(i,1);
end

for j=(m/2+1):m
   Y((j-(m/2)),1)= A(j,1);                    % unit in um
   B((j-(m/2)),2)=Y((j-(m/2)),1);
end

plot(T,Y);
Title('Profile plot');
xlabel('time (second) ');
ylabel('Displacement (micrometres)');
grid;
pause;

no_fn = fix((fn_u-fn_l)/fn_s)+1;
no_dr = fix((dr_u-dr_l)/dr_s)+1;
no_s = no_dr*no_fn
pause;

optf1 = zeros(no_s, 1);
optf2 = zeros(no_s, 1);
optap = zeros(no_s, 1);
opterr = zeros(no_s,1);
optfn = zeros(no_s,1);
optdr = zeros(no_s,1);

optm =zeros(1,8);
i_s = 0;

pause off;

for dr_i=dr_l:dr_s:dr_u
 for fn_i=fn_l:fn_s:fn_u
```

```
            a1 = 2*dr_i*fn_i;
            a0 = fn_i*fn_i;

            u1=0.5*(-a1+sqrt(a1*a1-4*a0));
            u2=0.5*(-a1-sqrt(a1*a1-4*a0));

            L1=exp(u1*t_step);
            L2=exp(u2*t_step);

            f1=L1+L2;
            f2=-L1*L2;

            PU = -u1*(1+L1*L1)*(1-L2*L2)+u2*(1+L2*L2)*(1-L1*L1);
            PL = 2*(u1*L1*(1-L2*L2)-u2*L2*(1-L1*L1));
            P= PU/PL

            ap1=-P+sqrt(P*P-1)
            ap2=-P-sqrt(P*P-1)

            if (abs(ap1)<=1)&(abs(ap2)>1)
                        ap = ap1
            end

            if (abs(ap1)>1)&(abs(ap2)<=1)
                        ap = ap2
            end

            mt=2;

            OFI=zeros(mt,1);
            OTI=zeros(mt-1,1);
            atm =zeros(mt-1,1);
            Xtp =zeros(m/2,1);
            Xtm = zeros(mt,1);
            Xtmp=zeros(mt,1);
            atmp = zeros(mt-1,1);
            Ep = zeros(m/2,1);
            sumsqerr=0;

            OFI(1,1)=f1;
            OFI(2,1)=f2;

            OTI(1,1)=ap;

            for j=1:m/2

                        Xtp(j,1)=dot(OFI',Xtm')-dot(atm',OTI');

                        perr=Y(j,1)-Xtp(j,1);
                        Ep(j,1)=perr;

                        %Reset the Xt vector by shift regrister
                        for i=2:mt
                                    Xtmp(i,1)=Xtm(i-1,1);
                        end

                        Xtmp(1,1)=Y(j,1);
                        Xtm=Xtmp;

                        %Reset the atm vector by shift regrister
                        for k=2:mt-1
                                    atmp(k,1)=atm(k-1,1);
                        end

                        atmp(mt-1,1)=perr;
                        atm=atmp;

                        sqerr = perr*perr;
                        sumsqerr=sumsqerr+sqerr;
            end

            plot(T(10:m/2), Y(10:m/2), T(10:m/2), Xtp(10:m/2));
            pause;

            i_s = i_s+1
            opta0(i_s,1)=a0;
            opta1(i_s,1)=a1;
            optf1(i_s,1)=f1;
            optf2(i_s,1)=f2;
            optap(i_s,1)=ap;
            optfn(i_s,1)=fn_i;
            optdr(i_s,1)=dr_i;
            opterr(i_s,1)=sumsqerr;
  end
end

pause on;

plot3(optdr, optfn, opterr);
title('Error Performance Surface');
ylabel('Natural freq (rad/s)');
xlabel('Damping ratio');
```

```
zlabel('Sum of square errors');
grid;
pause;

MOPW = [optdr, optfn, opterr];

min_err=10e12;

for i=1:i_s
  if        opterr(i,1)<min_err
            min_err=opterr(i,1);
            optm(1,1)=opta0(i,1);
            optm(1,2)=opta1(i,1);
            optm(1,3)=optf1(i,1);
            optm(1,4)=optf2(i,1);
            optm(1,5)=optap(i,1);
            optm(1,6)=optfn(i,1);
            optm(1,7)=optdr(i,1);
            optm(1,8)=min_err;
  end
end

oa0 = optm(1,1);
oa1 = optm(1,2);
of1 = optm(1,3);
of2 = optm(1,4);
oap = optm(1,5);
ofn = optm(1,6);
odr = optm(1,7);

n_freq = ofn
n_freqc = 2*pi*n_freq
d_ratio = odr
clf;

t_frame = uicontrol(gcf, 'Style', 'frame','BackgroundColor', 'm',...
            'HorizontalAlignment','Center','Position', [20 15 520 395]);

t1_head = uicontrol(gcf,'Style', 'text',...
            'Position', [80 375 430 20],...
            'String', 'THE HONG KONG POLYTECHNIC UNIVERSITY',...
            'BackgroundColor', 'm','HorizontalAlignment', 'Center');

t2_head = uicontrol(gcf,'Style', 'text',...
            'Position', [80 355 430 20],...
            'String', 'Department of Manufacturing Engineering',...
            'BackgroundColor', 'm','HorizontalAlignment', 'Center');

Hc_frame = uicontrol(gcf, 'Style', 'frame','BackgroundColor', 'b',...
            'HorizontalAlignment','Center','Position', [20 15 460 340]);

M_label = uicontrol(gcf, 'Style', 'text',...
                        'Position', [50 320 340 20],'BackgroundColor', 'c',...
                        'HorizontalAlignment','Center',...
                        'String', 'VIBRATION SYSTEM PARAMETERS (Work)');

ARMA_label = uicontrol(gcf, 'Style', 'text',...
                        'Position', [50 290 340 20],...
                        'BackgroundColor', 'y',...
                        'HorizontalAlignment','Center',...
                        'String', 'Parameters for ARMA(2,1) difference equation ');

ARMAEQN_label = uicontrol(gcf, 'Style', 'text',...
                        'Position', [50 260 340 20],...
                        'BackgroundColor', 'c',...
                        'HorizontalAlignment','Center',...
                        'String', 'X(t) - f1*X(t-1) - f2*X(t-2) = e(t) - ap*e(t-1)');

f1_label = uicontrol(gcf, 'Style', 'text',...
                        'Position', [50 230 220 20],...
                        'BackgroundColor', 'g',...
                        'HorizontalAlignment','Left',...
                        'String', 'Optimum value of f1 :');

Hc_opf1 = uicontrol(gcf, 'Style', 'edit',...
                        'Position', [290 230 100 20],...
                        'BackgroundColor', 'w',...
                        'HorizontalAlignment','Center',...
                        'String', num2str(of1),...
                        'Callback', 'get(Hc_opf1, "String");');

f2_label = uicontrol(gcf, 'Style', 'text',...
                        'Position', [50 200 220 20],...
                        'BackgroundColor', 'g',...
                        'HorizontalAlignment','Left',...
                        'String', 'Optimum value of f2 :');

Hc_opf2 = uicontrol(gcf, 'Style', 'edit',...
                        'Position', [290 200 100 20],...
                        'BackgroundColor', 'w',...
                        'HorizontalAlignment','Center',...
                        'String', num2str(of2),...
```

```
                    'Callback', 'get(Hc_optf2, "String");');

oap_label = uicontrol(gcf, 'Style', 'text',...
                    'Position', [50 170 220 20],...
                    'BackgroundColor', 'g',...
                    'HorizontalAlignment','Left',...
                    'String', 'Optimum value of ap :');

Hc_opap = uicontrol(gcf, 'Style', 'edit',...
                    'Position', [290 170 100 20],...
                    'BackgroundColor', 'w',...
                    'HorizontalAlignment','Center',...
                    'String', num2str(oap),...
                    'Callback', 'get(Hc_opap, "String");');

Sqerr_label = uicontrol(gcf, 'Style', 'text',...
                    'Position', [50 140 220 20],...
                    'BackgroundColor', 'g',...
                    'HorizontalAlignment','Left',...
                    'String', 'Sum of square error :');

Hc_sqerr = uicontrol(gcf, 'Style', 'edit',...
                    'Position', [290 140 100 20],...
                    'BackgroundColor', 'w',...
                    'HorizontalAlignment','Center',...
                    'String', num2str(min_err),...
                    'Callback', 'get(Hc_sqerr, "String");');

A2_label = uicontrol(gcf, 'Style', 'text',...
                    'Position', [50 110 340 20],...
                    'BackgroundColor', 'y',...
                    'HorizontalAlignment','Center',...
                    'String', 'Parameters for autoregressive system A(2)');

dr_label = uicontrol(gcf, 'Style', 'text',...
                    'Position', [50 80 220 20],...
                    'BackgroundColor', 'g',...
                    'HorizontalAlignment','Left',...
                    'String', 'Damping ratio : ');

Hc_dr = uicontrol(gcf, 'Style', 'edit',...
                    'Position', [290 80 100 20],...
                    'BackgroundColor', 'w',...
                    'HorizontalAlignment','Center',...
                    'String', num2str(d_ratio),...
                    'Callback', 'get(Hc_dr, "String");');

nfreq_label = uicontrol(gcf, 'Style', 'text',...
                    'Position', [50 50 220 20],...
                    'BackgroundColor', 'g',...
                    'HorizontalAlignment','Left',...
                    'String', 'Natural frequency (Hz) :');

Hc_nfreq = uicontrol(gcf, 'Style', 'edit',...
                    'Position', [290 50 100 20],...
                    'BackgroundColor', 'w',...
                    'HorizontalAlignment','Center',...
                    'String', num2str(n_freqc),...
                    'Callback', 'get(Hc_nfreq, "String");');

pause;
clf;

%display the optimum conditions
ou1=0.5*(-oa1+sqrt(oa1*oa1-4*oa0));
ou2=0.5*(-oa1-sqrt(oa1*oa1-4*oa0));

oL1=exp(ou1*t_step);
oL2=exp(ou2*t_step);

of1=oL1+oL2;
of2=-oL1*oL2;

oPU = -ou1*(1+oL1*oL1)*(1-oL2*oL2)+ou2*(1+oL2*oL2)*(1-oL1*oL1);
oPL = 2*(ou1*oL1*(1-oL2*oL2)-ou2*oL2*(1-oL1*oL1));
oP= oPU/oPL;

oap1=-oP+sqrt(oP*oP-1)
oap2=-oP-sqrt(oP*oP-1)

if (abs(oap1)<=1)&(abs(oap2)>=1)
        oap = oap1
end

if (abs(oap1)>1)&(abs(oap2)<1)
        oap = oap2
end

        mt=2;

        OF=zeros(mt,1);
        OT=zeros(mt-1,1);
```

```
                oatm =zeros(mt-1,1);
                oXtp =zeros(m/2,1);
                oXtm = zeros(mt,1);
                oXtmp=zeros(mt,1);
                oatmp = zeros(mt-1,1);
                oEp = zeros(m/2,1);
                osumsqerr=0;

                OF(1,1)=of1;
                OF(2,1)=of2;

                OT(1,1)=oap;

                for j=1:m/2

                        oXtp(j,1)=dot(OF',oXtm')-dot(oatm',OT');

                        operr=Y(j,1)-oXtp(j,1);
                        oEp(j,1)=operr;

                        %Reset the Xt vector by shift regnster
                        for i=2:mt
                                oXtmp(i,1)=oXtm(i-1,1);
                        end

                        oXtmp(1,1)=Y(j,1);
                        oXtm=oXtmp;

                        %Reset the atm vector by shift regnster
                        for k=2:mt-1
                                oatmp(k,1)=oatm(k-1,1);
                        end

                        oatmp(mt-1,1)=operr;
                        oatm=oatmp;

                        osqerr = operr*operr;
                        sumsqerr=sumsqerr+sqerr;
                end

plot(T(10:m/2), oXtp(10:m/2), T(10:m/2), Y(10:m/2));
title('Comparing the model performance at optimum conditions');
xlabel('time');
ylabel('Y (micrometers)');
pause;

plot(T(10:m/2), oEp(10:m/2));
title('Prediction error plot at optimum conditions');
xlabel('time');
ylabel('Error (micrometers)');

MET = [T, oXtp, Y, oEp];

save errvmpw.dat MET -ascii %save the error signal data
save optvmpw.dat optm -ascii            %save the vibration model parameters
save errsurfw.dat MOPW -ascii           %save the square error data

Hc_proceed = uicontrol(gcf, 'Style', 'push', ...
                'Position', [80 3 70 20],...
                'String', 'proceed',...
                'CallBack','clg; savevw1; fftsgs1;');

Hc_zoom = uicontrol(gcf, 'Style', 'push', ...
                'Position', [5 3 70 20],...
                'String', 'Zoom','CallBack', 'zoom on');
```

MVSINPM.M

```
%input for the MVS program (Merchant criterion)

load mvspara1.dat;

SP=mvspara1;
dia = SP(1,1);
f = SP(2,1);
v = SP(3,1);
d = SP(4,1);
trad = SP(5,1);
STT = SP(6,1);
STW = SP(7,1);
h_n = SP(8,1);
s_c = SP(9,1);
TS = SP(10,1);

t_frame = uicontrol(gcf, 'Style', 'frame','BackgroundColor', 'm',...
        'HorizontalAlignment','Center','Position', [20 15 520 395]);

t1_head = uicontrol(gcf,'Style', 'text',...
        'Position', [80 375 430 20],...
        'String', 'THE HONG KONG POLYTECHNIC UNIVERSITY',...
        'BackgroundColor', 'm','HorizontalAlignment', 'Center');
```

```
t2_head = uicontrol(gcf,'Style', 'text',...
        'Position', [80 355 430 20],...
        'String', 'Department of Manufacturing Engineering',...
        'BackgroundColor', 'm','HorizontalAlignment', 'Center');

Hc_frame = uicontrol(gcf, 'Style', 'frame','BackgroundColor', 'b',...
        'HorizontalAlignment','Center','Position', [20 15 460 340]);

M_label = uicontrol(gcf, 'Style', 'text',...
                'Position', [50 320 390 20],'BackgroundColor', 'c',...
                'HorizontalAlignment','Center',...
                'String', 'MACHINE PARAMETERS SETTING');

dia_label = uicontrol(gcf, 'Style', 'text',...
                'Position', [50 290 100 20],...
                'BackgroundColor', 'g',...
                'HorizontalAlignment','Left',...
                'String', 'Part diameter (mm) :'),

Hc_dia = uicontrol(gcf, 'Style', 'edit',...
                'Position', [160 290 60 20],...
                'BackgroundColor', 'w',...
                'HorizontalAlignment','Center',...
                'String', num2str(dia),...
                 'Callback', 'get(Hc_dia, "String");');

ts_label = uicontrol(gcf, 'Style', 'text',...
                'Position', [230 290 120 20],...
                'BackgroundColor', 'g',...
                'HorizontalAlignment','Left',...
                'String', 'Shear stress (N/sq. m) :');

Hc_ts = uicontrol(gcf, 'Style', 'edit',...
                'Position', [360 290 100 20],...
                'BackgroundColor', 'w',...
                'HorizontalAlignment','Center',...
                'String', num2str(TS),...
                'Callback', 'get(Hc_ts, "String");');

f_label = uicontrol(gcf, 'Style', 'text',...
                'Position', [50 260 230 20],...
                'BackgroundColor', 'g',...
                'HorizontalAlignment','Left',...
                'String', 'Feed Rate (mm/min) :');

Hc_feed = uicontrol(gcf, 'Style', 'edit',...
                'Position', [300 260 100 20],...
                'BackgroundColor', 'w',...
                'HorizontalAlignment','Center',...
                'String', num2str(f),...
                'Callback', 'get(Hc_feed, "String");');

s_label = uicontrol(gcf, 'Style', 'text',...
                'Position', [50 230 230 20],...
                'BackgroundColor', 'g',...
                'HorizontalAlignment','Left',...
                'String', 'Spindle speed (rpm) :');

Hc_sspeed = uicontrol(gcf, 'Style', 'edit',...
                'Position', [300 230 100 20],...
                'BackgroundColor', 'w',...
                'HorizontalAlignment','Center',...
                'String', num2str(v),...
                'Callback', 'get(Hc_sspeed, "String");');

d_label = uicontrol(gcf, 'Style', 'text',...
                'Position', [50 200 230 20],...
                'BackgroundColor', 'g',...
                'HorizontalAlignment','Left',...
                'String', 'Depth of cut (micrometre) :');

Hc_dcut = uicontrol(gcf, 'Style', 'edit',...
                'Position', [300 200 100 20],...
                'BackgroundColor', 'w',...
                'HorizontalAlignment','Center',...
                'String', num2str(d),...
                'Callback', 'get(Hc_dcut, "String");');

trad_label = uicontrol(gcf, 'Style', 'text',...
                'Position', [50 170 230 20],...
                'BackgroundColor', 'g',...
                'HorizontalAlignment','Left',...
                'String', 'Tool radius (mm) :');

Hc_trad = uicontrol(gcf, 'Style', 'edit',...
                'Position', [300 170 100 20],...
                'BackgroundColor', 'w',...
                'HorizontalAlignment','Center',...
                'String', num2str(trad),...
                'Callback', 'get(Hc_trad, "String");');
```

```
V_label = uicontrol(gcf, 'Style', 'text',...
                'Position', [50 140 400 20],...
                'BackgroundColor', 'c',...
                'HorizontalAlignment','Center',...
                'String','VIBRATION PARAMETERS SETTING');

EMT_label = uicontrol(gcf, 'Style', 'text',...
                'Position', [320 110 60 20],...
                'BackgroundColor', 'g',...
                'HorizontalAlignment','Center',...
                'String', 'Tool');

EMW_label = uicontrol(gcf, 'Style', 'text',...
                'Position', [390 110 60 20],...
                'BackgroundColor', 'g',...
                'HorizontalAlignment','Center',...
                'String', 'Work');

EM_label = uicontrol(gcf, 'Style', 'text',...
                'Position', [50 80 260 20],...
                'BackgroundColor', 'g',...
                'HorizontalAlignment','Left',...
                'String', 'Stiffness (N/um) :');

Hc_EMT = uicontrol(gcf, 'Style', 'edit',...
                'Position', [320 80 60 20],...
                'BackgroundColor', 'w',...
                'HorizontalAlignment','Center',...
                'String', num2str(STT),...
                'Callback', 'get(Hc_EMT, "String");');

Hc_EMW = uicontrol(gcf, 'Style', 'edit',...
                'Position', [390 80 60 20],...
                'BackgroundColor', 'w',...
                'HorizontalAlignment','Center',...
                'String', num2str(STW),...
                'Callback', 'get(Hc_EMW, "String");');

hn_label = uicontrol(gcf, 'Style', 'text',...
                'Position', [50 50 260 20],...
                'BackgroundColor', 'g',...
                'HorizontalAlignment','Left',...
                'String', 'Run-out amplitude (micrometre) :');

Hc_hn = uicontrol(gcf, 'Style', 'edit',...
                'Position', [320 50 120 20],...
                'BackgroundColor', 'w',...
                'HorizontalAlignment','Center',...
                'String', num2str(h_n),...
                'Callback', 'get(Hc_hn, "String");');

sc_label = uicontrol(gcf, 'Style', 'text',...
                'Position', [50 25 260 20],...
                'BackgroundColor', 'g',...
                'HorizontalAlignment','Left',...
                'String', 'Run-out frequency (Hz)');

Hc_sc = uicontrol(gcf, 'Style', 'edit',...
                'Position', [320 25 120 20],...
                'BackgroundColor', 'w',...
                'HorizontalAlignment','Center',...
                'String', num2str(s_c),...
                'Callback', 'get(Hc_sc, "String");');

Hc_proceed = uicontrol(gcf, 'Style', 'push', ...
        'Position', [480 30 60 30],...
        'String', 'Proceed',...
        'CallBack',[...
        'P = zeros(10,1); P(1,1)=eval(get(Hc_dia, "String"));...
        'P(2,1)=eval(get(Hc_feed, "String"));...
        'P(3,1)=eval(get(Hc_aspeed, "String"));...
        'P(4,1)=eval(get(Hc_dcut, "String"));...
        'P(5,1)=eval(get(Hc_trad, "String"));...
        'P(6,1)=eval(get(Hc_EMT, "String"));...
        'P(7,1)=eval(get(Hc_EMW, "String"));...
        'P(8,1)=eval(get(Hc_hn, "String"));...
        'P(9,1)=eval(get(Hc_sc, "String"));...
        'P(10,1)=eval(get(Hc_ts, "String"));...
        'save mvspara1.dat P -ascii;clf;mvibs3dm']);

Hc_close = uicontrol(gcf, 'Style', 'push', ...
        'Position', [480 70 60 30],...
        'String', 'Close',...
        'CallBack',[...
        'P = zeros(9,1); P(1,1)=eval(get(Hc_dia, "String"));...
        'P(2,1)=eval(get(Hc_feed, "String"));...
        'P(3,1)=eval(get(Hc_aspeed, "String"));...
        'P(4,1)=eval(get(Hc_dcut, "String"));...
        'P(5,1)=eval(get(Hc_trad, "String"));...
        'P(6,1)=eval(get(Hc_EMT, "String"));...
        'P(7,1)=eval(get(Hc_EMW, "String"));...
        'P(8,1)=eval(get(Hc_hn, "String"));...
```

```
'P(9,1)=eval(get(Hc_sc, "String"));,'...
'P(10,1)=eval(get(Hc_tu, "String"));,'...
'save mvspara1.dat P -ascii;clf;mvsinpm1']);
```

MVI8S3DM.M

```
%Prediction of surface roughness

%Define machining parameters.

load mvspara.dat;

SP = mvspara;

dia = SP(1,1);                          %part diameter (mm)
f = SP(2,1);                            %feed rate (mm/min)
v = SP(3,1);                            %spindle speed (rpm)
d = SP(4,1);                            %depth of cut (micrometre)
trad = SP(5,1);             %tool radius (mm)
STT = SP(6,1);                          %Stiffness of the tool system (MN/m)
STW = SP(7,1);                          %Stiffness of the work system (MN/m)
ampz = SP(8,1);                         %runout amplitude (micrometer)
frz = SP(9,1);                          %runout frequency (Hz)
ampz = 0.001*ampz;                      %unit conversion for amplitude of Z-axis vibration (mm)

ela = 80;                               %define view angle
ava = -80;


[fname, pname]=uigetfile('*.dat', 'Select force file to be processed');

fid = fopen(fname);
D = fscanf(fid, '%g', [1,inf]);
fclose(fid);

F = D';                                 %shear angle data

[mf,n] = size(F);

s = f/v                                 %feed rate (mm/rev)
r = dia/2;                              %Part radius (mm)
d = 0.001*d;                            %unit conversion for depth of cut (mm)

N = fix(r/s)                            %no. of revolutions

a_res = mf-1                            %angle resolution

a_step = (2*pi)/a_res;                  %step size of angular rotation

r_step = (s*a_step)/(2*pi);     %step size of radial movement

t_rot = 2*N*pi;                         %total angular rotation

c_mark = (60*frz)/v                     %number of cut marks per revolution of the work

%phase shift angle for z-axis vibration

pcon = (c_mark-fix(c_mark))

if pcon>0.5
  psz = 2*pi*(1-pcon)
else
        psz=2*pi*pcon
end

m = fix(t_rot/a_step)                   %number of steps

t_tot = (60*N)/v                        %total machine time (second)

t_step = (60/(v*a_res))                 %time step (second)

t_res = s/20;                           %tool resolution

s_rate= 1/t_res;                        %sample frequency for the roughness data (Hz)
%s_rate = m;

nt = round(sqrt(2*trad*d)/(t_res));     %number of tool points
ts = nt*(t_res);                        %tool span

%initiation
v_a = zeros(m,1);                       %angle vector
v_r = zeros(m,1);                       %radial vector
t_vector = zeros(m,1);
XS = zeros(m,1);
ZS = zeros(m,1);
YS = zeros(m,1);
XP = zeros(m,1);
ZP = zeros(m,1);
YP = zeros(m,1);
YEP = zeros(m,1);
```

```
TX = zeros(2*nt,1);
TY = zeros(2*nt,1);
RX = zeros(N*2*nt,1);
RY = zeros(N*2*nt,1);
RX = zeros(2*nt,1);
RY = zeros(2*nt,1);
PV = zeros(N,1);
RIX = zeros(N,1);
RIY = zeros(N,1);
RRX = zeros(N*2*nt,1);
RRY = zeros(N*2*nt,1);
fj = 0;
k = 0;
s_i = 0;

%Determine the vibration system parameters
load optvmpt.dat;
load optvmpw.dat;

SPT=optvmpt;
SPW=optvmpw;

%loading the tool vibration system parameters
a0t = SPT(1,1);
a1t = SPT(1,2);
f1t = SPT(1,3);
f2t = SPT(1,4);
apt = SPT(1,5);
nft = SPT(1,6);
drt = SPT(1,7);
sq_errt = SPT(1,8);

%loading the workpiece vibration system parameters
a0w = SPW(1,1);
a1w = SPW(1,2);
f1w = SPW(1,3);
f2w = SPW(1,4);
apw = SPW(1,5);
nfw = SPW(1,6);
drw = SPW(1,7);
sq_errw = SPW(1,8);

%Determine relative displacement between the tool the workpiece

hforce = zeros(m,1);
PSH_AR = zeros(m,1);
vforce = zeros(m,1);
TM = zeros(m,1);

SHA = F;

w_cut = 0.001*s;                                    %width of cut in m
TS = 45e6;                                          %shear stress in N/sq. m

for i=1:N
        for j=1:(mf)
                PSH_AR((i-1)*(mf)+j,1)=(SHA(j, 1)*pi)/180;
        end
end

for j=1:m
        %Merchant shear angle equation
        d_cut = 0.001*(d+ampz*sin(2*pi*frz*(j*t_step-psz)));      %depth of cut in m
        %hforce(j,1) = TS*d_cut*w_cut*2*cot(PSH_AR(j,1));
        %vforce(j,1) = TS*d_cut*w_cut*((1/(sin(PSH_AR(j,1))*sin(PSH_AR(j,1))))-2);

        %Lee and Shaffer equation
        hforce(j,1) = TS*d_cut*w_cut*(cot(PSH_AR(j,1))+1);
        vforce(j,1) = TS*d_cut*w_cut*(cot(PSH_AR(j,1))-1);
end

for i=1:m
        TM(i,1) = i*t_step;
end

plot(TM, hforce);
xlabel('Time (second)');
ylabel('Main Cutting Force (N)');
grid;
pause;

plot(TM, vforce);
xlabel('Time (second)');
ylabel('Thust Cutting Force (N)');
grid;
pause;

vcforce=[TM, 1000*vforce];
hcforce=[TM, 1000*hforce];

save vpforce.dat vcforce -ascii;                    %vertical force (mN)
save hpforce.dat hcforce -ascii;                    %horizontal force (mN)
```

```
u1t=nft*(-drt+sqrt(drt*drt-1))                    %characteristic roots of the tool system
u2t=nft*(-drt-sqrt(drt*drt-1))

u1w=nfw*(-drw+sqrt(drw*drw-1))                    %characteristic roots of the workpiece system
u2w=nfw*(-drw-sqrt(drw*drw-1))
pause;

GT = zeros(m,1);                                  %initial Green's function for tool system
GW = zeros(m,1);                                  %initial Green's function for work system

%GTU = zeros(m,1);
%GTL = zeros(m,1);
%GWU = zeros(m,1);
%GWL = zeros(m,1);

%Green's Function

for i = 1:m
        GT(i,1) = (exp(u1t*TM(i,1))-exp(u2t*TM(i,1)))/(u1t-u2t);
  GW(i,1) = (exp(u1w*TM(i,1))-exp(u2w*TM(i,1)))/(u1w-u2w);

  %GTU(i,1)=exp(u1t*TM(i,1))-exp(u2t*TM(i,1));
  %GWU(i,1)=exp(u1w*TM(i,1))-exp(u2w*TM(i,1));

end
pause;

subplot(2,1,1);
plot(TM,GT);
xlabel('Time (second)');
ylabel('Green function (tool system)');
grid;
pause;

MGT = [TM, GT];
save greent.dat MGT -ascii;   %save the Green's function value for tool system

subplot(2,1,2);
plot(TM, GW);
xlabel('Time (second)');
ylabel('Green function (work system)');
grid;
pause;

MGW = [TM, GW];
save greenw.dat MGW -ascii;               %save the Green's function value for work system

EMT = STT/(nft*nft)                       %equivalent mass of tool system (Nas/um)
EMW = STW/(nfw*nfw)                       %equivalent mass of work system (Nas/um)
pause;

%ZVT = vforce/EMT;
%ZVW = vforce/EMW;

%XVT = conv(GT, ZVT);                     %convolution for tool system
%XVW = conv(GW, ZVW);                     %convolution for work system

XVT=zeros(m,1);
XVW=zeros(m,1);

%Tool displacement determined by convolution of green function of tool system

for i=1:m
        sumXT=0;

        for k=1:m
                if i>=k
                        sumXT=sumXT+(vforce(k,1)/EMT)*((exp(u1t*((i-k)*t_step))-exp(u2t*((i-k)*t_step)))/(u1t-u2t));
                end
        end

        XVT(i,1)=sumXT;
        t_index = i
end

%Work displacement determined by convolution of green function of work system

for i=1:m
        sumXW=0;

        for k=1:m
                if i>=k
                        sumXW=sumXW+(vforce(k,1)/EMW)*((exp(u1w*((i-k)*t_step))-exp(u2w*((i-k)*t_step)))/(u1w-u2w));
                end
        end

        XVW(i,1)=sumXW;
        w_index = i
end

subplot(2,1,1);
```

```
plot(TM, XVT(1:m));
xlabel('Time (second)');
ylabel('Tool displacement(um)');
grid;

SVT = [TM, XVT(1:m)];

subplot(2,1,2);
plot(TM, XVW(1:m));
xlabel('Time (second)');
ylabel('Work displacement(um)');
grid;
pause;

SVW = [TM, XVW(1:m)];

XV = XVT(1:m)+XVW(1:m);                                    %relative displacement between the tool (m)

subplot(2,1,1);
plot(TM, XV(1:m));
xlabel('Time (second)');
ylabel('Tool-work displacement(um)');
grid;

SVTW = [TM, XV];

MXV = zeros(2*m,1);
for i = 1:m
        MXV(i,1) = TM(i,1);
end

for j = 1:m
        MXV(m+j,1) = XV(j,1);
end

%Spectrum analysis
time_res = 1/t_step
[Pxxv, faxv]=psd('XV', m, time_res);

subplot(2,1,2);
plot(faxv, Pxxv);
xlabel('Frequency of Z-axis vibration (Hz)');
ylabel('Power spectral density');
grid;
pause;

SVSP = [faxv, Pxxv];

%Tool path under vibration

%Tool geometry plot
for q=1:nt
  TX(q,1) = q*t_res-ts;
  TY(q,1) = (TX(q,1)*TX(q,1))/(2*trad);
  TX(nt+q,1) = q*t_res;
  TY(nt+q,1) = (TX(nt+q,1)*TX(nt+q,1))/(2*trad);
end

subplot(1,1,1);
plot(TX, TY);
title('Tool geometry');
xlabel('Tool span (mm)');
ylabel('Tool height (mm)');
grid;
pause;

ampx=0;
frx =0;

%Tool positions under vibration
r_angle =-a_step;

for i=1:m
        %vibration data
        v_a(i,1) = (i-1)*a_step;
        v_r(i,1) = i-r_step*(i-1);
        v_angle=(ampx/r)*sin(2*pi*frx*i*t_step);
        r_angle=r_angle+a_step+v_angle;
        v_r_diff = ((abs(r_angle-v_a(i,1))*s)/(2*pi));
        t_diff = (60*v_r_diff)/f;

        %vibration conditions
        if r_angle>v_a(i,1)
                s_i=s_i+1;
                XS(s_i,1)=v_r(i,1)*sin(v_a(i,1));
                YS(s_i,1)=v_r(i,1)*cos(v_a(i,1));
                YEP(s_i,1)=v_r(i,1);
                ZS(s_i,1)=ampz*sin(2*pi*frz*(i*t_step-psz))+0.001*XV(i,1);
                t_vector(s_i,1)=TM(i,1);
        end

        if r_angle<v_a(i,1)
```

```
                s_i=s_i+1;
                XS(s_i,1)=v_r(i,1)*sin(v_a(i,1));
                YS(s_i,1)=v_r(i,1)*cos(v_a(i,1));
                YEP(s_i,1)=v_r(i,1);
                ZS(s_i,1)=ampz*sin(2*pi*frz*(i*t_step-psz))+0.001*XV(i,1);          %unit in mm
                t_vector(s_i,1)=TM(i,1);
        end

        if r_angle==v_a(i,1)
                s_i=s_i+1;
                XS(s_i,1)=v_r(i,1)*sin(v_a(i,1));
                YS(s_i,1)=v_r(i,1)*cos(v_a(i,1));
                YEP(s_i,1)=v_r(i,1);
                ZS(s_i,1)=ampz*sin(2*pi*frz*(i*t_step-psz))+0.001*XV(i,1);          %unit in mm
                t_vector(s_i,1)=TM(i,1);
        end

        if rem(i-1,s_res)==0
          fj=fj+1
          YP(fj,1)=YS(i,1);
          ZP(fj,1)=ZS(i,1);
        end
end


ZPP = zeros(fj,1);
YPP = zeros(fj,1);

for i=1:fj
  YPP(i,1)=r-YP(i,1)
  ZPP(i,1)=ZP(i,1)
end

vtime = zeros(s_i/N,1);
ZSP = zeros(s_i/N,1);
for i=1:s_i/N
  vtime(i,1)=t_vector(i,1);
  ZSP(i,1)=ZS(i,1);
end

%plot(vtime,ZSP);
%grid;
%title('Motion of the tool');
%xlabel('Time (second)');
%ylabel('Tool position (mm)');
%pause;

plot(YPP,ZPP);
grid;
title('Effect of vibration on the tool position');
xlabel('Distance of travel (mm)');
ylabel('Tool position (mm)');
pause;

MTP=[YPP, ZPP];

i_i=1;                                                  %initiate the roughness vector
l=0;
i_r=0;
%determine the initial intercept point
RIX(i_i,1)=-s/2;
RIY(i_i,1)=(s*s)/(8*trad)-d;

for i=1:(N*2*nt)

  if rem(i-1,2*nt)==0
        i_i=i_i+1;
        l=l+1

        if l==1
                Top = (2*(ZPP(l,1))*trad)+(s*s)*(2*l-1);    %determine the intercept points
        else
                Top = (2*(ZPP(l,1)-ZPP(l-1,1))*trad)+(s*s)*(2*l-1);
        end

        RIX(i_i,1)=Top/(2*s);
        %RIY(i_i,1)=(Top*Top)/(8*s*s*trad)-d;
        RIY(i_i,1)=ZPP(l,1)+(((RIX(i_i,1)-(l)*s)*(RIX(i_i,1)-(l)*s))/(2*trad))-d;
  end

  RX(i,1)=TX((i-((l-1)*2*nt)),1)+(l-1)*s;
  RY(i,1)=TY((i-((l-1)*2*nt)),1)+ZPP(l,1)-d;

  if (RX(i,1)>=RIX(i_i-1,1))&(RX(i,1)<=RIX(i_i,1))
    i_r=i_r+1;
    RRX(i_r,1)=RX(i,1);
    RRY(i_r,1)=RY(i,1);
  end
end

plot(RX, RY);
grid;
```

```
title('Tool Interference plot for each feed position');
xlabel('Distance of travel (mm)');
ylabel('Tool position (mm)');
pause;

MTI=[RX, RY];

RXP = zeros(i_r,1);
RYP = zeros(i_r,1);

for i=1:i_r
   RXP(i,1)=RRX(i,1);
   RYP(i,1)=1000*RRY(i,1); %unit conversion mm to micrometre
end

comet(RXP, RYP);

[orx, ory]=size(RYP);
B=zeros(orx,2);
sumR=0;
sumP=0;

for i=1:orx
   B(i,1)=RXP(i,1);
   B(i,2)=RYP(i,1);
   sumR =sumR+RYP(i,1);
end

%Surface roughness determination - Ra
RAV=sumR/orx;

for j=1:orx
    sumP=sumP+abs(RYP(j,1)-RAV);
end

Ra=1000*(sumP/orx);                    %Ra in nanometre

%Geometrical Surface Roughness Determination - Rt

Rmax=-1000*d;
Rmin=-1000*d;

for i=1:orx
   if RYP(i,1)>Rmax
     Rmax=RYP(i,1);
   end

   if RYP(i,1)<Rmin
     Rmin=RYP(i,1);
   end
end

Rt=Rmax-Rmin;                          %geometrical roughness (P-V value)

Rth = 1000*Rt;                         %unit conversion for Rth (micrometre to nanometre)

MRTA = [Rth, Ra];

save roughval.dat MRTA -ascii;         %save the roughness values

Rt_hd = uicontrol(gcf,'Style', 'text', ...
                  'Position', [5 4 25 20],...
                  'BackgroundColor', 'g',...
                  'String', 'Rt :');

Rt_cur = uicontrol(gcf,'Style', 'text', ...
                  'Position', [30 4 50 20],...
                  'BackgroundColor', 'g',...
                  'String', num2str(Rth));

Rt_unit = uicontrol(gcf,'Style', 'text', ...
                  'Position', [80 4 17 20],...
                  'BackgroundColor', 'g',...
                  'String', 'nm');

Ra_hd = uicontrol(gcf,'Style', 'text', ...
                  'Position', [105 4 25 20],...
                  'BackgroundColor', 'c',...
                  'String', 'Ra :');

Ra_cur = uicontrol(gcf,'Style', 'text', ...
                  'Position', [130 4 50 20],...
                  'BackgroundColor', 'c',...
                  'String', num2str(Ra));

Ra_unit = uicontrol(gcf,'Style', 'text', ...
                  'Position', [180 4 17 20],...
                  'BackgroundColor', 'c',...
                  'String', 'nm');

plot(RXP,RYP);
grid;
```

```
title('Roughness profile');
xlabel('Distance travel (mm)');
ylabel('Surface height (micrometre)');
pause;
clf;

Hm_ex=uimenu(gcf, 'Label','Option');

Hm_exview = uimenu(Hm_ex, 'Label', 'View');

Hm_zoom = uimenu(Hm_ex, 'Label', 'Zoom', 'CallBack', 'zoom');

Hm_zoomon = uimenu(Hm_zoom, 'Label', 'On', 'CallBack', 'zoom on');

Hm_zoomoff = uimenu(Hm_zoom, 'Label', 'Off', 'CallBack', 'zoom off');

set(Hm_exview, 'Separator', 'on');

Hm_exv2d = uimenu(Hm_exview, 'Label', '2-D', 'CallBack', 'view(2)');

Hm_exv3d = uimenu(Hm_exview, 'Label', '3-D', 'CallBack', 'view(3)');

Hm_close = uimenu(gcf, 'Label', 'Close');

Hm_clfig = uimenu(Hm_close, 'Label', 'Close Figure', 'CallBack', 'clf; fffsgs1;');

Hm_clmenu = uimenu(Hm_close, 'Label', 'Remove Menu', ...
        'CallBack', 'delete(Hm_ex); delete(Hm_close); drawnow');

vw=get(gca, 'View');

SD=[XS, YS, ZS];

ZSM = 1e6*ZS;                          %unit conversion from mm to nm

subplot(1,1,1);
vw=get(gca, 'View');
plot3(XS,YS,ZSM);
EL1 = ela;
AZ1 = ava;
XC1 = 0.5+sqrt(3)/2*[cos(EL1)*sin(AZ1),-cos(EL1)*cos(AZ1), sin(EL1)];
T1=viewmtx(AZ1, EL1, 0, XC1);view(T1);
title('Tool Locus formed by vibration between tool and workpiece');
xlabel('X (mm)');
ylabel('Y (mm)');
zlabel('Z (nm)');
pause;

axis([-dia/4, dia/4, -dia/4, dia/4]);
axis(axis);

gs=s/5;
for g_is=1:1
                g_i=-(dia/(4*g_is)):gs:(dia/(4*g_is));
                [XGI, YGI]=meshgrid(g_i, g_i);
                ZGI=griddata(XS, YS, ZSM, XGI, YGI);
                mesh(XGI, YGI, ZGI);
                %surfl(XGI,YGI,ZGI);
                EL1 = ela;
                AZ1 = ava;
                XC1 = 0.5+sqrt(3)/2*[cos(EL1)*sin(AZ1),-cos(EL1)*cos(AZ1), sin(EL1)];
                T1=viewmtx(AZ1, EL1, 0, XC1);view(T1);
                caxis auto;
                colorbar('vert');
                title('Mesh Surface Wave induced by vibration between tool and workpiece');
                xlabel('X (mm)');
                ylabel('Y (mm)');
                zlabel('Z (nm)');
                shading interp;
                pause;
end

%plot3(XS, YS, ZS, 'o')
%hold off
pause;
surfl(XGI,YGI,ZGI)
shading interp;
colormap(gray);
shading interp;
EL1 = ela;
AZ1 = ava;
XC1 = 0.5+sqrt(3)/2*[cos(EL1)*sin(AZ1),-cos(EL1)*cos(AZ1), sin(EL1)];
T1=viewmtx(AZ1, EL1, 0, XC1);view(T1);
colormap(gray);
shading interp;
title('Surface Wave by vibration between tool and wprkpiece');
xlabel('X (mm)');
ylabel('Y (mm)');
zlabel('Z (nm)');
pause;
clf;
```

```
colormap('default');
contour(XGI,YGI,ZGI);
title('Contour Map for the Surface Wave');
xlabel('X (mm)');
ylabel('Y (mm)');
colorbar('vert');
pause;

caxis auto;
pcolor(XGI,YGI,ZGI);
title('Color Map for the Surface Wave by vibration between tool and workpiece');
xlabel('X (mm)');
ylabel('Y (mm)');
zlabel('Z (nm)');
colorbar('vert');
shading interp;
pause;
clf;


%Real surface generation

SYTP = zeros(N,a_res);
SZTP = zeros(N,a_res);
SYTPM = zeros(N,a_res);
SZTPM = zeros(N,a_res);
SXSP = zeros(3*m, 1);
SYSP = zeros(3*m, 1);
SZSP = zeros(3*m, 1);
SYIP = zeros(N, 1);
SZIP = zeros(N, 1);

%plot(YP, ZP);
%pause;

i_p=0;

%determine the initial intercept point

for j=1:a_res

        if j==1
                i_i=1;
                SYIP(i_i,1)=-s/2;
                SZIP(i_i,1)=((s*s)/(8*trad));
        end

        for i=1:N

                SYTP(i,j)=YEP((i-1)*a_res+j,1);
                SZTP(i,j)=ZS((i-1)*a_res+j,1);                                  %unit in mm
                i_p=i_p+1;
                SXSP(i_p,1)=(SYTP(i,j))*sin((j-1)*a_step);
                SYSP(i_p,1)=(SYTP(i,j))*cos((j-1)*a_step);
                SZSP(i_p,1)=SZTP(i,j);

                i_i=i_i+1;
                if i==1
                        Top = (2*SZTP(i,j)*trad)+(s*s)*(2*i-1);     %determine the intercept points
                else
                        Top = (2*(SZTP(i,j)-SZTP(i-1,j))*trad)+(s*s)*(2*i-1);       %determine the intercept points
                end

                SYIP(i_i,1)=Top/(2*s);
                SZIP(i_i,1)=SZTP(i,j)+(((SYIP(i_i,1)-i*s)*(SYIP(i_i,1)-i*s))/(2*trad));

                i_p=i_p+1;
                SXSP(i_p,1)=(r-SYIP(i_i,1)-(j-1)*r_step)*sin((j-1)*a_step);
                SYSP(i_p,1)=(r-SYIP(i_i,1)-(j-1)*r_step)*cos((j-1)*a_step);
                SZSP(i_p,1)=SZIP(i_i,1);

                if (i==N)
                        SYIP(1,1)=-s/2;
                        SZIP(1,1)=((s*s)/(8*trad));
                        i_i=1;

                        %i_p=i_p+1;
                        %SXSP(i_p,1)=(r-SYIP(1,1)-j*r_step)*sin(j*a_step);
                        %SYSP(i_p,1)=(r-SYIP(1,1)-j*r_step)*cos(j*a_step);
                        %SZSP(i_p,1)=SZIP(1,1);
                end

        end

        %plot(SYIP, SZIP);
        %pause;
end

SZPP = zeros(i_p,1);
SYPP = zeros(i_p,1);
SXPP = zeros(i_p,1);
```

```
for i=1:i_p;
        SXPP(i,1)=SXSP(i,1);
        SYPP(i,1)=SYSP(i,1);
        SZPP(i,1)=1e6*SZSP(i,1);    %unit convert from mm to nm
end

plot3(SXPP,SYPP,SZPP,'y.');
pause;

sgs=s/5;
for sg_is=1:1
        sg_i=-(dia/(4*sg_is)):sgs:(dia/(4*sg_is));
        [SXGI, SYGI]=meshgrid(sg_i, sg_i);
        SZGI=griddata(SXPP, SYPP, SZPP, SXGI, SYGI);
        mesh(SXGI, SYGI, SZGI);
        caxis auto;
        colorbar('vert');
        %surfl(SXGI,SYGI,SZGI);
        EL1 = ela;
        AZ1 = ava;
        XC1 = 0.5+sqrt(3)/2*[cos(EL1)*sin(AZ1),-cos(EL1)*cos(AZ1), sin(EL1)];
        T1=viewmtx(AZ1, EL1, 0, XC1);view(T1);
        title('Simulated Mesh Surface for the Workpiece');
        xlabel('X (mm)');
        ylabel('Y (mm)');
        zlabel('Z (nm)');
        shading interp;
        pause(1);
end

%plot3(XS, YS, ZS, 'o')
%hold off
pause;

surf(SXGI,SYGI,SZGI)
caxis auto;
colorbar('vert');
EL1 = ela;
AZ1 = ava;
XC1 = 0.5+sqrt(3)/2*[cos(EL1)*sin(AZ1),-cos(EL1)*cos(AZ1), sin(EL1)];
T1=viewmtx(AZ1, EL1, 0, XC1);view(T1);
title('Simulated Surface Texture for Workpiece');
xlabel('X (mm)');
ylabel('Y (mm)');
zlabel('Z (nm)');
pause;
clf;

surfl(SXGI,SYGI,SZGI)
shading interp;
colormap(gray);
shading interp;
EL1 = ela;
AZ1 = ava;
XC1 = 0.5+sqrt(3)/2*[cos(EL1)*sin(AZ1),-cos(EL1)*cos(AZ1), sin(EL1)];
T1=viewmtx(AZ1, EL1, 0, XC1);view(T1);
title('Simulated Surface Texture for Workpiece');
xlabel('X (mm)');
ylabel('Y (mm)');
zlabel('Z (nm)');
pause;
clf;

colormap('default');
contour(SXGI,SYGI,SZGI);
title('Contour Map for the Surface Texture of the Workpiece');
xlabel('X (mm)');
ylabel('Y (mm)');
caxis auto;
colorbar('vert');
pause;

caxis auto;
colormap('default');
pcolor(SXGI,SYGI,SZGI);
title('Color Map for the Surface Texture of the Workpiece');
xlabel('X (mm)');
ylabel('Y (mm)');
colorbar('vert');
shading interp;
pause;
clf;

pcolor(SXGI,SYGI,SZGI);
colormap(gray);
title('Gray Color Map for the Surface Texture of the Workpiece');
xlabel('X (mm)');
ylabel('Y (mm)');
colorbar('vert');
shading interp;
pause;
clf;
```

```
%Spectrum analysis
[Pxx, fss]=psd(RYP,orx,s_rate);
[fssm, fsan]=size(fss);
fsw=zeros(fssm-1,1);
Pxw=zeros(fssm-1,1);

for i=1:fssm-1
        fsw(i,1)=(1000/fss(i+1,1));
        Pxw(i,1)=Pxx(i+1,1);
end;

subplot(2,1,1);
plot(fss, Pxx);
xlabel('Freq. of roughness wave (no. of waves per unit length)');
ylabel('Power spectral density');
grid;
M=[fss, Pxx];

subplot(2,1,2);
semilogx(fsw, Pxw)
xlabel('Wave length (micrometre)');
ylabel('Power spectral density');
grid;
MS=[fsw, Pxw];
pause;

Hc_zoom = uicontrol(gcf, 'Style', 'push', ...
        'Position', [400 3 70 20],...
        'String', 'Zoom','CallBack', 'zoom on');


Hc_quit = uicontrol(gcf, 'Style', 'push', ...
        'Position', [5 3 70 20],...
        'String', 'Quit',...
        'CallBack','clf; fftsgs1;');

Hc_exit = uicontrol(gcf, 'Style', 'push', ...
        'Position', [80 3 70 20],...
        'String', 'Exit',...
        'CallBack','fftsave3; clf; fftsgs1;');
```